Transactions of the ASME®

Journal of Engineering for Gas Turbines and Power

Published Quarterly by The American Society of Mechanical Engineers

VOLUME 113 • NUMBER 3 • JULY 1991

Transactions of the ASME, Journal of Engineering for Gas Turbines and Power (ISSN 0022-0825) is published quarterly (Jan., Apr., July, Oct.,) for $125.00 per year by The American Society of Mechanical Engineers, 345 East 47th Street, New York, NY 10017. Second class postage paid at New York, NY and additional mailing offices. POSTMASTER: Send address changes to Transactions of the ASME, Journal of Engineering for Gas Turbines and Power, c/o THE AMERICAN SOCIETY OF MECHANICAL ENGINEERS, 22 Law Drive, Box 2300, Fairfield, NJ 07007-2300.
CHANGES OF ADDRESS must be received at Society headquarters seven weeks before they are to be effective. Please send old label and new address.
PRICES: To members, $36.00, annually; to nonmembers, $125.00.
Add $15.00 for postage to countries outside the United States and Canada.

INDEXED by Applied Mechanics Reviews and Engineering Information, Inc.
Canadian Goods & Services Tax Registration #126148048

TECHNICAL PAPERS

(Contents continued on page 364)

ANNOUNCEMENTS

Future Engine Technology: Lessons From the 1980s for the 1990s

J. B. Heywood
Massachusetts Institute of Technology,
Cambridge, MA 02134

The past twenty years has seen an explosion in our knowledge of engine processes, steadily improving engine power density and efficiency, major reductions in exhaust emissions, and a substantial increase in engine sophistication and complexity. This paper explains how engineering analysis has played a major enabling role in realizing these improvements in spark-ignition engine performance. Examples are given of the many different types of analysis tool in areas such as combustion, emissions, stress analysis, system dynamics, and fluid flow that have been found useful in resolving different engine development and design problems and opportunities. The significant improvements achieved in engine fuel consumption, power density, and emissions control are then reviewed. It is argued, however, that the improvements in urban air quality do not correspond to the reductions achieved in vehicle exhaust emissions. Our current understanding of the link between vehicle emissions and air quality does not explain this discrepancy. What matters is low enough in-use emissions, and future regulations do not adequately focus on this essential requirement. An available energy analysis of the four-stroke spark-ignition engine operating cycle is used to identify where opportunities for further increases in efficiency and power are to be found. Approaches that would improve combustion efficiency, reduce heat losses, increase expansion stroke work, reduce pumping work, and decrease friction are discussed. It is concluded that many analysis tools are now available to identify more precisely how large these opportunities are, and how best they might be realized. The potential of various modifications to the four-stroke cycle SI engine cycle, and alternative spark-ignition and diesel cycles, are reviewed. Finally, it is argued that relative to Europe and Japan, the United States lacks a sufficiently broad and organized research effort designed to support the exploration and development of these opportunities.

Rationale and Scope

The past two decades have seen major changes in engine technology. These have come about due to the need to reduce vehicle emissions very substantially, improve fuel consumption due to market pressures and regulation, increase engine specific power to improve vehicle performance and reduce engine size and weight, and improve vehicle drivability, which had deteriorated significantly in the early years of emission control. For the spark-ignition engine, these improvements have come from many different areas; most important, however, has been the development of much more sophisticated engine designs with electronic engine control, and the introduction and continued development of the catalytic converter.

You have generously honored me with the Honda Lectureship because of my research and writing on internal combustion engine technology over the past twenty or so years. So I thought it would be appropriate to use the opportunity this occasion provides to write a broader review of three topics in which I am much involved: (*a*) how engineering analysis has contributed to the engine improvements listed above; (*b*) how far we have progressed in our efforts to control air pollution; and (*c*) what potential exists for further improving current engine technology and for new engine options.

I will first discuss several areas of engine operation where the combination of analysis and extensive empirical data has led to significant gains. I will show that one essential feature of all these successful combinations of empirical and analytical (or computational) engineering is matching the type of analysis used to the specific problem. There are no universal analysis tools, though some are obviously more general than others. The major focus will be a spark-ignition engine performance, efficiency and emissions, since this has received the greatest emphasis during the 1970s and 1980s, will continue to be very important in the 1990s, and is my primary area of expertise. Diesel efforts are following this pattern too, but more slowly, because the problems of emission control and improved efficiency are more complex than in the SI engine, and the amount of resources available for diesel engine R&D is smaller.

Contributed by the Internal Combustion Engine Division and presented at the Twelfth Annual Fall Technical Conference, Rockford, Illinois, October 7–10, 1990. Manuscript received by the Internal Combustion Engine Division July 1990.

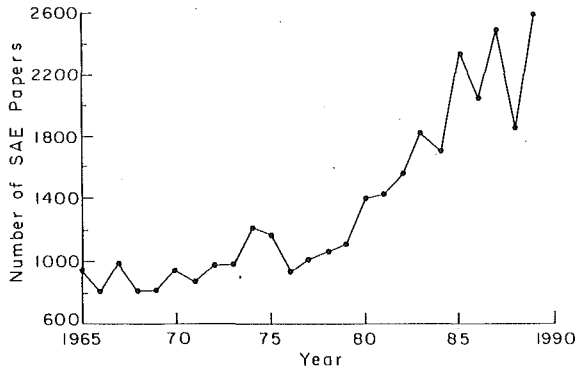

Fig. 1 Plot of number of papers presented at Society of Automotive Engineers technical meeting each year, 1965-1989

I will then focus on passenger car emissions and urban air pollution. We will see that one success story of the 1980s, the catalytic converter, has not apparently had the impact on the real problem—urban air quality—that it has had on spark-ignition engine exhaust emissions. A major reason is that the real problem—how all actual sources of emissions contribute to air pollution—has not received the same level of analysis as has the engineering "solution." Finally, I will discuss what I perceive to be the most important "engine" needs and opportunities for the 1990s.

The Role of Engineering Analysis

The Information Explosion and Escalating Complexity. Anyone who works with the technical literature on engines knows that it has been expanding at an enormous rate. As an illustration, I have plotted in Fig. 1 the number of technical papers published each year by SAE—which has become the largest source of such literature—over the past twenty-five years. Such literature records the expansion of our engine knowledge base, the analysis, computational, and diagnostic methods relevant to engine research and development, and the successful resolution of engine problems and realization of new engine opportunities.

In parallel, the complexity of automobile spark-ignition engines has escalated enormously. As illustration, one recent production engine design (Inoue et al., 1989) incorporates a four-valve cylinder head, cam switching between low and high speed, a tuned intake and exhaust system, sophisticated electronic engine control, and the sensors and actuators required to implement that control. Twenty years ago such geometric complexities would be the rare exception, and would only have been considered routine in special applications such as racing.

How Analysis Helps. Although many types of engineering activity have contributed to engine improvements over the past two decades, such developments would not have been possible without the contribution that has come from "engineering analysis." The 1970s and 1980s have demanded rapid changes in technology; the next decade and beyond will require changes of comparable magnitude, at least. As I discuss a number of engine technology improvements, and the problems they were or are intended to overcome, I will show that there is always an "appropriate" engineering analysis methodology that substantially aids the development and design process. Usually this analysis methodology comes into use because a sufficiently quantitative understanding of the phenomena or processes involved has been developed, and techniques for measuring this behavior are available. The knowledge framework that results helps the practicing engineer organize his otherwise empirical data base and extract and use the information that it contains much more effectively.

This discussion, based on many years of experience in engine research and extensive contact with engine development and design, will show that our current knowledge of engine phenomena has two distinct sources: a vast experimentally derived data base—largely empirical—which has been developed over the past several decades (and continues to be developed at a rapid rate), and an ever-broadening array of analysis tools based on our steadily increasing fundamental understanding of engine phenomena and processes. In this extremely detailed and complex engineering field, both are necessary for rapid progress, as I learned well during the ten years I worked on my recently published reference text on internal combustion engine fundamentals (Heywood, 1988), and as I will illustrate in this paper.

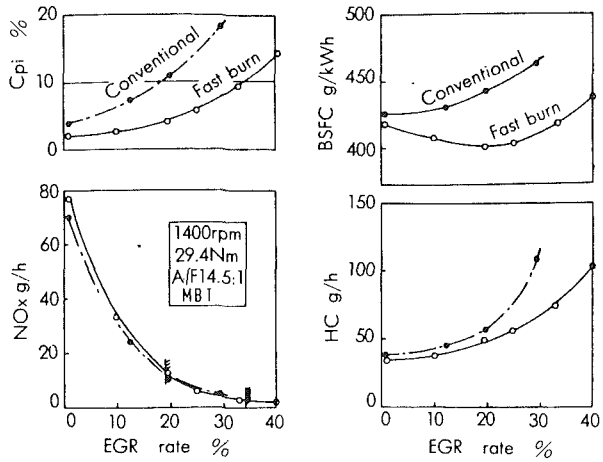

Fig. 2 Illustration of improvement in emissions and fuel consumption by fast-burn combustion system (Kuroda et al., 1980). Coefficient of variation in indicated mean effective pressure C_{pi}, NO_x and HC emissions, and brake specific fuel consumption at fixed part-load operating point are shown as a function of percent recycled exhaust (EGR).

How have engineers responded to this rapid increase in our knowledge of engine phenomena, the demands for improved performance (power, efficiency, and emissions), and the availability of new technologies (such as sensors and computer controls)? My assessment is that the increasing use of analysis tools has enabled development and design engineers to apply this expanding knowledge base and realize in large measure the opportunities that more sophisticated and better optimized engine systems offer.

One of the clearest examples of the interplay between analysis and engine design is the development of fast-burn spark-ignition combustion systems. Developed in the late 1970s and brought into production in the early 1980s, the fast-burn approach to engine combustion has provided significant improvements in engine NO and HC emission control, and fuel consumption.

Figure 2 indicates how "fast burn" provides all these benefits (Kuroda et al., 1980). It compares the operating and emissions characteristics of a fast-burn SI engine combustion system with those of the "conventional" or slower burn that it replaced. The objective is a combustion process that is sufficiently fast and robust that it will tolerate a significant amount of dilution of the fresh fuel-air mixture with burned gases—residual plus recycled exhaust—to control NO_x. The figure shows that the reduction in NO emissions depends only on the amount of added EGR, but that the amount of EGR the engine will tolerate before its performance becomes too erratic (defined by the cycle-to-cycle variability in indicated mean effective pressure C_{pi}; for example, see Fig. 2 upper left) depends on the burn rate. The fuel consumption benefit from the faster burn is in part direct (faster release of the fuel's chemical energy does improve cycle efficiency), but in larger part is due to the dilution of the fuel-air mixture with additional EGR, which

changes the thermodynamic properties of the burned gases to produce more expansion stroke work, reduces heat losses, and (at a constant part load) reduces pumping work.

One of the first companies to implement fast-burn technology was Nissan, and a series of papers published through the 1970s by their Engine Research Department describes step by step how this technology was developed. Table 1 lists these papers and the key step each paper provided.

One sees within the engine R&D department a pattern of developing a sequence of "appropriate" analysis tools, often based on research done a few years earlier elsewhere, then using these analysis tools together with carefully structured engine tests to sort out what combustion approach would both reduce engine emissions, and improve efficiency and driveability. Interestingly, these analysis tools did not push the then available state of the art. They contained just enough complexity to do their intended job—the essence of "appropriate analysis."

A major problem with engine design throughout the past two decades of emission control has been finding the calibration that gives good control of emissions during engine transients *and* good vehicle response and driveability. A very different type of model has been developed and used to assist in the solution of these complex system-dynamic problems. The many components of the engine and vehicle, and the processes that link them, are modeled in whatever way most simply describes those aspects of that component's behavior that contribute directly or through its interactions with other parts of the total vehicle system to the vehicle phenomena of concern.

An example of such a vehicle system model is shown in Fig. 3 (DeLosh et al., 1981). It is designed to explore problems like those that arise on rapid accelerations or decelerations due to mismatches between the dynamic characteristics of the processes that take place in the many subsystems that make up the total engine system. Its power is in its "number crunching"; that is, its ability to deal quantitatively with all the interactions between the many subsystems that are involved in a change in engine conditions, when the total system complexity goes well beyond what the human mind can follow. Because even the subsystems are extremely complex, many component models are based largely on experimental data. For example, regression

Table 1 Series of Nissan papers on fast-burn engine combustion phenomena

	Paper Title	*Contribution*
1	"Heat Capacity Changes Predict Nitrogen Oxides Reduction by Exhaust Gas Recirculation," S. Ohigashi, H. J. Kuroda, Y. Nakajima, Y. Hayashi, and K. Sugihara, SAE Paper No. 710010, 1971.	1 Showed that engine data on changes in NO and fuel consumption (sfc) with EGR were well correlated by changes in heat capacity.
2	"Potentiality of the Modification of Engine Combustion Rate for NO_x Formation Control in the Premixed SI Engine," H. Kuroda, Y. Nakajima, K. Sugihara, and Y. Takagi, SAE Paper No. 750353, 1975.	2 Used a computer simulation of SI engine cycle to calculate NO emissions and sfc as a function of burn profile. Showed that the tradeoff between NO and sfc depended little on burn rate.
3	"The Fast Burn with Heavy EGR, New Approach for Low NO_x and Improved Fuel Economy," H. Kuroda, Y. Nakajima, K. Sugihara, Y. Takagi, and S. Muranaka, SAE Paper No. 780006, 1978.	3 Used a detailed analysis of engine combustion patterns to show that faster burn rates allowed higher EGR rates (and therefore greater NO control and larger sfc gains) than slower burn rates.
4	"Lean Mixture or EGR—Which is Better for Fuel Economy and NO Reduction?" Y. Nakajima, K. Sugihara, and Y. Takagi, IMechE Paper No. C94/79, Proceedings of Conference on "Fuel Economy and Emissions of Lean Burn Engines," Institution of Mechanical Engineers, London, June 12–14, 1979.	4 Used engine data and burn rate analysis to show that excess air (lean operation) and EGR has comparable effects on fuel consumption, although the engine will tolerate more excess air. However, EGR has much larger impact on NO.
5	"Effects of Exhaust Gas Recirculation on Fuel Consumption," Y. Nakajima, K. Sugihara, Y. Takagi, and S. Muranaka, *Proceedings IMechE, Automobile Division*, Vol. 195, No. 30, 1981, pp. 369–376.	5 Used a thermodynamic model of the engine cycle, with engine data, to show that the fuel consumption gain with EGR and a fast burn was due to changes in heat capacity, heat losses to walls, and reduced pumping work.
6	"Nissan NAPS-Z Engine Realizes Better Fuel Economy and Low NO_x Emission," M. Harada, T. Kadota, and Y. Sugiyama, SAE Paper No. 810010, 1981.	6 Showed how fast burn and high EGR tolerance could be achieved in practice by creating a swirling flow within the cylinder during the intake process.

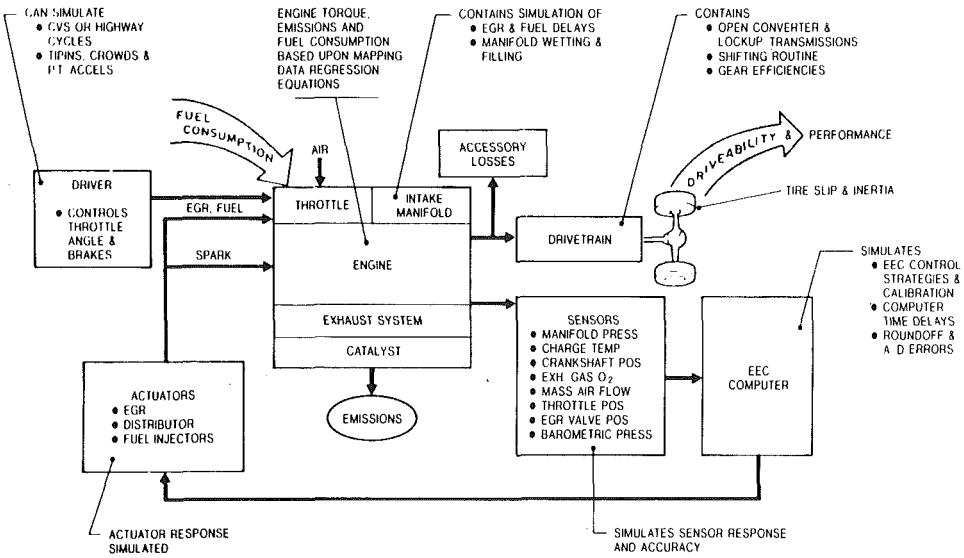

Fig. 3 Schematic diagram of vehicle system dynamic model use to examine problems like those that arise in rapid accelerations or decelerations due to mismatches in component dynamic characteristics (DeLosh et al., 1981)

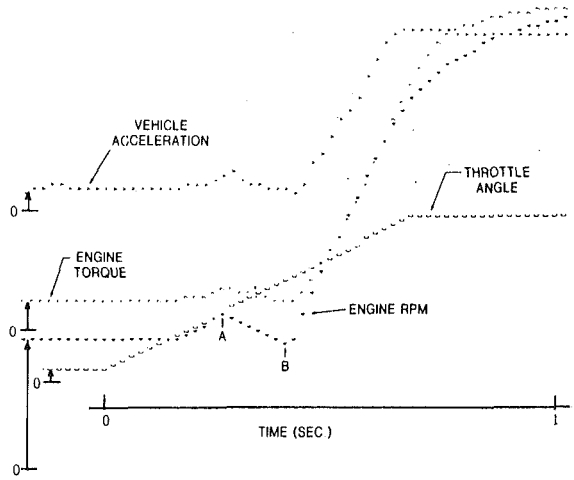

Fig. 4 Example of results from vehicle system dynamic model of Fig. 3. Shows engine speed, torque, and vehicle acceleration changes that occur during 25-deg throttle opening in 5-liter V8 engine. The increasingly lean mixture, which the throttle opening produces in the cylinder at A causes the engine to misfire, and speed and torque fall. At B the engine recovers, torque and speed increase smoothly, and the vehicle accelerates.

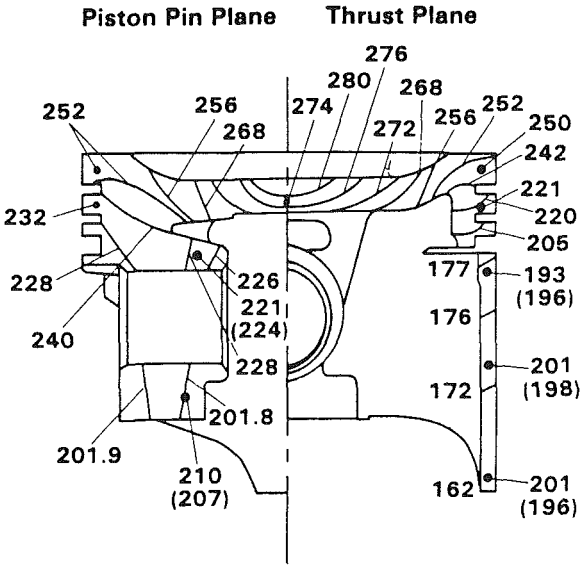

Fig. 5 Finite element analysis predictions of temperature (°C) distribution in a spark-ignition engine piston at 4600 rev/min and wide-open-throttle; dots show measured results (Li, 1982)

equations based on a measured engine performance map usually define the engine's response to changes in speed, inlet manifold pressure, air/fuel ratio, EGR, and spark timing; no analytic-based engine model can yet do that with sufficient accuracy and economy. Process models are often physically based; e.g., the flow of air and fuel into, within, and out of the inlet manifold is calculated from quasi-steady filling and emptying conservation equations.

Figure 4 shows an example of the type of results such analysis methodologies produce (DeLosh et al., 1981). Various engine and vehicle parameters are plotted versus time over a one second period during which the throttle on a 5-liter V8 throttle-body injection engine opens 25 deg. In the example shown, the fuel metering has not been adjusted to compensate for the increase in airflow (the "airflow error") due to the manifold filling that occurs during throttle opening. The increasingly lean mixture in the cylinder at point A causes poor combustion, power is lost, and the vehicle stumbles. The continued rotation of the engine continues to drive the system, and at B the major portion of the lean transient has passed and the vehicle accelerates smoothly.

This is an example of an analysis methodology that organizes large amounts of data, combines it with theory where appropriate, and thereby follows a complex set of subsystem interactions as the vehicle is "driven" through those speed-time sequences where problems have been observed, or are anticipated. The potential for examining engine-caused vehicle transient problems is obvious. Such models are *not* fundamentally based; they usually cannot be because the amount of detail that must be incorporated for them to be useful is much too large for theory to deal with. They are, however, powerful diagnostic tools.

Fundamentals have provided an extremely valuable engine component analysis tool in the area of mechanical and thermal behavior of materials: stress, thermal expansion, deformation. Finite element analysis (FEA) techniques are well developed and have proved valuable in the design of geometrically complex components such as pistons, which are heavily loaded, mechanically and thermally, where weight and geometric details are especially important. Figure 5 illustrates the level of sophistication the results of such calculations can provide (Li, 1982). It shows the predicted and measured temperature distribution within the piston at high speed and load. The agreement between analysis and data is generally good. The one region where agreement is not as good (the skirt) identifies where the major problems in FEA application remain, specifying the boundary conditions. In the calculation shown, the heat transfer coefficient between the skirt and liner has been overestimated. The complexity of and interrelations between engine phenomena are apparent: The successful resolution of one area of analysis then highlights the next related area where new knowledge needs to be developed, in this case the heat transfer processes that occur between the piston and the hot cylinder gases, the lubricant, and the liner.

Such finite-element based studies are now commonplace in the design of cylinder blocks, pistons, connecting rods, and crankshafts. However, since some of the important practical details still cannot be incorporated into the analysis methodology, due to lack of understanding or insufficient geometric detail, considerable skill is still required of the user to make simplifications in the problem and/or bridge these gaps with empirically based knowledge.

The equivalent methodology for the analysis of engine fluid flow phenomena rather than solid material phenomena—computational fluid dynamics (CFD)—though much more complex, is also proving useful in engine development. CFD codes for engine analysis have only recently reached the point where they can connect usefully with practical problems, though they have been important research tools for the past decade or so. These fluid-dynamic-based engine process analysis codes solve the partial differential equations for conservation of mass, momentum, energy, and species concentrations. The principal components of these "multidimensional" engine flow codes are the following: the models and equations used to describe the processes being analyzed (of which, for example, the turbulence model is critical); the procedures used to transform the differential equations into algebraic relations between discrete values of velocity, pressure, temperature, etc. at the grid points of the computing mesh which (ideally) matches the actual geometry; the algorithm for solving these algebraic equations; and the computer code that translates the numerical algorithm into computer language, and especially important, the interfaces for easy input and output of information (Heywood, 1988, Ch. 14).

Let me illustrate the power of these very sophisticated complex flow-analysis based codes, especially as engine development tools (they still lack the level of geometric detail required to aid engine design directly). At the current stage of devel-

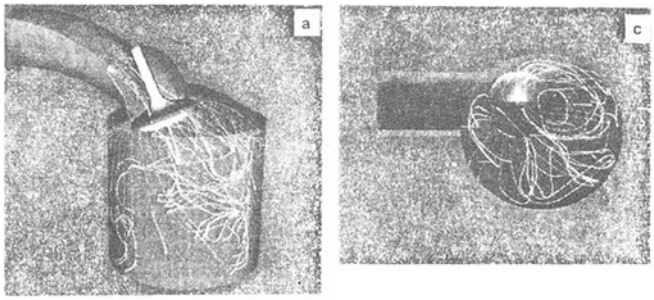

Fig. 6 Streamlines calculated with CFD engine code during the intake process, 160 deg ATC, in the inlet port and cylinder of a spark-ignition engine; the complexity of the flow field and the value of a predictive code that describes the flow field are obvious (Naitoh et al., 1990)

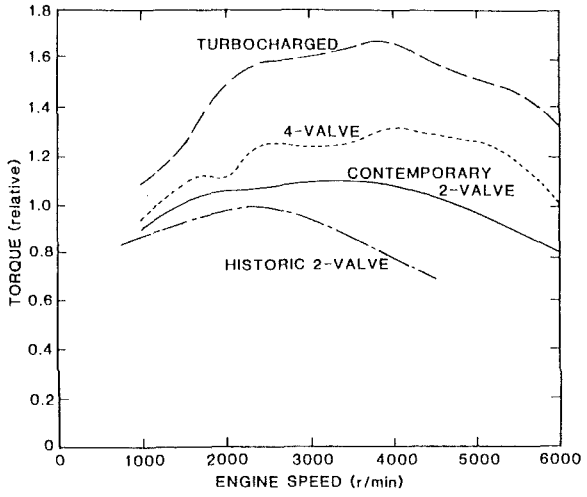

Fig. 7 Wide-open-throttle torque curves for modern two- and four-valve, and turbocharged spark-ignition engines, compared with standard design of two decades ago (Amann, 1989)

opment, their value lies in their ability to predict, with reasonable precision, the flow pattern within and around complex geometric shapes. Thus application areas include airflow under the hood around the engine and its associated components to predict underhood temperatures, flow through inlet ports, and flows within the cylinder. Figure 6 shows one recent example of predictions of the flow produced in the port and valve during the intake process (Naitoh et al., 1990; the original figures, in color, show much greater detail). Such streamline predictions help the port and cylinder head designer achieve the desired in-cylinder flow field. Especially important currently is the level of swirl (rotation about the cylinder axis), or tumble (rotation about an axis perpendicular to the cylinder axis). While it is still difficult to relate the details of these in-cylinder flows to the flame development rate and its cycle-to-cycle variability, a quantitative analysis tool that relates the flow field to the geometric details is now available.

These CFD analysis tools are being used to help develop improved port and cylinder head geometries, as well as in areas such as improvement of coolant flows through the block and cylinder heads, and under-hood packaging of the engine, its auxiliaries, and other components.

This brief review illustrates the wide variety of analysis tools that now play a major role in engine development and design. The essential feature of these tools is that they are "appropriate" to the problem they are used on. Here, appropriate means they contain enough of the physics (through equations and/or through data) to describe adequately the phenomena in the problem under investigation and provide information that can be related to the practical problem. My experience is that engine development and design practitioners are much more astute at judging whether an available analysis meets their needs than they are usually given credit for. I have seen many instances where complex computer codes are now used extensively despite the time required to learn how to use them, because it is clear that they are "useful."

Impact on Efficiency and Performance. The oil price shocks of the 1970s and the Corporate Average Fuel Economy standards established in 1975 have forced significant improvements in part-load spark-ignition engine efficiency. The average fuel economy of the new U.S. passenger-car fleet in each model year has increased from 16 miles per gallon in 1975 to about 28 miles per gallon in 1989. About one-third of this increase has come about due to engine and drivetrain improvements. In addition, the poor performance of many vehicles in the late 1970s and early 1980s led to a market demand for improved vehicle acceleration and driveability. How have engine designs responded to these challenges?

Increases in efficiency have come primarily from improvements in combustion and management of engine operation, modest increases in compression ratio, and reductions in engine friction (both in absolute magnitude and relative importance). The fast-burn combustion technology described previously in this paper raised engine efficiency at part load through more rapid completion of combustion, lower cycle-to-cycle combustion variability, and when used with increased EGR for NO_x control due to reduced heat losses, pumping work, and increased burned gas specific heat ratio. Friction has been lowered through careful attention to design details, through use of roller followers in the valve train, and because friction's relative importance decreased through use of higher output engine technology (see below).

Engine output has been increased significantly through use of highly tuned intake systems, and the introduction of multivalve technology. Figure 7 shows the torque improvements that have resulted. They are indeed large.

These efficiency and power density improvements have been achieved because the appropriate analysis tools were used to guide and support engine development and design. The role of analysis in the development of fast-burn technology has already been summarized. The development of tuned intake systems to increase the breathing capacity of engines over a surprisingly wide speed range would not have occurred without the use of unsteady gas dynamic models for flow in the intake system. Since the work of Benson in the early 1960s, one-dimensional computational fluid dynamic methods for predicting the wide-open-throttle pressure distribution and flow velocity in the intake system as a function of intake system geometry, in-cylinder engine processes, and speed, have been steadily developed and increasingly used to design intake systems (see for example Benson et al., 1964; Chapman et al., 1982; Morel et al., 1990).

Figure 8 shows a recent comparison of the predicted and measured intake manifold pressures in the inlet port of one cylinder of a 4-cylinder SI engine (Morel et al., 1990). The model predicts the airflow behavior in the manifold over the full speed range of the engine. Note that the tuned intake system provides a positive pressure pulse in the inlet port between bottom center at the end of the intake stroke and inlet valve closing. This is what increases the mass of air that enters the cylinder each cycle. As shown in Fig. 7, with well-designed tuned intake systems, substantial increases in torque in the engine's mid- and high-speed ranges can be and are achieved.

Summary. Will this trend of increasing use of analysis in engine engineering continue? Of course it will, because it is the best way to identify the opportunities for improving engine performance and target the necessarily empirical development required to realize these opportunities. However, support by

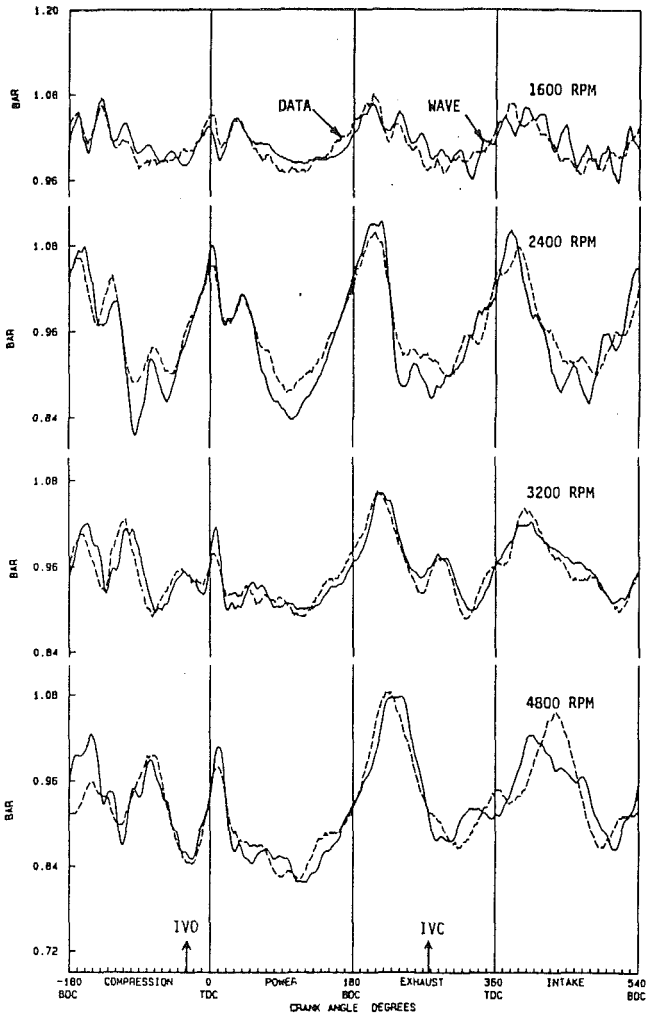

Fig. 8 Gas pressures in the intake manifold of 2.2-liter four-cylinder spark-ignition engine predicted by one-dimensional unsteady CFD analysis, compared with measured pressure variation (Morel et al., 1990)

industry and government in the United States, may not be sufficient to ensure the steady expansion of new engine knowledge, and its encoding in appropriate analysis tools that the future will require. Relative to Europe and Japan, the United States lacks a sufficiently broad and organized research effort designed to support the exploration and development of these opportunities.

The Automobile and Urban Air Pollution

Passenger Car Emissions. Exhaust emissions standards for unburned hydrocarbons, carbon monoxide, and oxides of nitrogen are now a small fraction (about one-twentieth for HC and CO; one-fourth for NO_x) of the exhaust emissions levels of cars produced in the late 1960s; see Table 2. The current exhaust emission standards of 0.41 g/mile HC, 3.4 g/mile CO, and 1.0 g/mile NO_x, were implemented in 1981 and have therefore been in place for almost a decade. Over this period, spark-ignition engine exhaust emissions have been controlled with the three-way catalyst technology where the engine operates with a close-to-stoichiometric air/fuel ratio to provide both oxidizing species for HC and CO removal in the catalyst and reducing species for NO removal. An exhaust oxygen sensor and control system modulates the engine's air/fuel ratio about the stoichiometric point to take advantage of species storage on the catalyst surface. The difficult remaining engine problem is adequate control of HC and CO during engine starting and warm-up, before the catalyst is hot enough to be effective.

Table 2 Automobile exhaust emission standards for HC, CO, and NO_x

Model year	HC emissions	CO emissions	NO_x emissions
Uncontrolled	8.2	89.5	3.4–4.4
1968	6.2	51	—
1970	4.1	34.0	—
1972	3.0	28.0	—
1973	3.0	28.0	3.1
1975	1.5	15.0	3.1
1977	1.5	15.0	2.0
1980	0.41	7.0	2.0
1981	0.41	3.4	1.0

Note: Standards g/mile.
Source: Grad et al., 1975; EPA, 1990.

Of course exhaust emission control is not as simple as this brief description suggests. Many computer-based analysis tools are used, from regression equations that smooth and correlate engine mapping data to define how an engine responds to changing operating conditions, to engine-in-vehicle simulations that are used to define the air/fuel ratio, spark timing, and EGR strategy as a function of speed and load, which maximizes vehicle fuel economy within the constraints of meeting the emissions requirements.

How well do these emission controls work? They do meet the requirements, since obviously all production models that are sold have been successfully certified. Recent EPA estimates based on vehicle emissions data, and a mobile source emissions model that adjusts for deterioration in emission control, mean vehicle speed, and ambient conditions (the latest version is "Mobile 4," EPA, 1990; see Atkinson et al., 1990), suggest that in-use emissions are higher than the standards for exhaust HC and CO, and about equal to the standards for NO_x. HC emissions are predicted to be between 1 and 3.4 times the applicable standard with an average multiplying factor of 1.8. The higher factors have occurred the first year a significantly stricter standard was imposed: e.g., in 1980 when the HC exhaust standard went down from 1.5 to 0.41 g/mile actual, HC emissions were estimated to decrease from 3 to 1.38 g/mile. Current production vehicles are estimated to have exhaust HC emissions of 0.66 g/mile. Actual CO emissions in g/mile are estimated by EPA to be consistently about a factor of 2 higher than the standards. NO_x emissions are estimated to be within about 10 percent of the applicable standard.

Complete Federal Test Procedure (FTP) emissions measurements by General Motors (Haskew and Gumbleton, 1988; Haskew et al., 1989) on in-use GM passenger cars from model years 1981 to 1986 show average 50,000 mile emission higher than the HC and CO standards for 1981 and 1982 (by about a factor of 2 for exhaust HC, and 1.5 (first year), 1.2 (second year), for CO) while close to the NO_x standard. In-use cars from model years 1983 to 1986 matched the HC and NO standard, and exceeded the CO standard by some 50 percent in 1983, 1984, and 1985.

These studies have identified a number of very high emitting vehicles in the vehicle population; e.g., the GM study showed that a few percent (1–4 percent) of the cars have HC and CO emissions more than six standard deviations above the mean.

Before we interpret this information, we must add the results from attempts to measure on-the-road emission directly, a difficult and rarely attempted task. Measurements of pollutant concentrations in the air flowing out of the Van Nuys tunnel in Los Angeles have been converted to average car emission rates based on measured traffic density. An inventory of vehicles entering the tunnel (over several periods of one hour) permitted an estimate to be made of expected emissions levels using the California Air Resources Board vehicle emissions factor program EMFAC7 (Ingalls, 1989). While the median vehicle speeds (usually about 40 mph) were higher than those

of the FTP, and the driving patterns are different, measured emission rates were some 2 to 7 times higher than model estimates for HC, up to 3.6 times higher for CO, and between 0.6 and 2.5 times NO g/mile values. One contributing reason to these high HC measurements may be high evaporative HC emissions, so-called running losses, from the vehicle fuel system, which must be added to exhaust emissions to get total HC emissions (Halberstandt, 1989).

A brief summary of the above would be: (1) Production vehicles meet the certification requirements; (2) in-use vehicles in the Federal Test Procedure have *average* emission levels (at 50,000 miles) that exceed the standards by factors of up to about 2 for HC and CO; (3) more recent model years do a better job of meeting the standards in practice; (4) a few percent of the in-use cars tested have very high HC and/or CO emissions (due to malfunctions and/or poor or no maintenance); (5) actual on-the-road emissions levels are difficult to determine, and one recent study suggests they may be much higher (at 40 mph, approximately constant speed) than the emissions levels that models used by regulators are predicting.

Urban Air Quality. Has urban air become cleaner during this 20 year period when exhaust emissions have been substantially reduced? The answer seems to be "yes," but neither as clean as Air Quality Standards require nor as clean as the achieved reduction in vehicle exhaust emission levels indicates should happen. Total United States CO emissions are estimated by the EPA to have decreased by 30 percent, 1970 to 1987, and the transportation systems CO emissions contribution decreased by 43 percent. In 1970 transportation was estimated to be the source of 80 percent of the total CO; in 1987 it is estimated to be 65 percent of the total. Extrapolation of average ambient CO concentrations collected by EPA back to 1970 suggests that about a 50 percent reduction in ambient CO concentrations has been achieved over this same time period, 1970 to 1987. Yet CO emissions per average car mile in 1990 should be about one-third what they were in 1980 (Haskew and Gumbleton, 1988), and in 1980 average CO emission rates should have been about one-half of the peak emission rate in 1968 (Grad et al., 1975): i.e., on a per-car basis, CO emissions should be about one-sixth the peak 1968 value. Two obvious additional problems are growth in vehicle miles traveled, and the absolute increase (and larger relative importance) of nontransportation CO emissions. That vehicles exceed the standards in actual use has already been factored in, at least to the degree to which we understand it.

The hydrocarbon problem is more complex still. What matters is oxidant levels; composite average ozone concentrations have decreased by about 20 percent since 1978. Both HC and NO_x contribute to oxidant production, and the ratio of HC and NO_x concentrations in the atmosphere has a major impact on the amount of oxidant produced. Pre-emission control volatile organic compounds (circa 1968) came about equally from transportation and nontransportation sources. In 1987, EPA estimates suggest that nontransportation HC emissions are essentially the same as they were in 1970, and the transportation emission contribution has been halved (Atkinson et al., 1990). Passenger car exhaust HC emissions on an average car mile basis have gone down by a much larger factor. However, there is concern that evaporative emissions from the vehicle fuel system are not adequately controlled, and have actually gone up as gasoline vapor pressure has risen, and HC reactivity may have increased due to the fuel composition trends of the past two decades. A major problem with volatile organic emissions is the large number of small stationary sources.

Summary. An important lesson from all this is that we do not adequately understand what is going on. While urban air pollution results from an extraordinarily complex set of processes, my own conclusion is that none of the players involved—auto industry, oil industry, regulators, politicians, and the public—have been willing to acknowledge the extent to which we *cannot* explain what is really going on (what progress we are making toward substantially cleaner air), nor are they willing jointly to commit the resources needed to understand the problems better.

I reach the conclusion that we have not cleaned up the air to the extent we should have, despite the very real engineering success of the catalytic converter and associated control equipment at reducing passenger car emissions. Although we can offer many possible explanations, we really do not know what is not working the way we thought it would. Sources of discrepancy could be some or all of the following: (1) Average real-world vehicle exhaust emission levels may be substantially higher (by more than a factor of two) than the applicable standards; (2) evaporative hydrocarbon emissions (running losses) are the major source of passenger HC emissions; (3) a significant number of vehicles (newer as well as older) may be really high emitters due to component failures, malfunctions, and inadequate maintenance; (4) the growth rates for vehicle miles traveled in urban areas with major pollutant problems may be significantly higher than the estimated growth rates; (5) the relative importance of mobile and stationary sources of emissions may have been incorrectly estimated: an error here could significantly change the expected reductions in emissions achieved to date; (6) the atmospheric chemistry that produces oxidants via photochemical smog may be much less sensitive to reductions in inputs (emission rates) than anticipated. Large questions, but a large and important problem! A much more extensive "engineering analysis" of this problem and its key components is required. Lower numbers for passenger car exhaust emission standards would not necessarily improve the situation as discussed below.

Engine Technology Prospects for the 1990s

What Are the Needs?

Emissions. As explained above we need effective control of emissions in new cars at levels that are low compared to the emissions of old cars the new cars (largely) replace. Since cars last about 10 years, what is required is an incremental reduction in emissions every four or so years, until in-use transportation system emissions are sufficiently below stationary source emissions so that stationary sources become the primary focus for control. For HC it is total vehicle HC emissions that matter, exhaust *and* evaporative. This has always been the objective of vehicle emissions regulation; however, its realization in practice falls short of the objective. Just lowering the values of new car exhaust emission standards will not solve the problem; other measures are needed.

Engine Size and Weight. Under-hood space is at a premium; reductions in vehicle weight are attractive for many reasons. So higher specific power (power per unit engine weight or bulk engine volume) will continue to be an important objective.

Engine Efficiency. Stricter fuel economy standards are almost certain for many reasons: magnitude of our oil imports, the balance of trade problem they create, and their strategic impact; concern with rising CO_2 emissions and global warming; need to show the rest of the world we will moderate our high per capita energy consumption.

Reliability and Maintainability. Increasing engine complexity, market competitiveness, need for durable emission control, and the rising cost of vehicle service place a high premium of inherent engine reliability, and low and straightforward maintenance requirements.

Manufacturability. Need for shorter design cycles, and higher inherent quality to lower total manufacturing cost and increase flexibility. These requirements encourage fewer different size engines in each producers' lineup and more modular engine concepts to reduce development and design effort, and

Table 3 Typical numbers for available energy engine analysis; four-stroke cycle spark-ignition engine at 2000 rev/min, inlet pressure 0.5 atm, stoichiometric operation, compression ratio = 10

	Indicated	Brake
Available energy of fuel	100	
Combustion inefficiency	5	
Combustion irreversibility	19	
Available energy loss due to heat loss	20	
Exhaust gas available energy (at cylinder exit)	20	
Indicated work	36	36
Pumping work loss		3.5
Mechanical friction and auxiliary loss		7.5
Brake work		25

discourages use of more than one or two basic engine technologies.

What is the Potential for Improvement? The concept of "available energy" is increasingly being used to analyze the energy conversion characteristics of engines. Internal combustion engines are devices that process a flow of fuel and air, and produce useful power: They release the chemical energy in our resource, the fuel, and from that energy produce a certain amount of mechanical work.

One can think of the fuel as "our system"; the key question is then how effectively can we produce useful work from this system, allowing it to interact with the atmosphere—our source of air, and also a constant pressure and temperature reservoir.

Application of the First and Second Laws of Thermodynamics to this system shows that the work producing potential of the fuel–air mixture as it goes through a device such as an engine that interacts with the atmosphere is given by the property availability or available energy, A, where

$$A = (U - U_0) + p_0(V - V_0) - T_0(S - S_0)$$

Here U is the internal energy of our system, p pressure, V system volume, S system entropy and the subscript zero denotes atmospheric values (e.g., $U_0 = U(T_0, p_0)$ where p_0 and T_0 are atmospheric pressure and temperature). One can understand the equation as follows. The first term $(U - U_0)$ is the change in internal energy of the system as it comes to *equilibrium* with the atmosphere. The last term $T_0(S - S_0)$ is the *minimum* heat transfer with the atmosphere required to bring the system and atmosphere to equilibrium. The $p_0(V - V_0)$ term is the work done by the atmosphere *on* the system as the system volume changes in this equilibrium process. The internal energy change *less* the minimum heat transfer *less* the work done *on* the atmosphere is clearly the maximum or *available* useful work. The final state of equilibrium with the atmosphere gives the *maximum* work. If the exhaust gases are not in equilibrium with the atmosphere, then additional work can, in principle, be produced.

An available energy balance through the engine cycle identifies where opportunities for producing useful work are lost through irreversibilities (such as friction) that destroy available energy, heat losses (which transfer energy and hence work producing potential out of the system) and flows (the hot exhaust gases transfer available energy out of the engine). See Heywood (1988), Primus et al. (1984), or Foster (1985) for a more complete explanation.

Table 3 shows typical numbers for the available energy losses and transfers for a spark-ignition engine at a part-load mid-speed operating condition. It is useful because it quantifies where opportunities for improving engine efficiency lie, and how large these opportunities are. The table is based on 100 units of fuel available energy. Let us look at each of the terms in turn.

The combustion inefficiency is the HC, CO, and hydrogen that exit the engine unburned in the exhaust. The unburned HC are about two of these five units, i.e., 2 percent of the fuel goes straight through the engine. In fact the impact on indicated work is greater than this. A larger fraction of the fuel, about twice as much, escapes the primary combustion process unburned in crevices, largely between the piston, rings, and cylinder liner. A substantial fraction of this oxidizes during the expansion and exhaust strokes prior to exiting the cylinder (Namazian and Heywood, 1982). Emissions control requirements will require some reduction in this loss. If the 5 units are reduced to 4, and that extra fuel burns during the combustion process, indicated work would increase by 1 percent.

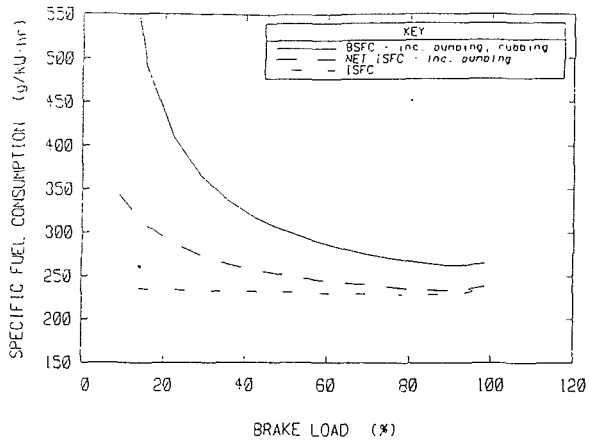

Fig. 9 Indicated (dash-dot line) and brake (solid line) specific fuel consumption of a standard spark-ignition engine over the full load range; dashed line shows effect of pumping work; 1000 rev/min (Patton, 1989)

A major loss of *available* energy is the combustion process itself. Energy is conserved, but combustion is an irreversible entropy-generating process; the *work producing potential* of the hot combustion products immediately after combustion is lower than that of the fuel–air mixture just prior to combustion by some 19 percent. There is little we can do about this; burning our fossil fuels is the only practical method currently available for utilizing the fuel's chemical energy. Interestingly, stoichiometric combustion from a high-temperature unburned mixture state minimizes this loss. Lean mixtures or EGR increase this loss modestly.

Heat losses from the hot burned gases to the combustion chamber walls remove about 20 percent of the fuel's available energy from the cylinder. (The actual heat loss is a slightly higher fraction of the fuel's *energy*.) Maximum heat loss rates occur right at the end of the combustion process. Reductions in heat loss would help, but are limited to modest amounts; see below. However, care should always be taken to hold heat losses to a minimum. A decrease in heat losses by x percent results in an improvement in fuel consumption by about $x/3$ percent. The exhaust gas carries a comparable amount of available energy out of the cylinder. A greater expansion ratio would reduce this; otherwise exhaust gas energy recovery devices such as a turbine or exhaust-heat driven Rankine cycle system are required.

The indicated work—that transferred to the piston over the compression and expansion strokes—for this condition corresponds to about 36 percent of the fuel's available energy. This quantity, the indicated efficiency of a spark-ignition engine, is remarkably constant over the speed and load range, lying between about 35 and 39 percent at these conditions. It obviously depends on compression ratio and mixture composition (lean, rich, dilution with EGR). It also depends on burn rate and cyclic variability of the combustion process. This latter area has been exploited by the fast-burn combustion technology.

Finally, at part load, friction decreases the brake output significantly below the indicated output. As indicated in Table 3 and Fig. 9, the cause is the pumping work requirement of

the four-stroke cycle, and mechanical and auxiliary friction. This is, and has always been, a major problem for the four-stroke cycle. It is an area that is being actively worked on for the obvious reason that its leverage on brake output is large: A 10 percent reduction in total friction at the conditions of Table 3 would yield a 4 to 5 percent improvement in brake efficiency.

In summary, based on this available energy analysis of the standard four-stroke spark-ignition engine cycle, I would rank the opportunities for improvement in this order: friction reduction (largest), expansion stroke work increase, heat loss reduction/combustion efficiency improvement (smallest).

What Are the Opportunities?

Emissions Situation. Obviously all new cars produced must meet the emissions standards. There is an increasing trend toward worldwide uniformity in test procedures and levels of standards (though with different timetables). One appreciates the logic behind this trend. However, it underlines the need for reality (low in-use emissions), and the standards and test procedures that define them, to be closely coupled. Also, different urban areas in the United States as well as different parts of the world often have quite different air pollution problems and control needs.

In the United States we need an orderly progression toward lower *total* in-use emissions. This requires effective control of evaporative HC emissions as rapidly as possible, an understanding of the role and causes of very high emitting cars, and procedures (imposed on car producers and car owners) that reduce their impact significantly. It may well require exhaust emissions levels significantly lower than current new car standards in some geographic areas in the future, evaluated at more demanding ambient conditions, but the rationale for that lacks adequate quantification. Current proposals in the Clean Air Act are pursuing some of these needs, though not all, and the politics of the situation unfortunately emphasizes the one option—much lower exhaust *standards*—that is probably not the most important need right now!

But, of course, all new engine options must show the potential of meeting the applicable standards. That gives a significant advantage to evolutionary developments of current production engine technology. Although we should remember that application of substantial engineering resources to the emissions control problem of the conventional spark-ignition engine and the diesel have proved remarkably effective at reducing their emission levels.

The Four-Stroke Cycle Spark-Ignition Engine. Let us look at combustion-related improvements, and then friction. We have already seen the efficiency advantages of fast-burn combustion technology with its rapid chemical energy release close to top center, lower cyclic combustion variability, and ability to absorb more EGR at part load for NO_x control. Some continued improvements here can be expected as the technology spreads across all engines and is better optimized as it matures. Improved control of fuel metering via increasing use of more sophisticated port fuel injection systems aids this trend. One can also expect reductions in engine HC emissions and improved mixture control to result in some decrease in combustion inefficiency.

Increasing use of knock sensors will permit engine operation closer to the knock limit, and modest increases in compression ratio should result. Perhaps variable compression ratio concepts (e.g., the variable height piston crown concept of Wirbeleit et al., 1990) may prove feasible; use of a significantly higher compression ratio at part load where the engine is not knock limited improves part-load fuel consumption substantially.

There are no obvious ways to obtain substantial reductions in heat losses in spark-ignition engines. The engine is knock limited already with standard water-cooled components. Use of significant thermal insulation is not therefore feasible, and even if it were the benefits are limited (Amann, 1989) because substantial heat "recycling" from the hot combustion gases to the incoming fresh charge via the walls then occurs. However, reductions in heat losses through careful optimization of combustion chamber shape to reduce the heat transfer surface area (Muranaka et al., 1984), improvements in surface finish (Tsutsumi et al., 1990) and surface coatings (Boehm and Harrer, 1990) offer useful incremental opportunities.

Friction is an extremely important opportunity. However, its many different components, and its link with wear and durability, make it a different engineering challenge. Here analysis can play an important role. A recently developed friction model (Patton et al., 1989) predicts each significant engine friction component via fundamentally based scaling laws that have been calibrated against available friction component data. The model relates details of the engine's geometry and operating conditions to the magnitude and thus relative importance of each friction component. Figure 10 shows the friction breakdown by component at part load and wide-open-throttle over the full speed range of a modern spark-ignition engine. The model results show the importance of pumping work at part-load, and at high speed WOT, that piston, ring, and connecting rod friction is especially important, and that valve train friction at low speed is a significant fraction of total fmep.

Mechanical rubbing friction and accessory drive reductions are already being partially exploited through use of roller followers in the valve train, smaller piston skirts, reduced ring tension, improved design, and sizing of accessories. Additional opportunities exist in the friction area, and they will have a significant impact on brake specific fuel consumption.

Reductions in pumping work are harder to realize. Use of

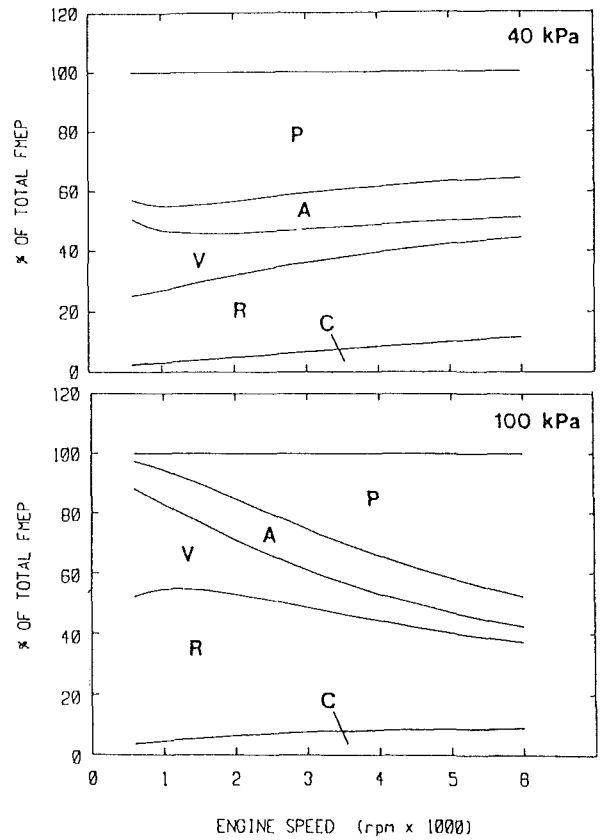

Fig. 10 The distribution of friction among its major components over the speed range of a 2-liter four-cylinder modern spark-ignition engine, at part load (40 kPa inlet manifold pressure) and wide-open throttle; *C* = crankshaft and seals; *R* = reciprocating components; *V* = valve train components; *A* = auxiliary components; *P* = pumping work (Patton et al., 1989)

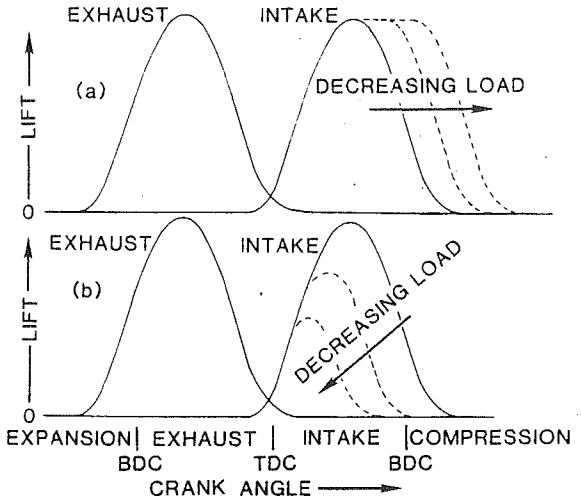

Fig. 11 Valve lift diagrams for (*a*) late intake valve closing, and (*b*) early intake valve closing as load is decreased. Both approaches reduce the pumping work at part load by changing the shape and enclosed area of the pumping loop on a *p–V* diagram (Amann, 1989).

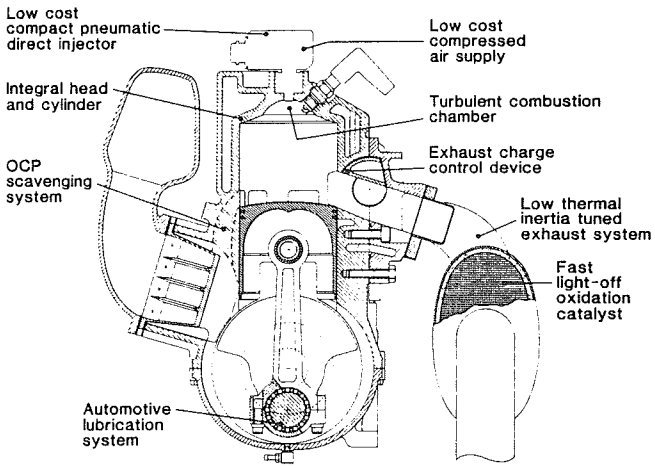

Fig. 12 Cross-sectional drawing of Orbital Combustion Process two-stroke cycle gasoline engine

significant amounts of EGR, well controlled, helps here. Improved design of inlet system, and especially ports and valves, helps at higher speeds and is especially important with fast-burn combustion technology since that requires intake flow control with special port and valve geometries.

Variable-valve-timing (VVT) is one option that is being explored. Many different VVT schemes are being considered for (*a*) improving the shape of the full-load torque curve as a function of engine speed, (*b*) improving idle combustion quality, and (*c*) reducing pumping work. Some cam shifting mechanisms are already in production (e.g., Inoue et al., 1989) for reasons (*a*) and (*b*), and significant benefits result. Here I will focus on pumping work reduction. Figure 11 illustrates two variable valve timing concepts, later and earlier intake valve closing as load is decreased. Conventional load control by throttling reduces the mass of fuel and air in the cylinder by decreasing inlet manifold pressure. Late intake valve closing (LIVC) decreases the mass retained in the cylinder by progressively delaying intake valve closing until late in the compression stroke so the piston pushes a portion of the already inducted mixture back into the intake. The intake pressure remains close to atmospheric so pumping work is significantly reduced. However, the compression ratio is reduced, even though the expansion ratio remains unchanged. So the efficiency of the compression/expansion part of the cycle is reduced, somewhat decreasing the benefit. Early inlet valve closing (EIVC) is an alternative approach. Here the mass in the cylinder is reduced by closing the inlet valve earlier, during the intake stroke. Once the valve is closed, the trapped mass is expanded as the intake stroke continues and then compressed again during the compression stroke. The compression ratio is unchanged, but the pumping work benefits are not as large as with LIVC. Only limited data on the performance of these VVT concepts are available to date. Recent tests with late inlet valve closing load control showed part-load brake specific fuel consumption benefits of up to 13 percent (Saunders and Abdul-Wahab, 1989). A different study of early intake valve closing showed improvements in bsfc up to about 8 percent (Lenz et al., 1989).

When late intake valve closing is combined with a higher expansion ratio even larger efficiency gains have been demonstrated. This is the Atkinson cycle (Saunders and Abdul-Wahab, 1989). One major problem, however, is low specific power. This characteristic can be improved with the addition of a supercharger and intercooler to compress the air prior to entering the cylinder and still, in principle, avoid the problem of knock. This has been called the Miller cycle.

Many variable valve timing mechanisms have been proposed (see Ahmad and Theobald, 1989, for a review). Those that are sufficiently flexible to have a significant influence on fuel economy are usually complex, and the cost, durability, reliability, friction, and (if electromagnetically controlled) the power requirements are potentially major problem areas. Whether these are promising *practical* concepts is not yet clear.

Two-Stroke Cycle Spark-Ignition Engines. A recent modification to the two-stroke-cycle spark-ignition engine has brought this engine concept to the position of serious contender as a passenger car power plant. The most important innovation is fuel introduction into the cylinder after the air charge has been trapped. This prevents the large carry through (20–40 percent) of unburned fuel that occurs with conventional small two-stroke cycle engines and causes their poor fuel consumption and very high hydrocarbon emissions. Figure 12 shows one arrangement of this concept, the Orbital Engine Company's "Orbital Combustion Process." The key features are the air assist fuel injection system, the exhaust port control valve, and the low thermal inertia exhaust and oxidation catalyst system. Air is drawn into the crankcase past the reed valves, by the upward motion of the piston during the compression stroke. Fuel is injected into the cylinder after the piston has covered both inlet and exhaust ports. The spark plug ignites the still stratified mixture toward the end of compression. Some two-thirds of the way through the expansion stroke the piston uncovers the exhaust ports and the burned gases start to flow rapidly out of the cylinder (the exhaust port valve is used to control this flow). The piston then uncovers the transfer ports, which allows crankcase-compressed air to enter the cylinder, further displacing burned gases. Some of this air blows straight through the cylinder; the rest is trapped with the residual burned gases for the next cycle.

The new type of two-stroke cycle offers the following advantages. The engine displacement, bulk size, and weight are lower than those of an equivalent power four-stroke cycle engine. The two-stroke cycle gives twice as many power strokes per unit time as the four-stroke cycle at the same engine speed. However, since scavenging is not as effective, the work produced per cycle per unit displaced volume is not as large. These two effects together yield the result that for equal maximum torque curves, the displaced volume of the two-stroke is three-quarters that of the four-stroke (Duret and Moreau, 1990). The twice as frequent torque pulses improve idle smoothness, though they increase engine noise.

Relative to the available energy analysis of the four-stroke cycle in Table 3, the two-stroke has these advantages. The pumping loop is eliminated, and the four-stroke pumping work

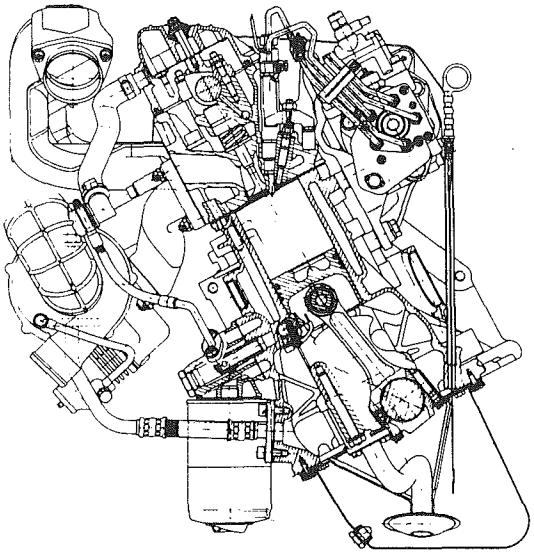

Fig. 13 Cross-sectional drawing of new five-cylinder turbocharged passenger car 2.46-liter direct-injection diesel engine (Bauder and Stock, 1990)

is replaced by the scavenge air pumping work. With crankcase pumping concepts, at light load this work is much less. Also rubbing friction is reduced because the valve train is not needed (at least in ported two-stroke cycle engines), and the rubbing friction of the pumping loop is eliminated. So the part-load fuel consumption of the two-stroke should be significantly better than that of an equivalent four-stroke. However, this does require good combustion characteristics.

The emissions problems of these two-stroke cycle concepts are different from conventional four-stroke emissions too. Since these are stratified-charge engines, they operate lean overall and NO_x must be controlled within the engine. An oxidation catalyst is used for HC and CO control. The straight-through flow of scavenging air cools the catalyst and may cause problems with oil carryover, so even the problems here are different. Low exhaust emissions levels have been achieved with prototype engine and catalyst systems. The durability of the emission control package has yet to be demonstrated.

Of greater significance are a number of more pragmatic engine design issues where differences from well-established four-stroke engine design practice will require extensive development. Examples of such problems are: higher thermal loading of the pistons; novel fuel injection technology; lubrication of critical components (e.g., piston pin); crankshaft and bearing design with dry sump.

Substantial engineering effort is currently being invested in developing several different "controlled injection" two-stroke cycle gasoline engine concepts in various organizations worldwide. Some employ poppet valves to retain four-stroke cycle technology, and some a wet sump with a separately driven blower for better scavenging control. Fuel-injection options other than air-assisted atomization include mixture preparation in a valved prechamber using conventional gasoline port injectors. Which of these concepts will prove superior, and whether any will replace the still evolving four-stroke cycle engine, remains to be seen (Amann, 1989).

Direct-Injection Diesel Engine. Based on the framework of Table 3, the largest efficiency improvements are achieved by the high-speed direct-injection diesel. The combustion inefficiency is reduced, the amount of expansion stroke work extracted is much greater due to the higher compression ratio and lean mixtures, the heat losses are comparable (as compared to the indirect-injection diesel engine where heat losses are significantly higher), and pumping work at light load is essentially eliminated. Figure 13 shows a new five-cylinder turbocharged direct-injection passenger car diesel developed by Audi. The turbocharger uses the available energy of the engine exhaust to increase the engine's power density at high load. Impressive output (maximum bmep of 13.5 bar at 2250 rev/min) and fuel consumption (best bsfc of 200 g/kW-h corresponding to a brake thermal efficiency of 43 percent) have been obtained (Stock and Bauder, 1990).

Improvements in conventional gasoline engines have reduced the efficiency advantage of the indirect-injection diesel to the point where the additional cost is hard to justify. However, the DI diesel has developed to the point where its light-load fuel consumption is some 20 percent better than that of the IDI. What is its potential for displacing gasoline engines?

Problem areas are increased and different noise, fuel issues and cold starting delays, higher initial cost, and especially emissions. NO_x and particulates emissions are high relative to applicable standards, and while traps and oxidation catalysts may with further development and low sulfur fuels help significantly with the latter, in-cylinder control of NO_x is especially difficult. However, progress in meeting European emission standards has been made, and the very high engine efficiency that this engine offers makes the control of its emissions an important engine research and development area.

Summary. There is much potential for improvement still remaining in the conventional four-stroke cycle spark-ignition engine. Evolutionary gains in combustion-related areas, friction, engine controls, and engine and catalyst emission reductions will continue to be realized. Power density improvements via more sophisticated intake tuning, increased use of multivalve heads, adoption of cam shifting mechanisms, and turbocharging will also occur. More radical changes in the engine such as variable valve timing and variable compression ratio concepts for efficiency gains have the potential for improving the four-stroke cycle where it needs it most, at part load. However, these more radical concepts have major practical implementation problems.

In my judgment, the new two-stroke cycle gasoline engines now under development are sufficiently promising in terms of engine size reduction and part-load fuel consumption improvement to warrant substantial development effort. Whether the emissions can be adequately controlled, and the practical design and manufacturing problems satisfactorily resolved, remains to be seen.

The direct-injection diesel is the most efficient engine concept we have available. When turbocharged, its low power density problem is removed though the engine's bulk size and weight is large. However, achieving low emissions, especially of NO_x, is a major yet-to-be-resolved problem. Its long-term promise is such that it too should stay high on our list of potential alternatives. After all, emissions problems do yield bit-by-bit to major engineering development effort.

References

Ahmad, T., and Theobald, M. A., 1989, "A Survey of Variable-Valve-Actuation Technology," SAE Paper No. 891674.

Amann, C. A., 1989, "The Automotive Engine—A Future Perspective," SAE Paper No. 89166.

Atkinson, D., Cristofaro, A., and Kolb, J., 1990, "Role of the Automobile in Urban Air Pollution," *Proceedings of Conference on Energy and the Environment in the 21st Century*, MIT, Cambridge, MA, Mar.

Benson, R. S., Garg, R. D., and Woollatt, D., 1964, "A Numerical Solution of Unsteady Flow Problems," *Int. J. Mech. Sci.*, Vol. 6, pp. 117–144.

Boehm, G., and Harrer, J., 1990, "Nickel Coated Pistons for Improved Durability in Knock Control Engines," SAE Paper No. 900453.

Chapman, M., Novak, J. M., and Stein, R. A., 1982, "Numerical Modeling of Inlet and Exhaust Flows in Multi-cylinder Internal Combustion Engines," in: *Flows in Internal Combustion Engines*, T. Uzkan, ed., ASME, New York.

DeLosh, R. G., Brewer, K. J., Buch, L. H., Ferguson, T. F. W., and Tobler, W. E., 1981, "Dynamic Computer Simulation of a Vehicle With Electronic Engine Control," SAE Paper No. 810447, SAE Vol. SP-487.

Duret, P., and Moreau, J.-F., 1990, "Reduction of Pollutant Emissions of the IAPAC Two-Stroke Engine With Compressed Air Assisted Fuel Injection," SAE Paper No. 900801.

EPA, 1990, "Combustion of Air Pollutant Emission Factors, Volume II: Mobile Sources," (Mobile 4), 5th ed.

Foster, D. E., 1985, "An Overview of Zero-Dimensional Thermodynamic Models for IC Engine Data Analysis," SAE Paper No. 852070.

Grad, F., Rosenthal, A. J., Rockett, L. R., Fay, J. A., Heywood, J. B., Kain, J. F., Ingram, G. K., Harrison, D., Jr., and Tietenberg, T., 1975, *The Automobile and the Regulation of Its Impact on the Environment*, University of Oklahoma Press, Norman, OK.

Halberstadt, M. L., 1989, "Effective Control of Highway Vehicle Hydrocarbon Emissions," *JAPCA*, Vol. 39, No. 6, p. 862.

Haskew, H. M., and Gumbleton, J. J., 1988, "GM's In-Use Emission Performance Past, Present, Future," SAE Paper No. 881682.

Haskew, H. M., Garrett, D. P., and Gumbleton, J. J., 1989, "GM's Results—The EPA/Industry Cooperative Test Program," SAE Paper No. 890185.

Heywood, J. B., 1988, *Internal Combustion Engine Fundamentals*, McGraw-Hill, New York.

Ingalls, M. N., 1989, "On-Road Vehicle Emission Factors From Measurements in a Los Angeles Area Tunnel," Southwest Research Institute, San Antonio, TX.

Inoue, K., Nagahiro, K., Ajiki, Y., and Kishi, N., 1989, "A High Power, Wide Torque Range, Efficient Engine With a Newly Developed Variable-Valve-Lift and -Timing Mechanism," SAE Paper No. 890675.

Kuroda, H., Nakajima, Y., Sugihara, K., Takagi, Y., and Maranaka, S., 1980, "Fast Burn With Heavy EGR Improves Fuel Economy and Reduces NO_x Emission," *JSAE Review*, No. 5, pp. 63-69.

Lenz, H. P., Geringer, B., Smetana, G., and Dachs, A., 1989, "Initial Test Results of an Electro-Hydraulic Variable-Valve Actuation System on a Firing Engine," SAE Paper No. 890678.

Li, C.-H., 1982, "Piston Thermal Deformation and Friction Considerations," SAE Paper No. 820086.

Morel, T., Flemming, M. F., and LaPointe, L. A., 1990, "Characterization of Manifold Dynamics in the Chrysler 2.2 S.I. Engine by Measurements and Simulation," SAE Paper No. 900679.

Muranaka, S., Ishida, T., Takagi, Y., and Nakagawa, Y., 1984, "Effect of Combustion Chamber Surface Volume Ratio on the Indicated Thermal Efficiency of S.I. Engine," *JSAE Review*, Vol. 15.

Naitoh, K., Fujii, H., Urushihara, T., Takagi, Y., and Kuwahara, K., 1990, "Numerical Simulation of the Detailed Flow in Engine Ports and Cylinders," SAE Paper No. 900256.

Namazian, M., and Heywood, J. B., 1982, "Flow in the Piston-Cylinder-Ring Crevices of a Spark-Ignition Engine: Effect on Hydrocarbon Emissions, Efficiency and Power," SAE Paper No. 820088, *SAE Trans.*, Vol. 91.

Patton, K. J., 1989, "Development and Evaluation of a Performance and Efficiency Model for Spark-Ignition Engines," M.S. Thesis, Department of Mechanical Engineering, MIT, Cambridge, MA.

Patton, K. J., Nitschke, R. G., and Heywood, J. B., 1989, "Development and Evaluation of a Friction Model for Spark-Ignition Engines," SAE Paper No. 890836.

Primus, R. J., Hoag, K. L., Flynn, P. F., and Brands, M. C., 1984, "An Appraisal of Advanced Engine Concepts Using Second Law Analysis Techniques," SAE Paper No. 841287; IMechE Paper No. C440/84; in: *Full Efficient Power Trains and Vehicles*, P-150, SAE, VECON '84.

Saunders, R. J., and Abdul-Wahab, E. A., 1989, "Variable Valve Closure Timing for Load Control and the Otto Atkinson Cycle Engine," SAE Paper No. 890677.

Stock, D., and Bauder, R., 1990, "The New Audi 5-Cylinder Turbo Diesel Engine: The First Passenger Car Diesel Engine With Second Generation Direct Injection," SAE Paper No. 900648.

Tsutsumi, Y., Nomura, K., and Nakamura, N., 1990, "Effect of Mirror-Finished Combustion Chamber on Heat Loss," *JSAE Review*, Vol. 11, No. 2.

Wirbeleit, F. G., Binder, K., and Gwinner, D., 1990, "Development of Pistons With Variable Compression Height for Increasing Efficiency and Specific Power Output of Combustion Engines," SAE Paper No. 900229.

Medium-Speed Engine Bearings—Development Experience

J. F. Warriner

D. L. Westerling

The Glacier Metal Company, Ltd.,
Somerset, United Kingdom

After a brief history of the introduction of galvanically applied overlays to the surface of thin-walled half-bearings, the paper goes on to describe experiences in service engines. This shows that from the mid-1970s, overlay life could be sharply reduced due to a variety (or combination) of factors. These are described, the possible causes explained, and various palliatives investigated. The principle factor in the mid-1970s was the rapid rise in the use of lower quality heavy fuels initiated by escalating oil costs. The consequence of using these fuels was often rapid overlay loss, which in turn resulted in further problems, particularly: large areas of exposed nickel interlay, corrosion of the overlay, and/or corrosion of the base lining material. Four palliatives, elimination of the overlay, harder overlays, elimination of the interlayer, and modified surface topography are described and results of development testing and field service experience are presented.

1 Introduction

Almost from the time that copper-lead and subsequently aluminum linings replaced white metal in reciprocating engines, some form of soft overlay coating has been applied. Initially this was a thin layer of lead on copper-lead for automotive engines to improve the embeddability and compatibility of the bearing surface. This was quickly replaced with a lead-tin material to provide some corrosion resistance, since oils at that time were readily oxidized. An alternative to tin is indium, which also provides the lead with corrosion resistance while maintaining good surface properties. Typically the lead-tin overlay contained 8–12 wt% tin, but another early development was to incorporate 1–3 wt% copper.

Until recently, the only attempt to delete the use of an overlay plate came in the late 1950s with the introduction of 20 percent reticular tin-aluminum lining material. In automotive applications this was extremely successful in its unplated form, but experience in medium-speed diesel engines was varied. In some engines it was totally successful, in others tolerable, and in a few unsatisfactory. In those instances where problems occurred, they were usually due to various combinations of inadequate filtration of the lubricating oil, misalignment, distortion of mating components, and production problems. As a consequence, overlay plating was also applied to this material in most medium-speed engine applications.

No general problems of any significance existed with the use of overlay plating until the mid-1970s. From that time higher engine ratings, bearing loadings, and oil operating temperature have gradually combined with the increasing use of progressively lower grades of residual fuel to cause premature loss of, and other damage to, the overlay plated surface. During this period several different options have evolved, the most common of which have been an increase in the tin content to 14–18 wt%, interrupted overlay surfaces, and deletion of the overlay.

2 Basic Method of Overlay Plating

Overlay plate is applied by conventional galvanic means from an anode, typically of lead-tin, and an electrolyte containing both tin and copper. The most significant feature of overlay plating that has affected the performance of engine bearings has been the use of an interlayer, typically nickel, between the lining and the overlay.

For aluminum bearing linings the use of an interlayer is currently an essential part of the procedure, although attempts are ongoing at T&N Technology to eliminate this necessity. (T&N Technology is the central Research and Development of the T&N plc group of Companies.)

With copper-lead linings application of an interlayer is not necessary during the manufacturing stage, but it has been established by various sources [1, 2, 3] that a reduction of bond strength between a cast copper-lead lining and the overlay, leading to total bond failure, can occur after a period of time in the engine. This phenomenon has never been properly understood, and is also being examined at T&N Technology. It is related to migration of tin from the overlay and formation of intermetallic compounds at the bond line, which have been thoroughly covered in the literature [2, 3, 4].

With sintered copper-lead linings such bond deterioration does not generally occur, and this was shown as long ago as 1965 by Perrin [1]. However, loss of tin from the overlay and the formation of intermetallic compounds occur more rapidly without the interlayer.

3 Overlay Life

In medium-speed diesel engines, it used to be considered that the overlay plate should be retained on the bearing surface throughout the major period of the life of a bearing, except

Contributed by the Internal Combustion Engine Division and presented at the Twelfth Annual Fall Technical Conference, Rockford, Illinois, October 7–10, 1990. Manuscript received by the Internal Combustion Engine Division July 1990.

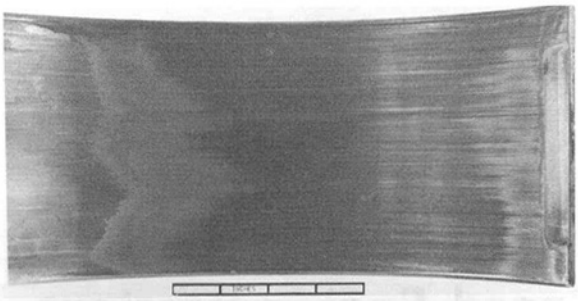

Fig. 5.1 Typical appearance of accelerated overlay wear

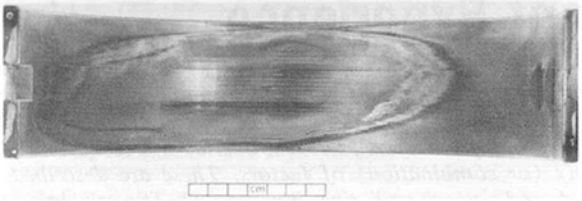

Fig. 5.2 Localized surface wear due to geometric error

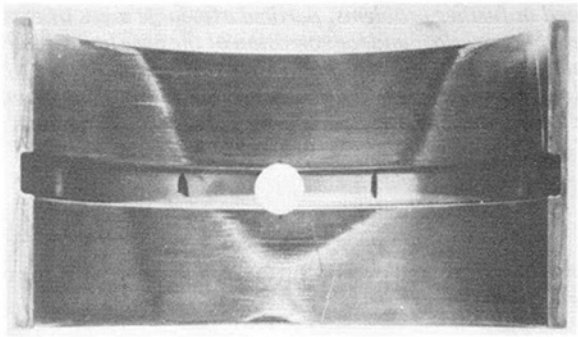

Fig. 5.3 Wear pattern related to axial misalignment

in cases where the overlay wore through locally to accept permanent distortion, regular deflections, or local inaccuracies within the total bearing assembly. Otherwise, it was considered that the bearing had reached the end of its useful life if the overlay were fatigued or generally worn through, but that this life could be expected to reach at least 20,000 hours.

Such bearings would require changing at a routine overhaul period, even though satisfactory performance had been achieved after the overlay had worn through. Typically, a bearing was rejected when the wear approximated to 30 percent of the bearing projected area.

However, during the late 1970s it became increasingly apparent that overlay life in some applications was being dramatically reduced.

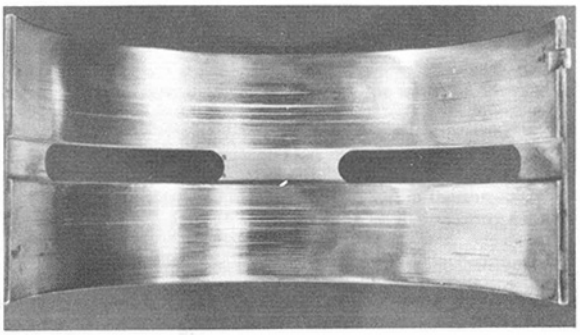

Fig. 5.4 Extensive wear arc

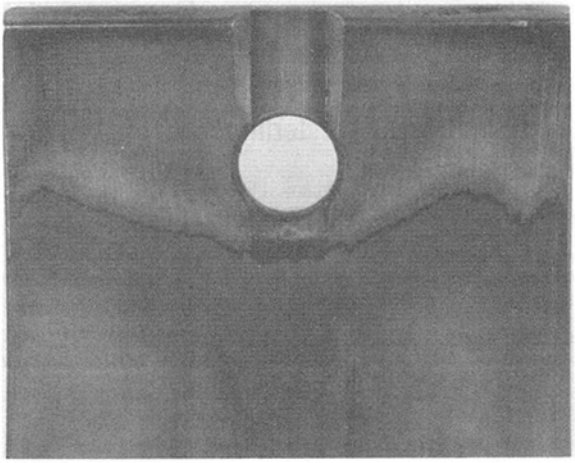

Fig. 5.5 Cliff edge wear, abrupt cutoff

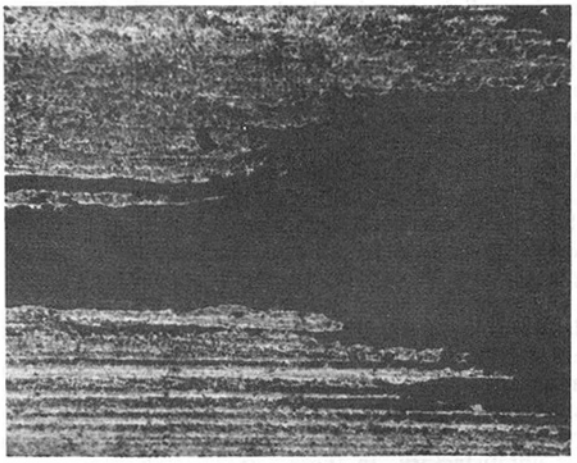

Fig. 5.6 Cliff edge wear, striated

4 Appearance of Damaged Overlay Bearings

Bearings began to show removal of overlay to expose a mixture of lining material, nickel interlayer, and various intermetallic compounds formed by tin, from the overlay, and either nickel from the interlayer or copper from copper-lead linings. Generally this overlay loss occurred over the full axial length of the bearing in an aligned pattern, reaching an arc of 40–60 deg in a very short period of time, typically 2000–5000 hours (see Fig. 5.1). Exceptions to the normal pattern of overlay loss occurred when geometric inaccuracies were present, and examples are shown in Figs. 5.2 and 5.3.

The arc of overlay removal began in the region of the bearing where maximum wear could be expected. However, with extended engine running it was found that the arc of overlay removal continued to increase circumferentially, but not in depth, as typified in Fig. 5.4. In many instances this resulted in very large arcs of exposed nickel interlayer or nickel-tin compound. Another effect that became very apparent was that the transition between intact and removed overlay was very abrupt, creating a "cliff edge" effect. This sometimes occurred in a relatively straight axial cutoff line, as shown in Fig. 5.5, but often generated "fingers" or a striation effect, as in Fig. 5.6.

Initially, instances of rapid overlay loss seemed to be associated only with engines running on heavy fuel, and certainly such engines were much more prone to the problem than those running on distillate. Investigation of bearings from heavy fuel engines repeatedly revealed the presence of numerous relatively small black particles embedded in the overlay, especially adjacent to the sharp, worn edge of the overlay (Fig. 5.7). These particles, typically in the size range 10–30 μm, were often

associated with the fine scores in the overlay but were also brittle, as shown by the embedded but broken particle in Fig. 5.8.

Identification of the particles by energy dispersive X-ray analysis (EDAX) indicated that the majority contained various proportions of sulfur and calcium, whereas a smaller number contained such elements as aluminum, silicon, vanadium, nickel, zinc, phosphorus, potassium, and iron as well as sulfur and calcium. Thus the majority were associated with products of heavy fuel combustion or of relevant lubricating oil additives, or both. Typical traces from two such analyses are shown in Figs. 5.9(*a*) and 5.9(*b*). Chemical analysis of the debris confirmed a generally held belief that the particles contained a high proportion of carbon, giving the typical black color.

The problem became so widespread that Det Norske Veritas [5] initiated a detailed investigation and, because of the carbon content of the particles, coined the phrase "soft particle wear." However, it has been Glacier's view that the particles were not soft but were responsible for the accelerated wear, a view supported by the results of investigations into the beneficial effects of Glacier centrifugal filters in heavy fuel engines. Comparative results from analyses of chemical content and particle size in sample filtrates removed from two engines, one operating on heavy fuel and the other on distillate, are shown in Tables 5.1 and 5.2.

To obtain the size analysis of particles in the sludge, the soluble oil residue was removed first and the resultant dispersion passed successively through graded fine PTFE filter elements with mesh sizes 14, 5, 3, 0.8, and 0.3 μm.

It can be seen that the particle sizes found on each element used for the filtrate from the heavy fuel engine were significantly greater than the mesh size of even the coarsest element, suggesting that reagglomeration had occurred. This effect could possibly explain how bearings can contain a high concentration of embedded particles that are coarser than the engine filtration level. It is also clear that the particle size in the sample from the heavy fuel engine was considerably larger than that in the sample from the engine running on distillate, thus possibly explaining the much greater wear rate of bearings from heavy fuel engines.

However, it was not only the bearings in heavy fuel engines that were subjected to high rates of overlay removal, although the incidences of similar problems in distillate fuel engines were less frequent. Detailed studies of the background to these other instances showed a variety of factors, such as:

(*a*) a mixture of different oils, which may have been incompatible,
(*b*) the presence of sulfur from some other source, or increased sulfur content in the distillate fuels,
(*c*) water leakage into the lubricating oil,
(*d*) oil change intervals two to three times longer than the engine manufacturer's specification,

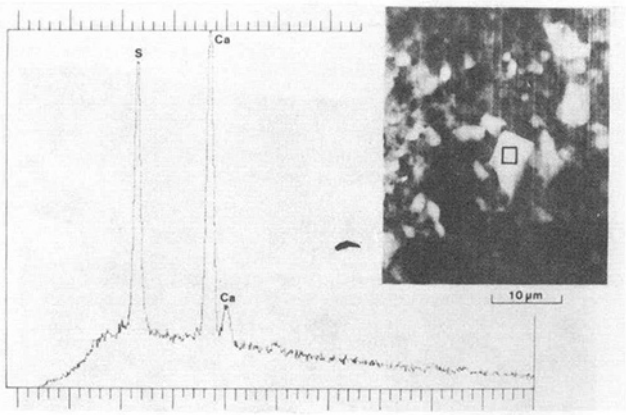

Fig. 5.9(*a*) EDAX traces of embedded particles

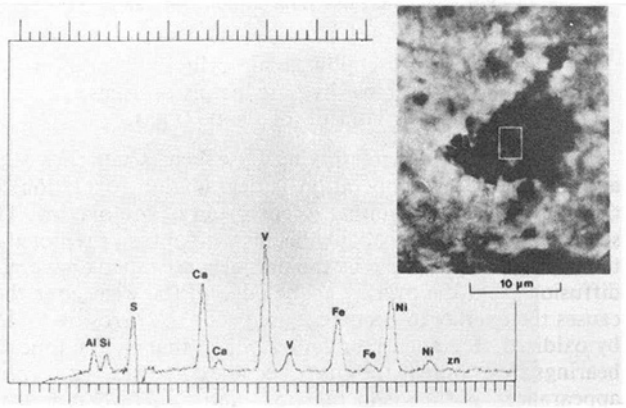

Fig. 5.9(*b*) EDAX traces of embedded particles

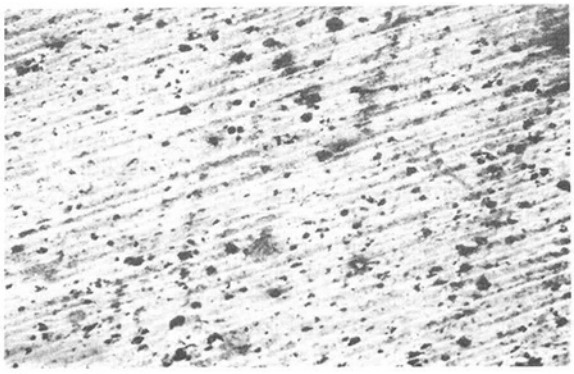

Fig. 5.7 Embedded particles and associated surface scoring

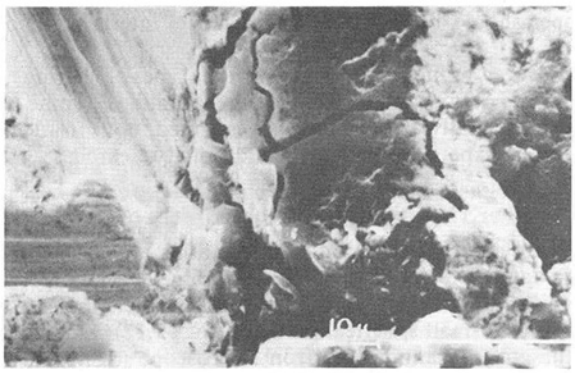

Fig. 5.8 Broken, brittle embedded particle

Table 5.1 Chemical analysis of sludge removed from filters of engines operating on heavy and distillate fuels

COMPONENT	% OF TOTAL SAMPLE ANALYSED	
	Heavy Fuel	Distillate Fuel
Oil + soluble hydrocarbons	41.4	77.3
Carbon (as soot)	22.7	11.7
Calcium	22.1	0.7
Sulphur	11.0	4.9
Copper	1.1	0.05
Lead	0.1	0.07
Tin	0.1	0.1
Phosphorous	0.7	1.14
Zinc	0.6	3.55
Iron	0.2	0.49

Table 5.2 Particle size analysis of sludge removed from filters of engines operating on heavy and distillate fuels

MATERIAL	FILTER MESH SIZE (μm)	MEAN PARTICLE SIZE (μm)	PARTICLE SIZE RANGE (μm)
Heavy fuel engine filtrate	0.3	8	1.5—20
	0.8	10	4—20
	3.0	9	3—20
	5.0	15	3—70
	14.0	27	8—50
Distillate fuel engine filtrate	14	4	2—7
Heavy fuel engine bearing		21	8—30

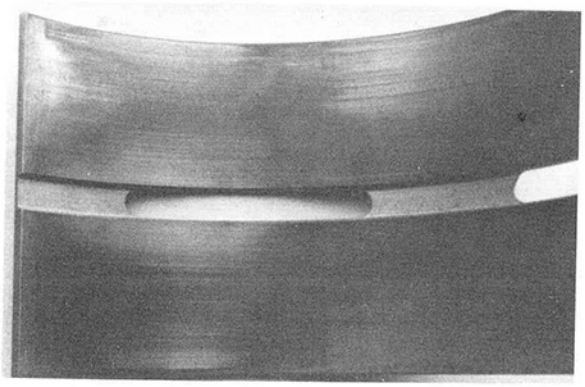

Fig. 5.10 Abrasive wear without corrosion

(*e*) low temperature (low load) cylinder conditions resulting in gas blow-by past the piston rings,
(*f*) combustion of landfill (or "sour") gas.

The common parameter linking these factors with each other and with heavy fuel operation is degradation (oxidation) of the lubricating oil, resulting in corrosion of the overlay. The sequence of damage probably begins with abrasive removal of the overlay, for example by the particles described above. Tin diffusion from the overlay at the edge of the wear zone then causes the overlay to become more prone to corrosion locally by oxidized, degraded lubricating oil, so that by the time the bearings are examined they have become corroded, with typical appearances as shown in Figs. 5.5 and 5.6. In comparison, Fig. 5.10 shows an extensively worn bearing taken from an engine running on heavy fuel before overlay corrosion has had time to occur, thus illustrating the difference between the early and later stages of the problem.

It has long been established that lead-based overlays can be corroded by organic acids and peroxides, which form as lubricating oil degrades. However, work by Wilson and Shone [6] indicated that the tin content in lead–tin or lead–tin–copper overlays needed to fall below 3 percent by weight and the indium content in lead–indium overlays needed to below 6 percent, for corrosion to proceed at a significant rate. From the time of the early pure lead overlays until the more recent cases of rapid overlay loss occurred, such corrosion was not considered to be a problem. However, corrosion certainly seemed to be a major contributory factor in the excessive overlay loss described above.

The problem with overlay corrosion is that there is no proof; it can only be deduced on the basis of circumstantial evidence. The occurrence of corrosion of the lead phase in a copper–lead lining is very clear, since the lead is "leached" out, leaving voids where it originally existed, as shown in Fig. 5.11. However, examination of the linings from bearings that have suffered excessive overlay loss often does not show corrosion of the lead phase, particularly in the majority of heavy fuel cases.

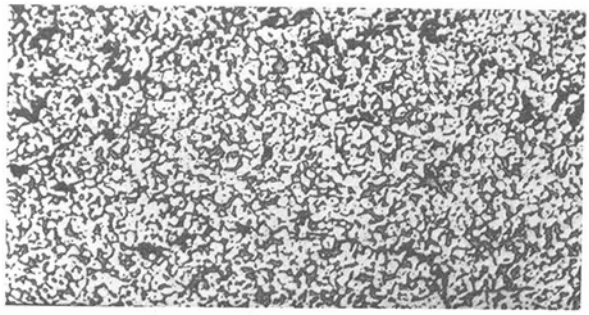

Fig. 5.11 Microsection of corroded lead–bronze bearing

5 Overlay Corrosion

Various investigators have carried out tests on overlay corrosion, and one of the best known early works was that by Wilson and Shone [6]. More recently Crooks and Eastman [4] investigated and reported on the effects of such parameters as tin content, the use of interlayers between overlay and lining, and operating temperature. This work showed very clearly that corrosion could be significant when tin contents were significantly above 3 percent, that it was slower with a nickel interlayer incorporated, that it increased at higher temperature, and that a small addition of copper in lead–tin was beneficial.

The basic outcome of the test work showed that:

1 Raising the tin content of the lead–tin overlay from 10 to 20 percent increased the rate of tin loss, both with and without a nickel interlayer, when heat treated at 100°C. After 4500 hours at this temperature the 10 percent tin content had reduced to between 3.7 and 4.4 percent, while the 20 percent tin had reduced to 5 percent.

2 The addition of 2.5 percent copper to 12.5 percent tin resulted in a residual tin content of 10.2 percent after 1000 hours heat treatment at 120°C compared to 8.5 percent with no copper. The samples included a nickel interlayer.

3 Corresponding figures after 1000 hours at 170°C were 9.2 and 6 percent.

4 Corrosion tests in medicinal white oil (a readily degradable mineral oil) showed a very marked reduction in overlay loss with either lead–tin or lead–tin–copper overlays when a nickel interlayer was incorporated.

5 The wear rate, during rig testing, was 50 percent greater with lead–tin than with lead–tin–copper.

6 Overlay thickness had a very marked effect on fatigue strength, which reduced as thickness increased.

Thus, on the basis of small-scale rig and heat treatment test work, it may be concluded that, to increase overlay life in terms of corrosion and wear resistance while maintaining the required fatigue strength, the tin content should be increased, copper should be included, and a nickel interlayer incorporated.

However, as indicated earlier, various types of bearing problems have occurred in service engines that allowed some of the possible palliatives above to be investigated, both from engine operating experience and from additional research.

6 Further Investigation of the Effects of Palliatives

Where overlay loss resulted in striations, or fingers, at the worn edge of the overlay as shown in Fig. 5.6, high-powered magnification of the surface between the fingers indicated the presence of small spherical particles (Fig. 5.12). Examination of these in a Scanning Electron Microscope (SEM) revealed that they consisted only of copper and tin. Other investigators

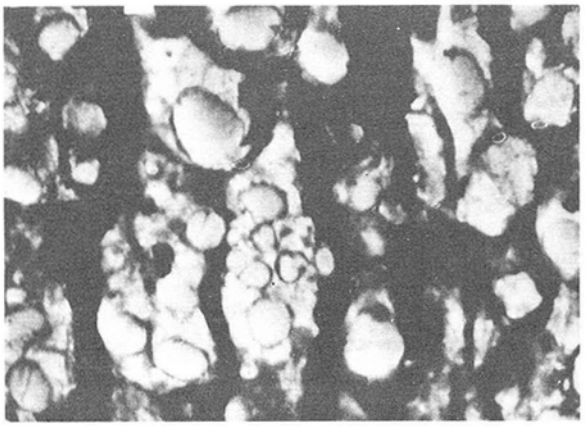

Fig. 5.12 Copper-tin spherical particles at wear edge

have reported the presence of "oil balls" in worn bearings, but it is believed possible that these started as similar copper-tin spherical particles. This finding led to some test work on the effect of copper and tin in the overlay.

It has been known for many years that the amount of tin in overlays is above the solid solubility level in lead (approximately 3 percent at 20°C), and that the surplus tin is present as "islands" within the overlay. This effect is clearly seen in Fig. 5.13, which shows (*a*) a microsection of a non-heat-treated overlay as manufactured, together with elemental identification of (*b*) lead, (*c*) tin, (*d*) copper, and (*e*) nickel. A microsection of the same bearing after heat treatment for 1000 hours at 160°C can be seen in Fig. 5.14, the corresponding parts of which show that tin has diffused to the nickel interlayer, forming a nickel-tin compound, and that the original tin islands have become less distinct (since tin from the islands has replaced that which has diffused to the nickel). Furthermore, some of the copper has been absorbed by the less prominent tin islands still remaining.

This mechanism has also been found in bearings from engines, and probably explains the copper-tin spheres that form on the bearing surface at the worn edge of the overlay; it also strongly indicates that the lead phase of the overlay has been lost by corrosion.

Thus if the tin content is to be increased to improve resistance to corrosive wear, and copper is incorporated for similar reasons, the copper level should not be so high as to negate the benefit from the extra tin.

Unpublished work at T&N Technology on the effect of increased tin overlay has shown that, on lead-bronze linings, if the tin content exceeds approximately 20 percent, a higher rate of tin diffusion and compound formation can cause removal of lead from the lining through the overlay (as shown in Fig. 5.15). This has several effects:

1 It roughens the bore surface with spots of lead.
2 It provides direct corrosion paths through the overlay to the lining.
3 It damages the bond of a nickel interlayer.
4 It may promote bond deterioration of an overlay without a nickel interlayer.

Although the above effects have not yet been thoroughly investigated and explained, the evidence is sufficiently strong to justify imposition of an upper limit on the tin content of overlays, at least for lead-bronze lined bearings.

The incorporation of a nickel interlayer between the overlay and the lining has been shown to improve the corrosion life of lead-tin overlays significantly. However, practice has demonstrated that if the overlay is removed over a large extent of the bearing surface to expose the nickel (and initially nickel-

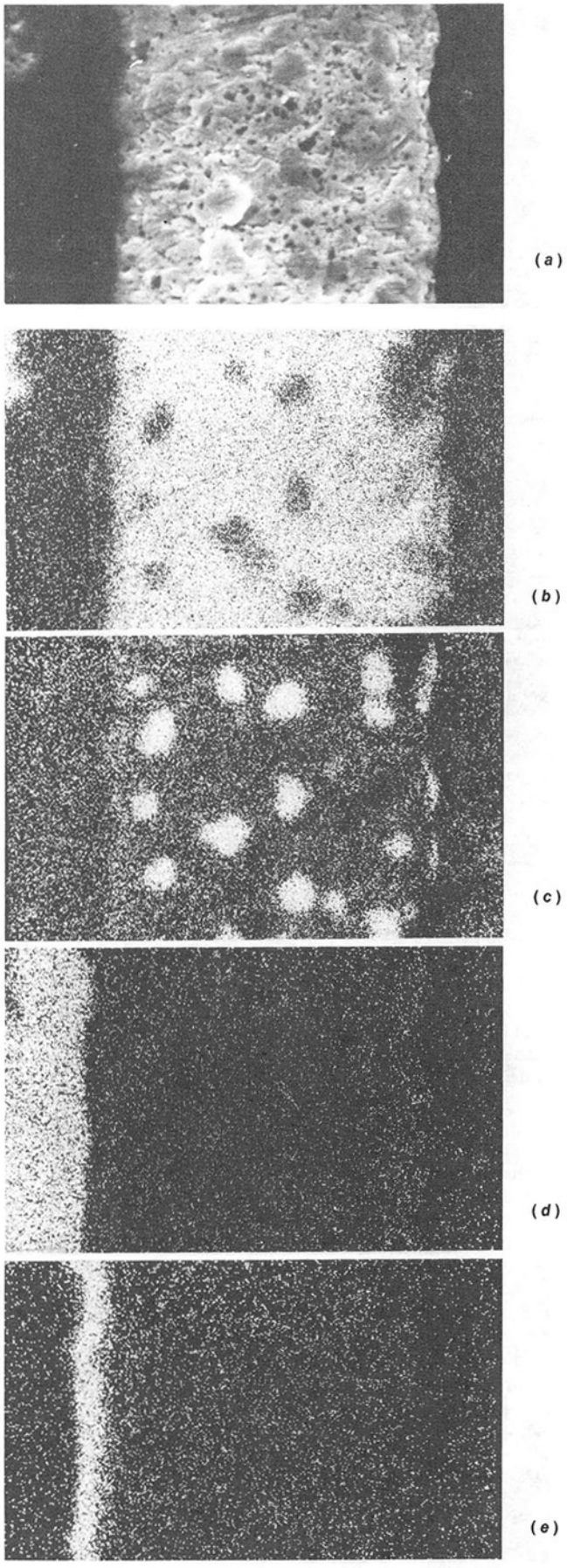

Fig. 5.13 Microsection *(a)* of unused overlay with elemental identification of *(b)* lead, *(c)* tin, *(d)* copper, and *(e)* nickel

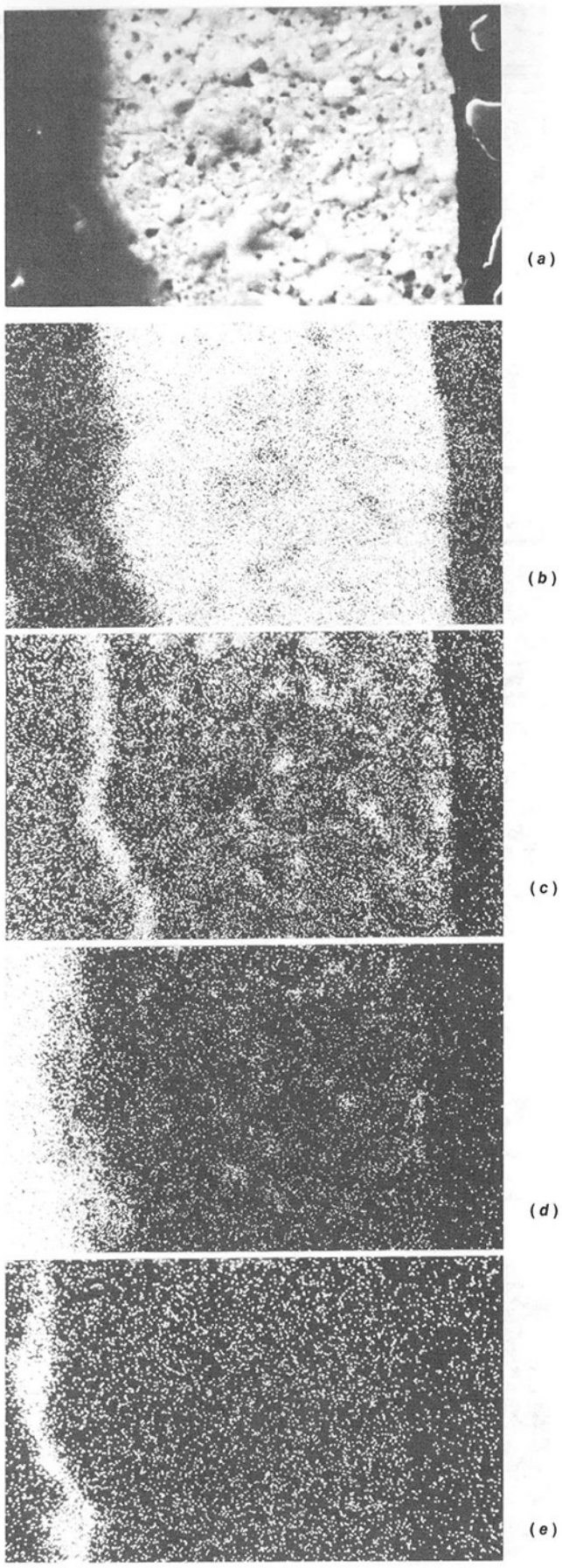

Fig. 5.14 Microsection *(a)* of overlay after 1000 hours at 160°C with elemental identification of *(b)* lead, *(c)* tin, *(d)* copper, and *(e)* nickel

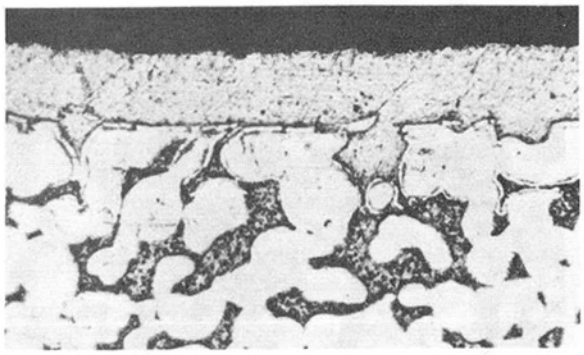

Fig. 5.15 Tin diffusion resulting in deformation of lining lead

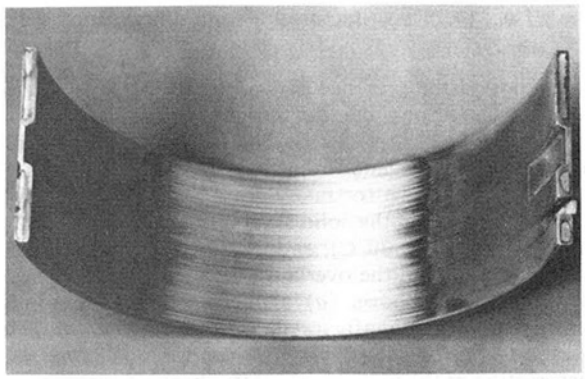

Fig. 5.16 Extensive wear arc through the nickel interlayer

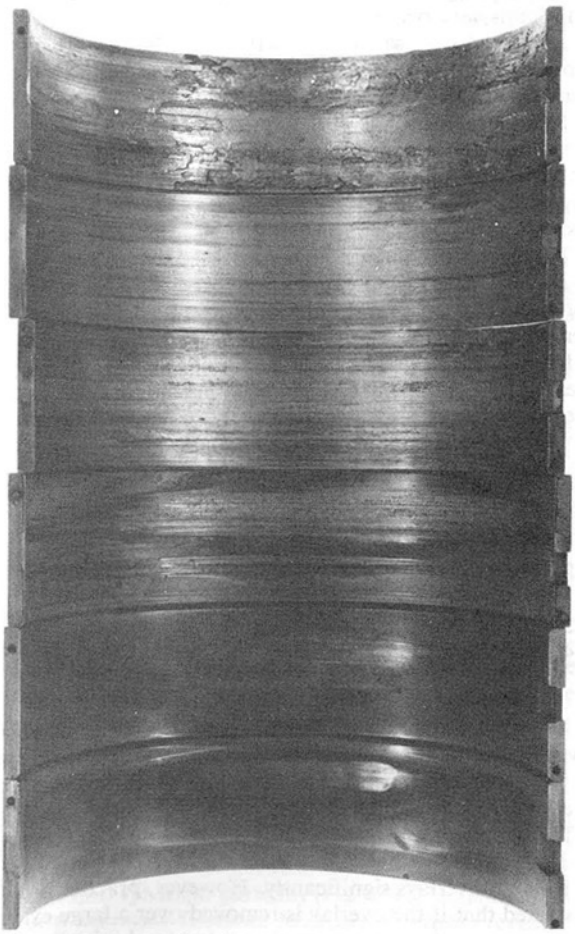

Fig. 5.17 Progressive damage related to the nickel interlayer

tin), seizure can be readily initiated when other adverse environmental conditions (e.g., debris) are present.

Bearings with large arcs of exposed nickel-based surfaces are particularly prone to seizure if refitted after removal, which often occurs because of their good visual appearance. Unexplained bearing seizures have also been experienced, totally unrelated to overhauls or bearing examinations, and deductions have been made on the basis of circumstantial evidence. The first argues that, as the exposed nickel surface wears through, the crank journal surface becomes roughened and in turn causes further wear of the bearing; the second argues that severe scoring of the bearing occurs because the worn nickel cannot be embedded by adjacent nickel.

The first of these deductions is supported by Fig. 5.16, in which the overlay and most of the nickel had been removed over an arc of 110 deg. Nickel was only present over relatively narrow arcs at each end of the wear zone and analysis showed no ferrous contamination except at each end of the wear zone. The surface of the worn region contained numerous circumferential scores. Surface finish measurements of the shaft revealed this to be N8, corresponding to the worn bearing, and N4 outside the bearing area, thus strongly implying that the exposed area that had worn through the nickel had caused the shaft roughening.

The second deduction is supported by the sequential photographs in Fig. 5.17, which shows how the bearing surface becomes progressively damaged following initial wear pattern due to a distortion effect in the assembly. The second bearing in the sequence indicates the mechanism of progressive breakdown by displaying fine tears through the exposed zone of nickel interlayer.

The two examples shown were of tin-aluminum lined bearings, for which the addition of an interlayer is currently an essential part of overlay plating, although problems have also been experienced with lead-bronze linings and a nickel interlayer. A paper by Baxter and Rawlings [7] is a typical account of the way in which an ongoing service problem was overcome by simply eliminating the nickel interlayer. It was pointed out earlier that this option is available with sintered lead-bronze linings but not with cast.

Thus the incorporation of a nickel interlayer needs to be a compromise between extending overlay corrosion life and avoiding potential seizure problems when overlay wear occurs. In cases where overlay is lost relatively quickly regardless of bearing metallurgy, it may be beneficial to omit the interlayer.

7 Overcoming the Rapid Wear Problem

The initial response to the accelerated overlay removal phenomenon was to establish the extent to which oil additive formulation could be effective. However, the main thrust of the oil companies has been to ensure particularly that the sulfur contamination of lubricating oils is neutralized before it combines with moisture to form sulfuric acid. Oil formulation cannot eliminate the particulate contamination of oils by combustion products, nor avoid ultimate degradation and oxidation of the lubricant.

Improvements to and maintenance of the filtration of the lubricating oil system are clearly beneficial. Poynton and Crowley [8] demonstrate the dramatic improvement in overlay life to be achieved by centrifugal filtration in addition to full flow element filtration. They also demonstrate the importance of the correct additive combination in the lubricant, in this instance ensuring a sufficiently high dispersancy rating.

Glacier has approached the problem from a metallurgical viewpoint and improved existing materials; it has also developed new materials to suit current diesel and gas engine fuels and conditions. The new generation of materials is expected to be more capable of withstanding future fuels, operating conditions, lubricating oils, and levels of maintenance.

8 Current Status of Bearing Materials

8.1 Unplated AS15. The lining is 20 percent reticular tin aluminum, roll bonded onto a steel backing. It is a well-established material that has been sufficiently improved to be of real value in the context of modern fuels; improvements in engine build and lubricating oil filtration have been of further assistance.

Figure 5.18 shows an AS15 bearing from a large medium-speed engine after 40,000 hours operation with heavy fuel. This bearing is one of a complete engine set, which were all in excellent condition and exhibited no measurable wear at the conclusion of the field tests. Recent advances in the oil additive formulations and fuel treatment should enable this reticular tin aluminum to perform more satisfactorily in landfill gas applications than the standard copper-lead bearings currently in use.

8.2 AS104. Developed from AS15, the lining consists of 10 percent reticular tin aluminum with finely dispersed silicon (4 percent) particles and 1 percent copper as a solid solution hardener. The fatigue strength of this material is slightly greater than that of AS15. It does not require an overlay for either surface property enhancement or corrosion resistance, and therefore is not prone to rapid overlay wear with consequential exposed interlayer problems.

The resultant structure of the material gives it outstanding surface properties, which include a shaft polishing effect, probably due to the silicon particles, and a considerably greater resistance to damage under seizure conditions. This was particularly demonstrated in tests against nodular cast iron shafts. Figure 5.19 shows the extent of damage exhibited by AS104 and overlay plated lead-bronze bearings when subjected to the same dynamic load pattern on an engine simulating test machine.

Generally the corrosion resistance, low wear rate, seizure resistance, and high fatigue strength makes this material very suitable for heavy fuel engines.

Various short and long term tests have been carried out in medium speed diesel engines, and for several years one particular engine builder has specified the material in standard production for a highly rated 250 mm bore engine. There have been no adverse reports, and some of the earlier bearings fitted will now have operated in excess of 20,000 hours. Figure 5.20 shows the condition of a crankpin bearing after an 11,000-hour field trial in a 400 mm bore engine; this was typical of the complete set of main and crankpin bearings, all with immeasurable wear.

8.3 "Mosaic." Some bearing manufacturers have also adopted an approach different from that of utilizing a suitable existing material or designing a new material, wherein the nickel surface is interrupted in order to avoid exposure of large areas of nickel in cases where the overlay is rapidly removed.

The Glacier solution is the "Mosaic" bearing, in which the bore surface is produced with variable indentations. This surface is overlay plated in the normal manner, including an interlayer, and is bored to produce a finely distributed mosaic pattern of lining and overlay, separated by thin borders of nickel. Figure 5.21 shows that this characteristic is maintained throughout the wear life of the bearing.

Following very successful preliminary testing in small high-speed diesel engines for several periods of 1000 hours duration, prototype testing has continued in a range of medium-speed diesel engines of up to 280 mm bore, with wear rates and visual appearances superior to those of the standard bearings. The process can readily be applied to any lining material and, while no increase in fatigue strength is claimed, there have been instances during preliminary testing where anticipated fatigue failures did not occur.

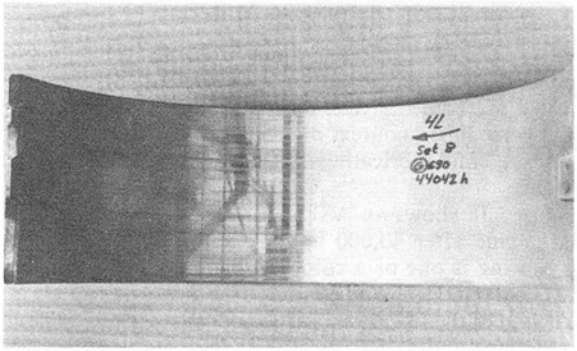

Fig. 5.18 Condition of unplated AlSn20 (AS15) medium-speed engine bearing after 40,000 hours operation

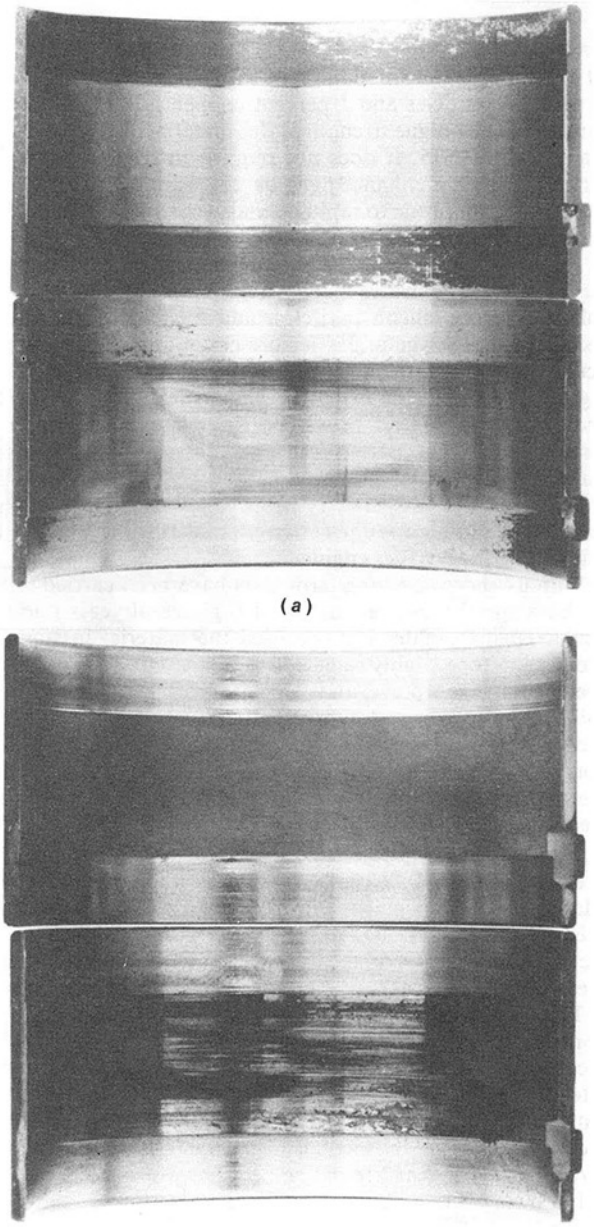

(a)

(b)

Fig. 5.19 Performance of *(a)* AlSn 10Si4 (AS104) and *(b)* overlay plated lead-bronze on seizure test rig

The main objectives of the "Mosaic" principle are reduced wear and improved compatibility throughout the life of the bearings, leading to increased life while retaining the benefits of overlay plate.

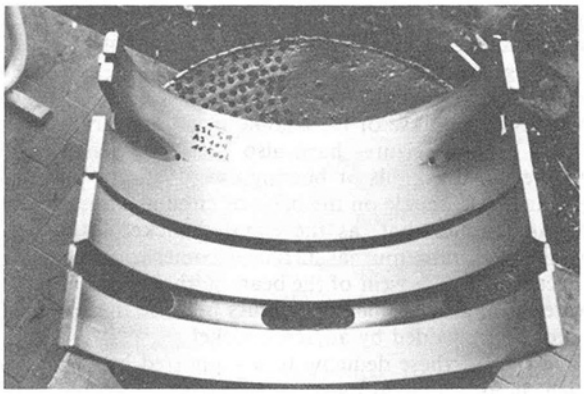

Fig. 5.20 Condition of unplated AlSn 10Si4 (AS104) medium-speed engine bearing after 11,000 hours operation

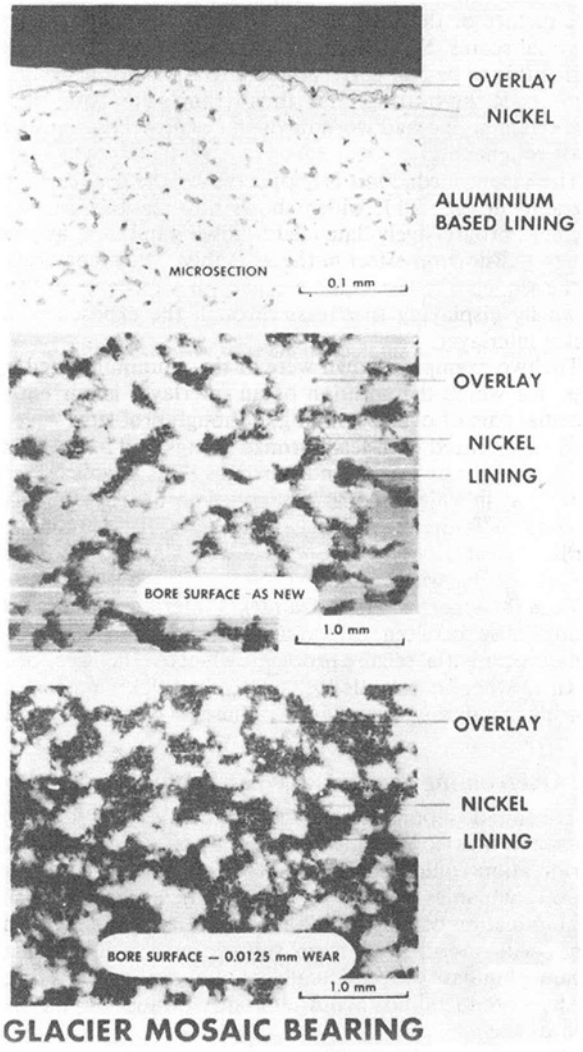

Fig. 5.21 Glacier "Mosaic" bearing microsection and surface appearance

8.4 Overlays. The standard overlay plate specification for medium speed engines now contains 14–18 wt% tin, 1–3 wt% copper, and the remainder lead, to take advantage of the corrosion resistance of the increased tin content and the higher wear resistance created by the copper content. This also avoids the potential difficulties associated with tin contents above 20 percent and undue interaction between the tin and copper.

The specification has been in use for over 8 years, and was initially adopted to overcome specific instances of rapid overlay

removal as previously described; it has gradually become more widely utilized to the extent that it is now supplied as standard.

An alternative for aluminum based linings is a plain tin overlay. This has the benefit of being totally corrosion free in a normal engine environment, with extremely good wear and cavitation erosion resistance. To date, this specification has only been supplied for development and field evaluation, and the longest known testing period has been 3000 hours. In spite of this, the full-scale engine testing has confirmed the projected benefits.

Where extensive overlay loss cannot be overcome in bearings lined with sintered lead–bronze, the option is available of omitting the nickel interlayer and thus of avoiding the potential consequences associated with its exposure. This solution is standard practice in several modern, highly rated medium-speed engines with bearing operating periods in excess of 20,000 hours.

9 Future Developments

Work will continue on the development of aluminum based lining materials to increase their fatigue strengths, while maintaining their excellent corrosion resistance and ability to operate without an overlay plate. In this respect AS124, which is a development of AS104, is already available in automotive bearing sizes. Compared with Glacier AS15 material, AS124 shows a fatigue strength improvement of 20 percent but is significantly harder. However, there is scope for further development.

The major advance with overlay plating will most probably occur with sputter coating (or vacuum deposition). Several bearing manufacturers are already developing the process and investigating different coating materials. T&N Technology is well to the forefront of this development and has already investigated a range of potential coating materials. Based on a combination of fatigue strength and seizure resistance, the most promising example so far is a coating of AlSn40. Development of the detailed structure of this and other alloys will continue.

Conventional electroplating will be further developed, particularly with the purpose of eliminating the interlayer on aluminum-based alloys but also with a view to increasing fatigue strength and wear resistance.

Acknowledgments

The authors express their appreciation to Waukesha Engine Division for their cooperation in the "Mosaic" Bearing Project, and particularly to Dr. Warren Snyder, Co-inventor, for support in the preparation of this paper and in the work on copper–tin spheres in overlays.

References

1 Perrin, H., "Bearing Problems in Internal Combustion Four-Stroke Rail Traction Engines," *7th Int. Cong. Combustion Engines (CIMAC)*, London, 1965, pp. 763–792.

2 Semlitsch, M., "Diffusion Process in Multilayer Plain Bearings Using Electron Microprobe Analysis," *5th Int. Cong. X-ray Optics and Microanalysis*, Turbingen, 1968, pp. 485–494.

3 Semlitsch, M., "Comparative Microanalysis Investigations on Multilayer Bearings Using Atomic Absorption, X-Ray Diffraction and Electron Probe," *Mikrochim. Acta*, Vienna, 1970, Supplement IV, pp. 157–169.

4 Eastham, D. R., and Crooks, C. S., "Plating for Bearing Applications," *Trans. Inst. Metal Finishing*, Vol. 60., 1982,

5 Karlsen, J. K., Brunborg, O., and Bulukin, J., "Bearing Damages in Trunk Diesel Engines," Det Norske Veritas Report No. 87-1031, 1987.

6 Wilson, R. W., and Shone, E. B., *The Corrosion of Overlay Bearings*, 1969, pp. 788–794.

7 Baxter, A. S., and Rawlings, R. E., "The Design and Development of the MB190: A High Speed Diesel Engine Based on Medium Speed Principles," Inst. Diesel and Gas Turbine Engineers, Publication No. 428, 1985.

8 Poynton, W. A., and Crowley, J. C. T., "Design and Development of Medium Speed Diesel Engines for High Reliability," Inst. Diesel and Gas Turbine Engineers, Publication No. 440, 1987.

3500 SI Engine Application Flexibility

R. L. Havran
Caterpillar Inc.,
Mossville, IL 61552

The 3500 Spark-Ignited Engine is a 170 mm bore by 190 mm stroke family including 8, 12, and 16-cylinder models rated at 54 bkW per cylinder. Initial production included low-emission versions of the 12 and 16 cylinder engines in 1986. This paper describes basic combustion and attachment developments that have broadened the product offering for improved performance in more varied fuel and high-temperature cogeneration applications.

Introduction

The initial 3500 SI engines were offered in 1986 in a turbocharged and aftercooled low-emission (LE) version with a single compression ratio. Continued development of these engines has focused in several areas with major emphasis on replacing applications of the G379, G398, and G399—159 mm bore by 178 mm stroke—which have been applied successfully in gas compression, electrical power generation, and oil field applications since the early 1960s [1]. This previous family of engines will be referred to in this paper as the 6.25 bore family. The developments described in this paper include naturally aspirated stoichiometric (NA) and turbocharged and aftercooled stoichiometric (TA) combustion versions, broader fuel tolerance, and elevated jacket water temperature configurations for making steam in cogeneration applications. Development continues on higher speed ratings and controls for increasingly stringent emissions regulations.

Objectives

1 Provide TA and NA combustion configurations of the 3500 SI engine to burn gaseous fuels ranging from propane (approximately 2300 Btu/scf) to pipeline quality natural gas (approximately 900 Btu/scf).

2 Broaden LE combustion to burn gaseous fuels ranging from propane to digester/landfill gas (approximately 500 Btu/scf).

3 Meet fuel consumption targets of 7000 Btu/bhp-h for LE combustion and 7500 Btu/bhp-h for TA combustion, both on pipeline quality natural gas and propane.

4 Provide capability of the 3500 SI engine to use the jacket cooling water to make steam in cogeneration applications.

Fuels

Gaseous spark-ignited engines are expected to burn a broad variety of fuels. One way of ranking these fuels is by lower heating value (LHV) per standard cubic foot (scf). However, detonation is the limiting parameter for carbureted spark-ignited engines and detonation tendency varies for constant LHV depending on composition of the fuel. Caterpillar has adopted a different ranking called the methane number that was developed in the early 1970s [2]. The methane number is a method to calculate the detonation tendency of a gaseous fuel mix and compares it to that of a methane and hydrogen mixture. Pure methane has a member number of 100 and pure hydrogen has a methane number of 0. A 50/50 mixture of the two has a methane number of 50. Figure 1 shows a plot of LHV versus

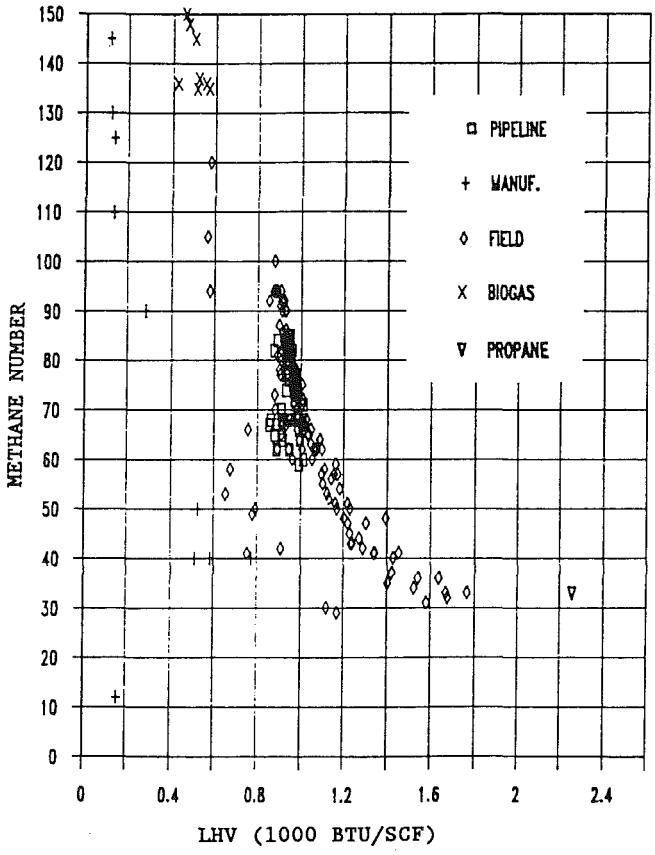

Fig. 1 LHV versus methane number

Contributed by the Internal Combustion Engine Division and presented at the Twelfth Annual Fall Technical Conference, Rockford, Illinois, October 7–10, 1990. Manuscript received by the Internal Combustion Engine Division July 1990.

methane number for a variety of naturally occurring and manufactured gases that was calculated based on the procedure outlined in [2].

SI engines are typically used for electrical power generation (EPG) and gas compression applications. Fuels used in EPG fall into three categories:

1 pipeline quality
2 propane, either as a primary or backup fuel
3 landfill/digester gas

Fuel for gas compression is typically field gas, which has a broad Btu range depending on composition. These four fuel types were targeted for combustion development. Their LHV and methane number ranges are shown in Table 1. Fuels with methane numbers higher than landfill/digester represent primarily a fuel/air ratio problem to obtain a proper combustion mix. For methane numbers lower than propane, derating or special lower compression ratio pistons woud be required.

Combustion

3500 SI engines were initially offered in LE versions with 10:1 compression ratio pistons. This configuration offered pipeline and limited field gas capability and was developed to run low-Btu landfill gas [3]. To replace the 6.25 bore family fully, NA and TA stoichiometric versions were planned. These combustion technologies are finding more limited application in developed countries because of increasingly stringent emission laws. However, NA and TA stoichiometric do find application in sites using catalytic converters and developing countries where less sophisticated engines are desirable. In addition, more flexibility was desired for LE combustion to provide better fuel consumption over different ranges of fuel methane number. The initial strategy to cover these various options is shown in Table 2.

TA Development

Since NA combustion does not push thermal limits as severely as TA versions, the strategy verification was focused on the TA engine. Experience and screening tests showed that two changes were required to the exhaust system. The first was removal of the stainless steel lining that provides an air gap between the exhaust and main exhaust chamber, as shown in Fig. 2. While this lining is needed to minimize exhaust energy losses for LE versions, additional heat rejection to the manifold was required to meet turbocharger temperature limits for the stoichiometric engines. The second change required was a larger capacity wastegate. While providing sufficient capacity for LE versions, the bypass area was too small to provide acceptable power limiting for TA ratings.

With these modifications, exhaust temperature measurements still showed the low compression ratio proposal to be unacceptable at target TA ratings. The backup plan that was pursued was an early inlet closing (EIC) cam and medium compression ratio piston. As depicted in Fig. 3, an EIC cam makes the combustion charge ignite like a lower compression ratio configuration by cooling the charge by expansion prior to compression. However, on the expansion stroke, the combustion gets the benefit of the higher geometric compression ratio in better fuel consumption and lower exhaust temperatures. As shown in Fig. 4, exhaust temperatures with the EIC camshaft and medium compression combination met the exhaust temperature goal and were chosen for further development.

A primary interest throughout the initial TA screening work was to provide the maximum rating and fuel flexibility with a minimum number of unique combustion hardware items. Once the EIC/compression ratio question was resolved, the finalized combustion strategy was revised as shown in Table 3.

Table 1 Fuel versus methane number

	LHV, Btu/SCF	Methane # Range
Landfill/Digester	450–600	130–160
Pipeline	850–1000	65–90
Field Gas	800–1600	25–85
Propane	2350	30–35

Table 2 Initial combustion strategy

C/R	Combustion	Methane #	Application
High	LE	65–150	pipeline, landfill/ digester
Medium	LE	30–100	pipeline, propane, field
Low	TA/NA	25–100	pipeline, propane, field

LE Development

The strategy to provide two different compression ratios for LE combustion was driven by three primary factors:

1 It was believed that a higher compression ratio piston would improve combustion stability on landfill/digester gas applications.

2 Improved fuel economy could be realized for high methane number applications with a higher compression ratio.

3 Propane backup capability in EPG applications and lower methane number field gas applications requiring low emissions combustion required a lower compression ratio to maintain competitive ratings.

Second generation landfill engines, incorporating the higher compression ratio (11:1) pistons and production version J-gap precious metal spark plugs described in a previous paper [3], have confirmed improved combustion stability over the pre-

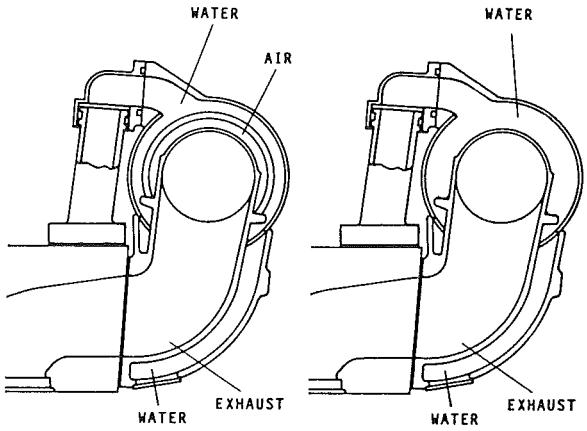

Fig. 2 3500 SI water-cooled manifolds

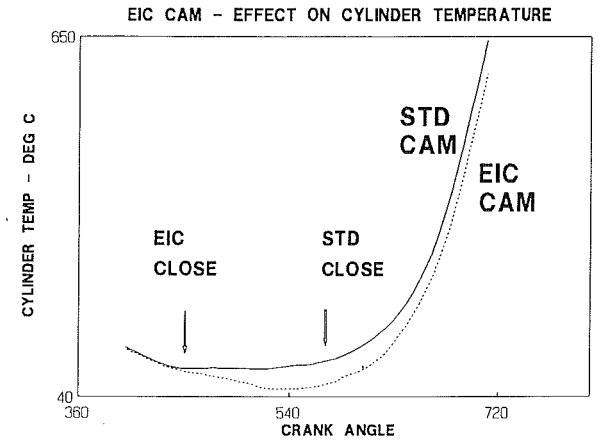

Fig. 3 EIC cam; effect on cylinder temperature

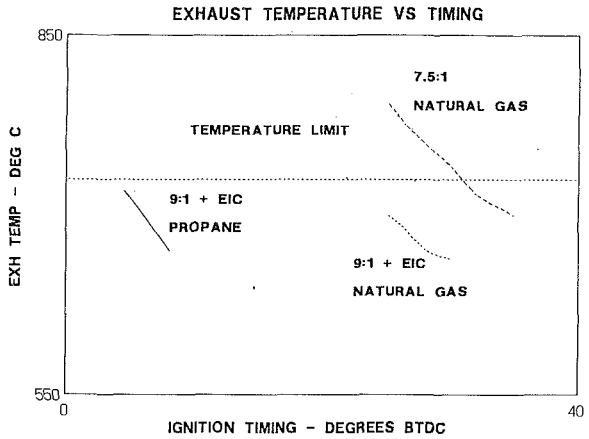

Fig. 4 Exhaust temperature versus timing

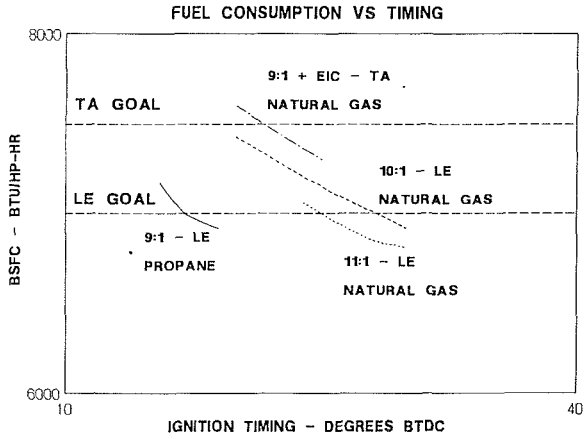

Fig. 5 BSFC versus timing and C/R

Table 3 Finalized combustion strategy

C/R	Cam	Combustion	Methane #	Application
11:1	STD	LE	65–150	pipeline, landfill/ digester
9:1	STD	LE	30–100	pipeline, propane, field gas
9:1	EIC	TA	25–100	pipeline, propane, field gas
9:1	STD	NA	25–100	pipeline, propane, field gas

Table 4 Power variation versus C/R and spark plug (3516 SI LE @ 800 bkW)

Piston C/R	Spark Plug	Power Variation, kW
10:1	STD	+/−50
11:1	J-GAP	+/−25

vious 10:1 version. Landfill engines typically power generator sets and are paralleled to the utility grid. Combustion instability in this application manifests itself as power fluctuations as engine speed is held constant. Table 4 shows a comparison of demonstrated power fluctuations with the two compression ratio/spark plug combinations.

Performance screening of the high (11:1) compression ratio piston on pipeline fuel confirmed the fuel economy improvements for the 11:1 piston compared to 10:1 predecessor. Likewise, the ability to maintain rating and emission goals with the 9:1 piston were demonstrated with propane fuel. These performance comparisons are shown in Fig. 5. Also shown is fuel consumption performance for the TA engine for comparison. Based on these performance results component and engine development work with these pistons was continued.

LE Cogeneration Application

Dramatic improvements in the overall fuel efficiency of a gas engine are realized when the thermal heat rejection of the jacket water, oil cooler, and exhaust can be recovered in a usable form. A typical method employed by the 6.25 bore predecessor of the 3500s was flashing the jacket water circuit to steam in an ebullient system. A schematic of this system is shown in Fig. 6.

In the ebullient system no jacket water pump is needed as coolant flow is sustained by convection. A special riser exhaust manifold is used to facilitate the convective flow and prevent steam pocket formation in this high heat flux, low static head area of the engine. While stringent water treatment guidelines

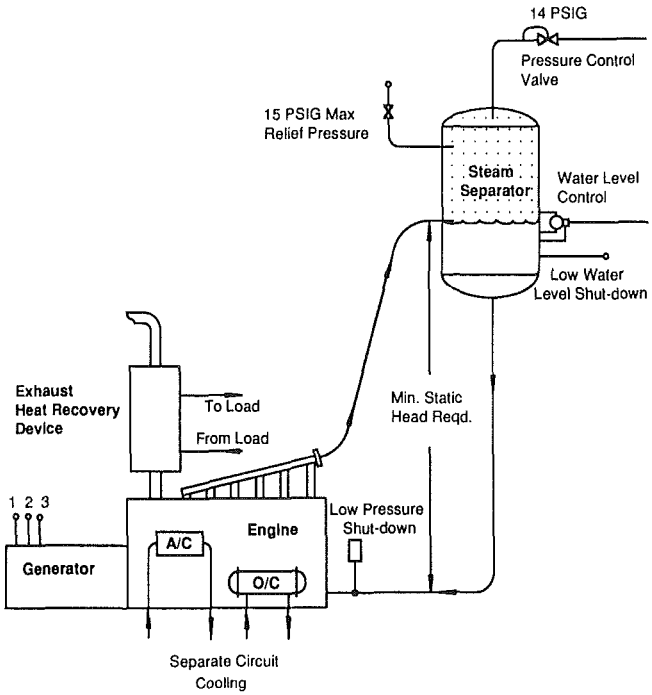

Fig. 6 6.25 bore ebullient schematic

are required to prevent deposit damage to the engine, using the jacket circuit directly provides the lowest engine operating temperature for a given quality of steam because no secondary heat exchanger is required. When properly applied these systems have been very successful with thermal shock from hot shutdowns being the most prevalent application problem. More recent installations have incorporated an auxiliary pump to provide forced flow for startup and shutdown conditions.

Development of cogeneration capability for 3500 SI LE built on the 6.25 bore experience. A solid water system like that shown in Fig. 7 with an external pump was developed for several reasons. The first was to provide more installation flexibility by reducing the height requirement for heat recovery equipment. Second, by having an external pump, hot engine shutdowns would not cause thermal shocks to the engine by formation of localized steam pockets and coolant conditioners can be kept in suspension by providing circulation while the engine is down for other reasons. Finally, the major job of developing an air shielded riser exhaust manifold was avoided. Using the jacket water as part of the steam circuit was continued because of successful water treatment guidelines and

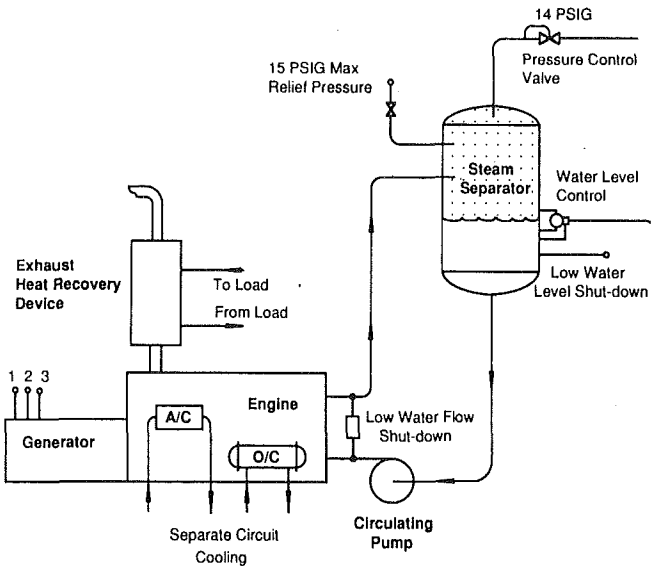

Fig. 7 3500 cogeneration schematic

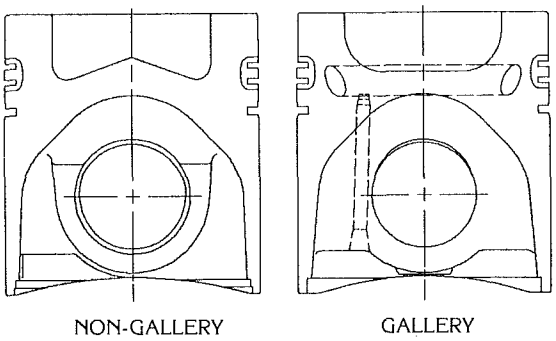

Fig. 8 Gallery versus nongallery piston: cross section

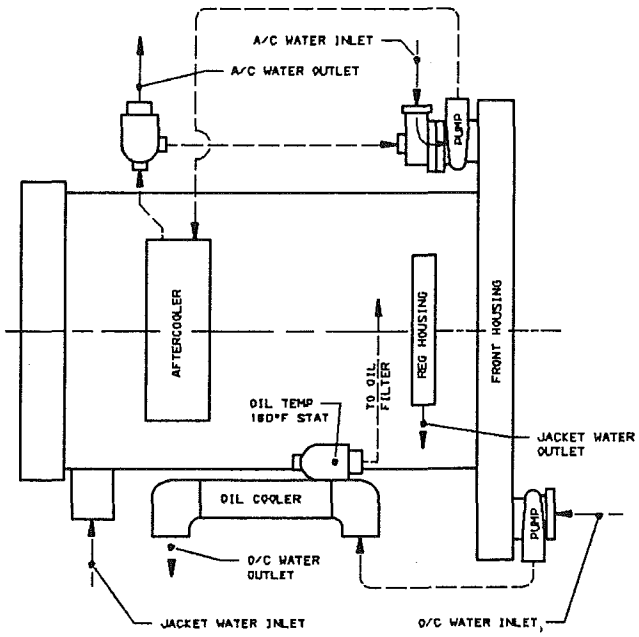

Fig. 9 Three-circuit cogen schematic

minimizing peak jacket temperatures for a given steam pressure.

Piston endurance testing at cogeneration conditions showed

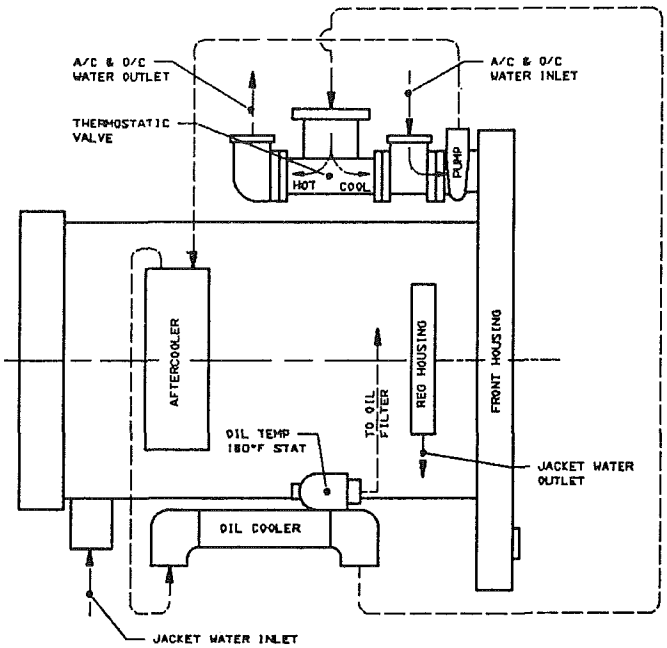

Fig. 10 Two-circuit cogen schematic

that the increased ring temperature caused by the elevated jacket temperature caused unacceptable land and ring deposits and potential stuck rings. Anticipating this possibility, pistons with a cooling gallery behind the ring band had been procured for evaluation. Figure 8 shows a comparison of the then production 10:1 nongalleried piston and the 11:1 galleried version. Caterpillar has had good success applying this piston design since first production of the 3500 diesel engine. Finite element modeling experience of diesel gallery designs applied to the SI piston gave a high confidence of success for subsequent development. Comparable squish characteristics to the nongalleried SI design and proportional cross sections for SI versus diesel pressure and thermal load were maintained in the galleried SI design.

To maximize versatility of the cogeneration feature on 3500, two different water circuitry options are offered. Figure 10 shows the two-circuit system where the aftercooler and oil cooler are flowed in series with a thermostatic control to maintain proper temperatures. This type of system is best for applications where low-temperature cooling is plentiful and no use for the oil cooler heat rejection can be found. The three-circuit system shown in Fig. 9 will be used where low-temperature cooling is at a premium or a use for the oil cooler heat rejection, such as heating water, is available.

Reliability Development

Insuring that reliable products are developed and provided to customers continues to be a prime objective at Caterpillar. A tool that has become widely used is Product Evaluation of Reliability Growth or PERG. This tool is a probabilistic model that calculates the development time required to demonstrate a given level of product reliability and serves as a management tool to provide an objective method for evaluating a product's fitness for production. Without going into great detail, the time required to develop a product depends on an objective assessment of "new content," which is a weighted average of system changes compared to existing products and the desired level of demonstrated reliability.

PERG evaluations were conducted for the 3500 TA stoichiometric engine and the 11:1 LE cogeneration engine. Figures 11 and 12 show how the predicted reliability of these engines developed. Steps upward on the chart indicate a failure incident. Steps downward indicate that validated fixes to one or

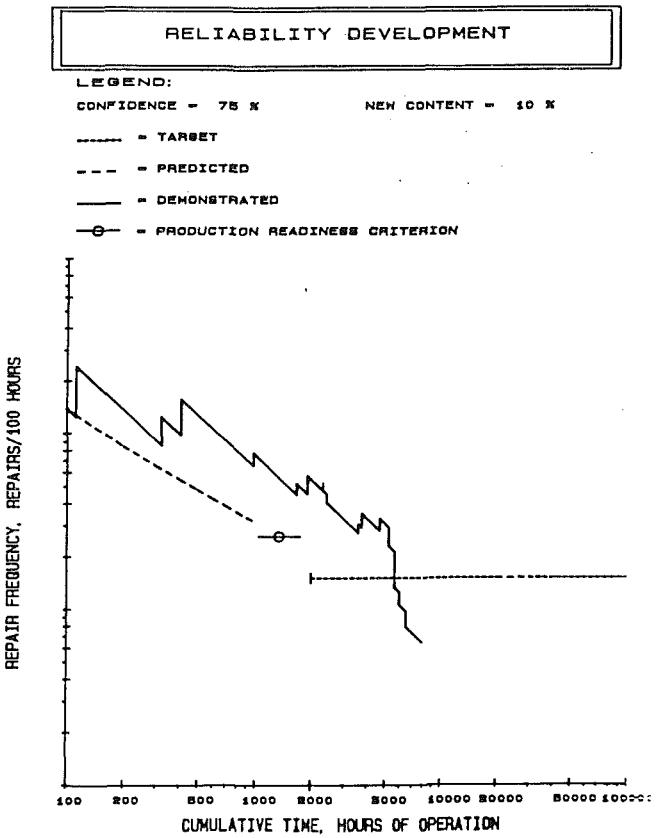

Fig. 11 TA stoichiometric PERG chart

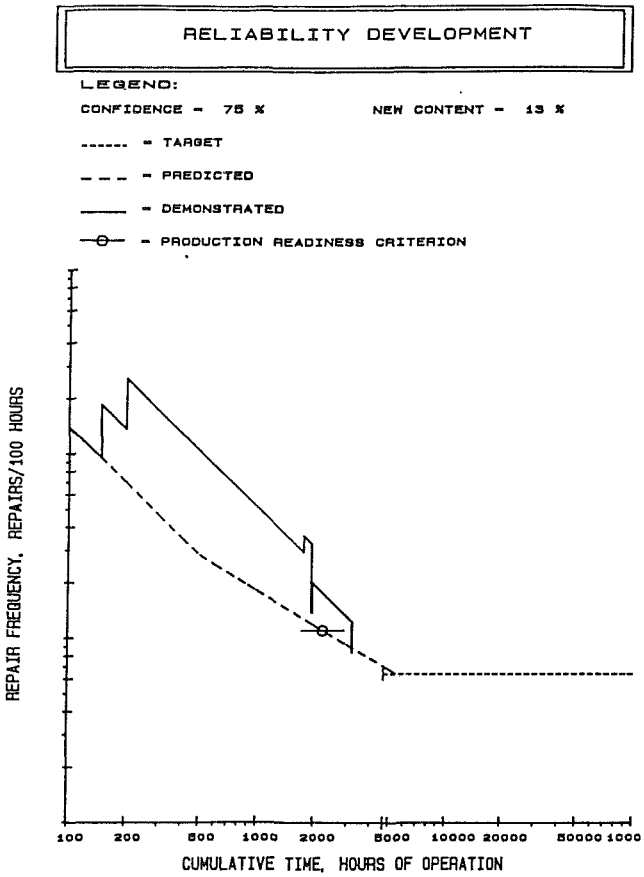

Fig. 12 LE cogen PERG chart

more problems have been implemented so that the specific failure can be edited out. The products were not put into production until the reliabiity criteria had been met.

Close field follow production units are being evaluated using the same analysis to confirm reliability results from production iron in customer applications. While the *new content* of these engine programs was relatively small, problems with wastegate fits, joint leaks, and piston ring wear were uncovered and resolved. A special detonation test was run on the TA stoichiometric engine to assess the robustness of the galleried piston compared to the flat top 6.25 bore it was effectively to replace. 500 hours of endurance at elevated detonation levels confirmed that the cooling gallery design piston has significantly improved heat dissipation characteristics for detonation tolerance compared to a nongallery design.

Conclusions

Over 10,000 hours of combustion, durability, and reliability testing have validated a combustion strategy for 3500 SI engines in three basic combustion configurations. Fuel consumption targets of 7000 and 7500 Btu/bhp-h for LE and TA ratings, respectively, have been demonstrated. The ability to burn fuels ranging from propane to landfill gas, while maintaining ratings, has been verified. Steam cogeneration capability has been applied at several sites. Ongoing production experience in addition to the extensive lab work continue to support the conclusion that the 3500 SI is a worthy successor to the 6.25 bore family of spark-ignited engines.

References

1 McClung, C. L., "Design and Development of the Caterpillar 3500 Series Spark-Ignited Engine Family," *New Developments in Large Bore Engines*, ASME, New York, 1985, pp. 47–57.

2 Leiker, M., et al., "Evaluation of Antiknocking Property of Gaseous Fuels by Means of Methane Number and Its Practical Application to Gas Engines," ASME Paper No.72-DGP-4, Apr. 1972.

3 Macari, N. C., and Richardson, R. D., "Operation of a Caterpillar 3516 Spark-Ignited Engine on Low Btu Fuel," ASME Paper No. 87-ICE-13, Feb. 1987.

A Turbocharger for the 1990s

E. R. Johnson
Cooper Bessemer Rotating Division,
Mt. Vernon, OH 43050

The large-bore engines of the 1970s and 1980s have seen tremendous amounts of technological improvements. The key buzzwords were: "Lower the emissions, and improve the fuel consumption." As we move into the 1990s, we see dramatic improvements in specific outputs along with continued research to further improve emissions and fuel consumption. One of the keys to success will have to be the degree to which the industry responds with improvements in turbocharger performance. In 1985, Cooper Bessemer Rotating Products Division began a program to develop the turbocharger of the 1990s. This paper will describe the development of the CB turbocharger series from concept to early production.

Introduction

In the early 1980s, it became apparent that the product line of turbochargers offered by Cooper Bessemer Rotating Products was beginning to show its age. Demands by our customers for higher efficiencies, increased reliability, and shorter lead times put us on a path to develop a replacement for the ET series of turbochargers.

The turbo of the 1990s must be capable of supporting engines that incorporate very lean combustion, increased scavenging efficiency, higher specific ratings (BMEP), and provide all the above at a lower fuel rate. What this means to the turbo is that it must provide additional compressor output with less energy input to the turbine, at a competitive cost delivered in a shorter time frame, with increased reliability.

A survey of the marketplace shows a strong need for improved turbochargers for two and four-cycle engines in the 600 kW to 13,000 kW range, with BMEPs ranging from 10 to 25 bar. It is this marketplace that the CB turbocharger product line is directed to serve (Fig. 1).

Project Goals

A set of design objectives was formulated in the concept stage of the project to give engineering direction and focus. They are as follows:

1 Improved overall efficiency.
2 High reliability.
3 Reduced production lead time.
4 Competitive cost.
5 User friendliness.

Accomplishments. 1 Actual turbocharger performance improvement exceeded our initial goals by a considerable margin. Total combined turbine, compressor, and mechanical adiabatic static-to-static efficiencies were improved on an average of seven to eight points across all frame sizes. Figure 2 shows typical examples of the improvement achieved in the CB series over the old ET series. Careful attention to the compressor and turbine design has resulted not only in an overall jump in performance, but the efficiency islands are much broader in the flow range and they also cover a much wider range of pressure ratios. This will allow the turbochanger to offer increased output across a much broader range of engine speeds and torque, which results in better emissions and fuel consumption at variable speed and load conditions at the user's level.

2 High reliability was achieved through a conservative design approach coupled with a very comprehensive field development program. From the very beginning of the project, it was decided to conduct all design, layout, and detail drawing work on a Schlumberger Bravo 3 CAD-CAM computer system. Use of the Graphem/IFAD Finite Element Analysis system within the CAD system allowed all rotating and structural components to be carefully analyzed and redesigned in keeping with the conservative design concept. A total of eight field prototype units of various frame sizes were placed in the field and have accumulated approximately 125,000 hours of operation without significant problems.

3 Reduced production lead time was accomplished by reducing the turbo Bill of Material items by 60 percent and

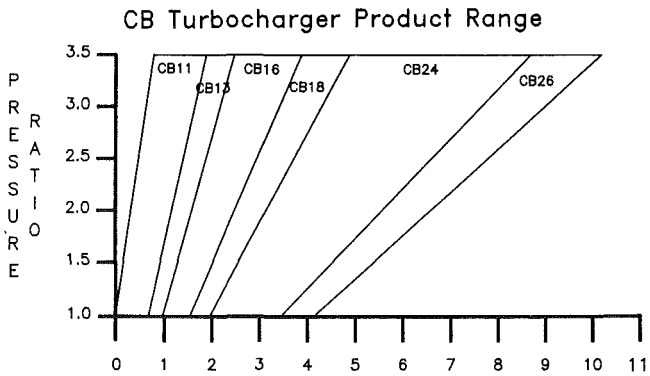

Fig. 1

Contributed by the Internal Combustion Engine Division and presented at the Twelfth Annual Fall Technical Conference, Rockford, Illinois, October 7-10, 1990. Manuscript received by the Internal Combustion Engine Division July 1990.

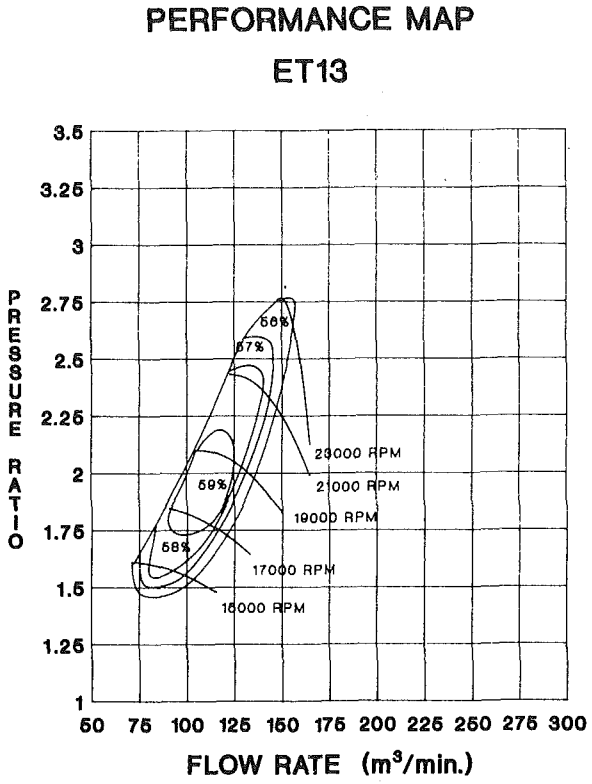

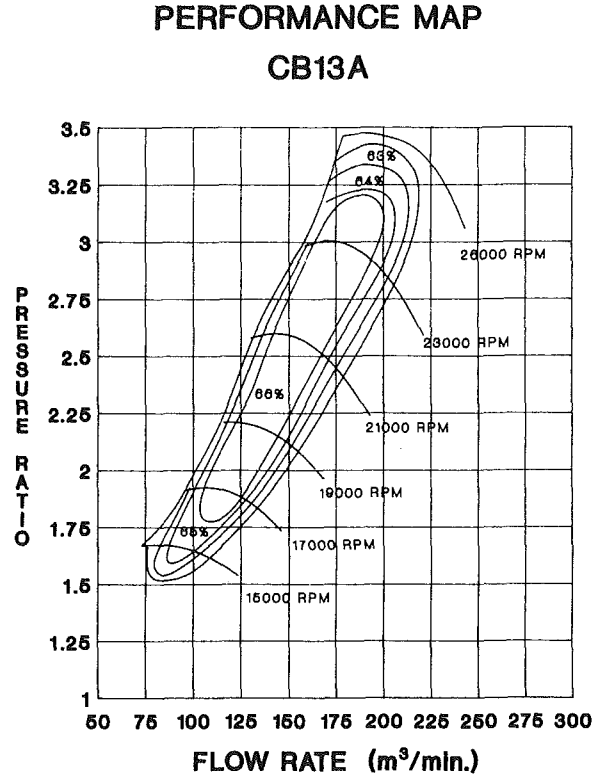

Fig. 2

utilizing the increased compressor performance range to standardize turbo designs. The Bill of Material reduction came about by carefully analyzing each component's function and then consolidating it with another.

The enhanced performance range noted above was used to standardize aero-assemblies. Each aero-assembly is related to a particular engine or group of engines. Based on forecasts by

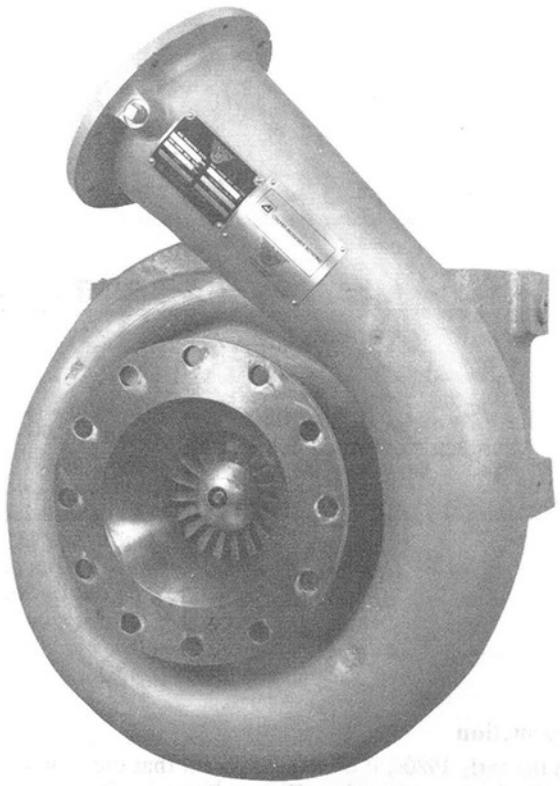

Fig. 3

engine types, a stocking program is put in place, thus allowing extremely quick responses to market change.

4 Competitive cost was accomplished by implementing a Manufacturing Integrated Design philosophy. From concept to final detail drawings, pattern shops, casting vendors, machinists, and assembly personnel were consulted. Each assembly was reviewed and revised, then a production prototype was constructed and tested. After field data were accumulated, the design was reviewed once again prior to final production release. Each step of the way, every component was reviewed to minimize cost without compromising integrity or lead times.

5 The final product (Fig. 3) had to be "user friendly." In the conceptual planning of the new product, a review of the customer's needs took place. The CB turbo product had to accommodate both Inline and "Vee" engines, so single and double discharge compressor scrolls were designed for each frame size. The turbocharger bearing system was designed to use standard engine crankcase oils, thus eliminating the complexity of separate lube oil consoles. Considerable time and effort were put into simplifying the assembly and disassembly of the turbo. Bearing clearances are preset, and only the compressor wheel running clearance must be set by assembly personnel.

Design Highlights

Compressor. The compressor section of a turbocharger (Fig. 4) supplies the combustion and scavenging air to the engine at pressure ratios approaching 4:1.

Two basic centrifugal compressor types are used in turbochargers. One uses a purely radial exit, and the other uses a lean-back at the exit. The radial exit wheel has the advantage of offering the highest head output per specific speed and is the simplest to analyze and control mechanical stresses. The disadvantage to a radial wheel is that the peak efficiency islands occur at or near surge. One of the goals stated above to offer

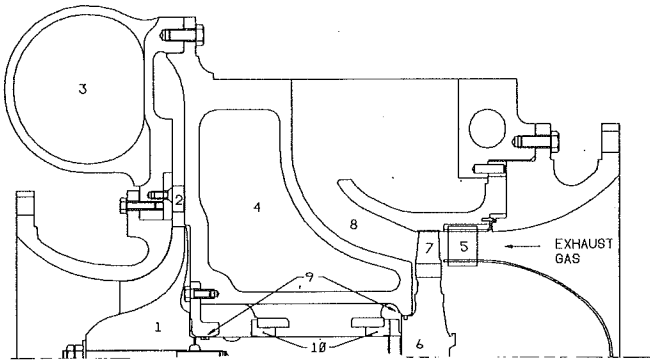

Fig. 4 (1) Compressor wheel; (2) vaned diffuser; (3) discharge scroll; (4) bearing casing; (5) nozzle ring; (6) turbine rotor; (7) turbine blades; (8) exhaust diffuser; (9) piston rings; (10) bearings

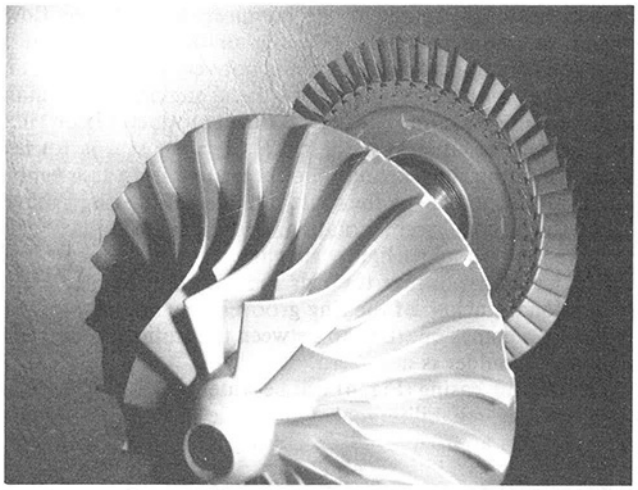

Fig. 5

very broad efficiency islands led us away from a radial to the lean-back design. The CB series of turbochargers uses a lean-back design with intermediate splitter vanes to control the extremes in blade loading required to achieve high efficiency with wide range (Fig. 5). To further extend the performance envelope, a multivane diffuser was added to the flow path immediately behind a short vaneless section at the compressor o.d.

Mechanically, two major items need consideration. The centrifugal stress must be controlled in the compressor wheel bore and at the o.d. where the blade lean-back occurs. The other consideration is avoiding acoustic stimulation of the blade vibratory modes by passing frequency interference with the vane diffuser. Finite Element Analysis was used to analyze the centrifugal stress situation in the aluminum compressor wheel. In keeping with our minimum cost goal, it was decided that the stress levels had to be controlled with adequate safety factor to within the material properties of a casting. The use of a five-axis milled forging was outside the affordable range. In addition to analyzing stresses, FEA was used to determine the wheel backwall contour required to minimize the tip (o.d.) deflection (lean) toward the inlet at speed. A mechanical shaker table was used to determine the blade natural frequencies (Fig. 6). These data were plotted on an interference diagram to confirm the vaned diffuser blade number selection.

Turbine. Once the compressor was selected and the turbo speed identified, a review of turbine designs was conducted. Once again, there are two basic types to choose from: radial inflow and axial (Fig. 7). A radial inflow turbine generally can

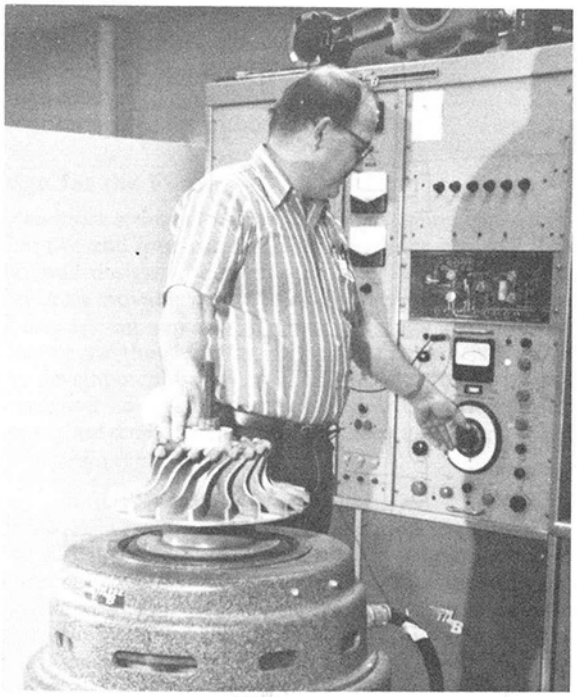

Fig. 6

be manufactured at a lower cost since the turbine wheel is cast, unlike an axial turbo, which uses individually machined blades inserted into a disk. Even with a cost advantage, the radial inflow design lost out to overall thermodynamic efficiency as the selected turbine design for the CB turbo. The radial inflow performance maps mirror a centrifugal compressor map, in that peak efficiencies are isolated to small islands. The trick is to size the turbine aeromap to overlay the peak compressor performance islands precisely. An axial stage turbine has essentially flat efficiency near design. Tip leakage losses can be controlled by abradable seals or with shrouded blades. The CB turbo will use a single-stage axial turbine (Fig. 4) with an upstream stator (nozzle ring) to accelerate the exhaust gas and to turn it to match the turbine blade gas entry angles for low incidence losses. To further enhance the overall stage efficiency, a diffuser is used at the rotor exit. The turbine nozzle ring is a stainless steel fabrication that locates an airfoil section at a precise exit condition determined by the individual engine match parameters ($M\sqrt{T}/P$). To control leakage, the nozzle ring is shrouded. The turbine blades are nonshrouded and held in the disk by a broached fir tree slot. Gas leakage at the blade o.d. is controlled through the use of an abradable seal, which is plasma sprayed into the stationary shroud.

Blade and disk stresses were analyzed using Finite Element Analysis. Particular attention was paid to the fir-tree area and to the shaft-to-disk attachment. The turbine disk is a nickel, high-strength, high-temperature alloy forging, and the blades are a high nickel super alloy casting.

Mechanical. Once the aerodynamic packages were determined, the real work began. It is very easy to overlook the importance of coordinating the aerodynamic design with the rotor dynamics. The best aerodynamic package in the world is useless if the rotor is unstable at speed. Concerns over bearing types, support stiffnesses, synchronous and nonsynchronous whirl, and even interaction between the rotating aero clearances present significant challenges to the design engineer.

Placing the journal bearings outboard of the rotating assembly simplifies the rotor dynamics since a "stiff" shaft response can be used; and it also allows the use of small journal bearing sizes, which result in low friction losses. The drawbacks

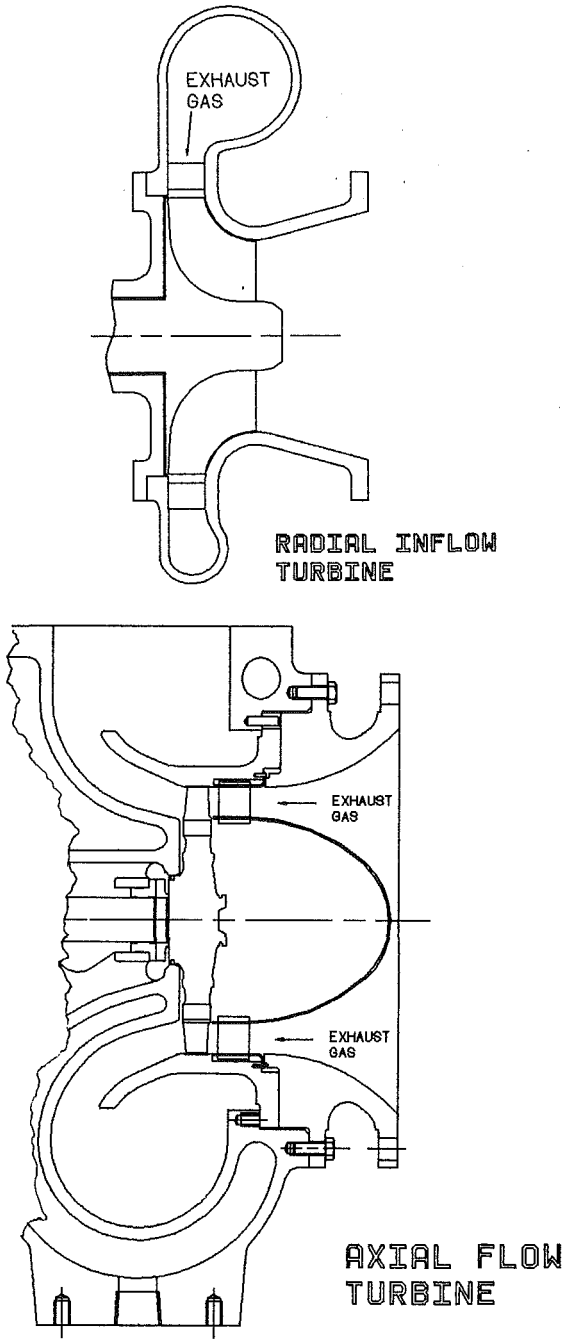

Fig. 7

to this concept are many. Putting the turbine bearing outboard of the rotor on an axial flow turbine places the bearing assembly in the gas path. To enable the bearing to live, a water jacket must surround the assembly. Thermodynamically, this is a disaster; you are taking energy out of the exhaust stream before the expansion stage. This does not lend itself to improved turbine efficiency. This concept also causes significant gas path obstruction and complicates the casing designs with provisions for joint seals.

The decision to put the bearings inboard (Fig. 4) on the CB turbo forced another set of decisions: journal bearing concepts. A first-level decision based on fluid film design versus rolling element had to be made. Use of a rolling element design with standard crankcase quality lubrication would result in very short intervals between turbo overhauls. For the CB turbo, two types of hydrodynamic fluid film bearing systems were tested: a converging lobe cylindrical sleeve bearing and a five-pad tilt pad bearing assembly. Both designs provided adequate oil film stiffness and dampening properties to control shaft vibration when running through the first critical and at other shaft resonance points. The sleeve bearing was less expensive than the tilt pad assembly; however, Cooper Bessemer experience with the large-frame turbine and compressor business has shown the tilt pad design to have an edge on 1/2 speed whirl stability, ruggedness, and overhaul intervals. The tradeoff of stability, ruggedness, and durability over cost made the tilt pad system the choice for the CB turbo.

The thrust bearing utilizes a tapered land design attached to the tilt pad assembly. Extensive testing including load cell, thermocouple embedment, and strain gages was used to confirm adequate design safety factors for all conditions of thrust loading.

To seal the oil system from the compressor and turbine flow path, a labyrinth style seal has traditionally been used. A labyrinth seal uses a series of knife edge steps with high-pressure "seal" air to effect an oil-tight seal. With a turbocharger, the high-pressure air source is the compressor discharge flow. Again, thermodynamically, bleeding air that has had significant compression work done to it is not very efficient; plus in some cases at very light loads on a diesel engine, the air manifold can be a vacuum. For the CB turbo product, piston rings (Fig. 4) will be used as a shaft seal. A tight seal is formed when the piston ring expands into the seal housing at assembly and is located axially by the shaft shoulder of the ring groove. When the turbocharger is rotating, the ring remains stationary and the shaft shoulder lightly rubs the ring as the thrust load shifts the rotor position towards the compressor. The entire dimensional stackup of the ring grooves is such that when the thrust load comes on, the gap between the stationary ring and the shaft shoulder is near zero.

The bearing casing (Fig. 4) will be water jacketed in keeping with the high reliability goal. Four-cycle engine turbine inlet temperatures approach 700°C. During unavoidable hot shutdowns, the possibility of oil coking due to heat soak is ever present in the turbine end of a turbocharger. By going to a water jacket around the bearing cavity, a high percentage of the heat soak will be transferred to the water jacket, thus avoiding premature maintenance on the bearing components.

Field Development. Many hours of development testing took place on a gas-fired test stand with the prototype turbos. Tests were run to evaluate aerodynamic performance, rotor dynamic response, thrust loads, etc.; but there is no substitute for field exposure to accumulate durability data. Below is a summary of the installations:

Installation #1
2) 6 Cyl/2-Cycle Integral Engines
(355 mm Bore/330 rpm/1000 kW)
Installed 2/86
Continuous service without problems.

Installation #2
1) 8 Cyl/4-Cycle Engine
(254 mm Bore/1000 rpm/1120 kW)
Installed 6/86
Continuous service since 3/87 without problems.

Installation #3
1) 8 Cyl/4-Cycle Engine
(254 mm Bore/900 rpm/775 kW)
Installed 7/87
Continuous service since 1/88 without problems.

Installation #4
1) 8 Cyl/4-Cycle Engine
(254 mm Bore/900 rpm/775 kW)
Installed 5/88
Continuous service since 6/89 without problems.

Installation #5
1) 8 Cyl/4-Cycle Engine
(254 mm Bore/900 rpm/775 kW)
Installed 4/89
Unit ran until 3/90 when a crack through the water jacket in the exhaust casing was noted. Metallurgical examination found the cause to be a casting flaw. The vendor was brought in and changes to the pattern equipment were made to rectify the problem.

Installation #6
1) 10 Cyl/2-Cycle Engine
(355 mm Bore/330 rpm/1670 kW)
Installed 5/89
Unit suffered thrust bearing failure after 8400 hours service. A forensic investigation of the incident took place and found low lube oil supply pressure to the turbo as the cause of failure.

Installation #7
1) 8 Cyl/4-Cycle Engine
(254 mm Bore/900 rpm/775 kW)
Installed 3/90
Continuous service without problems.

Installation #8
1) 8 Cyl/4-Cycle Engine
(254 mm Bore/900 rpm/775 kW)
Installed 3/90
Continuous service without problems.

Design for the Future

Even more stringent requirements governing emissions output on two and four-cycle engines are on the horizon. The CB turbo was designed in such a manner so as to be able to incorporate movable compressor diffuser vanes as well as turbine nozzle ring vanes as a future development. It would be natural to use the electronic engine control schemes currently under development by several manufacturers to trim the turbo performance to the on-demand engine conditions and still achieve good overall efficiency. This idea and others will drive turbo development through the 1990s.

Closing

The CB turbocharger represents a large increment in improvement in all facets of engineering. Innovative thinking in aerodynamic design and mechanical packaging has yielded a cost-effective and reliable product to fill the needs in large-bore engine development for the 1990s.

A Comparative Study of the Stiller-Smith and Slider-Crank Mechanisms for Eight-Cylinder Internal Combustion Engine Use

J. E. Smith

J. C. Smith

A. D. McKisic
Mechanical and Aerospace Engineering,
West Virginia University,
Morgantown, WV 26506

Of the possible alternatives to the slider-crank for internal combustion engine use, the Scotch yoke in its various forms and inversions has received considerable attention. Among these, the Stiller-Smith mechanism has shown promise as being a viable option. Kinetostatic models were formulated to determine loading within similar eight-cylinder, four-stroke, compression-ignition engines with emphasis placed on comparing the number and similarity of mechanism components, implications of component and linkage motions, the loading experienced by similar bearing surfaces, and the friction losses of specific components.

Introduction

Kinematically the slider-crank is modeled as a planar four-bar linkage. The crank throw serves as the input link, the connecting rod is the coupler, and the piston is the output link. All members are linked by revolute joints (journal bearings) except for the pistons and frame (block), which are joined by prismatic joints. Multicylinder engines can be considered as multiple slider-cranks sharing a common frame and coupled by a common crank. The kinematic behavior of the slider-crank, as in any other four-bar linkage, is easily described.

Of the possible alternatives to the slider-crank, the scotch yoke and its various kinematic inversions has been the object of several investigations. Its use in internal combustion engines has been patented by Hunter [1], Bourke [2], Reitz [3], and Flinn [4]. The Geisel engine [5] has also shown promise.

The Stiller-Smith mechanism represents a different approach to the motion conversion objective. The mechanism was originated at West Virginia University [6] and is the subject of two U.S. patents [7, 8]. Detailed descriptions of the mechanism can be found in these and other sources [9–11], so only a cursory introduction is included here. The mechanism is in the form of a double cross-slider, or elliptic trammel. The trammel link shown in Fig. 1 is replaced by a gear whose center is located midway between the pins, which constrain its motion with respect to the "connecting rods." These are not connecting rods as in a slider-crank engine because they are rigidly connected—that is, without a wrist-pin—to the pistons located at the opposite ends. As depicted in Fig. 1 as the connecting rods reciprocate linearly, the center of the trammel gear translates in a circular fashion about an axis, which is located at the intersection of the connecting rods and is perpendicular to both rods. As the center of the gear translates in a circle, the entire gear rotates about its geometric center in the opposite direction of the translation. The magnitude of the angular velocity of this rotation is equal to that of its angular translation but with the opposite algebraic sign. The same is true for the angular acceleration [9]. Herein lies the principle difference between the Stiller-Smith mechanism and other double cross-sliders. In previous attempts to employ the cross-slider, the trammel translation was harnessed by means of a crank, which rotated about the axis located at the center of translation. To compensate for the trammel rotation, a bearing was required at the trammel center. The Stiller-Smith mechanism utilizes this trammel rotation instead of eliminating it. This is accomplished by a trammel link in the form of a gear. This gear is in continuous mesh with one or more similar gears mounted eccentrically on one or more output shafts, as shown in Fig.

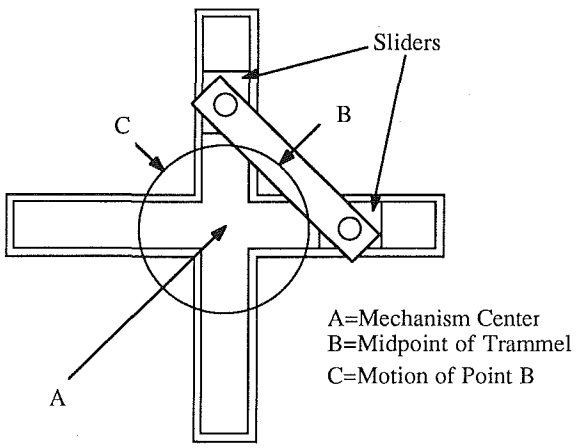

Fig. 1 The double cross-slider

Contributed by the Internal Combustion Engine Division and presented at the Twelfth Annual Fall Technical Conference, Rockford, Illinois, October 7–10, 1990. Manuscript received by the Internal Combustion Engine Division July 1990.

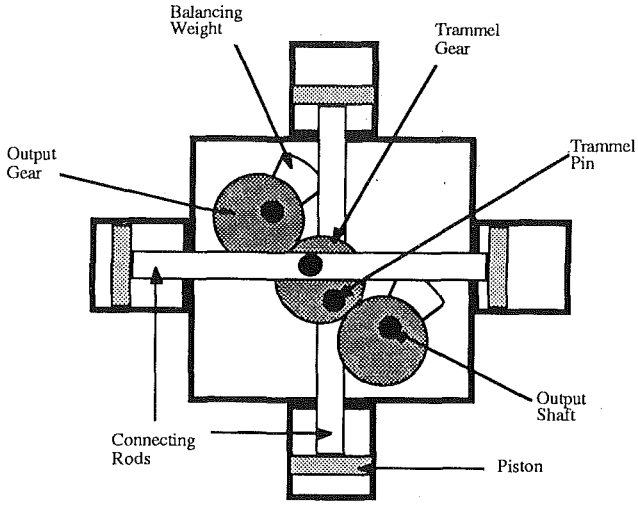

Fig. 2 The Stiller-Smith mechanism

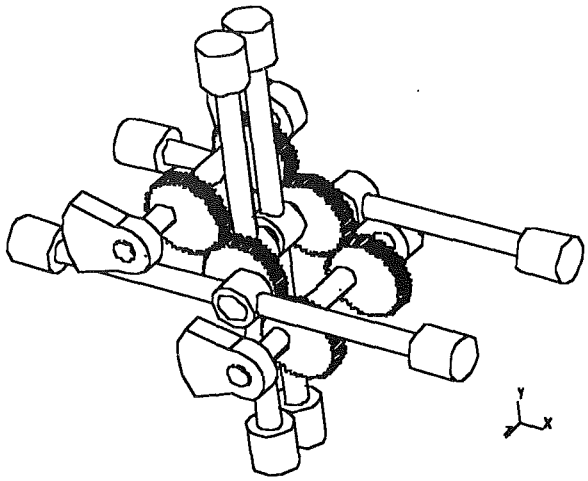

Fig. 3 The ABBA eight-cylinder configuration

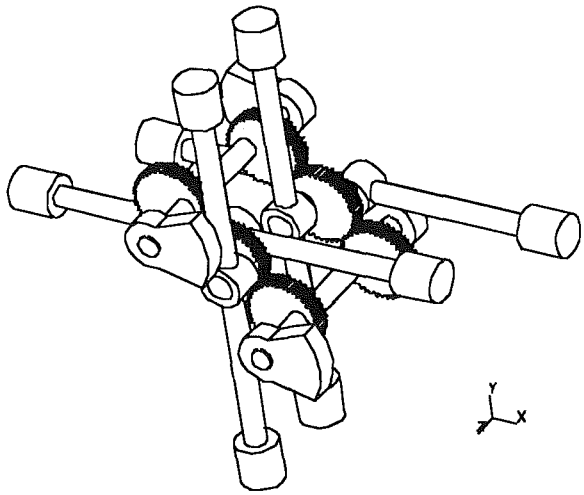

Fig. 4 The ABAB eight-cylinder configuration

2. The output gears are mounted eccentrically to compensate for the center translation. Otherwise a continuous mesh would not be possible. With this arrangement, as the trammel gear rotates, so does the output gear. Therefore, the angular velocities and accelerations of the output shafts are all identical to those of the translation of the trammel gear center [9].

A feature inherent in the Stiller–Smith mechanism, as in any double cross-slider, is that the motions of the pistons are all described by single harmonic terms. In the case of the slider-crank, the piston motion is often approximated as a two-term harmonic. This results in the need for complicated balancing schemes. Since these high-order terms are absent from the equations of motion in the Stiller–Smith mechanism, the mechanism is easily balanced [10–12].

The cruciform shape allows for multiple mechanisms to be linked via output shafts to form multicylinder (greater than four) arrangements. By the addition of balancing weights to the output shafts, two different eight-cylinder configurations can be balanced in three dimensions [12]. These configurations are illustrated in Figs. 3 and 4.

The first configuration, Fig. 3, is designated ABBA. While proceeding along an axis parallel to the output shafts, the connecting rods are encountered in the following order: horizontal, vertical, vertical, and then horizontal. Figure 4 shows the second balanceable configuration, the ABAB. The connecting rods are in the order of horizontal, vertical, horizontal, and vertical.

It is possible for a mechanism to contain up to five output shafts. One shaft can be used as the main drive shaft. It can also be externally coupled with another to change the internal

Nomenclature

B = distance between linear bearing supports
$D_{()}$ = gear diameter
$F_{()()}$ = force
$I_{()}$ = moment of inertia
$P_{()}$ = cylinder pressure
$R_{()}$ = bearing reaction
$T_{()}$ = shaft torque
$a_{()}$ = acceleration of center of gravity
$d_{()}$ = bearing diameter
$f_{()}$ = friction force
$m_{()}$ = mass
q = axial distance between bearings
$r_{()}$ = location vector magnitude
s = distance between parallel connecting rod
x = Cartesian coordinate
y = Cartesian coordinate
z = Cartesian coordinate
t = time
$\mathbf{F}_{()}$ = force vector
$\mathbf{i}$ = unit direction vector
$\mathbf{j}$ = unit direction vector
$\mathbf{k}$ = unit direction vector
$\mathbf{M}$ = moment vector
$\mathbf{R}_{()}$ = bearing reaction vector
β = mass center location angle
$\theta_{()}$ = location angle
$\mu_{()}$ = coefficient of friction
ρ = torque ratio
ϕ = pitch angle
$\chi_{()}$ = coordinate rotation angle

Subscripts

A = crank throw #1
B = crank throw #2
C = crank throw #3
D = crank throw #4
L = left bank
R = right bank
a = journal
b = bearing
f = friction circle
g = center of gravity
i = component number
j = component number
n = cylinder number
net = net
$/o$ = with respect to margin

Superscripts

x = component
y = component
$'$ = local cordinate
$\cdot$ = first derivative with respect to time
$\ddot{}$ = second derivative with respect to time

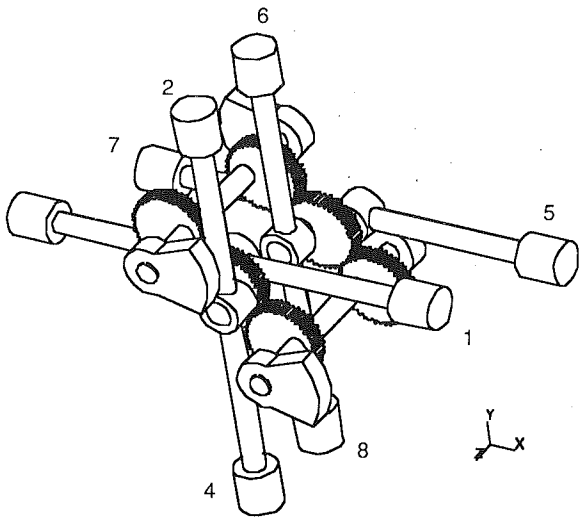

Fig. 5 Eight-cylinder ABAB cylinder designation

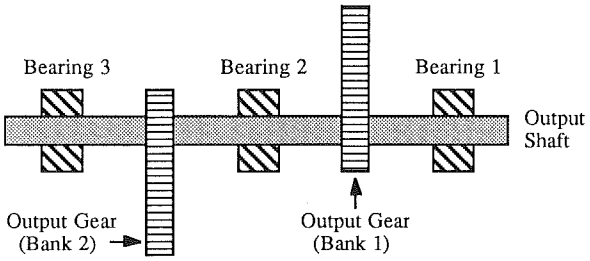

Fig. 6 Single output shaft, gears, and bearings

load distribution of the engine. Separate shafts can be used to drive accessories such as cooling fan, distributor, cam shaft, and generator. An auxiliary power-takeoff shaft is also readily available.

Analysis of an Eight-Cylinder Stiller–Smith Engine

Modeling. The kinematic through dynamic analysis of the Stiller–Smith engine has been well described in the literature with the corresponding development for the slider-crank left to the open literature [13–18]. Those readers interested in a detailed analysis or information on unique features of the Stiller–Smith mechanism are referred to the works of Smith et al. [9, 19], Sivaneri et al. [20], and Mucino et al. [21].

Stiller–Smith Firing Order. Since the Stiller–Smith eight-cylinder engine is still in the research stage, no firing order exists. Of the two possible arrangements of the engine that were discussed, this investigation will include only the ABAB configuration. This configuration and the cylinder numbering convention are shown in Fig. 5. Any firing order must be consistent with the balancing requirements. As determined in [12], cylinders 5–8 must be 180 degrees out of phase with cylinders 1–4 for three-dimensional balancing to be possible. This investigation will use a firing order of 1-2-5-4-7-8-3-6. This firing order is one of eight combinations and was chosen for ease of illustration.

Output Shaft Bearing Distributions. The open literature discusses several procedures for determining the load distribution on the five main bearings for a V-8 engine. For the load analysis for the six output shaft bearings for the eight-cylinder Stiller–Smith engine, each output shaft contains three journal bearings. Figure 6 shows one output shaft not including the balancing weights. In the slider-crank analysis, the loads on any main journal are assumed to be affected by only those arrows adjacent to the bearing. When two throws share a common

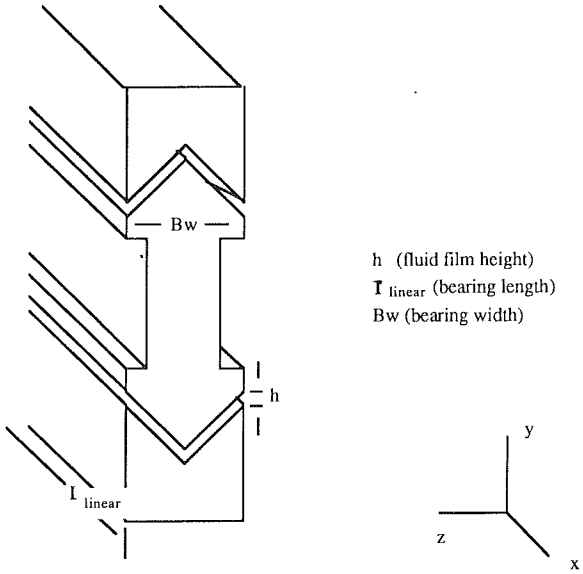

Fig. 7 Cross-sectional view of linear slider bearing

bearing, the loads on the bearing are determined by first assuming that each throw acts separately and then vectorially superimposing the loads resulting from the individual throws. In the Stiller–Smith analysis it is assumed that mechanism bank number 1 has no effect on bearing number 3. If the output gear is located midway between the two bearings, each bearing will support half the net reaction. The same procedure is followed for the second mechanism bank. In this case bearings 2 and 3 are involved. The net reaction due to the two mechanisms on the middle bearing is determined by superimposing the loads resulting from the two individual mechanism banks.

Balancing Weights. As can be shown in [17 and 22] the primary and secondary inertial forces in a 90 degree V-8 engine are inherently balanced. The same can be said for the secondary out-of-plane couple. The primary couple that exists can be easily eliminated by the addition of simple rotating counterweights. Higher order forces cannot be eliminated by the use of simple rotating counterweights. For the eight-cylinder Stiller–Smith mechanism, [12] shows that the primary shaking forces are also inherently balanced for the ABAB configuration. Due to its simple harmonic motion, the Stiller–Smith mechanism, unlike the slider-crank, contains no higher order harmonic forces. The same is true for higher order harmonic couples. However, a first-order couple does exist in the absence of rotating counterweights. This couple is easily eliminated by placing counterweights on the output shafts so that they are 180 degrees out of phase with the closest output gear [12]. This means that they are also out of phase with each other and contribute no net shaking force. They also induce no moment about the z axis [19].

Linear Bearing Analysis. The most significant difference resulting from a comparison of Stiller–Smith and slider crank mechanisms comes from the linear bearing analysis. A cutaway view of the linear bearing in the Stiller–Smith engine can be seen in Fig. 7. The reader may note that if these bearings are well designed and if the rod is sufficiently rigid, sidewall forces between the pistons and cylinder walls of the engine will be negligible. This will reduce wear and gas blowby past the rings and will negate the need for a piston skirt, thus reducing some moving mass.

In the first working prototype of the Stiller–Smith engine, the rods were round in cross section and ran in plain metal bushings in the engine casing so that they had a long unsupported span. For an engine with acceptable longevity this would

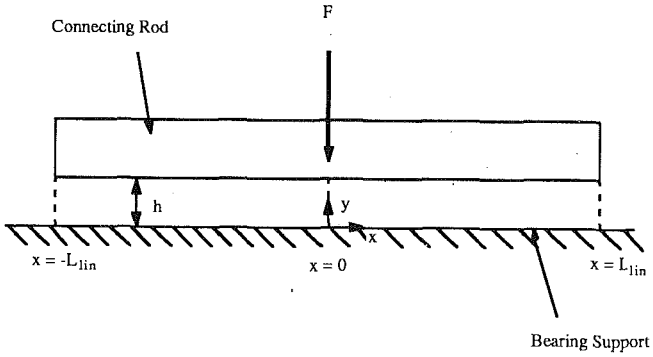

Fig. 8 Simplified linear slider bearing

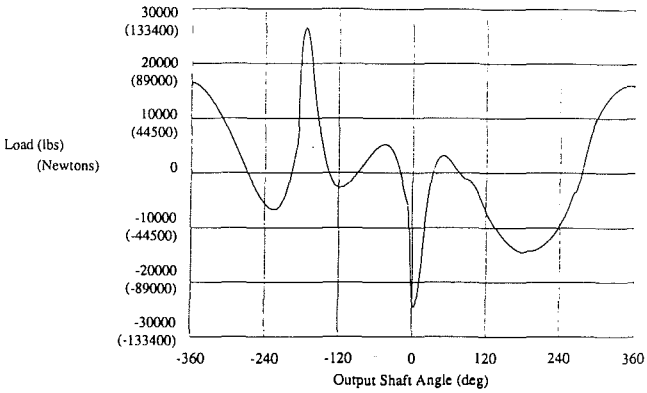

Fig. 9 Load history for linear bearings as a function of output shaft rotation (engine speed 2400 rpm)

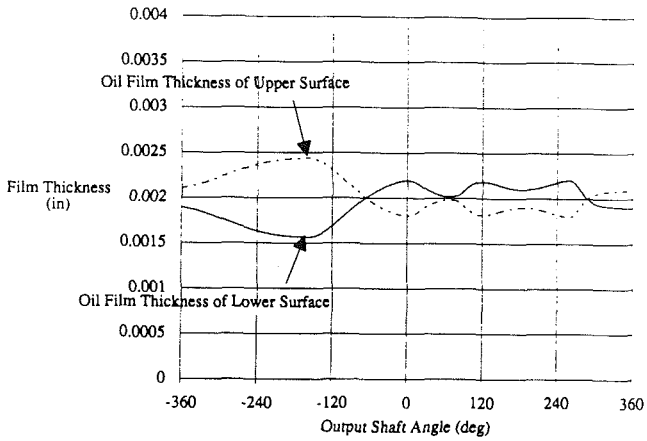

Fig. 10 Oil film thickness of upper and lower bearing surfaces for the linear bearing as a function of output shaft rotation (engine speed 2400 rpm)

prove unsatisfactory, so the new design in Fig. 7 has been proposed. A cross section of the new connecting rod is supported over much of its length by plain bearing surfaces on webs attached to the engine case. Oil may be fed to the bearing surfaces via holes in the webs.

With this configuration the reciprocating rod is permitted to move in the x direction. Vertical movement (y direction) is restricted to a few thousandths of an inch because of the bearing supports. This clearance is necessary for incorporation of an oil film, which will separate the connecting rod and bearing support preventing metal to metal contact. Movement in the z direction is likewise restricted. Once again some small movement in this direction is permitted; however, large displacements are restricted by the presence of the **V**-shape design of the bearing.

The load applied to this bearing is the result of the load imposed by the trammel pin in the connecting rod. As the engine runs, the linear reciprocating rods perform a linear sinusoidal translation at the same time the oil film thickness on each side of the bearing is changing as a result of the loading on the rod. This motion along with a load fluctuating in magnitude and direction pose a very difficult yet interesting lubrication problem. Due to the limited research in this type of bearing and the complexity of the problem, the analysis has been simplified. Consider the bearing system shown in Fig. 5.2. This differs from the true Stiller–Smith bearing in that the base is flat, and not a **V**-trough, and in that a film on only one side of the rod is considered. Power and pressure requirements have prescribed the use of a hydrostatic oil film, and analysis has shown that hydrodynamic (wedge) effects will be small. It is therefore proposed that the force on the center of the rod will be opposed solely by "squeeze-action" of the oil film. It will also be assumed for this analysis that no breakup of the film occurs during the linear motion.

Due to the complexity of the lubrication of this type of linear bearing system, several simplifying assumptions have been made in the solution of the Reynolds equation:

1 The linear connecting rod will not be permitted to move in the z direction.

2 The **V**-shape will be flattened and the bearing will be modeled as flat plates.

3 The oil viscosity is independent of direction.

4 A pressurized oil system will feed oil to the bearing surface via holes in the bearing support. For this reason the bearing surface will be assumed to possess a complete oil film.

With the simplifying assumptions imposed, the Reynolds equation can be reduced to a more workable form [23]. This work can be found in Smith [23] where the bearing load history was described by Fig. 9. The resulting oil film thickness for this analysis is represented in Fig. 10.

Results

Mechanisms. The objective of the study was to compare the slider-crank and Stiller–Smith mechanisms in eight-cylinder, four-stroke, compression-ignition engine environments. The slider-crank engine investigation is based on the Cummins VT-903 turbocharged diesel engine. All calculations for the Stiller–Smith mechanism were based upon an engine whose stroke, bore, and displacement are equivalent to those found in the Cummins VT-903 Specifications for the engine used in the investigation may be found in Tables 1 and 2.

Table 3 shows a breakdown of the moving parts of the engines. The members listed include only those involved in the motion conversion mechanisms themselves and are listed by functionally similar motions.

This table shows that the V-8 mechanism contains over twice as many moving parts as does the eight-cylinder Stiller–Smith. For members experiencing complex motion, that is motion other than just simple translation or rotation, the V-8 has four times as many members as does the Stiller–Smith. The complex motion experienced by the V-8's connecting rod also requires multiple harmonic terms for an accurate description. While both engines have eight cylinders, the Stiller–Smith has only four reciprocating parts. Its pistons are rigidly attached to the connecting rods, one at each end.

Joint Identification. Figure 11 shows the joint (bearing surface) types of the two mechanisms. A breakdown of the joints into bearing type is shown in Table 4 for both mechanisms. The slider-crank engine contains more bearing surfaces, by 42 percent, than the Stiller–Smith engine. The table also identifies bearing surfaces that serve similar purposes in the two mechanisms. Both mechanisms contain eight sets of piston rings, one per cylinder. These serve the function of containment of combustion gases and isolation of lubricant from the combustion chamber. While the rings will provide some support for lateral load, this is primarily accomplished by the piston skirt in the slider-crank and the linear bearings in the Stiller–

Table 1 V-8 engine specifications

General Specifications			
Base Engine		Cummins VT-903	
Stroke		12.1 cm	(4.75 in)
Bore		14 cm	(5.5 in)
Displacement		14.8 l	(903 cu. in.)
Operating Cycle		4-Stroke, CI	
Bank Angle		90o	
Compression Ratio		15.5:1	
Governed Speed		2400 rpm	
Crank Specifications			
Throw Length	rl	6.033 cm	(2.375 in)
Mass Rotation Radius	rlg	6.033 cm	(2.375 in)
Rotating Weight/Throw	W1	17.87 N	(4.017 lbf)
Main Bearing Diameter	dl	9.53 cm	(3.75 in)
Crank-Pin Diameter	d2	7.938 cm	(3.125 in)
Bearing Separation	q	17 cm	(6.6 in)
Con-Rod Separation	s	3.8 cm	(1.5 in)
Balancing Weight Separation	h	59.06 cm	(23.25 in)
Con-Rod Specifications			
Length	r2	20.81 cm	(8.193 in)
Mass Center Location	r2g	6.716 cm	(2.644 in)
Weight	W2	30.9 N	(6.94 lbf)
Moment of Inertia	I2	0.02977 N-m-s2	(.2635 in-lbf-s2)
Piston Specifications			
Weight	W3	33.26 N	(7.477 lbf)
Skirt Area		84.677 cm2	(13.125 in2)
Friction Coefficients			
Main Bearings	m1	0.01	
Crank Pins	m2	0.01	
Piston	m3	0.05	

Table 2 Stiller-Smith engine specifications

General Specifications			
Base Configuration		ABAB	
Stroke		12.1 cm	(4.75 in)
Bore		14 cm	(5.5 in)
Displacement		14.8 l	(903 cu. in.)
Operating Cycle		4-Stroke, CI	
Compression Ratio		15.5:1	
Governed Speed		2400 rpm	
Output Shaft/Gear Specifications			
Gear Diameter	D	15 cm	(6.0 in)
Mass Rotation Radius	r5g	3.0163 cm	(1.1875 in)
Rotating Weight/Gear	W5	54.94 N	(12.35 lbf)
Bearing Separation	q	17.1 cm	(6.75 in)
Con-Rod Separation	s	22 cm	(8.5 in)
Balancing Weight Separation	h	52.1 cm	(20.5 in)
Pitch Angle	f	20o	
Torque Ratio	r	0.111	
Output Shaft/Gear Specifications			
Gear Diameter	D	15 cm	(6.0 in)
Mass Rotation Radius	r2g	3.0163 cm	(1.1875 in)
Rotating Weight/Gear	W2	54.94 N	(12.35 lbf)
Pitch Angle	f	20o	
Pin Separation		2.375	
Con-Rod/Piston Specifications			
Bearing Mount Separation	B	44.133 cm	(17.375 in)
Weight	W2	143.8 N	(32.33 lbf)
Linear Bearing Area		280.3 cm2	(43.44 in^2)
Friction Coefficients			
Main Bearings	m1	0.01	
Trammel Pins	m2	0.01	
Linear Bearings	m3	0.05	

Table 3 Moving part breakdown

	VT - 903 (8-Cylinder)		Stiller-Smith (8-Cylinder)	
Motion	Component	Number	Component	Number
Reciprocating	Pistons	8	Piston-Rods	4
Rotating	Crankshaft	1	Output Shafts	2
Complex Motion	Con-Rod	8	Trammel Gears	2
	Total	17		8

Table 4 Bearing surface breakdown

	VT - 903		Stiller-Smith	
Bearing Type	Component	Number	Component	Number
Linear Reciprocating	Ring Sets	8	Ring Sets	8
	Piston Skirts	8	Linear Bearings	4
Rotating Journals	Main	5	Output Shaft	6
	Crank Pins	8	Trammel Pin	4
Oscillating	Wrist Pin	8	Wrist Pin	0
Gear Contacts	Gears	0	Gear Teeth	4
	Total	37		26

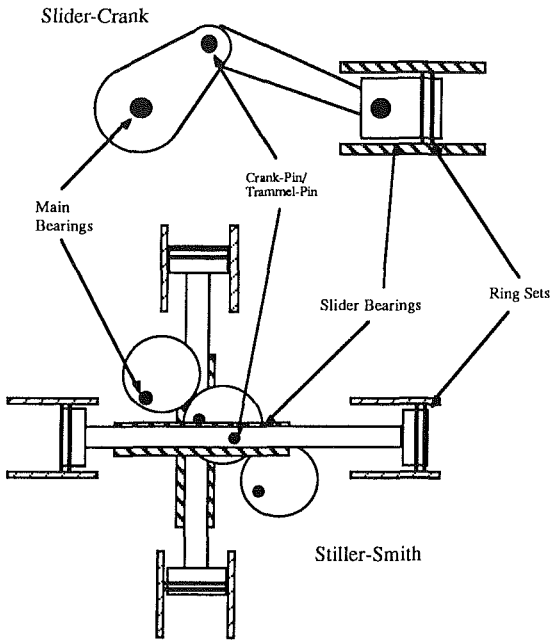

Fig. 11 Mechanism joint identification

Smith. The slider-crank engine therefore has twice as many linear reciprocating bearing surfaces. The slider-crank also has twice as many crank-pin, or big-end, bearings as the Stiller–Smith engine has trammel pin bearings. Conversely, the Stiller–Smith engine has six journal bearings for its two output shafts compared to the five main journal bearings supporting the V-8 crankshaft.

It should be noted that the Stiller–Smith engine can operate with one to five output shafts. A Stiller–Smith engine employing a single output shaft requires only three bearings. Overall the V-8 contains 13 rotating journals to the 10 for the Stiller–Smith. The Stiller–Smith engine contains no functionally similar bearing surface to the slider-crank oscillatory wrist-pin. Likewise there are no gear contacts or any higher order kinematic pairs in the slider-crank. Adding an auxiliary power-takeoff shaft to the V-8 will require the addition of a minimum of two journal bearings and one higher kinematic pair.

Comparison of Main Bearing and Output Shaft Bearing Load. The main bearings in the V-8 and the output shaft bearings in the Stiller–Smith engine are functionally similar. The load distributions for the main bearings are shown in Figs. 12 and 13. For the Stiller–Smith engine the outer bearings are the most heavily loaded, whereas the V-8 is most heavily loaded in the center bearings. In the Stiller–Smith engine, bearings 4, 5, and 6 have significantly higher peak loads than do bearings 1, 2, and 3. This is a direct result of 90 percent of the torque being carried by the output shaft containing these bearings. The following results presented will be for the Stiller–Smith bearing #6, which is the most heavily loaded Stiller–Smith bearing, and the first V-8 main bearing.

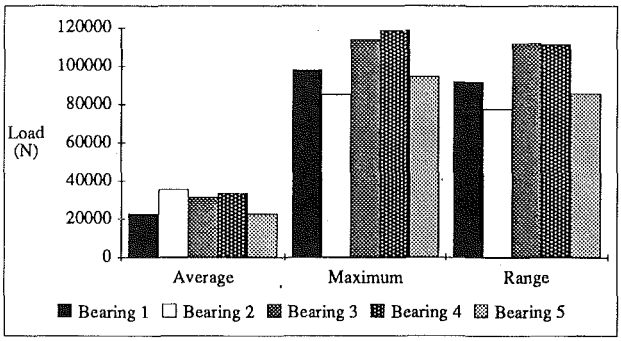

Fig. 12 V-8 main bearing load distribution

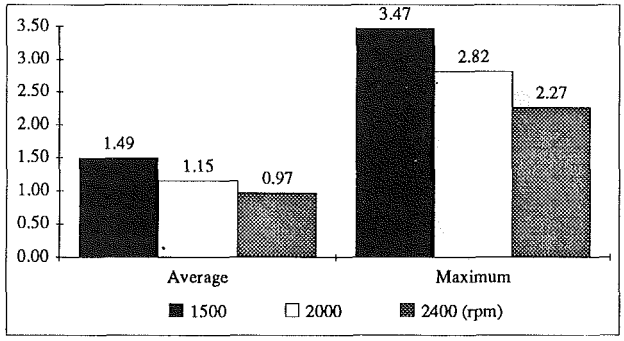

Fig. 15 Ratio of V-8 main bearing to Stiller-Smith output shaft bearing load

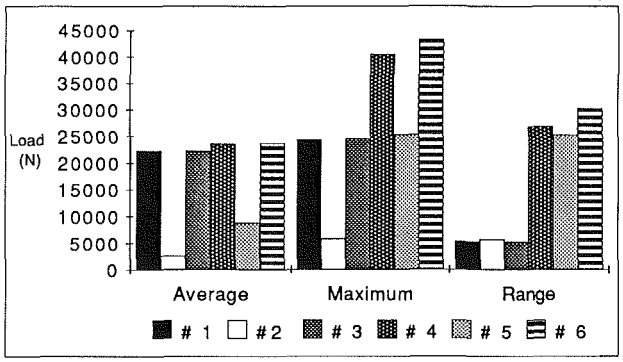

Fig. 13 Stiller-Smith output shaft load distributions

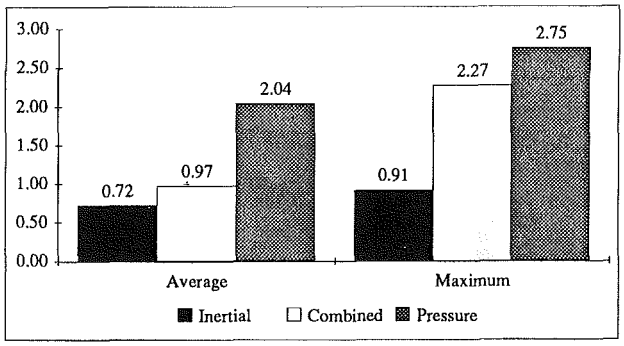

Fig. 16 Relative magnitude of contributing loads: V-8 main bearing load/ Stiller-Smith output shaft bearing load

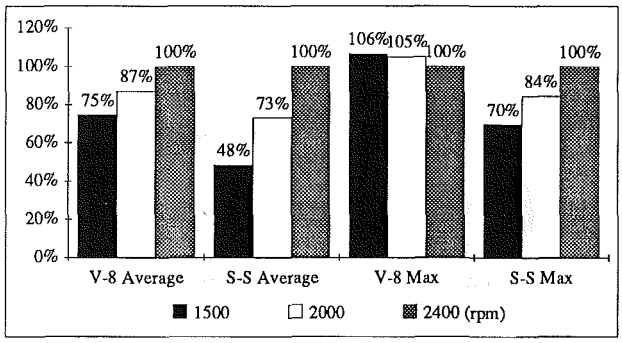

Fig. 14 Effect of engine speed on main bearing loads: normalized to 2400 rpm

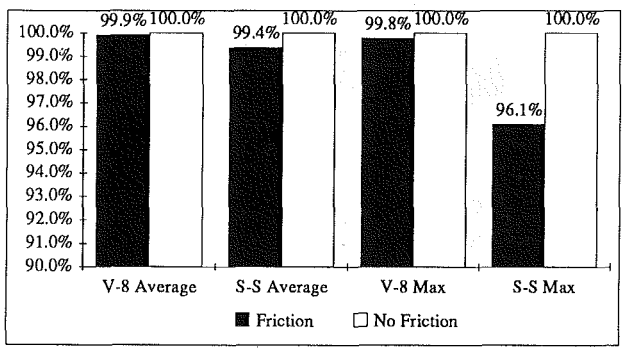

Fig. 17 Effect of friction on main bearing loads

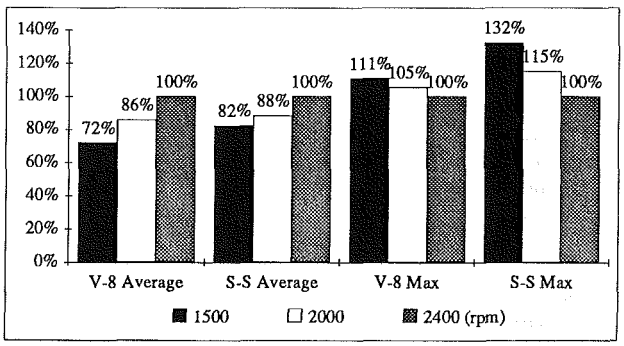

Fig. 18 Effect of engine speed on pin loads: normalized to 2400 rpm

It is assumed that the engine load is held constant over the range of engine speeds investigated where the maximum pressure was 12 MPa (1750 psi) with 30 percent supercharging. The effect of engine speed on the bearing load is similar in both engines. As shown in Fig. 14, bearing load increases with increasing engine speed except for the maximum V-8 load. This indicates that inertial forces and gas forces work together instead of in opposition. The effects are approximately the same with inertial forces having a greater influence for the Stiller-Smith engine. In a direct comparison of the loads, as shown in Fig. 15, the maximum V-8 load is nearly four times that of the Stiller-Smith at 2400 rpm. The maximum bearing load due to gas pressure, shown in Fig. 16, in the V-8 is 2.75 times that experienced in the Stiller-Smith. After comparing the maximum loads it is concluded that the V-8 bearings are more likely to fail due to fatigue.

The dual output shafts of the Stiller-Smith engine introduce possibilities for design variation not available to the V-8. As previously discussed, the difference in loading between bearings on the two output shafts is a result of the torque distributions. It was assumed in the analysis that the balancing weights were identical on both output shafts.

The difference between the output shaft and crankshaft bearing loading increases even more with the introduction of friction into the system. As seen in Fig. 17, the introduction of friction decreases the loading on all bearings. The effect is greatest in the Stiller-Smith engine. The percentages shown are based upon a Coulomb friction model.

Comparison of Crank-Pin and Trammel Pin Bearing Loads. The trammel pins on the Stiller-Smith and crank-pin in the slider-crank are functionally similar. As shown in Fig. 18,

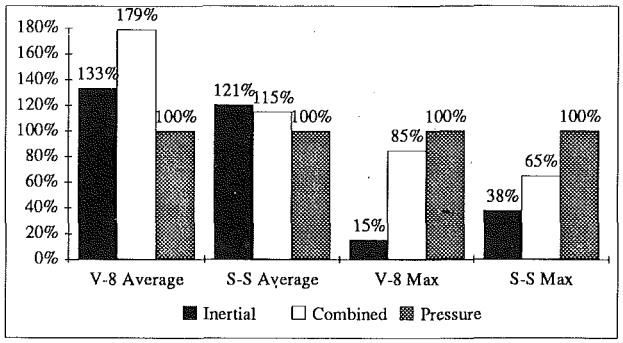

Fig. 19 Relative magnitude of contributing pin loads: normalized by pressure loads

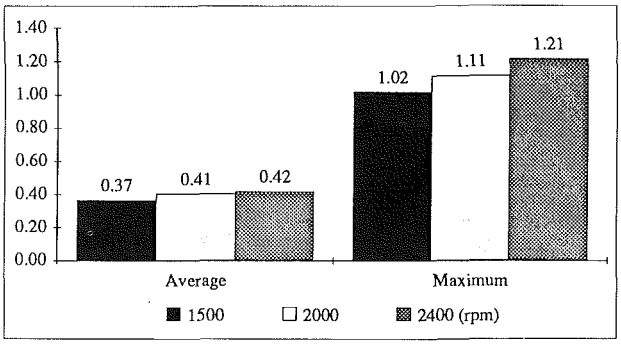

Fig. 20 V-8 pin loads/Stiller-Smith trammel pin loads

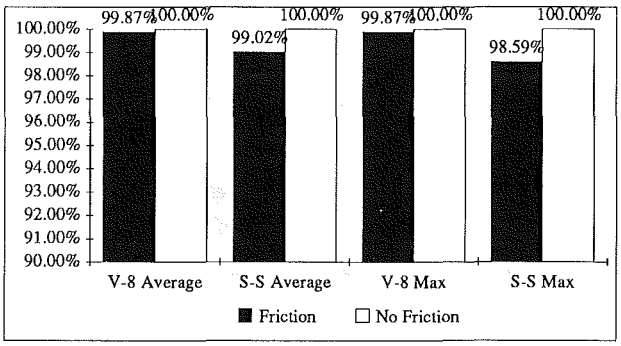

Fig. 21 Effect of friction on pin loads

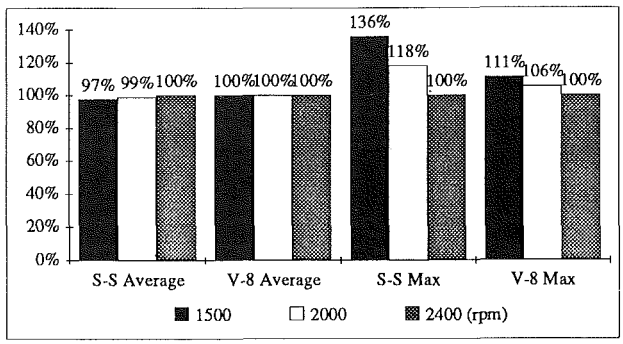

Fig. 22 Effect of engine speed on reciprocating bearing loads: normalized to 2400 rpm

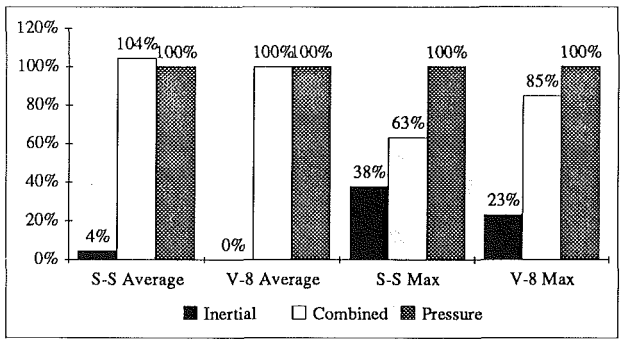

Fig. 23 Relative magnitudes of contributing reciprocating bearing loads: normalized by gas pressure loads

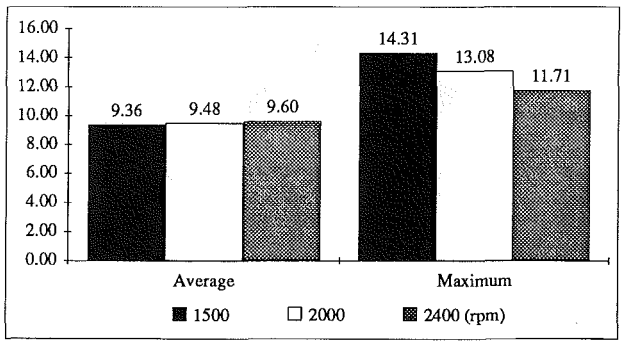

Fig. 24 Stiller-Smith linear bearing loads/V-8 piston sidewall load

average pin loads again increase with engine speed. The maximum pin loads decrease with increasing engine speed. This trend is again more pronounced in the Stiller-Smith engine. The trend in both shows that inertial and gas forces oppose each other in their contribution to the maximum pin load. Figure 19 helps to explain why engine speed has a greater effect on maximum load in the Stiller-Smith engine. Maximum inertial forces are 38 percent of the maximum gas forces in the Stiller-Smith engine. They account for only 15 percent of the maximum gas forces in the V-8. It is also noteworthy that the combined forces are 85 percent of the pressure forces in the V-8. Therefore the maximum inertial and gas forces occur nearly simultaneously and directly oppose each other. This is not the case on the Stiller-Smith engine. Because the maximum inertial forces in the Stiller-Smith are closer in magnitude to the maximum gas forces, the combined load is actually less than that in the slider-crank. The effect is increased with engine speed as seen in Fig. 20. Figure 21 shows that for all cases the introduction of friction reduces pin loads. Like the main bearings, the pin bearings in the Stiller-Smith engine are less susceptible to fatigue failure based on maximum loading.

Some important conclusions can be made from summarizing the preceding discussions on the journal bearing loadings for the two mechanisms. In all cases the maximum loads experienced by the V-8 journal bearings are greater than those in the corresponding Stiller-Smith journal bearings. If all other factors are considered equal, the journal bearings in the Stiller-Smith engine are less susceptible to fatigue failure. The drastic difference between the maximum loading on the main bearings can be attributed to the corresponding gas force reactions. In the V-8 engine, the large loads due to cylinder pressure are transmitted directly through the crank and must be supported by the main bearings. These same loads in the Stiller-Smith engine are carried by the linear bearings instead of the output shaft bearings. The introduction of friction in the system decreases the loads on all journal bearings. Given minimum capacity ratio, the Stiller-Smith journal bearings are less likely to have fluid film breakdown and suffer seizure.

Reciprocating Bearing Load Comparisons. In a standard slider-crank engine, the piston skirt serves as a bearing surface that must reciprocate linearly and at the same time support a load. The same purpose is accomplished by the linear bearings in the Stiller-Smith engine. Figure 22 shows the effect of engine speed on reciprocating bearing load for the two mechanisms.

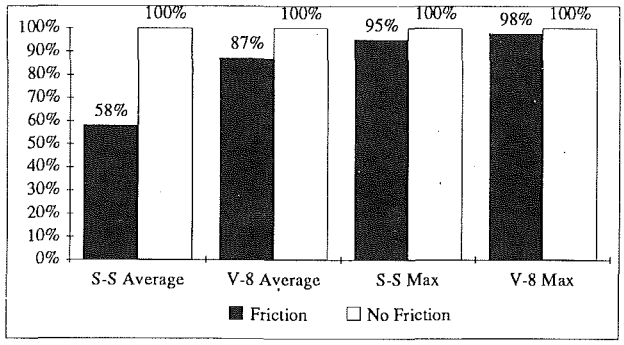

Fig. 25 Effect of friction on reciprocating bearing loads

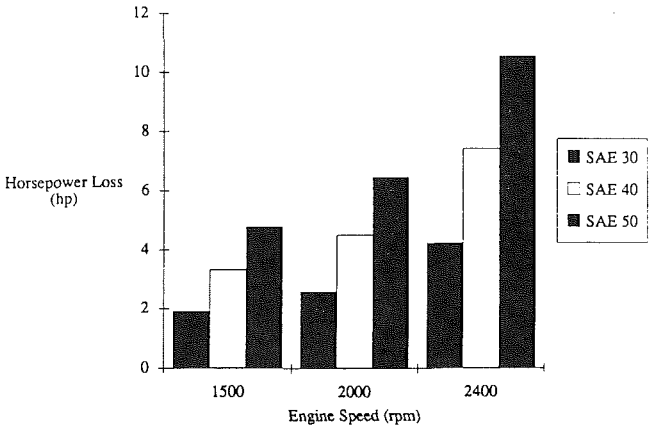

Fig. 26 Horsepower loss as a function of engine speed for linear bearings

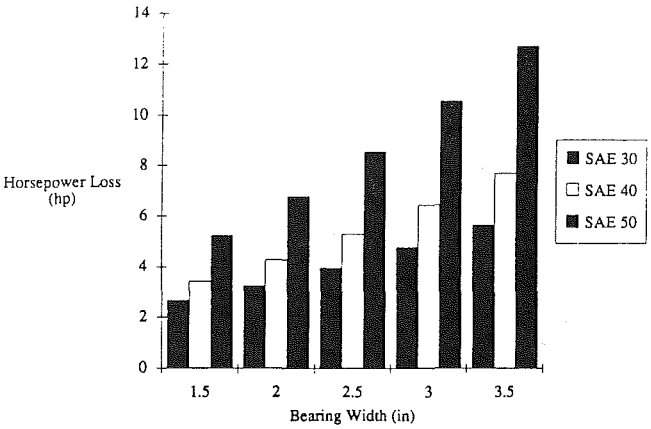

Fig. 27 Horsepower loss as a function of bearing width for linear bearings (engine speed 2400 rpm)

The maximum normal load decreases with increasing engine speed for both mechanisms indicating that inertial forces oppose gas forces for both. The effect is more drastic in the Stiller-Smith engine. This is reflected in Fig. 23 in that the maximum inertial and gas pressure forces are closer in magnitude in the Stiller-Smith engine than in the V-8. A direct comparison of the loads, Fig. 24, shows that the Stiller-Smith slider is much more heavily loaded than the V-8 piston sidewall. The ratio of average load increases with engine speed while that for maximum load decreases. As would be expected in both engines, the loads decrease with the introduction of friction. This is shown in Fig. 25.

The reason that the Stiller-Smith linear bearings are so much more heavily loaded is that they, like the V-8 main bearings, must experience the main force exerted on the piston by the cylinder pressure. One redeeming factor for the linear bearings is they carry their highest load at the time their velocity is the

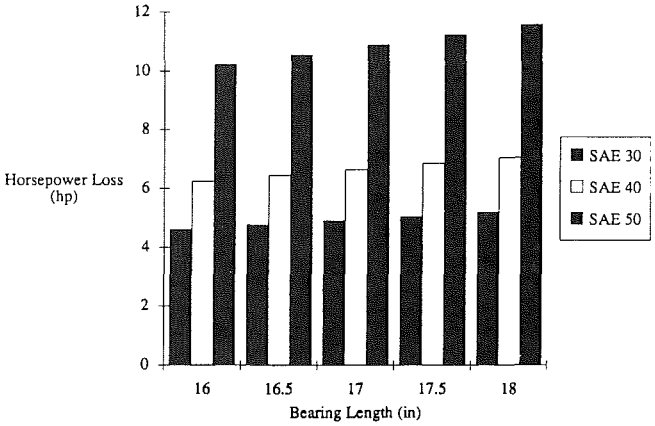

Fig. 28 Horsepower loss as a function of bearing length for linear bearings (engine speed 2400 rpm)

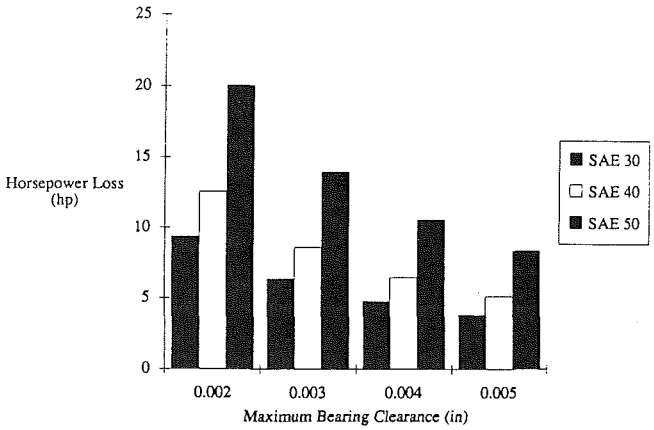

Fig. 29 Horsepower loss as a function of maximum bearing clearance for linear bearings (engine speed 2400 rpm)

greatest. This is very beneficial for hydrodynamic lubrication. Even though the Stiller-Smith linear bearings are much more heavily loaded than the slider-crank piston sidewall, there is no indication that these bearing surfaces will not provide the required support.

Friction Loss Implications. One of the strong points of the diesel engine is its good fuel economy. Shigley and Mitchell [24] state that the difference between a very good diesel engine and an average diesel engine is almost invariably due to a difference in their frictional losses. All other things being equal, a reduction in the number of bearings reduces the friction losses in the system containing those bearings. The extent of the resulting reduction of friction losses is dependent upon a number of conditions. Primarily, a significant friction loss reduction can be achieved if the number of bearings can be reduced without subjecting the remaining bearings to excessive loading.

It is commonly held that power losses are proportional to bearing width and the cube of the bearing diameter [25, 26]. If the bearing dimensions must be changed to obtain the same specific loading, the difference in losses can change considerably [25]. If a bearing system has high specific loadings after a reduction in the number of contained bearings, then the bearing dimensions must be changed accordingly. If the same diameter-width ratio is kept and dimensions are changed so that the same specific load is achieved, the friction losses are approximately the same as with a greater number of bearings [25]. Following the same logic, for an equal number of bearings with the same specific loading and diameter-width ratios, smaller bearings can result in significant reductions in friction losses.

For the remaining journal bearings in the engines, the tram-

mel and crank pins, the loadings are much more similar in magnitude. It must be assumed that the bearings are similar in size to be conservative. There are still indications that friction losses will be greater in the V-8 crank-pin bearings because there are twice as many bearings.

Predictions as to comparative losses in the reciprocating slider bearings are much less certain. The majority of published literature covering slider bearings friction losses concerns rotating bearings. The projected bearing area for a Stiller–Smith linear bearing is greater than that of a V-8 piston skirt. The smaller area of the V-8 piston skirt would provide more favorable friction losses [24, 26]. However, the V-8 contains twice as many pistons as the Stiller–Smith contains linear bearings and the total projected areas are actually closer than expected.

In this investigation, it was assumed that the only motion experienced by the piston was linear reciprocation in the cylinder bore. In actual engines clearances exist between the piston skirt and cylinder walls. This and the ability of the piston to rotate about the wrist-pin allows piston slap to occur. In their work on piston friction losses in diesel engines, Furahama and Takiguchi [25] hypothesize that a large frictional force is generated by the piston slap impulse. Due to the component construction in the Stiller–Smith engine, piston slap is not likely to occur. Without the piston slap it is possible that this large initial friction force is not present.

In addition to these friction losses on a slider-crank's piston skirt the loss in horsepower in the Stiller–Smith linear bearings can be predicted as a function of engine speed, bearing width, bearing length, and clearance (Figs. 26–29). While these results are not definitive without experimental backup they do correlate well with friction loss expectations for piston skirts.

Conclusions

It is impossible to predict the functional success of a machine from theoretical studies alone. Simulations are useful in identifying potential strengths and weaknesses without the expensive and time-consuming construction of the actual machines. This analysis attempted to examine specific components in internal combustion engines using two different motion conversion mechanisms and to make comparisons between the component's performance and the effects certain parameters have upon their performance.

On a basis of the number of components it is concluded that an eight cylinder engine using the Stiller–Smith mechanism is superior to a similar slider-crank design because it has less than half the moving parts. These parts are also less complex in construction. The number of bearing surfaces in the Stiller–Smith engine is again less than that in a standard V-8.

For comparable journal bearing surfaces, the performance of those in the Stiller–Smith engine equaled or exceeded that of those in the slider-crank engine in the areas of bearing fatigue and minimum capacity ratio.

For the linear reciprocating bearings the Stiller–Smith linear bearings were much more heavily loaded than the V-8 piston skirts. This is a direct result of the Stiller–Smith linear bearings directly receiving gas pressure loads. The Stiller–Smith linear bearings also control piston motion more effectively than the V-8 piston sidewall, minimizing piston slap and blowby.

In the case of constant load, it was determined that engine speed had a greater effect upon bearing loads in the Stiller–Smith engine. A comparison of relative magnitudes of contributing forces showed that the inertial forces in the Stiller–Smith engine were closer in magnitude to those due to gas pressure than was the case in the V-8. In direct comparisons of inertial loads, those in the Stiller–Smith engine were the greatest of the two engines. In both engines the inertial forces tended to reduce bearing loads due to gas pressure.

In general the introduction of friction into the system reduces the magnitudes of bearing loads. It was concluded that the journal bearings in the Stiller–Smith engine will produce fewer friction losses than those in the V-8, if properly designed.

References

1 Hunter, W. J., "Internal Combustion Engine," United States Patent No. 1181892, 1916.

2 Bourke, R. L., "Internal Combustion Engine," United States Patent No. 2122677, 1938.

3 Reitz, D. M., "Bourke Type Engine," United States Patent No. 4013048, 1977.

4 Flinn, H. L., Jr., "Linear to Rotary Motion Converter Utilizing Reciprocating Pistons," Great Britain Patent No. 2038984, 1979.

5 Hope, J., "The Geisel: A New Concept for Reduced Fuel Consumption in Internal Combustion Engines," Haeco, Inc., Report Cincinnati, OH, 1983.

6 Smith, J. E., "The Dynamic Analysis of an Elliptic Trammel Mechanism for Possible Application to an Internal Combustion Engine With a Floating Crank," Ph.D. Dissertation, West Virginia University, 1984.

7 Stiller, A., and Smith, J., "Oscillatory Motion Apparatus," United States Patent No. 4641661, 1987.

8 Stiller, A., and Smith, J., "Oscillatory Motion Apparatus," United States Patent No. 4682569, 1987.

9 Smith, J., Craven, R., and Cutlip, R., "The Stiller–Smith Mechanism: A Kinematic Analysis," SAE Paper No. 860535, 1986.

10 Smith, J., Nesbit, S., and Churchill, R., "The Stiller–Smith Cross-Slider Engine: A Balanced Engine Concept," SAE Paper No. 870614, 1987.

11 Nesbit, S., "A Two-Dimensional Analytical Model for Balancing the Stiller–Smith Engine," Thesis, West Virginia University, 1985.

12 McKisic, A. D., Smith, J., Craven, R., and Prucz, J., "Three-Dimensional Balancing of the Stiller–Smith Mechanism for Application to an Eight Cylinder IC Engine," SAE Paper No. 871917, 1987.

13 Taylor, C., *The Internal Combustion Engine in Theory and Practice*, Vol. 1, MIT Press, Cambridge, MA, 1985.

14 Norling, R., "Continuous Time Simulation of Forces and Motion Within an Automotive Engine," SAE Paper No. 780665, 1978.

15 Doughty, S., Smalley, A. J., and Evans, B. F., "Internal Dynamic Force Analysis for V-Type Engine/Compressor With Articulated Power Cylinder Connecting Rod Mechanism," ASME Paper No. 88-ICE-12, 1988.

16 Taylor, C. F., *The Internal Combustion Engine in Theory and Practice*, Vol. 2, MIT Press, Cambridge, MA, 1985.

17 Wilson, C. E., Sadler, J. P., and Michels, W. J., *Kinematics and Dynamics of Machinery*, Harper & Row, New York, 1983.

18 Nahvi, H., "Analytical Model of Friction in a Slider-Crank Mechanism With Hydrodynamic Bearings," Master's Thesis, West Virginia University, 1986.

19 Smith, J. E., and McKisic, A. D., "Stiller–Smith Versus Conventional V-8 Bearing Load and Friction Comparisons," *The Proceedings of the Institute of Mechanical Engineers*, Issue D4, Vol. 203, 1989.

20 Sivaneri, N. T., et al., "Unique Kinematic Features of the Stiller–Smith Mechanism," *Proceedings of the OSU 10th Applied Mechanisms Conference*, Dec. 6–9, 1987.

21 Mucino, V., Sivaneri, N. T., Smith, J. E., Wang, W. G., and Gokhale, M. R., "Dynamics of the 'Stiller–Smith' Mechanism in an Internal-Combustion Engine Environment," *Proceedings of the OSU 10th Applied Mechanisms Conference*, Dec. 6–9, 1987.

22 Patterson, D., "Engine Torque and Balance Characteristics," SAE Paper No. 821575, 1982.

23 Smith, J. C., "Analysis of Plain Bearings in and Eight Cylinder Internal Combustion Engine Utilizing the Stiller–Smith Mechanism," M.S. Thesis, West Virginia University, 1989.

24 Shigley, J., and Mitchell, L., *Mechanical Engineering Design*, 4th ed., McGraw-Hill, New York, 1983.

25 Pohlmann, J. D., and Kuck, H.-A., "The Influence of Design Parameters on Engine Friction," *Combustion Engines—Reduction of Friction and Wear*, I. Mech. E. Publication No. 1985-3, C73/85, Mechanical Engineering Ltd., London, 1985, pp. 67–74.

26 Rosenberg, R. C., "General Friction Considerations for Engine Design," SAE Paper No. 821576, 1982.

27 Furuhama, S., and Takiguchi, M., "Measurement of Piston Friction Force in Actual Operating Diesel Engine," SAE Paper No. 790855, 1979.

Heavy-Duty Spark Ignition Engines Fueled With Methane

M. Gambino

S. Iannaccone

A. Unich

Istituto Motori C.N.R.,
Napoli, Italy

Pollution reduction in urban areas is a major driving force to upgrade mass transportation systems. Options to the urban planner include electric traction and combustion engine upgrade. Electric traction centralizes the emission source, usually removed from urban areas, but requires substantial capital costs and lead time for the transportation infrastructure. Engine emission improvement is possible through both fuel changes and engine upgrade. Natural gas engines are a viable option for clean-operating urban buses. In the near term, conversion of existing diesel bus engines to spark-ignited natural gas is an attractive solution in terms of capital costs and lead time. This paper contains the analysis required to transform diesel engines into spark-ignited natural gas engines. Experimental data are shown for both a turbocharged and a naturally aspirated conversion. Emission data are presented showing the natural gas conversion to meet present EEC emission requirements.

Introduction

Low-emissions transportation systems are needed for urban areas due to the incompatibility of high population density and large concentration of emission sources. Low air quality has caused both health concerns and degradation of historic structures. Urban pollutant levels coupled with increased public concern have been the driving catalyst needed to identify measures needed to reduce urban pollution.

Mass transit affects both the fuel consumed and the pollutant emitted on a unit distance per passenger basis. An improvement to present mass transportation with increased ridership would therefore lower emissions. In the limit, where mass transit makes up a predominance of urban transportation, emissions from these sources could be identified and eliminated to a great extent. Solutions to remove emissions from mass transit are numerous. One solution, to electrify mass transit, would involve large capital expenditure as well as a new infrastructure. Solutions of this type require long lead times. It is necessary to identify solutions that can be implemented in the near term, thus reducing emissions and allowing time needed to optimize urban planning for more long-term solutions.

Improvement of exhaust emissions for urban transit buses is one of the near-term solutions. Capital costs for this system would be low due to the existing infrastructure. Using present technology, urban bus engines could be converted or retrofitted to meet present and future emission requirements. Engine-fuel relationships have been historically recognized and recently, fuel-emission relationships have been identified. Gaseous fuels are a prominent candidate for low-emissions engines. Natural gas, for instance, has a high fuel octane number and has been proven to be a safe fuel by a substantial number of accumulated passenger miles, both in Italy and other countries. Natural gas is made up primarily of the light hydrocarbon methane. Storage can be accomplished by compression or liquefaction. Either method has pros and cons as to which is the optimum.

An optimum solution for engine conversion is the heavy-duty spark ignition engine. At present, no optimized engine exists whose primary design is to operate on natural gas for the size and performance range needed for urban buses. This solution is one with high associated capital costs and significant lead time.

Diesel engines do not exist that require little hardware to modify for natural gas operation and are pre-engineered to fit the chassis requirements of present bus systems. These combinations make the conversion to natural gas fuel one that is available to users at present and is plausible in terms of capital costs.

The Istituto Motori of the Italian National Research Council is conducting research on spark-ignition natural gas engines, particularly those derived from diesel bus engines.

Natural Gas Engines

Conversion of existing diesel bus engines to natural gas use and spark ignition is the most logical start point and can have the greatest impact on near-term urban emissions if it finds widespread use. Engine conversions must retain the attributes of their predecessor if they are to gain market acceptance. Present diesel bus engines are characterized by high "low-speed" torque, low specific fuel consumption, long life and maintenance intervals.

Generally these attributes are found in large displacement, low mechanical stress engines operating at fairly low speeds for engines categorized as "high-speed internal combustion engines." Conversions of this engine type should maintain the high reliability and long life reputation these engines enjoy.

Goals and Setup

The goal of this research is to optimize the conversion of existing diesel bus engines to natural gas-fueled spark-ignition

Contributed by the Internal Combustion Engine Division and presented at the Twelfth Annual Fall Technical Conference, Rockford, Illinois, October 7-10, 1990. Manuscript received by the Internal Combustion Engine Division July, 1990.

engines and to conform to European emission limits (88/77 CEE-R49). The performance of the existing diesel engine that is the basis of the conversion is to be maintained. No heavy-duty spark-ignition engines exist in Europe and therefore there are no emission regulations presently enforced. The bases for maximum emissions are the regulations now in force for the parent engine 88/77 CEE-R49.

This regulation exists for diesel engines that normally operate at very high air/fuel ratios. It fixes the molecular weight of the working fluid at 29, approximately that of air. The natural gas conversion will be operating much nearer to stoichiometric and will have a lower air index, defined as

$$\text{Air Index} = \frac{\text{Air/Fuel operating}}{\text{Air/Fuel stoichiometric}}$$

To modify the diesel emission regulation, the molecular weight of the working fluid was calculated at each point in the 13-Mode cycle. The measured NO_x value was corrected for variations in relative humidity as well [1]. For hydrocarbon measurement, a Beckman Model 400 FID (flame ionization detector) was used. A Beckman 864 NDIR (nondispersive infrared analyzer) was used for CO emissions and a Beckman 951A CLA chemiluminescent analyzer was used to measure NO_x.

The Naturally Aspirated Engine Conversion

A fuel system for the addition of natural gas to the inlet manifold and a system to provide spark ignition to each cylinder was fabricated. For this particular engine, close attention was paid to the shape of the combustion chamber, the interaction between the combustion chamber and the valve porting, the valve timing, and the position and number of spark plugs.

Optimizing the number as well as the position of the spark plugs reduces flame travel, a very important factor to increase the "mechanical octane" number of a given engine with a large bore and semiquiescent combustion chamber. Methane fuels are usually characterized by a lower flame speed than higher molecular weight hydrocarbons usually used in transportation engines [2]. Multiple plugs in a combustion chamber can lower flame travel distance but may raise cylinder pressures and temperatures, thus increasing production of NO_x at a given speed and load [3]. An optimum combustion chamber can create adequate air motion to improve flame speed and reduce end gas exposure, thereby reducing the chance of detonation [4, 5]. Efficiency an be increased with the attainment of maximum brake torque spark timing; simultaneously, if this design is carried to an optimum, knock can be eliminated.

Interaction between the inlet and exhaust valve port and combustion chamber can ensure good fuel/air mixing and volumetric efficiency. In diesel baseline engines, the inlet valve port geometry generates swirl to ensure air/fuel mixing during the injection sequence. For the spark-ignition engine, the port can be redesigned to allow increased volumetric efficiency with the elimination of inlet port swirl, thereby allowing combustion chamber shape to govern turbulence.

Valve timing can be adjusted to eliminate the overlap required by the diesel engine to scavenge combustion products from the cylinder. Reduced valve overlap reduces the "blow-through" of fuel present in the inlet charge of an inlet manifold fumigated spark-ignition engine. Subsequently, a natural EGR will be produced in the cylinder with the net effect of charge dilution, thus lowering peak combustion temperature and NO_x production. Power loss produced by this natural EGR can be partially or in whole offset by the increase in volumetric efficiency mentioned previously.

In the spark-ignited natural gas-fueled engine, the advantage of the wide flammability limits and ease of fuel/air mixing can have a strong influence on the performance of an engine operating with lean air/fuel ratios. Spark advance also has a strong influence on the production of NO_x in these engines.

Table 1 IVECO 8220 technical data

Cylinders	6
Displacement	9572 cm³
Bore	125 mm
Stroke	130 mm
Compression Ratio	11:1 (17:1)
Maximum Power	136 kW @ 2600 rpm 151 kW @ 2600 rpm
Maximum Torque	572 Nm @ 1400 rpm 638 Nm @ 1600 rpm
Maximum Brake Efficiency	0.316 (0.351)
Electronic Ignition with Twin Spark Plug	
Two Carburetors IMPCO 200	

Note: The values in parentheses refer to diesel engines.

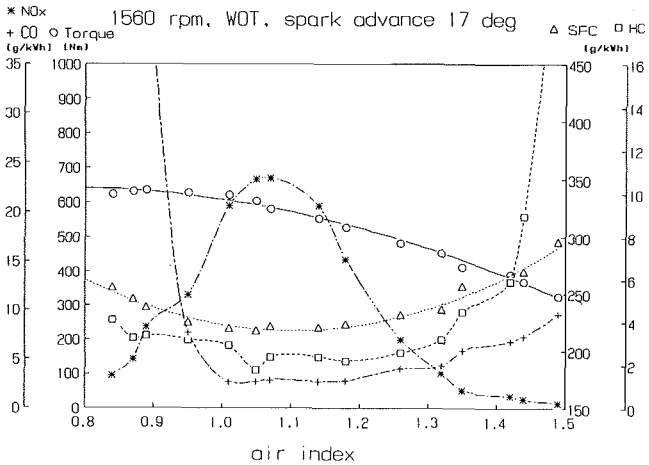

Fig. 1 IVECO 8220 torque: SFC, HC, CO, NO_x

These two parameters, when optimized, can achieve good results without system complexity in reducing emissions.

The test engine used in the conversion was an IVECO 8220 diesel with 9572 cm^3 displacement. A Landi Renzo fuel system was used to fumigate natural gas into the inlet manifold. A disk combustion chamber was fitted with dual spark plugs and an 11:1 compression ratio. The fuel system used two Impco carburetors, each fed from the same methane source, which had undergone pressure reduction through a two-stage regulator setup.

The electronic ignition system allowed the optimum spark advance to be set at each point throughout the speed and load grid. Technical specifications of the engine are reported in Table 1.

Figure 1 shows torque, specific fuel consumption, HC, CO, and NO_x versus the air index (actual air/fuel ratio divided by stoichiometric air/fuel ratio) at maximum manifold pressure and 1560 rpm. These particular tests were performed to optimize the carburetion system.

In these tests, it was evident that natural gas would run without misfire at lean air index values (air index = 1.4) without unduly increasing unburned hydrocarbon emissions. Initial tests also showed that lean mixtures could be burned in semiquiescent or quiescent combustion chambers. Figure 2 shows how lean mixture operation met the existing regulation (88/77 CCE-R49) that could not be met with stoichiometric operation.

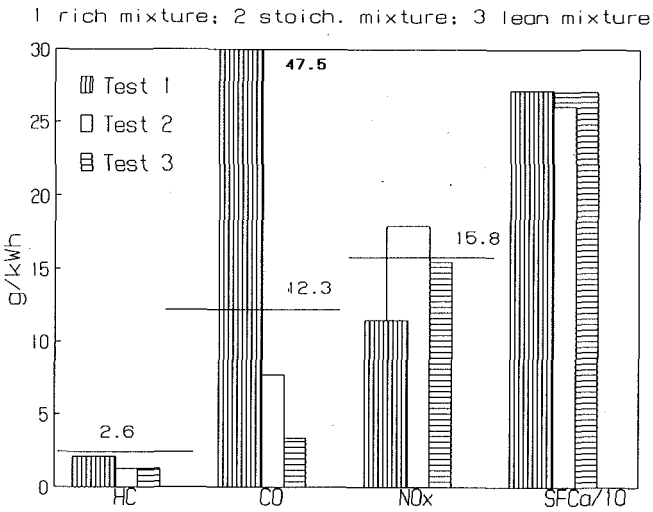

Fig. 2 13-Mode cycle: IVECO 8220

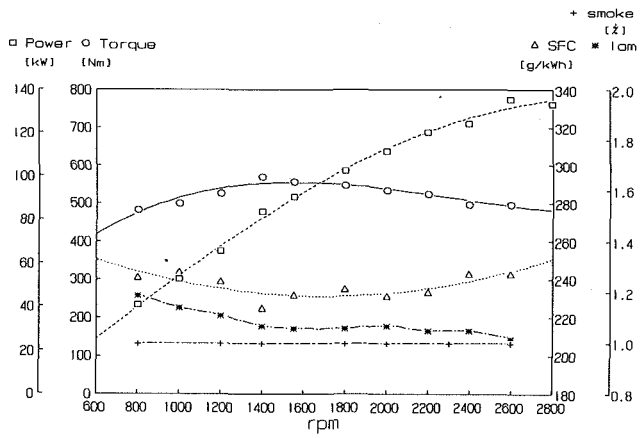

Fig. 3 Torque, power, SFC, lambda: smoke IVECO 8220

Table 2 13-Mode cycle IVECO 8220 engine fueled with methane*

Speed RPM	Torque Nm	Power kW	Air f. kg/h	Fuel f. kg/h	Lambda	BSFC g/kWh	Exhaust M.W. g/mol	S. Adv. deg.	HC	CO g/h	NO_x	Exhaust Temp. (°C)
650	0.7	0.0	28.7	2.02	0.83	--	26.38	5	5	32	2	405
1570	59.7	9.8	126.0	6.76	1.08	689	27.58	16	25	122	30	544
1555	143.9	23.4	193.0	9.17	1.22	391	27.69	15	56	137	40	561
1563	282.3	46.2	289.6	13.36	1.26	289	27.70	14	90	207	91	589
1548	428.3	69.5	362.0	17.08	1.23	246	27.68	14	93	129	294	628
1550	558.2	90.6	382.7	21.05	1.06	232	27.57	13	100	235	1600	674
640	0.7	0.0	24.5	1.86	0.77	--	25.89	5	5	26	2	415
2600	498.5	135.8	576.6	32.99	1.02	243	27.52	21	150	403	3162	764
2590	372.1	101.0	526.6	26.45	1.16	262	27.64	21	93	326	1839	765
2615	250.7	68.7	430.7	21.28	1.18	310	27.66	21	71	306	847	681
2575	123.6	33.3	312.2	15.30	1.19	459	27.66	21	56	249	255	659
2615	49.9	13.7	249.1	12.18	1.19	892	27.66	21	46	243	107	646
625	0.7	0.0	21.9	1.79	0.71	--	25.33	5	5	26	2	436

* *Total Emissions (g/kWh)*
HC = 1.29
CO = 3.36
NO_x = 15.51
Average Fuel Consumption = 271.g/kWh

Table 2 shows detailed results of the 13-Mode cycle using lean mixtures. Torque and power were similar to the diesel baseline while smoke levels were negligible, as can be seen in Fig. 3.

Turbocharged Engines

The conversion of the turbocharged engine is more complex due to the interaction of the turbocharger and the carburetor. Higher power-to-displacement ratios characterize the turbocharged engine. In the case of rich mixtures where the heating value of the fuel charge inducted is greater than the diesel baseline equivalent, very high levels of power can be produced. Because one goal of the engine conversion is to attain engine life that is common to diesel engines, this route was not taken. Equivalent diesel-fuel rates in terms of heating value of the inlet charge were maintained to promote diesel engine life at equivalent power output.

The turbocharged conversion used an IVECO 8460 diesel engine as a baseline. The engine displaced 9500 cm^3, used a disk-shaped combustion chamber with two spark plugs and a compression ratio of 9.0. Maximum boost pressure was 0.6 bar and the charge was air-to-air intercooled. Two stages of pressure regulation fed dual Impco 200 carburetors. Ignition was provided by the same system as that used on the naturally aspirated conversion. Camshaft overlap was reduced to zero to reduce the amount of blow through the fresh inlet charge. Table 3 shows the specifications of this engine.

Figure 4 shows the torque specific fuel consumption, HC, CO, and NO_x versus air index at maximum manifold pressure and 1300 rpm. Lean operation with the disk-shaped combustion proved to be an optimum combination allowing the adjustment of the air/fuel ratio to satisfy the emission regulations.

Tables 4 and 5 show the results of emission tests using lean mixtures. The 13-Mode cycle has been met using this method. Figure 5 shows the air/fuel ratios required to meet this regulation.

In comparison, the results of the turbocharged engine are similar to the naturally aspirated model, both of which passed the emission requirement. This can be seen in Fig. 6. Emissions for the turbocharged engine and the naturally aspirated engine are quite similar, while the torque curve for the turbocharged version is substantially higher over the rpm range, as shown in Fig. 7. By leaning the air/fuel ratio, it is possible to further reduce the emissions from the turbocharged engine. In this case a partial reduction of torque is noted, as shown in Fig. 8.

The use of the two spark plugs can be shown to increase NO_x emissions by increasing the rate of combustion. These single plug results are in agreement with the results from the tests on a Caterpillar TA130 engine using single spark plugs. The characteristics of the two engines—Caterpillar and IVECO

Table 3 IVECO 8460 technical data

Cylinders	6 (turbocharged)
Displacement	9500 cm³
Bore	120 mm
Stroke	140 mm
Compression Ratio	9:1 (16:1)
Maximum Power	152 kW @ 2050 rpm (154 kW @ 2050 rpm)
Maximum Torque	962 Nm @ 1300 rpm (882 Nm @ 1100 rpm)
Maximum Brake Efficiency	0.321 (0.390)
Boost Pressure	0.60 bar
Overlap Angle	0° (49.8°)
Electronic Ignition w/Twin Spark Plugs	
Two Carburetors (IMPCO 200)	
Intercooler	

Note: The values in parenthesis refer to diesel engines.

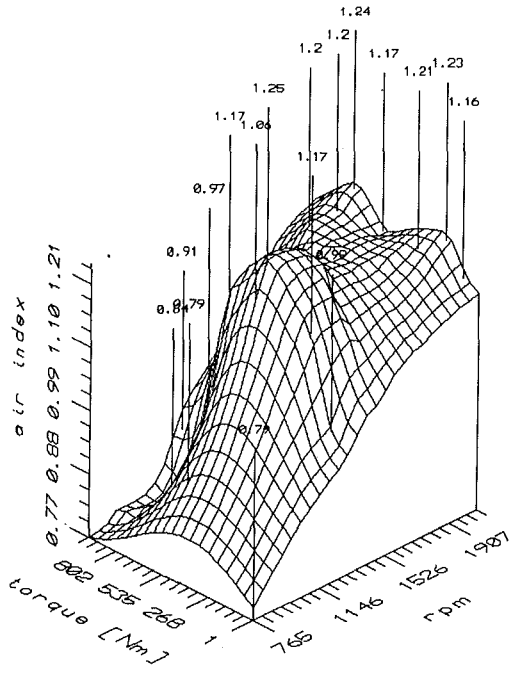

Fig. 5 Air index: IVECO 8460, methane

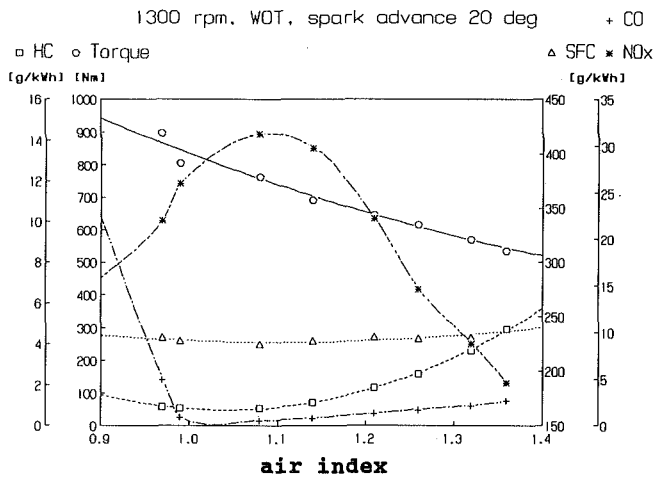

Fig. 4 IVECO 8460 torque, SFC, HC, CO, NO_x

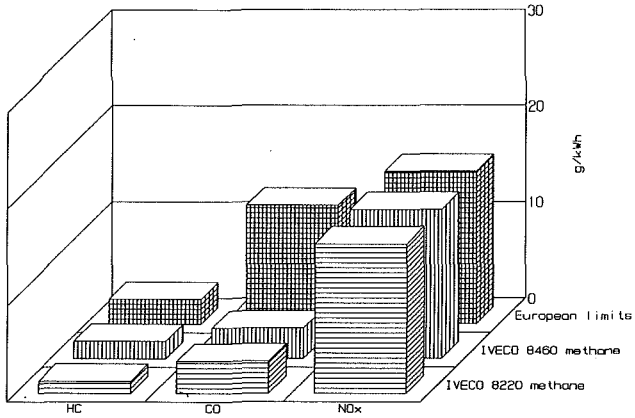

Fig. 6 13-Mode cycle: IVECO 8220 and 8460

Table 4 13-Mode cycle IVECO 8460 engine fueled with methane*

Speed RPM	Torque Nm	Power kW	Air f. kg/h	Fuel f. kg/h	Lambda	BSFC g/kWh	Exhaust M.W. g/mol	S. Adv. deg.	HC	CO g/h	NO_x	Exhaust Temp. (°C)
650	1.4	0.1	36.9	1.88	1.14	--	27.60	0	17	33	2	430
1310	98.3	13.5	147.5	6.80	1.26	504	27.69	8	88	81	13	556
1300	237.3	32.3	228.9	10.62	1.25	329	27.69	8	136	95	44	598
1300	477.5	65.0	379.2	17.07	1.29	263	27.72	10	229	136	134	618
1300	716.2	97.5	454.5	21.60	1.22	221	27.66	18	174	150	2326	619
1300	962.0	131.0	495.4	29.14	0.99	222	27.50	20	140	516	2329	705
740	1.4	0.1	40.0	2.23	1.04	--	27.52	0	15	29	3	477
2035	716.2	152.7	790.0	36.50	1.26	239	27.69	21	262	317	2722	693
2010	525.2	110.6	607.9	29.14	1.21	264	27.64	14	185	290	773	697
2045	358.1	76.7	508.3	24.00	1.23	313	27.65	10	161	235	193	713
2050	182.6	39.2	347.8	16.25	1.24	415	27.66	7	138	161	41	699
2050	74.4	16.0	246.6	12.04	1.19	753	27.63	7	94	154	18	606
660	1.4	0.1	33.0	1.92	1.00	--	27.46	0	16	29	2	456

Total Emissions (g/kWh):
HC = 1.83
CO = 3.19
NO_x = 15.48
Average Fuel Consumption = 252 g/kWh

Table 5 13-Mode cycle IVECO 8460 engine fueled with methane*

Speed RPM	Torque Nm	Power kW	Air f. kg/h	Fuel f. kg/h	Lambda	BSFC g/kWh	Exhaust M.W. g/mol	S. Adv. deg.	HC	CO g/h	NO_x	Exhaust Temp. (°C)
765	0.7	0.1	45.9	2.90	0.92	--	27.10	0	18	41	5	477
1300	94.8	12.9	118.8	6.76	1.02	524	27.53	8	80	140	58	596
1310	238.7	32.8	182.0	10.55	1.00	322	27.51	8	116	1096	256	631
1295	481.0	65.2	294.9	18.13	0.95	278	27.27	10	135	2488	745	644
1297	723.2	98.3	387.3	24.48	0.92	249	27.10	18	153	3262	1692	605
1302	947.9	129.3	501.0	29.60	0.98	229	27.52	24	149	3741	2787	714
756	0.7	0.1	40.7	2.16	1.10	--	27.61	0	17	61	5	681
2050	710.6	152.6	687.6	38.25	1.04	251	27.57	20	134	1205	3961	780
2050	535.0	114.9	518.5	30.60	0.98	266	27.55	14	134	198	2218	777
2060	361.6	78.0	408.0	23.60	1.00	302	27.52	10	159	264	1112	750
2050	179.0	38.4	285.0	16.60	1.00	432	27.61	7	73	739	1215	755
2085	77.2	16.9	201.4	11.91	0.98	706	27.53	7	31	226	103	741
800	0.7	0.1	42.5	2.39	1.03	--	27.57	0	17	48	5	485

Total Emissions (g/kWh):
HC = 1.46
CO = 23.90
NO_x = 20.30
Average Fuel Consumption = 264 g/kWh

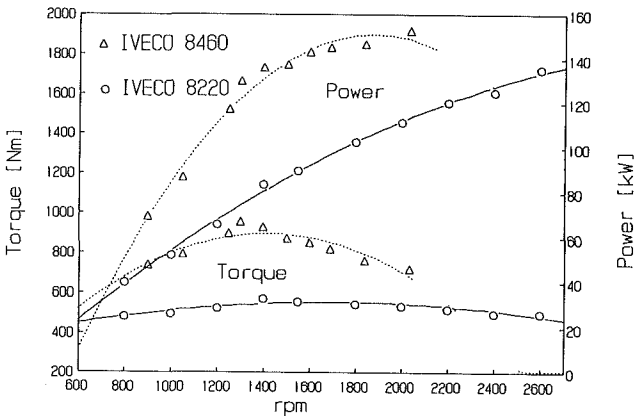

Fig. 7 Power, torque: IVECO 8220 and 8460

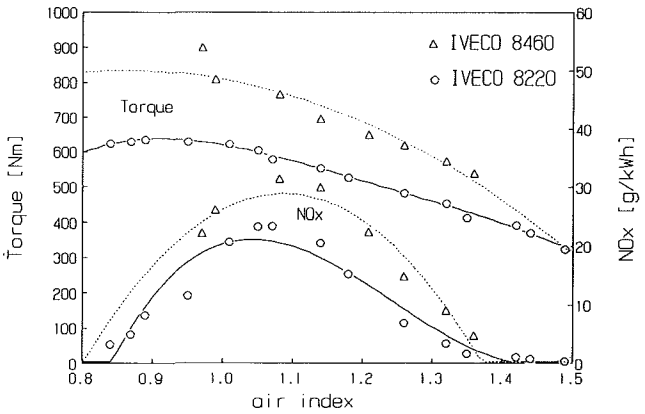

Fig. 8 Torque and NO_x: IVECO 8220 and 8460

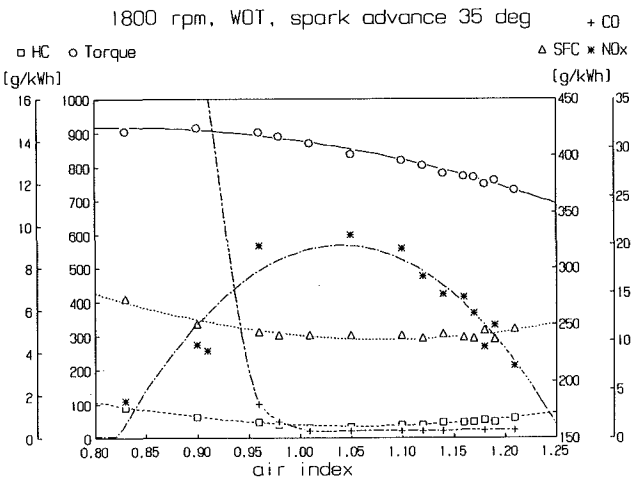

Fig. 9 Torque, SFC, HC, CO, NO_x: Caterpillar TA130

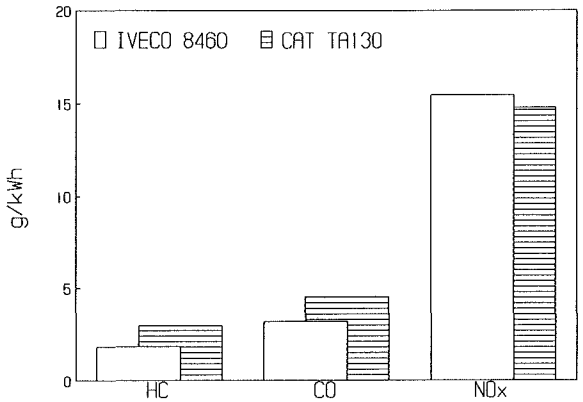

Fig. 10 13-Mode cycle: IVECO 8460 and Caterpillar TA130

8460—are similar. Performance parameters are shown in Fig. 9 for the Caterpillar engine. Lower NO_x is shown than that produced by the IVECO. Figure 10 shows the HC and CO emissions were higher for the Caterpillar engine due to the use of a single spark plug, which may be responsible for incomplete combustion at low loads.

Conclusions

Based on these tests, the performance and emissions of a spark-ignition engine fueled with methane derived from a diesel engine are satisfactory. No complex modifications were needed. With a simple combustion chamber geometry and a specific design of the inlet port, it was possible to reach the same performance of the diesel engine with emission levels lower than European regulations.

With a simple geometry disk combustion chamber, it was necessary to use a twin spark ignition system. In the case of the turbocharged engine, it was necessary to eliminate the valve overlap and to cool the intake charge.

References

1 Karim, G. A., and Wierzba, I., "Comparative Studies of Methane and Propane as Fuels for Spark Ignition and Compression Ignition Engines," SAE Paper No. 831196, 1983.

2 Heywood, J. B., *Internal Combustion Engine Fundamentals*, McGraw-Hill, New York, 1988.

3 Gambino, M., and Rizzo, G., "Lean Burn Engines, Fueled With Alcohol-Gasoline Blends," *Proceedings of the VIII International Symposium on Alcohol Fuels*, Tokyo, Japan, 1988.

4 Gambino, M., and Iannaccone, S., "New Technology on Fuels for Improving Engine Performance With Regulated Combustion," presented at the General Seminar of the U.O. of PFE [in Italian], Montecatini, 1989.

5 Ghezzi, U., and Ortolani, C., *Combustion and Pollution*, X. Y. Tamburini, ed. [in Italian].

6 Gambino, M., Iannaccone, S., and Migliaccio, M., "State-of-the-Art in Research in the Area of Mass Transit Using Natural Gas Fuels," presented at the II National Convention, ATIG, Florence, Italy, 1989 [in Italian].

7 Klimstra, J., "Catalytic Converters for Natural Gas-Fueled Engines: A Measurement and Control Problem," SAE Paper No. 872165, 1987.

8 Kummer, J. T., *A Catalyst for Automotive Emission Control*, Progress in Energy and Combustion Science, Vol. 6, Pergamon Press, New York.

9 Gambino, M., Iannaccone, S., and Unich, A., "The Use of Catalysts for Natural Gas-Fueled Vehicles," presented at the IV METANAUTO, Bologna, Italy, Mar. 1990.

R. R. Sekar

W. W. Marr

Argonne National Laboratory,
Argonne, IL 60439

D. N. Assanis
University of Illinois
Urbana, IL

R. L. Cole

T. J. Marciniak

Argonne National Laboratory,
Argonne, IL 60439

J. E. Schaus
AutoResearch Laboratories, Inc.,
Chicago, IL 60638

Oxygen-Enriched Diesel Engine Performance: A Comparison of Analytical and Experimental Results

Use of oxygen-enriched combustion air in diesel engines can lead to significant improvements in power density, as well as reductions in particulate emissions, but at the expense of higher NO_x emissions. Oxygen enrichment would also lead to lower ignition delays and the opportunity to burn lower grade fuels. Analytical and experimental studies are being conducted in parallel to establish the optimal combination of oxygen level and diesel fuel properties. In this paper, cylinder pressure data acquired on a single-cylinder engine are used to generate heat release rates for operation under various oxygen contents. These derived heat release rates are in turn used to improve the combustion correlation—and thus the prediction capability—of the simulation code. It is shown that simulated and measured cylinder pressures and other performance parameters are in good agreement. The improved simulation can provide sufficiently accurate predictions of trends and magnitudes to be useful in parametric studies assessing the effects of oxygen enrichment and water injection on diesel engine performance. Measured ignition delays, NO_x emissions, and particulate emissions are also compared with previously published data. The measured ignition delays are slightly lower than previously reported. Particulate emissions measured in this series of tests are significantly lower than previously reported.

Introduction

Argonne National Laboratory (ANL) has been studying the application of oxygen-enrichment technology to diesel engines, especially for industrial cogeneration systems (Assanis et al., 1990; Cole et al., 1990; Sekar et al., 1990a, 1990b). An initial assessment was based on a literature survey and a modified simulation code. The study indicated beneficial changes in engine power density, thermal efficiency, ignition delay, smoke, particulates, and other exhaust emissions. The only problem area was the increase in NO_x emissions. In order to control NO_x emissions, water was introduced into the combustion process in the form of emulsified fuel. It was also concluded that less-refined, cheaper fuel could be used with oxygen-enriched air. This fact could make the concept economically viable.

First-phase experimental work has been conducted on a single-cylinder, heavy-duty diesel engine. The experimental data have been used to fine-tune the simulation code for the oxygen-enriched diesel engine. The objective is to develop a reliable code, validated by experimental data. Such a tool would be very useful in predicting the performance of full-size cogeneration systems, using larger diesel engines, as opposed to conducting time-consuming and expensive experimentation.

Contributed by the Internal Combustion Engine Division and presented at the Twelfth Annual Fall Technical Conference, Rockford, Illinois, October 7–10, 1990. Manuscript received by the Internal Combustion Engine Division July 1990.

This paper summarizes the original model assumptions and the modifications that were implemented in order to simulate the performance of the single-cylinder test engine with various levels of oxygen enrichment. Then, ANL experimental data are compared with simulation predictions. Also, emissions and ignition delays from the ANL data set are compared with previously published data of other investigators.

Performance Prediction Code

A turbocharged and turbocompound diesel engine computer simulation has been developed by Assanis and validated against test results from a Cummins engine (Assanis and Heywood, 1986). The parent code was modified at the University of Illinois in order to allow for various levels of oxygen enrichment in the intake air and for operation with water-emulsified fuels. This section briefly summarizes the main assumptions of the simulation and describes changes implemented in order to conduct our study. Additional details on the parent code can be found from Assanis and Heywood (1986).

Summary of Parent Code. In the computer simulation, the reciprocator cylinders, the intake manifold, and the various sections of the exhaust manifold are treated as a series of connected open systems. In general, the systems are open to the transfer of mass, enthalpy, and energy in the form of work

and heat. The contents of each of these systems are represented as one continuous medium by defining an average equivalence ratio and a uniform temperature and pressure at all times.

Gas properties are calculated assuming ideal gas behavior. At low temperatures (below 1000 K), the cylinder contents are treated as a homogeneous mixture of nonreacting ideal gases. At high temperatures (above 1000 K), the properties of the cylinder contents are calculated by assuming the burned gases are in equilibrium, with allowance for chemical dissociation (Martin and Heywood, 1977). Provisions are incorporated in the thermodynamic property routines in order to model intake air with various levels of oxygen enrichment (i.e., with a desired N:O ratio).

The diesel four-stroke cycle is treated as a sequence of continuous processes: intake, compression, combustion (including expansion), and exhaust. Quasi-steady, adiabatic, one-dimensional flow equations are used to predict mass flows past the intake and exhaust valves. The compression process is defined to include the ignition delay period (i.e., the time interval between the start of the injection process and the ignition point). The total length of the ignition delay can either be specified or predicted using an Arrhenius expression based on the mean cylinder gas temperature and pressure during the delay period. Combustion is modeled as a uniformly distributed heat release process. The sum of two algebraic functions, one for the premixed and the other for the diffusion-controlled combustion phase, is used to describe the rate of fuel burning (Watson et al., 1980). The relative weight of each combustion phase depends on the length of the ignition delay period and on the engine load and speed.

Heat transfer is included in all the engine processes. Convective heat transfer is modeled using available engine correlations based on turbulent flow in pipes. The characteristic velocity and length scales required to evaluate these correlations are obtained from a mean and turbulent kinetic energy model. Radiative heat transfer, based on the predicted flame temperature, is added during combustion. The time-dependent temperature distributions in the piston, cylinder head, liner, and manifold walls are computed using coupled, transient heat conduction models for the wall structures.

Summary of Simulation Modifications. Since the heat release correlation in the original code did not capture the effect of oxygen enrichment on combustion, an alternative option was implemented in the code to use heat release profiles based on our experimental results. First, the cylinder pressure diagrams obtained from the experiments were used to generate heat release rate diagrams as a function of oxygen content. The heat release code that was used treats the combustion chamber contents as uniformly mixed and accounts for the effects of crevice volume and in-cylinder motion. If desired, the program can also approximate the gas-to-wall heat transfer according to the Woschni correlation (Woschni, 1967). More details on the heat release code are given by Bonne (1989). The experimentally derived heat release profiles were then used as inputs to the diesel computer simulation to model performance for different oxygen levels.

The original computer code could only be used with turbomachinery, and thus required specific map characteristics an an input. Simulations of naturally aspirated engines, or of single-cylinder laboratory engines with controlled intake/exhaust plenum conditions, were not possible. The new version of the code allows the option of treating the manifolds as constant pressure and temperature plenums, in addition to the option of determining these conditions from the solution of the manifold state equations. The modified diesel simulation can now be used to model a wide variety of engine systems ranging from complex intercooled, turbocompound engines to less complicated systems, such as the naturally aspirated engine.

The original computer model required a table of measured effective valve open areas to predict mass flow rates across the valves during the gas exchange process. Since these data are often not readily available, the polydyne cam model (Assanis and Polishak, 1990) was implemented in the simulation. Using this approach, the valve lift data are calculated after specifying the desired maximum lift and half-event angle. Transforming this valve lift curve into effective valve area at each crank angle involves a two-step calculation. First, a model is used to calculate the minimum area between the valve and the valve seat at each crank angle; second, the discharge coefficient for the given valve lift is calculated. The product of the minimum valve area and the discharge coefficient is equal to the effective valve area.

In order to calculate the minimum geometric valve area, the valve lift process is broken into three regimes. When lift first occurs and is still relatively small, the minimum valve area corresponds to the frustrum of a right circular cone; the conical face between the valve and seat, which is perpendicular to the seat, defines the flow area. The minimum area for the next regime is still the surface of the frustrum of a right circular cone, but this surface is no longer perpendicular to the valve seat. The base angle of the cone increases to 90 deg. Finally, when the valve lift is sufficiently large, the minimum flow area is the port flow area minus the sectional area of the valve stem. Details are given by Heywood (1988).

Once the minimum valve area has been defined, the discharge coefficient is determined based on experimental data correlated to the valve area calculations. This study utilizes the discharge coefficient algorithm developed by Noyes (1980). Noyes' analytical predictions are based on experimental data for pressure ratios between 1.125 and 2.5, valve rise (valve lift divided by the valve port diameter) between 0 and 0.408, and valve seat angles between 30 and 45 deg. A least-squares algorithm was used to determine the best correlation between pressure ratio, valve lift, and valve seat and the measured values of the discharge coefficient.

Method of Solution. When the individual submodels of the cycle simulations are brought together to form a complete model, the result is a set of first-order ordinary differential equations. To perform predictive calculations with the cycle simulation, these equations are simultaneously integrated over the full operating cycle. Results include profiles of the state variables (such as temperature and pressure, mass flows through the valves) at specified crank angle intervals, as well as integrated performance results. The latter include power, volumetric and thermal efficiencies, gross indicated and pumping mean effective pressures, total heat loss, burn duration, and an estimated mean exhaust temperature. Heat and work transferred during each process of the cycle and the results of an overall energy balance are also provided.

Experimental Setup

Single-Cylinder Engine. A single-cylinder, four-stroke, direct-injection diesel engine was used in this series of experiments. This is a one-cylinder version of a heavy-duty diesel engine commonly used in heavy-duty trucks and in other, off-highway applications. The major specifications of the base engine are given in Table 1. No hardware changes were made to the base engine, and the manufacturer's recommendations were followed in the setup and operating procedures.

Table 1 Test engine specifications

Number of Cylinders	1
Bore × Stroke	137 mm × 165 mm
Displacement	2.44 L
Engine Speed	1800 rpm
Injection Timing	33° btdc
Compression Ratio	14.5
Peak Cylinder Pressure	11.3 MPa

Oxygen Supply System. For the purpose of the tests reported here, compressed oxygen from a bank of cylinders was used. The oxygen and the combustion air were mixed in a large tank before entering the intake manifold of the engine. A micro-fuel-cell-type (Teledyne model 326A) oxygen sensor located in the engine intake manifold was used to measure and control the intake oxygen content of the air entering the engine. Elaborate safety systems were provided to handle the compressed oxygen. The engine crank case was purged with nitrogen for added safety while running the engine. The amount of oxygen supplied from the cylinders was measured separately.

Instrumentation. For the most part, standard engine test-cell instrumentation was used for these tests. Cylinder pressure diagrams were obtained with an AVL pressure transducer, an optical encoder, and a PC-based data-acquisition system developed at the University of Illinois. NO_x and O_2 concentrations were measured in the exhaust gas stream. A conventional filter method was used to measure the particulate emissions. Two Fiberfilm TG0A20 filters were used in series to ensure high particulate collection efficiency. Details of the experimental arrangement and data collection procedures can be found from Sekar et al. (1990a, 1990b).

Test Conditions. The oxygen level of the intake air was varied from 21 to 35 percent by volume by mixing oxygen purchased in commercially available tanks with shop air supply. For each oxygen level, engine performance and emissions were recorded at a speed of 1800 rpm and full load. Extensive data were obtained for #2 and #4 diesel fuels and their emulsions with water. The intake and exhaust manifold pressures were maintained at 140 cm Hg abs. and 81 cm Hg abs., respectively, throughout the tests. Engine fuel rate was increased until the maximum power was reached. Engine manufacturer's recommendations were followed in the selection of these parameters (i.e., "full load" setting, boost, and back pressures). This resulted in nearly constant total mass flow rate of air and oxygen. The maximum power potential at each oxygen level was reached when the exhaust oxygen level was the same as that for the base engine, or when the exhaust manifold temperature reached a generally accepted maximum value of about 630°C.

Comparison of Analytical and Experimental Results

In this section, the measured cylinder pressure, engine power output, thermal efficiency, and intake air/O_2 mixture mass flow rates are compared to the simulation results. Only the results for nonemulsified diesel fuel are discussed here, since modeling of the effects of water injection on combustion heat release is currently being refined. The experimental ignition delays and NO_x and particulate emissions are also compared with previously published data.

Measured cylinder pressure data for the baseline case (21 percent oxygen content) and for the highest oxygen enrichment level (35 percent oxygen content) are shown in Figs. 1 and 2, respectively. These data represent smoothed profiles, derived by averaging samples of 30 engine cycles. The measured data have been processed using our heat release analysis program. Since the Woschni heat transfer correlation was developed for engines operating with base oxygen levels, there is no reason to expect it accurately to predict heat transfer under oxygen-enriched operation. For this reason, all heat release calculations are performed on a net basis (i.e., without attempting to add back a term for heat loss to the walls). As a result, the cumulative net heat release, when normalized by the fuel energy content, will not approach 100 percent. Nevertheless, changes in heat transfer and combustion efficiency will still appear as changes in the net heat release.

Net heat release rates for the engine operating under 21 and 35 percent oxygen level are shown in Figs. 3 and 4, respectively.

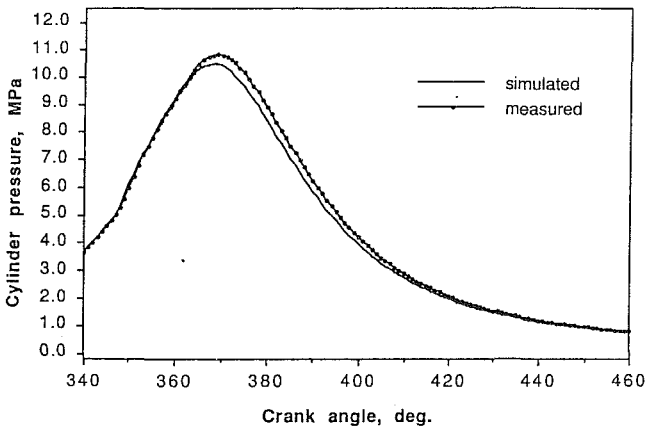

Fig. 1 Comparison of measured and predicted pressure traces for baseline engine operation with 21 percent oxygen

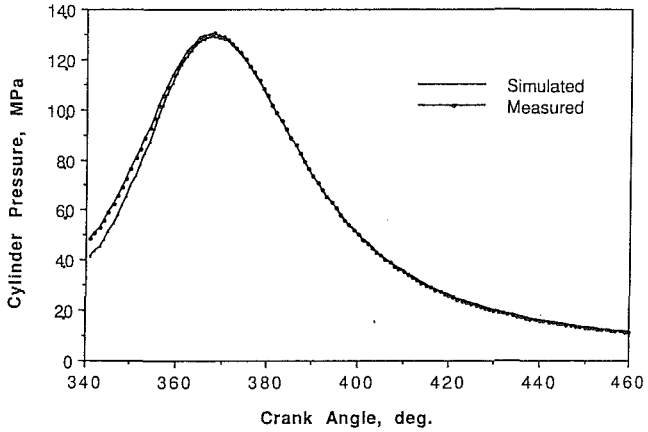

Fig. 2 Comparison of measured and predicted pressure traces for operation with 35 percent oxygen

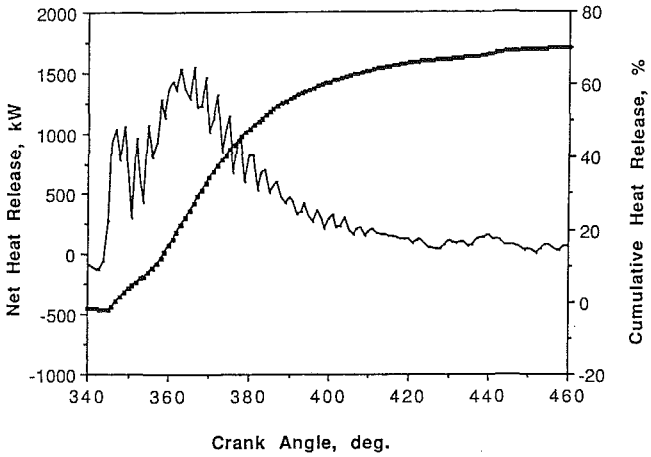

Fig. 3 Net heat release rates and cumulative heat release as a function of crank angle for baseline engine operation with 21 percent oxygen

Superposed on each of these figures is the cumulative net heat release. The injection timing is the same for both runs (i.e., 33 deg btdc). The effect of oxygen enrichment on heat release is noticeable. Ignition delay is shorter, so that there is almost no premixed burning. Combustion is overall more uniform with increasing oxygen content, reaches a higher peak, and ends earlier in the expansion stroke. Only 70 percent of the energy (on a net basis) is released with 21 percent oxygen, but more energy (approaching 76 percent) is released with 35 percent oxygen, indicating a more efficient combustion for the latter case.

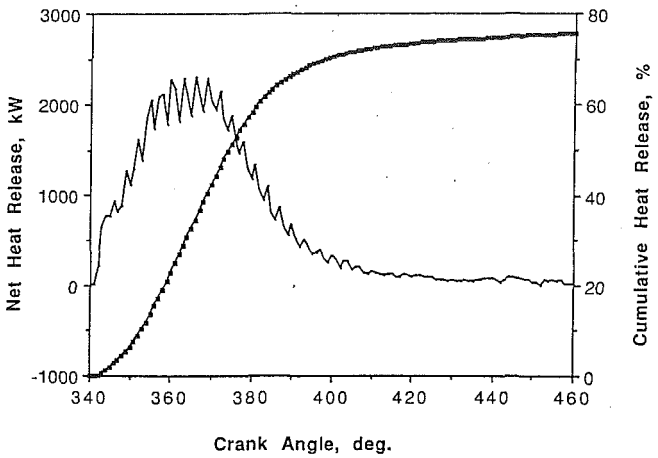

Fig. 4 Net heat release rates and cumulative heat release as a function of crank angle for operation with 35 percent oxygen

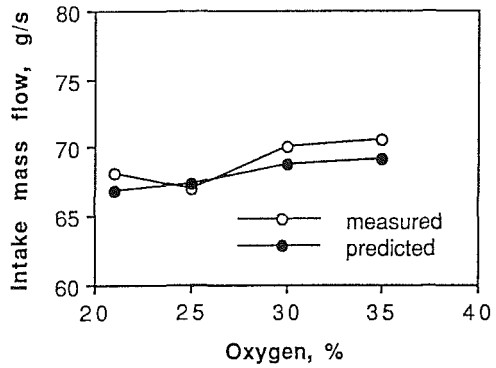

Fig. 5 Predicted and measured intake mass flow rates as a function of oxygen concentration in the combustion air

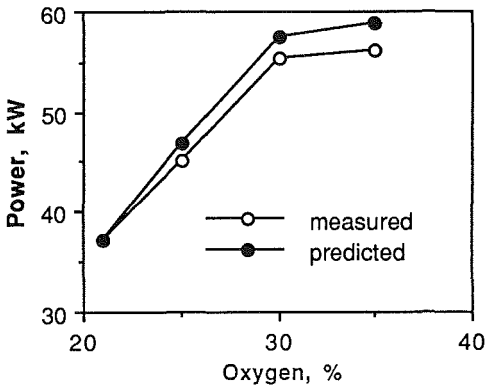

Fig. 6 Predicted and measured brake power as a function of oxygen concentration in the combustion air

The derived net heat release profiles were used to establish apparent rates of fuel burning; the latter were then provided as inputs to the simulation. The predicted pressure profiles for operation with 21 and 35 percent oxygen are compared to the measured pressure traces in Figs. 1 and 2, respectively. The same procedure was followed for the data obtained from running with 25 and 30 percent oxygen. Excellent comparisons of pressure levels and the rates of pressure rise are evident at all oxygen levels.

Figures 5, 6, and 7 compare predicted intake mass flow rates, brake power output, and brake thermal efficiencies against experimental data. Experimental motoring friction data for operation with 21 percent oxygen were used to develop a friction correlation that was used in the simulation. The variation of all three predicted performance quantities closely follows

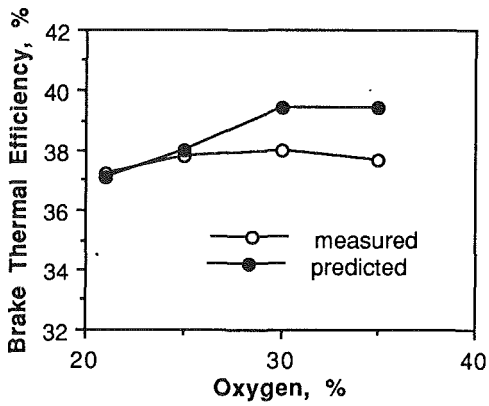

Fig. 7 Predicted and measured brake thermal efficiency as a function of oxygen concentration in the combustion air

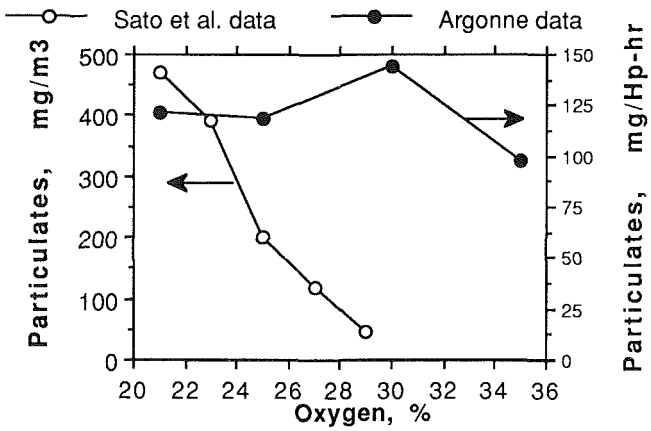

Fig. 8 Comparison of measured particulate emissions for various oxygen concentrations against previously published data (Iida et al., 1986)

the data in both magnitude and trend. The maximum difference between the calculated and measured power and thermal efficiency is under 5 percent, while mass flow rates compare within 2 percent. The small discrepancies are attributed to possible measurement errors and to inadequacies in heat transfer and friction modeling with higher loads under oxygen enrichment. Overall, the results confirm that the simulation can provide sufficiently accurate predictions of trends and magnitudes to be useful in parametric studies assessing the effects of oxygen enrichment on engine performance. Thus, we are planning to use the model to predict performance of large-scale diesel engines with oxygen-enriched combustion air.

Emissions data obtained by ANL followed predictable trends. In general, particulate emissions decrease and NO_x emissions increase when the oxygen level is increased. Particulate data are plotted in comparison with previously published data in Fig. 8. ANL data were obtained at maximum power for each Q_2 level. Since maximum power varies, it is more meaningful to plot NO_x and particulate data per kilowatt. Adequate information is not available to plot the data of Sato et al. in identical units. Hence, comparison of trends, rather than absolute values, is recommended in Figs. 8 and 9. The Argonne data do not show as large a reduction as Iida's data (Iida et al., 1986). It is possible, though, that the engine used by ANL had low particulate emissions to start with and, therefore, was not as sensitive to oxygen level.

The NO_x data in Fig. 9 agree well with previously published results (Iida and Sato, 1988). Since the adiabatic flame temperatures in oxygen-rich combustion are higher, it is expected that they would result in higher NO_x levels. It is very important to control the tendency for increasing NO_x emissions if this

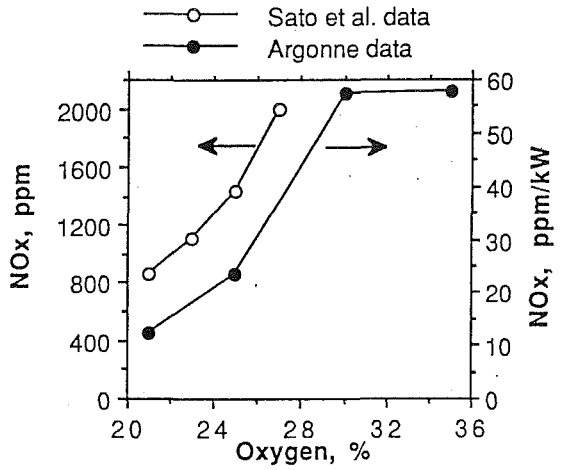

Fig. 9 Comparison of measured NO_x emissions for various oxygen concentrations against previously published data (Iida and Sato, 1988)

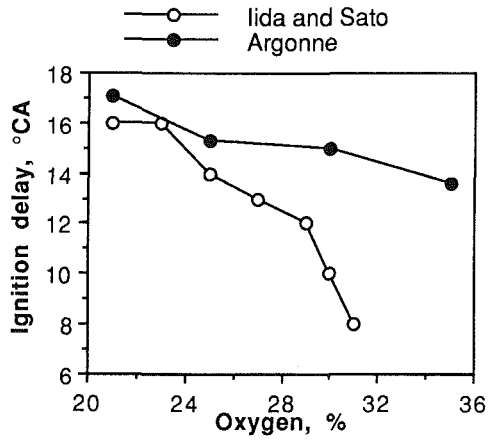

Fig. 10 Comparison of measured ignition delay for various oxygen concentrations against previously published data (Iida and Sato, 1988)

technology is to be commercialized. Retarding fuel-injection timing and addition of water into the combustion process are two possible means to control NO_x without adverse effects on engine performance. Experimental data on water-emulsified fuel are available (Iida et al., 1986), but data on retarded injection timing effects are not yet available. As shown in Fig. 10, the ignition delay is reduced with oxygen-enriched air. Hence, retarding the injection timing is expected to reduce NO_x without any fuel consumption penalties.

Conclusions and Recommendations

A computer simulation has been modified to model the performance of a diesel engine for operation with various levels of oxygen enrichment. The computer code predictions have been satisfactorily verified against experimental results. The model provides a useful tool for predicting the performance of a full-size diesel engine system using oxygen-enrichment technology. The methodology adopted here in correlating experimental data with simulation predictions should be extended to analyze results from tests with water-emulsified fuels. The measured heat release data for various oxygen and water content levels should used to develop a more generalized heat release correlation to account for operation with oxygen enrichment and water-emulsified fuels.

Both the analysis and the test program have indicated that oxygen-enriched combustion air significantly improves the performance of a diesel engine. Higher heat release rates and an overall increase in the engine power density have been obtained. The increased combustion rate associated with oxygen enrichment may provide the opportunity for using less volatile and less expensive grades of diesel fuel. Significant increases in cylinder temperatures and pressures are also associated with oxygen enrichment.

The experimental emissions data compare well with expected trends. It has been shown that oxygen enrichment reduces the particulate and hydrocarbon emissions. Although NO_x emissions would increase (due to the higher cylinder temperatures), they could be controlled through the use of water-emulsified fuels. Overall, results are encouraging, and the technology should be tested in a full-scale application.

Acknowledgments

This work is supported by the U.S. Department of Energy, Assistant Secretary for Conservation and Renewable Energy, under contract No. W-31-109-Eng-38. Accordingly, the U.S. Government retains a nonexclusive, royalty-free license to publish or reproduce the published form of this contribution, or allow others to do so, for U.S. Government purposes.

References

Assanis, D. N., and Heywood, J. B., 1986, "Development and Use of a Computer Simulation of the Turbocompounded Diesel System for Engine Performance and Component Heat Transfer Studies," *SAE Transactions*, Paper No. 860329.

Assanis, D. N., and Polishak, M., 1990, "Valve Event Optimization in a Spark-Ignition Engine," ASME JOURNAL OF ENGINEERING FOR GAS TURBINES AND POWER, Vol. 112, pp. 341–347.

Assanis, D. N., Sekar, R. R., Baker, D., Siambekos, C. T., Cole, R. L., and Marciniak, T. J., 1990, "Simulation Studies of Diesel Engine Performance With Oxygen Enriched Air and Water Emulsified Fuels," ASME Paper No. 90-ICE-17.

Bonne, M. A., 1989, "Development of Instrumentation and Analysis Techniques for Diesel Engine Combustion and Heat Transfer Studies," MS Thesis, University of Illinois, Urbana.

Cole, R. L., Sekar, R. R., Stodolsky, F., and Marciniak, T. J., "Technical and Economic Evaluation of Diesel Engine With Oxygen Enrichment and Water Injection," ASME Paper No. 90-ICE-1.

Heywood, J. B., 1988, *Internal Combustion Engine Fundamentals*, McGraw-Hill, New York.

Iida, N., et al., 1986, "Effects of Intake Oxygen Concentration on the Characteristics of Particulate Emissions From a D. I. Diesel Engine," SAE Paper No. 861233.

Iida, N., and Sato, G. T., 1988, "Temperature and Mixing Effects on NO_x and Particulates," SAE Paper No. 880424.

Martin, M. K., and Heywood, J. B., 1977, "Approximate Relationships for the Thermodynamic Properties of Hydrocarbon-Air Combustion Products," *Combustion Science and Technology*, Vol. 15, pp. 1–10.

Noyes, R. N., 1980, "Analytical Predictions of Discharge Coefficients for Engine Poppet Valves," GMR-3376.

Sekar, R. R., Marr, W. W., Schaus, J. E., Cole, R. L., and Marciniak, T. J., 1990a, "Diesel Engine Experiments With Oxygen Enrichment, Water Addition and Lower-Grade Fuel," to be presented at the Intersociety Energy Conversion Engineering Conference, Reno, NV.

Sekar, R. R., Marr, W. W., Schaus, J. E., Cole, R. L., Marciniak, T. J., and Eustis, J. N., 1990b, "Cylinder Pressure Analysis of a Diesel Engine Using Oxygen-Enriched Air and Emulsified Fuels," to be presented at the SAE Off-Highway and Powerplant Meeting, Milwaukee, WI.

Watson, N., Piley, A. D., and Marzouk, M., 1980, "A Combustion Correlation for Diesel Engine Simulation," SAE Paper No. 800029.

Woschni, G., 1967, "A Universally Applicable Equation for the Instantaneous Heat Transfer Coefficient in the Internal Combustion Engine," *SAE Transactions*, Vol. 76, Paper No. 670931.

Gaseous and Particulate Emissions From Diesel Locomotive Engines

S. G. Fritz
Department of Emissions Research,
Southwest Research Institute,
San Antonio, TX 78228

G. R. Cataldi
Research and Test Department,
Association of American Railroads,
Washington, DC 20001

Steady-state gaseous and particulate emissions data are presented from two 12-cylinder diesel locomotive engines. The two laboratory engines, a EMD 645E3B and a GE 7FDL, are rated at 1860 kW (2500 hp) and are representative of the majority of the locomotive fleet in North America. Each engine was tested for total hydrocarbons (HC), carbon monoxide (CO), oxides of nitrogen (NO_x), and particulate. Emissions were measured at all steady-state operating conditions that make up the eight discrete locomotive throttle notch positions, plus idle, low idle, and dynamic brake. Emissions are reported for each engine with two different diesel fuels: a baseline diesel fuel with a sulfur content of 0.33 weight percent, and a commercially available low-sulfur diesel fuel with a sulfur content of 0.01 weight percent.

Introduction

The current regulatory climate regarding engine emissions suggests that locomotive engine emissions (both gaseous and particulate) may soon be regulated beyond existing visible smoke standards. Because of their significant fuel consumption nationwide, regulatory agencies have periodically estimated the railroads' contribution to air quality problems. Previous studies by the EPA in the 1970s [1] and again in 1984 [2] have shown that the contribution of locomotive engine exhaust to the air pollution problem to be relatively small compared to other mobile sources. However, continuing nonattainment of National Ambient Air Quality Standards (NAAQS) in many urban areas has resulted in consideration of regulations in California for off-highway mobile sources (including locomotives). With the current national environmental activism and the resulting pressure on legislators and environmental regulators, off-highway mobile source emission regulations may extend to other parts of the nation (through the Environmental Protection Agency) within the next few years. Both the House and Senate versions of the Clean Air Act Amendments of 1990 authorize the EPA to study nonroad sources in nonattainment areas.

Background

Several factors must be emphasized regarding locomotive diesel engines as compared to on-highway heavy-duty diesel engines. These include engine size and speed, and wheel-engine speed independence. Almost all locomotives are powered by medium-speed diesel engines, with maximum operating speeds of 900–1100 revolutions per minute (rpm). Locomotive engines are designed to operate at relatively low speeds for high fuel efficiency and extremely long life. Cylinder diameters are in the range of 25 cm (10 in.). A new locomotive engine of current design costs about $400,000. In 1988, by far the most productive year for locomotive manufacturers and the most profitable one for railroads (in terms of revenue-ton miles) recently, approximately 500 locomotive-size diesel engines were produced in the U.S.; sales of approximately 700 were predicted for 1989.

Locomotive engines are coupled to the drive wheels through electric motors. There is no requirement that the drive wheel speed (and train speed) have any relation to the engine speed, as is the case with trucks and buses, which have automatic or manual transmissions essentially identical in function to those in passenger cars. The locomotive diesel engine drives an electric generator or alternator. The electricity is then used to drive direct current traction motors, which rotate the locomotive wheels. This allows the locomotive engine to be operated at a series of fixed settings (throttle notches), each providing a constant amount of power at a governed engine speed. Train speed is determined by the balancing of locomotive pulling force and the train resistance. At a given engine throttle notch with a short train, this may be a relatively high train speed. With a long or heavy train or severe grade, the same throttle notch will result in a much lower train speed. This means a train can accelerate or decelerate while the engine remains at a constant governed speed providing a fixed power output. Thus the use of a d-c traction motor allows the engine speed to be independent of train speed. Since electric traction motors are interposed between the locomotive engine and the driving wheels, virtually all operations (except switching) are characterized by relatively extended periods of constant engine speed and load.

U.S. Locomotive Engine Types. There are effectively only two basic engines represented in the U.S. locomotive population. One of these is the two-stroke cycle engine manufactured by Electro-Motive Division (EMD) of General Motors Corporation. The majority of Class I U.S. locomotives (approximately 70 percent) are powered by a variant of this engine. Nearly all of the remaining U.S. locomotives use the four-stroke cycle engine manufactured by the Transportation Sys-

Contributed by the Internal Combustion Engine Division and presented at the Twelfth Annual Fall Technical Conference, Rockford, Illinois, October 7–10, 1990. Manuscript received by the Internal Combustion Engine Division July 1990.

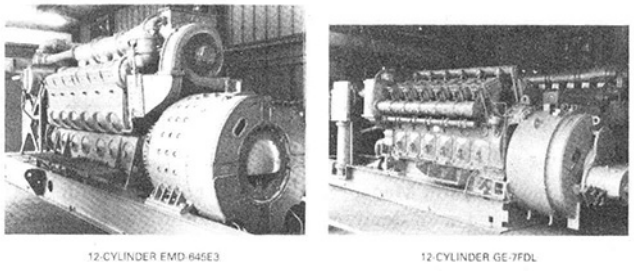

Fig. 1 Locomotive test engines at SwRI

tems Division of the General Electric Company (GE). Two engine designs manufactured by Caterpillar Inc. are being field tested in a limited number of locomotives. A variety of other engine designs can be found on older switcher locomotives owned by short line railroads and private industrial railroads.

Both EMD and GE have significantly increased horsepower and fuel economy in the last few decades. For instance, EMD has increased engine displacement and fuel injection pressure, and have expanded the use of turbocharging in this time period. Current locomotive engines are designed for high power and high thermal efficiency. Over the years, EMD and GE engines have been constantly upgraded and modernized.

Previous Locomotive Emission Studies. A very limited amount of information exists in the public domain on locomotive emissions. The Southern Pacific Transportation Company (SP) performed a study to develop certification procedures for visible smoke from locomotives in 1973 [3]. A field study was performed on GE locomotives by SwRI with GE and the SP in 1975 [4]. Several studies of locomotive engine emissions were performed by SwRI for the U.S. Department of Transportation, the Federal Railroad Administration, and the EPA in the mid-1970s [5–9]. These studies focused on gaseous emissions and visible smoke (or percent opacity based light extinction smoke meters) and were performed on engines that are now two generations old. Most of these locomotives have been retired, upgraded, placed in switcher service, or sold to short line railroads where they are used much less frequently.

A field study of in-service locomotive exhaust emissions was performed by the AAR in 1981–1983 [10]. Other studies by the AAR in the early and mid-1980s were performed primarily to determine engine performance while operating on alternative fuels, emulsions, or broadened specification diesel fuels. During some of these tests, gaseous emissions were recorded [11–14]. Since that time, however, significant engine upgrades in both the EMD and GE engine families have occurred and a corresponding upgrade of emission data is needed.

The fact that virtually all the locomotive emission data that are publicly available are unrepresentative of the current generation locomotive fleet, coupled with the increase in regulatory activity (particularly in California), prompted the AAR to acquire representative locomotive engine emission data (both gaseous and particulate). These new data are intended to serve as current locomotive baseline emission data in air quality inventory studies. The effort to develop new data was initiated in 1988 with the construction of a mobile emissions facility and the upgrade of the two 12-cylinder locomotive test engines at SwRI [14]. The work described below was performed as part of the 1989 AAR Diesel Fuel Specification and Locomotive Improvement Program [15].

Table 1 Locomotive test engine specifications

	EMD 12-645E3B	GE 12-7FDL
Number of Cylinders	12	12
Displacement L (in^3)	10.6 (645)	10.9 (668)
Bore and Stroke mm (in)	230 x 254 (9-1/16 x 10)	229 x 267 (9 x 10½)
Rated Speed (rpm)	904	1,050
Rated Power @ flywheel kW (bhp)	1,865 (2,500)	1,865 (2,500)
Compression Ratio	14.5:1	12.7:1
Cycle	2	4
Injection System	Unit Injector	Jerk Pump/ Nozzle

Experimental Test Plan

Description of Test Engines and Facilities. The EMD 12-645E3B engine shown in Fig. 1 is a two-stroke cycle engine, while the GE 12-7FDL operates on the four-stroke cycle. In the SwRI locomotive engine test facility, the EMD is loaded by a d-c generator and the GE by a d-c rectified alternator. The d-c power is absorbed by two sets of locomotive load grids equipped with cooling fans for heat dissipation. Both engines have their own cooling systems, which are modified versions of the standard locomotive system. Pertinent specifications for each of the test engines are shown in Table 1.

Both engines are operated at conditions that simulate the notch operation of their respective line-haul locomotives. Locomotive engines operate only at specified speed/power combinations defined by throttle "positions" or "notches." Since the power output and speed are constant at each notch position, the fuel consumption rate is also constant and can be defined for each position. EMD and GE engines in line-haul service operate at eight power-producing notches. There are also idle and, in some locomotives, low idle operating positions. The

Nomenclature

AAR = Association of American Railroads
a-c = alternating current
ASTM = American Society for Testing and Materials
bhp = brake horsepower
CL = chemiluminescent analyzer
CO = carbon monoxide
CO_2 = carbon dioxide
DB = dynamic brake
d-c = direct current
EMD = Electro-Motive Division of General Motors Corporation
EPA = United States Environmental Protection Agency
°F = degrees Fahrenheit
g = grams
GE = General Electric Company
GELH = General Electric Line Haul Duty Cycle
HC = hydrocarbons
HFID = heated flame ionization detector
hp = horsepower
h = hour
kW = kilowatt
NAAQS = National Ambient Air Quality Standards
NDIR = nondispersive infrared analyzer
NO_x = oxides of nitrogen
PM = particulate matter
rpm = revolutions per minute
SAE = Society of Automotive Engineers
SOF = soluble organic fraction
SP = Southern Pacific Transportation Company
SwRI = Southwest Research Institute

dynamic brake (DB) throttle notch position is used when the locomotive is braking the train and the traction motors are used as generators. The d-c power generated during the dynamic brake operation is dissipated through resistive load grids located on the roof of the locomotive. To facilitate laboratory testing, the positions were redefined in terms of speed and fuel mass consumption rate combinations (see Table 2). Notch 8 of each schedule represents rated speed and load of the engine. All other positions represent part-load conditions.

Amtrak Simulation. Because of the unique engine operating conditions of locomotives operated by the National Railroad Passenger Corporation (Amtrak), gaseous and particulate emission were measured on the 12-cylinder EMD 645E3B engine at speed and power settings different from those used for emulating freight locomotives. As shown in Table 3, Notches 8 through Idle are at a constant engine of 893 rpm. This engine speed represents synchronous speed for the main alternator, which provides a-c power to the trailing passenger cars. Engine power output is varied by changing the excitation to the alternator. At idle conditions, there is a "hotel" power requirement of approximately 32–35 kW for each passenger car, which represents a typical engine load at idle of 345 kW (462 bhp) at the flywheel. Therefore, the Amtrak idle condition is defined by an engine speed of 893 rpm and a load of 345 kW (462 bhp). The rated power at Notch 8 remains approximately 1864 kW (2500 bhp) at the flywheel. Since the hotel power requirement is relatively constant, even when the train is underway, additional tractive effort is provided by increasing the throttle notch position and is distributed between tractive effort and hotel power. Note that the standby mode represents engine operation at 720 rpm, which is synchronous speed for the auxiliary alternator.

Table 2 Throttle notch schedules

	EMD 12-645E3B		GE 12-7FDL	
Notch Position	Engine rpm	Fuel Rate (kg/hr)	Engine rpm	Fuel Rate (kg/hr)
Low Idle	255	**	NA	NA
Idle	300	**	450	**
1	315	25	450	23
2	387	72	536	48
3	488	101	707	93
4	565	147	765	145
5	650	183	879	206
6	736	249	879	268
7	820	340	964	316
8	904	396	1,050	391
DB-8	NA	NA	1,050	53
DB-5	NA	NA	879	37
DB-4	569	34	NA	NA
DB-1	300	12	NA	NA

** - Observed at idle speed

Gaseous Emission Measurement. Gaseous emission measurements during each steady-state test condition were obtained by sampling raw exhaust. Exhaust gases were analyzed for unburned hydrocarbons (HC), carbon monoxide (CO), oxides of nitrogen (NO_x), carbon dioxide (CO_2), and oxygen (O_2). Hydrocarbons were measured by a heated flame ionization detector (HFID) unit built to specifications given in SAE Recommended Practice J215. Carbon monoxide and carbon dioxide were measured by a nondispersive infrared (NDIR) analyzer in a system that conforms to SAE Recommended Practice J177a. Oxides of nitrogen were measured using a chemiluminescent (CL) analyzer.

Particulate Emission Measurement. Particulate measurements during each steady-state test condition were obtained using a "splitter" dilution system. The splitter system splits off a portion of the total raw exhaust flow and mixes it with dilution air. Mixing occurs in the dilution tunnel prior to sampling the mixture for particulate. The stainless steel dilution tunnel shown installed next to the GE engine in Fig. 2 is 20 cm (8 in.) in diameter and approximately 5 m (15 ft) long. Particulate mass samples were collected on dual 47 mm Pallflex T60A20 fluorocarbon-coated glass fiber filters. Dilution air and the split-off of total exhaust were regulated such that the maximum temperature at the filter sample zone was 52°C (125°F). All filters were weighed in an environmentally controlled chamber to ensure consistency of results.

Test Fuels Description. Two test fuels were evaluated in each of the 12-cylinder engines. For baseline measurements, an ASTM 2D diesel fuel was used. To assess the impact of fuel sulfur content on locomotive engine emissions, a low-sulfur ASTM 2D diesel fuel was also tested. The low-sulfur fuel was procured within the jurisdiction of the South Coast Air Quality Management District of California where a max-

Table 3 Amtrak EMD 12-645E3B throttle notch definitions

Throttle Notch	Engine Speed (rpm)	kW (flywheel)
8	893	1,864
7	893	1,820
6	893	1,418
5	893	1,157
4	893	908
3	893	731
2	893	595
1	893	468
Idle	893	345
Standby	720	345
High Idle	410	0
Low Idle	260	0
Dynamic Brake	893	345

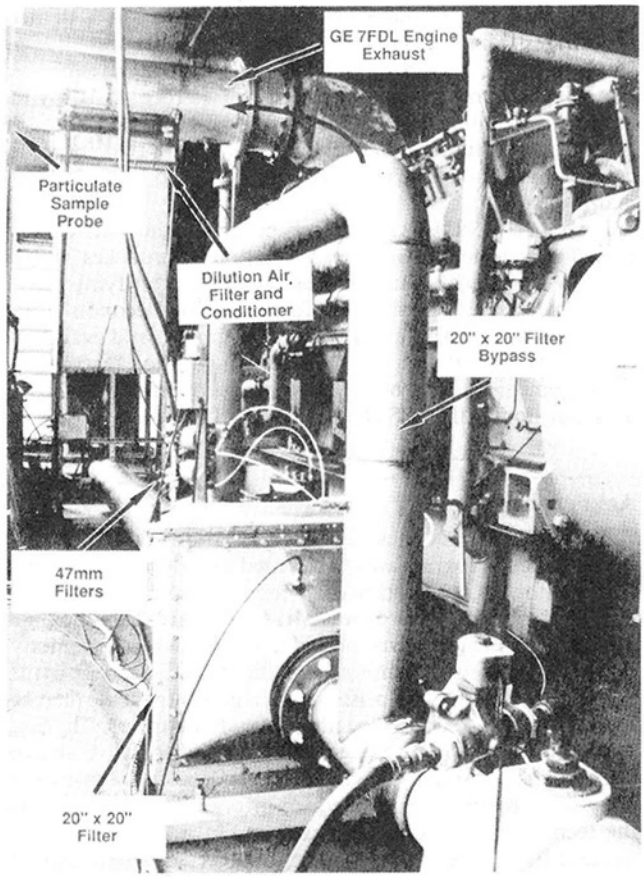

Fig. 2 Stainless steel CVS dilution tunnel used for particulate sampling installed next to GE 12-7FDL engine

imum of 0.05 weight percent sulfur is allowed for on-highway diesel fuel. The fuels were analyzed and the results are given in Table 4.

The engine test procedure used for the emissions measurements was essentially the same as has been developed for performance measurements. The engines were stabilized at rated conditions (Notch 8) for 2 hours prior to testing. One hour was spent at each notch position, with the first half hour being stabilization time. The emissions measurements took up to a full half hour at each test point.

Test Results

The average emissions for the three test days at each notch position, and for each fuel, are presented in the appendix (Tables A-1 through A-4), along with the weighting procedure used in determining the "GE Line Haul" (GELH) composite brake specific emissions. The weighting factors used in determining composite brake-specific emissions were the line-haul duty cycle supplied by GE. This duty cycle is thought to be fairly representative of locomotive operations throughout the U.S., with approximately 14 percent of the time spent at rated conditions (Notch 8) and a significant amount of time (55 percent) at idle. The remainder of the time is spent distributed over the other throttle notch positions. The GELH composite brake specific emissions for the EMD 12-645E3B and the GE 12-7FDL operated on both baseline ASTM 2D diesel and low-sulfur diesel fuels are shown in Table 5. Also shown in Table 5 is the GELH composite brake specific emissions for the EMD 12-645E3B while operating on the Amtrak duty cycle.

An example of the weighting procedure for determining the GELH composite brake specific emissions results using the Amtrak cycle data is included in the appendix as Tables A-5 and A-6. It was assumed that a cumulative idle time of 55 percent for the Amtrak cycle was equally distributed between idle, standby, high idle, and low idle, resulting in weighting factors of 13.75 percent for each idle test condition.

Table 4 Diesel fuel analysis

Determinations	Test Method	AAR89-B	AAR89-C
API Gravity @ 60°F	D1298	31.0	30.6
Flash Point °C (°F)	D93	64 (148)	96 (205)
Cloud Point °C (°F)	D2500	-8 (18)	-33 (-27)
Pour Point °C (°F)	D97	-9 (16)	-33 (-27)
Viscosity @ 40°C (cSt)	D445	3.16	3.55
Carbon Residue (%)	D524	0.13	0.14
Sulfur (Wt%)	D2622	0.33	0.01
Ash (Wt%)	D482	<0.01	<0.01
Water & Sediment (Wt%)	D2709	0.020	0.013
Cetane Number	D613	44.8	42.8
Cetane Index	D976	43.4	41.1
Cetane Index	D4737	43.5	40.8
Heat of Combustion	D240		
Gross MJ/kg (BTU/lb)		44.86 (19,288)	45.28 (19,466)
Net MJ/kg (BTU/lb)		42.28 (18,175)	42.60 (18,314)
Carbon-Hydrogen Ratio	D3178		
% Carbon		87.33	87.02
% Hydrogen		12.20	12.63
Hydrocarbon Type	D1319		
Aromatics (%)		38.8	29.8
Olefins (%)		1.9	2.9
Saturates (%)		59.3	67.3
Specific Gravity		0.8708	0.8729
Distillation	D86		
	% Recovered	Temp. °C (°F)	Temp. °C (°F)
	IBP	200 (392)	223 (434)
	5	228 (442)	237 (458)
	10	244 (471)	242 (468)
	20	252 (485)	251 (484)
	30	261 (501)	257 (495)
	40	269 (516)	265 (509)
	50	278 (532)	271 (519)
	60	287 (548)	277 (531)
	70	297 (567)	284 (543)
	80	311 (591)	294 (561)
	90	329 (624)	309 (588)
	95	342 (648)	322 (611)
	EP	354 (669)	334 (634)

Table 5 GE line-haul composite brake specific emissions summary for locomotive engines

	PM	HC	CO	NO_x
	GELH Composite (g/bhp-hr)			
Baseline fuel				
EMD 645E3B	0.28	0.33	0.80	11.7
GE 7FDL	0.26	0.60	2.24	10.7
Amtrak (EMD)	0.35	0.50	0.69	12.8
Low sulfur fuel				
EMD 645E3B	0.22	0.36	0.97	10.9
GE 7FDL	0.26	0.60	2.13	10.8
Amtrak (EMD)	0.27	0.48	0.72	12.1

Discussion

An examination of the data presented in Table 5 reveals emission levels of roughly what would be expected for a turbocharged diesel engine tuned for maximum fuel efficiency, with NO_x in the range of 10–12 g/bhp-hr. One notable result is the effect of low-sulfur diesel fuel on particulate emissions. For the EMD engine, use of the low-sulfur fuel resulted in a 21 percent reduction in particulates for both the standard freight notch definition and the Amtrak simulation operating conditions. However, the GE engine was unresponsive to the fuel change in terms of particulate emissions. A SOF determination was not made on the particulate filters, but this analysis is planned for future measurements to attempt to assist in understanding this observation. Note that previous studies by the AAR on these engines [11–15] have demonstrated that engine performance is generally insensitive to wide variations in fuel properties, with acceptable performance on broad-specification diesel fuels down to 32 cetane. This "performance insensitivity" may carry over to emission characteristics on this class of engines.

Assuming the GE line-haul weighting factors used in calculating the GELH composite brake specific emissions are representative of U.S. locomotive operations, these composite locomotive emissions can be expressed on a fuel specific basis (pounds of emittant/1000 gallons of fuel burned) and compared to locomotive emission factors previously used for air quality inventories. Recognizing the limitations to the current data, these results are shown in Table 6. Emission data from this program were calculated using the data presented in the appendix for the baseline 0.33 percent sulfur diesel fuel, and assumes 70 percent EMD's and 30 percent GE's in the U.S. fleet.

The particulate emission data in the AP-42 study were based only on highway diesel engine data available at that time since no locomotive diesel engine was available [1]. Particulate emission factors for locomotive engines are now quantified and can be included in future air quality studies.

The notable reductions in HC and CO emission factors of Table 6 can be partially explained by considering the age of the AP-42 data and the 1985 EPA update to the AP-42 locomotive emission factors. The 1985 EPA update [2] relied primarily on the locomotive emission data from studies in the 1970s [4–9], which were combined with up-to-date train traffic and locomotive inventory data from the early 1980s. Fuel shortages in the early 1970s and the early 1980s resulted in significant fuel economy improvements by the engine manufacturers. With these fuel economy improvements came decreases in HC and CO, with HC emissions reduced by roughly a factor of 2, and CO emissions by a factor of 5.

Future Work

Currently, a standardized test procedure for measuring locomotive engine emissions does not exist. Recognizing that a formal duty-cycle based test procedure for measuring gaseous and particulate locomotive emissions *must* be established, the AAR has initiated an industry working group to establish these procedures. The working group is made up of representatives from EMD, GE, Caterpillar, AAR, and SwRI. It is anticipated that the test procedure that evolves will be recognized by the locomotive engine manufacturers and will be adopted as an AAR Recommended Practice. This will ensure that future locomotive emissions are measured and reported in a consistent manner.

During the 1990 AAR research program, the generally accepted "first step" emissions reduction approaches will be evaluated in the laboratory. These include quantifying the effects on locomotive engine performance, fuel economy, and emissions while mapping fuel injection timing, and evaluating the effects of enhanced aftercooling. In addition, locomotive engine emissions will be assessed while operating on a low aromatic–low sulfur ASTM No. 1D fuel.

Table 6 Comparison of locomotive emission factors

	PM	HC	CO	NO_x
	pounds/1000 gallons fuel			
EPA AP-42 [1]	25	94	130	370
1985 EPA Update [2]	—	39	226	558
SwRI 1990 (a,b)	12	17	52	481

a - Using GE duty cycle with baseline diesel fuel.
b - Weighted using 70% EMD, 30% GE.

Acknowledgments

The AAR Phase X Diesel Fuel Specification and Locomotive Improvement Program was performed at Southwest Research Institute for the Association of American Railroads. The AAR Project Technical Monitor was Mr. G. Richard Cataldi. Guidance for the Program was provided by the AAR Locomotive Efficiency Review Committee and the AAR Energy Program Steering Committee comprised of individuals from the member railroads of the AAR and locomotive manufacturers. The Electro-Motive Division of General Motors Corporation and the Transportation Systems Division of the General Electric Company were frequently consulted for information and advice on the technical aspects of the program. In addition, their assistance in the form of donating the necessary parts for the engines is appreciated. Direct program participation and cooperation by AAR member railroads was also conducive to the program's success. The Southern Pacific Transportation Company and The Atchison, Topeka and Santa Fe Railway Company arranged for the procurement and transportation of the low-sulfur diesel fuel to San Antonio from California.

References

1 "Compilation of Air Pollutant Emissions Factors," EPA Report No. AP-42, 3rd ed., U.S. Environmental Protection Agency, Office of Air Quality Planning and Standards, Research Triangle Park, NC, Aug. 1977.

2 Ingalls, M. N., "Recommended Revisions to Gaseous Emission Factors From Several Classes of Off-Highway Mobile Sources," SwRI Report 03-7338-008, EPA Report No. 460/3-85-004, Contract No. 68-03-3162, Work Assignment 8, Mar. 1985.

3 "SP-AAR Program to Develop Certification Procedures With Respect to Visible Emissions from New and Out-Shopped Locomotives," SP Final Report, Aug. 1973.

4 Hoffman, J. G., Springer, K. J., and Tennyson, T. A., "Four Cycle Diesel Electric Locomotive Exhaust Emissions: A Field Study," ASME Paper No. 75-DGP-10, Apr. 1975.

5 Hare, C. T., and Springer, K. J., "Exhaust Emissions From Uncontrolled Vehicles and Related Equipment Using Internal Combustion Engines: Part 1—Locomotive Diesel Engines and Their Marine Counterparts," SwRI Report No. 11-2869-001, 1972.

6 Storment, J. O., and Springer, K. J., "Assessment of Control Techniques for Reducing Emissions From Locomotive Engines," SwRI Report No. AR-844, Apr. 1973.

7 Hare, C. T., Springer, K. J., and Huls, T. A., "Locomotive Exhaust Emissions and Their Impact," ASME Paper No. 74-DGP-3, May 1974.

8 Storment, J. O., Springer, K. J., and Hergenrother, K. M., "NO_x Studies With EMD 2-567 Diesel Engine," ASME Paper No. 74-DGP-14, May 1974.

9 Springer, K. J., and Davis, O. J., "Studies of NO_x Emissions From a Turbocharged Two-Stroke Cycle Diesel Engine," SwRI Report No. 11-2869-003, Oct. 1975.

10 Conlin, P. C., "Exhaust Emission Testing of In-Service Diesel-Electric Locomotives—1981 to 1983,"AAR Report No. R-688, Mar.1988.

11 Baker, Q. A., et al., "Alternative Fuels for Medium-Speed Diesel Engines Program, Fourth Research Phase Final Report," SwRI Report No. 03-7446-001, AAR Report No. R-569, Feb. 1984.

12 Wakenell, J. F., et al., "Alternative Fuels for Medium-Speed Diesel Engines Program, Fifth Research Phase Final Report," SwRI Report No. 03-7924, AAR Report No. R-602, Apr. 1985.

13 Wakenell, J. F., et al., "Alternative Fuels for Medium-Speed Diesel Engines Program, Sixth Research Phase Final Report," SwRI Report No. 03-8469, AAR Report No. R-615, Oct. 1986.
14 Wakenell, J. F., et al., "Diesel Fuel Specification and Locomotive Improvement Program, Eight Research Phase Final Report," SwRI Report No. 03-1542, AAR Report No. R-697, Dec. 1987.
15 Fritz, S. G., et al., "Diesel Fuel Specification and Locomotive Improvement Program, Ninth Research Phase Final Report," SwRI Report No. 03-2082, AAR Report No. R-731, Aug. 1989.
16 Fritz, S. G., et al., "Diesel Fuel Specification and Locomotive Improvement Program, Tenth Research Phase Final Report," SwRI Report No. 03-2695, Mar. 1990.

APPENDIX A

Locomotive Emissions Data

Table A-1 Average emissions from EMD 12-645E3B using baseline diesel fuel

				MASS EMISSION RATE					(WEIGHTED)				
Notch	Engine Speed	Fuel Flow (lb/hr)	BHP	PM (g/hr)	HC (g/hr)	CO (g/hr)	NOx (g/hr)	WF	BHP	PM (g/hr)	HC (g/hr)	CO (g/hr)	NOx (g/hr)
8	904	872	2,445	618	558	1,211	26,735	0.14	342	87	78	169	3,743
7	820	749	2,093	570	399	1,131	22,561	0.03	63	17	12	34	677
6	736	549	1,518	414	338	842	16,317	0.03	46	12	10	25	490
5	650	404	1,103	293	317	388	12,556	0.04	44	12	13	16	502
4	565	324	882	234	248	314	10,309	0.04	35	9	10	13	412
3	488	223	594	183	187	291	7,052	0.03	18	5	6	9	212
2	387	159	418	127	135	321	4,963	0.05	21	6	7	16	248
1	315	55	110	19	86	194	1,812	0.05	6	1	4	10	91
IDLE	300	27	12	21	88	297	776	0.275	3	6	24	82	213
LOW IDLE	255	18	0	28	84	269	480	0.275	0	8	23	74	132
DB-4	569	75	37	50	203	470	1,809	0.02	1	1	4	9	36
DB-1	300	27	12	21	88	297	776	0.02	0	0	2	6	16
							Sum =	1.00	579	165	193	462	6,771
							Composite g/bhp-hr =			0.28	0.33	0.80	11.7

Engine = EMD 12-645E3B

Table A-2 Average emissions from EMD 12-645E3B using low-sulfur diesel fuel

				MASS EMISSION RATE					(WEIGHTED)				
Notch	Engine Speed	Fuel Flow (lb/hr)	BHP	PM (g/hr)	HC (g/hr)	CO (g/hr)	NOx (g/hr)	WF	BHP	PM (g/hr)	HC (g/hr)	CO (g/hr)	NOx (g/hr)
8	904	872	2,468	510	610	1,407	25,022	0.14	345	71	85	197	3,503
7	820	749	2,108	384	486	1,558	22,168	0.03	63	12	15	47	665
6	736	549	1,525	353	368	1,046	15,206	0.03	46	11	11	31	456
5	650	404	1,113	221	294	434	11,693	0.04	45	9	12	17	468
4	565	325	895	192	240	327	9,922	0.04	36	8	10	13	397
3	488	222	596	140	179	308	6,488	0.03	18	4	5	9	195
2	387	158	419	101	127	301	4,771	0.05	21	5	6	15	239
1	315	54	109	9	92	213	2,072	0.05	5	0	5	11	104
IDLE	300	25	8	10	101	390	673	0.275	2	3	28	107	185
LOW IDLE	255	18	0	12	96	356	417	0.275	0	3	26	98	115
DB-4	569	74	35	21	200	600	1,798	0.02	1	0	4	12	36
DB-1	300	25	8	10	101	390	673	0.02	0	0	2	8	13
							Sum =	1.00	582	126	209	566	6,375
							Composite g/bhp-hr =			0.22	0.36	0.97	10.9

Engine = EMD 12-645E3B

Table A-3 Average emissions from GE 12-7FDL using baseline diesel fuel

				MASS EMISSION RATE					(WEIGHTED)				
Notch	Engine Speed	Fuel Flow (lb/hr)	BHP	PM (g/hr)	HC (g/hr)	CO (g/hr)	NOx (g/hr)	WF	BHP	PM (g/hr)	HC (g/hr)	CO (g/hr)	NOx (g/hr)
8	1050	862	2,513	460	778	3,393	26,460	0.14	352	64	109	475	3,704
7	964	697	2,010	401	545	4,358	21,671	0.03	60	12	16	131	650
6	879	590	1,669	337	356	5,486	18,672	0.03	50	10	11	165	560
5	879	455	1,260	280	276	2,961	13,948	0.04	50	11	11	118	558
4	765	320	859	212	235	1,988	9,041	0.04	34	8	9	80	362
3	707	205	535	122	162	800	4,430	0.03	16	4	5	24	133
2	536	105	265	78	126	383	1,981	0.05	13	4	6	19	99
1	450	51	111	78	114	237	880	0.05	6	4	6	12	44
Idle	450	18	0	36	252	378	260	0.55	0	20	139	208	143
DB-8	1050	116	97	432	1,205	2,445	1,094	0.02	2	9	24	49	22
DB-5	879	82	83	166	646	1,425	900	0.02	2	3	13	29	18
							Sum =	1.00	585	150	349	1,309	6,293
							Composite g/bhp-hr =			0.26	0.60	2.24	10.7

Engine = GE 12-7FDL

Table A-4 Average emissions from GE 12-7FDL using low-sulfur diesel fuel

				MASS EMISSION RATE					(WEIGHTED)				
Notch	Engine Speed	Fuel Flow (lb/hr)	BHP	PM (g/hr)	HC (g/hr)	CO (g/hr)	NOx (g/hr)	WF	BHP	PM (g/hr)	HC (g/hr)	CO (g/hr)	NOx (g/hr)
8	1050	862	2,563	371	900	3,245	28,002	0.14	359	52	126	454	3,920
7	964	697	2,045	569	659	4,125	20,636	0.03	61	17	20	124	619
6	879	590	1,698	390	414	5,242	18,164	0.03	51	12	12	157	545
5	879	455	1,282	395	311	3,111	13,184	0.04	51	16	12	124	527
4	765	320	876	230	258	2,152	8,807	0.04	35	9	10	86	352
3	707	205	550	114	180	725	4,793	0.03	16	3	5	22	144
2	536	105	294	61	107	334	2,439	0.05	15	3	5	17	122
1	450	52	120	68	102	229	1,043	0.05	6	3	5	11	52
Idle	450	17	0	49	225	358	272	0.55	0	27	124	197	150
DB-8	1050	118	120	465	1,353	2,598	1,098	0.02	2	9	27	52	22
DB-5	879	83	99	143	531	1,413	1,022	0.02	2	3	11	28	20
							Sum =	1.00	599	154	358	1,273	6,474
									Composite g/bhp-hr =		0.26	0.60	2.13	10.8

Engine = GE 12-7FDL

Table A-5 Emissions from EMD 12-645E3B simulating Amtrak operations using baseline diesel fuel

				MASS EMISSION RATE					(WEIGHTED)				
Notch	Engine Speed	Fuel Flow (lb/hr)	BHP	PM (g/hr)	HC (g/hr)	CO (g/hr)	NOx (g/hr)	WF	BHP	PM (g/hr)	HC (g/hr)	CO (g/hr)	NOx (g/hr)
8	893	881	2,474	763	676	952	31,727	0.14	346	107	95	133	4,442
7	893	870	2,447	665	482	1,000	30,801	0.03	73	20	14	30	924
6	893	689	1,902	535	431	513	22,648	0.03	57	16	13	15	679
5	893	573	1,526	457	420	499	17,874	0.04	61	18	17	20	715
4	893	484	1,218	412	423	441	14,218	0.04	49	16	17	18	569
3	893	418	981	379	439	576	11,318	0.03	29	11	13	17	340
2	893	370	803	334	481	530	9,572	0.05	40	17	24	27	479
1	893	324	627	301	505	587	7,668	0.05	31	15	25	29	383
IDLE	893	283	462	252	597	572	6,372	0.1375	63	35	82	79	876
STAND BY	720	226	463	158	392	446	5,813	0.1375	64	22	54	61	799
HIGH IDLE	410	38	0	30	164	516	1,138	0.1375	0	4	23	71	156
LOW IDLE	260	20	0	30	101	368	538	0.1375	0	4	14	51	74
DB	893	283	462	252	597	572	6,372	0.04	18	10	24	23	255
							Sum =	1.00	833	295	415	574	10,691
									Composite g/bhp-hr =		0.35	0.50	0.69	12.8

Engine = EMD 12-645E3B

Table A-6 Emissions from EMD 12-645E3B simulating Amtrak operations using low-sulfur diesel fuel

				MASS EMISSION RATE					(WEIGHTED)				
Notch	Engine Speed	Fuel Flow (lb/hr)	BHP	PM (g/hr)	HC (g/hr)	CO (g/hr)	NOx (g/hr)	WF	BHP	PM (g/hr)	HC (g/hr)	CO (g/hr)	NOx (g/hr)
8	893	870	2,474	499	588	850	29,212	0.14	346	70	82	119	4,090
7	893	862	2,443	477	581	902	29,448	0.03	73	14	17	27	883
6	893	684	1,902	392	488	453	21,377	0.03	57	12	15	14	641
5	893	573	1,524	345	435	455	16,623	0.04	61	14	17	18	665
4	893	479	1,218	329	464	528	13,512	0.04	49	13	19	21	540
3	893	414	981	314	554	572	10,778	0.03	29	9	17	17	323
2	893	366	799	276	471	603	9,368	0.05	40	14	24	30	468
1	893	322	627	251	530	594	7,484	0.05	31	13	27	30	374
IDLE	893	281	462	238	536	610	6,159	0.1375	63	33	74	84	847
STAND BY	720	225	462	105	366	426	5,741	0.1375	64	14	50	59	789
HIGH IDLE	410	37	0	26	186	681	1,142	0.1375	0	4	26	94	157
LOW IDLE	260	20	0	21	105	471	448	0.1375	0	3	14	65	62
DB	893	281	462	238	536	610	6,159	0.04	18	10	21	24	246
							Sum =	1.00	833	222	403	601	10,087
									Composite g/bhp-hr =		0.27	0.48	0.72	12.1

Engine = EMD 12-645E3B

R. W. Rice

A. K. Sanyal

A. C. Elrod

Clemson University
Clemson, SC 29631

R. M. Bata
West Virginia University,
Morgantown, WV 26506

Exhaust Gas Emissions of Butanol, Ethanol, and Methanol-Gasoline Blends

Emissions levels for CO, NO_X, and unburned fuel (UBF) from a stationary four-cylinder Chrysler engine were measured under a variety of operating conditions for gasoline and three different 20 vol percent alcohol-gasoline blends. In tests of separate isobutanol, ethanol, and methanol blends, lower CO and NO_X emissions were observed for the alcohol blends relative to gasoline, particularly for fuel-rich operation. Generally, on a volume (mole) basis unburned fuel emissions were highest for methanol blends and lowest for gasoline, but on a mass or OMHCE basis only small differences were noted. For a given fuel, the separate effects of engine speed, load, and equivalence ratio were examined.

Introduction

The combination of increasingly stringent restrictions on pollutant emissions from automotive engines, a progressive rise in the price of gasoline, and awareness of the desirability of renewable fuels has increased the incentive for using alcohol as an automotive fuel component. The main objective of the work described here was to compare the emissions characteristics of a variety of alcohol-gasoline blends with each other and with those for gasoline. Results are reported for three alcohols, i.e., methanol (CH_3OH), ethanol (C_2H_5OH), isobutanol (C_4H_9OH), but the emphasis in the study was on isobutanol because it, unlike methanol and ethanol [1-4], has not been extensively studied and because it appears to have some attributes that offer potential advantages. Isobutanol has been used as a surfactant/cosolvent to improve the stability of methanol-gasoline and ethanol-gasoline blends. It has a relatively low affinity for water and is much closer to gasoline in terms of fuel characteristics such as heating value, latent heat, etc., than are the lower molecular weight alcohols.

Differences in emissions characteristics for alcohols compared to gasoline can be attributed to differences in physical and chemical properties that affect combustion. In contrast to gasoline, which is a complex, widely variable mixture of true hydrocarbons, alcohols are single species of "partially oxidized hydrocarbons." The presence of the oxygen atom in an alcohol molecule, coupled with the lower carbon number, accounts for much of the difference in properties relative to gasoline shown in Table 1. The related issues of higher heat of vaporization and fuel delivery system adjustments when alcohols are used are intertwined with the air-fuel ratio and peak flame temperature, parameters that greatly affect exhaust emissions. With the equivalence ratio, ϕ, defined as

Table 1 Selected liquid fuel properties

PROPERTY	GASOLINE	ISO BUTANOL	ETHANOL	METHANOL
Specific Gravity (at 60 F)	0.72 - 0.75	0.81	0.794	0.796
Boiling Point (C)	30 - 225	108.1	78.3	65.0
Molecular Weight	111 (Avg)	74	46	32
Elemental Composition:				
(Wt.)% Carbon	85 - 88	64.9	52.1	37.5
% Hydrogen	12 - 15	13.5	13.1	12.6
% Oxygen	0.0	21.6	34.7	49.9
C/H Ratio	5.6 - 7.4	4.8	4.0	3.0
Stoichiometric A/F Ratio	14.6	11.1	9.0	6.4
Net Lower Heating Value				
(i) Mass, MJ/kg	43.5	33	27.0	20.1
(ii) Volume, MJ/l	32.0	26	21.3	15.9
Heat of Vaporization (KJ/kg)	400	579	900	1,100
Vapor Pressure at 100 F (KPa)	62 - 90	2.30	17	32
Octane Rating				
Research	91 - 100	113	111	112
Motor	82 - 92	94	92	91

$$\phi = \frac{\text{actual air-fuel mass ratio}}{\text{stoichiometric air-fuel mass ratio}}, \quad (1)$$

The terms "lean" and "rich" refer to operation in which $\phi > 1$ and $\phi < 1$, respectively. It is clear from the stoichiometric equations (2)-(5) for combustion of the three alcohols and gasoline (approximated as C_8H_{15}) that, for a given volumetric intake of a fuel vapor-air mixture, increasing the alcohol content of the fuel will have a "leaning" effect on the engine.

$$C_8H_{15} + 11.75O_2 \rightarrow 8CO_2 + 7.5H_2O \quad (2)$$

$$C_4H_9OH + 6O_2 \rightarrow 4CO_2 + 5H_2O \quad (3)$$

$$C_2H_5OH + 3O_2 \rightarrow 2CO_2 + 3H_2O \quad (4)$$

Contributed by the Internal Combustion Engine Division and presented at the Energy-Sources Technology Conference and Exhibition, Houston, Texas, January 20-24, 1991. Manuscript received by the Internal Combustion Engine Division September 1990. Paper No. 91-ICE-16.

$$CH_3OH + 1.5O_2 \rightarrow CO_2 + 2H_2O \quad (5)$$

The performance, emissions levels, and fuel economy of an automotive engine are complex functions of engine design, speed, spark timing, inlet manifold pressure, fuel–air ratio, and fuel composition. A survey of operational characteristics indicates that significant increases in fuel economy and decreases in pollutant emissions may be achieved by operating such engines on very fuel-lean mixtures [5] and/or at higher compression ratios. Varying the equivalence ratio has a profound impact on exhaust emissions due to the corresponding effects on peak flame temperature, flame propagation rate, and the concentration of species, particularly oxygen. Obviously, as the equivalence ratio is increased from rich to lean, the oxygen concentration relative to fuel vapor and carbon monoxide (CO) increases, resulting in a greater probability of complete combustion to carbon dioxide (CO_2) and water. Starkman et al. [6] estimated the CO and nitric oxide (NO) concentration in engine exhausts based on theoretical calculations for numerous single component fuels at various air–fuel ratios and suggested that lower CO and NO emissions might be realized with alcohol than with gasoline.

Conventional gasoline cannot be used to fully exploit the potential advantages of lean combustion because of the rapid decrease in flame speed as the mixture is leaned. Because of the proximity of the lean combustion limit to stoichiometric conditions, attempts to burn gasoline near the lean limit in automotive engines have been reported to result in erratic combustion, poor drivability, and an increase in hydrocarbon emissions [7]. Alcohol fuels allow leaner operation, but substitution of an alcohol blend for gasoline will require larger metering jets to attain a given equivalence ratio, given the lower energy content per mass of alcohol [8]. In this respect, isobutanol has an advantage relative to methanol or ethanol. Bata et al. [9] found only 2.5 percent reduction in thermal efficiency when 20 vol % of the gasoline was replaced by isobutanol (brake specific fuel consumption (BSFC) increased by 6.5 percent). It was further noted that, because isobutanol has a higher stoichiometric air–fuel ratio than the lighter alcohols, a higher percentage of isobutanol can be used as an extender without requiring significant engine adjustment/redesign.

Experimental Section

Figure 1 is a schematic diagram of the apparatus used in this study. It included a Chrysler 2.2-liter, four-cylinder spark ignition engine (compression ratio = 8.5) mounted on a Clayton hydraulic dynamometer. All automatic ignition and emission controls except the positive crankcase ventillation valve were either deactivated or removed from the engine. The dynamometer package included a tachometer and a load cell to measure engine speed and torque. Cooling water temperature was measured using a thermocouple and air flow rate was determined using a Superflow turbine flow meter. Fuel flow rate was measured using a calibrated buret and an electronic stopwatch. For all the tests reported here the ignition timing was fixed at 20 deg before top dead center.

Gases leaving the engine exhaust manifold were pumped through two separate sampling paths, as shown in Fig. 1. In one sampling system, carbon monoxide and total unburned fuel (UBF) were measured using an Analytical Instruments Corporation Model 610A gas chromatograph connected to a Spectra Physics Model SP 4200 computing integrator. The other sampling path was used for measuring the nitrogen oxides (NO_X) content by means of a Beckman Model 951A NO_X Analyzer. The exhaust gas sent to the NO_X analyzer was also periodically routed to the GC to check for in-leakage of room air into the sampling system.

The GC was operated isothermally at 85°C using helium as the carrier gas and was equipped with two pneumatically operated ten-port gas sampling valves, which allowed column

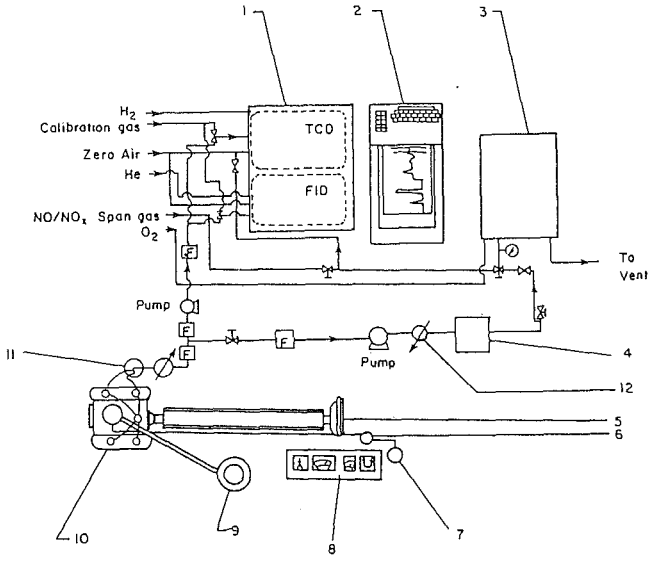

Fig. 1 Schematic diagram of the experimental system: (1) gas chromatograph; (2) computing integrator; (3) NO_X analyzer; (4) sample dryer; (5) dynamometer; (6) fuel pump; (7) fuel buret; (8) engine control panel; (9) air flow meter; (10) engine; (11) exhaust duct; (12) condenser

backflushing and/or switching to achieve separation (via adjusting valve switching times). For determination of CO, CO_2, O_2, and N_2 concentrations a thermal conductivity (TCD) detector was used in conjunction with a combination of a Porapak Q column and a 5A molecular sieve column. A flame ionization detector (FID) was used to measure unburned fuel emission. Separation of the various hydrocarbon and alcohol species was accomplished using a combination of a DC-200 column and a 10 percent TCEP column. Separate experimentally determined FID response factors relative to propane as a representative aliphatic hydrocarbon were used for aromatics and each of the three alcohols. The factor used for methanol was 0.82, for ethanol it was 0.91, and for isobutanol it was 0.95. The NO_X analyzer utilized the chemiluminescence method of detection in which NO is converted to NO_2 by reaction with ozone generated from oxygen. Separate measurements could be made of NO and NO_2 concentration, but generally the total NO_X values were only slightly higher, e.g., 5 percent, than the NO values.

Both the GC and the NO_X analyzer were frequently calibrated using certified gas mixtures of known composition in or near the range of actual engine exhaust samples. As indicated in Fig. 1, various filters and gas–liquid separators/condensers were used to prevent particulates and water droplets from reaching the analyzers. All sampling lines were kept hot using electrical heating tape in order to prevent condensation and a Hankison Model 8005 air dryer was installed upstream of the NO_X analyzer to remove water, which otherwise might have condensed in a transfer line and dramatically lowered the apparent NO_X value.

The controlled variables for the experiments were: (*i*) fuel composition, (*ii*) engine speed, (*iii*) load, and (*iv*) air–fuel ratio. Different combinations of speed and engine load resulted in changes in equivalence ratio for a particular fuel. The equivalence ratio was also varied by using different sets of carburetor jets. The main dependent variables studied were the exhaust gas concentrations for CO, NO_X, and unburned fuel (UBF), but brake specific fuel consumption was also monitored. Table 2 shows the values of stoichiometric air–fuel mass ratio for various alcohol–gasoline blends, assuming gasoline is approximated as C_8H_{15} with a stoichiometric A/F ratio of 14.6. Emissions data were taken only after the engine had reached normal operating temperature and, in general, analyses were consid-

Table 2 Comparison of air-fuel stoichiometric ratio for different alcohol-gasoline blends

ALCOHOL	ALCOHOL CONTENT IN FUEL BLEND		
	5 % (vol)	10 % (vol)	20 % (vol)
BUTANOL	14.38	14.21	14.0
ETHANOL	14.22	13.92	13.33
METHANOL	14.08	13.65	12.80

ered valid only if reproducible within ±10 percent in subsequent measurements.

Results and Discussion

Carbon Monoxide Emissions. As noted earlier, increasing a given alcohol's content in a fuel blend results in leaner combustion due to the partially oxidized nature of alcohols relative to true hydrocarbons. Consequently, for a given air-fuel ratio, the use of alcohol allows a higher relative concentration of oxygen to exist in the combustion gases and this, in turn, achieves a greater conversion of CO to CO_2 than for a gasoline-only case. This effect would be expected to be most pronounced for methanol since oxygen accounts for a larger percentage of its molecular weight than for any of the other alcohols. The data shown in Fig. 2 show this expected trend, namely that, at each of three engine operating conditions, use of the 20 vol % methanol blend (M20) resulted in the lowest CO emissions. The conditions used were: (*i*) 1250 rpm and 0 ft lb_f (no load, NL); (*ii*) 2200 rpm and 50 ft lb_f (68 Joules, intermediate load, IL); and (*iii*) 2500 rpm and 85 ft lb_f (115 Joules, full load, FL, at wide open throttle, WOT).

These differences in CO concentration for different fuels can be largely attributed to differences in air-fuel equivalence ratio because, for a given engine condition, i.e., speed and load, the methanol blend (M20) had the highest ϕ value, the ethanol blend (E20) had the next highest value, and gasoline had the lowest ϕ value. The variation of CO concentration with air-fuel ratio at different conditions observed in this study agree closely with the results of Lichty and Phelps [10]. Figure 3 shows that CO emissions decreased rapidly with increasing ϕ in the fuel-rich region, i.e., $\phi < 1$, with all the alcohol blends showing somewhat lower CO levels than did gasoline. In the vicinity of stoichiometric operation ($\phi = 1$) and in the lean region ($\phi > 1$) there was no statistically meaningful difference among the four fuels tested, with the CO concentration remaining between 0.1 and 0.15 vol. % in this operational region.

Unburned Fuel Emissions. The four fuels tested showed similar patterns for unburned fuel (UBF) emissions as a function of ϕ, as illustrated by Fig. 4. In all cases UBF concentration decreased with increasing ϕ in the rich region, reached a minimum at or just above $\phi = 1$, then increased slightly for gasoline, the ethanol blend, and the isobutanol blend (B20). The increase in UBF emissions for the methanol blend at very lean conditions was more pronounced than for the other fuels and may reflect a tendency to misfire. Of the alcohol blends, B20 showed the lowest UBF concentration with a value only slightly higher than for gasoline. A major factor having a bearing on the observed trend of UBF at a given ϕ (increasing as the molecular weight of the alcohol decreases) is the increased amount of unburned fuel in the quench layer and crevices of the combustion chamber [11, 12]. The amount of fuel in these areas would be expected to be highest for M20 because, at a given ϕ, the mass of fuel vapor per unit volume of air would be greater than for gasoline or the other blends. Jackson et al. [13] observed that minimum UBF emissions

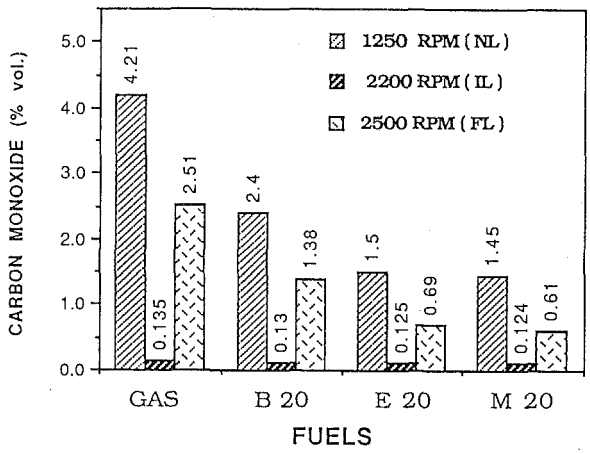

Fig. 2 Carbon monoxide emissions as a function of fuel composition for three different operating conditions

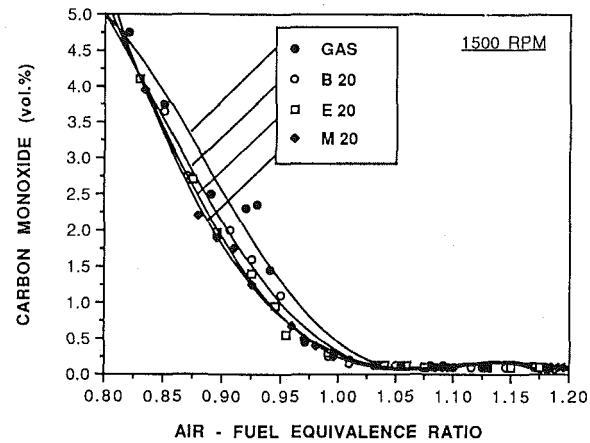

Fig. 3 Variation of carbon monoxide emissions with air-fuel equivalence ratio at 1500 rpm

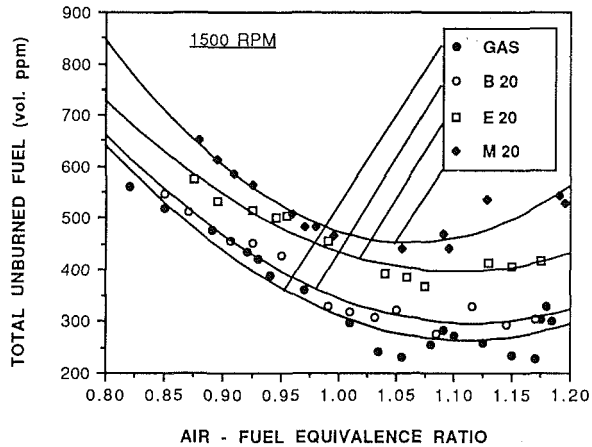

Fig. 4 Variation of unburned fuel emissions in vppm with air-fuel equivalence ratio at 1500 rpm

occurred at a ϕ value of roughly 1.1, which is also the optimum ϕ value as far as fuel economy is concerned.

The gas chromatographic columns used resolved the UBF mixture into numerous individual components or groupings of closely related compounds. Calibration of the GC with pure components allowed identification of the major constituent species or types. These included aliphatics (normal and branched chain alkanes), aromatics (benzene, toluene, xylenes), and alcohols. Because of the low concentrations of aldehydes in the exhaust gas, no meaningful measure for these species could be made with the GC, but based on other work

[3] aldehyde emissions would have been expected to be highest for M20 and lowest for gasoline. The results of this study are presented in terms of unburned fuel rather than the more commonly used term "hydrocarbons" because for alcohol blends a significant proportion of the UBF exhaust is a partially oxidized hydrocarbon, thus on a mass of carbon emitted basis the results for the alcohols at a given ϕ are closer to those for gasoline than the volume-based curves of Fig. 4 imply. A better comparison is provided by examining the quantity, "organic material hydrocarbon equivalent" (OMHCE), whose calculation equation for the case of a methanol-gasoline blend (ignoring any small contribution from aldehydes) is as follows:

$$\text{OMHCE} \approx \text{mass ppm hydrocarbon} + \frac{13.8756}{32.042} \text{ mass ppm methanol.}$$

Here the contribution of the alcohol to the total mass emission is adjusted by a multiplicative factor, which is the ratio of the molecular weight of a hypothetical species, $C_nH_{1.87n}$ to the molecular weight of the n-carbon atom alcohol. The H/C atom ratio of 1.87 used is representative of gasoline. Figure 5 is a plot of OMHCE versus ϕ, which shows that the isobutanol blend, B20, and gasoline had virtually identical OMHCE emissions, while E20 and M20 had somewhat higher values, particularly in the lean region. Table 3 shows the distribution of major types of UBF measured in mass ppm at a specific engine operating condition, 1500 rpm and 85 ft lb_f (115 J), and, as expected, the major contribution was from aliphatics. The percentage of alcohol in the UBF was somewhat lower than the original fuel value for all alcohols. At this time it cannot be said with certainty that this reflects actual differences in combustion behavior relative to true hydrocarbons or is merely an artifact of the sampling/detection system. In addition to difficulties in achieving an isolated GC peak for species such as methanol, it was noted that even a trace of condensed water in the sample line could measurably lower the apparent measured concentration of alcohol due to "capture" by water.

Table 3 Distribution of major constituent types in the exhaust at 1500 rpm, 85 ft lb_f (115 J) expressed in mass ppm

CONSTITUENT	GASOLINE EQ.RATIO = 0.94	BUTANOL(20%) EQ.RATIO = 0.95	ETHANOL(20%) EQ.RATIO = 0.98	METHANOL(20%) EQ.RATIO = 0.99
ALIPHATICS	795 (75.3%)	729 (70.3%)	668 (67.5%)	569 (63.6%)
AROMATICS	261 (24.7%)	202 (19.5%)	195 (19.6%)	202 (22.6%)
ALCOHOLS	-	105 (10.2%)	128 (12.9%)	123 (13.8%)

NO_X Emissions. The formation reactions for NO, principal constituent of NO_X, are relatively slow and the reactions do not reach equilibrium during an engine cycle, i.e., the NO_X formation rate (and thus amount produced) is governed by reaction kinetics rather than thermodynamic equilibrium. Consequently, NO_X formation is very dependent on combustion chamber temperature, which, in turn, is dependent on air–fuel ratio and, particularly, load. Figure 6 shows the variation of NO_X emissions with ϕ for the four fuels at 1500 rpm. As one moves away from stoichiometric conditions in the rich region, the decrease in ϕ results in decreased NO_X emissions because the NO_X formation reactions become progressively starved for oxygen and, secondarily, heat generation rate due to fuel combustion is also lower. In the lean region, an increase in ϕ leads to a decrease in NO_X emissions, even though oxygen is in excess, because increased dilution with air results in a lowering of peak combustion temperature [14]. At a given ϕ value, the "energy density" of an alcohol blend fuel charge is less than that for gasoline, resulting in lower flame temperatures and thus lower NO_X emissions. Figure 6 shows that all of the alcohol blends had lower maximum NO_X values than did gasoline, but that the difference in peak values was not large. In the rich region isobutanol along with ethanol and methanol gave appreciably lower NO_X emissions, but this advantage was not evident in the lean region. In general, these results compare favorable with those for methanol obtained by Most and Longwell [14].

As noted earlier, the air–fuel ratio in these experiments varied not only due to changes in carburetor jets, but also due to changes in engine speed, load, and fuel; thus the operational variables were coupled. For example, ϕ changed from a value of 0.93 to 0.90 for gasoline when speed changed from 1500 to 2500 rpm at a fixed load of 85 ft lb_f (115 J). Likewise, when load was changed from 25 ft lb_f (34 J) to 85 ft lb_f (115 J) at a fixed speed of 1500 rpm, ϕ varied approximately linearly from 1.18 to 0.93. For these tests the highest NO_X emissions occurred when the engine was at high load, thus reflecting the temperature effect cited previously as well as the expected explicit effect of ϕ.

Emissions on a Fuel Consumed Basis. The comparisons made thus far have been primarily on a basis of either mppm or vppm of exhaust, but perhaps a more relevant basis for comparison is mass of emission per mile driven. Given that the measurements were made on a stationary engine, direct measurements for the latter basis were not possible. However, reasonable g/mile estimates could be obtained by drawing upon actual measurements of fuel consumption and estimates of vehicle speed corresponding to a given engine speed. Figure 7 is a plot showing brake specific fuel consumption (BSFC) in

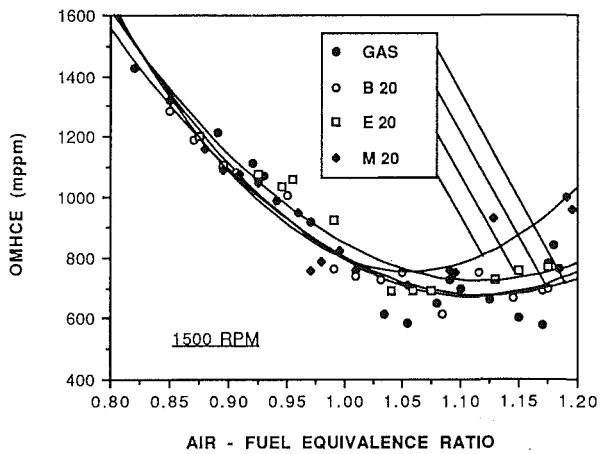

Fig. 5 Variation of organic material hydrocarbon equivalent in mppm with air-fuel equivalence ratio at 1500 rpm

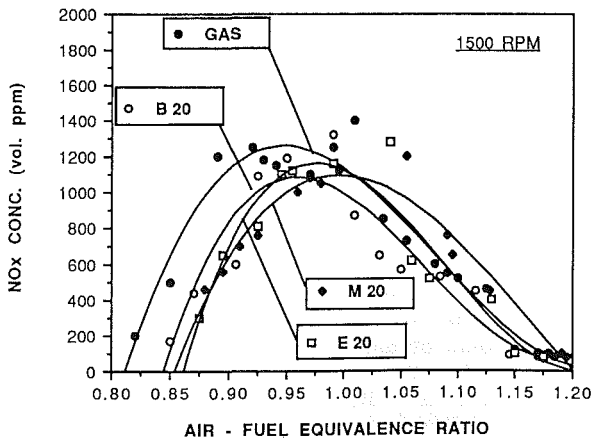

Fig. 6 Variation of nitrogen oxide emissions with air-fuel equivalence ratio at 1500 rpm

kg/hp h versus ϕ for the four fuels. Given the differences in energy content per unit mass, the results were as expected, with M20 showing the largest fuel consumption. Table 4 presents data for CO, UBF, and NO_X emissions on a "pseudo g/mile basis" for all four fuels at two different operating conditions. Direct comparisons with U.S. Federal Test Procedure emission standards are not practical because these tests were steady-state tests at a given condition with no transient cycle and were not at FTP conditions. Furthermore, the values reported here are "raw" exhaust, i.e., pre-catalytic converter values; and the speed (mph) values are only estimates. Even so, the results are useful for comparison of the relative behavior of the four fuels at a given condition. They show that at intermediate load conditions there was only a small reduction in CO and NO_X for the alcohols relative to gasoline, whereas at high load the reduction in CO was more substantial. Unburned fuel emissions displayed an opposite trend with all but isobutanol giving UBF emissions definitely higher than those for gasoline at intermediate load and all four fuels being comparable in UBF levels at high load. As discussed earlier, much of this behavior is understandable given the variation in ϕ involved.

Conclusions

Most earlier studies of exhaust emissions from alcohol-gasoline blend fueled spark ignition engines have focused on only one pollutant and/or involved only one alcohol; thus the current work is useful in providing a direct quantitative comparison of emissions for all three major pollutants for three different alcohols. The primary reason for the reduction in CO emissions for alcohol fuels relative to gasoline at a given air-fuel ratio is the "leaning" effect related to the lower stoichiometric A/F value for alcohols. This effect, coupled with a lowering of peak combustion temperature for alcohol blends, also accounts for a modest lowering of NO_X levels for alcohols. In contrast to improvements in CO and NO_X emissions when using alcohols, UBF emissions on a mass basis for such blends were higher than for gasoline at intermediate load but roughly equal or possibly lower at high load. Although currently not considered an economically viable alternative to ethanol or methanol as a gasoline extender, isobutanol appears to have

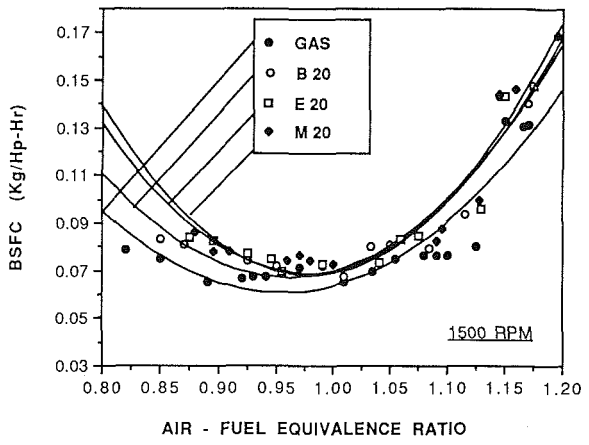

Fig. 7 Variation of brake specific fuel consumption with air-fuel equivalence ratio at 1500 rpm

Table 4 Comparison of exhaust emissions for different fuels on a g/mile basis

ENGINE OPERATING CONDITION	GASOLINE			BUTANOL (20%)			ETHANOL-(20%)			METHANOL (20%)		
	CO	UBF	NOx	CO	UBF	NOx	CO	UBF	NOx	CO	UBF	NOx
2200 RPM LOAD=50ft.lb (45 mph)	EQ. RATIO = 1.05			EQ. RATIO = 1.06			EQ. RATIO = 1.07			EQ. RATIO = 1.08		
	2.56	4.82	1.53	2.45	4.87	1.47	2.44	5.70	1.41	2.38	6.26	1.39
2500 RPM LOAD=85ft.lb (53 mph)	EQ.RATIO = 0.90			EQ. RATIO = 0.93			EQ. RATIO = 0.95			EQ. RATIO = 0.96		
	57.7	11.1	4.11	34.7	10.9	3.91	16.7	10.1	3.81	6.44	9.67	3.64

emissions characteristics similar to those alcohols. Given isobutanol's advantages in terms of low affinity for water, vapor pressure/latent heat compatibility with gasoline, etc., there appears to be incentive to explore potential inexpensive methods for butanol production, e.g., via fermentation.

Acknowledgments

The authors wish to thank the South Carolina Energy Research and Development Center, and Dr. L. P. Golan in particular, for the grant which made this study possible. The efforts of Mark Hooker and Alex Zheng in assembling the test apparatus are also gratefully acknowledged.

References

1 Ebersole, G. D., and Manning, F. S., "Engine Performance and Exhaust Emissions: Methanol Versus Isooctane," in: *Alcohol as Motor Fuels*, SAE Progress in Technology Series, No. 19, 1980, pp. 35–54.

2 Wigg, E. E., and Lunt, R. S., "Methanol as a Gasoline Extender-Fuel Economy, Emissions and High Temperature Driveability," in: *Alcohol as Motor Fuels*, SAE Progress in Technology Series, No. 19, 1980, pp. 71–82.

3 Furey, R. L., and King, J. B., "Evaporative and Exhaust Emissions From Car Fuels With Gasoline Containing Ethanol or Methyl Test-Butyl Ether," in: *Alcohol as Motor Fuels*, SAE Progress in Technology Series, 1980, pp. 299–315.

4 Bata, R. M., Elrod, A. C., and Rice, R. W., "Emissions From I. C. Engines Fueled With Alcohol-Gasoline Blends: A Literature Review," *Engine Emissions Technology for the 1990's*, ASME ICE-Vol. 4, Oct. 1988, pp. 141–151.

5 Bolt, J. A., and Wimmer, D. H., "Exhaust Emission Abatement of Fuel Variations to Produce Lean Combustion," in: *Alcohol as Motor Fuels*, SAE Progress in Technology Series, pp. 225–247.

6 Starkman, E. S., Sawyer, R. F., Carr, R., Johnson, G., and Muzio, L., "Alternate Fuels for Control of Engine Emission," *J. Air Pollution Control Association*, Vol. 20, No. 2, Feb. 1970, pp. 87–92.

7 Hansel, J. G., "Lean Automotive Engine Operation-Hydrocarbon Exhaust Emissions and Combustion Characteristics," SAE Paper No. 710164, Jan. 1971.

8 Bolt, J. A., "A Survey of Alcohol as a Motor Fuel," in: *Alcohol as Motor Fuels*, SAE Progress in Technology Series, No. 19, 1980, pp. 21–23.

9 Bata, R. M., Elrod, A. C., and Lewandowski, T. P., "Butanol as a Blending Agent With Gasoline for I. C. Engines," SAE Paper No. 890434, Mar. 1989.

10 Lichty, L. C., and Phelps, C. W., "Carbon Monoxide in Engine Exhaust Using Alcohol-Blends," *Ind. Eng. Chem.*, Vol. 29, 1937, p. 495.

11 Heywood, J. B., "Pollutant Formation and Control in Spark Ignition Engines," *Prog. Energy Combustion Sci.*, Vol. 1, 1976, p. 135.

12 Daniel, W. A., and Wentworth, J. T., "Exhaust Gas Hydrocarbons—Genesis and Exodus," in: *Vehicle Emissions*, SAE Progress in Technology Series, No. 6, June 1964, pp. 192–205.

13 Jackson, M. W., Wiese, W. M., and Wentworth, J. T., "The Influence of Air–Fuel Ratio, Spark Timing, and Combustion Chamber Deposits on Exhaust Hydrocarbon Emission," in: *Vehicle Emissions*, SAE Progress in Technology Series, No. 6, 1964.

14 Most, W. J., and Longwell, J. P., "Single-Cylinder Engine Evaluation of Methanol-Improved Energy Economy and Reduced NO_X," in: *Alcohols as Motor Fuels*, SAE Progress in Technology Series, No. 19, 1980, pp. 83–93.

An Integrated Model of Ring Pack Performance

R. Keribar

Z. Dursunkaya

M. F. Flemming

Ricardo-ITI, Inc.,
Westmont, IL 60559

This paper describes an integrated model developed for the detailed characterization and simulation of piston ring pack behavior in internal combustion engines and the prediction of ring pack performance. The model includes comprehensive and coupled treatments of (1) ring-liner hydrodynamic and boundary lubrication and friction; (2) ring axial, radial, and (toroidal) twist dynamics; (3) inter-ring gas dynamics and blowby. The physics of each of these highly inter-related phenomena are represented by submodels, which are intimately coupled to form a design-oriented predictive tool aimed at the calculation of ring film thicknesses, ring motions, land pressures, engine friction, and blowby. The paper also describes the results of a series of analytical studies investigating effects of engine speed and load and ring pack design parameters, on ring motions, film thicknesses, and inter-ring pressures, as well as ring friction and blowby.

Introduction

The operation of piston ring packs in internal combustion engines impacts the performance, efficiency, durability, and emissions of engines. The recognition of effects of ring pack performance on key aspects of engine design and development has resulted in a sustained research and development effort aimed at understanding the operation of ring packs and optimizing their design, via measurements and increasingly, by analytical methods and simulation. A large body of literature exists, and review papers by Ruddy and Dowson (1982) and Ting (1985) can be quoted as good sources. Some of the previous work in the area of integrated modeling of ring pack phenomena will be briefly discussed here. Ting and Mayer (1974a, 1974b) developed early models of ring lubrication and blowby. Their models were aimed at the eventual prediction of cylinder wear. The work of Dowson et al. (1979) and Ruddy et al. (1979, 1981) has resulted in the development of more integrated simulations, which include effects of ring dynamics. Rhode (1980) has incorporated into ring lubrication calculations a model of mixed lubrication, which allows more realistic calculation of ring friction; it has been since adopted by a number of other investigators. The efforts toward further integration of various submodels into what has become an established scheme of two-dimensional axisymmetric analysis of ring packs, has continued in the eighties (Truscott et al., 1983), with more studies involving effects of various design parameters as well as comparison to data (Ruddy et al., 1986; Banks and Lacy, 1989). Attention has recently been shifting from ring dynamics and blowby, which can be predicted with reasonable accuracy, to the modeling of oil consumption. The accuracy of the current oil consumption models, however, has not proven to be satisfactory (Ruddy et al., 1986; Maekawa et al., 1986; Munro, 1990).

Contributed by the Internal Combustion Engine Division and presented at the Twelfth Annual Fall Technical Conference, Rockford, Illinois, October 7–10, 1990. Manuscript received by the Internal Combustion Engine Division July 1990.

The objective of the work reported here is the development of an integrated model, which builds upon existing work by (1) using highly physically based representations and advanced, robust, and flexible numerical schemes; (2) by further enhancing interaction between submodels, thus establishing key cause–effect relationships; and (3) by contributing a submodel for accurate prediction of oil consumption. An extensive experimental validation of the integrated model is also planned. This paper covers progress to date, toward the stated objective; it excludes discussion of the oil transport and consumption model, which is still under development by the authors.

Modeling Approach

General Approach. The operation of ring packs is characterized by a highly complex and interactive behavior involving the motion of the piston, radial, axial and (toroidal) twist motions of rings, gas flows through ring end gaps and lands/grooves, as well as the hydrodynamics, hydrostatics, and transport of oil. Additional factors include piston, ring, and cylinder temperatures, bore distortion (ring-bore conformability), and piston secondary motions. The work undertaken by the authors aims at the prediction of the global quantities of friction, blowby, and oil consumption as a function of numerous engine, piston, and ring pack design parameters and engine operating condition. Information on a large number of intermediate quantities is also sought, in order to provide physical insight to the details of the phenomena modeled.

Given the magnitude of the task, a structured approach was taken: The model was conceived as an assembly of modules, each dedicated to the analysis of a particular aspect of the phenomenology. Figure 1 schematically illustrates the approach for the ring pack submodels; shown are the four major modules (ring dynamics, ring lubrication, gas dynamics, and oil transport), two auxiliary modules (ring-bore conformability and oil consumption), and some of the interactions between the modules. The following characterizes the modeling philosophy adopted for the development of the submodels:

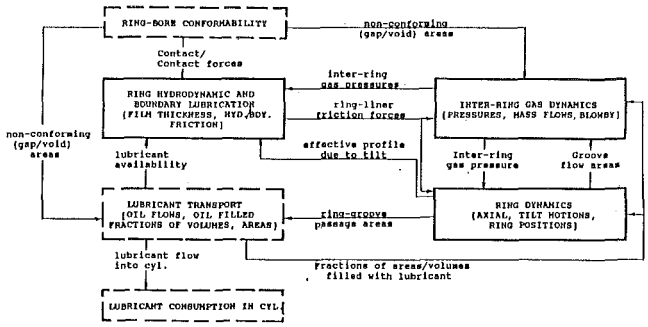

Fig. 1 Schematic of major elements (modules) of the integrated ring pack model and key interactions between them; solid blocks indicate submodels completed to date

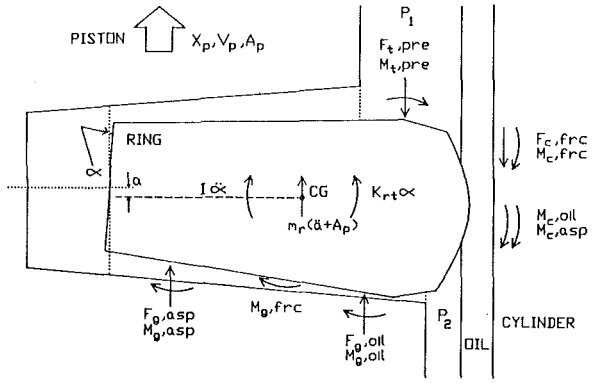

Fig. 2 Axial force and moment balance on cross section of a ring

(*a*) Physically based representations were used for the modeling of all key phenomena known to be important and understood. Lower-level (e.g., correlative and calibratable) models were used for the less well understood (and possibly only postulated) mechanisms, which are nevertheless thought or empirically known to have effects.

(*b*) An axisymmetric, two-dimensional mathematical treatment was adopted for the major elements of ring pack phenomenology. This choice was made on the basis of partial validity of the axisymmetric geometry assumption, and the impracticality of a three-dimensional approach. It is also the authors' belief that there is much knowledge and insight, not to mention valuable design guidance, to be gained from two-dimensional modeling of ring pack behavior.

(*c*) Emphasis was placed on representing all key interactions between phenomena, i.e., those indicated in Fig. 1.

To date, of the modules described above, those for ring dynamics, ring lubrication, and gas dynamics, as well as the representation of all interactions among them, have been completed and have been packaged in a single, integrated program. Modeling approaches used in individual submodels are described in more detail below.

Ring Axial and Twist Dynamics. The purpose of the ring dynamics submodel is the calculation of axial and rotational (toroidal twist) motions of rings within their grooves. Ring axial position and twist influence gas flow paths and ring-groove radial friction forces. Ring twist also affects the effective profile presented by the ring face to the cylinder bore and thus ring film thickness and friction. The equations for the two independent variables (ring axial position and twist angle) of this submodel are the equations of motion in the two respective degrees of freedom, i.e., a force and a moment balance,

$$m_r d^2a/dt^2 = F_{g,\text{oil}} + F_{g,\text{asp}} + F_{c,\text{frc}} + F_{l,\text{pre}} - m_r A_p \quad (1)$$

$$I_r d^2\alpha/dt^2 = M_{g,\text{oil}} + M_{g,\text{asp}} + M_{c,\text{frc}} + M_{l,\text{pre}} + M_{g,\text{frc}} + M_{c,\text{oil}} + M_{c,\text{asp}} - K_{rt}\alpha \quad (2)$$

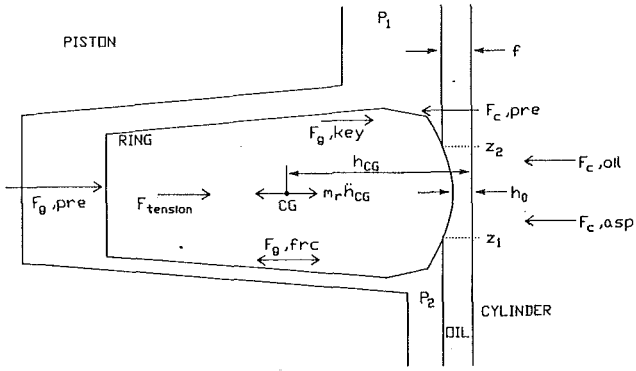

Fig. 3 Radial force balance on cross section of a ring

also schematically shown in Fig. 2; a is the axial ring position with respect to a reference frame fixed to the piston, and α the twist angle; m_r, I_r, and K_{rt} are ring mass, moment of inertia for toroidal rotation, and cross-sectional torsional stiffness; A_p is piston acceleration; F's and M's are axial forces and moments acting on various surfaces of the ring cross section, with the first subscript indicating location on ring (g = groove, c = cylinder; l = land) and the second subscript describing the source of the force or moment associated with it (oil = hydrostatic or hydrodynamic oil pressure; asp = normal pressure due to asperity contact; pre = gas pressure; frc = hydrodynamic or boundary friction). Terms associated with ring-groove contacts and land pressures are expressed as net forces and moments, i.e., as sums of forces acting on the top and bottom surfaces of the ring.

Forces and moments associated with land pressures (l,pre) are calculated using land pressure solutions provided by the gas dynamics/blowby submodel. Those related to the ring-cylinder oil film (c,oil, c,asp and c,frc) are supplied by the ring lubrication submodel. Ring-groove forces and moments are calculated from the hydrostatic oil and asperity contact pressures in the ring-groove films. The pressures are obtained by solving the Reynolds equation for the top and bottom ring-groove films, with groove back and appropriate land pressures as boundary conditions. Ring axial position and twist are used to update film geometries. Where local film thickness is comparable to groove/ring composite roughness, a simple asperity deformation model (a nonlinear spring) generates additional normal force. An "effective" viscosity is used in the Reynolds equation, which accounts for the presence of gas in the films, especially on the side with the large clearance.

Ring Hydrodynamic/Boundary Lubrication and Radial Motion. The primary purpose of the ring lubrication submodel is the calculation of ring radial position and hydrodynamic and boundary friction between the rings and the cylinder bore. The instantaneous friction forces and work are integrated over the cycle to provide mean frictional power loss. A secondary objective is the calculation of the ring-bore normal and friction forces (due to oil and asperity pressures) and their moments, which are passed to the ring dynamics submodel. The radial position of the ring cross section is passed to the gas dynamics model where it is used in the calculation of ring gap area. The ring radial position, expressed as minimum ring-bore film thickness h_0, is governed by the radial force balance on the ring cross section, shown in Fig. 3 and expressed by the following equation of motion:

$$m_r d^2h_{cg}/dt^2 = F_{g,\text{pre}} + F_{g,\text{key}} + F_{g,\text{frc}} - F_{c,\text{oil}} - F_{c,\text{asp}} - F_{l,\text{pre}} + K_{rr}(h' + h_0) \quad (3)$$

where the left-hand-side term and the last term on the right-hand side are inertia and ring tension forces, respectively; h_{cg} is the radial position of the center of gravity of the ring; K_{rr} is the ring's radial tension stiffness calculated from ring ten-

sion, and h', the reduction in ring radius at installation. Thus $K_r h'$ is the installed tension force. The remaining forces act on various surfaces on the ring: $F_{g,\text{pre}}$ is the force due to pressure in the back of the groove, $F_{l,\text{pre}}$ is due to land pressures acting on unlubricated portions of the ring face and chamfers, and $F_{g,\text{key}}$ is the radial component of the ring-groove normal force, present for keystone rings only. The oil pressure force is computed by integrating the hydrodynamic oil pressures on the ring face:

$$F_{c,\text{oil}} = \int_{z_1}^{z_2} P(z)dz. \tag{4}$$

$M_{c,\text{oil}}$ is calculated similarly by integrating the moment of the pressure with respect to the ring center and is passed to the ring dynamics submodel. The Reynolds equation is solved to obtain the axial film pressure distribution. Land pressures predicted by the gas dynamics/blowby submodel are used as boundary conditions:

$$\partial/\partial z(h^3 \partial P/\partial z) = -6\mu V_p \partial h/\partial z + 12\mu \partial h/\partial t, \tag{5a}$$

$$P(z_1) = P_1, \quad P(z_2) = P_2 \tag{5b}$$

where $[z_1, z_2]$ is the extent of the lubricated portion of the ring face and $h(z)$ is the film thickness profile calculated from the geometry of the ring face, minimum film thickness h_0, ring twist α, and thickness of oil available on the cylinder bore, as shown in Fig. 3, i.e.,

$$h = h(z, h_0, \alpha); \quad z_1 = z_1(h_0, \alpha, f); \quad z_2 = z_2(h_0, \alpha, f). \tag{6}$$

The load carried by deformation of contacting asperities where the film thickness is of the order of surface roughness, $F_{c,\text{asp}}$, is calculated by integrating the local asperity contact pressure P_{asp} over the entire ring face

$$F_{c,\text{asp}} = \int_0^{l_r} P_{\text{asp}}(z)dz. \tag{7}$$

$M_{c,\text{asp}}$ is similarly calculated and passed to the ring dynamics submodel. The local asperity contact pressure is computed from the Greenwood and Tripp (1971) model for the contact of two nominally flat surfaces, with a Gaussian distribution of asperity heights and fixed asperity radius of curvature:

$$P_{\text{asp}}(z) = \frac{16\sqrt{2}}{15}\pi(\sigma\beta\eta)^2 E\sqrt{\frac{\sigma}{\beta}}F[h(z)/\sigma] \tag{8a}$$

$$F(x) = \frac{2}{\sqrt{\pi}}\int_x^\infty (s-x)^{5/2}\exp(-s^2/2)ds \tag{8b}$$

where σ is the composite roughness of ring face and cylinder $(\sigma_r^2 + \sigma_2^2)^{1/2}$, η the asperity density, β the asperity radius of curvature, and E' the composite elastic modulus of the surface materials. Note that, as the ring face is not flat, the model was used to calculate local contact pressures (over a mesh) rather than a single force. Surface topography measurements of the more readily available type (rms height Rq and rms slope Dq) can be converted to the present input parameters using the transformation proposed by McCool (1987).

Ring friction is computed as the sum of hydrodynamic and boundary friction, i.e.,

$$F_{c,\text{frc}} = F_{c,\text{frc,oil}} + F_{c,\text{frc,asp}} \tag{9a}$$

$$F_{c,\text{frc,oil}} = \int_{z_1}^{z_2} [\mu V_p/h - 1/2h\ dP/dz]dz \tag{9b}$$

$$F_{c,\text{frc,asp}} = C_f F_{c,\text{asp}} \tag{9c}$$

where C_f is a specified dry friction coefficient for the ring-cylinder material pair.

The ring lubrication submodel allows ring "lift," i.e., a minimum film thickness h_0 above available film thickness f. When this occurs the force balance is solved with $F_{c,\text{oil}} = F_{c,\text{asp}} = 0$ until the ring re-enters the available film. A large spring force is activated to stop ring lift if the ring "collapses," i.e., $2\pi h_0$ equals the installed ring end gap. While the ring is lifted, the area of the gap between the ring face and the oil film on the bore (i.e., $\pi B[h_0 - f]$) is utilized in the inter-ring gas dynamics model as an additional gas flow area.

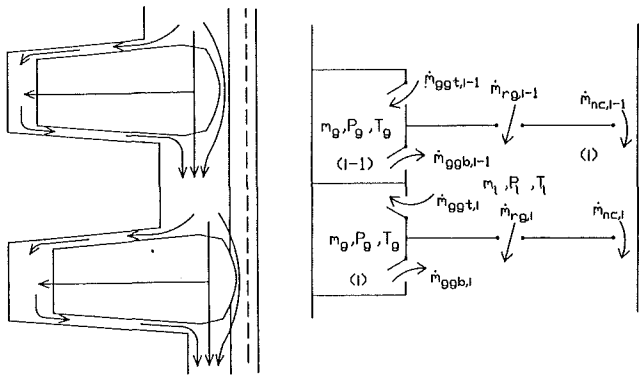

Fig. 4 Gas flow paths in ring pack and schematic of orifice-volume representation used

In a specialization of the ring lubrication submodel for double-rail oil rings, hydrodynamic and boundary lubrication equations (equations (4)–(9)) are solved for both rails; h_0, the minimum film thickness, occurs in one of the rails and film geometries for both rails are calculated accordingly. Total normal and friction forces as well as moments from the two rails are added. The sums are used in equations (1)–(3).

Inter-Ring Gas Dynamics (Blowby). The global objective of this submodel is the calculation of the rate of blowby or leakage of cylinder gas through the ring pack. In order to calculate the blowby, the instantaneous gas pressures in land and groove volumes between and behind rings are computed, as well as the rates of gas flow between these volumes. The latter are integrated over the cycle to give mean blowby rate. Land and groove pressures are used by the ring dynamics and ring lubrication calculations as already described.

The basic approach of the submodel is that of most previous studies of ring-pack gas dynamics, i.e., the unsteady flow between a series of gas volumes linked together by orifices. However, a more general description of volumes and flow paths was adopted. First, volumes in grooves as well as in lands are considered and calculated from piston, groove, and ring geometries and ring positions. Second, gas flow is allowed through gaps between rings and grooves (due to areas that become available during ring motions in grooves) and between ring and cylinder bore (due to ring "lift" or nonconforming rings), as well as to ring end gaps, as shown schematically in Fig. 4.

The primary independent variables of the inter-ring gas dynamics submodel are the masses of gas in land and groove volumes and are governed by a continuity equation for each volume:

$$dm_{l,i}/dt = \dot{m}_{rg,i-1} + \dot{m}_{ggb,i-1} + \dot{m}_{nc,i-1} \qquad i = 2, N_r \text{ (lands)}$$
$$- \dot{m}_{rg,i} - \dot{m}_{ggt,i} - \dot{m}_{nc,i} \tag{10a}$$

$$dm_{g,j}/dt = \dot{m}_{ggt,j} - \dot{m}_{ggb,j} \qquad i = 1, N_{r-1} \text{ (grooves)} \tag{10b}$$

where m is the mass in a volume and $\dot{m}$ denotes the mass flow rates through the various flow paths identified by subscripts rg (ring end gap), ggt/ggb (ring-groove gaps above and below rings) and nc (ring-bore nonconformability gap or gap due to ring "lift"). Gas mass flow rates are computed from the gas flow areas and velocities. The velocities are in turn calculated from the isentropic nozzle flow relationship for each orifice:

$$\dot{m} = KA\left(\frac{2\gamma}{R(\gamma-1)T_u}\right)^{1/2} P_u\left(\frac{P_d}{P_u}\right)^{1/\gamma}\left(1 - \left(\frac{P_d}{P_u}\right)^{\frac{\gamma-1}{\gamma}}\right)^{1/2} \tag{11}$$

where K is orifice flow coefficient (input), A is the orifice area,

R and γ are the gas constant and polytropic exponent, P_u and P_d are pressures upstream and downstream of the orifice, and T_u is the upstream temperature. A generalized nozzle flow module was used, which detects and applies choked flow conditions.

The gas pressures (which could alternately be considered as the independent variables) are related to the masses by the gas equation of state:

$$P_{l,i}V_{l,i} = m_{l,i}R_{l,i}T_{l,i} \quad i = 2,\ N_r \text{ (lands)} \tag{12a}$$

$$P_{g,j}V_{g,j} = m_{g,j}R_{g,j}T_{g,j}.\ \ j = 1,\ N_{r-1} \text{ (grooves)}. \tag{12b}$$

The first land and last groove pressures, not updated by equations (12), are set equal to cylinder and crankcase pressures, respectively. Gas temperatures are assumed to vary in a quasi-steady manner, i.e., always equal to the instantaneous area-weighted average of the temperature of surfaces surrounding each volume. Volumes are calculated from piston, groove, and ring geometries and ring position in the groove as predicted by the ring dynamics submodel. The locations of "orifices" between land and groove volumes are moved to the inner diameter of the ring or the outer diameter of the groove, depending on ring twist; groove/land volumes are adjusted accordingly.

Engine Cylinder Pressure and Other Data. An engine simulation code was utilized to produce engine data, which are utilized in addition to all ring pack, piston and liner/cylinder design parameters and oil properties specified as input to the integrated code. Crevice gas temperature history, average ring face, liner and piston land temperatures constitute the engine data required by the model.

Engine bore and parameters required to calculate piston primary (axial) motion (engine speed, stroke, connecting rod length, wristpin offset, TDC clearance) are also separately input. A module computes instantaneous piston axial position, velocity, and acceleration. Piston position is tracked to calculate, by interpolation, the temperature on the cylinder at the ring axial positions, which together with ring temperatures, are used to compute viscosity for the ring-cylinder oil films. Piston acceleration and velocity are used by the ring dynamics and ring lubrication submodels, respectively.

Numerical Solution Scheme. The primary differential equations are solved by first expressing the terms involving time derivatives by difference formulae and then applying the secant method (in its multivariate form if more than one equation is involved) on the resulting algebraic equations, to solve for the independent variables (e.g., minimum film thickness, ring twist, land pressure, etc.). The auxiliary equations relate dependent variables (e.g., film geometry, oil or asperity contact pressure, ring gap flow rates, etc.) to the independent ones and are also solved for each time step. The Reynolds equation, used for calculating the pressure distribution in both ring-cylinder and ring-groove oil films, is solved by finite differences, utilizing a 15-point mesh, distributed over the lubricated extent of the ring face.

Convergence of the solution is required at three levels: (1) Submodel level: A secant technique is applied within a submodel for a number of iterations until the solutions for all independent variables for all rings/lands etc., converge at the current time step; this is repeated for all other submodels. (2) Integrated model level: To ensure full interaction between the various submodels, the process is repeated for a number of "passes" until the differences between two passes in all the independent variables of all of the submodels become negligible; the solution then progresses to the next time step. (3) Cycle convergence: the process is continued until the solution is cyclic with respect to an engine cycle, i.e., repeats itself every 720 or 360 (for two-stroke cycle) crank angle degrees.

In order to resolve very rapid events, an automatic time step reduction/relaxation scheme was built into the solution technique. In addition to automatic time step reduction, damping schemes, which variably underrelax the solution, were adopted. Most simulations are run with a master time step (used for communication between submodels) of 5 crank angle degrees. During a typical cycle the master time step is reduced only a few times, to 2.5 or 1.25 degrees; within a master time step, time step reduction varies from one submodel to another and from ring to ring, allowing the solution to "zoom in" and resolve events with time scales of as low as 0.01 degrees.

Selected Predictions

The integrated model consisting of ring dynamics, ring lubrication, and inter-ring gas dynamics submodels, was applied to the three-ring pack of a four-stroke heavy-duty truck diesel (125 mm bore). The ring pack consists of a barrelled keystone top compression ring, a tapered (scraper) second ring, and a double rail oil control ring. All three rings were of conventional size and shape; land and groove clearances were also of typical magnitudes. Cylinder pressure histories, generated for the subject engine by an engine simulation code over a matrix of speed and load conditions, were used in the analyses.

The sensitivity of the model to many input parameters and the built-in interactions between submodels make possible a very large number of parametric studies and hence investigations of distinct design issues. A limited set of studies will be reported here, which demonstrate the capabilities of the model and features distinguishing it from prior models.

Baseline Cases. Cyclic variation of key ring pack quantities are shown in Figs. 5–10 for a "baseline" case selected as the 1900 rpm, full-load condition with fully flooded rings. Figure 5 shows axial motions of rings within their grooves. The results indicate only the *top ring* alternates its position between the bottom and top of its groove, spending part of the exhaust stroke and all of the intake stroke near the top. The transfer to the top of the groove is precipated by a favorable inertia force; the ring's position at the top is then maintained by a reduced cylinder pressure and a pressure differential in favor of second land pressure during the intake stroke. Except for a period during combustion, only the outside diameter of the ring is in close contact with the bottom of the groove. Similarly during the intake stroke the inside diameter only contacts the top of the groove. This is caused by the difference between the keystone angles of the ring and groove (ring angles are larger). When cylinder pressure drops after combustion the pressure force balance is favorable for ring motion upward; there is some motion but it is checked by the viscous and inertia forces. The *second ring* is always flush with the bottom of its groove; this is due to a second land pressure, which is always higher than that in the third land. The same is true for the oil ring; however, the pressure differential is much smaller for the oil ring and it is not enough to keep it flush with the crankcase side of its groove. Also as a result of a smaller pressure differential the effect of the inertia force on the ring motion is more discernible. Predicted toroidal twist histories for the three rings are shown in Fig. 6 where the top ring is seen to be the only one exhibiting any significant twist motion. This is due to the keystone angle difference as noted above and also due to a large ring-groove clearance. This allows relatively rapid motion in the center of the groove and causes "separation" and "impact" spikes in twist angle. The top ring twist angle is constant (it is equal to the difference between the ring and groove keystone angles) during combustion when the ring is flush with the bottom groove surface. The second ring twist is small and present only during downstroke (scraping) when the moment arm of the linear contact force is larger and thus this moment is amplified. An even smaller twist is seen for the oil ring and its direction indicates it is caused by the friction force on the rails.

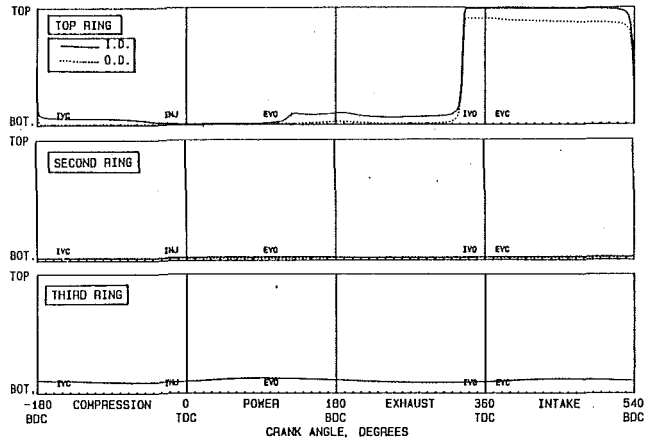

Fig. 5 Predicted cyclic history of ring axial motions for baseline case (1900 rpm, full load)

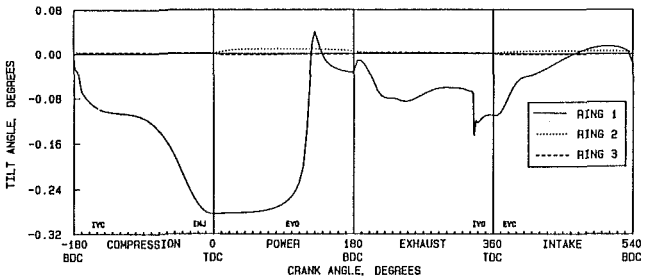

Fig. 6 Predicted cyclic history of ring twist for baseline case (1900 rpm, full load)

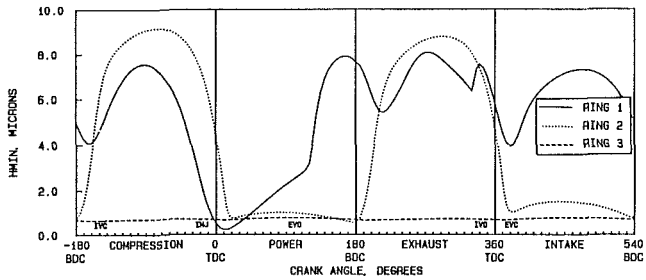

Fig. 7 Predicted cyclic history of minimum film thickness for baseline case (1900 rpm, full load)

Cyclic variation of ring minimum film thickness is shown in Fig. 7. Results indicate that the top ring radial motion has some features in addition to conventionally calculated behavior (i.e., small thickness at TDC's and BDC's, "humps" during strokes). One feature is the sustained small film thickness during the first half of the power stroke. This is associated with the constant twist during this period (Fig. 6), which causes the top ring to behave like a scraper ring. The behavior during exhaust stroke is a product of a relatively large second land pressure as well as increase in twist at the end of the stroke. The second ring exhibits a behavior typical of scraper rings, with much smaller film thickness during downstroke. The oil ring maintains an almost constant and small film thickness as its narrow rails cannot generate a hydrodynamic load carrying capacity. Its load (mostly tension) is supported almost entirely by asperity contact. The friction force histories for the three rings are shown in Fig. 8 and are consistent with the variation of minimum film thickness. Periods of boundary friction appear as spikes for the top and second rings and are prominent near the beginning and end of strokes. For the oil ring boundary friction is continuous and is augmented with a small hydrodynamic friction component, which is highest in the middle of each stroke. Instantaneous power loss associated with friction forces is shown in Fig. 9, which indicates that the oil ring causes the highest mean frictional power loss.

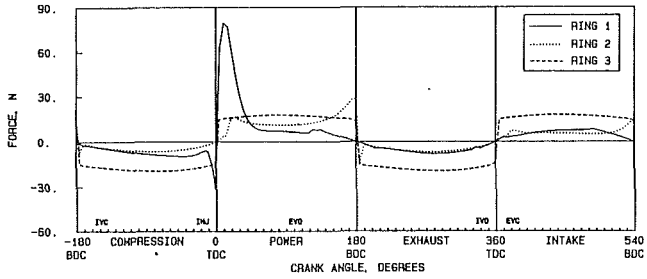

Fig. 8 Predicted cyclic variation of instantaneous ring friction force for baseline case (1900 rpm, full load)

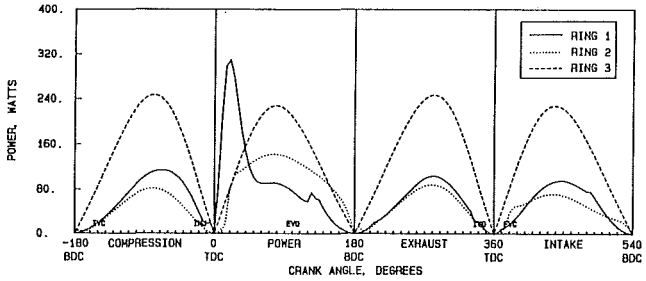

Fig. 9 Predicted cyclic history of instantaneous ring frictional power loss for baseline case (1900 rpm, full load)

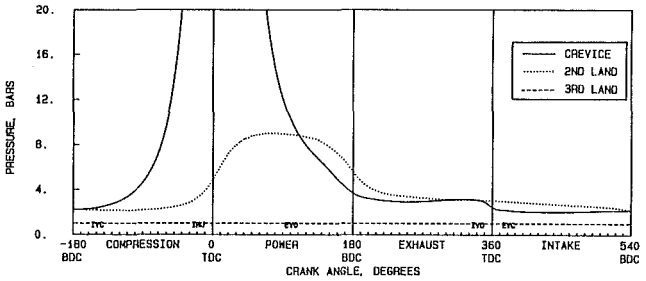

Fig. 10 Predicted cyclic history of land pressures for baseline case (1900 rpm, full load)

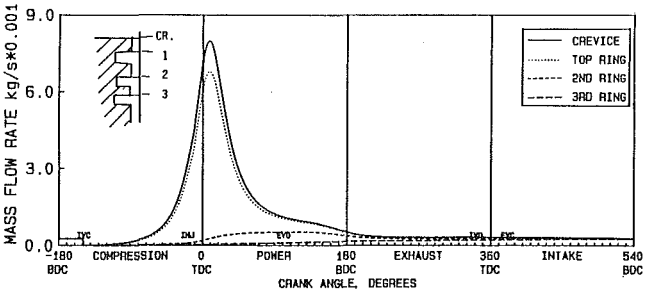

Fig. 11 Predicted cyclic history of cumulative mass past rings for baseline case (1900 rpm, full load)

Predicted cyclic variation of land (inter-ring volume) pressures is shown in Fig. 10. Second land pressure is seen to rise to 8 bars during combustion. Depressurization of the second land is slower as the reverse flow is driven by a smaller pressure difference after the cylinder and second level pressures cross over at about exhaust valve opening (EVO). The two pressures equalize again near intake valve opening but cylinder pressure drops again during intake. The corresponding history of cumulative gas mass past each ring is shown in Fig. 11, which shows that first and second rings both experience reverse flows. The flow is integrated at the top of each groove as shown in the inset diagram. Eighty to eighty-five percent of all mass past the top of the piston into the crevice is admitted into the first ring groove and the second land. This is mostly due to a

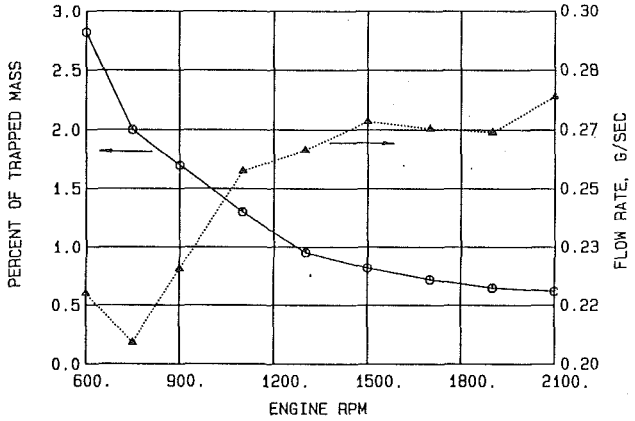

Fig. 12 Effect of speed on blowby at full load

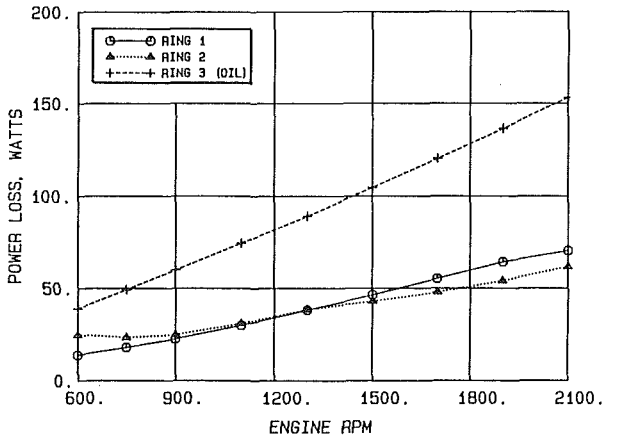

Fig. 13 Effect of speed on ring (hydrodynamic + boundary) friction at full load

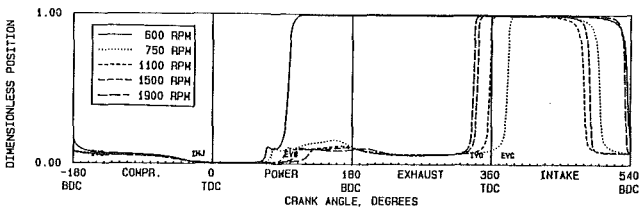

Fig. 14 Effect of speed on top ring axial motion, at full load

large ring-groove clearance in the first groove. For the full cycle, cumulative mass past all rings integrates to the same level (seen near IVC), which is the calculated *blowby* for the ring pack.

Speed Study. Predictions of blowby and frictional power loss for full-load operation over a speed range between 600 and 2100 rpm are shown in Figs. 12 and 13. Blowby (Fig. 12) exhibits the expected trend, i.e., the engine becoming more "gas-tight" with speed. The actual blowby mass flow rate, also shown in Fig. 12, increases with speed but the trend has perturbations associated with details of ring dynamics at various speeds, as will be seen below. It is important to note that the levels of blowby shown in Fig. 12, which are in line with typical observed levels, could *not* have been predicted by a simple model, which only takes into account gas flow through ring end gaps. It is the consideration of gas flow through ring grooves (during ring axial/tilt motions) and its effect on land pressures that has made a key contribution to the predicted blowby, bringing it to a realistic level. Total (hydrodynamic + boundary) frictional power loss for each ring, shown in Fig. 13, increases with speed; the oil control ring exhibits the highest level of mean friction as already implied by instantaneous

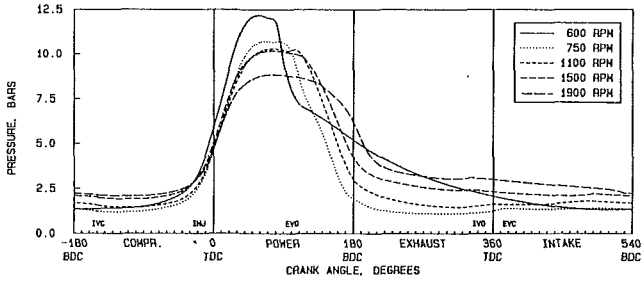

Fig. 15 Effect of speed on the cyclic history of second land pressure, at full load

power loss results (Fig. 9). The trend of friction increasing with speed is seen to reverse for the second (scraper) ring below 750 rpm. As speed is reduced hydrodynamic friction as well as the load carrying capacity due to the wedge film effect is decreased, thus increasing asperity contact and boundary friction eventually to the point where it is the dominant factor in the magnitude and trend of total friction. This will happen for all rings as speed is further reduced; however, scraper rings will reach this point (the minimum point on the Stribeck curve) at higher speed, as they do not normally have a significant hydrodynamic load carrying capacity during the downward stroke.

The effects of speed on the cyclic variation of key predicted parameters are also of interest as they help explain trends in the global quantities and provide insights relative to interactions between the various phenomena modeled. Figure 14 shows the effect of speed on top ring axial motion. For all speeds except 600 rpm, the motion upward after combustion is stopped after 10–20 percent of the groove gap distance is traversed, due to deceleration of the piston. As speed is reduced from 1900 rpm, the equalization of first and second land pressures and thus top ring motion upward takes place earlier and the motion is arrested after more travel, due to lower combustion pressures. Between 750 and 600 rpm the motion begins at a point where the inertia force (now favorable due to higher piston accelerations earlier in the power stroke) is added to the upward pressure force and causes the ring to transfer to the top surface of its groove. The result is a switch to a regime where the top ring spends most of the cycle at the top of its groove, except during the compression and early power strokes. The switch in regime at 600 rpm causes a more rapid depressurization of the second land as additional area becomes available during ring motion to the top of its groove. However, once the motion is complete, sealing of the first groove is more effective than at higher speeds; mass remaining in the second land drains to the third land causing the increase in blowby mass flow rate seen in Fig. 12. The corresponding trend in cyclic history of second land pressure is seen in Fig. 15. Similar analyses of trends in other quantities (ring twist, film thickness, ring friction) showed that they are consistent with the ones described above.

Effect of Load. The effect of engine load on the ring pack performance was studied at a constant engine speed at 1900 rpm, and the engine load was varied from full load to 25 percent of full load in increments of 25 percent. Combustion chamber pressure drops with decreasing load, resulting in lower blowby (Fig. 16). Similarly lower land and thus groove pressures at part loads cause both hydrodynamic and especially boundary components of total frictional power loss (Fig. 17) to decrease. As would be expected, the effects are on the top two rings only; as the oil ring groove is vented to the crankcase, gas pressure in the groove and thus load on the ring remains unaffected by engine load.

Effect of Oil Availability. During engine operation the thickness of oil film available for the lubrication of each ring varies through the cycle and is determined from the instantaneous

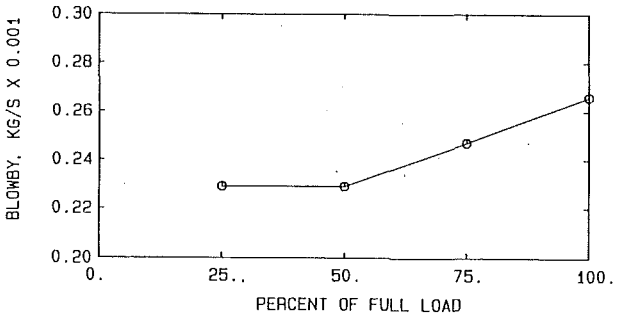

Fig. 16 Effect of load on blowby: 1900 rpm.

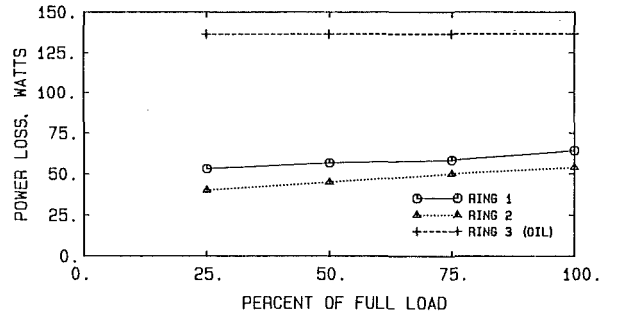

Fig. 17 Effect of load on (hydrodynamic + boundary) friction: 1900 rpm.

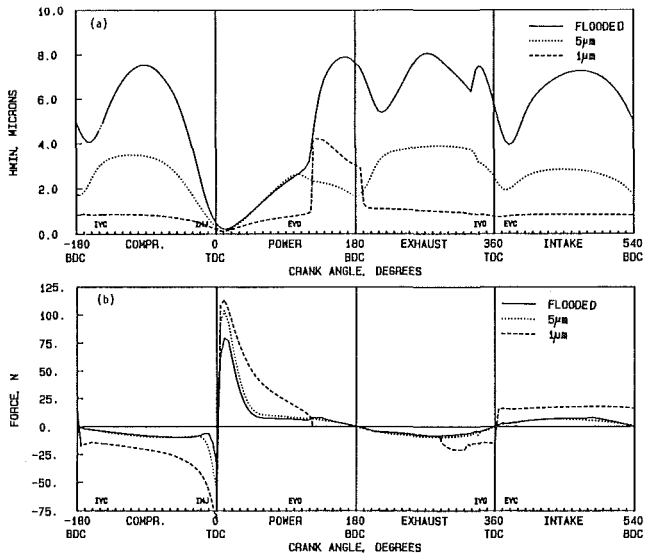

Fig. 18 Effect of available oil film thickness on (*a*) ring minimum oil film thickness; (*b*) ring instantaneous friction force

film thickness trailing the next upstream ring. The calculation of this quantity was left to the oil transport submodel, currently under development. However, the current model allows specification of a constant oil film thickness (available on the liner), which is utilized for all rings at all times, except for the oil ring during downstroke, when it is assumed to be flooded. Figure 18 shows the effect of oil film availability on the baseline case top ring film thickness and friction. As oil film thickness is reduced the top ring minimum film thickness also decreases as the force balance on the ring keeps it inside the film. For a 1 μm oil film the ring is seen to "lift" above the film after EVO due to an inward net radial force; as the cause of this (high pressure in the second land) is eliminated due to gas flow through the opening area, the ring settles into the film again. The friction of the top ring is affected as shown in Fig. 18(*b*). New periods of boundary friction appear as oil availability is

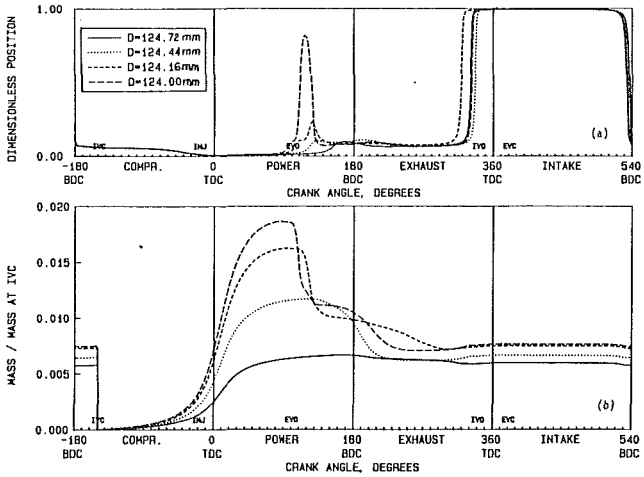

Fig. 19 Effect of second land volume (as modified by varying second land diameter) on (*a*) top ring axial motion; and (*b*) cumulative flow past second ring

reduced and existing ones become more dominant. The effect on the mean frictional power loss of all three rings is as follows (W):

	Flooded	h_{film} = 5 μm	h_{film} = 1 μm
Ring 1	64.5	74.5	161.9
Ring 2	54.1	54.5	164.2
Oil ring	136.5	146.2	148.9

Most affected by oil starvation are the first and second rings, which are forced to operate with boundary friction even in midstroke. The oil ring, which has little hydrodynamic lift due to its narrow rails and always operates with boundary friction, is not significantly impacted.

Effect of Second Land Volume. Second land volume is known to be an important quantity with significant effects on ring dynamics and blowby. Figure 19(*a*) shows the effects of second land volume on top ring axial motion. A large second land volume is seen to induce a second switch in top ring position due to low rate of depressurization of the second land. The prolonged high pressure in the second land also causes more mass flow through the second ring (Fig. 19*b*) and increases blowby.

Effects of Coupling Between Ring Dynamics and Inter-ring Gas Dynamics: The importance of a coupled treatment of ring motions and inter-ring gas dynamics, already implied by some of the results presented, is made clear by Figs. 20(*a*, *b*) and 21(*a*, *b*). Figure 20 shows the top ring motion (measurement) and second land pressure (prediction and measurement) results obtained by Graham and Munro (1982). Speed, load condition, and ring geometry for the results are not described. However, the predictions are qualitatively and quantitatively similar to those at the 600 rpm full-load case in the present study, shown in Fig. 21(*a, b*). Note however, that the second land pressure prediction shown in Fig. 20(*b*) does not respond to the axial motion of the top ring, as the measured pressure evidently does, resulting in a discrepancy between prediction and measurement.

The present model on the other hand produces a sharp drop in second land pressure as seen in Fig. 21(*b*). As the top ring groove clearance (the flow area) is large, the cylinder and second land pressures remain equal until the ring seals against the top of its groove. Characterization of such coupling between ring dynamics and gas pressures is extremely important for accurate calculation of blowby.

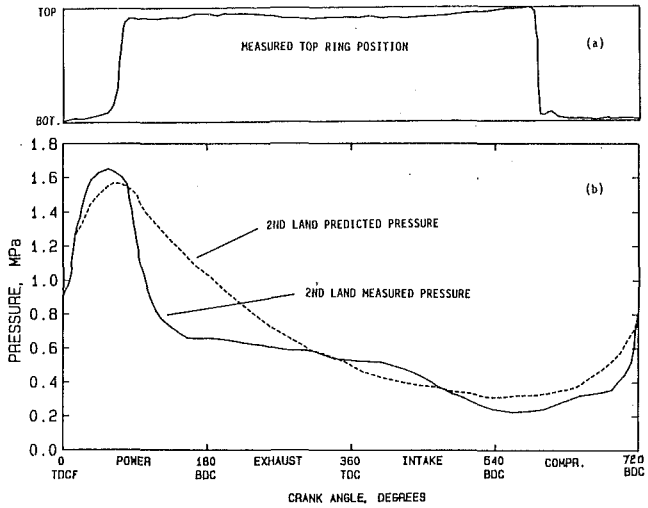

Fig. 20 Top ring axial motion (*a*) and correlation of predicted and measured second land pressure (*b*); data from Graham and Munro (1982)

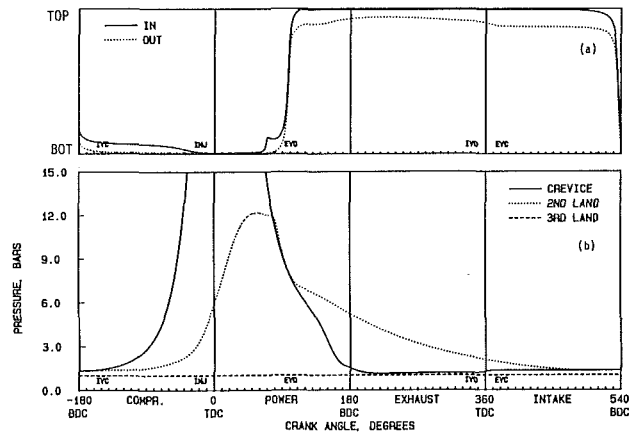

Fig. 21 Predicted cyclic variation of (*a*) top ring axial motion; and (*b*) inter-ring pressures: 600 rpm, full load

Similar relationships have been demonstrated using the present model, which are less readily understandable and even initially questionable. Examples are links between oil viscosity and blowby, torsional stiffness of rings and friction, surface finish, and land gas pressures. In every instance, however, detailed analysis of cyclic histories of several key quantities revealed a plausible reason for the link, within the context of the present model. An extensive validation of the model is planned during which experimental verification of the nature of some of these relationships will be sought.

Summary

1 A comprehensive model for the prediction of ring pack performance has been developed. The model currently consists of submodels of ring dynamics, inter-ring gas dynamics, and ring lubrication; it will be further augmented by oil transport and ring-bore conformability submodels. The model is characterized by advanced treatments of the phenomena analyzed and also by intimate coupling between the submodels.

2 The model has been applied to a heavy-duty diesel engine ring pack across a speed and load range spanning the operating condition map of the engine, producing the expected trends and magnitudes in global quantities (blowby, friction) and also interpretable behavior of and trends in cyclic variation of intermediate quantities such as ring motions, film thicknesses, and land pressures.

3 It was demonstrated through a series of analytical parametric studies that the built-in interactions (between submodels) in the code do affect the predicted behavior, and in some cases, such as the link between ring motions and inter-ring gas dynamics, are essential for correct characterization of the modeled behavior.

Acknowledgments

This work was supported by DOE/NASA contract DEN3-374, under subcontract to Caterpillar, Inc. It was monitored by Project Managers Joseph Notardonato of NASA Lewis Research Center, and Herbert Larson of the Caterpillar, Inc. Technical Center.

References

Banks, T. J., and Lacy, D. J., 1989, "The Application of Analysis to Piston Ring Performance," IMechE Paper No. C375/003.

Dowson, D., Economou, P. N., and Ruddy, B. L., 1979, "Piston Ring Lubrication—Part II: Theoretical Analysis of a Single Ring and Complete Ring Pack," in: *Energy Conservation Through Fluid Film Lubrication Technology: Frontiers in Research and Design.*

Graham, N. A., and Munro, R., 1982, "Investigation of Analysis of Oil Consumption and Blowby in Relation to Piston and Ring Features," presented at AE Symposium, Paper No. 28.

Greenwood, I. A., and Tripp, J. H., 1971, "The Contact of Two Nominally Flat Surfaces," *Proc. I. Mech. E.*, Vol. 185, pp. 625–633.

Maekawa, K., Mitsutake, S., and Morohoshi, S., 1986, "A Study of Engine Lubricating Oil Consumption by Computer Simulation," SAE Paper No. 860546.

McCool, J. I., 1987, "Relating Profile Instrument Measurements to the Functional Performance of Rough Surfaces," ASME *Journal of Tribology*, Vol. 109, pp. 264–270.

Munro, R., 1990, "Emissions Impossible—The Piston and Ring Support System," SAE Paper No. 900590.

Rhode, S. M., 1980, "A Mixed Friction Model for Dynamically Loaded Contacts With Application to Piston Ring Lubrication," *Proceedings of the 7th Leeds-Lyon Symposium on Tribology.*

Ruddy, B. L., Dowson, B., and Economou, P. N., 1979, "Piston Ring Lubrication, Part III: The Influence of Ring Dynamics and Ring Twist," in: *Energy Conservation Through Fluid Film Lubrication Technology: Frontiers in Research and Design.*

Ruddy, B. L., Dowson, D., and Economou, P. N., 1981, "A Theoretical Analysis of the Twin-Land Type of Oil-Control Piston Ring," *J. Mech. Eng. Sci.*, Vol. 23, pp. 51–62.

Ruddy, B. L., Dowson, D., and Economou, P. N., 1982, "Review of Piston Ring Studies," *Proc. of 9th Leeds-Lyon Symposium: Tribology of Reciprocating Engines.*

Ruddy, B. L., Reid, T. J., and Veshagh, A., 1986, "Ring Pack Performance Predictions," presented at AE Symposium, Paper No. 30.

Ting, L. L., and Mayer, J. E., 1974a, "Piston Ring Lubrication and Cylinder Bore Wear Analysis, Part I—Theory," ASME *Journal of Lubrication Technology*, Vol. 96, pp. 305–314; Paper No. 73-Lub-25.

Ting, L. L., and Mayer, J. E., 1974b, "Piston Ring Lubrication and Cylinder Bore Wear Analysis, Part II—Theory Verification," ASME *Journal of Lubrication Technology*, Vol. 96, pp. 258–266; Paper No. 73-Lub-27.

Ting, L. L., 1985, "A Review of Present Information on Piston Ring Tribology," SAE Paper No. 852355.

Truscott, R., Reid, T., and Ruddy, B. L., 1983, "Ring Dynamics in a Diesel Engine and Its Effects on Oil Consumption and Blowby," SAE Paper No. 831282.

On the Development of Modern Analysis Techniques for Single Cylinder Testing of Large-Bore Engines

G. M. Beshouri
Advanced Engine Technologies Corporation, San Leandro, CA 94578

The world-wide consolidation of many engine manufacturers, along with the relatively low production rate of new engines, has resulted in a significant reduction in the facilities, engines, and personnel available for conducting full-engine laboratory quality tests against calibrated dynamometers. Concurrently, the continued pressure for further reduction in exhaust emissions, along with improvements in fuel consumption, has created a growing aftermarket for the retrofit/upgrade of new technologies requiring further engine development. Regrettably, the prohibitive cost and capital investment associated with full engine tests, along with the lack of facilities, makes such tests prohibitive. Therefore, a number of new experimental techniques and associated analysis methods have been developed for conducting laboratory quality single-cylinder tests on commercial engines without interfering with their profitable operation. Such tests have been successfully conducted on both spark-ignited and dual fuel engines. Many details of the methods utilized, along with estimations of their accuracy and reliability, are described.

Introduction

The past two decades has witnessed a significant reduction in the number of domestic builders of large-bore engines, with the associated reduction in available test facilities and experienced test personnel. Simultaneously, various Federal, state, and local regulatory bodies have continued to introduce increasingly more stringent limitations on emissions while energy costs encourage engine operators to minimize fuel consumption. As a consequence, the industry faces technological challenges (equal to those that faced the originators of reciprocating engine technology) at a time when test facilities and expertise are at a numerical minimum.

Therefore, while the heightened interest in emissions and efficiency has created a growing aftermarket for engine retrofit packages that reduce engine fuel consumption and/or reduce emissions, there are few firms equipped to perform extensive full-engine testing on a dynamometer. Rather, these retrofit packages are offered by small firms (often with extravagant claims) with limited resources and little test backup. The author has examined a variety of retrofits ranging from ceramic coatings to water-in-fuel emulsification to fuel injection system modifications that claim substantial reductions in fuel consumption (typically 5–10 percent) and emissions (an order of magnitude). In general, the test backup is limited, usually performed on an engine in service with little to no special instrumentation, and therefore does not stand up to careful scrutiny.

However, the need to perform verification testing in the field on a production engine does not necessarily exclude laboratory quality results. In fact, engine manufacturers have historically performed field performance testing to ASME codes [1] for decades with uncertainties of less than ± 0.5 percent and repeatability better than 0.2 percent. Based on techniques described in the literature and extensive experience working as service and research engineers, AETC engineers have developed a number of specialized techniques for performing laboratory quality testing and development on a single cylinder of a production engine. The use of these techniques, in conjunction with modern data acquisition systems, data processing algorithms, and curve fitting methods permits real time data reduction and analysis. By carefully bounding the extremes of operating conditions and then selectively recording a minimum number of data sets between the extremes, the development cycle can be reduced from several months to a few weeks or less.

The recent application of these techniques to a feasibility and development test of a dual fuel engine utilizing electronic pilot fuel injection resulted in a projected reduction in NO_x emissions to as low as 0.5 g/bhp-hr with little to no penalty in fuel consumption [2]. The test, including instrument installation; baseline, feasibility, and development testing; and teardown, took less than two weeks, without compromising normal plant operations.

Contributed by the Internal Combustion Engine Division and presented at the Twelfth Annual Fall Technical Conference, Rockford, Illinois, October 7–10, 1990. Manuscript received by the Internal Combustion Engine Division July 1990.

This paper first reviews key test parameters utilized in this and similar single cylinder field development tests. It then evaluates the associated instrumentation and special test and calculation techniques. Finally, it gives examples of typical results as applied to various engine types.

Performance Evaluation Parameters

As noted, most after-market product development for large-bore engines focuses on reducing emissions (primarily NO_x) and improving fuel consumption. While a wide variety of parameters are available for evaluating, understanding, and optimizing engine performance, five have proven particularly effective. A brief description of each follows.

Indicated Power/MEP. Generally, most users require that any engine improvement or modification not de-rate the unit or reduce the available output. This is most easily assessed by determining the Indicated Power (IHP) on variable speed applications such as pump drives and marine main propulsion engines, or Mean Effective Pressure (MEP) on fixed speed applications such as generator drives. Typically the output for the test cylinder is obtained by measuring cylinder pressure and speed as a function of crank angle. Based on the geometry of the rod/crank mechanism, the cycle average torque can be determined and the MEP and/or IHP calculated according to well-established formulas [3].

Fuel Consumption. As noted, the threat of ever-increasing fuel costs encourages operators to minimize engine fuel consumption. Moreover, most methods of reducing emissions often result in fuel penalties, increasing an operator's sensitivity to obtaining optimal efficiency.

While most easily understood in terms of thermal efficiency, the domestic engine industry has traditionally expressed fuel consumption performance in terms of Brake Specific Fuel Consumption (BSFC—in lbm/bhp-hr) or Brake Specific Energy Consumption (BSEC—in Btu/bhp-hr or Btu/kW-hr). Either is effectively a measure of the fuel energy required to generate a unit of mechanical work and they are calculated as follows:

$$\text{BSFC} = \frac{m}{P_{av}\tau} \tag{1}$$

$$\text{BSEC} = \frac{E}{P_{av}\tau} \tag{2}$$

Emissions Levels. Typically, engine users operating under emissions limitations are restricted to generating a maximum annual mass of pollutants. As it is virtually impossible to measure the mass of annual pollutant formation, most operators (and the regulatory bodies) instead determine the annual energy output (in bhp-hr or kW-hr) and multiply by the brake specific emissions level, expressed in units of g (of pollutant)/bhp-hr. Recently, many regulatory bodies have moved to limiting brake specific emissions directly, in addition to annual outputs.

At this date, $BSNO_x$, BSCO, and BSNMHC are most commonly monitored and regulated. As an example, $BSNO_x$ emissions are calculated as follows:

$$\text{BSNO}_x = \frac{m_{\text{NO}}}{P_{av}\tau} \tag{3}$$

Combustion Stability. When driving a synchronous generator running against an infinite bus (during which the flywheel has no effect), an engine must have relatively stable cycle-to-cycle combustion. If it does not, the generator will produce large swings in current resulting in significant fluctuations in electrical power generation. In particular, this poses a problem for gaseous fueled engines, which inherently suffer from cycle-to-cycle instability due to inconsistencies in gas charging, gas ignition, and charge stratification [1].

Nomenclature

MEP = Mean Effective Pressure, psi
BSFC = Brake Specific Fuel Consumption, lbm/bhp-hr
BSEC = Brake Specific Energy Consumption, Btu/bhp-hr
τ = time interval during which the measurement is conducted, hr
m = mass of standard heating value fuel consumed during time τ, Btu
P_{av} = average brake power generated during τ (brake horsepower)
E = fuel energy consumed during time τ, Btu
$BSNO_x$ = Brake Specific NO_x emissions, g/bhp-hr)
BSCO = Brake Specific CO emissions, g/bhp-hr
BSNMHC = Brake Specific Non-Methane Hydro-Carbon Emissions, g/bhp-hr
m_{NO} = mass of NO_x released during time τ, g
ROHR = Rate of Heat Release, Btu/θ
P_{comb} = average peak combustion pressure for n cycles, psi
P_{comp} = cold compression pressure, psi
SD = Standard Deviation for n cycles, psi
P_{man} = intake manifold (gage) pressure, psi
P_{atm} = atmospheric (ambient) pressure, psi
γ = ratio of specific heats
CR = Compression Ratio
BSEM = Brake Specific Emissions, g/bhp-hr
V'_{EM} = average volume flow rate of pollutant emission during time τ, scfm
C_{EM} = concentration of pollutant emission
V'_{ex} = volume flow rate of exhaust gas during time τ, scfm
R_{EM} = density of pollutant emission at standard conditions, g/ft^3
M'_{ex} = mass flow rate of the exhaust gas, lbm/min
M'_{in} = mass flow rate of the intake air, lbm/min
M'_{fu} = mass flow rate of the fuel(s), lbm/min
V'_{in} = volume flow rate of intake air, scfm
η_{ve} = engine volumetric efficiency
DI = Cylinder Displacement, ft^3
N = engine rotative speed, rpm
T_{in} = intake air manifold temperature, °F
P_{in} = intake air manifold pressure, in. Hg
P_{bar} = barometric pressure, in. Hg
Q_{app} = apparent rate of heat release, Btu/deg
θ = instantaneous crank angle, deg
P = instantaneous pressure, psi
V = instantaneous volume, in.^{3}
Q_{wall} = heat loss to the wall, Btu/deg

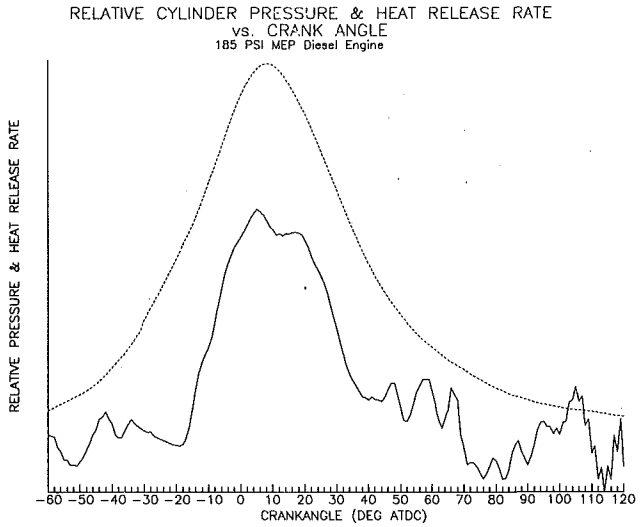

Fig. 1 Typical pressure and rate of heat release diagrams for a highly turbocharged diesel engine as a function of crank angle

Traditionally, combustion stability (along with low BSFC) was obtained by operating at relatively low (i.e., fuel rich) air/fuel ratios. However, the resultant $BSNO_x$ emissions levels are no longer acceptable, necessitating operation of gaseous fueled engines at leaner mixtures with the associated increased instability. Therefore optimum performance entails a tradeoff between combustion stability (and BSFC) and $BSNO_x$ emissions.

While the combustion stability can be quantified directly in terms of load fluctuation for full engine tests, single-cylinder tests require a method of evaluating combustion stability based on individual cylinder traces. While no definitive industry-wide method for calculating combustion stability exists, one particularly promising method, the Combustion Quality Index (CQI, see [4]), has been used extensively and is described below.

Combustion Performance. While perhaps a bit more nebulous than the other parameters, any after-market modification must not compromise the engine's "combustion performance," i.e., its ability to burn the fuel effectively and efficiently with a minimum of smoke. While MEP, BSFC, combustion stability, and even $BSNO_x$ are all indicators of combustion performance (or lack thereof) they are effects, not causes. Moreover, none really allow the development engineer to look effectively into the test cylinder and determine the beginning, magnitude and duration of the various phases of combustion.

These combustion events are most effectively determined by calculating and plotting the Rate of Heat Release (ROHR) versus crank angle. Originally developed in the 60s [5], ROHR is essentially a calculation of the rate of energy release based on the application of the first law of thermodynamics to a measured Pressure-Volume (P-V) trace. ROHR immediately reveals the beginning and duration of combustion, which is virtually impossible to discern from pressure traces of highly turbocharged diesel engines alone (Fig. 1). In addition, ROHR diagrams make it possible to discern different phases of combustion, i.e., premixed versus diffusion controlled for diesels, or in the case of dual fuel engines, liquid versus gaseous fuel combustion.

While ROHR analysis has been applied to automotive size engines since its inception, a continuing review of the literature reveals very little application of this powerful diagnostic tool to large-bore engines. This may be in part due to the relatively late introduction of high-speed digital data acquisition systems in the large-bore engine industry.

It should be noted that ROHR is not a parameter of optimization or even a direct measure of optimization effectiveness. Rather, like the cylinder pressure trace from which it is derived, ROHR is a sort of diagnostic permitting detailed examination of the combustion events occurring during an engine cycle. Based on its interpretation, it is possible more effectively and intelligently to optimize combustion controlling parameters such as injection timing, air/fuel ratio, etc., thereby minimizing speculation and test time.

Instrumentation

In order to calculate the desired performance parameters, a variety of engine operating parameters must be measured and recorded. Some parameters, such as air manifold pressure, air manifold temperature, etc., are readily available at the engine instrument panel. If the appropriate instruments are properly calibrated, they typically yield suitable data. Other parameters, such as cylinder pressure, TDC, fuel consumption, and emissions concentrations, must be obtained using more specialized instrumentation. A brief discussion of the required instrumentation and its successful application follows.

Cylinder Pressure

In Cylinder Versus Out. The difficulties of accurately and reliably indicating cylinder pressure as a function of crank angle are well documented, particularly for small engines [6-8]. Optimal results are obtained when utilizing water-cooled, temperature-compensated, piezoelectric transducers slightly recessed from the cylinder head flame face.

Extensive testing on large-bore engines will generally confirm these conclusions. In particular, large-bore engines are typically fitted with "Indicator" passages for measuring peak firing pressures and blowing the engine down. Due to the ease of access, much development work has been based on measurements taken at this location. However, the long narrow indicator passage, which often includes one or more turns, usually retards the pressure signal (Fig. 2). In addition, the relatively rapid rate of pressure rise encountered in gas engines near TDC creates a sonic pressure wave, reflecting back and forth in the passage canceling and adding to the basic pressure signal (Fig. 3) resulting in significant deviations. Gas engines may also experience detonation in the passage itself.

In contrast, very reliable in-cylinder measurements can usually be obtained on large-bore engines by replacing the air start valve in the test cylinder with a "dummy" fitted with a removable, water-cooled pressure transducer.

Piezoelectric Versus Strain Gage. Traditionally, the automotive engine industry has utilized piezoelectric (quartz) transducers for measuring cylinder pressure, presumably due to their higher frequency response. However, the inherent zero drift of these transducers usually prohibits calibration with a dead weight tester. In addition, an auxiliary means of determining the minimum pressure level is required.

However, several high-quality, water-cooled and temperature-compensated strain gage transducers are now available, specifically designed for cylinder pressure measurement. Affording ease of calibration utilizing a dead weight tester, they are preferred for large-bore engines where loss in frequency response appears negligible due to the relatively low rotative speed of these engines. For example, in a comparative test, a piezoelectric and strain gage transducer were mounted in the same adapter connected to the indicator cock of a 275 psi BMEP diesel engine. When corrected for zero drift and converted to engineering units, the pressure waveforms from the two transducers exhibited no discernible difference.

Regrettably, strain gage transducers, like the piezoelectric transducers, do suffer zero drift, albeit not as great. This drift appears to be a strong function of cooling water temperature, and to a lesser degree, load. While automatic regulation of

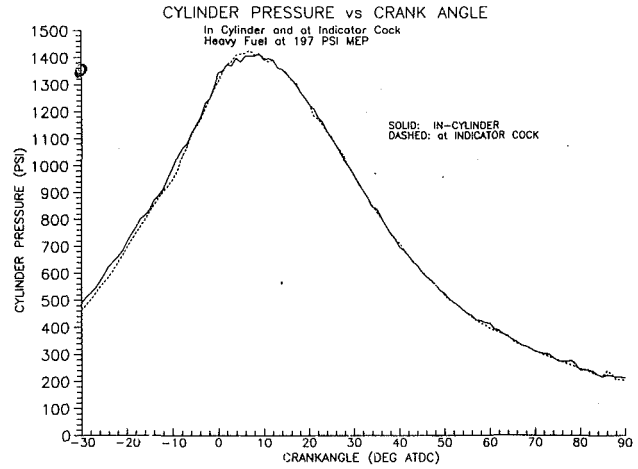

Fig. 2 Comparison of in-cylinder versus at indicator cock pressure measurements for a highly turbocharged diesel engine

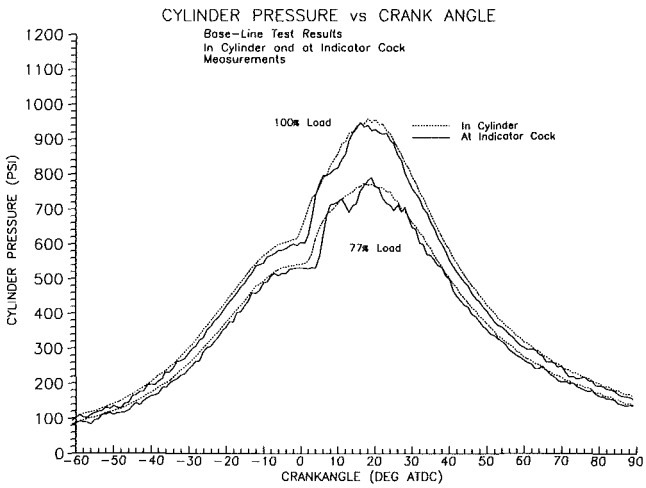

Fig. 3 Comparison of in-cylinder versus at indicator cock pressure measurements for a highly turbocharged dual fuel engine

cooling water temperature might resolve the problem, simple numerical compensating techniques have been developed for evaluating the minimum pressure based on air manifold pressure.

Sampling Rates. It is a well-established fact that errors as small as ±1 deg in the measurement of TDC can result in significant errors in indicated power, thus encouraging the use of high sampling rates (as high as 0.1 deg/sample) to minimize the uncertainty in the location of TDC. However, this high acquisition rate must be balanced by the need to minimize data file size and data processing time. With the careful location and triggering of TDC, a data acquisition rate on the order of 1 deg/sample will yield consistent MEPs, with 1000 points captured per file ensuring that one complete two-revolution cycle can be reduced from the data.

When a large number of continuous cycles are required, such as for calculation of combustion stability, sampling rates must be held to a minimum to obtain the maximum number of cycles for a fixed buffer size. An acquisition rate of 5 deg/sample generally ensures the capturing of the peak pressure of each cycle to within ±1 percent, even on relatively unstable gas engines.

TDC/Speed

Effects of Error. As noted, relatively small errors in the determination of TDC can yield significant errors in the determination of MEP. An error of 1 deg can reportedly change

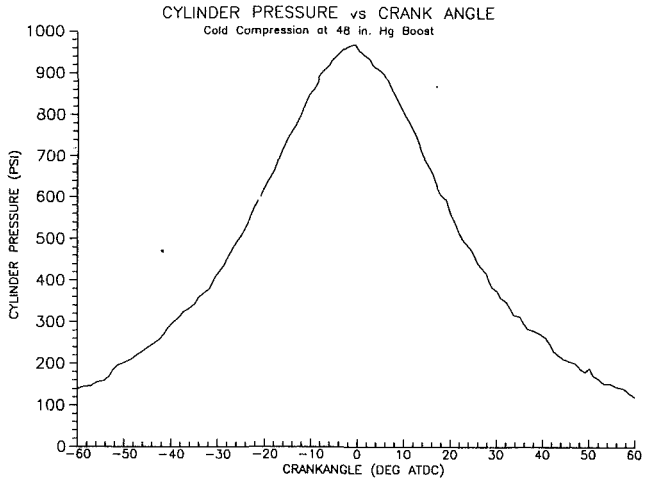

Fig. 4 Typical cold compression trace

calculated MEP by up to 10 percent on medium bore (< 10 in.) diesel engines [9]. Similarly, testing indicates a 1 deg error will typically create a 7–8 percent error in MEP on high-output large-bore diesels and 4–5 percent on a similarly rated dual fuel version of the same engine. The latter's lower sensitivity to TDC errors is attributed to the relatively flat pressure curve in the vicinity of TDC (Fig. 3) encountered on this engine type. To minimize the effects of this uncertainty, methods for finding and then consistently indicating dynamic TDC are required. The problem is somewhat less critical during comparative optimization testing when relative changes in MEP are of particular interest, providing TDC is repeatable and the speed remains constant.

Methods of Locating TDC. Methods of finding TDC fall into two categories, static and dynamic. Large-bore engines are particularly well suited to the former method as the relatively long stroke permits reasonably precise determination of TDC (±0.5 deg) when tramming with a dial indicator. Alternatively, the flywheel can be marked at fixed piston travel above the bottom of the liner on either side of TDC (typically ≈ ±60 deg) and TDC then found by bisecting the flywheel travel.

TDC is commonly located on small-bore engines via motoring. However, blow-by and thermal losses will often result in maximum pressure occurring before minimum volume (i.e., TDC) is obtained, resulting in a low evaluation of MEP [8]. Compensating techniques using a "Thermal Loss Angle" (TLA) or curve fitting of the compression curve [9] have recently been developed and applied to smaller bore engines.

A large-bore engine can similarly be motored by cutting off the fuel supply to the test cylinder (Fig. 4). Typically, pressure peaks about 1.0 deg before the statically determined location of TDC. This, along with an immediate drop in pressure at TDC, suggest that blow-by and thermal losses act similarly in large-bore engines. Therefore, the static method of TDC determination is preferred, though even then the indicated MEP is typically several percent less than expected.

Methods of Indicating TDC and Speed. In general, TDC is indicated during engine operation either by a free end mounted crankshaft encoder or a flywheel mounted Magnetic Pick-Up (MPU). While the former offers the additional advantage of triggering each point of data acquisition, it is subject to uncertainty created by the free-end vibratory motion of the crankshaft and prohibits the installation of other free-end instrumentation such as a torsiograph.

In contrast, torsional oscillation at the flywheel is minimal. An MPU can trigger the beginning of data acquisition, with the computer's internal clock controlling the acquisition rate. Variations in engine speed can be detected (and the speed

calculated) by changes in the time increment between TDC events and the data adjusted during post process smoothing (see below).

Fuel Burn. Reliable methods for measuring fuel burn rates in the field are well established [1]. However, many field development tests appear to be performed using rather crude methods. For example on liquid fuel engines, fuel burn can be estimated based on fuel rack settings, provided calibration curves are available and the fuel injected does not vary significantly from the calibration fluid in density or bulk modulus. However, the author has reviewed a number of test reports in which the proposed enhancement (such as water emulsification or injection system alteration) significantly alters the actual volume of fuel injected. In one particular example, "before and after" tests utilizing water emulsion at a fixed rack setting resulted in a significant reduction in fuel consumption. However, the reduction in real fuel delivery (due to the inclusion of water) moved the engine operating down into a lower load where better turbocharger efficiency naturally enhances performance.

The effects of density and compressibility can easily be eliminated by measuring the weight, rather then the volume of fuel burned. By connecting a separate fuel supply mounted on a beam or digital scale to the test cylinder, fuel burn can be measured with precision of 0.5 percent or better. The engine can be set to the desired load and the rack setting of the test cylinder adjusted (by recording the pressure versus time wave and calculating the MEP) until an indicated power level equal to the previously recorded "before" (or baseline) condition is obtained.

Gaseous fueled engines provide a more difficult problem. If the test cylinder is burning a separate gas, a Roots type gas meter can be used to measure gas consumption precisely and the fuel supply adjusted to obtain the desired MEP. If the test cylinder is burning the same gas as the remainder of the cylinders, measurement of fuel burn rate is more problematic. The author has attempted to infer changes in fuel burn by maintaining the engine gas header pressure at a constant value and measuring the change in indicated power on the test cylinder. Regrettably, on gas-injected engines, pulsations in the gas supply header create substantial variations in test cylinder charge, creating variations in MEP of several percent. This in turn creates uncertainties of several percent in calculation of fuel consumption, making it quite difficult to discern real changes in fuel burn.

Emissions. Methods for measuring stack emissions from stationary engines are well established [10] and reliable instrumentation now available [11]. However, experience has shown that the measurement of individual cylinder emissions can prove quite difficult, particularly on highly turbocharged engines. To determine the emissions level at the test cylinder effectively, a probe must be installed downstream of the exhaust valves and prior to any pulse convertor or nozzle that mixes exhaust streams from other cylinders.

While traditional stack sampling occurs at virtually atmospheric pressure in a well-mixed stream of essentially uniform flow, preturbine exhaust flow occurs under positive pressure with a large pressure pulsation each cycle. In addition, long valve overlaps tend to pack the probe with fresh scavenging air significantly (and incorrectly) biasing the NO_x concentration down by as much as 70 percent. To date, no practical method of eliminating this effect has been found. However, by simultaneously measuring stack and individual cylinder emissions during baseline testing, a correction factor can be obtained, which can then be applied to subsequent concentration measurements.

Digital Data Acquisition. While many factors work against the successful test and development of new technologies in the field, the advent of inexpensive portable microcomputers and peripheral data acquisition cards has placed a powerful tool in the development engineer's hands, largely compensating for the lack of normal test facilities. Several years ago AETC engineers developed a microcomputer-based portable high-speed Data Acquisition System (DAS) specifically tailored to engine field testing. Built around a Compaq Portable III, the current generation system can digitize up to 16 channels of data at combined rates of up to 27 kHz in up to 20,000 point bursts. Postprocessing algorithms permit real time postprocessing including conversion to engineering units, averaging, filtering, etc., in addition to the nearly instantaneous calculation of MEP and ROHR. While more powerful mini-based systems are available, the portability and flexibility, along with low cost, of the micro-based system is unmatched.

Utilizing this system during engine mapping tests, data reduction for a single test run was reduced from 4 hr, utilizing traditional methods to less than 10 min, permitting real time analysis. In conjunction with instantaneous curve fitting and plotting, the diligent development engineer can exploit this ability and detect and eradicate bad test data, avoid meaningless operating regimes, and explore particularly sensitive operating conditions without ever stopping the engine. The resultant reduction in test time can offset many of the disadvantages of field development testing.

Methods of Calculation

Indicated MEP and Power. Once the necessary TDC and cylinder pressure data are recorded, the indicated MEP and power are calculated in a series of postprocessing programs as described below. First, the 2.8 revolutions of raw pressure data is converted to engineering units by multiplying through by the appropriate gain without any compensation for zero drift. The resultant data file along with the associated MPU output is then run through a phasing program, which first scans the MPU data to locate two successive TDC peaks. Based on the located TDC events, the program segregates out points representing the 720 deg of rotation from TDC combustion to TDC combustion and then performs an Akima Spline Fit on these data to generate 720 smoothed data points (i.e., one per degree). The average speed during the cycle is also determined at this time.

To compensate for zero drift, another program reads the resultant pressure data file and determines the average pressure during the cylinder filling portion of the cycle. It then adjusts this pressure level to a user-specified value (typically the air manifold pressure recorded with a calibrated precision bourdon tube type pressure gage). The resultant data are now ready for the determination of MEP and power utilizing standard formulas and the known engine geometry, or any other subsequent analysis such as ROHR.

Combustion Quality Index (CQI). When attempting to minimize engine NO_x emissions while maximizing engine efficiency, the development engineer is faced with a difficult analysis problem, particularly when conducting single-cylinder tests. One must discriminate between engine configurations that create low NO_x emissions due to poor combustion stability and therefore low power and efficiency and those that consistently ignite the very lean mixture yet yield very low emissions levels without a loss in power or combustion stability.

To assist in rapidly evaluating combustion stability during single cylinder tests, Kaiser [4] developed a new dimensionless parameter designated the Combustion Quality Index or CQI for evaluating combustion stability. CQI is mathematically defined as follows:

$$\mathrm{CQI} = \frac{(P_{\mathrm{comb}} - P_{\mathrm{comp}})}{(SD + 1)} \tag{4}$$

where P_{comb} and P_{comp} are expressed as "gage" pressures for the sake of simplicity.

The "Cold Compression" pressure can in turn be estimated from the thermodynamic relationship for adiabatic compression, i.e.,

$$P_{comp} = \{ (P_{man} + P_{atm}) CR^{\gamma} \} - P_{atm} \quad (5)$$

Based on tests measurements a specific heat ratio of $\gamma = 1.3364$ appears appropriate.

By subtracting the "Cold" compression pressure from the average peak combustion pressure, CQI factors out the stable cold compression pressure and evaluates only combustion induced pressure variations. The "1" in the denominator prevents the CQI from approaching infinity (due to the mathematical singularity encountered for $SD = 0$) in the case of extremely stable combustion. Typical values of CQI for various engine types (based on measurements at the indicator cock) are shown in Table 1 below. As can be seen, the CQI very effectively expresses quantitatively what is known qualitatively; diesel engines are very stable having high CQIs and leaned out gas engines marginal at best yielding very low CQIs.

Recent comparisons of CQI calculations based on measurements at the indicator cock versus in the cylinder reveal that pressure fluctuations induced in the indicator passages of lean dual fuel engines bias the CQI down 3–4 points. Presumably other gaseous fueled engine types suffer from the same problem, so care must be taken when comparing CQI values to ensure relevant comparisons.

Brake Specific Emissions. As noted, stationary engine emissions levels are most commonly measured and regulated in terms of brake specific levels, i.e., is the mass of pollutant generated per unit of work created (usually expressed in hp-hr). However, in general it is not possible to measure the mass flow rate of the pollutants of interest directly. Rather the concentration of the pollutant in the exhaust gas stream is measured and the pollutant volume flow rate then calculated by multiplying the measured concentration by the exhaust gas volume flow rate, usually expressed in Standard Cubic Feet per Minute (SCFM), i.e.,

$$V'_{EM} = C_{EM} V'_{ex} \quad (6)$$

The Brake Specific Emission (BSEM) level then may be calculated as follows:

$$\text{BSEM} = \frac{C_{EM} V'_{ex}}{P_{av}} R_{EM} \quad (7)$$

with the appropriate conversion from minutes to hours.

Exhaust gas volume flow rate is often measured directly at the exhaust pipe with pitot tubes. However, experience has shown that unless extreme care is taken, erroneous results will occur. In one particular instance, a nationally reputed emissions measuring company performed a pitot tube traverse on the exhaust pipe of a dual fuel engine and obtained exhaust volume flow rates over twice the actual value. As this effectively doubles the apparent BSEM, such an error is intolerable.

A more reliable method is to determine exhaust gas volume flow via the measured mass flow, i.e.,

$$M'_{ex} = M'_{in} + M'_{fu} \quad (8)$$

The fuel mass flow can either be obtained by measuring fuel burn rates or be estimated based on expected efficiencies. As the fuel mass flow typically constitutes significantly less than 10 percent of the total exhaust mass flow, a reasonable estimate will not compromise the overall reliability of the calculation.

Determination of the intake air mass flow is more problematic. When possible, a calibrated (ASME nozzle) meter can be installed at the engine intake. However, as most field installations are hard piped between the intake filter and the turbocharger inlet, most installations require an alternative method. One method originally developed by Kaiser for field emissions testing [12], and since modified for more general application, has proven particularly useful.

Basically, the method estimates the intake air volume flow (and thereby the mass flow) based on the volumetric efficiency and displacement of the engine, and then corrects to standard conditions, i.e., for a four-stroke cycle engine:

$$V'_{in} = \eta_{ve} DI \frac{N}{2^*} \times \frac{(520\ \text{R})}{(T_{in} + 460)} \times \frac{(P_{in} + P_{bar})}{30.0} \quad (9)$$

(*Note: The 2 should be replaced with a 1 for two-stroke cycle engines.)

The volumetric efficiency, η_{ve}, is most easily obtained by curve fitting shop stand test data measurements of intake air flow (typically measured with a calibrated orifice) as a function of P_{in}. Based on experience, a logarithmic fit is particularly effective in covering a wide range of air flows, i.e.,

$$\eta_{ve} = A \log (P_{in}) + B \quad (10)$$

where A and B are constants for a particular engine based on the curve fit test data. Alternatively, depending on the individual engine, a linear fit may prove satisfactory over the relatively narrow operating range over which most optimization occurs.

Utilizing this method, an error of less than ± 1 percent is typically introduced when compared against calibrated nozzle measurements of V_{in}.

With both the air and fuel mass flow rates available, the total exhaust gas mass flow can now be calculated, converted to volume flow at standard conditions and entered into equation (8). The calculation method can be further simplified for (air) lean burn engines by approximating the exhaust products as air. The fuel mass flow can then be converted into volume flow via the density of air at standard conditions. Then the exhaust gas flow (in SCFM of air) is simply the sum of the intake air flow (in SCFM of air) and the fuel mass flow (in SCFM of air).

Rate of Heat Release (ROHR) Analysis. To facilitate "real time" analysis of Rate of Heat Release diagrams, a simplified analysis method based on work by Sorenson [13] and applied as a diagnostic to measured pressure data by Hayes et al. [14], is utilized. This simplified method ignores chemical equilibrium, rather assuming that the working fluid is air with properties based on the calculated instantaneous temperature. In addition, a uniform wall heat transfer coefficient based on Eichelberg's correlation [15] is used with a constant and equal wall temperature for all surfaces.

Considering a control volume that surrounds the combustion chamber, the first law of thermodynamics under these assumptions becomes

$$\frac{Dq_{app}}{d\theta} = \frac{V}{\gamma - 1} \frac{Dp}{d\theta} + \frac{K}{\gamma - 1} P \frac{Dv}{d\theta} - \frac{Dq_{wall}}{d\theta} \quad (11)$$

The first two terms to the right of the equality represent the actual work performed on the control volume as indicated by the pressure time diagram while the third term is the heat lost from the control volume to the walls (as indicated by the negative sign).

A computer code based on equation (9) was developed with one additional modification. To compensate for the approximate nature of the estimated wall heat transfer coefficient,

Table 1 Combustion quality index for typical turbocharged combustion systems (based on measurements at the indicator cock)

SYSTEM	CQI
Diesel	25–35
Standard dual fuel	9–16
Standard spark ignited	4–9
Lean dual fuel	4–12
Lean spark ignited	<5
Prechambered spark	14–21

the new method iterates on the convective heat transfer coefficient until Q_{app} equals the energy input to the cylinder.

The code runs as follows: after reading in the desired pressure data file and associated cylinder filling conditions, the program determines the cylinder filling mass at intake valve closing based on the known engine geometry. It then calculates the instantaneous rate of apparent heat release, $Dq_{app}/d\theta$, based on a first estimate of the heat transfer coefficient. It next integrates the apparent heat release rate for a complete 720 deg cycle, and compares the result with the expected heat input based on the power generated and estimated BSFC. The program then iteratively scales the convective heat transfer coefficient until the total apparent heat release is equal to the energy released by the fuel.

The various assumptions involved do introduce approximations in the analysis. In particular, comparisons by Hayes (on a naturally aspirated diesel) against more exact methods revealed that the approximate method offered good qualitative information, indicating the beginning of combustion, phases of combustion, etc., rather well. However, the method was substantially off quantitatively in predicting peak Rates of Heat Release. Hayes demonstrated the majority of this error was attributed to incorrect estimates of the mass charge at valve closure, rather than the lack of modeling of chemical equilibrium. While the author has not made similar comparisons for highly turbocharged engines, the problem should be far less pronounced due to the substantial valve overlap and fresh air scavenging of these engine types. A cylinder mass estimate based on the volume at intake valve closing and the air manifold pressure should closely approximate actual conditions.

In general, the deletion of chemical equilibrium will yield much less satisfactory results for gaseous fueled engines due to their lower air/fuel ratios. However, virtually all modern stationary gas engines are highly turbocharged, utilizing either a dual fuel or torch ignition cycle, and therefore running at essentially diesel engine level air/fuel ratios. The lack of chemical equilibrium modeling should not significantly impair the validity of the approximation for these engine types either.

In addition, the primary interest in obtaining Rate of Heat Release diagrams is as a diagnostic aid for detecting gross changes in combustion performance. Therefore any approximations introduced by the simplifying assumptions are more than offset by the greatly enhanced speed of analysis.

Some Examples

To demonstrate the power offered by the methods described above, several examples of their application follow.

Combustion Instability in Dual Fuel Engines. The author has been very interested in causes of dual fuel engine instability for many years. As noted, combustion instability becomes particularly problematic when leaning out the air/fuel ratio and reducing pilot fuel quantities to minimize NO_x emissions.

During previous proprietary test work on standard mechanical fuel injection systems at dual fuel turn down ratios ($\approx$5–6 percent), the author noted fuel injection was very inconsistent, with significant variations in peak injection pressure (often no greater than nozzle opening pressure) and injection duration. This was attributed to compressibility effects associated with the low delivery levels.

Attributing much of the dual fuel engine cyclic instability to this phenomenon, the author had the opportunity to perform combustion performance testing on a standard dual fuel engine as part of a benchmark test for other work. As expected, measurements of in-cylinder pressure revealed substantial cyclic variation with peak combustion pressure varying from 850 to 1100 psi and MEPs from 178 to 195 psi (Fig. 5). All the cycles appeared to initiate combustion within a degree of TDC with

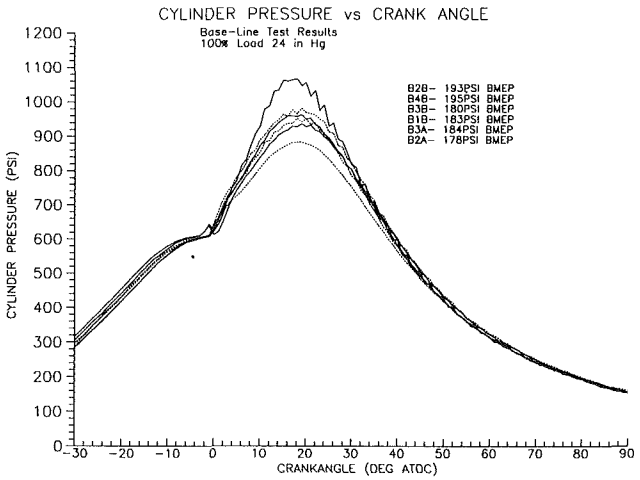

Fig. 5 Typical pressure angle traces for a highly turbocharged dual fuel engine

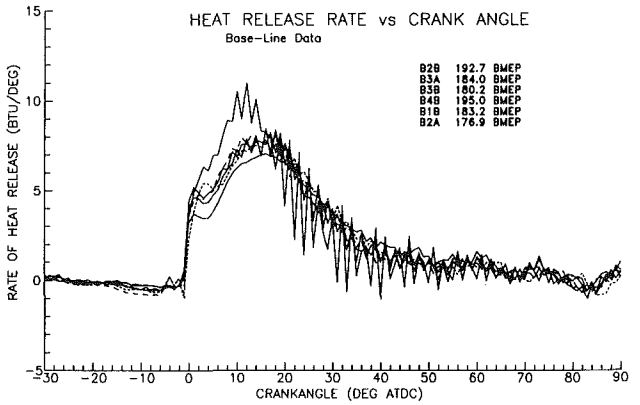

Fig. 6 Rate of heat release diagrams for the pressure data shown in Fig. 5.

initially equal rates of pressure rise. However, the curves started to depart drastically at $\approx$4 deg ATDC.

Examination of ROHR diagrams indicated most of the traces exhibited three distinct phases of combustion. First, approximately 30–50 percent of the injected diesel fuel ignites and burns in premixed combustion just after TDC. The ROHR then rolls off at 2–3 deg ATDC as the premixed fuel is consumed and the liquid fuel combustion shifts to a slower diffusion-controlled phase. The ROHR then begins to rise rapidly in the third phase as pockets of the premixed gas/air mixture in the vicinity of burning liquid fuel mixture reach their ignition temperature. The pools of burning gas link and lead to a rapid rise in ROHR typical of homogeneous phase combustion.

This result confirmed the authors' suspicions that the liquid fuel was not being properly atomized and therefore not all burning in the premixed phase. However, this did not appear to explain the cyclic variations noted. In particular the second highest MEP cycle (data set B2B on Fig. 6) exhibited premixed liquid fuel combustion levels identical to the other cycles. However, rather than suffering a subsequent dip in ROHR, the ROHR continues to rise, apparently indicating an immediate and rapid transition to premixed gas combustion. The large oscillations in ROHR reflect pressure oscillations in the cylinder, possibly due to the rapid movement of the flame front as it engulfs the gas.

But what makes this cycle so particularly effective? It appears that charge stratification due to inconsistent gas injection occasionally created a near-stoichiometric pocket of fuel/air mixture in the vicinity of the injector. This encouraged the immediate transition to gas phase combustion noted. Work

by Tice [16] certainly indicates local charge stratification in the vicinity of the ignition source can drastically impact combustion. Subsequent measurement of fuel gas header pressure confirmed the presence of large pressure fluctuations, resulting in both charge stratification and overcharging (as evidenced in trace B4B with extended combustion well after TDC).

Without ROHR analysis it would have been impossible to discern variations in the various phases of combustion that resulted in the identification of gas stratification as an important contributor to cyclic instability in this engine model. Rather, based on the cylinder pressure data alone, the instability would have been solely (and erroneously) attributed to the fuel injection system.

Low Pilot Fuel Dual Fuel Engine. Many of the techniques discussed in this paper were applied to the test and optimization of a low pilot, high-pressure electronic injection system for reducing dual fuel engine emissions. While the test program and results are summarized in detail elsewhere [2], one particular example of the power of the diagnostic tools available follows.

When reducing the pilot injection from 2.9 to 2.2 percent, a drastic reduction in $BSNO_x$ emissions was encountered, proportionately much greater than that encountered in moving from 6 percent pilot with the baseline mechanical system to 2.9 percent with the electronic (Table 2). As all previous work (albeit at in the 3–8 percent delivery range) had indicated $BSNO_x$ emissions were fairly linear with pilot quantity, the result was quite a surprise.

Examining the ROHR diagrams, the development team noted rather drastic changes in the three phases of combustion between the 2.9 percent to 2.2 percent pilot runs (Fig. 7). At 2.9 percent delivery, virtually all the pilot fuel was consumed in the first phase of combustion followed by a brief second phase dip in ROHR and then a rapid increase during third phase combustion of the gas (with some ringing). In contrast, at 2.2 percent pilot delivery, a little over half the pilot fuel burns in the first phase, followed by no dip, but rather slow transition to premixed gas combustion as the remaining diesel fuel burns in diffusion. The third phase peaks both later and at a lower ROHR than encountered at 2.9 percent pilot, with no ringing, indicative of lower flame speeds and gas temperatures. Much of the emissions reduction then must be attributed to this drastic change in second and particularly the third phase of combustion, rather than the reduction in pilot alone. The effect became even more pronounced at 1.4 percent pilot delivery, with so low a CQI and MEP that this delivery level did not even represent an operable condition.

As a note, the poorer first phase of combustion encountered at 2.2 percent pilot is attributed to the lower statistical volume of diesel fuel droplets capable of initiating and sustaining premixed combustion, thereby raising the temperature to a high enough level to vaporize and ignite the remaining liquid fuel in a premixed mode.

Again, without ROHR analysis, the development team could not have discerned these complex multiphase interactions and understood the cause of the drastic NO_x reduction.

Heavy Fuel Versus Diesel Fuel Combustion. While most large-bore engine development today focuses on gaseous fuel engines, liquid (i.e., diesel) fuel engine development continues. In particular, the author has encountered various after-market products and modifications including water emulsification, fuel additives, ceramic coatings, and fuel system alterations, which reputedly lower emissions and/or enhance fuel consumption. The author has also encountered various situations in which failures have been attributed (erroneously) to the more aggressive combustion characteristics of "Heavy Fuel."

In one particular instance, unusual crankshaft vibratory response was attributed to heavy fuel operation, as heavy fuel operation induced higher exhaust temperatures and peak pressures than diesel fuel at what was claimed the same load. Investigation revealed that the claims were based on the incorrect assumption that a similar rack setting on each fuel indicated a similar load. In cylinder pressure measurements confirmed (as expected) that the heavy fuel was in fact generating more power at the same rack setting due to its greater energy per unit volume.

Adjusting the rack settings to obtain approximately equal MEPs (Fig. 8) on each fuel resulted in essentially identical operating parameters. Comparisons of the pressure wave forms revealed little discernible difference between the two fuels, though the ROHR diagrams (Fig. 9) did reveal some interesting differences. In particular, while both fuels initiated premixed combustion at approximately 16°BTDC, less prepared heavy fuel was available resulting in the drop in ROHR just after TDC, followed by a gradual increase in ROHR as diffusion controlled combustion took over. In contrast, the diesel fuel combustion continued in a premixed phase until 12 deg ATDC. Combustion of the slower burning heavy fuel also lasted longer into the cycle. Both these differences are attributed to the greater volatility of the diesel fuel.

While not critical to the question at hand, the ROHR dia-

Table 2 NO_x emissions for varying pilot fuel quantities at equivalent air manifold pressures and injection timings

Pilot fuel delivery, percent	NO_x emissions, g/bhp-hr
≈6 (baseline)	7.0 (estimated)
2.9	4.5
2.2	2.0

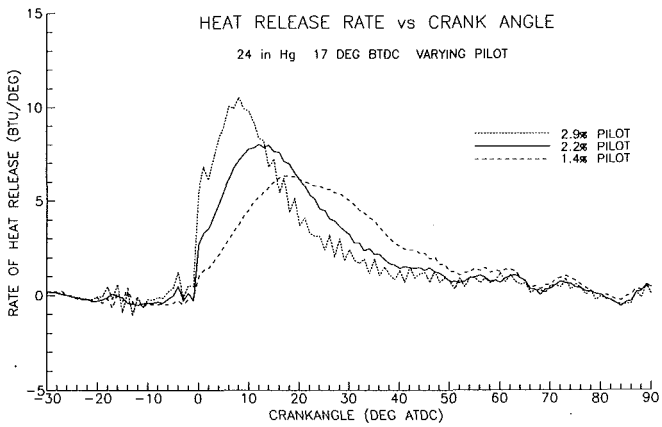

Fig. 7 Rate of heat release diagrams for varying pilot delivery, low pilot dual fuel engine

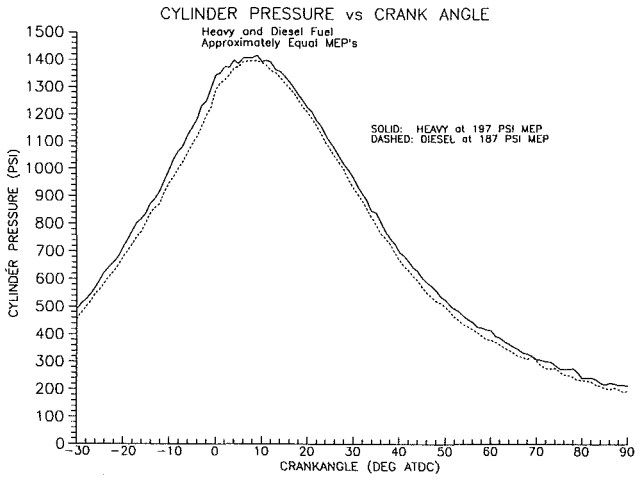

Fig. 8 Comparison of pressure traces for heavy and diesel fuels at approximately equal MEPs

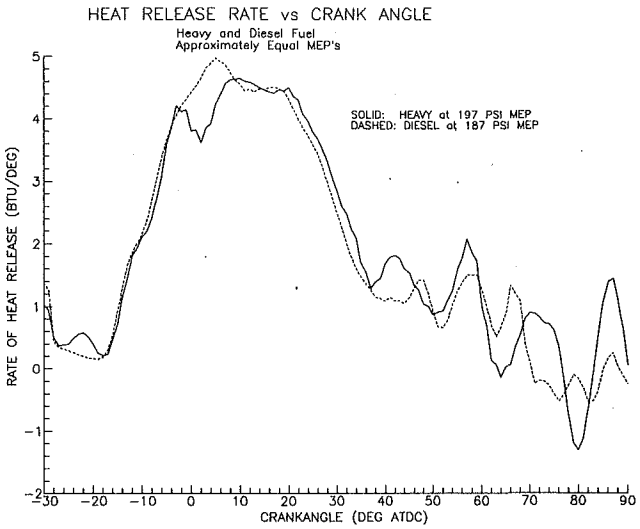

Fig. 9 Rate of heat release diagrams derived from the pressure traces shown in Fig. 8

grams proved quite useful in demonstrating the differences in combustion characteristics between fuel types to the operator.

Conclusions

(A) Utilizing state-of-the-art instrumentation and data acquisition systems, the research engineer can conduct laboratory quality development testing in the field on a single cylinder.

(B) In addition to performing data acquisition functions, modern microcomputers can be programmed to perform quickly a variety of data reduction processes, such as the calculation of MEP, IHP, BSEM levels, etc., permitting rapid alteration of the test agenda, thereby minimizing the time required to optimize and map a new engine technology.

(C) Analysis of Rate of Heat Release diagrams, based on simplified calculation methods, can provide the development engineer with a powerful real time diagnostic tool. As a result, engine development can be performed in the field today faster than previously possible, and of comparable quality and scope to factory-based programs.

References

1 *Reciprocating Internal Combustion Engines*, ASME Power Test Code PTC 17-1973, New York, 1973.

2 Workman, J., and Beshouri, G. M., "Single Cylinder Testing of a High-Pressure Electronic Pilot Fuel Injector for Low NO_x Emission Dual Fuel Engines, Parts I and II," ASME JOURNAL OF ENGINEERING FOR GAS TURBINES AND POWER, Vol. 112, 1990, pp. 413–430.

3 Lilly, X. Y., *Diesel Engine Reference Book*, Butterworth, Boston, MA, 1984.

4 Kaiser, R. M., "Exhaust Gas NO_x Reduction Through Combustion Modification Using PRECOM, a Two Stage, Torch Ignition, Precombustion Chamber Technique," *ASME Proceeding, Internal Combustion Engine Division Technical Conference*, West Middlesex, PA, Oct. 8, 1985.

5 Krieger, R. B., and Borman, G. L., "The Computation of Apparent Heat Release for Internal Combustion Engines," ASME Paper No. 66-WA/DGP-4, 1966.

6 Brown, W. L., "Methods for Evaluating Requirements and Errors in Cylinder Pressure Measurements," SAE Paper No. 670008, 1967.

7 Lancaster, D. R., et al., "Measurements and Analysis of Engine Pressure Data," SAE Paper No. 750026, 1975.

8 Lecuona, A., and Rodriguez, P. A., "Evaluation of Pressure and Crank Angle Errors From Reciprocating Engine Indicator Diagrams," SAE Paper No. 860027, 1986.

9 Zeelenberg, A. P., and Vos, B., "Combustion Efficiency of Residual Fuels," *Fuels Combustion and Lubrication*, ASME ICE-Vol. 11, 1990.

10 *Federal Register*, Vol. 44, No. 142, "Standards for Performance of New Stationary Sources; Stationary Internal Combustion Engines," July 23, 1979.

11 Fanick, E. R., "Test Procedures for Measuring Exhaust Emissions From Natural Gas Transmission Engines," ASME JOURNAL OF ENGINEERING FOR GAS TURBINES AND POWER, Vol. 112, 1990, pp. 408–412.

12 "Field Test Report for East Bay Municipal Utility District Transamerica Delaval Engines S/N 82003/5 Model DGSR-46," Transamerica Delaval Inc., Apr. 30, 1986.

13 Sorenson, S. C., "Simple Computer Simulations for Internal Combustion Engine Instruction," *International Journal of Mechanical Engineering Education*, Vol. 9, No. 3, 1981.

14 Hayes, T. K., et al., "Cylinder Pressure Data Acquisition and Heat Release Analysis on a Personal Computer," SAE Paper No. 860029, 1986.

15 Benson, R. S., and Whitehouse, N. D., *Internal Combustion Engines*, Pergamon Press, New York, 1983.

16 Tice, J. K., and Nalim, M. R., "Control of NO_x Emissions in Gas Engines Using Pre-stratified Charge-Applications and Field Experience," ASME Paper No. 88-ICE-11, 1988.

A Study of Indicator Passage Error Correction Schemes

B. G. Shiva Prasad

F. L. Heidrich
Dresser-Rand, EPCD,
Painted Post, NY 14870

The passage length between the cylinder and the measuring transducer is known to cause distortion of pressure time traces due to pulsations caused by dynamic effects. This paper attempts to arrive at a simple and efficient calculation scheme for correcting those distortions. Both time domain (method of characteristics approach) and frequency domain methods are evaluated to assess the importance of considering various effects for improving the prediction accuracy. The predictions from both methods are compared with experimental data as well as the results of Heidrich [6], who used simpler versions of these methods.

Introduction

Accurate measurement of the P–V card of reciprocating compressors and engines is essential for the calculation of capacity and horsepower. This in turn necessitates accurate measurement of the pressure inside the cylinder. It is not always possible to mount the pressure sensor directly inside the cylinder, either for mechanical reasons or for protecting the transducer from the harsh temperature, particulate and even combusting environments. Hence in many cases, the sensors are mounted at the end of well-designed passages and adapter systems. Elson and Soedel [1] and Bucholz [2] have discussed the effects of adapter systems on pressure measurement and ways of designing them to minimize those effects. In some cases, passages as long as 18 in. or more become a necessity and these might distort the pressure signals and even induce resonances. Such effects will cause erroneous estimation of horsepower and capacity in the case of healthy machines, while in the case of unhealthy ones with, say, leakage, it may lead to faulty diagnosis. Also in some cases, the P–V cards with channel resonance effects might imply valve flutter problems even if there is none.

In the absence of any means to eliminate those effects completely, there arises a need for developing techniques to account for the gas dynamic effects that occur in indicator passages. This would enable prediction of the actual pressures inside the cylinder from the measurements taken by transducers at the end of those passages. Although the problem appears to be important, surprisingly, to the authors' knowledge, there are very few investigations reported in the literature addressing this issue. Bradley and Woollatt [3], starting from one-dimensional equations for unsteady flow in a duct and using the method of characteristics approach, have developed a technique for predicting the actual pressures from the measured pressures at the end of a passage. They used an unsteady pipe flow facility to demonstrate the validity of their technique. They also noted that the unsteady flow in the passage produces most of the distortion, while the effect of any volumes in the passage or friction in the pipe or pressure losses at junctions are only secondary. Xiagxing [4] has devised a digital filter to reduce the distortions occurring due to channel resonance. Harris and Smalley [5] have used a frequency domain technique to correct for channel resonance, which has shown good agreement with their experimental data. However, the details of their technique are not available in their paper.

The work reported in this paper is a continuation of the earlier work of one of the authors, Heidrich [6], who investigated various techniques in order to arrive at a simple and efficient correction scheme for routine use in data acquisition. He concluded that the basic method of characteristics approach suggested by Bradley and Woollatt as well as a simple frequency domain approach neglecting the dynamic flow effect on damping would satisfy the need. In this paper, the authors have tried to assess the usefulness of considering the neglected effects in the two techniques from the point of view of improving the prediction accuracy. In the method of characteristics approach, the effects of volumes in the passage, pipe friction, and junction losses are considered, while in the frequency domain approach, the effect of dynamic flow on frictional damping is considered.

Experimental Data

The laboratory tests were conducted at the Dresser-Rand closed loop facility in Painted Post, New York. For a detailed description of this facility see [7]. The test apparatus was a high-speed, low-horsepower compressor pumping nitrogen in a single-stage configuration. Two passages of 6 and 12 in. lengths were designed that would allow an Ashcroft K8 transducer to be placed at the end of the passage and secured in place. Another passage of minimal length was used to record a "channel resonance free" signal. The transducer's electrical output was transmitted to one of four channels of a Nicolet 4094 oscilloscope. A timing trace was transmitted to a different channel for top dead center definition. Each test point was recorded on a floppy disk through a disk drive connected to the oscilloscope. A BASIC computer program was written to establish communication between the oscilloscope and an IBM PC via a RS232 cable. The test data were transferred to the PC in ASCII format for later analysis and manipulation.

Contributed by the Internal Combustion Engine Division and presented at the Energy-Sources Technology Conference and Exhibition, Houston, Texas, January 20–24, 1991. Manuscript received by the Internal Combustion Engine Division September 1990. Paper No. 91-ICE-9.

The dynamic pressure data used to evaluate channel resonance correction procedures were measured at two pressure ratios (1.6 and 2.5) and two compressor speeds (1515 and 1770 rpm). For each condition, pressure time traces were obtained at the minimal, 6 in. and 12 in. channel lengths. For the sake of brevity, this paper will consider the 1.6 ratio, 1515 rpm and the 2.5 ratio, 1770 rpm test conditions only.

Time Domain Solution

This section will describe and analyze results found using a time domain solution method. The following solution was originally introduced by Bradley and Woollatt [3], whose results showed good agreement with their test data. A simplified version of this solution was presented at the 1990 Purdue University Compressor Conference by Heidrich [6] in which good comparison with experimental data was reported at compressor speeds and operating pressures higher than in [3]. The focus here is to investigate the time domain solution in greater detail by considering the additional effects neglected in [6] with a view to improve the accuracy of results.

The method of characteristics is used to calculate the cylinder pressure at any given time by determining the transducer pressures a certain time increment before (P_1) and after (P_3) that instant. The time increments are found by dividing the passage lengths by the pressure wave velocity (i.e., the slopes of the left and right running characteristics). As Fig. 1 illustrates, the left and right running characteristics can be shown to be:

$$A-\frac{k-1}{2}U \text{ is constant along } \frac{dx}{dt}=-A+U \tag{1}$$

and

$$A+\frac{k-1}{2}U \text{ is constant along } \frac{dx}{dt}=A+U \tag{2}$$

The isentropic change of state law is used to calculate the local speed of sound at any point from

$$A=A_{\text{ref}}\left\{\frac{P}{P_{\text{ref}}}\right\}^{(k-1)/2K} \tag{3}$$

The reference pressure and temperature are used to define the entropy of the gas in the indicator passage and must be chosen accordingly. For this application, it is acceptable to use the mean pressure and temperature inside the cylinder. The reference temperature is used to calculate the reference speed of sound:

$$A_{\text{ref}}=\sqrt{kg_c z_{\text{ref}} R_g T_{\text{ref}}} \tag{4}$$

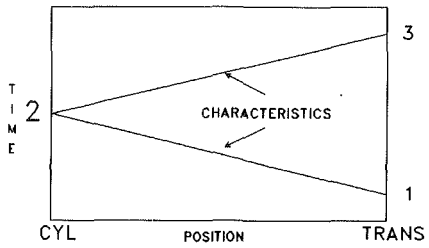

Fig. 1 Method of characteristics

It should be noted that a reference speed of sound can also be determined by measuring the time step between successive peaks of the quarter wave resonance seen in the measured pressure distribution.

The solution uses an iterative approach to calculate the pressure time history inside the cylinder. The iteration begins by assuming the speed of the pressure waves (the slope of the characteristic lines) as the reference speed of sound. With this, the speeds of sound from both ends (A_1 and A_3) are found. The cylinder gas velocity (U_2) is found by subtracting the two characteristic equations

$$A_2+\frac{k-1}{2}U_2=A_3+\frac{k-1}{2}U_3 \tag{5}$$

$$A_2-\frac{k-1}{2}U_2=A_1-\frac{k-1}{2}U_1 \tag{6}$$

from which

$$U_2=\frac{A_3-A_1}{k-1} \tag{7}$$

because the gas velocities U_1 and U_3 are 0, since points 1 and 3 are closed ends. Once U_2 is found, the average gas velocity for each characteristic can be written as

$$\frac{U_2+0}{2}=\frac{A_3-A_1}{2(k-1)} \tag{8}$$

The characteristic slopes can then be written as the average of the gas velocity plus or minus the average speed of sound

$$\left[\frac{dx}{dt}\right]_{\lambda I}=\frac{A_3-A_1}{2(k-1)}-\frac{A_2+A_1}{2} \tag{9}$$

$$\left[\frac{dx}{dt}\right]_{\lambda II}=\frac{A_3-A_1}{2(k-1)}+\frac{A_2+A_3}{2} \tag{10}$$

Nomenclature

A = local speed of sound, ft/sec
A_{ref} = reference speed of sound, ft/sec
C = capacitance of the pipe $=g_cF/A^2$
d = passage diameter, ft
F = passage cross-sectional area, ft^2
f = Darcy friction factor
g_c = gravitational constant
H = complex pressure head, ft
h' = pressure head fluctuation about the mean, ft
i = $\sqrt{-1}$
K = loss coefficient for sharp-edged entrances
k = ratio of specific heats $=C_p/C_v$
L = inertance of the pipe, $1/g_cF$
l = passage length, ft
P = local pressure, psia
Pr = Prandtl number
P_{ref} = reference pressure, psia
Q = complex flow rate, ft^3/sec
Q_v = volumetric flow rate in the passage, ft^3/sec
q' = flow rate fluctuation about the mean
R = frictional resistance/unit length
R_g = gas constant = 1545/gas mole weight, ft lbf/lbm R
T_{ref} = reference temperature, R
U = local gas velocity, ft/sec
Vol = passage volume, ft^3
w = forcing function frequency, rad/sec
z_c = characteristic impedance
z_{ref} = reference compressibility factor
Υ = propagation constant
μ = absolute viscosity, lbm/ft sec
ρ = density, lbm/ft^3

Subscripts

1, 2, 3 = different time steps during an iteration loop
D = conditions at the source end of the passage
t = time
U = conditions at the boundary end of the passage
x = distance along the passage

With these slopes, new values for time at 3 and time at 2 can be found. If sufficient agreement (0.5 percent) in t_3 and t_2 is found between two successive iterations, then the iteration is terminated and a cylinder pressure (P_2) is found using

$$P_2 = \left[\frac{P_1^{(k-1)/2k} + P_3^{(k-1)/2k}}{2} \right]^{2k/(k-1)} \tag{11}$$

If agreement is not found, the speed of sound at 3 (A_3) is recalculated and the iteration continued.

Reference [6] has reported good agreement with experimental data using the previous method. This paper considers the following three additional effects: (*a*) pressure drop at the cylinder passage entrance, (*b*) pressure drop due to friction in the passage, and (*c*) the effect of a volume at the transducer end of the passage.

Entrance Loss

To determine the pressure drop at entrance to the passage, a loss coefficient for a sharp-edged entrance was used and multiplied by one half the square of the gas velocity:

$$\Delta P = \frac{\rho U^2 K}{2 g_c (144)} \tag{12}$$

where $K = 0.5$ for sharp-edged entrances.

The solution was designed to calculate the pressure drop at the end of iteration, i.e., when a value for the cylinder pressure was found. The pressure drop was subtracted from the cylinder pressure and recorded with the appropriate time. This process was continued throughout the compression cycle.

This method did not show any improvement in accuracy. This is due to the relative magnitudes of the pressure loss compared to the working pressures. The pressure drop calculated remained between 0.5 and 1 psi. For low-pressure applications (atmospheric suction), the entrance loss will have a greater impact on the accuracy and should be taken into consideration, but for natural gas compression, the effect is not appreciable.

Friction Effects

To determine the passage frictional effects, the gas flow can be considered to be either laminar or turbulent. Since the gas velocity varies from zero at the transducer to some value at the cylinder, it is difficult to determine for certain what type of flow is present. For the sake of simplicity, laminar flow was assumed throughout the passage. The pressure drop in a horizontal pipe for laminar flow can be determined using an equation derived from Hagen's experiment:

$$\Delta P = \frac{8 \mu L Q}{\pi (d/2)^4 g_c (144)} \tag{13}$$

As with the entrance losses, frictional effects are minimal. Pressure loss values are only 1–2 psi and do not show any appreciable improvement over the previous method. As the equation clearly points out, frictional losses would be more substantial at higher gas velocities and longer passage lengths. However, if the gas velocities increase, turbulent flow conditions would exist and a more detailed method of solution would have to be developed. For the laboratory data presented here, this loss is negligible.

Volume Effects

Since the passage used (see Fig. 10) did not have any volume increase before the transducer, the effect is not important for the present test case. The method of including this effect was given by Bradley and Woollatt [3] and will not be repeated here. With a volume increase at the end of the passage, the solution assumes that a gas velocity exists at the transducer. This velocity is found from

$$U_t = \frac{\text{Vol}}{kF} \frac{1}{P_v} \frac{dP_v}{dt} \tag{14}$$

From this, the speed of sound and gas velocity in the cylinder is calculated as

$$A_2 = 0.5 \left(A_1 + A_3 - \frac{k-1}{2} U_1 + \frac{k-1}{2} U_3 \right) \tag{15}$$

$$U_2 = \frac{A_3 - A_1}{k-1} + \frac{U_3 + U_1}{2} \tag{16}$$

The slope of the left and right running characteristics can then be determined and the iteration process applied as mentioned in the previous section.

As shown in Figs. 2–5, the results obtained by including the additional effects agree reasonably well with the pressure distributions measured directly inside the cylinder. Also Figs. 6–9 show good agreement with the results of Heidrich [6], who had neglected these effects. This would indicate that at least for the simple, weakly resonant passages of the type used in the present experiment, the additional effects are not important.

Frequency Domain Method

Most of the digital pulsation simulation techniques start with

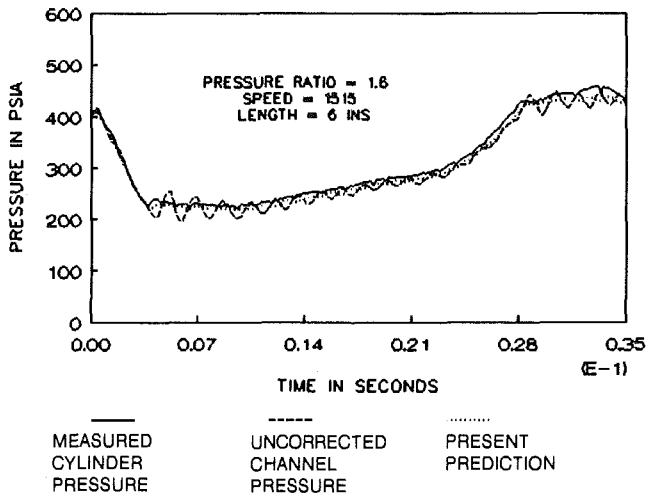

Fig. 2 Comparison of measured and predicted pressures using the time domain method

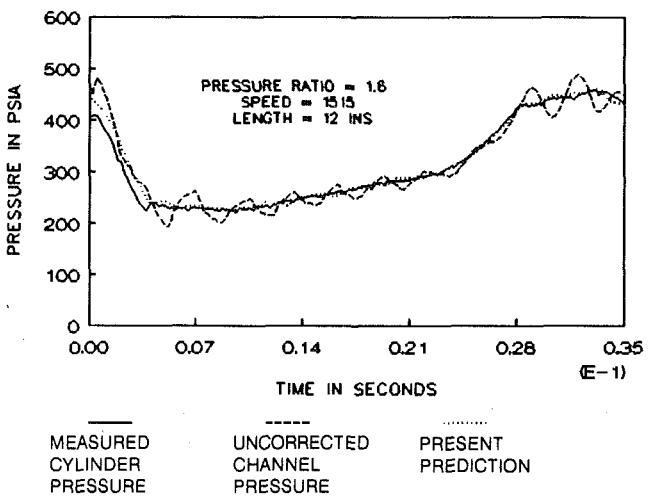

Fig. 3 Comparison of measured and predicted pressures using the time domain method

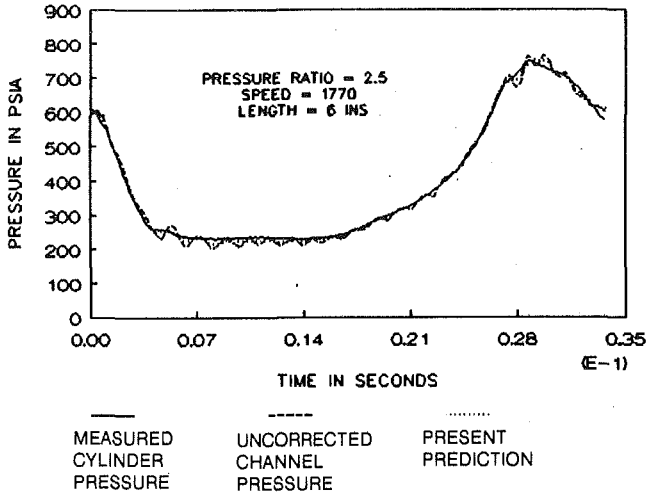

Fig. 4 Comparison of measured and predicted pressures using the time domain method

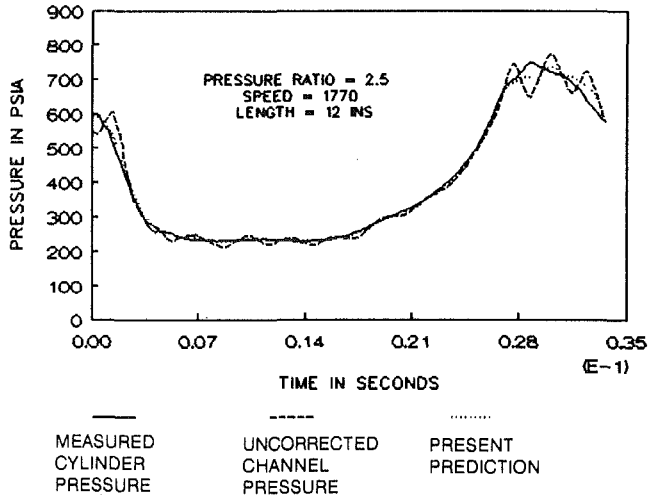

Fig. 5 Comparison of measured and predicted pressures using the time domain method

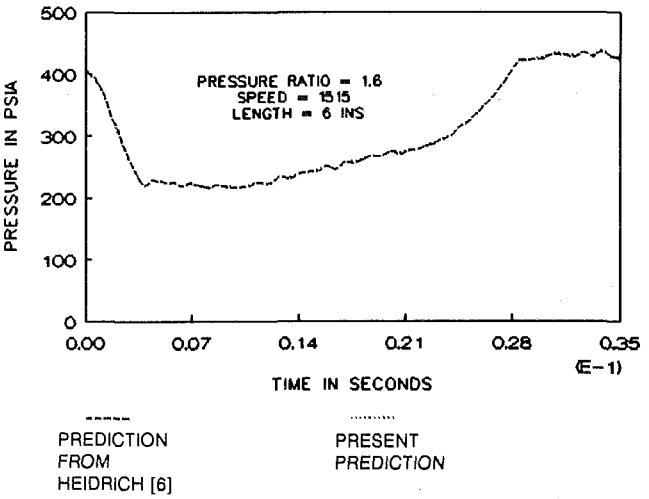

Fig. 6 Comparison of the present predictions with the results of Heidrich [6]

the one-dimensional conservation equations for fluid flow in a pipe to obtain the linearized equations for oscillatory flow (see Wylie and Streeter [8]) as

$$h_x' + Lq_t' + Rq' = 0 \tag{17}$$

$$q_x' + Ch_t' = 0 \tag{18}$$

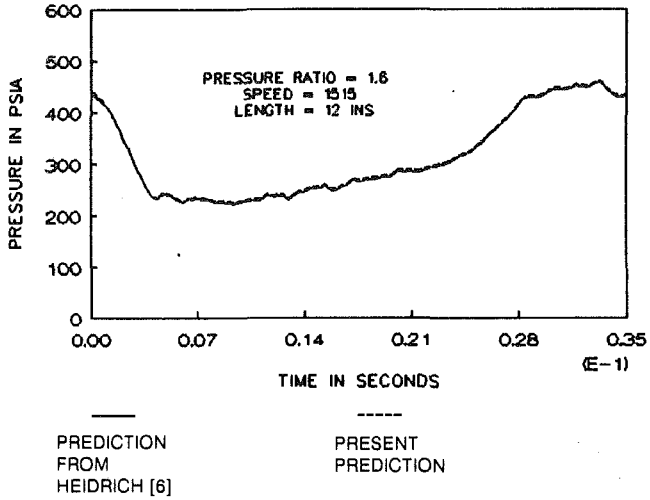

Fig. 7 Comparison of the present predictions with the results of Heidrich [6]

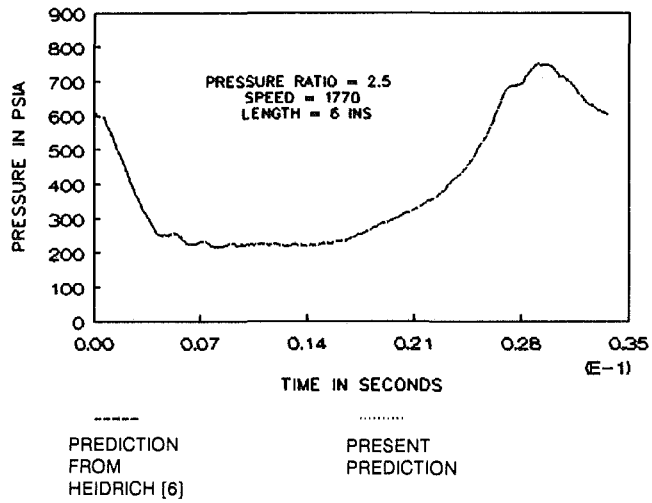

Fig. 8 Comparison of the present predictions with the results of Heidrich [6]

where L = inertance of the pipe = $1/g_cF$; C = capacitance of the pipe = g_cF/A^2; R = resistance/unit length = fQ_{rms}/g_cdF^2.

Equations (17) and (18) are solved in the frequency domain to obtain the following relations for H and Q at any point in the pipe in terms of its upstream or downstream values:

$$H_D = H_U \cosh \Upsilon l - Z_c Q_U \sinh \Upsilon l \tag{19}$$

$$Q_D = -H_U \sinh \Upsilon l / Z_c + Q_U \cosh \Upsilon l \tag{20}$$

The propagation constant Υ and the characteristic impedance Z_c are the most important parameters that control the response of the fluid to the forcing function. The propagation constant includes a resistance term, which provides the necessary damping. Proper modeling of this damping term is very crucial for predicting the correct response.

The geometry of the indicator passage used in the present measurements is shown in Fig. 10. Since the transducer terminates the channel at one end, the flow at that boundary, Q_U, is zero. Hence equations (19) and (20) can be simplified by neglecting Q_U to

$$H_D = H_U \cosh \Upsilon l \tag{21}$$

$$Q_D = -H_U \sinh \Upsilon l / Z_c \tag{22}$$

where

$$\Upsilon = \sqrt{Cw(-wl + iR)} \tag{23}$$

and

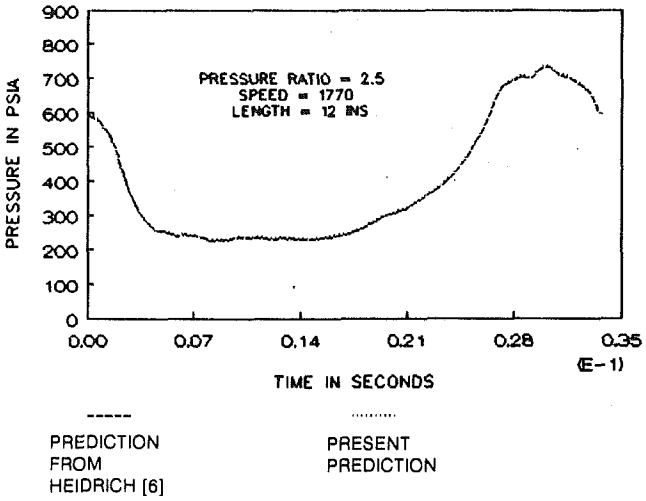

Fig. 9 Comparison of the present predictions with the results of Heidrich [6]

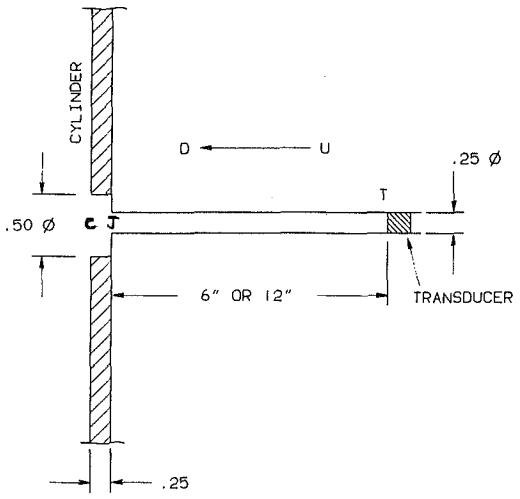

Fig. 10 Sketch showing the geometry of the passage

$$Z_c = -i\Upsilon/Cw \tag{24}$$

In the method used in [6], the effect of the portion CJ of the passage was neglected and equation (21) was used to compute the cylinder pressure from the transducer pressure measured at T. Also, Υ was modeled by neglecting the frictional resistance (since the mean flow, $\bar{Q}=0$ in the passage) and assuming that only thermal and viscous effects contribute to the resistance term.

In the present method, the frictional resistance due to the fluctuating flow in the pipe was also considered. For this purpose, the channel JT was divided into 20 strips and the fluctuating flow at the midpoint of each strip was computed using equation (22), first by neglecting the frictional resistance for finding R and then adding a frictional resistance based on the rms velocity over the strip during the successive iterations. The total resistance R was written as

$$R = fQ_{\text{rms}}/gdF^2 + w^2\mu/\rho gFA^2[4/3 + (\Upsilon - 1)/\text{Pr}] \tag{25}$$

Frictional Viscous Thermal

The pressure was propagated first from T to J using equation (21), and then a junction pressure loss due to the contraction at J was added before propagating it further to C using equation (19). During the iterative procedure (second iteration onward) the Darcy-Weisbach friction factor f was computed using the rms velocity at each strip and a total resistance for the channel was found by adding the individual resistances of

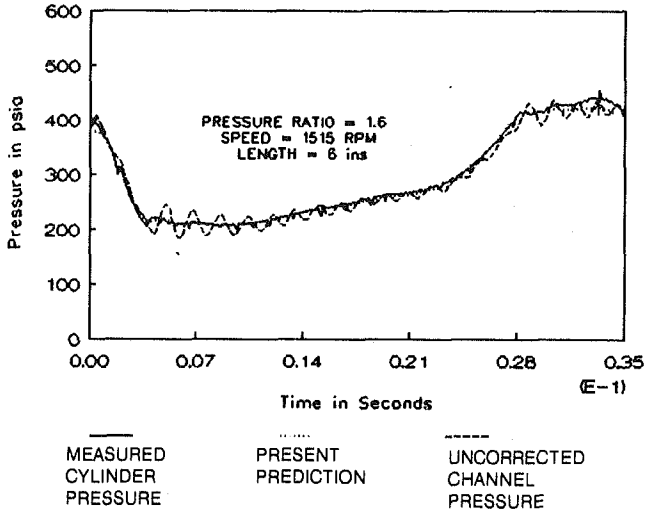

Fig. 11 Comparison of measured and predicted pressures using the frequency domain method

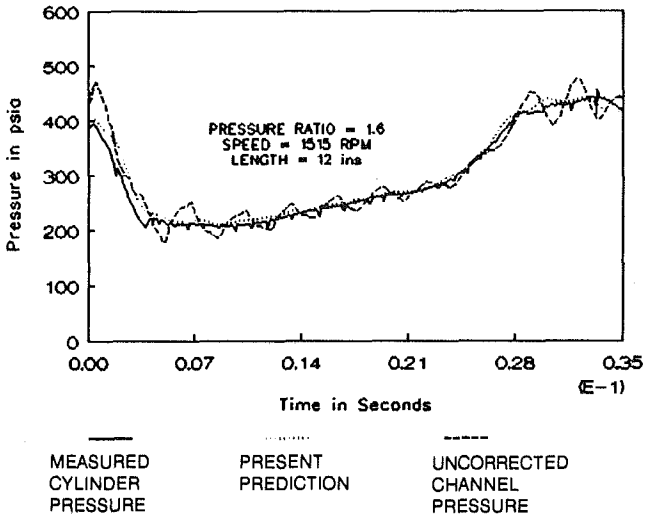

Fig. 12 Comparison of measured and predicted pressures using the frequency domain method

all the strips. The iterations were continued until the cylinder pressures calculated for successive iterations agreed to an accuracy of less than 0.05 percent for all 20 harmonics. The equations for head and flow are functions of frequency. Hence the time series for the measured pressures was expressed in terms of its harmonic components using Fourier transformation before starting the computation and the computed cylinder pressures were transformed back to the time domain.

Figures 11-14 show the comparison of computed pressures in the cylinder with the pressures measured inside the cylinder (at C) as well as those at the channel end (at T) for two speeds and two channel lengths of 6 and 12 in. Also, Figs. 15-18 show the comparison of the present results with the distributions obtained by Heidrich [6] earlier, by neglecting the effect of dynamic flow on damping. The present computation filters out all the pulsations and demonstrates a reasonable agreement with the measured pressures inside the cylinder for all four cases studied. However, it does not show any improvement in the agreement compared to that reported in [6]. The possible reasons could be the simple geometry of the passage used and the absence of any serious channel induced resonances. Hence a simple, noniterative frequency domain correction technique without considering the dynamic flow effects appears to be sufficient, at least in the case of simple passages without any volumes, valves, etc. Such a technique could easily be incor-

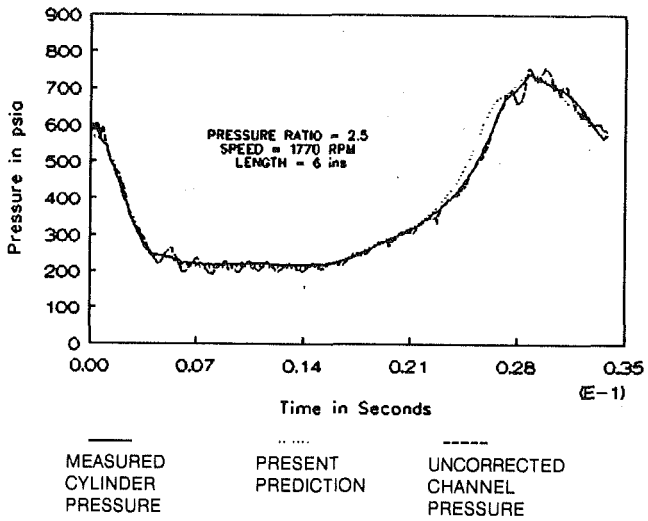

Fig. 13 Comparison of measured and predicted pressures using the frequency domain method

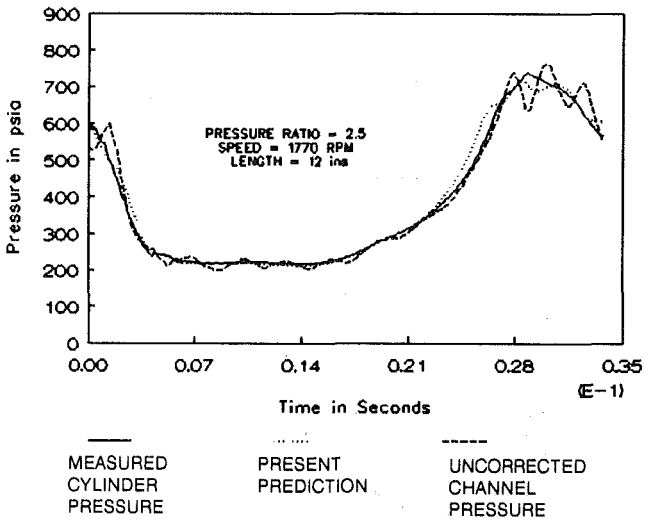

Fig. 14 Comparison of measured and predicted pressures using the frequency domain method

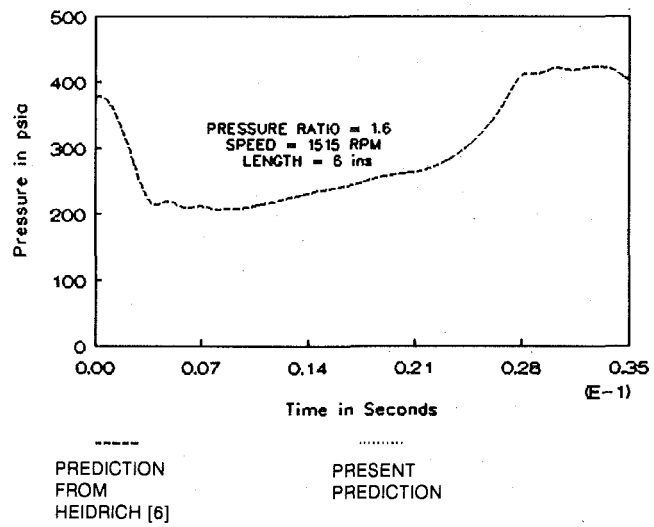

Fig. 15 Comparison of the present predictions with the results of Heidrich [6]

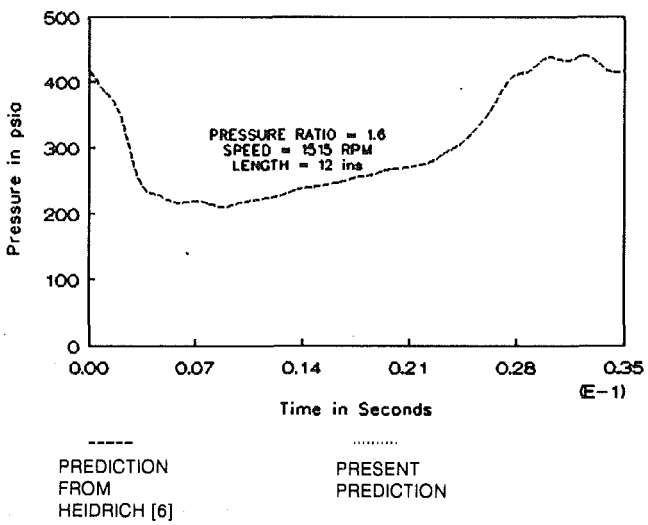

Fig. 16 Comparison of the present predictions with the results of Heidrich [6]

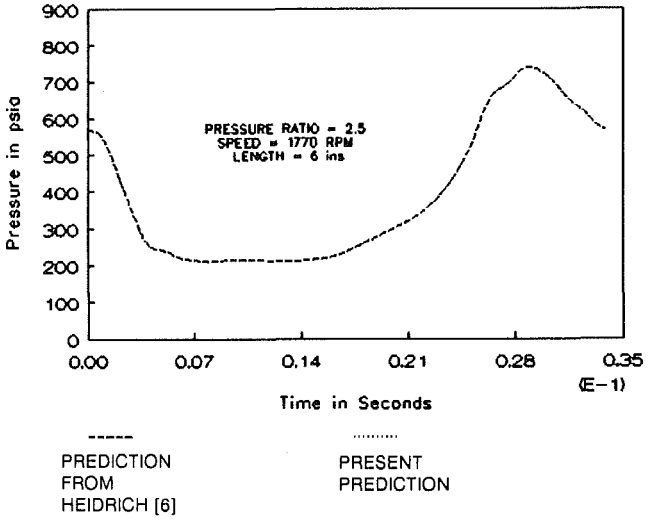

Fig. 17 Comparison of the present predictions with the results of Heidrich [6]

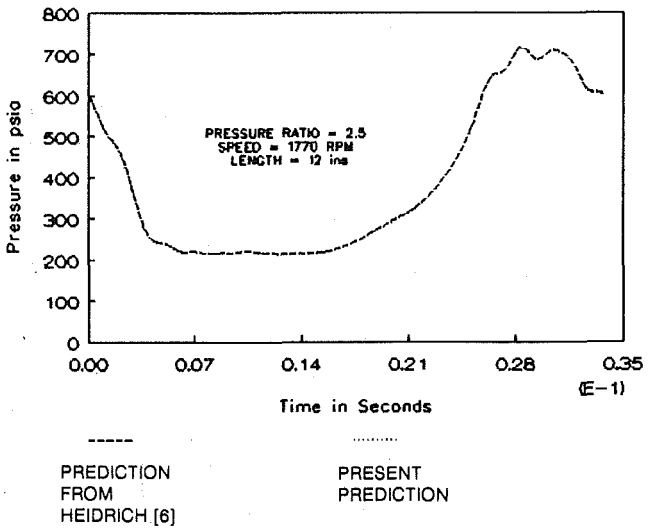

Fig. 18 Comparison of the present predictions with the results of Heidrich [6]

porated in a computer-based data acquisition system for diagnostic field measurements of reciprocating engines and compressors.

Conclusions

Comparison of pressure measurements obtained at two speeds, with and without passage effects, clearly demonstrated the need for a correction technique in order to assess the true performance of the compressor. This paper has investigated two such techniques in detail considering frictional effects, volume effects, and also the effect of dynamic flow in the passage.

The predictions from both methods showed good agreement with the pressures measured directly inside the cylinder over a complete cycle. However, the results of more detailed methods studied in this paper do not indicate any appreciable improvement over the results of simpler versions reported earlier in [6]. Hence, one could conclude, that at least for simple, weakly resonant passages, without large frictional effects, a simple frequency domain or time domain technique would suffice. Such techniques could easily be incorporated in computer-based data acquisition schemes for diagnostic measurements of reciprocating engines and compressors.

Acknowledgments

The authors would like gratefully to acknowledge the time and effort of the Dresser-Rand Development Laboratory group, namely Mr. David Decker, Mr. Donald Mason, Mr. Bill Glosick, and Mr. Richard Ellison. The authors would also like to thank Mr. Donald Draper, Dr. Derek Woollatt, and Mr. Joel Sanford for their technical support and guidance.

References

1 Elson, J. P., and Soedel, W., "Criteria for the Design of Pressure Transducer Adapter Systems," *Proceedings of the 1972 Purdue Compressor Technology Conference*, 1972, pp. 390–394.

2 Buchholz, A. B., "Investigation of Pressure Transducer Adapter Dynamics," *Proceedings of the 1978 Purdue Compressor Technology Conference*, 1978, pp. 275–282.

3 Bradley, P. G., and Woollatt, D., "Correction of Errors in Indicator Diagrams: Passage Effects," *The Engineer*, Mar. 9, 1968, pp. 511–516.

4 Xiagxing, S., "The Effect of Pressure-Inducting System of Transducers on Dynamic Pressure Measurement," *Proceedings of the 1986 Purdue International Compressor Engineering Conference*, 1986, pp. 714–723.

5 Harris, R. E., and Smalley, A. J., "Computer Based Diagnostic Tools for Compressor Performance Evaluation," ASME Paper No. 90-ICE-28, 1990.

6 Heidrich, F. L., "Channel Resonant Errors on *P–V* Indicator Diagrams for Reciprocating Compressors," *Proceedings of the 1990 Purdue International Compressor Engineering Conference*, 1990.

7 Draper, D. C., "Advanced Closed Loop," *Compressed Air*, 1983.

8 Wylie, E. B., and Streeter, V. L., *Fluid Transients*, McGraw-Hill, New York, 1978.

Optimum Probe Design for Precise TDC Measurement Using a Microwave Technique

T. Yamanaka
Senior Researcher.

M. Kinoshita
Researcher.

Toyota Central Research & Development Laboratories, Inc.,
Yokomichi, Nagakute, Nagakute-cho,
Aichi-gun, Achi-ken, Japan

The microwave method has advantages, such as a high degree of precision and dynamic measurement capability, for measuring TDC (Top Dead Center) in an engine. However, there are marked discrepancies between the calculation from a simplified model and experiments. Especially in the indirect-injection diesel engine, the concept of this method is not generally understood and the probe design for this method has not been established. It has been experimentally clarified that these discrepancies result mainly from the structure of the main chamber in the indirect-injection diesel engine and the measuring method of the sharpness of a microwave resonance. An optimum probe design for measuring TDC is proposed. A simple laboratory engine simulator is also proposed to simplify determination of the design parameters.

Introduction

The reference point used for determining crank position in engine analysis is TDC. Reliable and precise measurement of the dynamic TDC is necessary for evaluating engine operating parameters. Therefore, many papers have been published on various methods to measure TDC (Lancaster et al., 1975; Douaud and Eyzat, 1977; Amann, 1985; Rocco, 1985; Ferguson et al., 1987).

The microwave method has advantages, such as a high degree of precision and dynamic measurement capability; the difference between the microwave result and an optical crank angle marker technique was 0.08 deg. The optical technique measures directly piston positions for determining TDC using an optical rotary encoder as crank angle marker at an engine speed of 10 rpm (Yamanaka et al., 1985). The abovementioned advantages have attracted much attention (Merlo, 1970, 1981; Lienesh and Krage, 1979; Krage et al., 1982; Yamanaka et al., 1985). This method utilizes microwave resonance for detecting piston positions.

Based on the concept of acoustic phenomena, a resonance has two characteristics: frequency and sharpness of resonance. Since there are marked discrepanices between the calculation from a simplified model and experiments in these characteristics, the concept of this method is not well understood by some engine engineers and the probe design has not been established.

The main purpose of this paper is to clarify the causes of these discrepancies and to give an optimum probe design for applying this method to the indirect-injection diesel engine.

Contributed by the Internal Combustion Engine Division for publication in the JOURNAL OF ENGINEERING FOR GAS TURBINES AND POWER. Manuscript received by the Internal Combustion Engine Division August 18, 1989.

Principle of the Microwave Method

The upper part of Fig. 1 is a schematic representation of this method. The combustion chamber of a diesel engine can be regarded as a variable-length microwave resonator comprised of a probe, a prechamber, and a main chamber (Merlo, 1970). Therefore, there is absorption on each microwave resonance and the detected microwave signal exhibits a peak at each resonance. Thus reflected signals from the cavity vary in amplitude as the piston ascends during the compression stroke and descends during the power stroke, as shown in the lower part of Fig. 1. Although these signals are complicated and difficult to analyze in production engines, they should be symmetric with respect to TDC in principle because of their resonating property. Therefore, TDC can be measured by determining the center of symmetry. Each peak position on the microwave signal corresponds to the microwave resonance frequency for the mode. The microwave resonance frequency can be theoretically calculated from the physical dimensions of the chamber when it has a disk-shaped chamber with a flat piston and a flat head (see Appendix A). However, as previously mentioned, the calculation of the resonance frequency in the production engine cannot be made by use of the above simplified model but only by experimental data.

Procedure and Apparatus

Both a production engine (2.0-liter diesel engine by Toyota) and a laboratory engine simulator were used. Figure 2 shows a schematic diagram of the experimental setup in the case of the simulator. In the production engine experiment we used the setup similar to the previously reported one (Yamanaka et al., 1985).

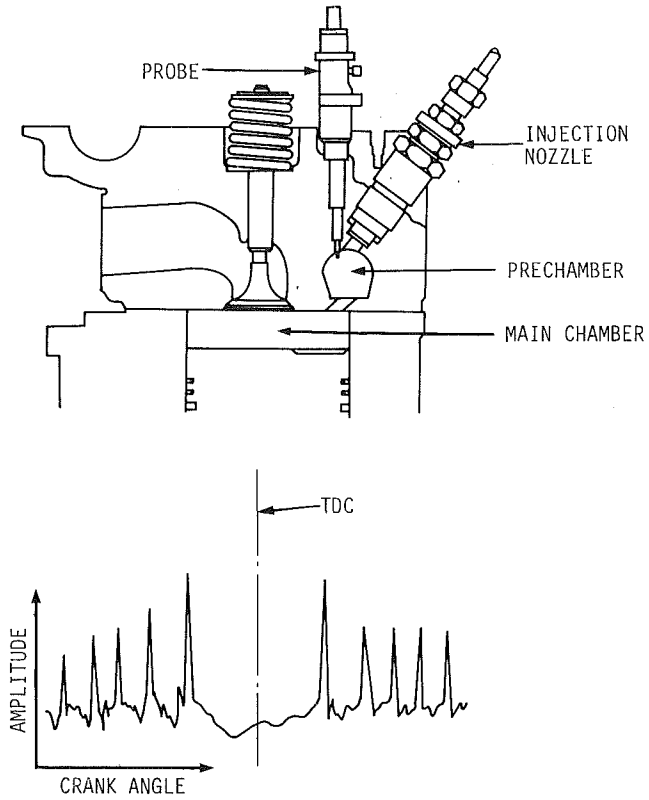

Fig. 1 Cutaway view of a probe installed in a diesel engine (top) and a typical microwave signal near TDC (bottom)

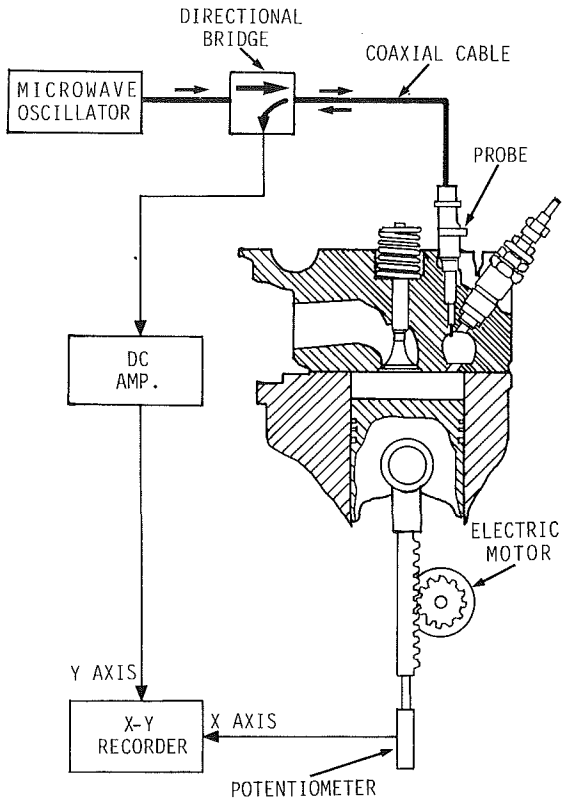

Fig. 2 Schematic diagram of the experimental setup

Experimental Procedure

The microwave frequency and the prove insertion length were varied and the resonance positions of the piston and Q factors (see Appendix B) were measured, respectively.

Secondly, measurements were obtained while varying the microwave frequency in the production engine. Results of the production engine were compared with those of the simulator.

Finally, the structure of the simulator was varied in two steps and the same measurements as in the first simulator were made. Experimental results were compared with theoretical values (see Appendix A) and the effect of the prechamber on resonance characteristics was estimated.

Chambers

Simulator Chambers. One cylinder of a production engine was used; the cylinder head was also made from a part of a production engine (see Fig. 2). As previously mentioned, several types of the simulator structure, namely types A, B, and C were used; the type A chamber had the same engine structure as the production engine, the type B chamber had the flattened combustion chamber (piston head and cylinder head) covered by copper foil, and the type C chamber had a structure with the prechamber in addition to the type B chamber. In the case of the type A chamber the probe was mounted in the hole for the glow plug of the prechamber and on the center of the main chamber for the type B and the type C chambers.

Production Engine. Piston positions were measured using the rotary encoder mounted on the engine crankshaft and the engine was motored.

Probe

As shown in Fig. 1, the probe couples the microwave with the engine chamber and determines the reflection coefficient of the microwave signal. The structure of the probe is similar to a miniature whip antenna used on automobiles. Usually the probe is made from a coaxial cable. Three probes were used: Probe 1 and probe 2 were designed for the simulator and probe 3 for the production diesel engine. Figure 3 shows the cross-sectional view of probe 3 and the dimensions of the three probes.

Instrumentation

In the simulator experiment a sweep generator was used as the microwave oscillator. The output frequency can be varied from 2 to 20 GHz. The microwave was routed to the combustion chamber through the connecting passage in the prechamber; it is coupled between the main chamber and the probe through the prechamber. A directional bridge separates the reflecting wave through the probe from the transmitting wave and detects the amplitude of the reflecting wave. The microwave resonance waveforms were recorded on an X-Y recorder in the case of the simulator experiment; the amplitude of the reflecting wave was recorded as the ordinate on the X-Y recorder and the piston position signal from the potentiometer linked with the piston was recorded as the abscissa on the recorder. In the frequency domain measurement the microwave frequency was recorded on the abscissa. The reflection coefficient, R, Q, and resonance piston positions were measured by using these recorded data.

Nearly the same apparatus used in the simulator experiment was used in experiments with the production engine. Resonance piston positions were measured using a personal computer with a resolution of 0.03 deg (Yamanaka et al., 1985).

Results

Measurement in the Type A Chamber. This chamber has the same structure as the production engine shown in Fig. 1. In these experiments, the microwave signal waveforms are very

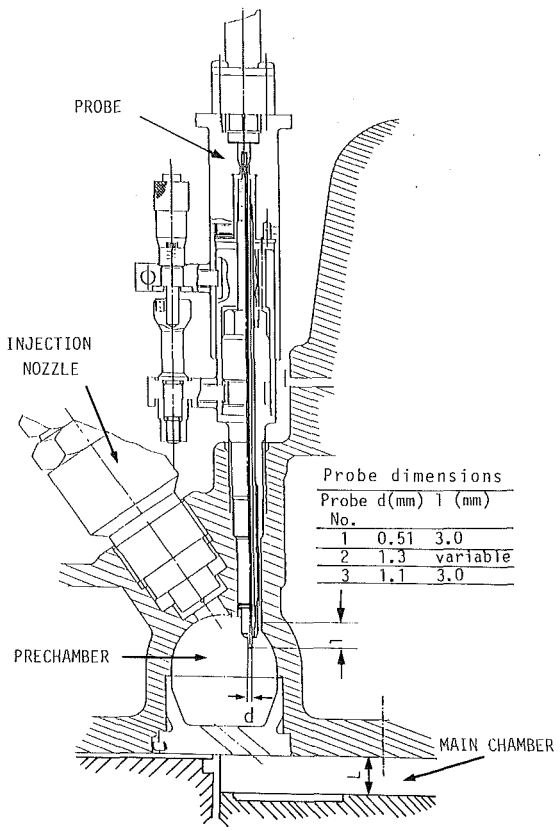

Fig. 3 Cross section of probe 3; L is the piston position

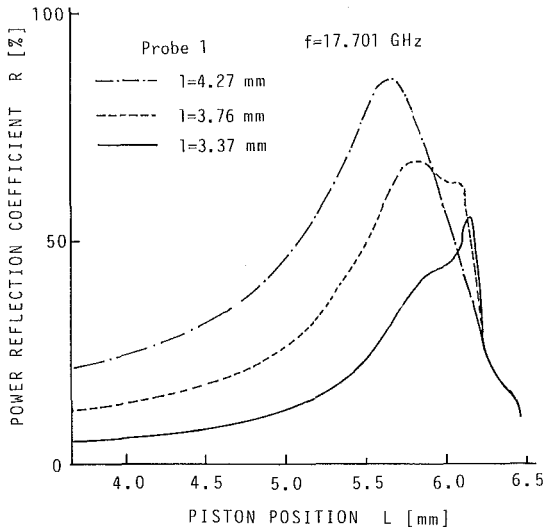

Fig. 4 Examples of the resonance waveform in a type A chamber

complicated as shown in Fig. 4. Therefore in this case it was very difficult to identify the resonance mode; the mode was identified when referred to the experimental results of the type B chamber in which it was easier to identify the mode.

Piston resonance positions in type A and type B chambers are shown as a function of frequency in Fig. 5; the piston was moved at each frequency until resonance was detected (see Fig. 4). Calculated values shown in Fig. 5 are obtained from equation (1), which is shown as follows:

$$L = -0.4987f + 17.39 \qquad \text{for the } TM_{011} \text{ mode} \qquad (1)$$

where L is the piston position (mm) and f is the microwave

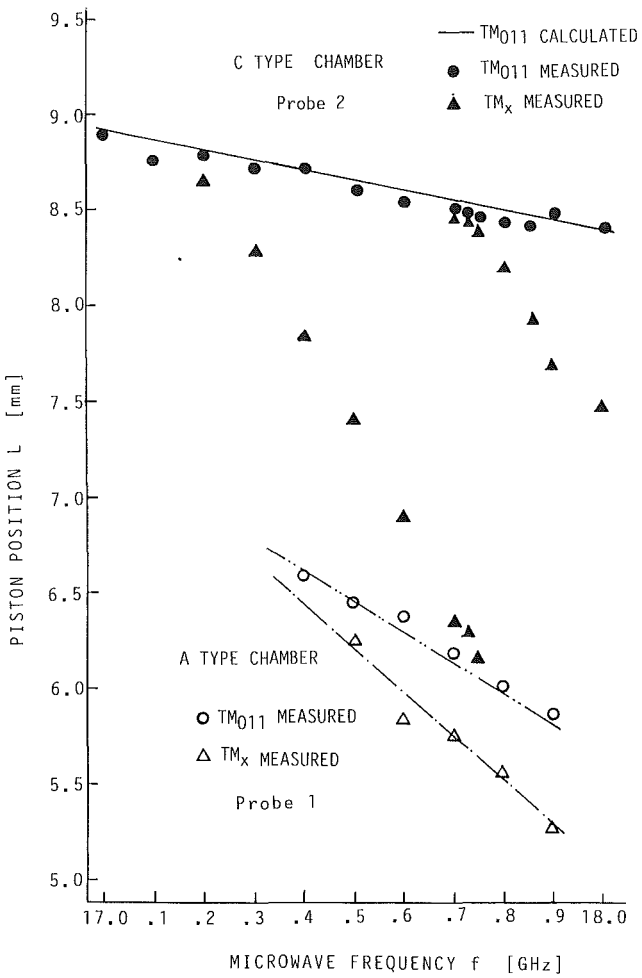

Fig. 5 Piston resonance position between 17 and 18 GHz in the simulator; dash-dotted lines are to guide the reader's eye

frequency (GHz). As Fig. 5 shows, the difference between calculated (see Appendix A) and experimental resonant positions was approximately 2.5 mm. It means that the theoretical model, namely the simple cylindrical cavity, is not appropriate for the resonator structure of the type A chamber. The dash-dotted lines in Fig. 5 are first-order equations fit to the experimental data.

These equations are shown as follows:

$$L = -2.271f + 45.96 \qquad \text{for the } TM_x \text{ mode (to be described)} \qquad (2)$$

$$L = -1.598f + 34.42 \qquad \text{for the } TM_{011} \text{ mode} \qquad (3)$$

The Q measurement is made by varying the piston position because the general method (frequency swept method) cannot be adopted (see Appendix B). In Fig. 6 only the coupling factor, β, is shown as experimental results because β determines Q and R of the microwave cavity as shown in Appendix B and Fig. 9. As shown in Fig. 6, they are determined as a function of the insertion length, l, of a probe (see Fig. 3); Q/Q_0 is determined by the probe insertion length, l, in this chamber. The measured and calculated Q_0 (see Appendix A) in this chamber are shown in Table 1 including results in other type chambers. The measured Q_0 is low as compared with the theoretically calculated value where the ohmic loss on the iron wall of the main chamber is taken into account; other losses are dominant.

Measurement in the Production Engine. The experimental setup is similar to that described in our previous paper (Ya-

Table 1 Theoretical and measured Q_0 (TM_{011} mode)

simulator type	frequency (GHz)	theoretical value	measured value	assumption
A	17.5	3293	129*	material:Fe
B	17.2	7963	432	material:Cu
	17.7	7846	790	
C	17.2	7963	380	

* Q_0 is corrected by the correction factor k.

manaka et al., 1985). In this experiment, piston positions were measured indirectly using the rotary encoder mounted on the engine crank shaft. Crank angles corresponding to resonance piston positions can be calculated using experimental equations (2) and (3), the engine geometry and the piston top clearance, *CR*. The experimental and calculated values are shown in Fig. 7; the piston top clearance ($CR = 0.7$ mm) was measured from the highest point of piston travel. As Fig. 7 shows, resonance piston positions in the production engine can be determined to an accuracy of the order of one degree from experimental values obtained in the simulator; the reason why the results differ for 30 rpm and 780–1000 rpm is supposed to be their dependence on engine speed.

Measurement in the Type B and Type C Chambers. The same experiments as in the type A chamber were also performed in the type B and type C chambers. Figures 5 and 6 show the experimental results for the type C chamber. Two unidentified resonance mode TM_xs exist in the type C chamber. There was little difference between results of the type B and the type C chambers for the other points. As shown in Fig. 5, there is a good coincidence between the experimental and calculated values obtained from equation (1). Therefore, it was concluded that the prechamber of the type C chamber has a small effect on the piston position of the microwave resonance. The difference between the structures of the type A and the type C chambers exists in each main chamber as previously described. The main type A chamber had depressions for valve seats in the block head and for combustion in the piston head, respectively. Therefore, the resonance positions of the type A chamber are shorter than those of the type B and the type C chambers, as shown in Fig. 5. In the type C chamber the coupling factor is also determined by the insertion length of the probe, as shown in Fig. 6.

As previously mentioned, calculated and measured values of Q_0 are shown in Table 1. Even in the type B chamber, which is considered to be a cylindrical resonator, which is the structure of the simplified model, the calculated Q_0 could not be realized. Since Q_0 depends on the degree of the microwave loss in the resonator, an extraordinary decrease of Q_0 in the type B chamber may result from the microwave loss in the clearance between the piston and the cylinder wall.

However, Q_0 of the type B chamber is several times as great as that of the type A chamber. Therefore, the other losses exist in the type A chamber as previously mentioned.

Probe Design Method

Choice of Microwave Frequency. Figure 8 shows a theoretical piston position, L, and its differentiation, $dL/d\theta$, as a function of the crank angle, θ. The $dL/d\theta$ determines the sensitivity, or resolution, of this method. Bearing clearances are within approximately ± 0.01 mm and 0.1 deg is usually required as the minimum resolution. Therefore, 0.01/0.1 or 0.1 mm/deg is the minimum value of $dL/d\theta$. This means that the resonance position should be larger than 25 deg or 5.2 mm from the result shown in Fig. 8 for the condition when $dL/d\theta$ is larger than 0.4 mm/deg. The f value of 24 GHz is obtained

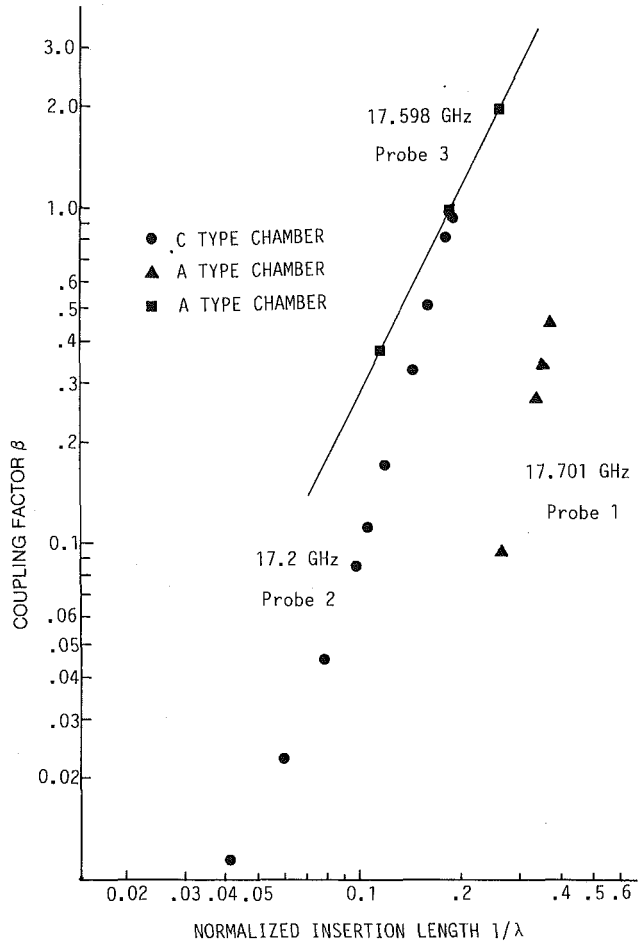

Fig. 6 Coupling factor versus normalized insertion length by the wavelength λ in the simulator

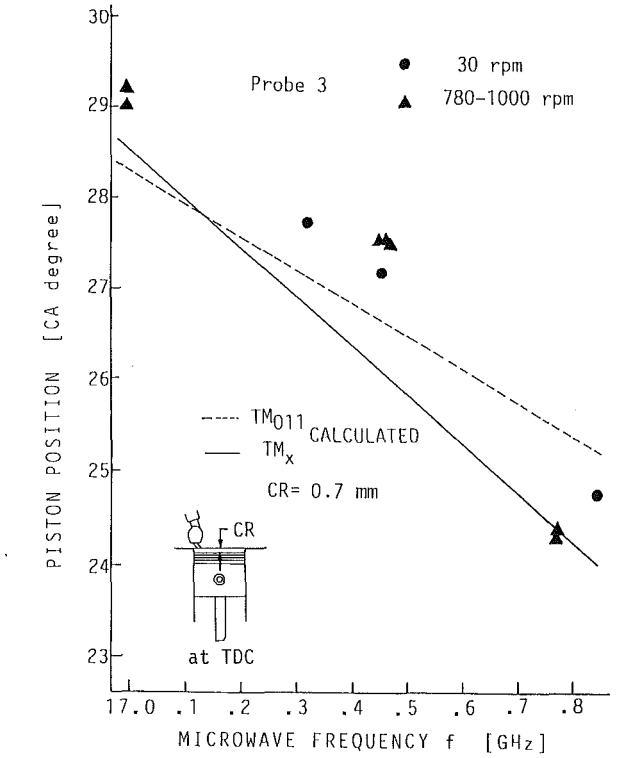

Fig. 7 Piston resonance position in a production engine; *CR* is the measured piston top clearance

by substituting 5.2 mm into L in equation (1). However, the frequency should be determined from the experimental results of Fig. 7 instead of the calculated one; the frequency is 17.8 GHz, which corresponds to 25 deg. Thus an upper limit for the frequency can be determined.

The probe insertion length, l, should be as short as possible to minimize the combustion disturbance and heat damage by the flame. However, the normalized insertion length by the wavelength (λ), l/λ, has a lower limit to detect the peak of the reflected microwave signal. Therefore, the microwave frequency should be higher than a certain value.

Taking into account all of these factors, the frequency was chosen between 17 and 17.8 GHz for this engine.

Probe Design. There is not much difference between resonance frequencies in the type A chamber using either of the three probes; the diameter of the probe d (see Fig. 3) has little effect on the resonance frequency. Therefore, the determination of the insertion length, l, is important.

Resonance positions are detected as positions of amplitude peaks in reflected microwave signals. Therefore, the sharpness Q of these peaks should be large because of the detection simplicity. Q and R depend on the insertion length, l; there is a trade-off between Q and R. Figure 9 shows such a relation; as R goes to zero, that is, the peak of the waveform reaches the maximum value, normalized Q/Q_0 approaches 1/2 of the maximum Q, namely Q_0. R should be chosen between 0 and 0.5. Therefore, the coupling factor β should be between 0.17 and 1 as shown in Fig. 9. From these values of β, the normalized insertion length by the wavelength, l/λ, should be between 0.08 and 0.2 using the experimental results in Fig. 6 if probe 3 is chosen. That is, as λ is 17.05 mm l should be between 1.4 and 3.4 mm. As above described the insertion length can be determined.

Simulator. A microwave frequency range and an approximate insertion length of the probe may be determined without experimental results. However, a detailed design should be made using experimental results because no practical calculation model exists in the production engine. In particular, the acceptable place for mounting the probe is generally restricted in the production engine; the optimum insertion length of the probe should be determined experimentally for the restricted mounting place. Motoring the production engine may be used for such experiment. However, the probe is heated and its temperature increases up to 200°C. Therefore the prototype probe for motoring the production engine should be specially designed for protection against such heat damage. Furthermore, the motoring wastes much time and money. On the other hand our simulator does not have such shortcomings. We recommend the use of a laboratory engine simulator.

Conclusions

1 The agreement between the theoretical calculation from a simplified model and the simulator experiment is good on the piston resonance position. Resonance positions in the production engine are shifted not by the presence of the prechamber but by the structure of the main chamber.

2 The microwave frequency determines the resonance position of the piston. An equation of the first degree between them is deduced from the experimental results in the production engine.

3 The Q factor and the reflection coefficient are uniquely determined by the insertion length of the probe.

4 An optimum probe design is proposed for the indirect-injection diesel engine. The simulator is useful for determining the design parameters.

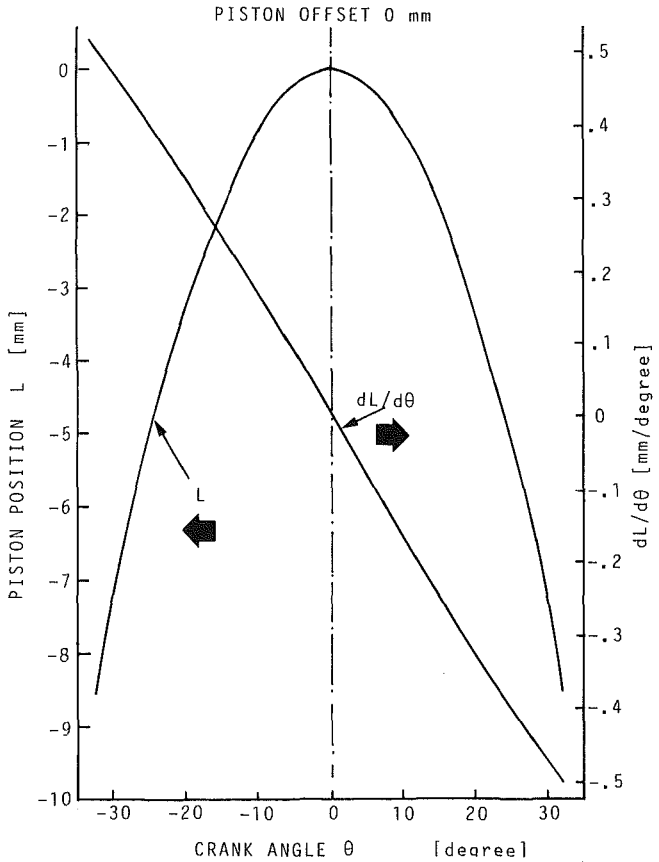

Fig. 8 Theoretical piston position L and the derivative of L with respect to the crank angle versus the crank angle in a production engine

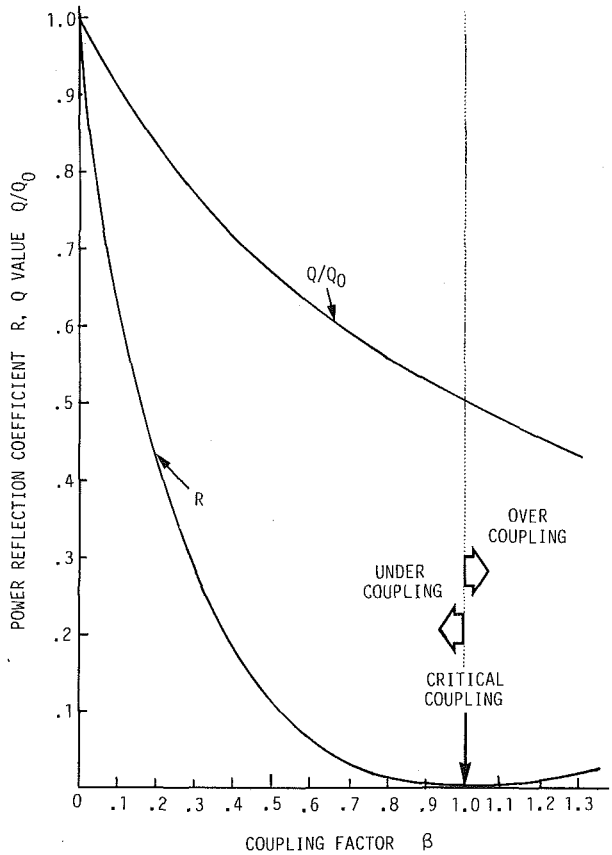

Fig. 9 Calculated R and Q/Q_0 as a function of the coupling factor; Q_0 is the value of Q measured inside the cavity

Acknowledgments

The authors would like to acknowledge Dr. H. Hattori of the University of Nagoya for his helpful comments. The authors are also grateful to Drs. I. Igarasi and N. Takahashi of Toyota Central Research and Development Laboratories, Inc., for encouragement and guidance in this study.

References

Amann, C. A., 1985, "Cylinder-Pressure Measurement and Its Use in Engine Research," SAE Paper No. 852067.

Douaud, A., and Eyzat, R., 1977, "DIGITAP—An On-Line Acquisition and Processing System for Instantaneous Engine Data-Applications," SAE Paper No. 770218.

Ferguson, C. R., et al., 1987, "Using an Optical Proximeter to Phase Cylinder Pressure to Crankshaft Position," SAE Paper No. 870478.

Krage, M. K., Lienesh, J. K., and Violetta, D. K., 1982, "Dynamic Diesel Engine Timing With Microwaves—The General Motors Approach," SAE Paper No. 820053.

Lancaster, D. R., Krieger, R. B., and Lienesh, J. H., 1975, "Measurement and Analysis of Engine Pressure Data," SAE Paper No. 750026.

Lienesh, J. H., and Krage, M. K., 1979, "Using Microwaves to Phase Cylinder Pressure to Crankshaft Position," SAE Paper No. 790103.

Merlo, A. L., 1970, "Combustion Chamber Investigations by Means of Microwave Resonances," *IEEE Trans. on Industry Electronics and Control Instrumentation,* Vol. IECI-17, No. 2, Apr., pp. 60–66.

Merlo, A. L., 1981, "Microwave Signal Analysis for Engine Diagnostics," *MIDCON Conf. Record,* Nov.

Rocco, V., 1985, "Dynamic T.D.C. and Thermodynamic Loss Angle Measurement in a D.I. Diesel Engine," SAE Paper No. 851546.

Yamanaka, T., Esaki, M., and Kinosita, M., 1985, "Measurement of TDC in Engine by Microwave Technique," *IEEE Transactions on Microwave Theory and Techniques,* MTT-33, No. 12, Dec., pp. 1489–1494.

APPENDIX A

Microwave Resonance Frequency and Quality Factor Q

As with mechanical waves, microwaves exhibit a phenomenon called resonance whenever the wave is confined between two reflecting surfaces separated by an integral number of half-wavelengths. When a metal cylinder is closed by two metal surfaces perpendicular to its axis, a cylindrical cavity is formed. The cylinder, that is the circular wave guide, has modes of transmission. For any mode, the transverse electromagnetic field may be resolved into two components, tangential and radial. It is customary to identify individual modes by using subscript notations. The resonant modes in this cavity are designated by adding a third subscript to indicate the number of half-waves along the axis of the cavity: The resonant modes are called TE_{nms} or TM_{nms}, where the integers n, m, and s refer to the number of electric field maxima in the standing wave pattern along the circular path, the radial path, and the axis, respectively.

A resonance has two characteristic features, the resonance frequency and the quality factor. The resonance frequency, f_0, for a mode is calculated from the wavelength and the condition above. The equation is shown as follows:

$$f_0 = c/2[(p_{mn}/a3.14)^2 + (s/L)^2]^{1/2}$$

where c is the velocity of light and a is the radius; L is the length of the axis, and p_{mn} is the constant for the mode. For example, $a = 90$ mm, $L = 8.8$ mm, $p_{01} = 2.41$, $s = 1$, $f_0 = 17.2$ GHz for TM_{011}.

Quality factor of the cavity itself, Q_0, can also be calculated by taking into account dissipated loss in the wall of the cavity

$$Q_0 = a(\pi f_0 \mu\sigma)^{1/2}/(1 + 2a/L) \text{ for } TM_{lms}$$

where μ is magnetic permeability and σ is conductivity.

APPENDIX B

Measuring Method of the Quality Factor Q

The quality factor Q represents the quality of the resonator.

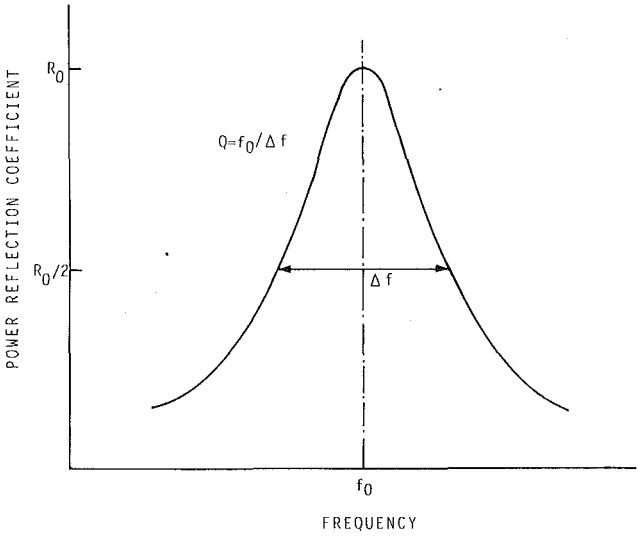

Fig. 10 Definition of the Q factor

Table 2 Correction factor k

mode	frequency (GHz) 17.0	17.5	18.0
TMx	5.25	6.40	8.02
TM_{011}	3.74	4.33	5.09
TM_{111}	2.98	3.36	3.82
TM_{021}	2.92	3.29	3.74

An approximate definition of Q, which can be applied to many types of resonant structures, is that Q is the ratio of the resonance frequency to the bandwidth between those frequencies on opposite sides of the resonant frequency (known as half-power points) where the response of the resonant structure differs by 3 decibels from that at resonance. Figure 10 shows this definition of Q; Q determines the sharpness of the resonance. The Q measurement is generally made on this definition in the case of the high Q resonator (Q is greater than several hundreds). However, this method is hardly applied to such low Q resonators as a production engine because the resonance curve in the frequency domain shown in Fig. 10 cannot be detected clearly and precisely. On the other hand, a similar resonance curve is obtained from varying the piston position, L. The relation between Q ($=f_0/\Delta f$) in the frequency domain and pseudo-Q ($=L_0/\Delta L$) in the piston position domain can be easily deduced. As equations (2) and (3) show, there is the first degree relation between the resonance position, L_0, and the resonance frequency, f_0. That is,

$$L_0 = af_0 + b \tag{4}$$

$$\begin{aligned} Q &= f_0/\Delta f \\ &= (L_0/\Delta L)/(1 - b/L_0) \\ &= (L_0/\Delta L)\,(1/(1 + b/a/f_0)) \\ &= -k(L_0/\Delta L) \end{aligned} \tag{5}$$

where k is the correction factor.

We can easily calculate k of any mode by using equations (4) and (5). For example, substituting a and b of equations (2) and (3) into equation (5), k can be calculated in each mode. The results are shown in Table 2. $L_0/\Delta L$ determines the resolution of the peak position, namely the sharpness of the microwave resonance waveforms. The microwave resonance waveform in Fig. 4 is complicated because $L_0/\Delta L$ is small (Q

is low and k is much greater than unity). On the other hand k of the type B and C chambers is almost unity. Therefore, microwave waveforms in such chambers have sharper peaks than those shown in Fig. 4.

APPENDIX C

Coupling Factor

The probe couples the transmission line with the resonator. The coupling factor, β, represents the degree of coupling and β equals unity in the critical coupling. The critical coupling results in the maximum transfer of energy between the transmission line and the resonator at the resonance frequency. There are close relationships among Q, β, and the power reflection coefficient, R.

$$Q/Q_0 = 1/(1+\beta) \tag{6}$$

$$R = ((\beta-1)/(\beta+1))^2 \tag{7}$$

where Q_0 is a constant, namely Q of the resonator itself (unloaded Q). This relation is shown in Fig. 9. Varying β, that is the probe insertion length in this case, R and Q are measured. β and Q_0 can be calculated from equations (7) and (6), respectively. In this process it is assumed that Q_0 is independent of β.

Study of the Nonsteady Flow in a Multipulse Converter

P. Flamang

R. Sierens

Laboratory of Machines and Construction of Machines,
University of Gent,
B-9000 Gent, Belgium

In a previous paper [1] a simplified model has been proposed to calculate the pressure loss coefficients of a multipulse converter under steady-state flow conditions. Therefore a special test rig has been built, which simulates the nonsteady but cyclic flow in the exhaust system of a real engine. Pressure and velocity measurements (with LDA) are compared with the results of the numerical simulation for the flow through the multipulse converter of the test rig. Finally, a comparison is made between measurements and calculations of the pressure history in the exhaust system of a real engine. This paper proves that this simplified model accurately predicts the behavior of the multipulse converter under nonstationary flow conditions.

Introduction

Pulse converters are widely used as exhaust pipe junctions for turbocharged diesel engines. They have the aim to combine the advantages of constant pressure and pulse turbocharging systems, i.e., simplicity of exhaust pipe arrangements, high turbine efficiency, and better energy recuperation at low load conditions.

The three most adapted pulse converters are the symmetric three-way pulse converter, the compact converter, and the multipulse converter [5, 9, 10].

An extensive research program on pulse converter systems has already been carried out at the laboratory. The flow through compact converters and multipulse converter systems have been analyzed on a fundamental level by means of pressure and LDA-velocity measurements [1, 3]. Two and three-dimensional flow calculations of these junctions have already been given in the literature [6, 7, 12].

During the research program, it is shown that the optimal dimensions are dependent on the engine conditions; therefore, a purely experimental optimization is a time-consuming and expensive job. Obviously, computer optimization seems to be the more attractive solution to the problem.

To study the nonsteady flow in the inlet and exhaust pipes of IC engines, the method of characteristics is extensively used [15]. The inlet and exhaust pipes are divided in a number of ducts. At the beginning and end of each duct, the flow in the duct interacts with boundaries. Such boundaries are the inlet or exhaust manifold, the inlet to the turbine, a junction of two pipes, etc. The interaction between the flow and these boundaries is described in the so-called boundary conditions. The method of characteristics itself and the different boundary conditions have been described extensively in the literature [8–11].

A converter is then treated as a junction of three or more ducts with an adiabatic pressure loss at the junction for each of the possible flow directions, or even simpler with an equal pressure assumption for all the duct ends (constant pressure model). The loss coefficients necessary for the first model are obtained from experiments under stationary flow conditions [1, 3]. When no experimental data are available the constant pressure model is normally used.

In [1] the authors have proposed a simplified model to calculate the (pressure) loss coefficients of a multipulse converter under stationary flow conditions. This model was based on assumptions that followed from the insight in the complex flow phenomena, and were derived from the fundamental flow analysis mentioned above.

Hereafter it is shown that also under nonsteady flow conditions the simplified model for the calculated loss coefficients (coupled to the method of characteristics) results in a good agreement with measurements. This way time-consuming measurements are no longer necessary. It is also shown that the constant pressure model is not suitable for simulation of the multipulse converter.

This paper gives only a summary of the study that has been carried out on pulse converter systems in the laboratory. A full description can be found in [12]. A larger number of velocity measurements (with LDA) in the multipulse converter on the test rig are given in [13].

Experimental Setup

Test Rig Description. The examined multipulse converter is a 1/4-scale model of the converter for the eight-cylinder 8 DZC-1000-166 engine of the Anglo Belgian Corporation.

The multipulse converter consists of four entries and one connection pipe to the turbine (see Fig. 1). The construction of the real converter is quite rudimentary; the four pipes are welded to each other with an angle of 23 deg to the axis of the converter.

Partitions are brought in (welded) at the end of the entry pipes to create the convergent part of the converter. The pulse converter has a throat ratio of 0.54. The area ratio between the connection pipe and the entry pipes is 1.16.

A special test rig has been developed to generate periodic

Contributed by the Internal Combustion Engine Division and presented at the Energy-Sources Technology Conference and Exhibition, Houston, Texas, January 20–24, 1991. Manuscript received by the Internal Combustion Engine Division September 1990. Paper No. 91-ICE-1.

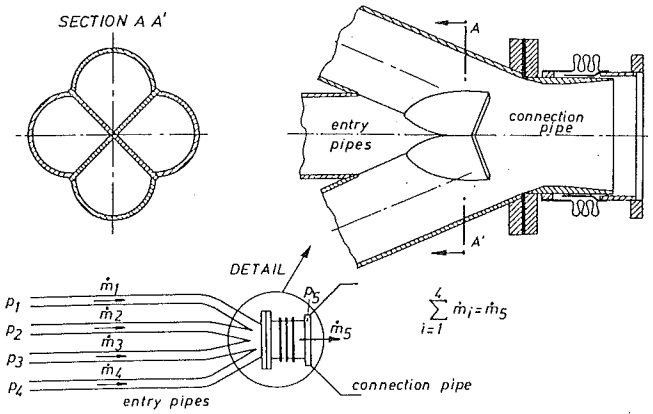

Fig. 1 Pipe arrangement of the multipulse converter

pressure pulses at each of the four inlet pipes of the multipulse converter.

Figure 2 shows a principal view of the test rig. A compressor delivers compressed air through the inlet (1) into a tank (2). On this tank four drums (3) are mounted, in which a rotor rotates. In each rotor there are compartments, which are filled in turn from the tank, and are emptied through the corresponding inlet pipe (4) of the pulse converter (5).

The rotors are operated with a gear belt by an electric motor. A disk provided with slots is mounted on the gear of rotor 1. By means of two photodiodes, one reference pulse and 90 (or 180) positioning pulses are generated each cycle.

At the end of the outlet pipe of the multipulse converter a nozzle (6) creates a back pressure, simulating the turbine.

Figure 3 shows in a cross section of the rotor and the different compartments separated from each other by partitions.

The principal dimensions are:

tank diameter:820 mm
tank height: 150 mm
tank volume: 79 liter
drums diameter: 284 mm
drums height: 172 mm
compartment volume I: 3.65 liter

The dimensions of the rotors are given in Fig. 3.

In the described tests only compartment I has been filled and emptied in turn. It is also possible to fill (and empty) compartment II (together with the use of compartment I). This results in two pulses for each inlet pipe of the converter per revolution of the rotor.

Compartment I fills when the orifice (ϕ 40 mm) in the underplate of the rotor overlaps with the orifice (ϕ 90 mm) in the tank. Figure 3 shows also a ring-shaped orifice in the top plate of the rotor. When this orifice overlaps with the outlet orifice of the house of the drum, a blowdown pulse in the corresponding converter inlet pipe is generated.

To minimize leakage flow through the inlet of the drum and

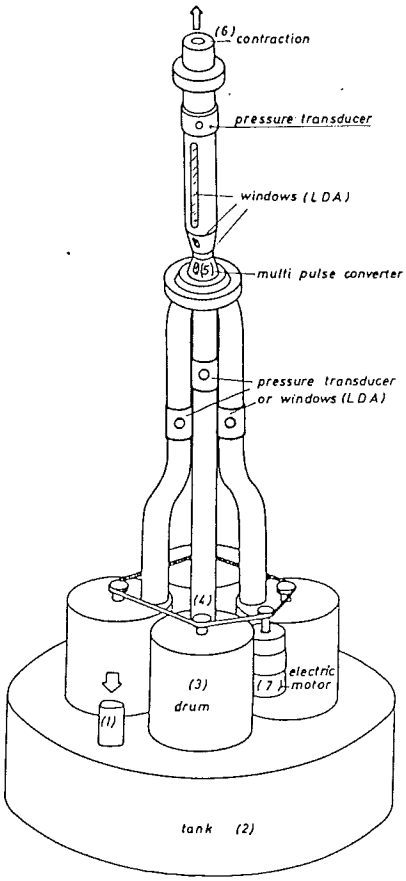

Fig. 2 Principal view of the test rig

the outside of the rotor housing, O-rings are located at the rotor contour. Other precautions were taken to reduce leakage at the bearings to the atmosphere.

The scale model of the multipulse converter is provided with windows in the inlet pipes, the mixing zone, and the outlet pipes to allow the LDA velocity measurements. On Fig. 2, the locations of the pressure transducers are also indicated.

LDA and Data Acquisition System. The velocity measurements are carried out with an LDA system composed of a He–Ne laser, beam splitter, Bragg cell, focusing, and receiving optics with photomultiplier and a counter-type signal processor. Only on-axis forward scatter applications were used.

The LDA system is mounted on a table with three possible translation directions. The photodetector and optics are adjustable to obtain a correct alignment of the system.

The counter is connected to a data acquisition system for subsequent data processing. To reconstruct the velocity profiles

Nomenclature

a = velocity of sound, m/s
F = pipe cross-sectional area, m^2
f_c = pressure drop coefficient
h = enthalpy, m^2/s^2
K = resistance coefficient
L = pressure loss coefficient
M = Mach number
$\dot{m}$ = mass flow rate, kg/s
p = static (mean) pressure, Pa
Δp = static pressure loss, Pa
PGEM = mean value of static pressure, bar
q = heat transfer/unit mass/unit time, m^2/s^3
t = time, s
TWF = turbine work function, J
u = velocity, m/s
W = wall friction, m/s^2
$\dot{W}_{is}$ = power that can be released in the turbine, J/s
x = distance, m
η = efficiency
κ = ratio of specific heats
ρ = density, kg/m^3

Subscripts

i = upstream
1, 2, 3, 4, i = inlet pipe
5 = connection pipe
o = reference condition

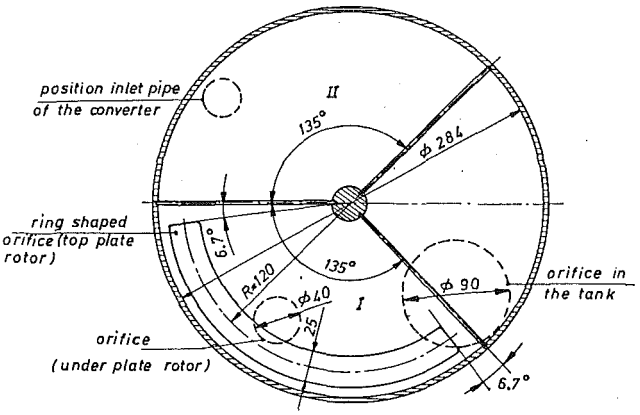

Fig. 3 Cross section of rotor

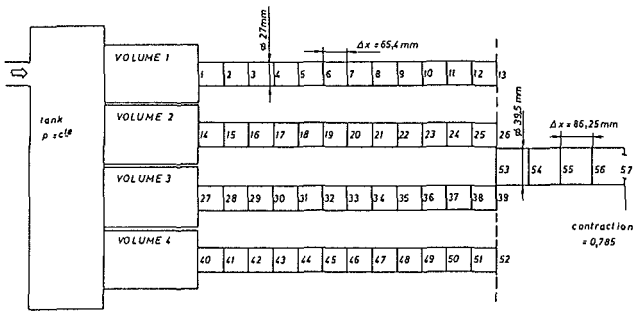

Fig. 4 Outline for the simulation of the test rig

the mean value and the standard deviation are calculated from the first and second-order moments of a probability distribution. More extended description of the used LDA system and a detailed error analysis of the system are given in [1–3].

Numerical Simulation of the Test Rig

Model Description. The outline for the numerical simulation of the test rig is given in Fig. 4.

The volume change in the different reservoirs (compartments of the rotors) is calculated with the filling and emptying method, which uses the conservation equations of mass and energy. The equations are solved with an Euler-predictor-corrector method with double corrector.

The calculation of the flow in the pipes is done with the method of characteristics, based on the following equations:

$$\frac{\partial \rho}{\partial t}+\frac{\partial u}{\partial x}\rho+u\frac{\partial \rho}{\partial x}+\frac{\rho u}{F}\frac{dF}{dx}=0$$

$$\frac{\partial u}{\partial t}+u\frac{\partial u}{\partial x}+\frac{1}{\rho}\frac{\partial p}{\partial x}+W=0$$

$$\frac{\partial p}{\partial t}+u\frac{\partial p}{\partial x}-a^2\left(\frac{\partial \rho}{\partial t}+u\frac{\partial \rho}{\partial x}\right)-(\kappa-1)\rho(q+uW)=0$$

This method is well known [8, 9, 11, 15], and the algorithm is available at the laboratory [4].

The coupling between the volumes and the pipes is done with the valve boundary of the method of characteristics [4]. The geometric area (the valve area in the boundary) is calculated from the overlap between the inlet pipe of the converter and the ring-shaped orifice in the top plate of the rotor. When there is no outflow from the compartment (no overlap), and the close end boundary is used at the end of the inlet pipe.

A constant mass flow rate is delivered to the tank (reservoir). Considering the tank as a separate volume, and calculating this volume with the filling and emptying method, has proved that the pressure variations in the tank were negligible. Therefore the tank is considered as a reservoir at a constant pressure.

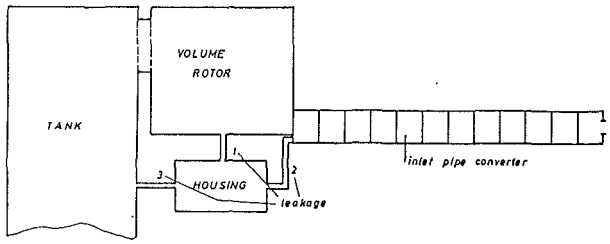

Fig. 5 Calculation of leakage flows

Leakage. The leakage occurring between the turning rotors and their housings (drums) is of little concern, but it has to be taken into account in the calculations. The different leakages are:

1 between the volumes (rotors and their housings)
2 between the housing and the inlet pipe of the converter
3 between the tank and the housing.

By introducing an extra volume for the housing (see Fig. 5), the different leakage flows can be calculated. A first estimation of the different leakage parameters was made from the construction clearances.

To obtain the correct leakage areas, separate test measurements are carried out. The multipulse converter is replaced by one pipe (with a contraction at the pipe end) and the nonsteady pressure in the pipe is measured for different rotor speeds and tank pressures. This procedure is repeated for each rotor. From a comparison of these measurements with the calculated pressures, the following leakage areas were obtained: 0.00042, 0.000045, and 0.000235 m^2 for (1), (2), and (3), respectively (see Fig. 5). These leakage areas are then used in the total simulation calculation.

Multipulse Converter Boundary. In the method of characteristics the multipulse converter is considered as a boundary, which interacts with the different inlet and outlet pipes of the converter. The converter is treated as a junction with five ducts. Different models are possible to simulate the multipulse converter boundary. These are described below.

Constant Pressure Model. When there are no data available from the converter, one may assume an equal pressure for all the duct ends. Even when the converter geometry is correctly defined, this model is not realistic for a pulse converter system.

Model With Experimental Pressure Loss Coefficients. The converter is treated as a junction with an adiabatic pressure loss at the junction for each of the possible flow directions [9]. The loss coefficients have to be obtained under steady flow conditions for all possible flow configurations and for all possible mass flow ratios through the different ducts. The multipulse converter is then seen as a black box, with the measured loss coefficients describing its transfer function.

In a symmetric multipulse converter with four inlet pipes and one connection pipe (pipe 5) to the turbine, eight flow combinations are possible. Assuming that there is always a positive flow to the turbine, the flow combinations can be reduced to four.

The pressure loss coefficient L_i is defined as

$$L_i=\frac{\Delta p_i}{p_5}=\frac{p_i-p_5}{p_5} \quad (i=1,\ 4)$$

The static pressure loss Δp_i is the difference of two static (mean) pressure readings in sections at equal distance from the junction. Index 5 is for the connection pipe (see Fig. 1).

Under steady-state flow conditions the pressure drop Δp_i across the converter (for pipe i) is of the form

$$\Delta p_i=f_{c_i}\frac{1}{2}\rho_i u_i^2$$

where ρ_i and u_i are the density and velocity upstream of the converter and f_{c_i} is a constant or pressure drop coefficient.

With the basic steady flow equations:

Energy

$$a_0^2 = a_i^2 + \frac{\kappa - 1}{2} u_i^2 = a_5^2 + \frac{\kappa - 1}{2} u_5^2$$

Continuity

$$F_i \rho_i u_i = F_5 \rho_5 u_5$$

Velocity of sound

$$a = \sqrt{\kappa p / \rho}$$

and the definition of the resistance coefficient

$$K_i = \frac{f_{c_i} \kappa}{2} = \frac{\Delta p_i \kappa}{\rho_i u_i^2} = \frac{p_i - p_5}{p_i} \frac{\kappa p_i}{\rho_i u_i^2}$$

or

$$\frac{p_5}{p_i} = 1 - K_i \mathrm{M}_i^2$$

After rearranging and combining these equations one obtains a relation between the Mach numbers in one of the inlet pipes and the outlet pipe of the converter with the resistance (or loss) coefficient

$$\frac{\frac{2}{\kappa - 1} + \mathrm{M}_5^2}{\frac{2}{\kappa - 1} + \mathrm{M}_i^2} = \left(\frac{F_i}{F_5}\right)^2 \frac{\mathrm{M}_i^2}{\mathrm{M}_5^2 (1 - K_i \mathrm{M}_i^2)^2}$$

The resistance coefficient K_i and the pressure loss coefficient L_i are functions of the Mach number M_5 and the mass flow ratios $\dot{m}_i / \dot{m}_5$

$$K_i = f(\dot{m}_1/\dot{m}_5,\ \dot{m}_2/\dot{m}_5,\ \dot{m}_3/\dot{m}_5,\ \mathrm{M}_5)$$

$$L_i = f(\dot{m}_1/\dot{m}_5,\ \dot{m}_2/\dot{m}_5,\ \dot{m}_3/\dot{m}_5,\ \mathrm{M}_5)$$

These coefficients, normally obtained from experiments, are then used as input data for the multipulse converter boundary. Although the pressure loss (or resistance) coefficients are obtained under steady-state flow conditions, these coefficients are used in the nonsteady simulation model (quasi-steady-state calculations). A full description of the application of these equations under nonsteady flow (and the rearranging of the equations to characteristic values) is beyond the scope of this paper and is described in [4].

Model With Calculated Pressure Loss Coefficients. The previous model gives good results [9, 11] and would be very attractive if it was not for the enormous and time-consuming work of measuring the pressure loss coefficients for each junction geometry.

In a previous paper [1], the authors have described a simplified model for the calculation of the pressure loss coefficients of a multipulse converter. It has already been proved that this simplified model gives good agreement with the steady flow measurements [1].

The "model with calculated pressure loss coefficients" in fact is the same as the previous model, except that the loss coefficients now are completely calculated, thus avoiding any measurements to be carried out!

Comparison of the Different Models for the Multipulse Converter. The different models of the multipulse converter boundary have been simulated for the nonsteady flow test rig (see Fig. 4 for outline of the test rig).

A comparison is made of the calculated pressures and velocities in the inlet and outlet pipes (for different converter geometries). In these calculations two volumes of each rotor have been considered to deliver a blowdown flow for each inlet pipe and per revolution of the rotor. The results are given at mesh point 1 (inlet of inlet pipe I to the converter) and at mesh point 55 (after the multipulse converter).

To compare the calculations with the different models, the following parameters are used:

PGEM(1): mean value of the static pressure in mesh point 1. This is a measure of the obstruction of the converter in the exhaust system.

PGEM(55): mean value of the static pressure before the turbine (or before the obstruction simulating the turbine).

TWF: turbine work function.

The turbine work function gives an idea how the energy of the exhaust gases, available at the exhaust valve of the engine, is transferred to the turbine [14]. At each moment and at each mesh point this function is equal to the power $\mathring{W}_{is}$ that can be released in the turbine, by an isentropic expansion to the ambient conditions

$$\mathring{W}_{is} = \dot{m}(h_0 - h_{0_{is}})$$

where h_0 = initial total enthalpy (per unit of mass); $h_{0_{is}}$ = enthalpy after isentropic expansion to the ambient pressure; $\dot{m}$ = instantaneous mass flow rate.

The parameter TWF is the integrated value of $\mathring{W}_{is}$ during one cycle at mesh point 55.

The efficiency of the multipulse converter is then defined as the ratio of TWF with the integrated value of $\mathring{W}_{is}$ before the multipulse converter.

The following runs were executed:

1 constant pressure model for the multipulse converter boundary

2 model with experimental pressure loss coefficients

3 model with calculated pressure loss coefficients (the throat ratio for runs 1-3 is equal to 0.54)

4 model with calculated pressure loss coefficients (throat ratio = 0.425).

The calculated results are summarized in Table 1 and shown in Figs. 6 and 7 (all results are for a constant pressure in the reservoir of 2.24 bar and a rotor speed of 500 rpm).

The results also show that for the constant pressure model the blowdown pulses and the obstruction of the converter are well simulated (PGEM(1) differs by only 0.3 percent). This is probably due to the real simulated geometry of the converter in the different pipe ends.

However, the average pressure PGEM(55) before the turbine (obstruction) is underestimated (by about 6.5 percent), as well as the total mass flow through the converter, resulting in an underestimation of the efficiency of the converter of about 11 percent!

The difference in the results for the calculations with the experimental and calculated pressure loss coefficients (for the throat ratio of 0.54) is less than 1 percent. Also the shapes of the pressure profile before the turbine and back flow nearly coincide (contrary to the constant pressure model).

The calculations show that in the cone of the converter a pressure recovery during most of the cycle is found with the

Table 1

	Constant pressure model	Experimental pressure loss coefficients	Calculated pressure loss coefficient	
			Throat ratio 0.54	Throat ratio 0.425
Mass flow (kg/s)	0.1279	0.1386	0.1379	0.1388
PGEM(55) (bar)	1.562	1.670	1.662	1.675
PGEM(1) (bar)	1.704	1.699	1.697	1.717
TWF (J)	5101.02	6182.50	6100.11	6241.42
ηMPC (percent)	83.91	95.02	94.24	94.30

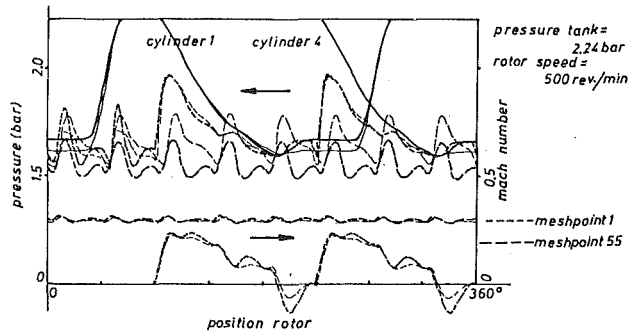

Fig. 6(*a*) Comparison of calculated results with the different models for the mpc (constant pressure model and model with experimental pressure loss coefficients): —— constant pressure model; —— experimental pressure loss coefficients

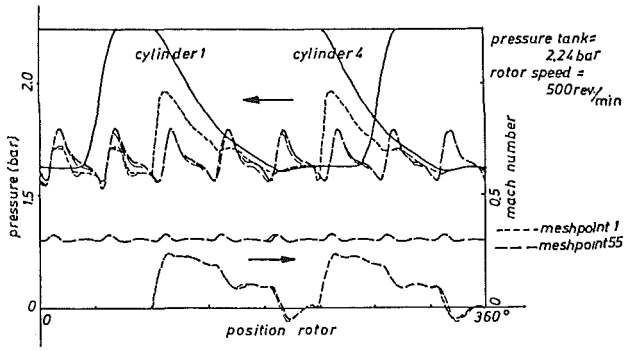

Fig. 6(*b*) Comparison of calculated results with the different models for the mpc (models with experimental and calculated pressure loss coefficients): ——— experimental pressure loss coefficients; ——— calculated pressure loss coefficients

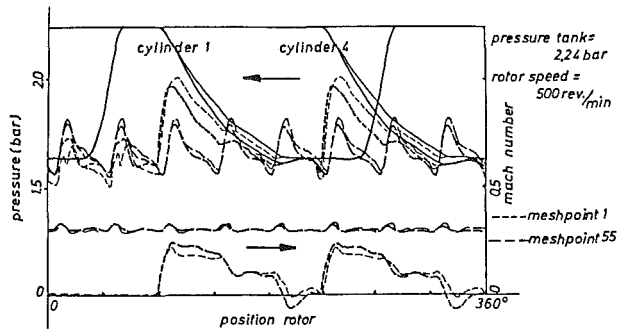

Fig. 7 Comparison of calculated results for different throat ratios: — throat ratio = 0.425; ——— throat ratio = 0.540

models of the pressure loss coefficients. This is because, contrary to the constant pressure model, both models with loss coefficients take into account the pressure changes resulting from the exchange of impulse in the mixing zone.

Also the back flow through the inlet pipes is incorrectly simulated with the constant pressure model, as it does not take into account the high pressure drop because of the 180 deg turning of the flow.

The influence of the throat ratio on the flow characteristics is seen in Table 1 and Fig. 7.

The converter with throat ratio 0.425 gives a greater obstruction to the blowdown pulses. This results in a slower decrease of the pressure in the cylinders (volumes of the rotor), nearly no back flow in the converter, a higher mean pressure before the turbine, a higher mass flow, more power available at the turbine, and a nearly equal efficiency of the converter.

From this one can conclude that the optimum dimensions of the converter have to be defined at the real engine situation.

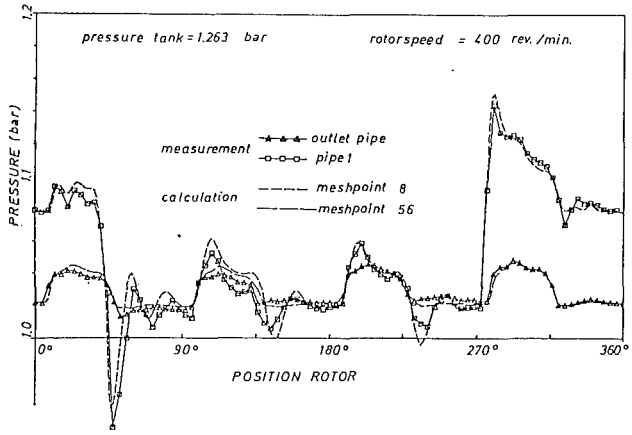

Fig. 8 Comparison of measured and calculated pressures

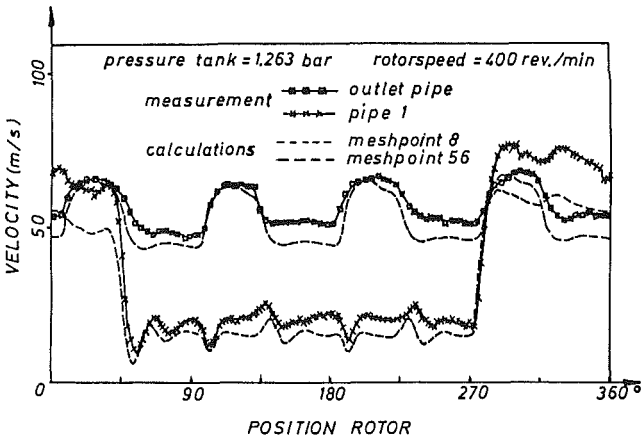

Fig. 9 Comparison of measured and calculated velocities

The influence of the converter on the flow through the exhaust system is also dependent on the conditions of the engine (speed and load), on the valve timing, and on the turbine characteristics.

Comparison of Experimental and Calculated Results

On the Test Rig. Figures 8 and 9 show a comparison between experiments and calculations of the test rig for a rotor speed of 400 rpm and a tank pressure of 1.263 bar. Each rotor gives one blowdown pulse per revolution (one compartment in use) and the calculations are done with the method of calculated pressure loss coefficients for the multipulse converter boundary.

Figure 8 shows close agreement for the measured and calculated pressures at the same location in inlet pipe 1 (at mesh point 8) and in the outlet pipe (at mesh point 56).

Figure 9 shows the comparison of the measured and calculated velocities at the same location as for Fig. 7. The agreement between the two results is qualitatively very good. Nevertheless the measured velocity in the inlet pipe is higher than the calculated one. One reason for this is that the measurements are taken in the middle of the pipe and that the maximum value of the velocity profile is compared with a one-dimensional and thus mean calculated value.

Also in the exhaust pipe, there is a very good qualitative agreement. The quantitative differences in this pipe are nevertheless even more complicated to understand, as here very high flow nonuniformities can occur.

For a Real Engine Situation. Pressure measurements have been carried out in the exhaust system of an eight-cylinder

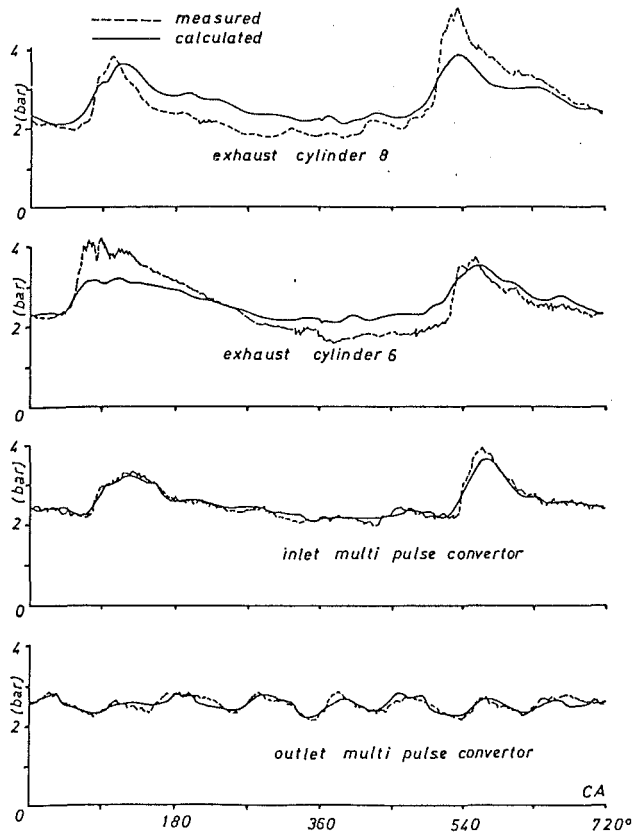

Fig. 10 Calculated and measured pressures in the exhaust system of an eight-cylinder ABC engine

ABC 8 DZC diesel engine for different load and speed conditions [4].

In the laboratory a total simulation program of the power and gas exchange process of this engine is developed [4]. The multipulse converter is simulated with the model of the calculated pressure loss coefficients.

Figure 10 shows the measured and calculated pressure just before and after the multipulse converter (for the engine condition of 1000 rpm and full load = 1768 kW). The agreement is excellent.

Further calculations have shown that for this engine situation, by changing the throat ratio from 54 to 100 percent (by leaving out the partitions in the converter) the specific fuel consumption could be decreased by 2 g./ikWh. The only snag was a small increase of the mean temperature of 2.5°C before the turbine.

In a subsequent paper, more details of this total simulation program, especially of the gas exchange process, and its applications and comparison with experiments will be given.

Conclusions

On a special test rig, which simulates the nonsteady but cyclic flow in the exhaust system of a real engine, pressure and velocity measurements (with LDA) have been carried out.

The measurements have been compared with a numerical simulation of the flow through the multipulse converter of the test rig.

The multipulse converter is considered as a boundary in the method of characteristics. Three different models are used for this boundary: constant pressure model; model with experimental pressure loss coefficients; model with calculated pressure loss coefficients.

The three models are compared. It is clearly seen that the models with pressure loss coefficients (experimental or calculated) take into account the essential features of the pulse converter working principle, such as backflow losses and exchange of momentum in the mixing zone. Neither of these effects is considered by the constant pressure model, which is therefore not suitable for modeling the multipulse converter.

Finally, the numerical model is compared with the measurements on the test rig (pressure and velocity diagrams) and with the measurements in the exhaust system of a real engine (pressure diagrams).

All this proves that the proposed simplified model to calculate the pressure loss coefficients of a multipulse converter [1] results in good agreement with the measurements and can thus be used to optimize the converter geometry for given engine conditions.

Acknowledgments

The research reported in this paper was supported by the Belgian Institute for the Encouragement of Scientific Research in Industry and Agriculture (IWONL IRSIA).

References

1 Flamang, P., and Sierens, R., "Study of the Steady-State Flow Pattern in a Multipulse Converter by LDA," ASME JOURNAL OF ENGINEERING FOR GAS TURBINES AND POWER, Vol. 110, 1988, pp. 515-522.

2 Snauwaert, P., and Sierens, R., "A Study of the Swirl Motion in Direct-Injection Diesel Engines by Laser Doppler Anemometry," *XXIe Fisita Congress*, Belgrade, 1986, Vol. I, pp. 47-54; Paper No. 865007.

3 Sierens, R., and Snauwaert, P., "Study of the Flow Pattern in Compact Manifold Type Junctions by LDA," ASME JOURNAL OF ENGINEERING FOR GAS TURBINES AND POWER, Vol. 109, 1987, pp. 452-458.

4 Van Hove, W., "Simulatiemodel voor de thermodynamische en gasdynamische cyclus van viertakt scheepdieselmotoren (Simulation of the Thermodynamic and Gasdynamic Cycle of Four Stroke, Ship Diesel Engines)," Ph.D. thesis, University of Gent, Belgium, 1989.

5 Flamang, P., and Sierens, R., "Experimental and Theoretical Analysis of the Flow in Exhaust Pipe Junctions," *Trans. IMechE*, 1989, pp. 461-469; Paper No. C382/082.

6 Dimitriadis, C., and Leschziner, M. A., "Computation of Three-Dimensional Flow in Duct Junctions by a Zonal Approach," *Proceedings 4th Int. Conference on Numerical Methods in Laminar and Turbulent Flow*, Swansea, United Kingdom, July 1985, pp. 306-317.

7 Dimitriadis, C., Leschziner, M. A., Winterbone, D. E., Alexander, G. I., and Sierens, R., "Computation of Three-Dimensional Flow in Manifold Type Junctions," *ASME Int. Symposium on Flow and Flow Related Phenomena in Reciprocating Combustion Engines*, Vol. III, ASME SED-Vol. 28, Nov. 1985, pp. 57-62.

8 Baruah, P. C., "A Generalised Computer Program for Internal Combustion Engines Including Gas Exchange Systems," Ph.D. thesis, University of Manchester, United Kingdom, 1973.

9 Benson, R. S., "The Application of Pulse Converters to Automotive Four Stroke Cycle Engines," SAE Paper No. 770034, 1977.

10 Winterbone, D. E., Nichols, J. R., Alexander, G. I., and Sinha, S. K., "The Evaluation of the Performance of Exhaust Systems Equipped With Integral Pulse Converters," Cimac, Int. Congress on Combustion Engines, Oslo, 1985, Paper No. D 62.

11 Winterbone, D. E., Alexander, G. I., and Nichols, J. R., "Developments in Methods of Considering Wave Action in Pipes Connected to I.C. Engines," *ASME Int. Symposium on Flow and Flow Related Phenomena in Reciprocating Combustion Engines*, Vol. III, ASME FED-Vol. 28, Nov. 1985, pp. 71-77.

12 Flamang, P., "Studie van de stroming in juncties van uitlaatsystemen van opgeladen dieselmotoren," Ph.D. thesis, University of Gent, Belgium, July 1989.

13 Vermeersch, K., and Vleurinck, J., "Laser Doppler Anemometrie van de niet-stationaire stroming in een multi pulse converter," End of year thesis, University of Gent, Belgium, 1989.

14 Winterbone, D. E., and Alexander, G. I., "Efficiency of the Manifolds of Turbocharged Engines," *Proceedings of the IMechE*, Vol. 199, No. D2, 1985.

15 Benson, R. S., *The Thermodynamics and Gas Dynamics of Internal Combustion Engines*, Vol. I, J. H. Horlock and D. E. Winterbone, eds., Clarendon Press, United Kingdom, 1982.

A Study of Inlet Flow Distortion Effects on Automotive Catalytic Converters

G. Bella

V. Rocco

Dipartimento di Ingegneria Meccanica
II Universitá di Roma,
00173 Rome, Italy

M. Maggiore

IBM European Center for Scientific and
Engineering Computing,
159-00147 Rome, Italy

This paper will focus on the influence exerted by a nonuniform flow distribution at the inlet of oxidizers to catalytic converters on conversion efficiency evaluated channel by channel. To this aim the flow inside the whole domain, constituted by the exhaust manifold and an elliptic-cross-sectional pipe connecting it with the converter shell, is simulated by means of a three-dimensional fluid-dynamic viscous model. In this way, after assigning typical converter size and geometry (i.e., elliptic) the gas flow rate distribution can be described at its inlet surface, also varying the total mass flow rate. After calculating the flow field at converter inlet by means of a three-dimensional model, evaluation is possible of local flow distortion in comparison with the ideal conditions of constant velocity of the gas entering the honeycomb converter channels. The abovementioned distorted flow field is then assigned as a local boundary condition for another model, developed by the authors, able to describe, through a one-dimensional fluid-dynamic approach, the reacting flow into the converter channels. It was also shown that, due to this flow distortion, honeycomb converters are not uniformly exploited in terms of pollutants of different quantities to be converted in each channel (i.e., a nonuniform exploitation of all the metals coating the ceramic monolith). Finally, the positive effects determined by a diffuser upstream of the converter on flow distribution are analyzed.

Introduction

In order to meet the 1992 European standard limits imposed on pollutant emissions [1] in the community countries, very widespread utilization is to be foreseen of catalytic converters, which have already proved for several years the most effective technical solution able to reduce gaseous emissions from S.I. engines. The most commonly used configuration consists of a honeycomb structure (ceramic or metal) [2], washcoated with a highly porous alumina layer impregnated with active catalyst material promoting pollutant conversion reactions.

The turbulent gas flow coming from the engine first crosses the semiconical pipe connecting the exhaust manifold with the converter shell. Then it enters the monolith passageways (typically of square cross section) inside which, due to their very small dimensions (of about 1 mm), it becomes laminar. Besides many other factors, chemical and thermal processes occurring in converters are then strictly dependent on the mass transfer rate between gas and catalysts, thus determining a great influence of the gas flow field at monolith inlet section [3].

Since evaluation of exhaust gas after-treatment efficiency and monolith thermal stresses is very difficult under any possible engine operating condition, converters are often overdimensioned in terms of both structural strength and catalytic loading in order to meet the required characteristics of high conversion efficiency, reliability, and service life [3]. In fact, since most of the design studies consider the exhaust gas flow uniformly entering the monolith, in each zone of the inlet section, that is assuming a one-dimensional flow field upstream of the converter (while this assumption holds inside monolith channels), the behavior of the whole monolith can only be described by a single channel. In this way such an approach proves to be unable to represent chemical and thermal processes (e.g., reaction rate, gas velocity, etc.) as they occur in each channel [4] as well as, consequently, thermal gradients developing in radial and axial directions in the monolith. Therefore its correct stress and local conversion degree analysis prove to be extremely ineffective.

In fact, in real operating conditions, even if under steady-state flow rate, due to the shape of converter frontal section (generally ellipse shaped), exhaust gas flow coming from manifold tends to enter the central channels of the converter. Therefore peripheral channels are crossed by a smaller gas flow rate, causing a remarkably different exploitation of catalysts, conversion activity being concentrated in the center of the monolith.

Accordingly, an accurate description of the gas flow field at the inlet of the converter has to be performed in order to evaluate how the exhaust gas streamlines are distributed, allowing calculation of the conversion efficiency in each single channel of the monolith.

After considering that in such passageways gas flow is laminar and that the monolith inlet section is usually nonaxisym-

Contributed by the Internal Combustion Engine Division and presented at the Energy-Sources Technology Conference and Exhibition, Houston, Texas, January 20–24, 1991. Manuscript received by the Internal Combustion Engine Division September 1990. Paper No. 91-ICE-13.

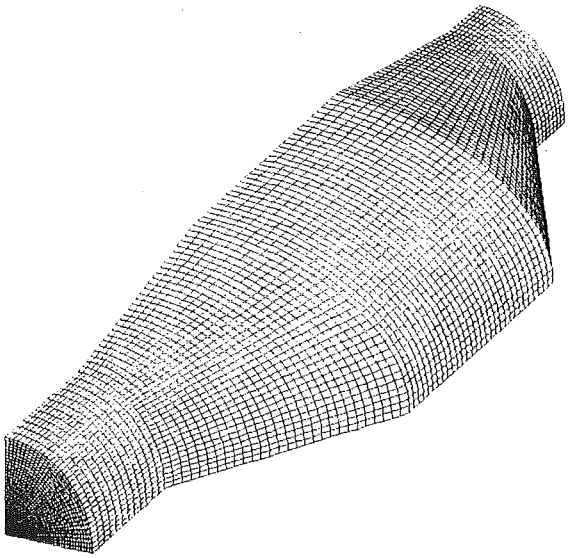

Fig. 1 Computational grid of the exhaust system

Table 1 Properties and design parameters for catalytic converter

Length of the active part of the converter	=	0.15 m
Ellipse maximum radius	=	0.076 m
Ellipse aspect ratio	=	0.566
Surface to volume ratio	=	933.0
Void fraction	=	0.695
Hydraulic radius	=	0.0745 cm
Effective diameter	=	0.00298 m
Number of cells per square inch	=	200
Equivalent open diameter	=	0.0834 m
Thickness of a layer of catalyst	=	.00254 cm
Thickness of wash coat	=	.0127 cm
Wash coat used	=	γ-alumina
Catalyst used	=	Platinum-Palladium
Pre-exponential factor of chemical rate equation for CO	=	1.76 E8 [sec $^{-1}$]
Pre-exponential factor of chemical rate equation for HC	=	0.35 E8 [sec $^{-1}$]
Ratio of activation energy to gas constant for CO and HC	=	8944 [K]

metric, the problem was approached by coupling two different fluid-dynamic mathematical models:

- a three-dimensional model able to describe the flow in the whole exhaust system (Fig. 1) and particularly in the pipe (ellipse-shaped section) connecting the manifold with the converter shell [5];
- a one-dimensional model able to describe the laminar reacting flow occurring in each monolith channel.

In this way the axial flow rate distribution obtained by means of the three-dimensional model can be assigned as boundary condition for the one-dimensional model, which allows one to follow with good accuracy, but without overly long calculation time, chemical and thermo-fluid-dynamic processes in the channels [6, 7].

In order to investigate the nonuniform exploitation degree of noble metals coating ceramic material, a parametric analysis has been performed by varying both exhaust gas flow rate (i.e., engine rpm) and temperature, in the case of an oxidizing catalytic converter; furthermore to the end of reducing the flow distortion, the effect of a diffuser, composed of four semiconical concentric surfaces of infinitesimal thickness placed upstream of the converter (Fig. 2), in this first fluid-dynamic analysis, has been simulated. Besides, it must be underlined that an accurate mathematical optimization of diffuser design could allow a much more uniform exploitation of noble metals covering the reaction surface of catalytic converters.

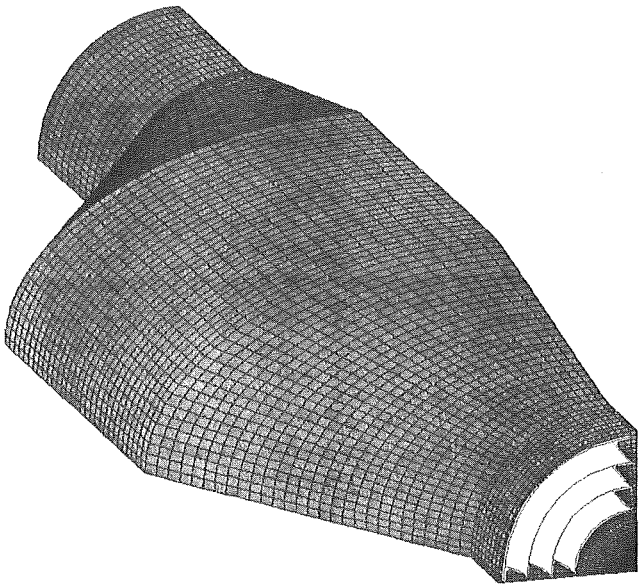

Fig. 2 Schematic of diffuser inlet layout

Theoretical Models

Two different dimensional models have been used to study the influence exerted by a nonuniform flow distribution at the inlet of the oxidizer catalytic converter (whose characteristics are reported in Table 1) on conversion efficiency. To the aim of simulating the behavior of the three-dimensional fluid flow

Nomenclature

A = pre-exponential factor of chemical rate constant, 1/s
D_i = diffusivity of the i species in the gas, m^2/s
D_e = equivalent diameter of the channel, m
E = activation energy of chemical rate constant, J/mole
h = heat transfer coefficient, J/m^2/s/K
k = rate constant m/s
M_w = mean molecular weight of the gas mixture
Q = heat of reaction, J/kg
Re = Reynolds number
R_u = universal gas constant, J/mole/K
S = surface of the channel, m^2
Sc = Schmidt number
$(Sh)_{lim}$ = limiting Sherwood number
t = time, s
T = temperature, K
P = pressure, Pa
u_i = velocity in direction x_i, m/s
u_i' = fluctuating velocity components in direction x_i, m/s
V = volume of the channel, m^3
x = Cartesian coordinate ($i = 1$, 2, 3), m
Y_i = mass fraction of i species
ΔL = converter step length m
μ = gas viscosity, kg/m/s
ρ = gas density, kg/m^3
ω_i = mass rate of production of species, i, $kg/s/m^3$
$(\bar{\ })$ = time-averaged quantity

Subscripts

ch = chemical
g = gas
mt = mass transfer
s = substrate layer of the catalyst
t = total

inside the diffuser connecting the exhaust manifold with the elliptic converter inlet section, the Star I computer code assembled by Computational Dynamics Ltd. has been employed. In fact, this code is able to analyze general three-dimensional problems of incompressible fluid flow, heat and mass transfer by means of a numerical finite volume procedure. In this particular case, in order to describe the gas flow rate distribution inside the whole domain constituted by the exhaust manifold and an automotive catalytic converter, the equations solved by the code Star I are the well-known differential conservation equations

$$\frac{\partial}{\partial x_j}(\rho u_j)=0 \tag{1}$$

$$\frac{\partial}{\partial x_j}(\rho u_j u_i+\tau_{i,j})=-\frac{\partial p}{\partial x_i} \tag{2}$$

in which the stress tensor τ_{ij} for Newtonian turbulent flow is

$$\tau_{ij}=-\mu\left(s_{ij}+\frac{2}{3}\frac{\partial u_i}{\partial x_j}\delta_{ij}\right)+\bar{\rho}\,\overline{u_i' u_j'} \tag{3}$$

where δ_{ij} is the Kroneker delta and s_{ij} is the rate of strain tensor given by

$$s_{ij}=\frac{\partial u_i}{\partial x_j}+\frac{\partial u_j}{\partial x_i} \tag{4}$$

In order to determine the Reynolds stresses and turbulent scalar fluxes a k–ϵ turbulence model has been used, comprising differential transport equation for the turbulent kinetic energy k and its dissipation rate ϵ. The conventional form of the k–ϵ model assumes that the turbulent Reynolds stresses and scalar fluxes are linked to the time-averaged flow properties by

$$\bar{\rho}\,\overline{u_i' u_j'}=-\mu_t s_{ij}+\frac{2}{3}\left(\mu_t\frac{\partial u_i}{\partial x_j}+\rho k\right)\delta_{ij} \tag{5}$$

where the turbulent viscosity η_t is linked to k and ϵ by

$$\mu_t=\frac{C_\mu \rho k^2}{\epsilon} \tag{6}$$

The transport equations used in Star to determine the turbulence energy and its dissipation rate are

$$\frac{\partial}{\partial x_j}\left(\rho\mu_j k-\frac{\mu_t}{\sigma_k}\frac{\partial k}{\partial x_j}\right)=\mu_t s_{ij}\frac{\partial u_i}{\partial x_i}-\rho\epsilon-\frac{2}{3}\left(\mu_t\frac{\partial u_i}{\partial x_j}+\rho k\right)\frac{\partial u_i}{\partial x_j} \tag{7}$$

$$\frac{\partial}{\partial x_j}\left(\rho\mu_j\epsilon-\frac{\mu_t}{\sigma_\epsilon}\frac{\partial \epsilon}{\partial x_j}\right)=C_{\epsilon 1}\frac{\epsilon}{k}\mu_t s_{ij}\frac{\partial u_i}{\partial x_i}-\frac{2}{3}\left(\mu_t\frac{\partial u_i}{\partial x_j}+\rho k\right)\frac{\partial u_i}{\partial x_j}$$
$$-C_{\epsilon 2}\rho\frac{\epsilon^2}{k}+C_{\epsilon 3}\rho\epsilon\frac{\partial u_i}{\partial_i} \tag{8}$$

in which C_k, σ_k, σ_ϵ, $C_{\epsilon 1}$, $C_{\epsilon 2}$, $C_{\epsilon 3}$, $C_{\epsilon 4}$ are further empirical coefficients whose values are given below.

C_μ	σ_k	σ_ϵ	$C_{\epsilon 1}$	$C_{\epsilon 2}$	$C_{\epsilon 3}$	$C_{\epsilon 4}$
0.09	1.0	1.20	1.44	1.92	−0.33	1.44

The mass flow rate, at the inlet section of the catalytic converter, calculated by means of the Star I code has been utilized as boundary condition for a one-dimensional fluid dynamic program, developed by the authors, describing the reacting flow inside every single channel of the converter, so allowing calculation of gas composition along the channel length.

The catalytic converters may usually be represented as a duct of constant cross-sectional area in which the flow is unsteady and chemical reactions occur. The basic equations used to describe these phenomena are:

- one overall mass continuity equation

$$\frac{\partial \rho}{\partial t}+\frac{\partial(\rho u)}{\partial x}=0 \tag{9}$$

- one momentum equation

$$\rho\left(\frac{\partial u}{\partial x}+u\frac{\partial u}{\partial x}\right)=-\frac{\partial p}{\partial x}+\frac{\partial}{\partial x}\left(\mu\frac{\partial u}{\partial x}\right) \tag{10}$$

- one energy equation

$$\rho\frac{De}{Dt}+p\frac{\partial u}{\partial x}=\dot{Q} \tag{11}$$

- N-1 species equations

$$\frac{\partial Y_i}{\partial t}+u\frac{\partial Y_i}{\partial x}+\frac{1}{\rho}\frac{\partial(\rho Y_i u_i)}{\partial x}=\frac{\omega_i}{\rho} \tag{12}$$

In this case N is equal to 13 and the species considered are H_2O, H_2, OH, H, N_2, NO, N, CO_2, CO, O_2, O, Ar, and C_3H_8.

- one equation of state for gas

$$p=\rho R_u T\Sigma\frac{Y_i}{W_i} \tag{13}$$

To the end of evaluating the overall reaction rate k_{T_i} and the heat released during the reactions the methodology proposed by Benson has been applied. The chemical reactions used in the model include the oxidation of CO and HC. The conversion of NO_x cannot be currently predicted due to the lack of a reliable kinetics model. In addition, in the present work the fresh catalyst condition has been considered. Thus only the two following chemical reactions take place on the catalyst surface:

$$CO+\frac{1}{2}O_2\rightarrow CO_2 \tag{14}$$

$$C_3H_8+5O_2\rightarrow 3CO_2+4H_2O \tag{15}$$

Therefore, the overall process of conversion of the reactants into products in an automotive catalytic converter involves a number of sequential steps. At first the reactants transfer from the flowing streamline to the external surface of the catalyst. Then they diffuse into the porous of the substrate of alumina layer and, finally, they are adsorbed on the active catalyst sites when the reaction occurs [8, 9]. In the same manner reaction products come back to the gas flowing through the channel. For these reasons the overall rate constant can be represented by two rate-limiting processes in series:

- the mass transfer of the reactants from the gas to the active catalyst sites;
- their effective chemical reactions.

Thus the overall rate constant k_T can be represented for each reactive species as:

$$\frac{1}{k_{T_i}}=\frac{1}{k_{mt_i}}+\frac{1}{k_{ch_i}} \tag{16}$$

in which the mass transfer and chemical reactions rate can be evaluated by means of

$$K_{ch_i}=A_i\exp\left(-\frac{E_{a_i}}{RT_s}\right) \tag{17}$$

$$k_{mt_i}=\frac{D_i}{D_e}(\mathrm{Sh})_{\lim}\left(1+0.095 D_e \mathrm{Re}\frac{\mathrm{Sc}}{\Delta L}\right)^{0.45} \tag{18}$$

In this paper, as stated before, the authors only consider oxidation reactions of CO and HC and assume the oxidation rate of these two species on catalyst sites proportional to their concentrations in the gas flow, to overall rate constant, and to the characteristic geometric ratio between the total surface of converter channels and its volume.

Then the mass conversion rate for the ith species can be expressed by

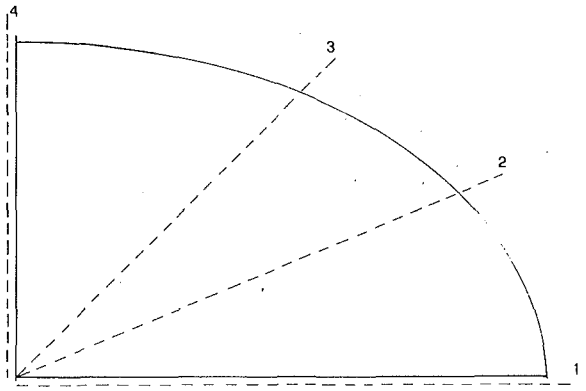

Fig. 3 Frontal section of the converter with reference planes (dashed lines)

$$\omega_i = -k_{T_i} \frac{S}{V} x_i \rho_g \tag{19}$$

Oxidation rate is independent of the concentration of oxygen, only if enough oxygen is present in the gas streamlines. The heat generated from oxidizing reactions can be evaluated by means of

$$Q = \frac{\Delta X_{CO} Q_{CO} + \Delta X_{C_3H_8} Q_{C_3H_8}}{M_w} \tag{20}$$

Finally, the surface temperature of the substrate layer of the catalyst, utilized to evaluate the chemical reaction rate, can be calculated by

$$T_s = T_g + \frac{\rho u Q}{h \Delta L (S/V)} \tag{21}$$

Equations (1)–(23) have been solved by means of a numerical finite difference technique.

Three-Dimensional Flow Steady-State Analysis

The flow field at converter inlet has been calculated by means of the abovedescribed three-dimensional finite volumes fluid-dynamic model applied to the whole control volume (Fig. 1) constituted by:

- the last part of exhaust manifold;
- the abovementioned ellipse-shaped duct connecting it with the converter shell;
- the honeycomb monolith itself and the exhaust final duct.

In the same figure the computational grid schematizing the system, in which 125,000 calculation cells have been considered, is represented.

Thanks to the fluid-dynamic symmetry, the controlled volume reduces to the one shown in Fig. 1. For this reason, besides wall surfaces, physical boundary conditions have been imposed only at the inlet and the outlet of calculation domain as follows:

- inlet section: constant gas velocity;
- outlet section: zero gradients along flow streamlines (fully developed flow field).

In Fig. 3 the frontal section of converter is illustrated and the four dashed lines indicate the orthogonal planes corresponding to the cross sections on which, the tangential components of gas velocity being nearly negligible in all the examined cases (maximum value is always smaller than 10 percent of bulk axial velocity), the calculated flow distributions have been visualized in two-dimensional form.

The two-dimensional flow fields (vector length denotes velocity intensity) shown in Figs. 5(*a–d*) have been calculated for an average steady-state velocity at the exit of exhaust manifold of 10 m/s, corresponding to about 1000 rpm for a two-liter engine, and respectively refer to the above mentioned sections 1–4.

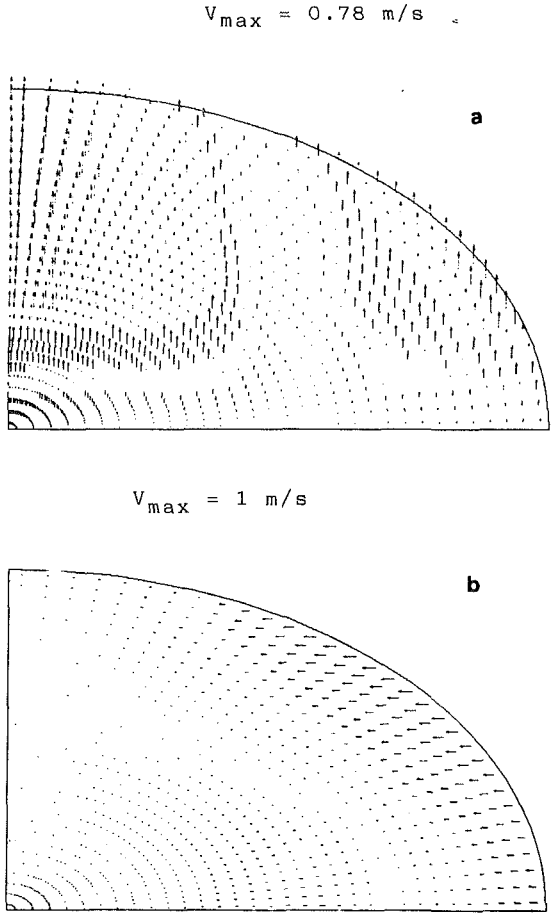

Fig. 4(*a, b*) *U, V* velocity components at inlet section of converter for inlet velocity of 10 m/s

Figure 5(*a*) corresponds to the less favorable flow condition. In fact, in this case the divergence angle of the semiconical duct connecting the exhaust manifold with the converter shell reaches maximum value, causing the flow separation and a well-developed vortex in the corner region of converter inlet section.

As a consequence of the vortex, total pressure drops and a reverse flow through the monolith peripheral channels occurs in this region.

This vortex, as expected, tends to be extinguished while moving toward sections (see Fig. 4) corresponding to divergence angles decrease. Figures 5(*b–d*) well illustrate how vortex (intensity and extension) decreases in the flow fields (Figs. 5*b*, *c*) and finally disappears (Fig. 5*d*) when the divergence angle is very small. Figure 6 represents the frontal view of velocity axial component flowing through the converter passageways.

What is observed in Figs. 5(*a–d*) is well depicted by the isolevel curves in Fig. 6, which represent the axial flow intensity that, as previously noticed, achieves maximum value in the proximity of the converter inlet section central zone.

The effect of junction-duct divergence angle is also clearly shown in this figure. In fact, significant flow recirculation can be noticed on the left side of the converter inlet corresponding to the maximum divergence angle (see also Figs. 5*a–c*), while where this angle is smaller (see also Fig. 5*d*) no recirculation occurs.

Moreover Fig. 6 clearly shows how under such flow field conditions, a large portion of monolith inlet section (marked with dashed lines) is actually not utilized, since it is not intersected by the crossing flow and, consequently, all the channels included in such a zone are not involved in exhaust gas aftertreatment.

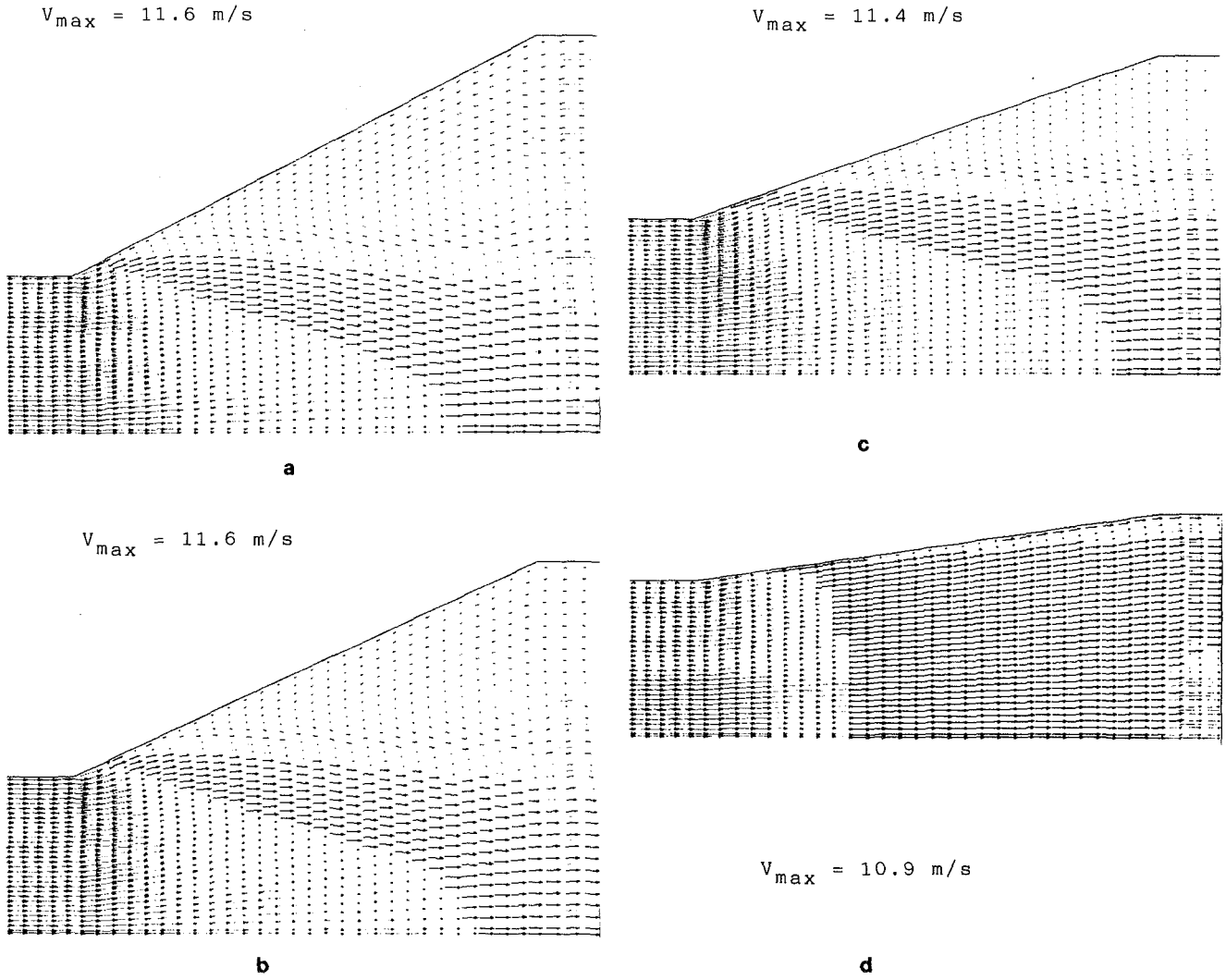

Fig. 5(*a, b, c, d*) Flow distribution for reference axial planes 1, 2, 3, and 4, respectively, for inlet velocity of 10 m/s

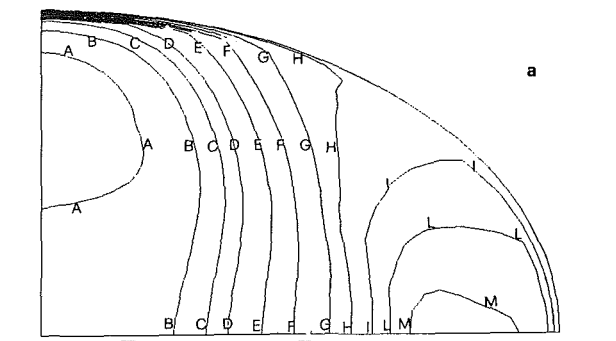

[M/S]		C	=	5.1	F	=	3.2	I	=	1.3
A	=	6.3	D	=	4.4	G	=	2.6	L	=	-0.6
B	=	5.7	E	=	3.8	H	=	1.9	M	=	-1.2

Fig. 6 Iso-axial velocity plot at converter frontal section for inlet velocity of 10 m/s

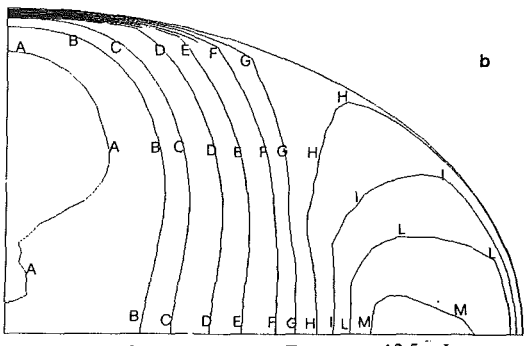

[M/S]		C	=	20.1	F	=	12.5	I	=	4.8
A	=	25.3	D	=	17.6	G	=	9.9	L	=	-2.8
B	=	22.7	E	=	15.0	H	=	7.4	M	=	-5.4

Fig. 7 Iso-axial velocity plot at converter frontal section for inlet velocity of 40 m/s

In order to evaluate the influence exerted by velocity intensity on flow distribution, the three-dimensional analysis has also been performed by assigning the average gas velocity at the exhaust manifold outlet a greater value equal to 40 m/s, corresponding to about 4000 engine rpm.

As in the latest analyzed case, Figs. 8(*a–d*) illustrate the flow pattern in two-dimensional form visualized in the same sections orthogonal to converter frontal surfaces shown in Fig. 3.

A comparison between these flow fields with the corresponding ones described in Figs. 5(*a–d*) shows that while vortex intensity increases, gas momentum being greater at exhaust manifold outlet, its extension substantially remains unchanged

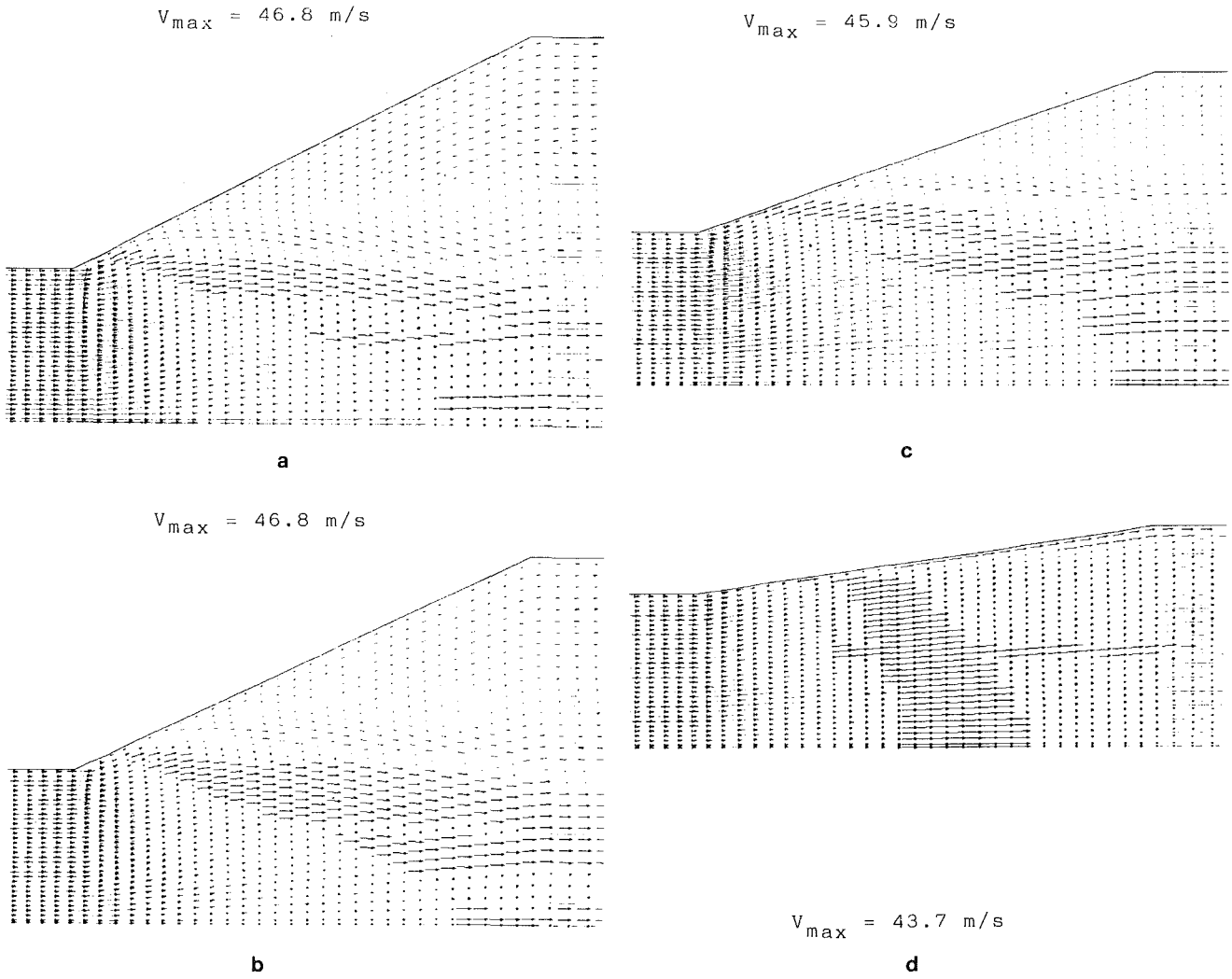

Fig. 8(*a*, *b*, *c*, *d*) Flow distribution for reference axial planes 1, 2, 3, and 4, respectively, for inlet velocity of 40 m/s

(see, respectively, Figs. 8*a–c* and Fig. 5*a–c*). This behavior can be explained by the consideration that, varying average gas velocity from 10 to 40 m/s, the Reynolds number does not change significantly in both the examined flow fields and, in any case, assumes very high values ($>10^5$).

Figure 7 shows the same situation already shown in Fig. 6 of a large portion of monolith inlet section intersected by gas flow recirculation.

After analyzing the free flow condition at the exhaust manifold exit, the influence exerted by the above described diffuser (see Fig. 2), inserted upstream of the converter, on gas rate distribution through honeycomb monolith channels is presented in the following paragraph.

Since we are only interested in the influence exerted by the diffuser on flow distortion, the less favorable geometric condition previously found (Figs. 5*a* and 8*a*) is illustrated.

Diffuser effect is well described in the Figs. 9(*a*) and 10(*a*) and Figs. 9(*b*) and 10(*b*), which respectively represent in two-dimensional form the flow patterns calculated for 10 and 40 m/s. In fact by comparing these graphs (Figs. 9*a* and 9*b*) with the analogous ones obtained for the free flow condition (Figs. 5*a* and 8*a*) a nearly complete absence of vortices in flow fields can be immediately recognized, also in this case of maximum divergence angle value of semiconical duct. Finally it has to be remarked that besides eliminating gas recirculation in converter channels, the diffuser action greatly affects the distribution of the mass rate entering the monolith channels. In both the cases represented in Figs. 10(*a*) and 10(*b*), as a consequence of the free vortex flow, it can be observed that nearly all passageways are crossed by exhaust gas and, in addition, the axial velocity intensity moving from peripheral to central channels still increases, but with a smaller radial gradient (compared respectively with Figs. 6 and 8), allowing a better, even if not yet uniform, catalyst exploitation.

One-Dimensional Analysis of Reacting Flow

The one-dimensional calculation model previously described has been utilized in order to analyze the effects of inlet gas velocity and temperature on catalytic conversion efficiency.

The composition expressed in molar fraction of the reactant species present in gas flow entering the converter monolith is

$$CO = 0.0015 \quad HC = 0.000275 \quad O_2 = 0.012$$

In addition, this composition has been chosen according to slightly lean combustion conditions. So it is to be observed that in such cases, as remarked before, oxygen mass fraction is sufficient to assure the complete oxidation of carbon monoxide and unburned hydrocarbons.

As shown by three-dimensional fluid-dynamic analysis, axial velocity of the flow entering the converter monolith differs

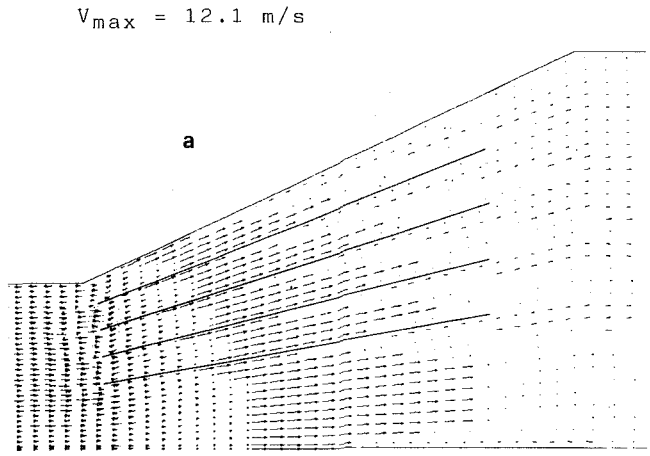

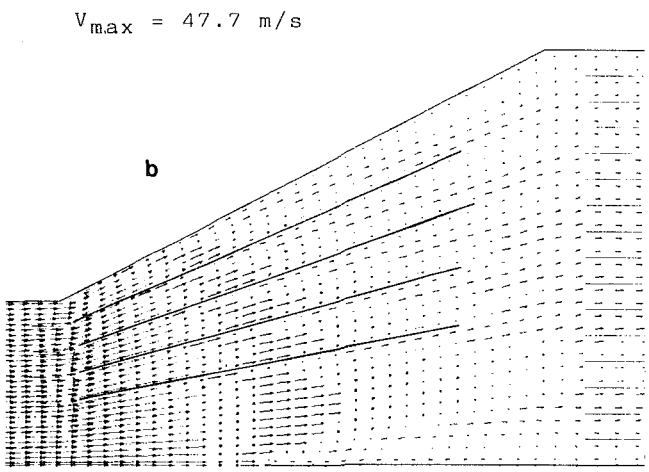

Fig. 9(*a*, *b*) Flow distribution with diffuser (bold lines) for reference axial plane 1 and inlet velocities of 10 and 40 m/s, respectively

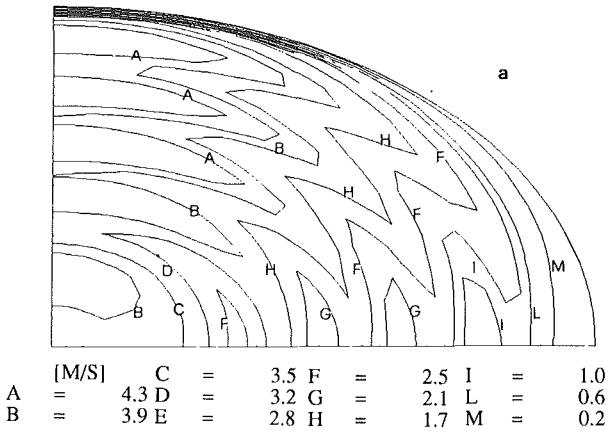

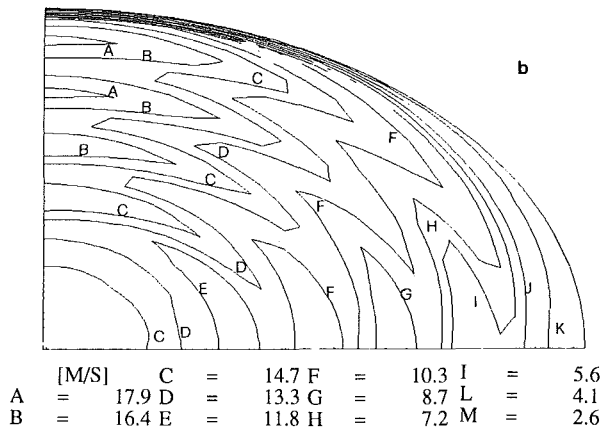

Fig. 10(*a*, *b*) Iso-axial velocity plot of converter frontal section for inlet velocities of 10 and 40 m/s, respectively

substantially while moving from peripheral to central channels and maximum values (of about 25 m/s) are usually achieved under free flow condition.

For this reason the one-dimensional calculation of the reacting flow has been performed by varying axial velocity between 5 and 25 m/s in order to represent any possible mass rate distribution at the converter inlet; while, with the aim of evaluating exhaust gas temperature influence on oxidizing reaction rate, two values have been considered: 700 and 900 K.

Figures 11(*a*) and 11(*b*) show the effect of inlet velocity, for a fixed exhaust gas temperature, equal to 700 K, on the CO and HC conversion versus nondimensionalized channel length.

As far as the CO species is concerned, an almost complete conversion is achieved for residence times corresponding to inlet gas velocities not greater than 10 m/s. The same behavior can be observed in Fig. 11(*b*) for HC species, even if, in such a case, the conversion reaction needs longer time, requiring the exploitation of a greater portion of channel surface.

When gas enters monolith passageways at higher velocities (i.e., 20 and 25 m/s) CO and HC behave differently. In fact, in the less favorable case of 25 m/s (generally achieved in the proximity of monolith central zone) as shown in Fig. 11(*a*), a good CO conversion efficiency is still reached (roughly 90 percent). On the contrary, as a consequence of lower values of chemical reaction rate, unburned hydrocarbon conversion efficiency remains lower than about 50 percent in the monolith channels into which exhaust gas enters at highest velocity.

The effect due to exhaust gas temperature can be analyzed by comparing Figs. 12(*a*) and 12(*b*) (referring to 900 K), respectively, with Figs. 11(*a*) and 11(*b*). As expected, a higher gas temperature, by promoting faster chemical reactions, improves conversion efficiency for both CO and HC species, the latest thus achieving a significantly greater value of about 70 percent.

Conclusions

A three-dimensional fluid-dynamic model (running on an IBM 3090 VF 600 E) has been used to investigate the flow pattern at a converter inlet, in order to provide the distribution of the exhaust gas rate entering the monolith passageways. By assuming such a flow distribution, the reacting flow inside the single channels has been simulated by means of a one-dimensional model developed by the authors.

After pointing out the effectiveness demonstrated by a diffuser, inserted upstream of the converter inlet, in eliminating flow separation and in more uniformly distributing the flow entering the converter, some concluding remarks can be made.

In the case of free flow a large portion of converter inlet section does not remain involved by gas coming from exhaust manifold. In this case the most part of pollutant conversion is concentrated in the central monolith passageways; for this reason a large nonuniform catalyst exploitation occurs.

As a result of this behavior, a fast depletion of the noble metals covering the surface of central channels can occur with a consequent undoubtable influence in efficient converter operating life.

Besides these effects, as previously shown in one-dimensional analysis of reacting flow, because of overly high velocities of exhaust gas entering some zones of the converter inlet

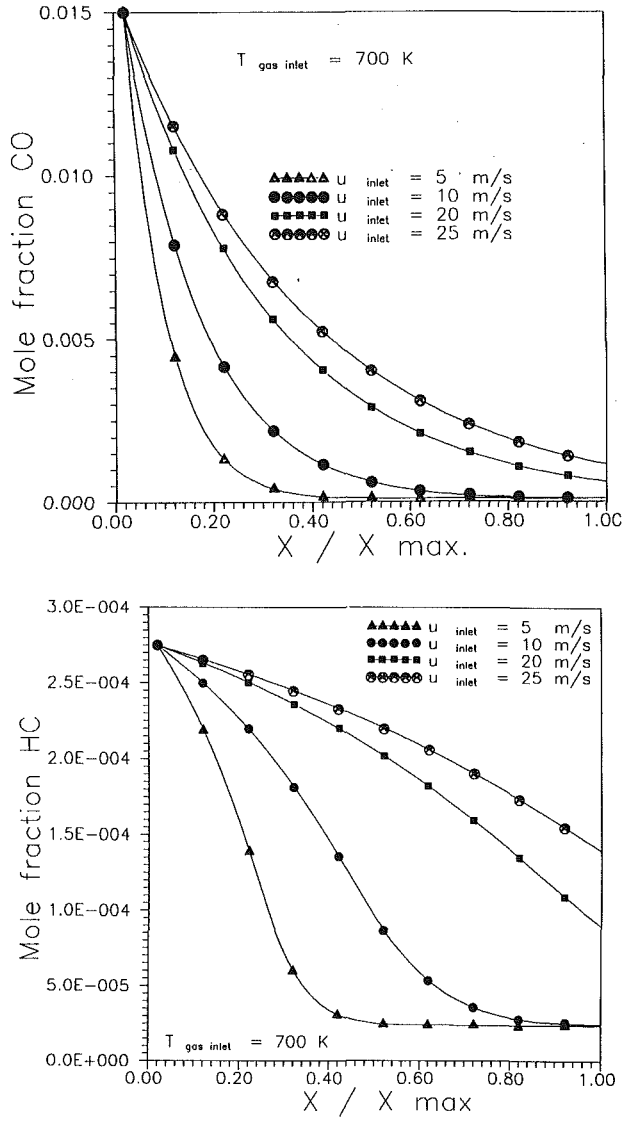

Fig. 11(*a*, *b*) HC and CO molar fraction plot versus nondimensional channel length for inlet gas temperature of 700 K and different inlet gas velocities

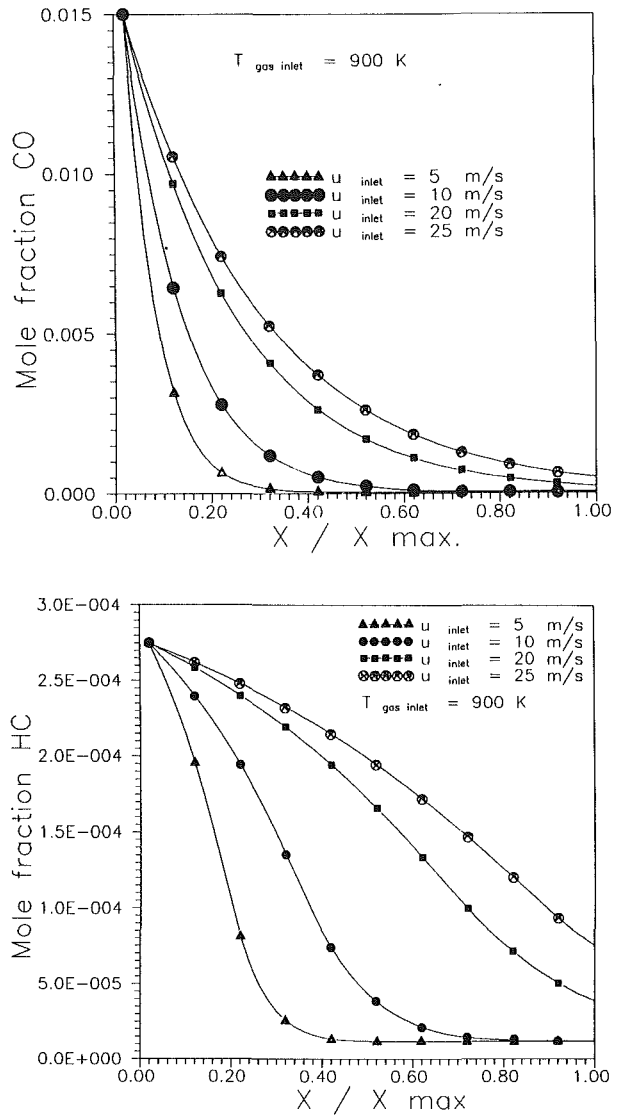

Fig. 12(*a*, *b*) HC and CO molar fraction plot versus nondimensional channel length for inlet gas temperature of 900 K and different inlet gas velocities

section, particularly unburned hydrocarbons can only be partially oxidized.

In order to minimize the two undesirable effects of nonuniform catalyst exploitation and of too short gas residence time in the monolith, both due to free flow distortion, the action of a diffuser has been investigated. As expected, the diffuser presence, even if not carefully designed in this first study, provided a significative improvement of catalytic converter operating conditions, demonstrating the usefulness of investigating diffuser geometric shape.

An optimization of such diffuser design, due to the large number of possible shapes to be tested, can be solved through a computational fluid-dynamic approach. In fact, in this way, the number of probable best shapes can be substantially reduced to only few configurations to be finally tested.

References

1 Bonardo, R., and Mortara, W., "Emission Control System to Meet European Standards and Insure Low Fuel Consumption," SAE Paper No. 905117, 1990.

2 Baruah, P. C., Benson, R. S., and Gupta, H. N., "Performance and Emission Predictions for a Multi-cylinder Spark Ignition Engine With Catalytic Converter," SAE Paper No. 780672, 1978.

3 Chen, D. K. S., Bisset, E. J., Oh, S. H., and Van Ostrom, D. L., "A Three-Dimensional Model for the Analysis of Transient Thermal and Conversion Characteristics of Monolithic Catalytic Converters," SAE Paper No. 880282, 1988.

4 Chen, D. K. S., and Cole, C. E., "Numerical Simulation and Experimental Verification of Conversion and Thermal Responses for a Pt/Rh Metal Monolithic Converter," SAE Paper No. 890798, 1989.

5 STAR I Manual, Computational Dynamics Ltd., 1988.

6 Bella, G., Feola, M., and Rocco, V., "Analisi delle Caratteristiche Funzionali dei Convertitori Catalitici Ossidanti per Motori a C.I. as Accensione Comandata," presented at the XLII Congresso Nazionale A.T.I., Genova, Italy, 1987.

7 Johnson, W. C., and Chang, J. C., "Analytical Investigation of the Performance of Catalytic Monoliths of Varying Channel Geometries Based on Mass Transfer Controlling Conditions," SAE Paper No. 740196, 1974.

8 Vaneman, G. L., "Performance Comparison of Automotive Catalytic Converter: Metal vs. Ceramic Substrates," SAE Paper No. 905115, 1990.

9 Gulati, S. T., Summers, J. C., Linden, D. G., and White, J. J., "Improvements in Converter Durability and Activity via Catalyst Formulation," SAE Paper No. 890796, 1989.

10 Kuo, K. K., *Principles of Combustion*, Wiley, New York, 1986.

Three-Dimensional Computations of Flow and Fuel Injection in an Engine Intake Port

T.-W. Kuo

S. Chang

Engine Research Department,
General Motors Research Laboratories,
Warren, MI 48090

An existing multidimensional in-cylinder flow code, KIVA, was modified to calculate gas flow and fuel injection in a simplified (no valve stem and simplified valve-head geometry) engine intake port. A single-cylinder engine simulation program was used to specify the initial and boundary conditions for flow calculations. A previously developed spray model was also used to simulate pressure-atomized spray with iso-octane as the fuel. Three cases with increasing degrees of complexity were considered: (1) an impulsively started port flow with both port ends open (the inlet-boundary velocity was changed from zero to a finite value at the start of computation), (2) an impulsively started port flow with one port end partially blocked to simulate gas flow through the valve annulus, and (3) port flow driven by the time-varying gas flow rate through the valve annulus calculated using a single-cylinder engine simulation program. A spray calculation was also made for each case. The calculations indicate that the KIVA code can be modified to conduct computations with complicated port geometries and open flow boundary conditions. The results also indicate that both gas flow and fuel-injection processes and port geometry have a strong influence on the details of fuel induction into the cylinder. This confirms that consideration of both gas flow and fuel-injection processes is necessary in order to understand the mechanisms of fuel–air mixing in an engine intake port employing port fuel injection.

Introduction

Engines with port fuel injection (PFI) systems have become popular as a means of improving vehicle performance through faster response and higher specific output. A recent study by Quader [1], however, has revealed the importance of fuel injection and vaporization on smoke and hydrocarbon (HC) emissions in a single-cylinder PFI engine. In particular, smoke formed under high-speed and heavy-load driving conditions can cause soot contamination of the engine oil. Furthermore, previous studies with PFI engines [2] indicated that the poorest engine performance resulted when beginning of injection was timed during the first 90 crack-angle degrees of the intake stroke. The reason for the combustion degradation is, however, not well understood. Also, there is current interest in engines that operate on alternative fuels such as methanol. The lower energy content per unit mass and higher latent heat of vaporization of methanol could add additional difficulties in using alternative fuels with PFI systems. Understanding and optimizing the fuel-injection related parameters are needed for better PFI system design.

The research described in this paper represents a first step aimed toward establishing a comprehensive computer model for analyzing the fuel-injection process in PFI engines. To this end, the General Motors Research Laboratories (GMR) version of the KIVA code was used. It was chosen because of its proven performance [3–5]. In particular, the same code with some modifications has been used quite successfully to consider in-cylinder flow, fuel injection, and combustion in both four- and two-stroke premixed-charge and fuel-injected engines employing practical chamber geometries and open flow boundaries. Furthermore, GMR's version of the KIVA code includes a state-of-the-art spray model that considers the effect of spray/wall impingement, which is important to the success of this study. Thus, the objectives of this work are (1) to modify the multidimensional in-cylinder flow code KIVA to study gas flow and fuel injection in an engine intake port, and (2) to apply the port-flow code to a port-fuel-injected engine to demonstrate the detailed information and understanding that can be added to port-fuel-injection related studies.

This paper is organized as follows. First, the flow model used in this study is briefly described. Then, details are given of the geometry and spray models. The results are divided into three parts according to three case scenarios with increasing degrees of complexity.

Submodel Descriptions

Flow Model. The computations were made using the KIVA computer program, which solves three-dimensional equations of transient chemically reactive fluid dynamics. Since chemical

Contributed by the Internal Combustion Engine Division and presented at the Energy-Sources Technology Conference and Exhibition, Houston, Texas, January 20–24, 1991. Manuscript received by the Internal Combustion Engine Division September 1990. Paper No. 91-ICE-4.

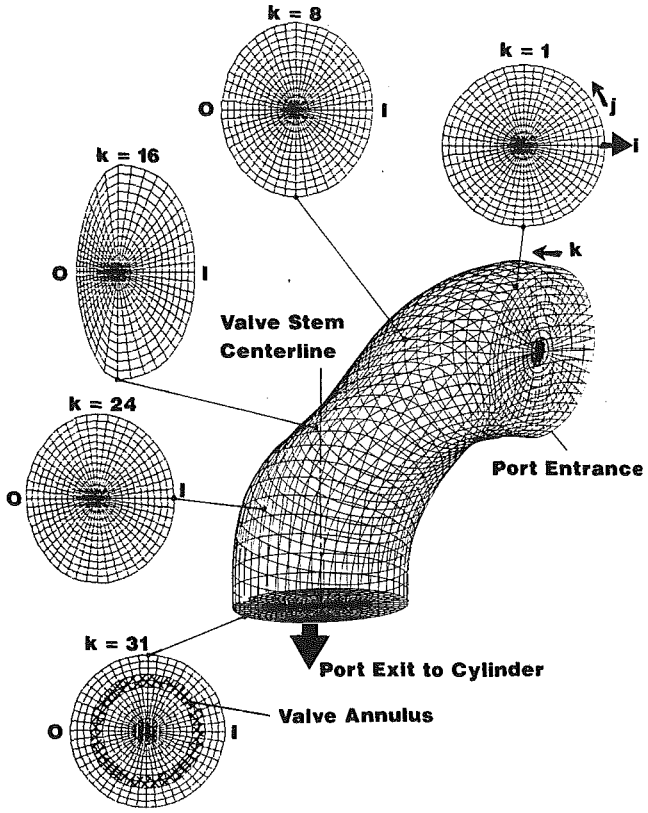

Fig. 1 Three-dimensional perspective and two-dimensional section (at five k index positions) views of the computational grids used for port-flow calculations; *I*: inside of bend; *O*: outside of bend; *i, j, k*: grid indices in the radial, circumferential, and forward flow directions, respectively

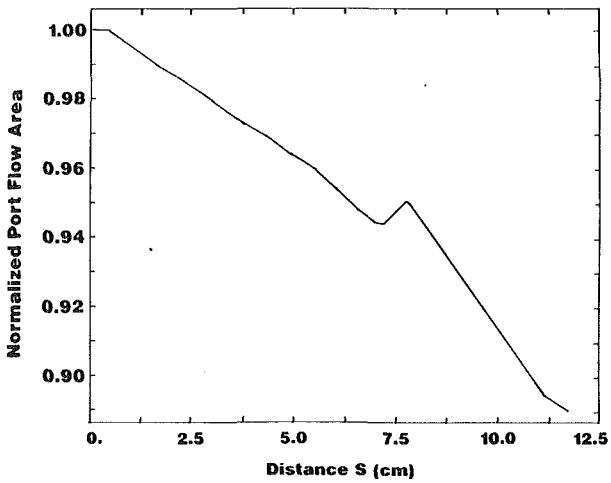

Fig. 2 Normalized port flow area as a function of distance from port entrance along the port centerline

reactions are relatively unimportant in port-flow calculations, they were not considered in this study. The equations and the numerical-solution method are discussed in detail by Amsden et al. [6, 7]. Brief descriptions of the grid generation and spray model used in the present study are presented in the following sections.

Port Geometry. The finite difference grid used in the computation is shown in Fig. 1. This port was designed for a research-type two-valves-per-cylinder engine except that the valve stem and guide have been ignored. There are 13 grid points in the radial direction (i), 49 grid points in the circumferential direction (j), and 31 grid points in the forward flow direction (k) resulting in 19,747 computational grid points. The port length along the centerline is approximately 11.5 cm and the bend angle is 90 deg. The gas flow in the port is expected to be highly three dimensional due to changes in both flow direction and cross-sectional shape. In particular, circular cross sections were used at the inlet ($k=1$) and the outlet ($k=31$). For intermediate planes, however, ellipses of different aspect ratios were used.

Furthermore, the port flow area decreases with increasing distance (S) away from the port entrance as shown in Fig. 2 (note the scale used on the vertical axis). In particular, the flow area at the port exit is about 11 percent smaller than that at the port entrance for the port examined. (The slight increase in port flow area at S = 7.5 cm was introduced to account for the existence of a valve stem. The effective port flow area actually decreases if the valve stem is inserted. However, due to difficulty in grid generation, the valve stem was not considered in this study.) The simultaneous change in cross-sectional area and shape in the intake port is needed for minimum pressure loss of internal flow bends, which eventually translates into better engine breathing and higher power output.

Spray Model. The fuel-injection process was modeled using a computationally efficient stochastic, parcel-injection method [6, 7]. In this technique, each computational parcel represents a group of drops with similar physical attributes. The drops exchange mass, momentum, and energy with the gas through source terms in the gas equations. Turbulence dispersion, drop breakup and coalescence, drop vaporization, and spray/wall impingement effects are included in the model as described in [8–10]. Further details about the spray model are given by Amsden et al. [6, 7].

A solid cone, pressure-atomized spray was simulated in this study. The initial drop size was assumed to be 20 μm in diameter for all cases examined. The injected drop velocity was specified and held constant during the injection. It had a value of 60 m/s unless otherwise stated. The injected drop temperature was 320 K and the spray half angle was assumed to be 15 deg. The amount of fuel injected was 10 mg for all cases, and the fuel used was iso-octane.

Nomenclature

BTDC = before top dead center
EOI = end of injection
H = minimum value plus 90 percent of the difference between the maximum and minimum value in the port
i = grid index in the radial direction
I = inside of bend
IMEP = indicated mean effective pressure
IVC = intake-valve closing
IVO = intake-valve opening
j = grid index in the circumferential direction
k = grid index in the forward flow direction
L = minimum value plus 10 percent of the difference between the maximum and minimum value in the port
NP = number of spray drops
O = outside of bend
S = distance from port entrance along port centerline
SOI = start of injection
UMAX = maximum vertical-velocity component
WMAX = maximum horizontal-velocity component

Case Scenarios

This section is separated into three parts according to the three test cases computed. These calculations were made with an increasing degree of complexity to ensure that the KIVA code was working properly. The three cases are: (1) an impulsively started port flow with both port ends open (the inlet-boundary velocity was changed from zero to a finite value at the start of computation), (2) an impulsively started port flow with one port end partially blocked to simulate flow through the valve annulus, and (3) port flow driven by the time-varying gas flow rate through the valve annulus calculated using the engine simulation program.

Impulsively Started Port Flow With Both Port Ends Open

Initial and Boundary Conditions. The working fluid used in this calculation was air, and the initial thermodynamic conditions (temperature and pressure) in the port were assumed to be uniform at 320 K and 101 kPa corresponding to engine operation at wide open throttle. The initial gas velocity was zero everywhere except at the port entrance ($k = 1$, see Fig. 1) where a fixed inflow air velocity of 24 m/s was specified at the start of computation. The boundary condition at the port exit was zero velocity gradient in the direction of flow.

Results and Discussion. Figure 3 shows the computed (a) velocity vectors and (b) pressure contour plots at 4 ms after the start of computation in a vertical plane cutting through the port centerline. The flow fields remain essentially unchanged thereafter since the computation has reached its steady state value. The 4 ms required for this impulsively started port flow to reach the steady-state solution agreed quite well with that estimated using the empirical steady-time correlation of Kuo et al. [11]. This finding is interesting since the empirical steady-time correlation [11] was derived based on calculations with impulsively started flow in a straight pipe rather than the complicated port geometry considered in the present study.

The computed velocity fields were plausible and showed an increase in velocity in the direction of flow due mainly to the reduction of port flow area mentioned earlier. (UMAX and WMAX represent the maximum vertical- and horizontal-velocity components in the cutting plane.) In particular, the exit velocity peaks near the inside of the bend due to a shorter flow path and a lower wall shear resistance over the inside of the bend. Furthermore, no flow separation on the inside of the bend was predicted.

The computed pressure fields were also plausible. (The contours marked by the letters H and L are drawn through those points having pressures of 90 and 10 percent of the difference between the maximum and the minimum pressure in the cutting plane, respectively. The interval between the contours is 10 percent of the difference between the maximum and the minimum values.) In particular, for flow in the outside of the bend, the high-pressure contours were found at the concave regions. This is caused by flow acceleration and deceleration as a result of port flow area change in the direction of flow (see Fig. 2).

At 4.0 ms, the spray model was activated and injection started for a duration of 0.75 ms. The input parameters used for spray calculations were given previously in the section on the spray model and the direction of injection is indicated in Fig. 4. Also shown in Fig. 4 are computed spray drops, velocity vectors, and fuel-vapor contour plots at (a) 4.5 ms during fuel injection), (b) 5.0 ms (0.25 ms after the end of injection), and (c) 6.5 ms after the start of computation. The spray-drop distributions are line-of-sight plots of all computational parcels existing in the port (the total number of parcels equals NP). Each dot or open circle represents the location of a parcel. The circle diameter, however, represents the size of the droplets contained in the parcel.

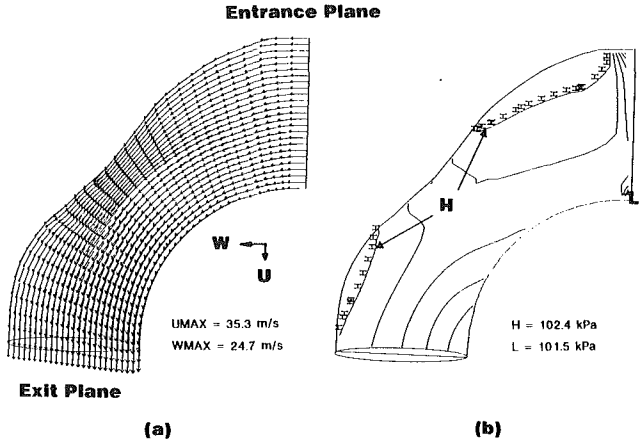

Fig. 3 Computed *(a)* velocity vectors and *(b)* pressure contour plots at 4 ms after the start of computation for the case of impulsively started port flow with both port ends open

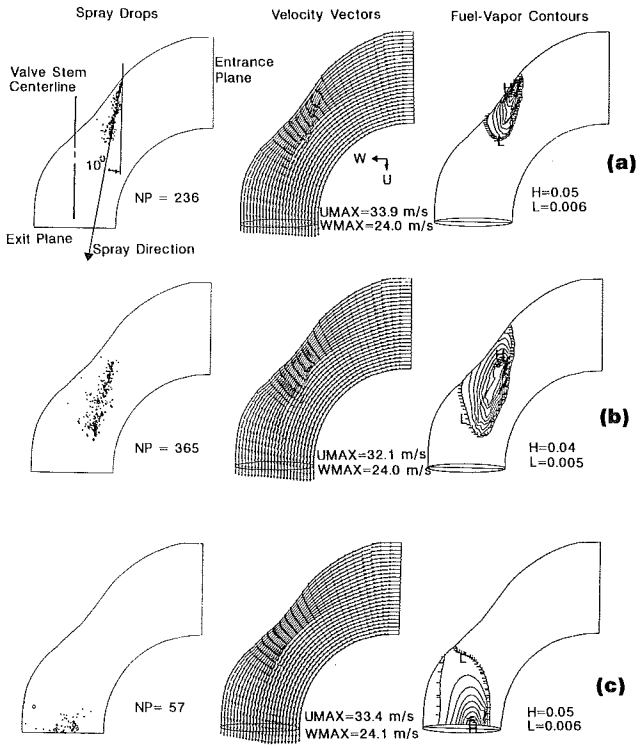

Fig. 4 Computed spray drops, velocity vectors, and fuel-vapor contour plots at *(a)* 4.5 ms, *(b)* 5.0 ms, and *(c)* 6.5 ms after the start of computation (injection at 4.0 ms) for the case of impulsively started port flow with both port ends open

Three observations can be made from Fig. 4. First, Fig. 4(a) indicates that the fuel-injection process influenced the gas flow near the injector somewhat due to the high drop injection velocity. (The drop injection velocity was 60 m/s and the local gas velocity at the injector tip was about 30 m/s.) The high drop injection velocity, as compared to the local gas velocity, also resulted in minimal spray deflection, although the fuel-vapor contours were deflected somewhat by the gas flow.

Second, Figs. 4(b) and 4(c) show that, after the end of injection, both the drops and fuel vapor continue to penetrate and eventually leave the port. After the majority of the spray has left the port, the initial flow field is recovered as shown by comparing the velocity-vector plots of Figs. 4(c) and 3(a).

Third, this study has demonstrated the capability to make three-dimensional gas flow calculations under both steady flow and transient fuel injection conditions.

Impulsively Started Port Flow With One Port End Partially Blocked

Initial and Boundary Conditions. The working fluid and the initial thermodynamic properties and velocities in the port were the same as those used in the previous calculation. At the port entrance, a fixed value of 24 m/s was again imposed to start the calculation. At the port exit, however, the flow area was partially blocked, and the gas was forced to leave the port through a simulated valve annulus. In particular, all computational grids at the port exit (k = 31, see Fig. 1) with an i index between 7 and 9 were assigned as open boundaries. Otherwise, a solid-wall boundary condition was imposed. The width of the annulus was 4.5 mm. The geometric flow area through the annulus was equivalent to that of a valve with a diameter of 26 mm, a lift of 6.4 mm, and a seat angle of 45 deg.

The velocity at the port exit was calculated using gas dynamical equations of nozzle flow based on pressure differences between the port and ambient. The ambient pressure was assumed fixed and equal to the port pressure at the start of calculation. The direction of gas flow at the port exit was arbitrarily chosen to be perpendicular to the port-exit plane (see Fig. 5a).

Results and Discussion. Figure 5 shows the computed (a) velocity vectors and (b) pressure contour plots at 4 ms after the start of computation in the plane cutting through the port centerline. The flow fields remain essentially unchanged thereafter since the computation had reached it steady-state solution.

The computed velocity fields were plausible and the maximum velocity vector was located at the port exit. The high-pressure contour was also near the port exit and serves as the driving force for exit flow. The observed increase in pressure along the port centerline was due to an increase in the gas density (the gas temperature remains unchanged) that was the consequence of the in-flow boundary condition (fixed in-flow velocity) and the compressibility of the fluid used (air).

At 4.0 ms, the fuel injection started and lasted for 0.75 ms. The input parameters used for spray calculations were the same as those used in the previous calculation. Figure 6 shows the computed spray drops, velocity vectors, and fuel-vapor contour plots at (a) and 4.5 ms (during fuel injection), (b) 5.0 ms (.025 ms after the end of injection), and (c) 6.5 ms after the start of computation.

By comparing results of Fig. 6 with those of Fig. 4, it is clear that both calculations gave qualitatively and quantitatively similar results. In particular, with or without partial blockage of the port, the spray penetration and dispersion remained essentially unchanged until the spray reached the port exit plane. For the case with the port partially blocked, a large fraction of the injected drops impinged on the simplified valve head (see Fig. 1) and remained in the port (this is indicated by the large difference in the number of spray drops NP shown in Figs. 6(c) and 4(c). More discussion on this aspect will be given in the next section.

Finally, this study has demonstrated our capability of making three-dimensional gas flow and fuel injection calculations with one end partially blocked to simulate gas flow through the valve annulus under both steady-state and transient conditions.

Port Flow Driven by the Time-Varying Boundary Conditions

Initial and Boundary Conditions. This study was intended to test the robustness of the code to handle time-varying boundary conditions typical of firing engine operating conditions. To this end, a single-cylinder engine simulation program [12] was used to generate typical gas flow rate data through the intake port as shown in Fig. 7.

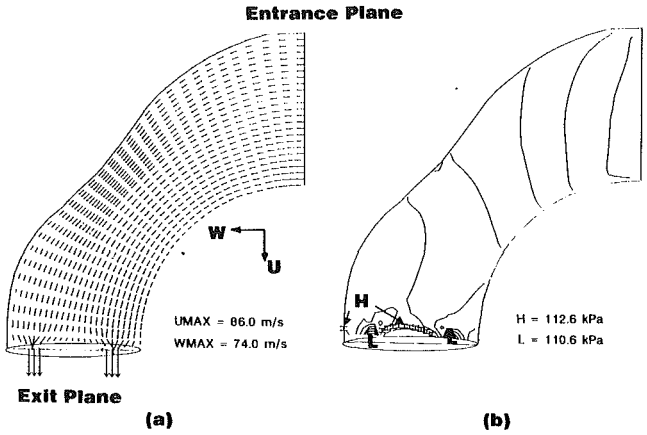

Fig. 5 Computed *(a)* velocity vectors and *(b)* pressure contour plots at 4 ms after the start of computation for the case of impulsively started port flow with one port and partially blocked to simulate flow through the valve annulus

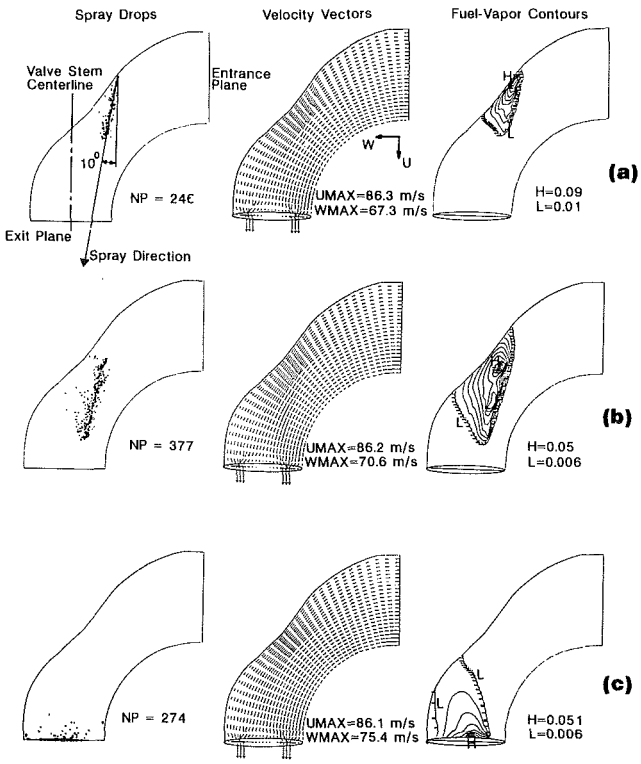

Fig. 6 Computed spray drops, velocity vectors, and fuel-vapor contour plots at *(a)* 4.5 ms, *(b)* 5.0 ms, and *(c)* 6.5 ms after the start of computation (injection at 4.0 ms) for the case of impulsively started port flow with one port end partially blocked to simulate flow through the valve annulus

Figure 7 indicates the existence of a back flow from the cylinder to the intake port right after intake valve opening (IVO) (from 380 deg BTDC firing the 345 deg BTDC firing). Afterward, the forward gas flow enters the cylinder and continues until 180 deg BTDC firing before back flow starts again. The intake valve closing (IVC) timing is at 122 deg BTDC firing.

Also shown in Fig. 7 are the start of injection (SOI) and end of injection (EOI) timings at 290 deg BTDC firing and 230 deg BTDC firing, respectively. The injection had a velocity of 15 m/s and lasted for 60 deg crank angle, which is typical of port-fuel-injection engines [2].

Computations were started at the time of intake valve opening. The initial pressure and temperature were assumed to be uniform in the port and were specified to be at 65 kPa and 320 K, respectively. The initial velocity was zero everywhere.

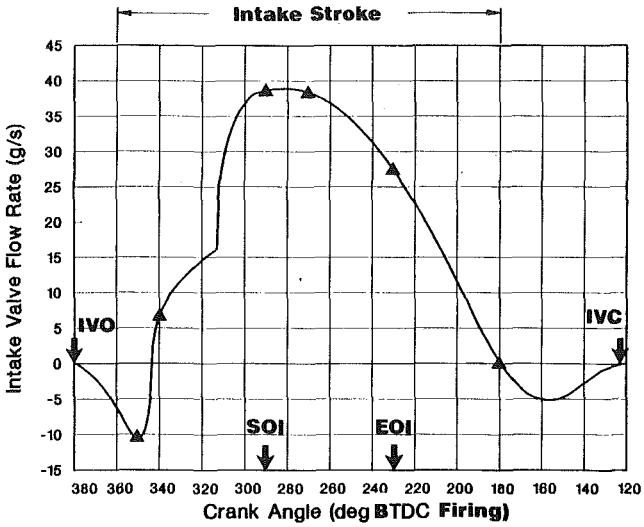

Fig. 7 Computed intake valve gas flow rate, using the single-cylinder engine simulation program, as a function of crank angle during the intake process; IVO: intake valve opening; IVC: intake valve closing; SOI: start of injection, EOI: end of injection

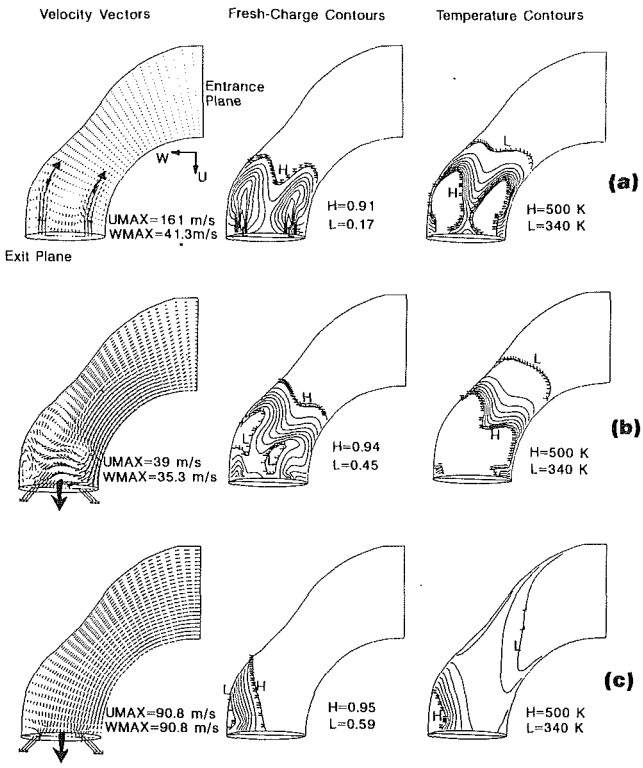

Fig. 8 Computed velocity vectors, fresh-charge and temperature contour plots at *(a)* 350 deg BTDC firing, *(b)* 340 deg BTDC firing, and *(c)* 290 deg BTDC firing for the case of port flow driven by the time-varying flow rate through the intake valve calculated using the single-cylinder engine simulation program

The velocity boundary condition at the port exit ($k = 31$) was calculated employing the valve-flow-rate data shown in Fig. 7. During the back-flow period, the cylinder temperature and burned-gas density (about 900 K and 0.384 mg/cm^3, respectively) from the simulation program were used to calculate the velocity through the valve annulus. The effect of valve lift was considered by adjusting the annulus area with time corresponding to the actual valve lift schedule. For simplicity, the back flow was assumed to have a direction normal to the port exit plane.

During the forward flow period, the local gas properties at the valve annulus were used for the velocity calculation. The flow direction, however, was assumed to follow the valve seat, which has an angle of 45 deg.

In this study, the same flow-rate data of Fig. 7 were also used to specify the velocity boundary condition at the port entrance ($k = 1$). This assumption could be in error if strong wave dynamics exist in the port due to cylinder-cylinder interactions. The information on gas flow rate through the port entrance could have been calculated using a multicylinder engine simulation program [13]; however, this was not done in the present study.

Finally, the solid triangles shown in Fig. 7 represent the crank angle positions at which detailed computed results will be presented. As can be seen, results encompass processes such as back flow, forward flow, and fuel-air mixing during and after fuel injection until 180 deg BTDC firing.

Results and Discussion. Figure 8 shows the computed velocity vectors, fresh-charge and temperature contour plots at (*a*) 350 deg BTDC firing, (*b*) 340 deg BTDC firing, and (*c*) 290 deg BTDC firing in a cutting plane through the port centerline. The fresh-charge contour plots represent fresh charge mass fraction distribution in the port. A value of 1 means pure air and a value of 0 represents burned gas due to back flow from the cylinder.

Figure 8(*a*) clearly indicates that the hot burned gas (from the temperature contours) entets the intake port as an annular jet (from the velocity vectors) during the back-flow period and fills up one-fourth of the port length (from the fresh-charge contours). Figure 8(*b*) shows that, right after the flow reversal, an extremely complicated flow pattern tends to promote mixing between burned gas and fresh charge (as indicated by the higher L contour value in Fig. 8*b* than in Fig. 8*a*). Figure 8(*c*) indicates that, at 290 deg BTDC firing, the flow disturbance generated by the back flow has diminished and exhibits a flow field similar to that shown in Fig 5(*a*). However, hot burned gas remains in the port as indicated by the existence of low fresh-charge and high temperature contours near the port exit.

Figure 9 shows the computed spray drops, fuel vapor contours, and velocity vectors plots at (*a*) 270 deg BTDC firing, (*b*) 230 deg BTDC firing, and (*c*) 180 deg BTDC firing in a cutting plane through the port centerline. In particular, the spray drop plots showed large spray deflection in the direction of gas flow due to the use of low injection velocity. (The drop injection velocity is 15 m/s and the local gas velocity at the injector tip is about 20–30 m/s during injection.) The low injection velocity also gives minimal disturbance to the gas flow (compare Figs. 9*a*, 9*b*, 6*a*, and 5*a*) and the spray drops are found concurrently with the fuel-vapor contours. In addition, the velocity vector plot of Figs. 9(*c*) shows that the forward flow through the valve annulus has ended at 180 deg BTDC firing. An extremely complicated flow pattern resulted due to deceleration of port flow in the later stage of the intake process.

Furthermore, Fig. 9(*c*) shows that, at the end of intake flow, there are still liquid and vapor in the port. The details of fuel induction into the cylinder are best illustrated in Fig. 10 where the fraction of fuel that has been injected (solid lines) and remains in the port (dashed lines) is plotted as functions of crank angle. As can be seen from Fig. 10, the injected fuel starts to enter the cylinder near the end of the injection (see group A). At the end of injection (230 deg BTDC firing), less than 5 percent of the injected fuel is vaporized. After the end of the injection, there is a steady decrease of total fuel mass in the port due to fuel entering the cylinder.

At 180 deg BTDC firing where the forward flow ceases, only 57 percent of the total injected fuel has entered the cylinder. For fuel that remains in the port, only 15 percent is vaporized. The remaining liquid fuel will continue to vaporize in the port during the valve-closed period and will be inducted first into the cylinder during the next intake stroke. In particular, the

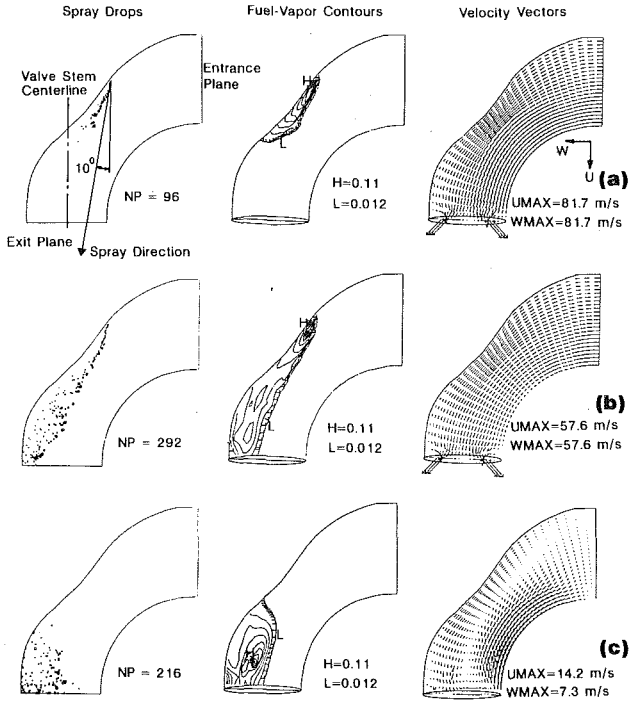

Fig. 9 Computed spray drops, fuel-vapor contour plots, and velocity vectors at *(a)* 270 deg BTDC firing, *(b)* 230 deg BTDC firing, and *(c)* 180 deg BTDC firing for the case of port flow driven by the time-varying flow rate through the intake valve calculated using the single-cylinder engine simulation program

hot burned gas entering the intake port during the back-flow period (see Fig. 8*a*) should help evaporate any liquid fuel left from the previous cycle. It is, of course, assumed that no misfire occurred in the previous cycle. Thus, the valve-overlap period can be an important design parameter in the optimization of PFI systems.

The amount of fuel entering the cylinder from the present injection cycle can be increased simply by injection timing advance. This can be seen clearly from group B in Fig. 10 where the start of injection timing was set at 90 deg crank angle before IVO as contrasted to 90 deg crank angle after IVO for group A. In particular, the fraction of injected fuel entering the cylinder increases from 0.57 to 0.93. The results confirmed that the fuel injection process has a strong influence on the details of fuel induction into the cylinder.

Finally, to maximize vaporization, it has been a common practice for production sequential PFI engines to start fuel injection right after intake valve closing to increase vaporization time. However, this approach alone has been shown to be inadequate for a wide range of engine operating conditions. Other methods, such as port- and injection-system optimization and charge motion should be considered as well [2]. Thus, the port-flow model, in conjunction with the in-cylinder flow model, which also accounts for chemical reaction [3], can be a useful tool in evaluating various mixture preparation strategies for optimal PFI system design.

Summary and Conclusion

This work represents a first step in successfully modeling the fuel-injection process in an engine intake port and incorporates a simplified valve model with no valve stem. The calculations indicate that the KIVA code can be modified to conduct computations with complicated port geometries and open flow boundary conditions. The results also indicate that both gas flow and fuel-injection processes and port geometry have a strong influence on the details of fuel induction into the cylinder. This confirms that consideration of both gas flow and fuel-injection processes is necessary in order to understand

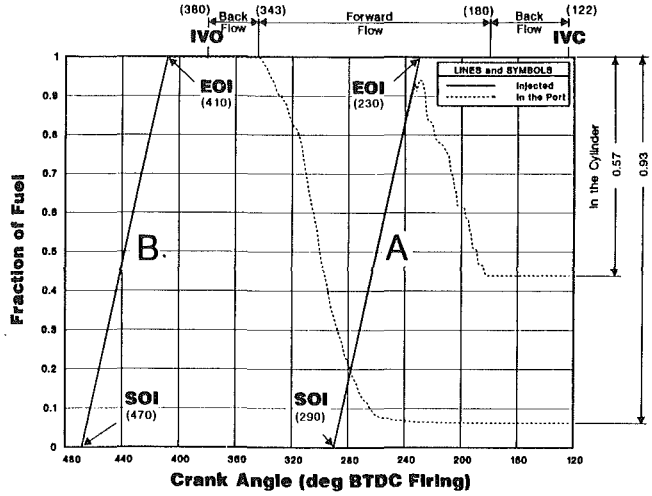

Fig. 10 Fraction of fuel that (1) has been injected and (2) remains in the port as functions of crank angle for two injection timings. Fraction of fuel inducted into the cylinder by IVC is also noted. IVO: intake valve opening; IVC: intake valve closing; SOI: start of injection; EOI: end of injection

the mechanisms of fuel-air mixing in an engine intake port employing PFI systems.

However, because of the model's inability to consider the valve stem effect, the present results are more qualitative than quantitative. Additional work is needed to address this issue. Furthermore, more work is needed in order to establish the link between the in-cylinder and port-flow calculations for a complete characterization of mixture preparation and charge motion effects on combustion in the PFI engine. Finally, model validation is needed before it can be used effectively as an analysis code.

Acknowledgments

The authors would like to thank Mason Yu, Ron Herrin, Rod Rask, and Don Siegla at the General Motors Research Laboratories for helpful comments.

References

1 Quader, A. A., "How Injector, Engine, and Fuel Variables Impact Smoke and Hydrocarbon Emissions With Port Fuel Injection," SAE Paper No. 890623, 1989.

2 Bandel, W., Fraidl, G. K., Mikulic, L. A., Quissek, F., and Carstensen, H., "Investigation of Mixture Preparation and Charge Motion Effects on the Combustion of Fast-Burn Gasoline Engines," SAE Paper No. 890160, 1989.

3 Kuo, T.-W., and Reitz, R. D., "Computation of Premixed-Charge Combustion in Pancake and Pent-Roof Engines," SAE Paper No. 890670, 1989.

4 Kuo, T.-W., "What Causes Slower Flame Propagation in the Lean-Combustion Engine?" ASME JOURNAL OF ENGINEERING FOR GAS TURBINES AND POWER, Vol. 112, No. 3, 1990, pp. 348-356.

5 Reitz, R. D., and Kuo, T.-W., "Modeling of HC Emissions Due to Crevice Flows in Premixed-Charge Engines," SAE Paper No. 892085, 1989.

6 Amsden, A. A., Ramshaw, J. D., O'Rourke, P. J., and Dukowicz, J. K., "KIVA: A Computer Program for Two- and Three-Dimensional Fluid Flows With Chemical Reactions and Fuel Sprays," LA-10245-MS, Los Alamos National Laboratories, Feb. 1985.

7 Amsden, A. A., Ramshaw, J. D., Cloutman, L. D., and O'Rourke, P. J., "Improvements and Extensions to the KIVA Computer Program," LA-10543-MS, Los Alamos National Laboratories, Oct. 1985.

8 Kuo, T.-W., and Yu, R. C., "Modeling of Transient Evaporating Spray Mixing Processes—Effect of Injection Characteristics," *SAE Trans.*, Vol. 93, Section 2, 1984, pp. 16-29.

9 Reitz, R. D., "Modeling Atomization Processes in High-Pressure Vaporizing Sprays," *Atomization and Spray-Technology*, Vol. 3, 1988, pp. 309-337.

10 Naber, J. D., and Reitz, R. D., "Modeling Engine Spray/Wall Impingement," SAE Paper No. 880107, 1988.

11 Kuo, T.-W., Syed, S. A., and Bracco, F. V., "Scaling of Impulsively Started, Incompressible, Laminar Round Jets and Pipe Flows," *AIAA Journal*, Vol. 24, No. 3, 1986, pp. 424-428.

12 Lienesch, J. H., "Engine Simulation Identifies Optimum Combustion Chamber Design," Paper No. 80.4.4.7, 18th FISITA Congress, 1980.

13 Benson, R. S., "Thermodynamics and Gas Dynamics of Internal Combustion Engines," J. H. Horlock and D. E. Winterbone, eds., Clarendon Press, Oxford, 1982.

Intake Swirl Process Generated by an Engine Head: a Flow Visualization Study

B. Khalighi
Staff Research Engineer,
Engine Research Department,
General Motors Research Laboratories,
Warren, MI 48090-9055

In-cylinder charge swirl is used in many internal combustion engines to promote combustion. The purpose of this work is to investigate the in-cylinder swirl characteristics generated by an engine head during the induction process by means of flow visualization and Particle Tracking Velocimetry (PTV). The study was carried out for an engine head with a shrouded intake valve in a special single-cylinder transient water analog. The results revealed that the in-cylinder swirl generated by the shroud is characterized by a strong single vortex with its center of rotation eccentric to the cylinder axis. The location of the center rotation differs from plane to plane along the cylinder axis. Furthermore, velocity data obtained for this study suggest that the in-cylinder swirl is not solid body rotation. Finally, the velocity fields were integrated and an equivalent swirl was calculated for the engine under transient conditions.

Introduction

The in-cylinder fluid motion in internal combustion engines is one of the most important factors controlling the combustion process. It governs the flame propagation rate in homogeneous charge spark-ignition engines; it controls the fuel-air mixing and burning rates in diesels (Heywood, 1987). Therefore, a good understanding of fluid motion inside the engine cylinder is critical to developing engine designs with the most attractive operating and emissions characteristics.

Flow visualization is widely used to investigate the in-cylinder flow process in internal combustion engines (Willas et al., 1966; Ekchian and Hoult, 1979; Hirotomi et al., 1981; Komatsu and Shirea, 1986; Khalighi and Huebler, 1988; Eaton and Reynolds, 1989; Kent et al., 1989; Khalighi, 1990). Combination of the flow visualization and the cycle-resolved full-field velocity information provide useful insights of the highly unsteady in-cylinder flow during the intake stroke. Full-field velocity measurement refers to techniques in which a mulitple exposure image of the light scattered from small suspended particles moving with the fluid is used to record the particle displacements and, hence, the fluid velocity over an extended region of the flow (Hjelmfelt and Mockros, 1966; Imaichi and Ohmi, 1983; Marko and Rimai, 1985; Adrian, 1986; Agui and Jimenez 1987; Gharib and Willert, 1988; Reuss et al., 1989; Khalighi and Lee, 1989).

The aim of the present investigation is to study the swirl characteristics in an engine during the intake stroke using flow visualization and Particle Tracking Velocimetry (PTV). For this study, air motion in the cylinder during the induction process is simulated by water. This of course requires a special experimental apparatus, which should mimic the engine functions (i.e., piston and valve motions) while it maintains the dynamic and kinematic similarities between the model and the real engine. It should be mentioned that such a system is only suitable for examining the induction process and cannot be used for visualizing the fluid motion during the compression stroke.

Contributed by the Internal Combustion Engine Division for publication in the JOURNAL OF ENGINEERING FOR GAS TURBINES AND POWER. Manuscript received by the Internal Combustion Engines Division April 30, 1990.

Model Similitudes

A special single cylinder transient water analog (Khalighi and Huebler, 1988) was used for the in-cylinder flow visualization studies. This engine model features a transparent cylinder and cylinder head, which provides maximum optical access to the flow inside the engine. In order for the water analog flow to be completely analogous to that in an engine cylinder, the following similarity criteria should be retrained as described by Willas et al. (1966): (1) thermal, (2) geometric, (3) kinematic, and (4) dynamic. Thermal similarity does not apply to our model because of the absence of compression and combustion strokes. The geometric similarity can be satisfied by constructing the model to scale, in our case 1:1. The importance of the remaining similarities is considered and discussed below.

Kinematic Similarity. In this study, air, which is a compressible fluid, is replaced by water, which is an incompressible fluid. This raises the question of how significant the errors will be if air is replaced by water. We attempt to answer this question by considering one-dimensional compressible flow theory. From this theory (Zucrow and Hoffman, 1976) it can be shown that

$$\frac{\Delta P}{\frac{1}{2}\rho V^2} = 1 + \frac{M^2}{4} + \frac{M^4}{40} + \ldots \quad (1)$$

where M is the Mach number, ΔP is the pressure drop, V is the flow velocity, and ρ is the fluid density. For incompressible flow, this expression is unity. However, even at high subsonic velocities (for compressible flow), deviations from unity are

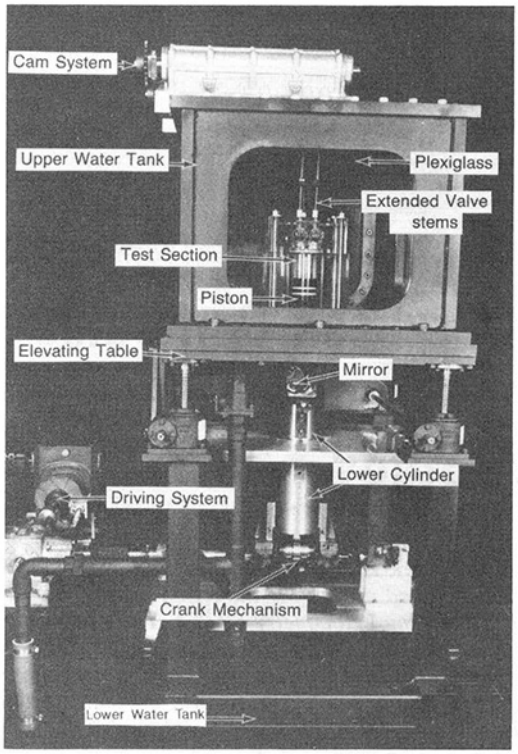

Fig. 1 Photograph of the transient water analog

small. The data obtained for typical production engines show that compressibility has only a minor effect on fluid velocities (during the induction stroke) over most of the engine speed range particularly at low engine speeds (2000 rpm and less). For example, in a typical engine, the maximum Mach number at the intake is about 0.5, for which the error will be less than 6 percent based on the above expression (Ma et al., 1986). This implies that the fluid motion during the intake stroke can be considered incompressible. The present assumption is only valid for the induction process and can not be used for rest of the engine cycle (i.e., exhaust stroke).

Dynamic Similarity. Since the flow during the induction process is almost incompressible, one can use the nondimensional momentum equation for an incompressible fluid

$$[\mathrm{St}]\frac{\partial \mathbf{V}}{\partial t} + \text{Convective term} = \text{pressure term} + \left[\frac{1}{\mathrm{Re}}\right]\nabla^2\mathbf{V} \quad (2)$$

Two parameters—Reynolds number ($\mathrm{Re} = U_pD/\nu$) and Strouhal number ($\mathrm{St} = D/tU_p$)—appear in the above equation and must be matched in the model and the engine. In these parameters, U_p is the piston velocity, D is the cylinder or piston diameter, t is a proper time scale, and ν is the kinematic viscosity of the fluid. The equality of these parameters between the model and the prototype is discussed below.

Reynolds Number. Matching Reynolds numbers between the model and the actual engine leads to

$$\left(\frac{U_pD}{\nu}\right)_{\text{model}} = \left(\frac{U_pD}{\nu}\right)_{\text{engine}} \quad (3)$$

or

$$\frac{U_p \text{ model}}{U_p \text{ engine}} = \frac{\nu \text{ model}}{\nu \text{ engine}}$$

For the conditions of this study, this ratio is 1:20.

Strouhal Number. A proper time scale applicable to internal combustion engines is the engine crankshaft speed $\omega(t \sim 1/\omega)$. Therefore, the Strouhal numbers for the model and prototype will automatically be the same, since the angular velocity of the crankshaft ω is directly proportional to the piston velocity (Ekchian and Hoult, 1979; Willas et al., 1966)

$$\omega \sim U_p \quad (4)$$

Experimental Setup and Procedures

Experimental Apparatus. The basic configuration of the transient water analog is shown in Fig. 1. The model is divided into three sections: top, middle, and bottom. The top section is a transparent water tank, which houses the test section (transparent cylinder and the cylinder head) and the cam systems for actuating the intake and exhaust valves. This tank is filled with water and small suspended particles for flow visualization purposes.

The engine cycle begins with the piston at top dead center (TDC). As the piston moves downward during the intake stroke, the intake valves open and water flows into the cylinder. Since water is incompressible, the piston must remain stationary at bottom dead center (BDC) during the normal compression and power strokes (during this period the intake and exhaust valves are closed). This is achieved by a solenoid mechanism (latching and unlatching mechanism) that operates by a switching circuit connected to the engine crankshaft. During this period, the decay process of the large-scale flow motion can be assessed. At the end of this period the exhaust valve starts to open, and by de-energizing the solenoid-driven mechanism, the piston resumes motion and completes the cycle at TDC.

The middle section of the water analog consists of an extended piston (primary) with top window, a secondary piston, the latching and unlatching mechanism, and an elevating table. The primary piston, which is driven by the secondary piston, is also used to view the in-cylinder flow motion on diametrical planes.

The bottom section of the system provides the main support for the water analog and consists of a water supply tank and the main driving system. The analog is powered by a variable speed d-c motor (5 hp, 2750 rpm maximum) via a reduction gear (10:1). Table 1 lists basic engine specifications used for the present study.

An engine head from a dual-intake-valve engine was mounted

Nomenclature

ABDC = after bottom dead center
ATDC = after top dead center
BBDC = before bottom dead center
BDC = bottom dead center
BTDC = before top dead center
D = cylinder bore diameter
dm = mass of the volume element
M = Mach number
n = engine speed
PTV = particle tracking velocimetry
r = radial distance
Re = Reynolds number
S = swirl ratio on each plane
S_{av} = average swirl ratio
St = Strouhal number
t = time
TDC = top dead center
U = fluid velocity
U_p = piston speed
v = velocity of the element
V = velocity
W = mass per unit length
X = streak length
Z = distance from cylinder head
ΔP = pressure drop
ν = kinematic viscosity
ρ = density
ω = engine angular speed

Table 1 Engine specifications

Bore (mm):	92.0
Stroke (mm):	85.0
Compression ratio (nominal):	7:1
Intake-valve head diameter (mm):	35.5
Exhaust-valve head diameter (mm):	30.0
Intake valve opens (°BTDC):	22.0
Intake valve closes (°ABDC):	50.0
Exhaust valve opens (°BBDC):	64.0
Exhaust valve closes (°ATDC):	20.0

on the water rig. In order to generate a relatively high in-cylinder swirl during the induction period, one of the intake valves of the engine was shut, and a 180 deg shroud (mask) was installed on the other intake valve. The location of the shroud with respect to the engine geometry is depicted in Fig. 2.

Particle Tracking Velocimetry (PTV). The working fluid was water, which was seeded with a small amount of neutral density particles. Particles used for the flow visualization were Pliolite spheres with sizes of 100–125 μm. A 2-W argon-ion laser was used as the illumination source. Figure 3 shows the light source setup for the flow visualization and velocity measurement experiments. The laser beam was passed through a series of optical components to produce a sheet of laser light (1 mm thick).

In order to perform PTV, the laser sheet was pulsed using an Acousto-Optic Modulator (AOM) to produce a desired coding pattern. The coding signal (Fig. 3) begins with two short pulses (dots), a long pulse (streak) in the middle, and a short pulse at the end. The advantages of this coding pattern are twofold: (1) Flow direction can be determined, and (2) one can be certain that the particles generating the streaks are within the light sheet during the illumination period.

A S-VHS Panasonic video camera and a 35 mm camera were used to record flow visualization and coded streak images. This resulted in photographic negatives and video images containing streak images that resemble the pulse pattern. By measuring the streak lengths and knowing the pulse duration, the instantaneous velocities were obtained using the following expression:

$$U = X/t \tag{5}$$

where U is the local instantaneous velocity vector in the illuminated plane, X is the streak length, and t is the pulse duration. The total duration of the coding pattern used in this study was 2.8 ms.

The PTV flow images (35 mm negatives and/or video images) were digitized through an Imaging Technology processing board. An IBM PC/AT was used to drive the digitizing board and provided storage of the image files on both the hard and floppy drives. The original image was converted into a 512×512 pixel matrix with an 8-bit gray scale. Digitized images were then sent from the PC to the IBM mainframe computer for image processing and analysis. The analysis begins by establishing a real-world coordinate system with respect to the pixel image. Next, flow boundaries are specified by moving the cursor along the flow boundaries. As soon as flow boundaries are defined, processing for velocity extraction can begin. Using the cursor, the end points of individual streaks are located on the screen and their pixel coordinates are stored in the buffer. Together with specified streak time scale (total duration of the pulse pattern), these data are used to calculate the flow velocities.

Upon completion of the image processing, the particle trajectories are replaced by vectors whose lengths are proportional to the particle velocities at the corresponding locations in the flow field. Due to the nature of the seeding process, the velocity data density is random and dispersed in nature. Thus an interpolation procedure was used to identify more details of the in-cylinder tumbling flow structure. The interpolation scheme

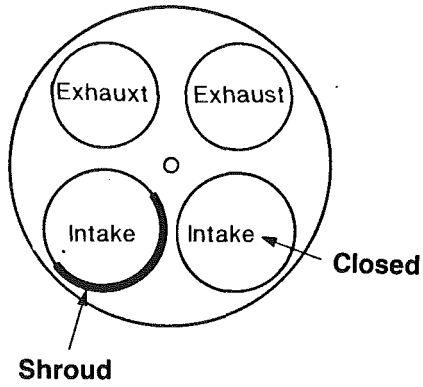

Fig. 2 Schematic of the engine head and shroud position

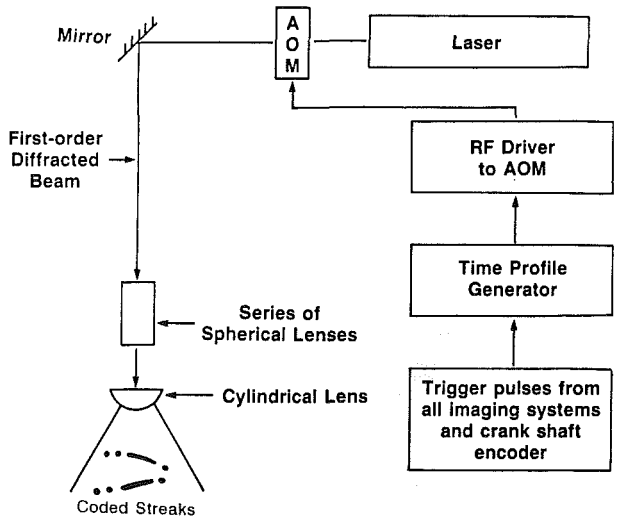

Fig. 3 Laser light setup for generating coded streaks (PTV images)

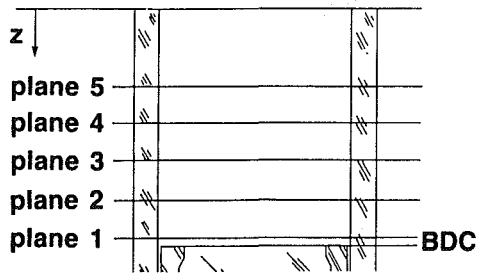

Fig. 4 Location of the measurement planes along the engine cylinder

used in the present study is similar to the one presented by Imaichi and Ohmi (1983).

Measurement Errors

Error sources affecting the accuracy of the velocity measurement by PTV have been discussed by Imaichi and Ohmi (1983) and Gharib and Willert (1988). In this study the most serious potential errors are:

1 Tracking error—this is because the particles do not strictly follow the motion of the fluid. Using the analysis described by Gharib and Willert (1988), the error due to tracking was calculated to be less than 0.4 percent for the present study.

2 Distortion of the image—distortion of photographic or video images due to the optical effects (i.e., lenses, glass, and water).

3 Measurement errors—errors in operating the digitization tablet (mouse) by the operator.

4 Error of computing Eulerian velocity field from Lagrangian measurements—This error is mostly introduced due

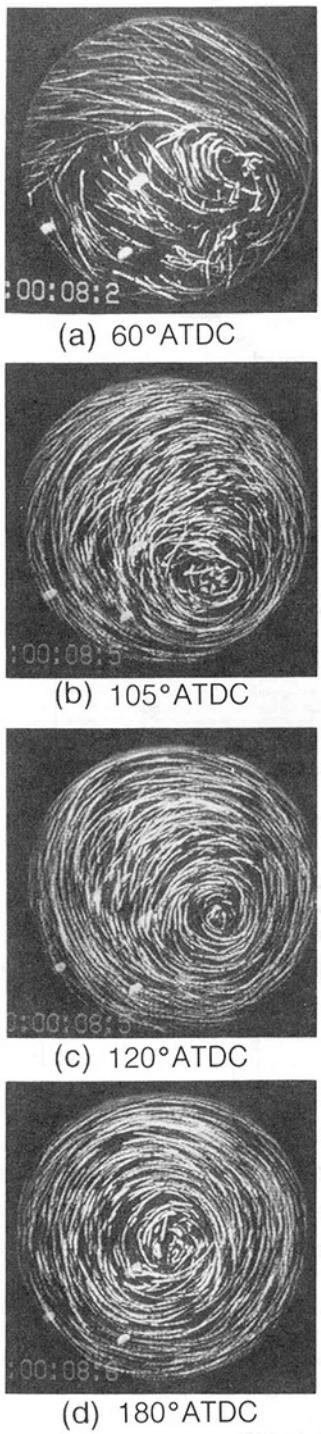

Fig. 5 Intake swirl development during an engine cycle on plane 5

to the trace curvature and acceleration of the particles (Gharib and Willert, 1988).

An attempt was made to assess the total error in the present investigation. PTV and image processing were performed for a known velocity field (fully developed turbulent flow in a tube). The results showed a compounded error of 4 percent in measuring velocities.

Results

For the present investigation, the transient water analog was operated at 65 rpm, which corresponds to approximately 1300 rpm equivalent engine speed. The in-cylinder swirl was studied on five different radial (horizontal) planes along the cylinder axis. Figure 4 shows the locations of these planes with respect to the engine cylinder head. For convenience a number is assigned to each plane as:

1 Radial (horizontal) plane 1; the horizontal laser sheet enters the cylinder at $Z = 92$ mm. Z is defined from the cylinder head (Fig. 4).
2 Radial plane 2, $Z = 77$ mm.
3 Radial plane 3, $Z = 62$ mm.
4 Radial plane 4, $Z = 47$ mm.
5 Radial plane 5, $Z = 32$ mm.

Global Observations. As mentioned earlier, the intake shroud position was selected such that it generated a relatively high in-cylinder swirl flow. The evolution of the in-cylinder swirl on one of the light planes during the intake stroke is shown in Fig. 5. This figure shows sequences of the video frames of the swirl generation on plane 5 (see Fig. 4 for the location of this plane). The in-cylinder swirl is characterized by a single clockwise vortex with its center of rotation eccentric to the cylinder axis. Furthermore, the center of rotation apparently tends to rotate about the cylinder axis as it is formed. The vortex becomes more stable as the piston reaches BDC. At BDC, the center of the vortex almost coincides with the cylinder axis, as shown in Fig. 5(*d*). Further investigations of the flow visualization images revealed that the in-cylinder swirl was highly repeatable from cycle to cycle.

Figure 6 shows the in-cylinder swirl flow on all five radial planes. These pictures were taken at BDC (bottom dead center). As shown in these figures, the swirl profile at all planes is characterized by a strong unsymmetric vortex with its center of rotation eccentric to the cylinder axis. These figures also indicate that the centers of rotation differ in locations for different radial planes.

Velocity Measurement. Flow visualization images (Fig. 6) were digitized and processed according to the procedure described earlier in which the local instantaneous velocities on the measurement planes were obtained. Figure 7 shows the PTV image and its corresponding velocity field on plane 1. This figure contains three separate pictures and plots. The first (top) picture is the PTV image taken at BDC. The second (middle) plot presents the measured velocity vectors obtained directly from the image processing procedures applied to the corresponding PTV image. The third (bottom) plot gives the corresponding interpolated velocity field. The origins of the velocity vectors are indicated by dots. It should be mentioned that equivalent velocities inside the actual engine would be approximately 20 times larger than the velocities shown here for the water analog.

Velocities were measured on all five planes. From these data the exact location of the center of the swirl is estimated visually and depicted in Fig. 8. This figure shows the centers of the swirl on all five planes with respect to the cylinder axis (eccentricity) and the distance from the cylinder head. It is evident that the center of the swirl is strongly influenced by the distance from the cylinder head, which is also reported by Willas et al. (1966).

The flow visualization and velocity measurements revealed that the flow field generated by the present shrouded intake valve was not characterized by pure swirl. In this case the flow field was a combination of swirl and tumble flows. The study of the tumble flow field is beyond the scope of the present investigation and will be discussed elsewhere.

Figure 9 shows the tangential velocity profiles along the diametrical line through the cylinder axis and the center of the swirl for all five planes. It is clear that the velocity profiles viewed on these planes do not resemble solid body rotation (usually assumed for multidimensional in-cylinder flow calculations). Finally, the velocity field obtained in this study can

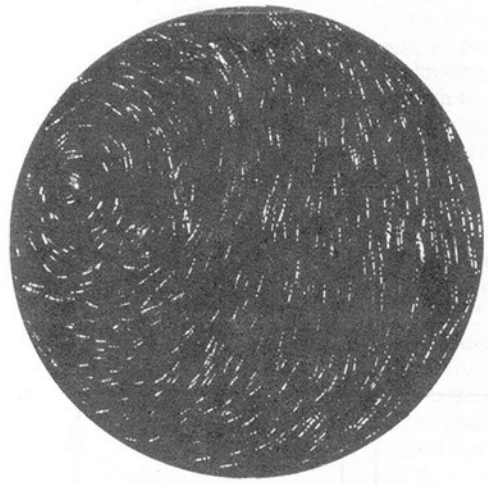

Plane 1

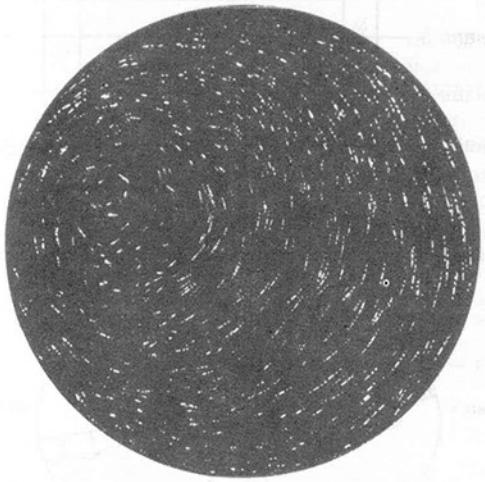

Plane 2

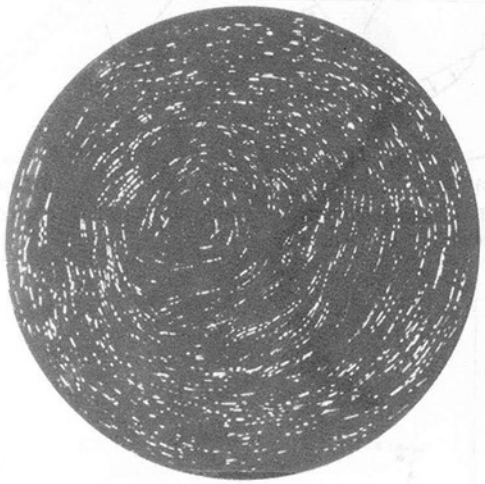

Plane 3

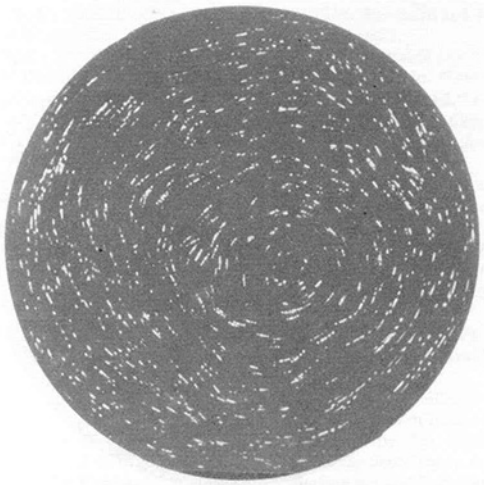

Plane 4

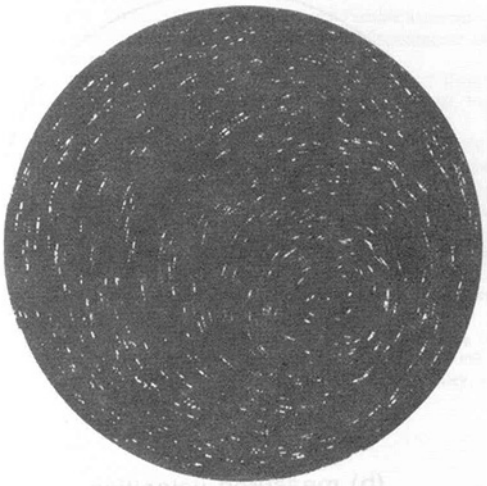

Plane 5

Fig. 6 Swirl flow structure on various radial planes taken at BDC

be integrated to obtain a transient swirl ratio. Swirl ratio is defined as the ratio of the angular speed of the swirling flow and the engine crank speed. The swirl ratio is usually measured using steady flow benches due to lack of swirl velocity data under transient condition.

Swirl Ratio Calculation. The local swirl ratio was calculated for each experimental plane using a similar approach suggested by Komatsu and Shirea (1986). The calculations were made for the velocity fields presented in this paper, which were taken at BDC. The following equation was used to calculate the equivalent swirl ratio (S) with respect to the cylinder axis:

$$S=\frac{60}{WR^2\pi n}\int_0^{2\pi}\int_0^{R}\int_Z^{Z+\partial Z}\rho r^2 v d\theta dr dz \qquad (6)$$

It expresses a ratio of the equivalent solid-body angular speed of the swirling flow (obtained from integrating the measured velocities) to the engine crank speed. W denotes mass per unit length (δZ), R is the cylinder radius, ρ is the density, n is the engine speed, and v is the tangential velocity in the cylinder.

Using the above definition, a swirl ratio (S) was computed for each plane with respect to the cylinder axis. Figure 10 shows the variation of the swirl ratio as a function of distance from the cylinder head (Z). The result shows that the local swirl ratio varies throughout the cylinder. In order to compare the transient swirl ratio and the steady-flow air bench data, an average value for the swirl ratio inside the engine cylinder was

(a) PTV image

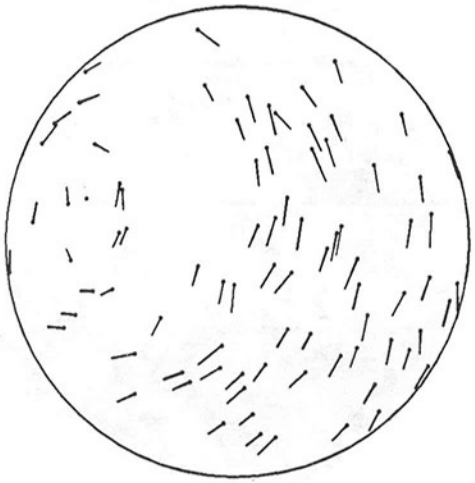

(b) measured velocities

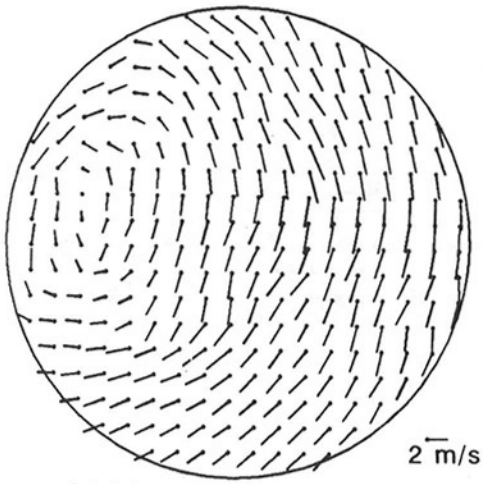

(c) interpolated velocities

Fig. 7 PTV image and its corresponding velocity field on plane 1 at BDC

computed. The average swirl ratio (S_{av}) obtained from the above values is

$$S_{av} = 7.80 \tag{7}$$

In a separate experiment a steady-flow air bench was used to evaluate the swirl ratio for this test configuration. Flow bench measurements included discharge coefficients and torque imparted to a torque meter as a function of valve lift. These data

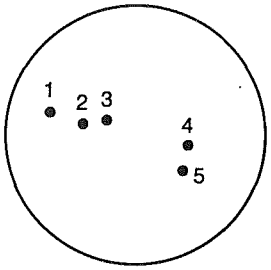

(a) Top view

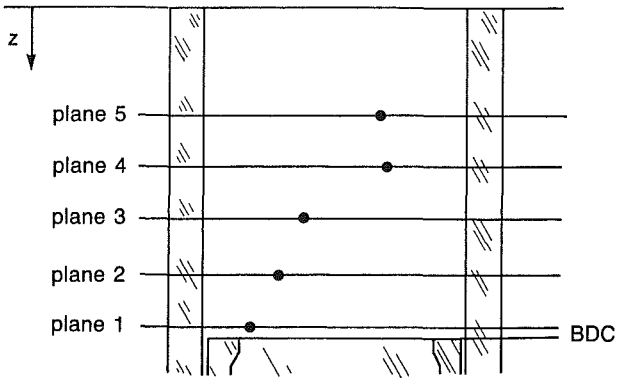

(b) Side view

Fig. 8 Location of the swirl centers obtained from processing the PTV images

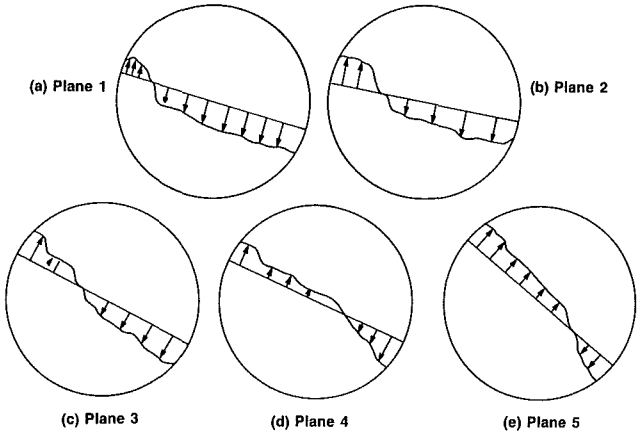

Fig. 9 Tangential velocity profiles along diametral lines on five different radial planes

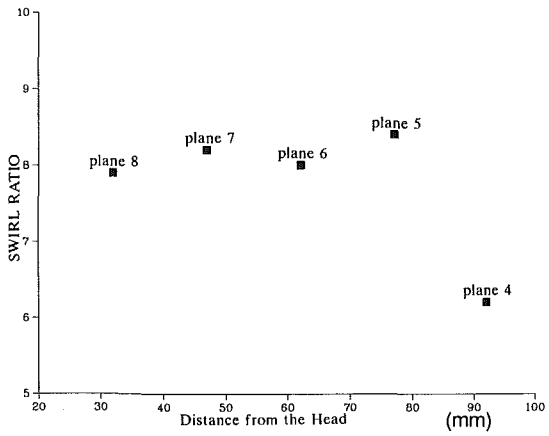

Fig. 10 Local swirl ratios on different radial planes

were then fed into an engine simulation program to calculate the swirl ratio. The swirl ratio obtained through this procedure was 9.2. This means that the steady flow bench experiment overpredicts the swirl ratio, which is consistent with the results reported by Kent et al. (1989). However, a fair comparison between the steady and transient swirl ratios would require a large number of data from several engine heads.

Closure

An experimental investigation was conducted to study the in-cylinder swirl characteristics in an engine by means of low visualization and Particle Tracking Velocimetry. The main conclusions derived from the flow visualization studies are:

- The in-cylinder swirl profile is characterized by a strong vortex with its center of rotation eccentric to the cylinder axis.
- On each horizontal plane, the center of rotation tends to rotate about the cylinder axis as it is formed during the intake stroke.
- The in-cylinder swirl is very stable and highly repeatable from cycle to cycle.
- Tangential velocity profiles on horizontal planes cannot be described as solid body rotation.

Generating a swirl flow in any direction inside the engine cylinder during the intake process in one of the more promising ways to achieve a fast burning rate (Heywood, 1987). A well-defined swirl flow structure is more stable than other large-scale in-cylinder flows, and therefore, breaks up later in the cycle giving higher turbulence during combustion. This higher turbulence gives both faster flame front progagation and higher reactive flame surface area.

References

Adrian, R. J., 1986, "Multi-point Optical Measurements of Simultaneous Vectors in Unsteady Flow—A Review," *Intl. Heat and Fluid Flow*, Vol. 7, pp. 127–145.

Agui, J. C., and Jimenez, J., 1987, "On the Performance of Particle Tracking," *J. Fluid Mech.*, Vol. 185, pp. 447–468.

Eaton, A. R., and Reynolds, W. C., 1989, "Flow Structure and Mixing in a Motored Axisymmetric Engine," SAE Paper No. 890321.

Ekchian, A., and Hoult, D. P., 1979, "Flow Visualization Study of the Intake Process of an Internal Combustion Engine," SAE Paper No. 790095.

Gharib, M., and Willert, C., 1988, "Particle Tracing: Revisited," *Proceedings of the AIAA/ASME/SIAM/APS 1st National Fluid Dynamics Congress,* Vol. 3, pp. 1935–1943, The American Institute of Aeronautics and Astronautics, Cincinnati, OH.

Heywood, J. B., 1987, "Fluid Motion Within the Cylinder of Internal Combustion Engines—The 1986 Freeman Scholar Lecture," ASME *Journal of Fluids Engineering,* Vol. 109, No. 3.

Hirotomi, T., Nagayama, L., Kobayashi, S., and Ymamasu, M., 1981, "Study of Induction Swirl in a Spark Ignition Engine," SAE Paper No. 810496.

Hjelmfelt, A. T., and Mockros, L. F., 1966, "Motion of Discrete Particles in a Turbulent Fluids," *Appl. Sci. Res.,* Vol. 16, pp. 149–161.

Imaichi, K., and Ohmi, K., 1983, "Numerical Processing of Flow-Visualization Pictures—Measurement of Two-Dimensional Vortex Flow," *J. Fluid Mechanics*, Vol. 129, pp. 283–311.

Kent, J. C., Mikulec, A., Rimai, L., Adamczyk, A. A., Mueller, S. R., Stein, R. A., and Warren, C. C., 1989, "Observation of the Effects of Intake-Generated Swirl and Tumble on Combustion Duration," SAE Paper No. 892096.

Khalighi, B., and Huebler, M. S., 1988, " A Transient Water Analog of a Dual-Intake-Valve Engine for Intake Flow Visualization and Full-Field Velocity Measurements," *SAE Transactions*, Vol. 97, pp. 877–892, Paper No. 880519.

Khalighi, B., and Lee, Y. H., 1989, "Particle Tracking Velocimetry: an Automatic Image Processing Algorithm," *Applied Optics*, Vol. 28, No. 20, pp. 4328–4332.

Khalighi, B., 1990, "Intake-Generated Swirl and Tumble Motions in a 4-Valve Engine With Various Intake Configurations—Flow Visualization and Particle Tracking Velocimetry," SAE Paper No. 900059.

Komatsu, G., and Shirea, S., 1986, "Flow Visualization of Process of Producing Induction Swirl Using Water Model," *Bulletin of JSME*, Vol. 29, No. 254, pp. 2592–2597.

Ma, T., Davis, M., and Collings, N., 1986, "Low Speed Dynamic Similarity Modeling in Internal Combustion Engines," SAE Paper No. 860239.

Marko, K. A., and Rimai, L., 1985, "Video Recording and Quantitative Analysis of Seed Particle Track Images in Unsteady Flows," *Applied Optics,* Vol. 24, No. 21, p. 3666.

Reuss, D. L., Adrian, R. J., Landreth, C. C., French, D. T., and Fansler, T. D., 1989, "Instantaneous Planar Measurements of Velocity and Large-Scale Vorticity and Strain Rate in an Engine Using Particle-Image Velocimetry," SAE Paper No. 890616.

Willas, D. A., Meyer, W. E., and Birnie, C., 1966, "Mapping of Airflow Patterns in Engines With Induction Swirl," SAE Paper No. 660043.

Zucrow, M. J., and Hoffman, J. D., 1976, *Gas Dynamics,* Wiley, New York.

Global What? Control Possibilities of CO_2 and Other Greenhouse Gases

K. J. Springer
Southwest Research Institute,
San Antonio, TX 78228

Global what? is a frequent response by those who first hear of the potential for global warming, global climate change, and global catastrophe, potentially brought on by excessive greenhouse gases in the upper atmosphere. The principal greenhouse gas, CO_2, is joined by methane, N_2O, and other trace gases in absorbing infrared radiation, which would otherwise escape into space, a process thought to be responsible for gradual increase in temperature that will melt ice caps and raise ocean levels. This paper discusses control possibilities that could be considered once there is agreement that CO_2 must be controlled. Many of the responses to the energy crisis of 1974 are applicable for CO_2 control. A variety of technologies, energy sources, and ideas are offered that, in combination, could be the basis for a global energy policy. Conversion and replacement of coal, oil, and eventually natural gas fired electric power plants with other energy sources such as nuclear, solar, wind, tidal, and geothermal, could significantly reduce CO_2 emissions. There are, however, no good alternatives to fossil fuels used in transportation that significantly reduce CO_2 emissions. Of all the fossil fuels, natural gas has the least CO_2 production. Electric vehicles and hydrogen-fueled engines are future possibilities, but the electricity for the electric cars and for making hydrogen must be from nonfossil fuel driven generators. Conservation, efficiency, and tax incentives are other parts of a control strategy, once the amount of control considered necessary is established. Renewed interest in nonfossil fuel energy sources and their research and development is obviously needed.

Introduction

Human progress has been marked by the conversion of carbon-containing fuels to useful forms of heat energy. From the discovery of fire, civilization has capitalized on the use of natural resources to bring about a better standard of living. To the extent one region or country has had an abundance of such resources such as wood, coal, or petroleum, their living conditions could be propelled forward. The USA has enjoyed a high rate of development in large part due to the abundance of fossil fuel natural resources. The "greenhouse effect" has, however, placed us on the "horns of a dilemma." There is no easy or simple solution to one of the most perplexing of problems we carry with us into the 21st century than what, if anything, must be done about CO_2 and other greenhouse gases. It is not just a problem for the USA, Western Europe, or Japan, but for all countries and regions striving for improvement in the quality of life.

A trial lawyer once said, "There are no facts, only viewpoints of the facts until the judge or jury rules. Then it becomes a fact." Consider a court case where science and technology are on trial. Each side assembles its scientific experts who provide their opinions in as convincing a way as possible as to what has happened or will happen or what was or was not a contributing factor. The case of global warming [1] due to CO_2, methane, water vapor, chlorofluorocarbons (CFCs), ozone, and nitrous oxide in the upper atmosphere is currently on trial. Such gases absorb infrared radiation that would otherwise escape into space and are beneficial in maintaining the earth's temperature at habitable levels. However, it is postulated that higher concentrations of such gases could result in global warming, accompanied by changing weather patterns and increasing sea levels, causing significant social and economic problems. The arguments for and against catastrophic global warming come from a number of experts who provide their opinion of what will happen based on observation of the past. There are several sides or viewpoints of the facts, each with computer models attempting to predict the future, that are varied and inconsistent [2]. World opinion, the jury, seems undecided and swings with each new revelation as the process of discovery continues to draw out more and more testimony. The jury is overwhelmed by the complexity of the issue, the contradictory evidence, and the antics of those who play to the crowd through fear-provoking news headlines.

Regardless of the number of viewpoints predicting a disaster by the world's leading scientists, there remains a small but

Contributed by the Internal Combustion Engine Division and presented at the Energy-Sources Technology Conference and Exhibition, Houston, Texas, January 20–24, 1991. Manuscript received by the Internal Combustion Engine Division September 1990. Paper No. 91-ICE-10.

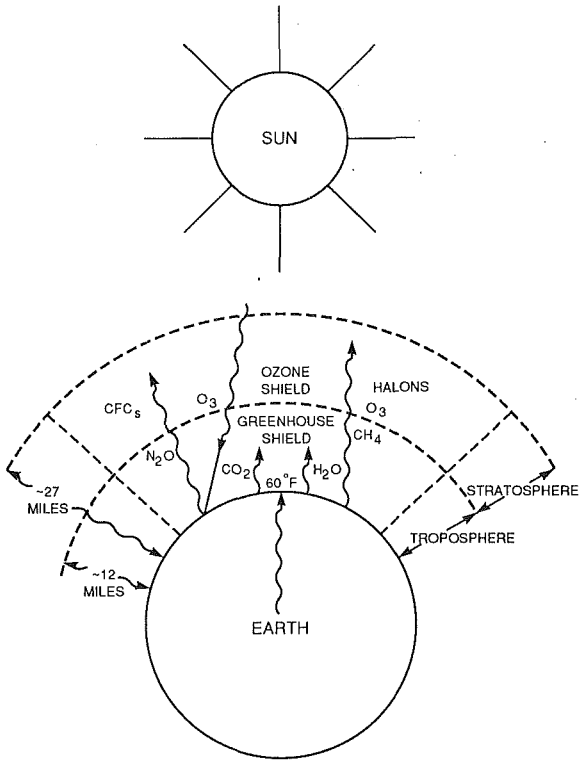

Fig. 1 Schematic of the Earth's Protective Shields

vocal minority arguing that too much is made about CO_2 and methane as causes of global warming [3]. Their viewpoint of the data does not support the often-quoted trend of increased temperature of this planet [4, 5]. Who is right? The jury, world opinion, will eventually decide, but not until the last minute because it probably is not able to make an informed decision due to its diverse background and the diversity of viewpoints. However, when it becomes decision time, a judgment will probably be made based on the preponderance of the evidence at that time, because it is unlikely any projection can be "beyond a shadow of a doubt." When more than 50 percent become convinced, world opinion will begin demanding changes to reduce CO_2, methane, and other greenhouse gas emissions. In the meantime, heads of state [6] and other government spokesmen will appoint themselves to rule on their impression of the evidence available, insofar as their own country goes. Some will ignore the entire proceedings, some will heed the alarms being sounded, and some will agree with those who say wait until more is known. A few may side with those who believe it is a nonproblem.

Figure 1 depicts the beneficial greenhouse effect of the troposphere, a region extending about 7 miles from the earth's surface to the stratosphere. This layer acts like panes of glass in a greenhouse and makes the earth habitable at an overall average temperature of about 60°F (15°C). CFCs (used as refrigerants and industrial solvents and in foam packaging) and halons (used in some fire extinguishers) act as greenhouse gases. However, CFCs and halons are much more important in that they destroy the protective shield of ozone found in the stratosphere at about 8 to 22 miles above the earth's surface. Stratosphere ozone absorbs much of the sun's ultraviolet radiation, unlike ground level ozone that in high concentrations can cause harmful respiratory effects on humans. For example, energy from the sun can decompose CFCs and release chlorine. Chlorine reacts in a chain reaction with ozone, and this is believed to be the reason for the hole in the ozone layer observed over the South Pole during late winter and early spring. Halons are thought also to destroy ozone through a similar, perhaps more efficient, chain reaction involving bromine: specifically bromine monoxide along with chlorine monoxide [7].

World reaction to the noticeable ozone depletion resulted in the 1987 Montreal Protocol on Substances that Deplete the Ozone Layer signed by 24 countries. By the year 2000, major reductions of at least 50 percent of the 1986 production rate of CFCs and halons are to be achieved. The ultimate goal is a total ban on the production of CFCs and halons. The major reductions planned for CFCs and halons will eventually eliminate them as significant to the greenhouse effect.

Table 1 The greenhouse gases

	Carbon Dioxide CO_2	Methane CH_4	CFCs and Halons	Nitrous Oxide, N_2O	Tropospheric Ozone O_3
Global Increase, Annual Basis, %	0.5	1	6	0.4	2
Life, years	7	10	110	170	renewed
Effect Relative to CO_2, times	1	30	20,000	150	2,000
Contribution to the Greenhouse Effect, %	50	18	14	6	12
Sources	(1)	(2)	(3)	(4)	(5)

(1) Fossil fuel burning, deforestation, and changing land use, burning of biological matter.

(2) Byproduct of bacterial breakdown of organic matter in swamps, paddy field, waste dumps, animals and natural gas leaks.

(3) Coolants in refrigerators, air-conditioners, aerosols, production of plastic foams, solvents, fire extinguisher testing.

(4) Fertilizers, fossil fuel, and bio-mass burning, changing land use, vehicle emissions.

(5) Photochemical reaction of sunlight on nitrogen oxides and reactive volatile hydrocarbons from vehicle emissions.

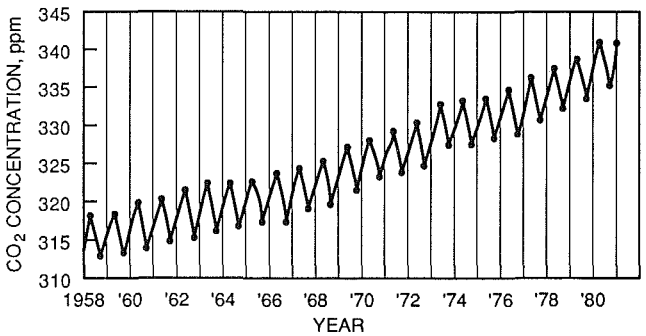

Fig. 2 Atmospheric CO_2 concentration at Mauna Loa Observatory, Hawaii

Control Considerations

CFCs and halons are man-made chemicals that can be discontinued. CO_2, methane, and water vapor, however, have been a part of our atmosphere/environment since the beginning of time. The most that can be done is to reduce emission of CO_2 and methane into the atmosphere and to consider ways to mitigate their effect. The concern is how to control these gases to a proper level in the face of the growing population and growing consumption to support a growing standard of living. The control of CO_2 and methane forms the basis of an energy policy. The relative importance of the greenhouse gases in terms of relative effect, life, and percent contribution are shown in Table 1 [8].

The Need for Control. Figure 2 shows that atmospheric CO_2 increased from 315 ppm in 1958 to 343 ppm in 1980 as measured at the Mauna Loa Observatory, Hawaii [9]. This increase, of about 0.35 percent per year, is attributed to the increased burning of carbon-containing substances such as wood, coal, natural gas, and petroleum products such as gasoline and diesel fuel. The yearly oscillations in CO_2 of about 6 ppm (about 2

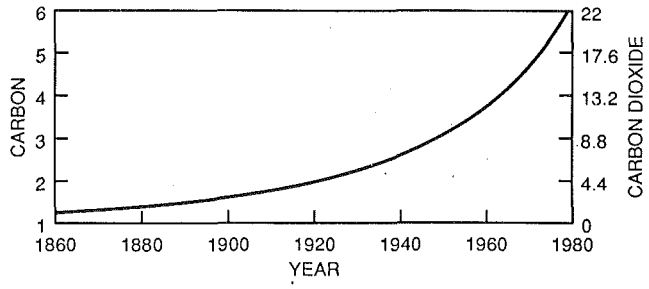

Fig. 3 Worldwide carbon and carbon dioxide from fossil fuel combustion (billions of tons per year)

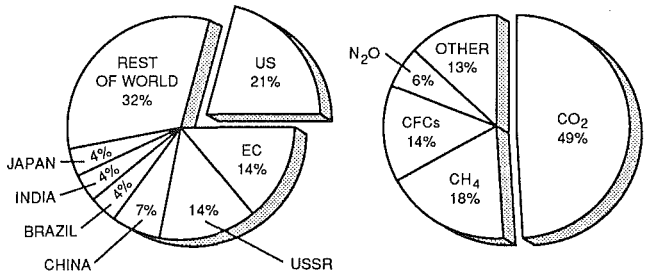

Fig. 4 Global greenhouse gases and the relative emissions by the United States

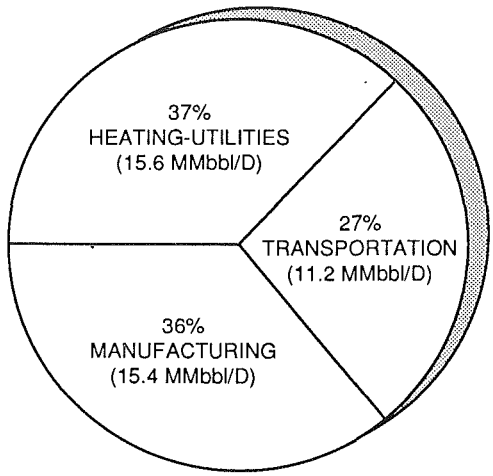

Fig. 5 Daily US energy usage (millions of barrels per day oil equivalent)

percent) shown in Fig. 2 relate to the growing seasons. At the start of the 19th century, before industrialization, the level of CO_2 is estimated to have been about 270 ppm. The trend of carbon releases, and equivalent CO_2 emissions, from fossil fuel combustion for the period 1860 to 1980 is shown in Fig. 3 [10].

Attempts to predict future CO_2 levels abound. One such projection estimates atmospheric CO_2 to be 400 to 600 ppm by 2050 [11]. What has prompted many observers to action was that, worldwide, the five warmest years in the past 125 were 1980, 1981, 1983, 1987, and 1988. Most scientists agree that the average temperature of the earth, taken to be 59°F, has increased about 1°F, or less, since 1861. During that time, the warming has been erratic; the average was essentially constant between 1861 to 1900 and 1940 to 1975. There was a warming trend between 1900 and 1940 and from 1975 to date. The increase in CO_2 during the period 1940 and 1975 was significant, yet most computer models failed to correlate this increase in CO_2 with changes in global temperature. In general, most computer models predicted a global temperature significantly higher than that actually observed. A review of the available global warming models and computer predictions is beyond the scope of this paper, as is an attempt to determine which estimate is correct.

For the purposes of this paper, it is assumed that unabated emission of CO_2, methane, and other greenhouse gases into the atmosphere will result in a major increase of the surface temperature of the earth. To some, this is pure speculation. However, what if the doomsdayers are correct? What then? Prudence dictates that we at least consider what measures could be taken to reduce CO_2, and other greenhouse gas emissions. This "worst case" *assumption* is the basis for the remainder of this paper, the objective of which is to consider ways and means to control, once the amount of control needed is known.

Amount of Control. Figure 4 [12] uses EPA estimates to show that CO_2 contributes the most to the greenhouse effect and that the U.S. emits the most greenhouse gases of all countries. These charts are based on the relative properties from Table 1 and atmospheric concentrations. Texas is the USA's leading CO_2-producing state, producing more than Great Britain or Italy, according to a Natural Resources Defense Council Report [13]. There is no consensus regarding how much control of CO_2, methane, and other greenhouse gases is necessary; CFCs have already been discussed. What is the upper limit of concentration of such gases in the upper atmosphere, without producing major global warming? Some scientists believe that CO_2 emissions must be roughly halved to stabilize tropospheric CO_2 levels. This would be difficult, as human activity is projected roughly to double the level of CO_2 in the atmosphere in 65 years [9].

Others apply roll-back proposals to a specific source such as transportation. Senator Stafford introduced a bill in the U.S. Congress calling for a 50 percent reduction in CO_2 emissions by the year 2000 and a 75 percent reduction by the year 2010. These reductions are to be accomplished by doubling fuel economy to 44.4 mpg (2000) and then redoubling to 88.8 mpg (2010). Another roll-back bill introduced by Senator Wirth calls for doubling of corporate average fuel economy from 1985 to 2010, with the intent of halving CO_2 emissions. The less fuel consumed per mile, the less CO_2 per mile. The South Coast Air Quality Management District of California has announced plans for a 20 percent cut in CO_2 by 2000 and a 40 percent cut by 2010. No similar aggressive roll-backs have surfaced for other, much more significant sources of CO_2 emissions, such as fossil-fueled electric power generation.

Such proposed legislation could be improved. For example wording such as, "upper atmosphere concentrations of CO_2 and methane must not exceed, for example, those measured in the year 2000." Then, if the ratio of ground level CO_2 to that found in the troposphere were known, losses due to interactions and other transport mechanisms could be estimated. A global inventory of CO_2 sources and emission rates could be achieved by estimated fuel consumption from various sources burning various types of fossil fuels. For example, daily energy consumption in the USA is equivalent to 42.2 million barrels of oil, split as shown in Fig. 5 [14].

Winter to summer changes in CO_2 emissions by each country will help define emission patterns. Given the levels based on say the year 2000, it will be possible to establish targets and a control strategy could be constructed. One obvious result of this analysis would be a better understanding of the per nation and per capita emission rate. For example, there is an immense difference between the USA and those countries striving to improve their standard of living. The "have" countries are worried not only about their own rate of consumption of fossil fuels and resultant CO_2, but by the trend toward higher consumption in the developing countries. While some countries put into place policies to reduce fossil fuel consumption, other "have" countries, unconvinced of the arguments, will do noth-

ing to increase the cost of energy (a likely result of some strategies that use alternative fuels or energy sources). The "haves" fear the consequences of the increase in cost: inflation and possible lack of competitiveness to other countries.

Meanwhile, the developing countries, eager to satisfy their populations' desire for a better life derived from higher fossil fuel consumption, will not listen to pleas by the "haves" to maintain their rate of fuel consumption at existing levels. Many of these countries have a rapidly expanding population and economy and feel it is their right to achieve the energy based living standards of other countries using available fossil fuels. What right does the USA or a European country have to deny upwardly mobile third world countries the better life afforded through higher fossil fuel consumptions? The determination of the allowable levels of global CO_2 is expected to bring out the best and the worst in us.

How to Control. Although many scientists believe the earth is warming due to CO_2 and other greenhouse gases, there is little consensus about how to control these gases. Some ideas, such as dumping hundreds of thousands of tons of iron into the ocean to create giant blooms of algae that could soak up excess CO_2 [15, 16], are unconventional and remain to be justified before attempting to use. Of the six billion tons of carbon per year emitted into the atmosphere, about half is absorbed by the oceans, soil organisms, and plants. Other ideas to mitigate the trend to global warming are based on common sense that makes sense but don't sell in some places. Resistance to change and lethargy are high on the list of reasons why even the simplest and easiest to implement common sense ideas are ignored.

It is axiomatic that the more people, the more consumption, and the more pollution. Some families, governments, and cultures have realized this and have put into effect voluntary or government mandated limits on the number of children per family. Table 2 gives a breakdown of the population of the world by continent [17]. This information is included for illustration purposes only, because the topic of population control is beyond the scope of this paper. Population, however, should not to be overlooked in the global CO_2 calculation.

$$\text{Global } CO_2 = (\text{Number of people}) \times (\text{Average consumption of fossil fuel energy}) \times \left(\frac{\text{grams } CO_2}{\text{kg fuel}}\right)$$

where the Consumption of fossil fuel energy is determined by the standard of living, type of fossil fuel used, and the overall energy efficiency.

In 1970, 87 out of every 100 persons added were in developing countries. In 1989, 93 of every 100 persons added to the world's population were in developing countries [18]. Countries that already have large populations with high rates of growth have greater difficulty in increasing the average standard of living, even if blessed with cheap, plentiful fossil fuels. These countries sometimes view the richly endowed, highly industrialized, countries as "overdeveloped" in terms of consumption of the world's fossil fuel energy reserves. To the extent the economy fosters more consumer goods and creature comforts based on energy and products derived from coal, oil, and gas (e.g., more cars and increased vehicle miles traveled), then that country or region can become a major contributor to world CO_2. It will be difficult to limit a developing nation or to expect it to adopt conservation or other measures just because the more industrialized nations decide they must. It has to do with the ability to do so through both technology and cost to the nation.

CO_2 production from countries with large populations and economies that are incapable of embracing a rising standard of living will be less important in terms of global warming. Countries that are developing (i.e., a population that not only expects a better material standard of living, but has an economy that requires greater energy consumption) will have major net increases in fossil fuel consumption and CO_2 emissions. An "upwardly mobile" country will have a difficult choice, when it comes time to reduce CO_2 production. It is impossible to predict what such a country may do, but in all likelihood they will continue to go for the cheapest, most abundant energy available to them, just as the USA did years ago. If that happens to be coal, oil, or natural gas, then CO_2 control is unlikely. It is thought that only the most advanced technology based countries with rich economies will be able to reduce or maintain some control over CO_2.

Control Responsibility. The industrialized countries of Europe, Asia, and North America must provide leadership in CO_2 reduction, because underdeveloped countries are unable and developing countries probably will not. In most of the industrialized countries, populations are not increasing rapidly, but that still leaves them to grapple with maintaining their lifestyle with reduced energy consumption. It is in these countries where the bulk of the man-made CO_2 and methane emissions come from, so it is appropriate that control begin there. Who can better afford to do so? Who has more to lose if the $CO_2 \rightarrow$ global warming linkage is real?

Given the range of standard of living, fossil fuel supplies, and the highly competitive nature of the industrialized nations, how can these nations come to parity on the issue of reduced use of fossil fuels? Competition, cost of living, and inflationary influence are dependent, more or less, directly on the cost of energy. For example, it can be argued that it was and still is cheap, abundant, and available energy, from coal, oil, and natural gas that made the USA an industrial giant and gave rise to the enviable life style currently enjoyed by most Americans. The double digit inflation experienced soon after the oil embargo of the mid-seventies was a direct result of the energy crisis best remembered for shortages, gas lines, and resultant steep price increases. Aside from the fact that no one wants to pay more for fuel or energy, it remains that reducing reliance on fossil fuels in the USA, or anywhere else, will likely result in a higher energy bill. If everyone took the same increase in price at the same time, such changes, although traumatic for a while, would eventually be considered as merely the price to pay to preserve the earth's climate. The major concern is the unequal way each industry, culture, and country will have to cope with reduced fossil fuel reliance and the impact on individual or national standards of living and in international trade and commerce.

There are no easy solutions to these expected inequities, and this is the main reason for the range of responses to the impending $CO_2 \rightarrow$ global warming warnings. The desire for more proof, through research and other studies, is natural before deciding on a course of action. The 68-nation conference on global warming held in November 1989 failed to reach an agreement to stabilize CO_2 emissions by the year 2000 [12, 19]. The USA, Japan, and the USSR refused to sign an accord specifying immediate CO_2 emissions reductions in industrialized nations. Many attendees were critical of the USA attitude. Perhaps those critics should review the history of the recent

Table 2 Estimated world population—1989

Continent	Area, 1000 Sq. Miles	% of Earth	Population Millions 1850	1900	1950	1989	% World 1989
N. America	9,400	16.2	39	106	219	420.1	8.1
S. America	6,900	11.9	20	38	111	287.5	5.5
Europe	3,800	6.6	265	400	530	685.4	13.2
Asia	17,400	30.1	754	932	1418	3130.6	60.3
Africa	11,700	20.2	95	118	199	642.1	12.4
Oceani, incl Australia and	3,300	5.7	2	6	13	26.3	0.5
Antarctica	5,400	9.3					
World	57,900		1175	1600	2490	5192	

Clean Air Act Amendments. Control of acid rain, through reduced oxides of sulfur emissions from power plants operating on high-sulfur coal, were under discussion for over 8 years. The acid rain issue is a classic case, not unlike the $CO_2 \rightarrow$ global warming trial now in progress. As significant as SO_2 and acid rain control is to the affected coal miners and electric power generators, it pales in comparison to the ramifications of mandatory control of CO_2.

Alternative Fuels. This section discusses a few of the prevalent, popular, strategies for reduction of methane and fossil fuel-derived CO_2 [20]. The second term of the equation, "average consumption of fossil fuel energy," draws significantly from experiences gained during the 1974 energy crisis. Incidentally, the per capita yearly energy consumption in the USA is 300 million Btu. This value is approximately equal to the sum of the energy per capita consumed in Brazil, Japan, and West Germany [21].

The degree of heating, cooling, lighting, transportation, processing and preparation of food, and delivery of water and other utilities and services, along with the array of clothing, furniture, housing, and appliances, all represent consumption of fossil fuels in one way or another. Consumption of fossil fuels produces CO_2 emissions. Where methane is a byproduct of combustion or is from a natural gas leak, it too becomes part of the greenhouse effect and influences global warming. A simple way to reduce CO_2 is to use less energy in the making and delivery of goods and services as well as in the creature comforts that current lifestyles demand. Smaller, more fuel-efficient cars, reduced vehicle miles traveled through enlightened land use planning, and restrictions on private car use are but a few of the proposals. Born of the energy crisis of the seventies, these proposals have reappeared, even though (prior to August 1990) there was no energy crisis in terms of price, shortage, or availability. Add to the shopping list those proven methods of energy conservation: better insulation, building materials, and construction methods and improved efficiency of appliances for heating, air conditioning, refrigeration, cooking, lighting and television. Alternative sources of energy, like nuclear, solar electric heating [22], hydroelectric, wind electric, geothermal, and tidal, all became popular research projects in the USA before the energy crisis was officially pronounced over in 1982. These sources have re-emerged as excellent alternatives in terms of zero CO_2 or methane emissions.

Beginning with wood, then coal, oil, and natural gas, there has been a competition between hydrogen and carbon as fuel-energy sources with hydrogen winning [23]. The preferred fuels are those with a high usable hydrogen-to-carbon ratio. Beyond methane, which comprises approximately 90 ± 5 percent of natural gas, hydrogen will eventually become the principal carrier for chemical energy in the fuel system. Hydrogen, with no carbon, produces no CO_2 in combustion.

Fuels used in transportation may be ranked on the basis of their energy specific CO_2 rates as shown in Table 3. Some carbon-containing transportation fuels will, because of the type and design of the engine, produce less CO_2 than others. The rankings in Table 3 change when the efficiency of the engine is considered. For example, diesel fuel, burned in a diesel engine with its superior brake specific fuel consumption, is not necessarily the worst transportation fuel in terms of CO_2 emissions, as its H/C ratio would indicate. Relative to the diesel engine burning diesel fuel, a spark ignition engine burning methane (natural gas) produces less CO_2, while an engine burning gasoline or methanol (methyl alcohol) generally produces more CO_2 per unit of work or per mile.

A third method for comparison of CO_2 production, and perhaps the best, is to consider the entire fuel cycle; this includes raw material production, manufacture, transportation, and combustion of the fuels. Table 4 [24] lists the percent change in greenhouse gas emissions per mile relative to petroleum-powered internal combustion engines. Fuels made from biomass assume processes that do not use fossil fuel and use crops grown every year so that CO_2 from fuel used is taken up by the crops involved in producing the fuel. An interesting observation is that because of coal's lower H/C ratio, using coal as a feedstock with current conversion technology for making methanol would significantly increase CO_2 per mile. Additional details on fuel life cycle CO_2 rankings are given in [25, 26].

Table 3 Approximate H/C and energy specific CO_2 rates for four transportation fuels

Fuel	H/C Ratio	Energy Specific CO_2 Rate, (1) grams of CO_2 per million joules energy
Methane	4.00	55
Methanol	2.00(2)	69
Gasoline	1.85	73
Diesel	1.80	74

(1) Based on Lower Heating Value
(2) Effective H/C in combustion. Chemical H/C is 4.00.

Table 4 Approximate greenhouse gas emissions per mile relative to petroleum-powered internal combustion engines

Fuel and Feedstock	Percent Change
Gasoline and diesel from crude oil	0
Less CO_2	
Methanol from natural gas	–3
CNG from natural gas	–19
Methanol, CNG, gasoline or diesel from biomass	–100
More CO_2	
Gasoline from oil shale	(50 ± 30)
Methanol from coal	98

Natural Gas. It is hard to find acceptable alternative fuels to gasoline and diesel fuel that do not produce CO_2. However, one fossil fuel stands out in all rankings, and that is natural gas [27]. Natural gas suffers from some of the same problems as hydrogen: storage, energy density, and distribution. Also, depending on the care of the engine conversion, increased methane exhaust emissions are expected, because methane is difficult to oxidize in an oxidation catalyst. And, of course, the more conversions to natural gas, the more potential for leaks. From Table 4, other potential fuels are either trivial in improvement, 3 percent for methanol from natural gas, or trivial in quantity, as with methanol from biomass. Figure 6 illustrates that all alternative transportation energy sources, including methanol, ethanol, natural gas, propane, and electricity, currently account for just 3 percent of USA transportation energy needs in 1984 [14].

Hydrogen and Electricity. Hydrogen, as a primary fuel, may be many years away because of supply and cost relative to fossil fuels, even though very limited introduction may begin as soon as the year 2000. This does not mean it should not be given serious consideration, especially in ways to make it in large quantities at reasonable cost. As a vehicle fuel, it suffers from storage density, but this concern is not shared by stationary engine applications. There is no doubt that hydrogen could be a transportation fuel [28, 29] given some way to store and distribute the fuel. It could become a popular fuel, given

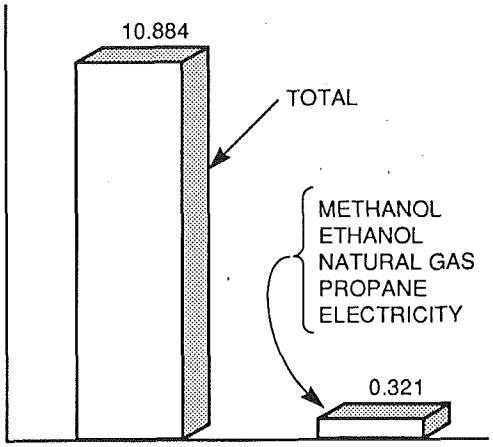

Fig. 6 Transportation energy, estimated 1989 US daily average (millions of barrels per day oil equivalent)

some way to make hydrogen at a reasonable cost. Electricity could be used as a transportation fuel quicker than hydrogen and would be just as attractive for some applications. But like hydrogen, it would have to be made by one of the non-CO_2 producing sources of electricity, such as nuclear, solar, hydro, or wind to have zero CO_2 impact.

Strategies for Controlling CO_2

With the overview of alternative non-CO_2 emitting energy sources and some description of alternative fuels to traditionally used fossil fuels for transportation, what might be some control strategies essential to planning and policy? In addition to a clear policy on population growth, consider the following.

Conservation. Conservation can begin now by simply using less energy and materials that are made by energy-intensive processes. Two main ways to encourage this are through standards of performance, as in energy efficiency ratings on appliances, and fuel economy standards [9, 30] for automobiles. The other way is through taxes, such as tax rebates for purchase and installation of home insulation or a solar heating system, or as a tax on fossil fuel derived energy for industrial, commercial, and residential use. Although an energy tax has been debated in the past, that tax would only apply to electricity made from fossil fuels or other commercial and domestic consumption of natural gas, coal, or oil. A consumption tax lacks the positive incentive that tax reductions have. Perhaps tax policy could even be double-edged, so as to penalize the use of fossil fuel-derived energy and reward conservation measures and the use of nonfossil fuel-derived energy. In this way, the penalties and rewards could offset one another and achieve greater CO_2 reduction, while having less impact on inflation than if only a straight energy tax alone is used. Representative Fortney Stark of California has proposed a CO_2 emission tax of $30 per ton [31]. Under this approach, automobiles that emit 58 tons of CO_2 average in a lifetime would have a tax of about 8 cents per gallon. This is not the only such greenhouse gas tax proposal. Sweden may become the first country to enact legislation to tax CO_2 production [12]. Support for such a carbon tax by the White House Chief of Staff, John H. Sununu, has drawn public protest from some oil and gas producers [32].

Incentives such as buybacks, rebates, or tax deductions to introduce new, lower polluting, more efficient products, is not new. For example Chrysler, among others in the auto industry, in the early 1980s, suggested a bounty be paid on gas guzzling, pre-emission controlled cars. These old vehicles would be converted into scrap (must be shredded and/or baled) and the price of the new car reduced by the bounty. Either the government or the government plus the car company, would pay the bounty, say $2000, to be applied to the purchase of a highly fuel-efficient and low pollution car. Unocal, for example, has offered to pay $700 each for up to 7000 pre-1971 cars turned into scrap metal in an attempt to remove high emitters from Los Angeles [33].

Alternative Energy Sources. Development of improved alternative sources of energy that produce substantially less CO_2 or methane emissions should be encouraged. On May 16, 1990, the Senate Energy and Commerce Committee completed mark-up of S.324, a modified version of Senator Tim Wirth's (D-CO) global warming legislation. This new scaled-down bill would require the Department of Energy (DOE) to develop a least-cost national energy plan to roll-back carbon dioxide and other greenhouse emissions by 20 percent, before the year 2005. Bill S.324 would also require DOE to establish research and development initiatives into renewable energy resource alternatives and the use of natural gas as a motor vehicle fuel.

If the government discontinued granting permits for new electric generation using fossil fuel combustion of coal, oil, or natural gas, communities would quickly begin construction of other ways to generate electricity. A time limit could be placed on existing fossil fuel fired electric generation for replacement and conversion. In the meantime, coal could be replaced with natural gas, where possible. In time, some form of nuclear power for electricity generation will and must be accepted, albeit safer. The greatest concern about nuclear energy is what to do with high-level radioactive wastes. Simply burying or similar storage solutions to these hazardous byproducts tarnishes the image of clean power, regardless of the safety record of the power industry.

Boiler Conversion. A plan could be established to convert industrial and process boilers to natural gas, geothermal, or solar heat. This diverse and fragmented sector will require ingenuity and perseverance to achieve, and only some boilers will be capable of being converted. Perhaps a "sunset law" will be needed on manufacture and sale of fossil fuel-burning boilers.

Transportation. Transportation-related CO_2 will be impacted by a range of controls, including limitations on use, limitations on manufacture of vehicles, tax incentives to buy very fuel-efficient vehicles, vehicles that operate on natural gas or LPG, and electric-powered light rail and street cars. On-highway vehicles are estimated to produce 2.2 gigatons of CO_2 per year, 10 percent of the global fossil fueled CO_2 [9]. Transportation is only one source among many sources, and its relative importance depends on the specific country. For example, transportation accounts for 0.9 gigatons of CO_2/year in the US, 4.2 percent of global fossil fueled CO_2 [9] and 19 percent of the US total.

Alternative Fuels. The ultimate substitute fuel is one that results in no emission of CO_2, methane, or greenhouse gases. Hydrogen requires ways to produce, distribute, and store compactly, primarily in the case of vehicle use. Hydrogen, as a byproduct of unused, nighttime nuclear power, might prove to be a useful and practical fuel for some stationary sources. Given suitable on-board fuel storage, hydrogen could displace some gasoline and diesel fuel vehicles. Much research and development remains to make hydrogen practical, yet hydrogen is the best example of the ultimate alternative fuel form.

Electric Vehicles. Given sufficient electricity (off-peak demand) from nonfossil fuel power plants, electric cars and city delivery vehicles promise to provide major reductions in CO_2. As nuclear and other sources are developed to make electricity, and conventional electric power stations are replaced, excess nighttime capacity should be available to recharge vehicle batteries. Important to this technology will be further improve-

ments in the capacity, life, and recharge rate of storage batteries. Improvements in controls, magnets, and perhaps even the application of super conductivity should be considered. During the transition to electric, some vehicles will profit from a hybrid engine-electric approach as a range/power extender. In all such vehicles, regenerative (electric) braking is essential. Substantial research remains to extend the practicality and use of electric vehicles, but developments to date are encouraging [34].

Deforestation. Deforestation of rain forests is reported to occur at the rate of more than 1 acre per second [35], a most disturbing statistic. Not only do these trees sequester CO_2, but the burning of the resultant biomass produces CO_2. There are many other negative aspects of such clear-cutting of rainforests as regards atmospheric humidity, soil erosion, etc., that have been extensively reported on and go beyond the intent of this paper. Deforestation has been estimated to account for about 27 percent of the total manmade CO_2 worldwide [9].

One response has been to plant trees, millions and millions of trees. However, reforestation is limited by space, moisture, photosynthesis, and soil nutrients. Only young forests efficiently remove CO_2 from the atmosphere and store it in wood and soil. As trees reach maturity, they reach equilibrium and remove less and less CO_2. What do we do with millions of old trees? Lumber companies harvest certain trees for their lumber, and new trees are planted that in time mature and are harvested. As long as the clear-cut area is replanted and the harvested trees are not burned, the CO_2 reduction is greater than if the trees are allowed to grow until death due to fire or other causes. As an aside, the biomass can be a source for alcohol, if collected and processed, thus making total use of the harvest.

It would seem that proposals to plant millions of trees should be for the purpose of eventually making lumber, paper, or alcohol, and not indiscriminant plantings to be eventually chopped down and used for firewood. Land clearing and deforestation occurred in the USA in an unprecedented scale in the 18th and 19th centuries. Perhaps unused farm and pasture land should be replanted with trees useful for lumber or other wood products as part of the CO_2 control strategy. In this way, the USA could provide even more wood products to the world and further reduce CO_2.

Summary

None of the above elements of an overall plan will be achieved easily. One problem is that the entrenched interests, public and private, national and international, will resist any change unless there is a clear and compelling reason. Perhaps the prediction of future catastrophe will persuade people to demand these major changes and pay the price. Aside from a clear and impending calamity, how will these changes take place in a free, democratic, and capitalistic society, such as the USA? Some point to the rapid agreement, both technical and political, regarding what to do about CFCs. Global warming through fossil fuel combustion, however, is several orders of magnitude more complex than elimination of CFCs. Reduction of CO_2 emissions strikes at the very basis of the world standard of living, not just a few products mainly isolated to the industrialized nations, as is the case with the use of the CFC refrigerant-12.

How can government reverse deforestation, discontinue fossil fuel electric powerplants, require nuclear and other nonfossil fuel energy sources, get an energy tax approved, and make the necessary shifts away from combustion of coal and oil? Conservation, development, and sale of even more fuel-efficient vehicles is possible. How do you get people to use cars less, given the land use incentives of the past? Perhaps policies that encourage urban sprawl, highway construction, and reliance on automobiles for transportation [36] will be reversed in the next century. None of these control possibilities are easy. Yet, there are clear and consistent approaches for policy and planning available for use in an energy strategy that would control manmade CO_2 and methane emissions to current levels.

There is no doubt that each day more and more CO_2, methane, and other greenhouse gases are emitted. It would seem prudent to develop contingency plans on what can be done, when, where, and how. It would also seem prudent to authorize continued research work on nuclear, solar, and other alternative energy sources, including hydrogen and electric hybrid vehicles. Regardless of the outcome of the debate over CO_2, such research will always find application against the day when fossil fuels [37] such as oil and natural gas become scarce or impractical to extract from the earth.

Conclusions

In conclusion, the following thoughts are offered.

- There is no shortage of fuels and energy sources or shortages of ways to efficiently use them, merely a shortage of determination to align our self-interest with the national and world interest.
- Capitalism and frontierism must soon reconcile themselves with conservation and the environment.
- Better management and use of the energy sources we currently use can mitigate the inevitable transition to alternatives.

For further reading on this subject, a special publication, *Greenhouse Mitigation*, FACT Vol. 7, 1989, edited by Alex E. S. Green, Fuels and Combustion Technologies Division, ASME, is available from ASME, New York.

References

1 *Radian Report*, "Global Warming and the Greenhouse Effect: How Hot Is Too Hot?," Oct. 1989.

2 *Forbes*, "The Global Warming Panic," Dec. 25, 1989.

3 *San Antonio Light*, "Weather Study Cools Off Global Warming Theory," May 23, 1990.

4 *Houston Chronicle*, " 'Greenhouse' Doesn't Warrant Climate of Fear," Jan. 29, 1989.

5 *San Antonio Light*, "Some Scientists Doubt Threat of Global Warming," Oct. 29, 1989.

6 *San Antonio Light*, "Thatcher Issues Call for Environmental Conduct Guidelines," Nov. 9, 1989.

7 *Radian Report*, "Chlorofluorocarbons and Global Ozone Depletion: Helping Prevent an Environmental Nightmare," Dec. 1988.

8 *Financial Times*, "The Greenhouse Gases," Mar. 16, 1990.

9 Hammerle, R. H., Shiller, J. W., and Schwarz, M. J., Ford Motor Company, "Global Warming," *Ford Research Technology Assessment Series*, June 1989.

10 *National Wildlife Federations Conservation 90*, Vol. 8, No. 6, Aug. 17, 1990.

11 NRC, 1983, "Changing Climate," National Research Council Report, National Academy Press, Washington, DC.

12 *C&EN*, "International Negotiations Inching Toward Global Climate Treaty," Mar. 5, 1990.

13 Tyson, R., "10 States Rank 3rd in World-Class Pollution," *USA Today/International Edition*, July 28, 1990.

14 *Energy Focus*, "Alternative Transportation Fuels: No Simple Solutions Available," Society of Petroleum Engineers, Apr. 1990.

15 *International Herald Tribune*, "Greenhouse Effect: Can the Oceans Iron It Out?" May 21, 1990.

16 *The China News*, "Battling the Greenhouse Effect," Aug. 1, 1990.

17 *The World Almanac and Book of Facts 1990*, Scripts Howard Company, New York, 1990.

18 Vobejda, B., "The Over Population Scare Has Gotten Lost in the Crowd," *The Washington Post National Weekly Edition*, July 9-15, 1990.

19 *San Antonio Light*, "U.S., Japan Scorn Global Pact to Curb 'Greenhouse' Effect," Nov. 7, 1989.

20 ASME General Position Paper on Energy and The Environment, June 1989.

21 *Energy Research & Development News*, Vol. 4, No. 1, July 1989, S. Carolina Energy Research and Development Center.

22 Ullmann, O., "When Does Solar Energy Come Again," presented at the Conference on Diffusion of Technologies and Social Behaviour at International Institute for Applied Systems Analysis (IIASA), June 14-16, 1989.

23 Marchetti, C., "When Will Hydrogen Come?" *International Journal of Hydrogen-Energy*, Vol. 10, No. 4, 1985, pp. 215-219.

24 NRC, "1990 Fuels to Drive Our Future," *National Research Council Report*, National Academy Press, Washington, DC.

25 DeLuchi, M., "Hydrogen Vehicle: An Evaluation of Fuel Storage Per-

formance, Safety Environmental Impacts, and Cost," *International Journal of Hydrogen Energy*, Vol. 14, No. 2, 1988, pp. 81–130.

26 DeLuchi, M., Johnston, R. A., and Sperling, D., 1988, "Transportation Fuels and the Greenhouse Effect," *Transportation Research Record*, Vol. 1175, pp. 33–44.

27 Wilke, T. L., "Global Climate Change: The Role of Natural Gas," *Viewpoint*, GRID Spring 1990.

28 *San Antonio Express-News*, "Scientists Say Hydrogen Is Fuel of Future," Sept. 3, 1989.

29 Marchetti, C., "The Future of Hydrogen, An Analysis at World Level, With Special Look at Air Transport," Invited paper presented at The Hydrogen Link Conference of the Hydrogen Industry Council, Montreal, Mar. 24–26, 1986.

30 *Automotive News*, "Curry Questions Data Supporting Boost in CAFE," May 7, 1990.

31 *San Antonio Express-News*, "Let Energy Pay for Deficit Fight," June 10, 1990.

32 *San Antonio Light*, " 'Carbon Tax' Proposal Attracts Protest From Permian Basin," July 1, 1990.

33 *San Antonio Light*, "Unocal to Pay Cash for Old Clunkers," Apr. 29, 1990.

34 *Nuclear Industry*, "Clearing the Air," First Quarter 1990.

35 *San Francisco Chronicle*, "Climate Peril," June 17, 1990.

36 *Bus Ride*, "A Farewell to Responsibility," May 1990.

37 *San Antonio Light*, "U.S. Oil Reserves, Discovery Rate Down Again," Sept. 14, 1989.

Global Climate Change

R. H. Hammerle

J. W. Shiller

M. J. Schwarz

Ford Motor Company,
Dearborn, MI 48121

This paper reviews the validity of the greehouse warming theory, its possible impact on the automotive industry, and what could be done. Currently there is very limited evidence that man's activity has caused global warming. Mathematical models of the earth's heat balance predict warming and associated climate changes, but their predictions have not been validated. Concern over possible warming has led to several evaluations of feasible CO_2 control measures. Although cars and trucks contribute only a small fraction of the CO_2 buildup, the automotive industry may be expected to reduce its share of the atmospheric CO_2 loading if controls become necessary. Methods to reduce automotive CO_2 emissions, including alternative fuels such as methanol, natural gas, and electricity, are discussed. Also, control of the other greenhouse gases. which may currently contribute about 45 percent of the greenhouse warming, is considered.

General Background

The heat and drought in the summer of 1988 have been cited in both Congress and the media as evidence that man has caused global warming. Indeed, 1988 was the hottest year on record. Worldwide, the five warmest years in the last 125 were 1980, 1981, 1983, 1987, and 1988. Recent elevated temperatures tend to uphold the greenhouse theory that man-made gases, such as carbon dioxide (CO_2), methane (CH_4), ozone (O_3), nitrous oxide (N_2O), and chlorofluorocarbons (CFCs), which are accumulating in the atmosphere, may be warming the earth. However, over the past 100 to 200 years the temperature changes and the ambient levels of the greenhouse gases are not well correlated, suggesting the recent temperature changes may have a natural origin. Overall there are reasons for concern that the accumulation of these gases may be warming the earth, and further investigation is necessary.

The scientific foundation for the greenhouse theory of climatic change goes back to Arrhenius (1896) who proposed that the glacial epochs occurred largely because reductions in atmospheric CO_2 levels lowered the earth's average temperature. His proposal is gaining acceptance as recent analyses of gases trapped in glacial ice samples, which were formed during those epochs, show some of the predicted CO_2 fluctuations.

In the late 1930s, Callendar concluded that human activities were causing a worldwide increase in atmospheric CO_2 and that this increase could initiate global warming by the greenhouse effect (Callendar, 1938). Since then, a lot of research has focused on CO_2. In only the last 15 years, the effect of other trace gases accumulating in the atmosphere has been recognized as well. Public awareness, media coverage and regulatory concern for the issue has varied significantly over this time period.

Atmospheric CO_2 has increased from 315 ppm in 1958 to about 343 in 1980; an average rate of about 0.35 percent per year; see Fig.1. The yearly CO_2 oscillations of roughly 6 ppm, seen in that figure, occur as a result of growing seasons. In

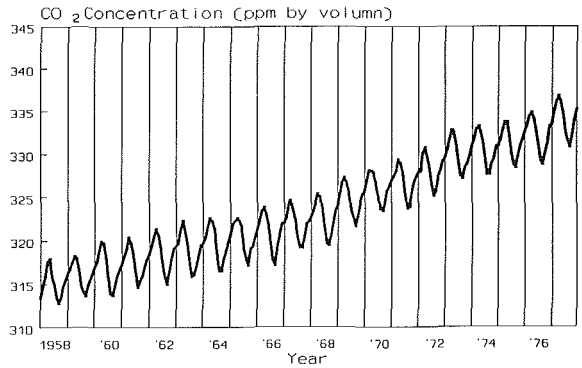

Fig. 1 Atmospheric carbon dioxide levels at Mauna Loan Observatory, Hawaii

1990, the level was 353 ppm, and it is increasing by 0.5 percent per year. Current estimates place the pre-industrial (circa 1790) CO_2 level at 270 ± 10 ppm and the 2050 level at 400 to 600 ppm (NRC, 1983). The observed increases are primarily attributable to mankind burning coal, oil, and gas; large increases are predicted for the future on the basis of expected fossil fuel combustion. Deforestation and land-use changes over the last 100 years have added to the increase by releasing large quantities of CO_2.

Widespread temperature measurements began on land in the 1850s and on the ocean only recently. There are hundreds of millions of temperature observations with several uncertainties. Jones et al. (1986) analyzed these data to remove much of the uncertainty and then argued that the global temperature between 1861 and 1984 has increased about 0.5°C; see Fig. 2.

While the data of Jones et al. suggest a 0.5°C increase, temperature measurements (Karl and Jones, 1989) in the continental U.S. between 1901 and 1984 do not. The raw data show an apparent 0.2°C increase, which is removed when one considers urban bias. Here urban bias means that many temperature monitoring sites that were rural in 1901 are now urban. Heat island effects that make cities warmer than the countryside also make these sites warmer today than they were in 1901.

Contributed by the Internal Combustion Engine Division and presented at the Energy-Sources Technology Conference Exhibition, Houston, Texas, January 20–24, 1991. Manuscript received by the Internal Combustion Engine Division September 1990. Paper No. 91-ICE-12.

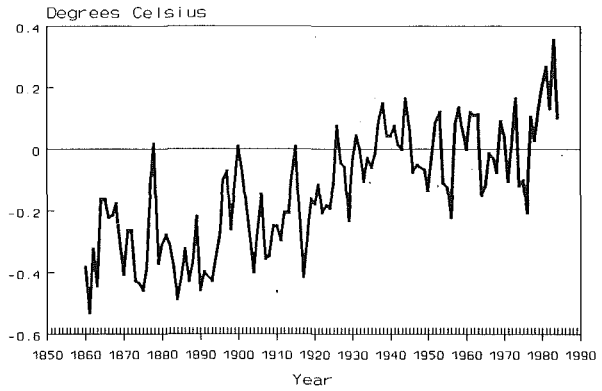

Fig. 2 Observed temperature trend

This heat island effect can be removed by estimating the effect of city size on its temperature. Estimates add between 0.1 and 0.4°C to the observed annual average temperature, an amount as large, or larger, than the apparent 0.2°C increase. The magnitude of the urban bias in other countries is uncertain.

The 0.5°C increase suggested by Jones et al. (1986) is approximately equal to the increase predicted by the greenhouse theory (0.4 to 1.4°C depending on the preindustrial CO_2 concentration and other assumptions). However, the increase is not as steady as the theory predicts (Jones et al., 1986). The global temperature data show little trend from 1861 to 1900, marked warming from 1900 to 1940, steady temperatures from 1940 to 1975, and subsequent rapid warming. The nearly constant global temperatures from 1940 to 1975 is very puzzling. This 35-year period saw great increases in CO_2 emissions in clear contradiction to the theory. While the agreement between the observed global temperature increase and the increase predicted by the greenhouse theory adds credence to the theory, it does not demonstrate a causal relationship.

Studies modeling the future greenhouse effect of CO_2 suggest that doubling the CO_2 level would cause a global warming of 1.3 to 4.8°C. Some early studies are listed in Table 1.

The models also predict a 3 to 11 percent increase in rainfall (Schlesinger and Mitchell, 1985) and more evaporation. There is substantial uncertainty in the geographical distribution of the changes in precipitation; however, they generally indicate more rain in latitudes between 30 and 70 deg North, the latitudes of the United States (Bradley et al., 1987). Measurements since 1850 show precipitation in the US declined from 1880 to the 1930s, and generally increased since then. It has increased markedly in the last 30 years, especially in autumn, winter, and spring, with no change in summer rainfall.

The longer-term impact of man-made greenhouse warming is even more uncertain. Early studies modeling the future greenhouse effect of four times higher CO_2 levels showed that there would be less summer rain in the US (Manabe et al., 1981). This trend was not confirmed by other studies assuming two times higher CO_2 levels (Schlesinger and Mitchell, 1985) or by historical measurements (Bradley et al., 1987).

The rainfall issue is not resolved, nor is the effect of a possibly warmer and dryer climate on agriculture (NRC, 1983). Yet, drought and crop damage are often cited to be the results of man-made greenhouse warming. A rise in sea level is similarly cited. Many scientists view the man-made increase in atmospheric CO_2 levels as an inadvertent global experiment, which, like it or not, may demonstrate the impact of greenhouse warming before that impact can be accurately predicted (Ramanathan, 1988).

Other gases, besides CO_2, which have accumulated in the atmosphere since the 1790s, may also contribute to today's greenhouse warming. In the 1795 to 1985 time period, the same model suggests that these other gases have added 0.3 to 1.1°C to the CO_2-induced warming as shown in Table 2 (Dickinson and Cicerone, 1986). Over that time period, CO_2 caused about 60 percent of the warming.

Table 1 Warming predictions of various greenhouse models induced by increases in atmospheric CO_2 from 300 ppm to 600 ppm

Model	Temperature Change (°C)	(°F)
Manabe & Wetherald (1975)	2.9	5.2
Manabe & Wetherald (1980)	3.0	5.4
Schlesinger (1983)	2.0	3.6
Washington & Meehl (1984)	1.3	2.3
Hansen et al. (1984)	4.2-4.8	7.6-8.6
Manabe & Wetherald (unpubl)	4.0	7.2

Source: WMO, 1985

Table 2 Global warming due to other gases from 1795 to 1985 predicted by greenhouse model (Dickinson and Cicerone, 1986)

Gas	Temperature Change (°C)	1985 Conc	Pre-Ind Conc
Carbon Dioxide	0.4 to 1.4	345 ppm	275 ppm
Methane	0.2 to 0.7	1.7 ppm	0.7 ppm
Ozone	0.03 to 0.1	10-100 ppb	0-10% less
Nitrous oxide	0.01 to 0.06	304 ppb	285 ppb
CFC 11	0.02 to 0.07	0.22 ppb	0 ppb
CFC 12	0.03 to 0.13	0.38 ppb	0 ppb
Total	0.69 to 2.5		

By the year 2030, the greenhouse warming caused by gases other than CO_2 will be approximately equal to that of CO_2; see Fig. 3 (Ramanathan et al., 1985). In the 2030 projection, CFC use was assumed to grow 3 ± 2 percent per year. Of course, the Montreal Protocol and EPA rules limiting the production and sale of CFCs, both of which occurred after these estimates were made, should reduce the impact by 2030.

Technical Facts

The basic idea for the greenhouse theory (Arrhenius, 1896) is that the earth's temperature is stable if the radiant energy it receives from the sun is balanced by the outgoing radiant energy that the earth emits into space. The solar radiation that hits the earth and its atmosphere could supply up to 342 W/m^2, when averaged over the earth surface (Dickinson and Cicerone, 1986). However, on average about 30 percent of this incident energy is reflected back into space from clouds, airborne dust, and surfaces. The percent reflectivity is called the albedo; it varies from about 10 percent for clear sky to nearly 80 percent for the tops of cumulus clouds (Huschke, 1959). The earth and its atmosphere absorb 70 percent of the sun's radiation on the average, or 239 W/m^2; see Fig. 4.

In describing the radiation emitted from earth, an understanding of thermal radiation is useful. Thermal radiation from an object is usually infrared unless it is very hot, above 500°C. The energy is proportional to its surface temperature in absolute degrees to the fourth power and is often idealized to "blackbody" radiation. By definition, a "blackbody" is an object that absorbs all radiant energy that strikes its surface (no reflected radiation, hence it appears black at low temperatures). The earth's surface (not including the atmosphere) radiates like a blackbody.

The earth's surface and the atmosphere emit infrared thermal radiation back into space. If, for a moment, we neglect the atmosphere's role in emitting radiation but not its role in absorbing the sun's energy, the earth would emit 390 w/m^2,

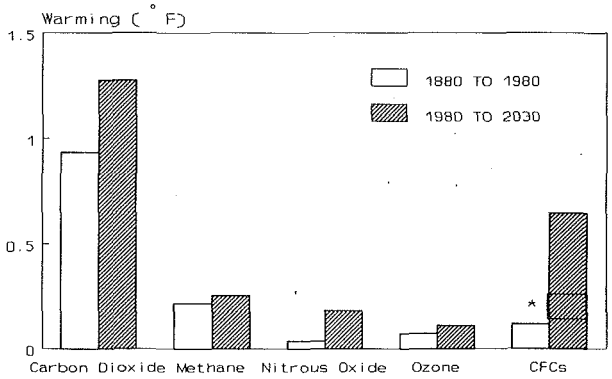

Fig. 3 Calculated greenhouse warming

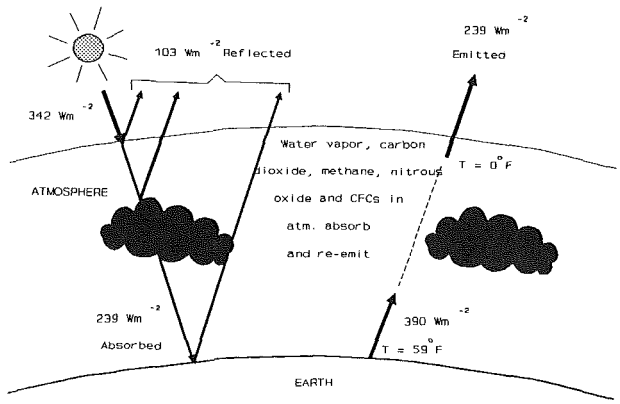

Fig. 4 Global energy balance

the thermal energy radiated by a blackbody at the earth's average surface temperature, 15°C (59°F or 288 K). Since this is greater than the 239 W/m^2 absorbed from the sun, the earth would gradually cool to about −18°C (0°F or 255 K), the blackbody temperature needed to radiate the 239 W/m^2. At an average surface temperature of −18°C (0°F), the earth would be covered with ice, and agriculture would be impossible.

Gases present in the atmosphere absorb and then re-emit most of the thermal radiation from the earth's surface. However, the atmosphere emits less energy into space than the earth's surface would because the atmosphere's average temperature is lower, roughly 0°F. The temperature in the first 10–15 km of the atmosphere, which is radiatively active, decreases from that of the earth's surface by 5–7°C per km. At roughly −18°C (0°F), the atmosphere radiates 239 W/m^2, the same as that absorbed from the sun.

Thus, the difference between the energy emitted by the earth and that emitted by the atmosphere (390–239 = 151 W/m^2) is absorbed by the atmosphere. This energy-trapping process is called the greenhouse effect; here the atmosphere plays the same role as the glass panes in a greenhouse. The greenhouse effect is critical for mankind's survival; it keeps the global temperature at a habitable 15°C (59°F), rather than a hostile −18°C (0°F).

When the energy trapping is enhanced, for example, as resulting from a doubling of the atmospheric concentration of carbon dioxide to 600 ppm, about 4 W/m^2 more of the thermal radiation emitted from the earth's surface is absorbed in the atmosphere. The number of W/m^2 needed to raise the earth's surface temperature by 1°C is called the feedback factor; it is the major uncertainty of the greenhouse theory, and it has been studied extensively for 29 years. Estimates vary from 3.6 to 0.9 W/(m^2°C) yielding a 1.1 to 4.5°C warming, respectively, for the CO_2 doubling (Ramanathan, 1988).

Uncertainties in the feedback factor stem from gaps in our understanding of polar ice and glacier melting, ocean heating and evaporation and cloud formation. For example, the heat capacity of the oceans is enormous, if surface and deep waters are well mixed; it is much smaller, if only surface water is heated.

In addition, some of these processes are especially difficult to model because they also affect the earth's albedo. For example, a 1.0 percent increase in albedo removes 3.4 W/m^2 heat load, almost canceling the effect of doubling the CO_2 level. Indeed, more clouds are expected to form because of the greenhouse warming, and, if they do, they will reflect more sunlight back into space and tend to slow down the warming of the earth. This effect is not included in the current greenhouse models.

The ability of the radiatively active gases to absorb the earth's infrared emission is well known to vary with the wavelength of the radiation. This is shown in Fig.5, which gives the radiant energy from the earth and atmosphere detected by a satellite over the tropical Pacific. The active gases are water vapor, CO_2, CH_4, O_3, N_2O, and CFC 11 and CFC 12.

Water is by far the strongest absorber. Its absence in desert air, for example, allows escaping thermal radiation to lower nighttime temperature drastically. Roughly 70 to 90 percent of the thermal radiation emitted by the earth's surface with wavelengths between 7 and 13 μm escapes into space because those wavelengths are not strongly absorbed by the abundant gases, such as water and CO_2. This wavelength region is called the atmospheric window because it is relatively transparent. A number of manmade trace gases, such as ozone and CFCs, absorb strongly in this region.

Per molecule, energy trapping by the other gases is much more efficient than for CO_2 for three main reasons: The other gases absorb more efficiently than CO_2 on a molecular basis; the other gases absorb in the atmospheric window where a relatively large large portion of the earth's radiation escapes into space; and finally there is so much CO_2 in the atmosphere already that much of the earth's radiation in the CO_2 absorption region is currently absorbed.

For example, an increase of either CFC 11 or 12 from 0 to 2 ppb leads to trapping about 0.6 W/m^2, and a global temperature increase of 0.2 to 0.7°C for each gas, while an increase of CO_2 from 300 to 600 ppm leads to trapping of about 4 W/m^2, and a temperature rise of 1.1 to 4.5°C. Thus, one molecule of a CFC has about the same greenhouse effect as about 3×10^4 molecules of CO_2. Only the low atmospheric levels of CFCs, 10^6 times lower than CO_2, keep their greenhouse warming contributions low; see Table 2.

Finally, before leaving this discussion of the greenhouse theory, let's return to Arrhenius's idea that the greenhouse effect caused the glacial epochs. As described above, the greenhouse models predict approximately a 0.5°C increase in global temperature due to a 70 ppm CO_2 increase from 270 to 340 ppm for 1861 to 1984. This requires a feedback factor close to 3.5 Ws/(m^2°C).

That feedback factor is too large to predict a 7–10°C temperature increase needed for the glacial-interglacial epochs where the CO_2 increase from 190 to 280 ppm was recently observed in glacial ice formed during those epochs. One possible explanation, if Arrhenius's idea is correct, is that the oceans have indeed slowed the current global warming but that as thermal equilibrium is established much higher temperatures will result.

However, another theory on the glacial epochs, which was championed by M. Milankovitch during the first half of this century, suggests that glacial epochs are due to periodic variations in the geometry of the earth's orbit about the sun (Covey, 1984). If the glacial epochs were caused by variations in the earth's orbit, the 0.5°C warming from 1861 to 1984 may be due to these variations rather than to the greenhouse effect.

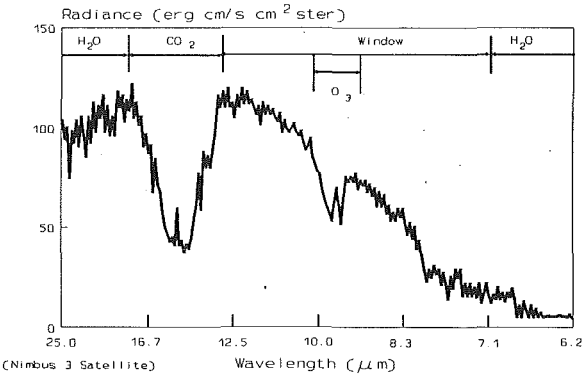

Fig. 5 Observed spectra of outgoing longwave emission

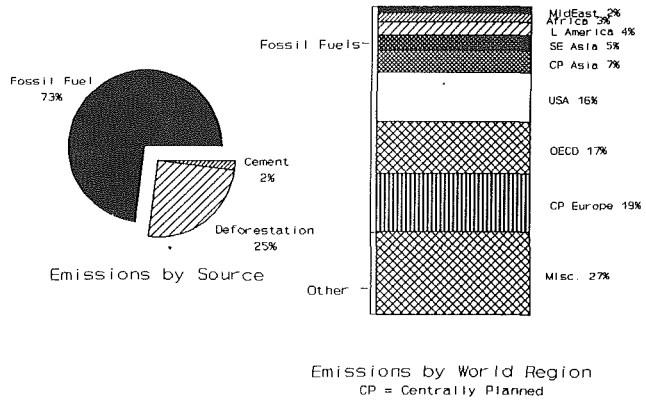

Fig. 6 Carbon dioxide emissions by source and world region

The earth's orbit is currently near the highest temperature conditions. This is consistent with the glacial epoch record in which the earth is approaching the high-temperature interglacial period, having just come out of a major glaciation 18,000 years ago (Covey, 1984). The glacial epoch issue is not yet settled.

Current Emissions

Global fossil fuel combustion generates roughly 21.3 gigatons (10^9 metric tons) of CO_2 per year (IEA, 1989). Deforestation releases roughly 8 gigatons of CO_2 per year (Woodwell, 1988), and cement manufacturing releases about 0.5 gigatons of CO_2 per year from the calcination of carbonate rock, in addition to the CO_2 from the fossil fuel used, which was included above in fossil fuel combustion (World Resources, 1990). Thus, total man-made CO_2 emissions (fossil fuel, deforestation plus cement manufacturing) worldwide are about 30 gigatons per year; see Fig. 6 (Blair, 1988).

While these emission rates are huge, the atmosphere into which they are emitted is also huge, but obviously not limitless. Currently, the 350 ppm of CO_2 in the atmosphere represent 2800 gigatons. The current estimated 0.5 percent annual increase in atmospheric CO_2 requires an unabsorbed carbon emission of 14 gigatons of CO_2 per year. Therefore, the difference, about 16 gigatons of CO_2 per year, is absorbed apparently by the earth.

However, estimates of CO_2 absorption by the oceans are only about 11 gigatons of CO_2 per year (Bolin, 1970). In any case, about half of the man-made CO_2 emissions, 15 gigatons per year, appear to be absorbed by natural processes and half remain to build up in the atmosphere.

Fossil fuel usage in the US generates 16.8 percent of the global man-made CO_2 emissions, and 23.5 percent of the global fossil-fuel CO_2 emissions; see Fig. 6 and Table 3. Considering combustion only, worldwide highway vehicles and those in the US generate 3.0 (14.3 percent) and 1.16 (5.5 percent) gigatons of CO_2 per year, respectively; see Table 3. When CO_2 emissions from fuel production are included, worldwide and US highway vehicles emit 3.2 (15.1 percent) and 1.22 (5.7 percent) gigatons of CO_2 emissions per year, respectively. Highway vehicles in the US generate about 23.2 percent of the US fossil fuel CO_2 emission inventory from fuel combustion only and 24.4 percent from both fuel combustion and processing. Highway vehicles worldwide generate about 10.7 percent (estimates range from 7 to 13 percent) of the global man-made CO_2 emissions.

Biomass emission from deforestation, which includes wood burning, is not considered a fossil fuel, but its burning does contribute roughly 8 gigatons CO_2 per year or about 27 percent of the man-made global CO_2 emission inventory. Deforestation is expected to continue at a rate of a few percent loss of global forests per year. This rate, if not reduced, will completely eliminate forests in 30 to 50 years.

Table 3 Approximate vehicle CO_2 emission rates using 21.3 and 29.8 gigatons/yr for global fossil fuel and man-made CO_2 emission rates, respectively

Source	CO_2 Emissions (Gigatons/yr)		Fraction of Global Fossil Fuel		Fraction of Global Man-made	
	Comb Only	Comb +Proc	Comb Only	Comb +Proc	Comb Only	Comb +Proc
Global Highway Vehicles	3.0	3.2	14.3%	15.1%	10.2%	10.7%
U.S. Highway Vehicles	1.2	1.2	5.5%	5.7%	3.9%	4.1%
U.S. Total Fossil Fuel Use		5.0		23.5%		16.8%

There is disagreement about whether significant regrowth of forests has occurred in some areas. Part of the debate is that deforestation is occurring roughly with human population growth, while reforestation is limited by photosynthesis, soil nutrients, moisture, and the space available, many of which are hard for man to control. Also only immature forests remove CO_2 from the atmosphere and store it in wood and in soil. As they reach maturity, they reach equilibrium and no longer store additional carbon. No evidence for regrowth has been found, so the issue is not yet settled (NRC, 1983).

It should be noted that in comparing percentage numbers, such as those given above, one must be careful to use the same base. For example, worldwide highway vehicles emit 15.1 percent of the global fossil fuel CO_2 emissions, but only 10.7 percent of the global man-made CO_2 emissions; see Table 3.

More stringent passenger car fuel economy standards by themselves would have very little impact on the US or global CO_2 emission inventory. If feasibility issues were temporarily neglected, and, for example, if the US passenger car CO_2 emissions were immediately reduced by 20 and 50 percent over the 1985 level, the US fossil fuel CO_2 emission inventory would be reduced by 2.2 and 5.6 percent, respectively, based on 1985 MVMA fuel consumption data. Global man-made CO_2 emissions would be reduced by 0.4 and 1 percent, respectively. If, in a similar manner, US highway vehicle CO_2 emissions were reduced by 20 and 50 percent over 1985, the US fossil fuel CO_2 emission inventory would be reduced by 4 and 10 percent, respectively.

Halving vehicle CO_2 emission rates internationally, i.e., doubling fuel economy, would achieve about a 5 percent reduction in global man-made CO_2 assuming miles traveled remained constant. This shows that vehicle fuel efficiency improvements,

by themselves, offer limited leverage for reducing global CO_2 levels, thus making it clear that any effort to reduce CO_2 emissions would have to be implemented for a wide range of CO_2 emitters.

Global emissions of CFC 11 and 12 are about 0.26 and 0.33 megatons per year, respectively. Currently the 0.37 ppb atmospheric concentration of CFC 12 represents 8.1 megatons. There are no natural sources of CFCs. Their tropospheric lifetimes are 65 and 110 years, respectively. With a 110-year lifetime, approximately 0.09 megatons of CFC 12 is removed from the atmosphere per year. This loss is about one third of the annual emissions.

The potential of the other greenhouse gases to cause global warming depends on their atmospheric lifetimes relative to CO_2. For example, a methane molecule in the atmosphere has about 26 times the global warming potential of a single molecule of CO_2. However, most of the methane emitted from any source will be gone in 10 to 20 years because its atmospheric lifetime is about 10 years, while the CO_2 will last more than 200 years. Thus, to compare the effect of methane emissions on global warming to that of CO_2, the effect of fresh methane emissions should be averaged over the CO_2 lifetime. When this is done, a molecule of methane has about four times the global warming potential of a molecule of CO_2.

In a recent report (Unnasch et al., 1989), the global warming caused by methane attributed to current passenger vehicles was about 7 percent of the greenhouse warming of the CO_2 attributed to the same vehicles. About 95 percent of the methane emissions attributed to vehicles came from methane releases during oil production; only 5 percent comes from the tailpipe. Because worlwide highway vehicles contribute only 10.7 percent of global man-made CO_2 emissions, methane emissions attributed to cars contribute only 0.7 percent to the global warming potential.

In addition, that report (Unnasch, 1989) showed that the use of CFC 12 for vehicle air conditioning has a huge potential greenhouse impact. About 50,000 metric tons of CFC 12 is sold for use in US mobile air conditioners per year. Currently all of this eventually leaks into the atmosphere. In 1984, there were 1,711,485 miles driven (MVMA, 1988), which yields 0.027 g/mile. The global warming potential for CFC 12 is about 30,000 times that of CO_2 on a molecular basis when atmospheric lifetimes are not considered and about 16,000 including lifetimes. Thus, using the potential with lifetimes, CFC 12 contributes the equivalent of about 160 g/mile of CO_2 compared to the tailpipe CO_2 emissions of about 310 g/mile! This surprising result is due to the fact that CFC 12 has between 1.6 and 3×10^4 higher greenhouse potential on a molecular basis than CO_2.

Seventy-four percent of the passenger vehicles sold in 1986 in the US had air conditioners, and 56 percent of such vehicles in use in 1986 had air conditioners. CFC use in mobile air conditioners contribute 23 percent of the US CFC emissions of 0.2 megatons per year; see Fig. 7 (Black, 1988). However, CFCs have not yet accumulated in the atmosphere to the point where they contribute significantly to the greenhouse warming; see Table 2.

In addition, the Montreal Protocol with the London Revision of 1990 and the EPA rules on CFCs will completely eliminate future emissions by the year 2000 because they deplete stratospheric ozone. It is obviously important to replace CFC 12 in highway vehicle air conditioning systems as soon as safe alternatives are found.

Possible Impact on the Automotive Business

Assuming that greenhouse warming is confirmed and its reduction is required at some point, the most significant additional requirements on the motor vehicle industry would be control of CO_2 and CFCs. Of these, the most difficult is CO_2 control. While CO_2 is already controlled indirectly by the fuel economy standards and CFCs will shortly be eliminated to protect stratospheric ozone under the revised Montreal Protocol, at issue is the need for additional controls.

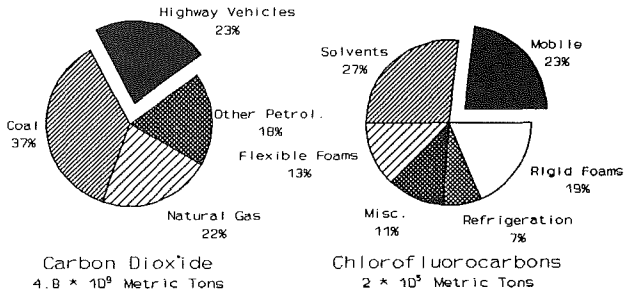

Fig. 7 1985 US CO_2 and CFC emissions by source category

Modification of existing CFC 12 facilities to produce a fluorocarbon, HFC 134a ($C_2H_2F_4$), which is a CFC 12 substitute, has already begun. Also processes to produced foam for most automotive applications using water vapor instead of CFC 11 have been developed.

The automotive industry plans to eliminate CFC 12 as soon as possible. Toxicological studies of HFC 134a will take about 3 years to complete, with a fairly accurate estimate of its safety due in the early 1990s. These toxicological studies control the introduction timing. HFC 134a will require some modification of vehicle air conditioning systems because it is less efficient at cooling.

While HFC 134a has a similar infrared absorption band and cross section to CFC 12, HFC 134a is not expected to accumulate in the atmosphere because its lifetime in the atmosphere is only 15 years compared to 110 years for CFC 12. Therefore, HFC 134a has roughly one tenth the global warming potential of CFC 12 when lifetimes are considered. HFC 134a has no chlorine so it is not expected to deplete stratospheric ozone.

A number of bills have been introduced in the US Congress that called for drastic CO_2 emission reductions. Those requiring reductions of 20 percent or more by the year 2000 have not received widespread support.

A bill introduced by Senator Wirth (S.324) called for the establishment of a national energy policy that will identify cost-effective strategies to lessen the generation of greenhouse gases and consider othe important national goals. The bill includes efforts to improve our scientific understanding, to stabilize greenhouse gas emissions, and to investigate the possibility of reducing CO_2 emissions by 20 percent by the year 2005.

These control objectives are broadly consistent with the recommendations of the 1989 Noodwijk Conference. The 67 countries represented support stabilization of CO_2 emissions by the year 2000 as a first step and urge feasibility studies for ways to reduce emissions by 20 percent sometime thereafter.

Reductions in all sources of CO_2 emissions of 20 percent by the year 2005 and of 50 percent ultimately have been suggested as needed to stabilize atmospheric CO_2. These correspond roughly to 25 and 100 percent improvements in fuel efficiency, respectively.

Advances in fuel economy are not considered limited by technology in the sense that 25 to 100 percent improvements in fuel economy are impossible. Technology does limit the fuel economy that can be achieved with a given vehicle description, and, therefore, technology may force a reduction in vehicle size and performance to achieve a specific fuel economy. Additionally, even if technology were not a limitation, practicality would be. There are limits to how much size and performance can be reduced, and costs can be increased.

In 1983, the Office of Technology Assessment of the US Congress estimated that new car average fuel economy could be increased from the 27.5 mpg, which was then required by

1985, to 51 mpg by the year 2000 (Alic et al., 1983). These improvements were projected from weight reductions, improved engine, transmission, and accessory efficiencies, aerodynamics, and decreased drive train resistance. Today, this report is considered outdated and is being redone.

Congress may choose other approaches, such as increasing the federal excise tax on gasoline. If the problem is perceived to be very serious, more drastic measures might be considered, such as forcing mass transit, or taxing individuals or businesses purchasing low-mpg vehicles. Alternatively, there could be various restrictions on highway access like requiring special lanes for high-occupany and/or high fuel efficiency vehicles or increased government involvement in community planning to reduce traffic congestion and vehicle miles traveled.

Obviously, fuel conserving laws would have a huge impact on consumers and the automotive manufacturers, but they would be only a part of a much larger program to restrict CO_2 emissions from other sources in the US and in the world. Measures to achieve overall CO_2 reductions would also significantly affect automotive manufacturing operations, such as plant heating, painting, and using and generating electrical power.

Change in Fuel Use

Attempts to control man-made greenhouse warming could substantially alter the use of the various fossil fuels. In general, the amount of CO_2 formed from the use of a fuel depends upon the ratio of carbon to hydrogen in the resource from which that fuel was derived. If the resource is mainly carbon, like coal, its direct combustion produces about 20 percent more CO_2 for the same amount of energy as petroleum; see Fig. 8.

If, on the other hand, the resource has relatively high hydrogen, like methane, its combustion releases about 20 percent less CO_2 for the same energy as petroleum because some of the energy is derived from the oxidation of hydrogen to water. Therefore, coal users would want to shift to natural gas or petroleum, if there were no other constraints.

However, coal is such a plentiful resource, especially in the US, and the industry employs so many people, it is hard to imagine a strategy that would eliminate coal completely. To the extent that coal is eliminated, much, if not all, of the gas and oil production capacity idled by improved efficiencies for those fuels may be used to replace coal. Also because the role of nuclear power is uncertain, it is questionable whether it will help replace coal.

Unfortunately, US domestic production of petroleum has not kept pace with consumption as illustrated in Fig. 9. With the growth of the nation, total US energy consumption reached 74 quadrillion Btu in 1986 (Hoffman, 1988). Figure 10 illustrates the trend in total energy consumption from major energy sources, except biomass, over the period 1955 to 1986. In 1986, 43 percent of total US energy consumed, excluding biomass, was supplied by petroleum. Highway vehicles consumed nearly 50 percent of the petroleum or 21 percent of the total non-biomass energy used in the US, as shown in Fig. 11.

Because the recoverable resources of fossil fuels have been so large and relatively inexpensive, they have been very difficult to displace in man's global energy system. This is particularly true for transportation. Over 97 percent of the energy used by the transportation sector in the United States comes from oil (US Department of Energy, 1988).

There are many reasons for this dominance. Petroleum-based fuels have very high energy densities providing good vehicle driving range. There has been significant investment in engine design to improve the efficiency of combustion. Also, the handling, storage, and use of petroleum-based fuels have been optimized to the point where these procedures are both convenient and relatively safe. A significant change from petroleum would seriously impact the design and function of motor vehicles.

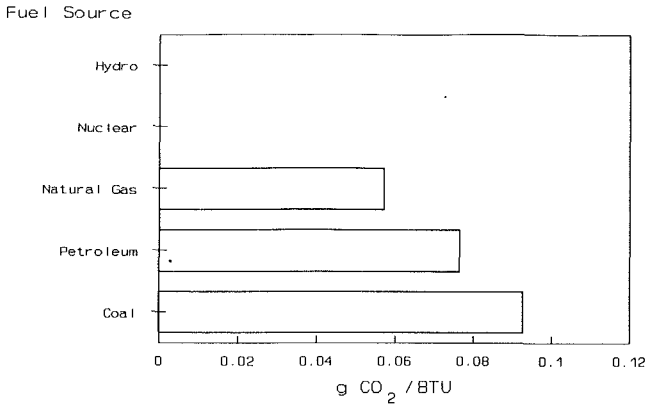

Fig. 8 CO_2 emissions per Btu from combustion only

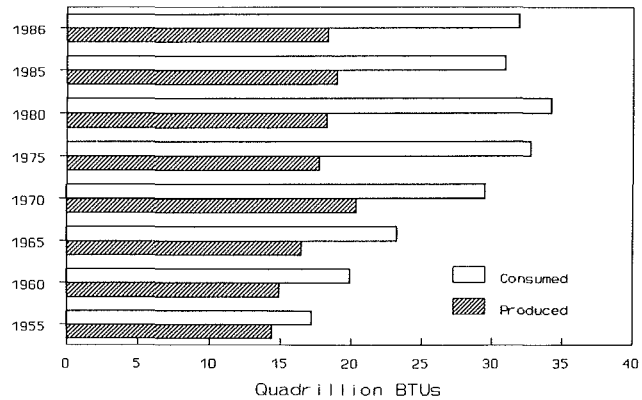

Fig. 9 US total petroleum consumption and domestic production

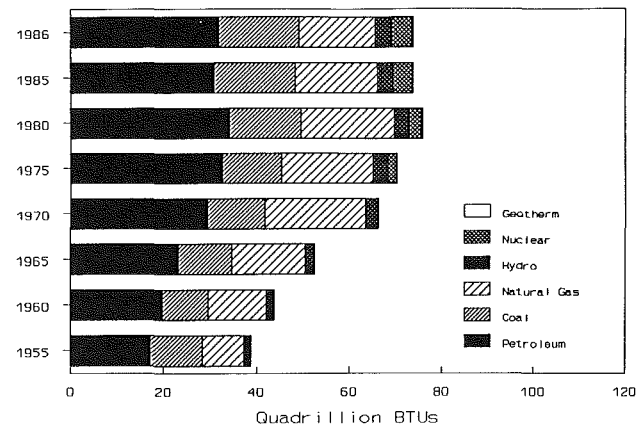

Fig. 10 US total energy consumption by source

As crude petroleum supplies are used up, conversion of coal, or shale, to methanol or gasoline may become more attractive, but significant amounts of CO_2 may be released in the process of conversion in addition to that released in combustion. A recent report (Unnasch et al., 1989) on the impact of methanol-fueled vehicles on the greenhouse effect concluded that methanol from coal would have a 50 to 70 percent greater greenhouse effect than gasoline from petroleum. However, methanol from natural gas would have about 5 to 10 percent less greenhouse warming than vehicles fueled with gasoline. Clearly, methanol or gasoline produced from coal offers no greenhouse advantage.

The agriculture lobby in the US argues that making ethanol

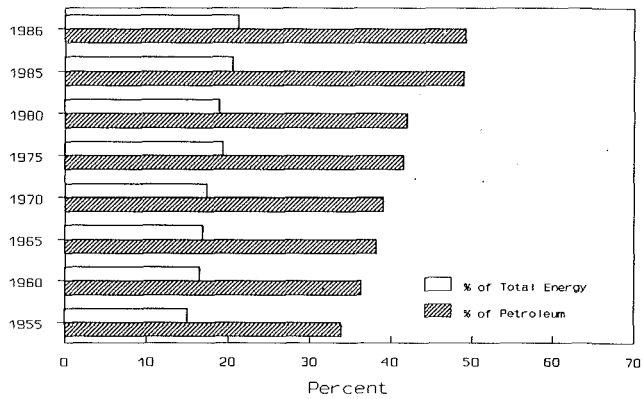

Fig. 11 US highway vehicle energy usage as a percentage

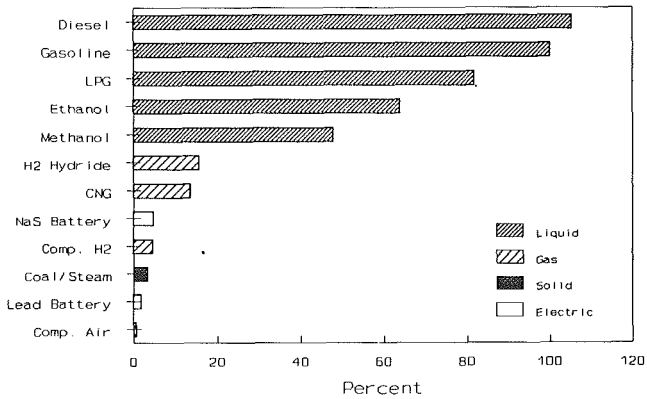

Fig. 12 Specific energy available to drive a vehicle as a percent of gasoline

from grain for transportation fuel could recycle the CO_2. Growing grain does consume CO_2; however, the operation of motorized agricultural equipment, and the fermentation and distillation processes used to produce the ethanol also release CO_2. Grain supply, conversion efficiency, and cost are important issues (Bungay, 1981).

To help describe the driving range possible with different fuel systems, we define "specific energy" as the energy available to drive a vehicle per unit mass of the fuel, fuel container, and fuel transfer equipment. On current gasoline vehicles, the fuel container and transfer equipment are the gas tank and fuel pump, but, on electric vehicles, they are the battery and electrical cables. Approximate specific energies for a number of energy storage systems are shown in Fig. 12.

The ranking of the systems is approximate because it depends on variables, such as the development status, safety, and cost, which affect the system mass. Systems with high specific energy allow vehicles with long range and large carrying capacity, while those with low specific energy, such as electric and hydrogen vehicles, have restricted range and hauling capacity compared to current vehicles.

In spite of these limitations, some scientists have suggested conversion to pure hydrogen fuel, but the short-term feasibility of such an approach is very doubtful because pure hydrogen does not exist as a natural resource and, thus, would require energy to separate it from other compounds. Also vehicles with either compressed hydrogen or hydrogen stored in metal hydride have very low range and limited interior room.

Electric power vehicles have similar range and room disadvantages. However, the fact that significant R&D efforts have gone into electric vehicles and that they are being planned for use in the south coast area of California for ozone control during the first quarter of the next century, gives them a higher probability than hydrogen. Of course, electric vehicles are only viable in the context of global warming if the electricity is produced from sources other than fossil fuels, for instance, hydroelectric, solar, or nuclear.

Reforestation and Disposal of CO_2

Reforestation may be considered a way to help reduce atmospheric CO_2 levels, but its effectiveness appears limited to offset only a small fraction of fossil fuel emissions. While trapping and disposing of CO_2 emissions have also been mentioned, the quantity of material that would have to be controlled makes feasibility doubtful. For example, each gallon of gasoline produces nearly 20 lb of CO_2. If the CO_2 gas were converted to a solid, such as $CaCO_3$, for easy handling the weight would be nearly 540 lb per gallon.

Conclusions

Based on the above discussion, the following conclusions are made:

Although the quality of temperature data is uncertain, many scientists agree that a 0.3 to 0.6°C average global temperature increase has most likely occurred over the last 100 years, but there is little direct evidence that it is due to the greenhouse effect.

Since 1958, the atmospheric CO_2 concentration has risen from about 315 ppm to about 353 ppm in 1990. Currently, the level is rising at 0.5 percent per year. Estimates place the preindustrial CO_2 level at 270 ppm.

The magnitude of the estimated average global temperature change is consistent with the predicted warming due to the changes in atmospheric greenhouse gas concentrations. There are many uncertainties in these model predictions, but research to resolve the uncertainties is increasing.

Although man-made greenhouse warming has not yet been proven, it might be proven over the next few years especially if the unusually warm weather persists. However, it is impossible to say for sure when, or if, man-made greenhouse warming will be proven.

Most current estimates predict that atmospheric CO_2 concentrations will pass 600 ppm (the nominal doubling of the recent levels) in the third quarter of the next century. Modeling studies suggest that a doubling of CO_2 would cause a global surface warming of 1.3–4.8°C. The climate record between 1850 and 1940 and the estimate of CO_2 changes during that period suggest warming changes in the lower half of the range predicted by the models. With much less certainty, the models also predict some specific regional climate changes, including changes in rainfall.

The effects of such climate changes on agriculture in the United States are highly uncertain and could depend strongly on the outcome of future agricultural developments.

Besides CO_2, the other man-made greenhouse gases, including methane, nitrous oxide, ozone, and CFCs, contribute about 45 percent to the prediction of the 1985 greenhouse warming. By the year 2030, these other gases are predicted to contribute about 50 percent of the greenhouse warming if the CFC reductions resulting from the Montreal Protocol are not taken into account.

While our estimates of CO_2 emissions are somewhat uncertain and constantly being improved as better data become available, we cited the following: On a global basis, motor vehicles account for about 10.7 percent of the total man-made CO_2 emission inventory. A doubling of the worldwide motor fleet fuel economy with constant vehicle miles traveled (halving of fuel consumption) could achieve only a 5.4 percent reduction in greenhouse warming attributable to CO_2 or a 3 percent reduction when all greenhouse gases are considered. US highway vehicles account for about 4.1 percent of the global man-made CO_2 emissions inventory, and cars account for 2 percent. A doubling of the US fuel economy for cars at constant vehicle miles traveled could achieve about a 1 percent reduction in the

CO_2 portion of the greenhouse warming or about 0.5 percent reduction when all greenhouse gases are considered.

References

Alic, J. A., Jenny, L. L., and Bull, T. E., 1983, "Future Automobile Fuel Economy: Technology and the Marketplace," Society of Automotive Engineers, Paper No. 830983.

Arrhenius, S., 1896, "On the Influence of Carbonic Acid in the Air Upon the Temperature of the Ground," *Philosophical Magazine*, Vol. 41, p. 237.

Black, F., 1988, "Motor Vehicles as Sources of Compounds Important to Tropospheric and Stratospheric Ozone," presented at the Ozone Symposium, Nijmegen, the Netherlands, May 9–13.

Blair, P. D., 1988, "Testimony of the Program Manager of Energy and Materials, Office of Technology Assessment" on Technologies for Remediating Global Warming before a joint hearing of the Subcommittee on Natural Resources, Agriculture Research and the Environment and the Subcommittee on Science, Research and Technology of the House Committee on Science, Space and Technology, June 29.

Bolin, B., 1970, "The Carbon Cycle," *Scientific American*, Vol. 223, p. 125.

Bradley, R. S., Diaz, H. F., Eischeid, J. K. Jones, P. D., Kelly, P. M., and Goodness, C. M., 1987, "Precipitation Fluctuations Over Northern Hemisphere Land Areas Since the Mid-19th Century," *Science*, Vol. 237, pp. 171–175.

Bungay, H. R., 1981, *Energy, The Biomass Options*, Wiley Interscience Publications, New York, pp. 36, 268, and 271.

Callendar, G. S., 1938, *Q.J.R. Meteorological Society*, Vol. 64, p. 223.

Covey, C., 1984, "The Earth's Orbit and the Ice Ages," *Scientific American*, Vol. 250, pp. 58–66.

Dickinson, R. E., and Cicerone, R. J., 1986, "Future Global Warming From Atmospheric Trace Gases," *Nature*, Vol. 319, pp. 109–115.

Hoffman, M. S., ed., 1988, *The World Almanac and Book of Facts: 1988*.

Huschke, R. E., 1959, "Glossary of Meteorology," American Meteorological Society, Boston, MA, p. 21.

IEA, 1989, "Energy Balances of OECD Countries 1986/1987," and "World Energy Statistics and Balances 1971–1987," International Energy Agency, Paris.

Jones, P. D., Wigley, T. M. L., and Wright, P. B., 1986, "Global Temperature Variations Between 1861 and 1984," *Nature*, Vol. 322, pp. 430–434.

Karl, T. R., and Jones, P. D., 1989, "Urban Bias in Area-Averaged Surface Air Temperature Trends," *Bulletin of American Meteorological Society*, Vol. 70, pp. 265–270.

Manabe, S., Wetherald, R. T., and Stouffer, R. J., 1981, "Summer Dryness Due to an Increase of Atmospheric CO_2 Concentration," *Climate Change*, Vol. 3, p. 347.

MVMA, 1988, "Motor Vehicle Facts and Figures," Motor Vehicle Manufacturing Association, Detroit, MI.

NRC, 1983, "Changing Climate," National Research Council Report, National Academy Press, Washington, DC.

Ramanathan, V., Cicerone, R. J., Singh, H. B., and Kiehl, J. T., 1985, "Trace Gas Trends and Their Potential Role in Climate Change," *Journal of Geophysical Research*, Vol. 90, pp. 5547–5566.

Ramanathan, V., 1988, "The Greenhouse Theory of Climate Change: A Test by an Inadvertent Global Experiment," *Science*, Vol. 240, pp. 293–299.

Schlesinger, M. E., and Mitchell, J. F. B., 1985, "Projecting the Climatic Effects of Increasing Carbon Dioxide," M. C. MacCracken and F. Luther, eds., Department of Energy Report, Washington, DC, p. 81.

US Department of Energy, 1988, "Assessment of Costs and Benefits of Flexible and Alternative Fuel Use in the U.S. Transportation Sector," Progress Report One: Context and Analytical Framework, DOE/PE-0080.

Unnasch, S., Moyer, C. B., Lowell, D. D., and Jackson, M. D., 1989, "Comparing the Impact of Different Transportation Fuels on the Greenhouse Effect," California Energy Commission Report, Sacramento, CA.

Woodwell, G. M., 1988, "CO_2 Reduction and Reforestation," *Science*, No. 242, pp. 1493.

World Resources, 1990, *A Guide to the Global Environment*, World Resources Institute, Oxford University Press, p. 350, ISBN 0-19-506229-9.

WMO, 1985, "Atmospheric Ozone 1985, Assessment of Our Understanding of the Processes Controlling Its Present Distribution and Change," World Meteorological Organization, Global Ozone Research and Monitoring Project, Report No. 16, Vol. III.

Flame Speeds of Low-Cetane Fuels in a Diesel Engine

B. J. Stroia
Cummins Engine Company, Inc.,
Columbus, IN 47202

D. L. Abata
Michigan Technological University
Houghton, MI 49931

A theoretical and experimental investigation of the flame speeds of low-cetane fuels during the initial stage of heat release in a Diesel engine is described. This information is important for developing a fundamental background in the understanding of fuel injection rate-controlled heat release in a Diesel engine. In this study, a theoretical model based on droplet size, turbulent intensity, and equivalence ratio was developed for the flame propagation through a fuel droplet/air matrix. The results of the theoretical model were compared to experimental high-speed photographs of flame growth in a Diesel engine. For successful injection rate controlled heat release to occur using pilot injdection, the model determined that the combustion zone due to a pilot fuel spray must flow to a distance of at least 30 orifice diameters from the nozzle tip before the main injection event can take place. Results of the model were verified by experiment for the two limiting cases of X/D less than 30 and X/D greater than 30. As expected, rate-controlled heat release was to achieved for the case of X/D less than 30. However, for the case of X/D greater than 30, the main fuel injectin ignited upon injection into the cylinder, and heat release was controlled by rate of injection.

Introduction

The measurement of flame growth in Diesel engines can be very important since it relates actual combustion of the fuel to various operating parameters such as engine speed and load, and injection characteristics. In the case of low-cetane fuels, the flame development is particularly important since it is directly related to the ignition of the fuel. In fact, the ignition quality of the fuel (or, rather, autoignition quality) is the exact parameter investigated to determine the cetane rating of the fuel. In the direct injection Diesel engine, liquid fuel is injected into the combustion chamber and a noticeable delay occurs before ignition of the fuel spray takes place. If the ignition delay of the fuel is small, the flame will propagate throughout the entire combustion chamber with a gradual rise in cylinder pressure, resulting in complete combustion of the fuel. If the ignition delay of the fuel is large, as is the case with combustion of low-cetane fuels, more and more fuel is injected into the cylinder before complete combustion can take place, resulting in a rapid detonation of the fuel. Consequently, detonation or knock in a Diesel engine is seen to be directly related to the ignition delay of the fuel. If the initial flame growth of low-cetane fuels is fast enough to allow combustion to proceed readily during the injection of the fuel, then knock would not occur. Therefore, if the flame speed of low-cetane fuels could somehow be controlled, then combustion of the fuels would be improved, possibly eliminating the knocking problem.

In the past, the characteristic long ignition delay of low-cetane fuels has been somewhat lessened by the use of various techniques to control the combustion of the fuels. Ideally, combustion would be initiated near the center of the cylinder be some ignition source and would proceed outward from the injector tip in a radial direction toward complete combustion of the fuel. The problem then becomes where to locate the ignition source as related to the fuel spray so successful combustion will result. If the ignition source is placed too close to the injector orifice, the speed of the initial flame growth may not be able to overcome the spray velocity, and lift off and incomplete combustion of the fuel will occur. Conversely, if the ignition source is placed too far downstream of the developing spray, then knock will occur before the complete combustion of the fuel can take place. It soon becomes apparent that the successful combustion of low-cetane fuels is strongly dependent upon the location of the ignition source and characteristics of the fuel spray within the cylinder. Of primary concern is the effect of injection characteristics on the fuel spray and, subsequently, the combustion of low-cetane fuels.

The Diesel spray combustion process is very complex, depending on parameters such as injection characteristics, droplet size and distribution, atomization and fuel/air mixing, and ignition delay, to name a few. Of paramount importance to the understanding of diesel flame combustion is the link between fuel spray characteristics and the initial propagation and heat release of the flame. An understanding of this relationship is a key factor for the successful combustion of low-cetane fuels of the future. The purpose of this paper is to present the results of a detailed investigation of the initial stage of flame development of a Diesel spray flame as a function of various spray characteristics.

Contributed by the Internal Combustion Engine Division and presented at the Energy-Sources Technology Conference and Exhibition, Houston, Texas, January 20–24, 1991. Manuscript received by the Internal Combustion Engine Division September 1990. Paper No. 91-ICE-14.

Background

Ignition Delay. The main problem with the use of low-cetane fuels in a direct injection Diesel engine is the ignition delay of the fuel. Investigators at Michigan Technological University have visually observed the ignition and combustion of selected alternate fuels in a direct injection Diesel engine under normal operating conditions [1–6]. Although much useful information was obtained as a result of their investigation, preliminary results indicate a need for detailed study of the initial combustion and subsequent flame growth in order to achieve a complete understanding of the combustion of low-cetane fuels.

Both the physical and the chemical aspects of ignition delay must be considered when studying the combustion of low-cetane fuels. The physical delay of the fuel in itself consists of three parts: injection of the fuel, atomization of the fuel, and mixing of the fuel with air. Early investigations of ignition delay in Diesel engines indicate that the physical delay is not a small quantity and may be larger than the chemical portion under certain operating conditions [7]. The physical part of the ignition delay is heavily dependent on the formation process of the Diesel fuel spray and, in fact, may be the limiting factor in the ignition delay of the fuel [8]. The chemical part of the ignition delay is more dependent on the properties of the fuel [9–11] and temperatures existing in the combustion chamber (kinetics). For low-cetane fuels the chemical part of the ignition delay may vary significantly according to the fuel in question. For instance, the ignition delay of low-volatility, heavy-end fuels is usually limited by the physical formation of the spray, and the chemical part of the delay may be quite small in comparison. On the other hand, the exact division of the ignition delay into two parts for the combustion of high-volatility, light-end fuels is difficult since the fuel mixes so rapidly with the air in the cylinder.

Low-cetane alternate fuels used in a Diesel engine may not have fuel qualities similar to traditional Diesel fuel (such as volatility, self-ignition temperature, etc.); therefore, total reliance on the autoignition of the fuel may not be appropriate. New methods of introducing the fuel into the combustion chamber may have to be developed. Low-cetane fuels inherently have a large ignition delay and are not prone to rapid autoignition in the Diesel engine. Ideally, if the ignition delay of the fuel could be minimized or reduced to a negligible level, then a broader range of fuels could be used in the Diesel engine.

One way to decrease the ignition delay of low-cetane fuels in the diesel engine is to provide some type of auxiliary ignition source. The ignition source could be either a spark or glow plug, or even a zone of combustion material from a pilot fuel charge. It is hoped that the ignition delay of the fuel will be reduced sufficiently to allow acceptable combustion of the fuel. Ideally, the ignition delay of the fuel could be reduced to a negligible level, and heat release of the fuel would be controlled by rate of injection.

The idea of combustion being controlled by rate of injection would overcome several problems. The light-load combustion problem (low equivalence ratios) associated with direct injection Diesel engines would be significantly reduced since the fuel would burn at the stoichiometric fuel/air region at the periphery of the spray plume. Also, the tendency for the fuel to knock would be eliminated since the fuel would be ignited at the center of the cylinder upon injection. Some of the conditions required to achieve rate-controlled combustion of low-cetane fuels (as related to flame speed) will be presented later in the results section of this paper.

Flame Propagation Through a Droplet Matrix. The combustion of the Diesel fuel spray has been regarded to occur in three phases. These three phases are: (I) an initial or premixed part with a characteristic rapid rate of heat release, (II) a diffusion part where combustion is mixing controlled, and (III) the remaining combustion with a very low rate of heat release. if one is interested in the initial stage of flame development, the initial or premixed portion of the heat release must be studied in detail.

The premixed portion of the Diesel fuel spray occurs where the mixing process is most rapid—the edge of the spray. The edge of the spray may be represented as a homogeneous collection of fuel droplets immersed in a fuel vapor/air mixture. The initial portion of heat release may then be thought of as occurring in a two-phase droplet matrix existing at the periphery of the fuel spray. Results of such a two-phase flame speed model would yield much information about the ignition and subsequent heat release of low-cetane fuels.

Several researchers have investigated the burning rate through a two-phase droplet matrix. Using Spalding's [12] low-pressure vaporization model. Ballal and Lefebvre [13] developed a flame speed correlation for the laminar flame speed through a droplet matrix. Myers and Lefebvre [14] determined that flame speed is inversely proportional to the Sauter Mean Diameter (SMD); and for large drop sizes, evaporation rates may be controlling flame speed. Cekalin [15] studied the progagation of a flame in turbulent flow of a two-phase fuel/air mixture and determined that flame speed was dependent on droplet size and spacing, concentration of fuel vapor in the combustion zone, and intensity of turbulence. Mizutani and Nishimoto [16] did an extensive investigation of the turbulent flame velocity in premixed spray and developed a flame-speed correlation based on SMD, equivalence ratio, and intensity of turbulence. More recently Chan and Wu [17] developed a model for the laminar

Nomenclature

A = area of flame surface
aTDC = after top dead center
bTDC = before top dead center
C_p = specific heat
D = diameter
$\mathfrak{D}$ = diffusivity
f = fuel/air mass ratio
k = coefficient of mass transfer
M = mass
P = pressure
r = radius
Re = Reynolds number
R = gas constant
S = flame speed
Sc = Schmidt number
Sh = Sherwood number
t = time
T = temperature
u' = fluctuating velocity
V = velocity
V = volume
v = specific volume
w = boundary layer ratio
X = mole fraction
Y = mass fraction
ZID = zero ignition delay
α = thermal diffusivity
δ = thickness of flame front
δ_m = boundary layer thickness
ν = kinematic viscosity
ξ = equimolar counterdiffusion of vapor
ρ = density
ϕ = fugacity coefficient

Subscripts

c = chemical
ch = chamber
e = evaporation
f = fuel
g = gas
ig = ignition
l = liquid
L = laminar
m = mass
o = initial
q = quench
T = turbulent
v = vapor

flame speed through a *polydisperse* fuel spray and studied the effect of droplet size and distribution on the propogation of the flame. The monodisperse case was compared to the polydisperse case, and results were shown to be in good agreement with existing experimental data.

From the above discussion several independent variables are seen to have a significant effect on the flame speed through the droplet matrix. There flame speed is shown to be inversely related to SMD, approaching the homogeneous flame speed asymptotically as the SMD decreases to zero. The effect of equivalence ratio on flame speed is indirectly related through droplet vaporization with slower flame speeds at high equivalence ratios. Since the Diesel flame is inherently very turbulent, the intensity of turbulence has a great effect on the mixing-controlled propagation of the flame. The model presented later in the theory section of this paper incorporates all of the above variables in its development. In addition, a high-pressure model for droplet vaporization was used to account for the near/super-critical conditions existing in the combustion chamber. Results of the flame propagation model will be compared to experimental flame-speed results taken from actual flame photographs obtained from a modified Diesel engine.

Theory

A flame propagation model was developed to study the controlling factors that affect the flame speed through the premixed portion of the Diesel fuel spray. As mentioned previously, the edge of the spray may be represented as a homogeneous collection of fuel droplets immersed in a fuel vapor/air mixture. Therefore, the initial portion of heat release may then be thought of as occurring in a two-phase droplet matrix existing at the periphery of the fuel spray. The model is based on a two-phase droplet matrix concept and includes the effect of droplet size and intensity of turbulence on flame speed.

Flame Speed in a Fuel Vapor/Air Droplet Matrix. The basis of the theory is that under pseudo-steady-state conditions, the rate of flame propagation through a fuel droplet–air/vapor mixture is such that the total time in the reaction zone is equal to the sum of the evaporation and chemical reaction times:

$$t = t_e + t_c \tag{1}$$

This event is shown schematically in Fig. 1. The model assumes sufficient pre-ignition vaporization of the droplets ahead of the flame front causing a transient behavior from heterogeneous spray to homogeneous gas phase combustion to occur [17]. The characteristic reaction time is defined as:

$$t_c = \frac{[fuel]_o}{r_f} \tag{2}$$

where r_f is the overall reaction rate. Westbrook and Dryer [18] give an expression for quasi-global reaction kinetics for the combustion of decane (used in the model to represent DF2) as:

$$C_{10}H_{22} + 15.5O_2 \rightarrow 10CO_2 + 11H_2O$$

$$r_{C_{10}H_{22}} = 12.0 \times 10^6 \exp\left[-(15{,}000)\frac{1}{T}\right][C_{10}H_{22}]^{0.25}[O_2]^{1.5}\frac{\text{mol}}{\text{m}^3\text{S}} \tag{3}$$

Therefore, if the initial concentration of fuel is known, the chemical reaction time may be determined.

The total evaporation time may be determined by dividing the total mass of fuel in the the reaction zone by the average rate of fuel evaporation:

$$t_e = \frac{m_\delta}{m_v} \tag{4}$$

where $m_\delta = f\rho_g A\delta$, f = fuel/air mass ratio, ρ_g = density of mixture; A = flame surface area; δ = thickness of flame.

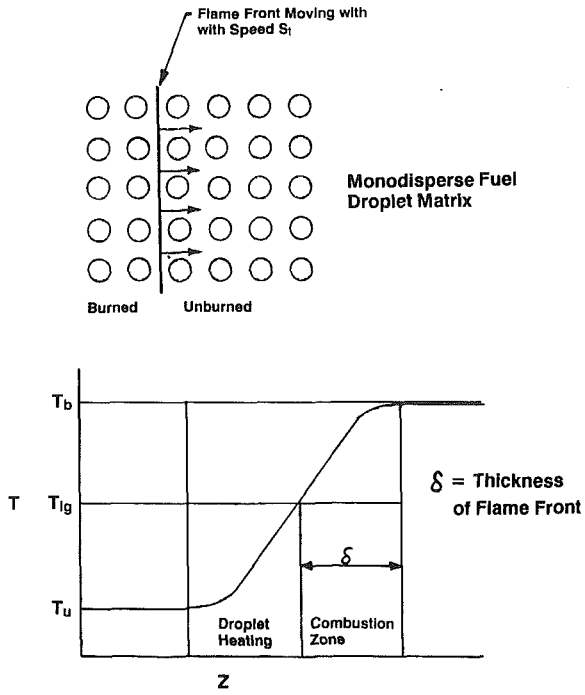

Fig. 1 Flame propagation through a fuel droplet/air mixture

To determine the rate of fuel evaporation form the droplet, the high-pressure theory of Kadota and Hiroyasu [19] was applied. The theory involves a quasi-steady-state analysis of the droplet evaporation. The model includes the effects of forced convection and accounts for the effects of nonideal gas behavior on the calculation of vapor–liquid equilibrium mole fraction boundary condition and for the effects of nonideality of the enthalpy of vaporization at supercritical temperatures and pressures. Using the evaporation model, the total evaporation time may be expressed as:

$$t_e = \frac{\rho_f D_1[1-(1+\xi)]Y_{FR}}{6K^*(Y_{FR} - Y_{F\infty})} \tag{5}$$

A detailed solution technique for equation (5) is given in [40]. In order to get an expression for the flame speed through the fuel droplet matrix, an energy balance on the reaction zone must be made. For steady flame propagation the heat conducted ahead of the flame must be equal to the energy required to heat the unburned gases from their initial temperature, T_{ch}, to the ignition temperature, T_{ig}. The enthalpy rise of the fuel–air mixture in the preheat zone is then:

$$f_{mass}C_p(T_{ig} - T_{ch}) \tag{6}$$

where f_{mass} is the mass flux through the flame front. The enthalpy is supplied by conduction from the reaction zone. The energy balance may then be represented as:

$$f_{mass}C_p(T_{ig} - T_{ch}) = k\frac{dT}{dx} \tag{7}$$

where k is the thermal conductivity of the gas. The mass flux (f_{mass}) is related to the laminar flame speed through the cold fuel/air–droplet mixture by:

$$f_{mass} = \rho_g S_L \tag{8}$$

The temperature gradient may be approximated by the linear relationship:

$$\frac{dT}{dx} = \frac{(T_f - T_{ig})}{\delta} \tag{9}$$

where δ is the flame thickness and T is the flame temperature. The laminar flame speed can then be expressed as:

$$S_L = \frac{k}{\rho_o C_p}\frac{T_f - T_{ig}}{T_{ig} - T_{ch}}\frac{1}{\delta} = \alpha\left(\frac{T_f - T_{ig}}{T_{ig} - T_{ch}}\frac{1}{\delta}\right) \tag{10}$$

The flame thickness can be expressed as:

$$\delta = S_L t_c \tag{11}$$

Therefore, the final form of the laminar flame speed through the fuel droplet matrix is:

$$S_L = \left(\frac{\alpha(T_f - T_{ig})}{t_q(T_{ig} - T_{ch})}\right)^{\frac{1}{2}} \tag{12}$$

where t_q is the sum of the chemical reaction time (t_c), and the droplet evaporation time (t_e). Fuel properties such as kinematic viscosity, thermal diffusivity, and specific heat were determined from Reid et al. [25].

Modification for Turbulence. When considering turbulent flame-seed correlations, two separate groups may be formed. One group of correlations is based on some length scale of the turbulent eddies, usually measured form the actual combustion process. The second group of correlations is based on the laminar flame speed and the intensity of the turbulence. Many researchers have modeled turbulent flame propagation as a function of length scale of the turbulent eddies [26–30]. However, for I.C. engine studies, Lancaster et al. [31] state that turbulent intensity may be the only characteristic of turbulence that influences flame speed. The reason for this is that the energy of the turbulent flow is not contained in a monodisperse collection of eddy sizes but is distributed over a large range of eddy sizes [32].

One of the first researchers to model turbulent flame speed as a function of laminar flame seed and turbulent intensity was Damkohler [33]. He developed an expression for flame speed as follows:

$$\frac{S_T}{S_L} = 1 + \frac{u'}{S_L} \tag{13}$$

The main drawback with Damkohler's equation is that it tends to overpredict flame speed at moderate levels of turbulent intensity. Shchelkin [34] developed a correlation based on a wrinkled conical laminar flame:

$$\frac{S_T}{S_L} = \left[1 + B\left(\frac{u'}{S_L}\right)^2\right]^{\frac{1}{2}} \tag{14}$$

Notice that the equation contains a coefficient (B) that is used to represent different combustion geometries. Karlovitz et al. developed a correlation based on the wrinkled laminar flame with the addition of flame-generated turbulence:

$$S_T = S_u + (2S_u u')^{1/2} \tag{15}$$

This equation is more applicable to engine flames since flame-generated turbulent intensity is much greater than u' for strong turbulent flow.

A comprehensive review of "laminar flame speed based" turbulent flame speed correlations was made by Wohl et al. [36]. He determined that for situations where u'/SL is much greater than 1 (similar to situations existing in a combustion chamber) most correlations reduce to the form:

$$\frac{S_T}{S_L} \cong \frac{\sqrt{2u'}}{S_L} \tag{16}$$

As a result of his investigation, he developed an expression for the turbulent flame propagation:

$$\frac{S_T}{S_L} = 1 + \left[2\left(\frac{u'}{S_L} - 1 + \exp\left(\frac{-u'}{S_L}\right)\right)\right]^{\frac{1}{2}} \tag{17}$$

This equation is readily applicable to engine combustion flames since it was obtained from experiments of high-velocity turbulent streams. Notice that equation (17) is in terms of the laminar flame speed and turbulent intensity. The laminar flame speed is calculated with the equations presented previously. Values of turbulent intensity for high velocity fuel spray can be obtained from Faeth [37] and Shuen et al. [38].

Experimental

Engine and Equipment. The engine used in the study was a modified Detroit Diesel Allison (DAA) 3–53 (model 5033–8300). The engine is a three-cylinder, two-stroke, direct injected Diesel engine with angled intake ports and four exhaust valves per cylinder providing moderate swirl with "through" scavenging. A detailed presentation covering the modification of the engine for optical access is given in [1]. A schematic of the modified engine is shown in Fig. 2. Specifications of the engine as supplied by Detroit Diesel are given in Table 1.

The high-speed camera used in this study was a HYCAM model 41-0004. Actual film speed of up to 10,000 frames per second are made possible through the use of high-speed rotating prisms used in the design of the camera. The film used was 250-foot rolls of 16 mm high-speed Kodak ektachrome (color) video news film. Approximately ten engine cycles were recorded on each 250-foot roll of film. Photography lasted about three seconds at maximum film speeds of 5000 to 8000 frames per second.

Experimental Test Fuels. The two test fuels used in the experimental portion of the study were a low-cetane–high-volatility fuel (Type I) and, for comparison purposes, No. 2 Diesel fuel. Properties of the low-cetane Type I fuel along with Diesel No. 2 are given in Table 2. The relationship of Type I fuel to Diesel No. 2 in terms of volatility is shown in Fig. 3. Notice that Type I fuel is more volatile than Diesel No. 2 fuel, which leads to greater rates of fuel/air mixing in the cylinder.

n-Decane was the fuel used for calculations in the theoretical

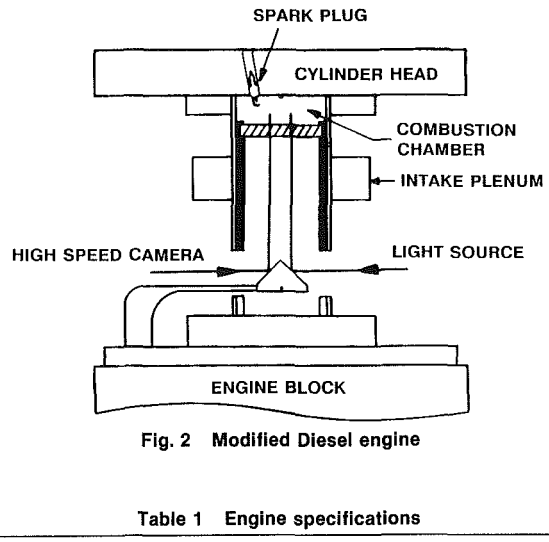

Fig. 2 Modified Diesel engine

Table 1 Engine specifications

Detroit Diesel Model #	5033-8200
Engine Type	2 Cycle
Combustion Type	Direct Injection
Number of Cylinders	3
Displacement	159 in.^{3}
Bore	3.875 in.
Stroke	4.5 in.
Aspiration	Blower, Turbocharger
Cool. Normal Operat. Temp.	1800F
Compression Ratio	18.7:1
Combustion Chamber	Mexican Hat Open
Injector (5A60)	8 Hole
Nozzle Opening Pressure	3500 psig
Airbox Pressure	37 in. Hg

Table 2. Experimental fuels

	Type 1 High Volatility AL-10999-F	Diesel No. 2 (AMOCO Premier)
Gravity, °API	49.0	38.8
Cetane Number	27.8	49.7
Viscosity, Kinematic @ 40°C, cST	0.76	2.31
Heat of Combustion, KJ/Kg		
Gross	44,503	45,069
Net	41,882	42,245

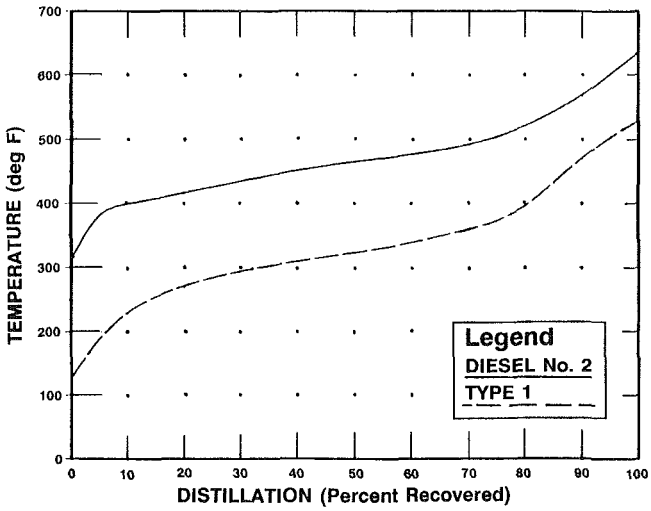

Fig. 3 Distillation Curve for the test fuels

flame-speed model. This single component fuel has properties similar to the fuels used in the experimental portion of the study. Properties of *n*-decane were obtained from [25].

Flame-Speed Measurement. The measurement of the flame speed from the high-speed photographs was made in the following manner: For each cycle of combustion, the time and location of ignition were recorded. As the flame traveled up the spray plume, the location of the traveling flame front was taken as the average of three positions: Centerline, +5 deg, and −5 deg. This distance traveled by the flame was recorded at specified time increments resulting in a average apparent flame speed for each case investigated. A schematic of the measurement technique is shown in Fig. 4.

Results

Theoretical results of the flame-speed model are presented in this section. The results of the model are also compared to experimental results of flame seed measured from high-speed photographs in order to characterize the zone of initial flame development at the edge of the fuel spray.

Results of the Flame-Speed Model. The results of the flame-speed model as a function of droplet size and turbulence intensity are shown in Fig. 5. It can be noticed that the flame speed through the droplet matrix is inversely related to droplet size with the flame speed increasing with a decrease in droplet size. Also, the effect of droplet size on flame speed is less apparent at larger droplet sizes due to the limiting effects of vaporization. These results (as related to droplet size) are consistent with the experimental results obtained by Ballal and Lefebvre [13]. The flame speed is shown to be directly related to the intensity of turbulence with the flame speed increasing

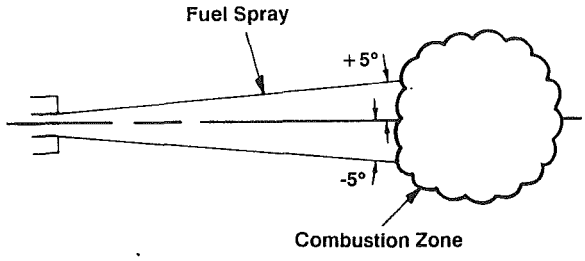

Fig. 4 Flame measurement technique

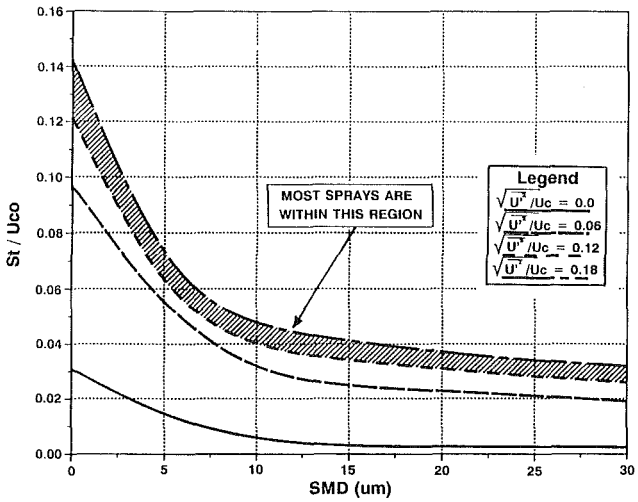

Fig. 5 Effect of droplet size and turbulence intensity on flame speed as predicted by the model

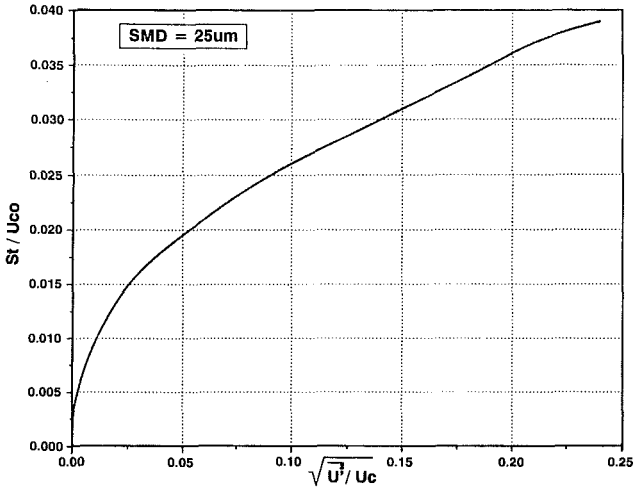

Fig. 6 Effect of turbulence intensity on flame speed as predicted by the model

as the intensity of turbulence increases. When the turbulence intensity is decreased to zero, the model predicts the laminar flame speed as expected. The effect of turbulence on the flame speed decreases as the droplet size increases indicating the dominance of flame speed on the vaporization of fuel for larger droplet sizes.

The effect of turbulence intensity on flame speed for the case of SMD equal to 25 μm is shown in Fig. 6. The nonlinear effect of turbulence on flame speed is clearly visible in the figure with a small increase in turbulence resulting in a corresponding large increase in flame speed. According to [38], the majority of turbulent jets fall within the range of U'/U_c

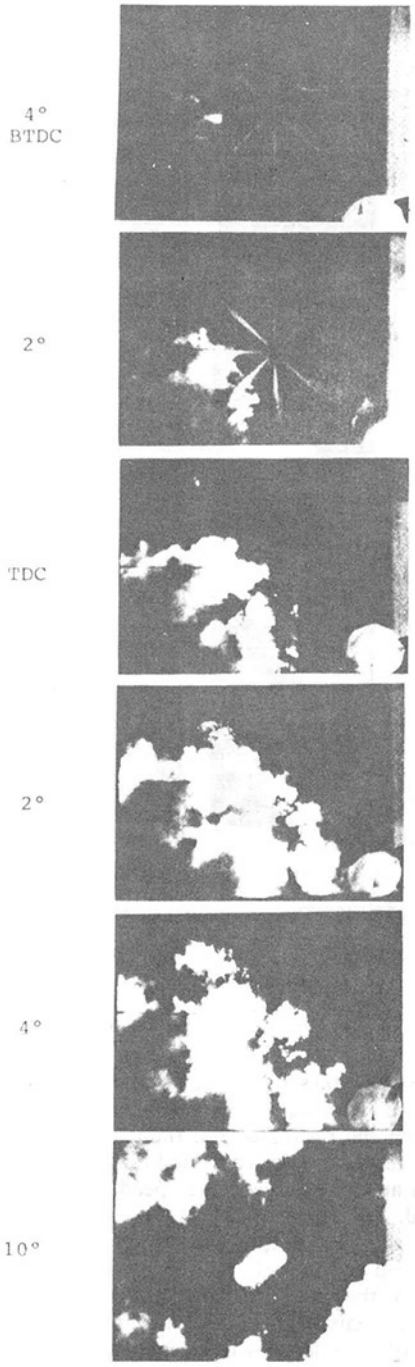

Fig. 7 Combustion of low-cetane fuel in a Diesel engine

between 0.12 and 0.18. The turbulence intensity for fuel sprays generally has a large value near the orifice and decreases in a nonlinear fashion as the spray develops. On the other hand, the scale of turbulence generally starts out small near the orifice and increases as the spray develops. This relatively large-scale mixing process is confined mainly to the edge and tip of the spray resulting in the first occurrence of an ignitable mixture of fuel and air.

Comparison of Model to Experiment. Using the flame-measurement technique explained in the theory section, experimental results of flame speed were obtained from the high-speed photographs. A representative sequence of photographs used in the measurements is shown in Fig. 7.

The results of the flame-speed model (for the case of $U'/Uc_o = 0.12$) are compared to the experimental flame-speed

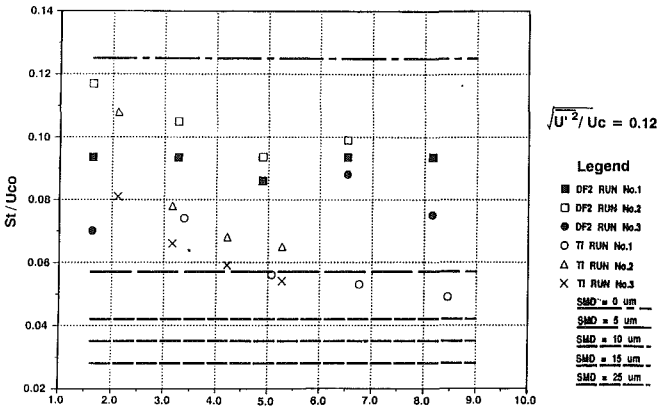

Fig. 8 Comparison of theoretical result to experiment

measurements in Fig. 8. Diesel No. 2 fuel is compared to the low-cetane (TI fuel) by calculating an apparent flame speed (as described previously) for the fuel. The apparent flame spark values for diesel fuel can be thought of as the speed of the *autoignition wave* and are shown here for comparison purposes only. According to the results, experimental values of speed ratio (S_l/Uc_o) for the low-cetane fuel are approximately equal to 0.07. The speed ratio is only slightly higher for the Diesel fuel with values in the range of 0.09. The flame-speed model predicts values of speed ratio in the range of 0.07 to 0.09 at droplet sizes of approximately 3 μm, indicating that the majority of the droplets at the edge of the spray are very small—less than 5 μm. At these sizes of droplets, it is very unlikely that any droplet burning is occurring, and the majority of the droplets vaporize prior to the passage of the flame surface. The results of the model indicate that the premix zone at the edge of the spray may be represented by a mixture of fuel vapor and air, containing very small droplets. In fact, results of flame speed for the case of a pure vapor/air mixture show little error when compared to the actual flame-speed measurements obtained from the photographs.

Prediction of Rate-Controlled Combustion. The combustion of low-cetane fuels becomes much more complete (elimination of knock, burning at low equivalence ratios, etc.) if an auxiliary ignition source is provided to initiate the combustion process. Efforts to improve the combustion of low-cetane fuels in a Diesel engine are described in another paper [5]. More recently [39], researchers at Michigan Technological University have successfully used pilot injection to ignite the spray of a low-cetane fuel in the center of the cylinder resulting in essentially zero ignition delay of the fuel (ZID).

If spray conditions such as velocity, intensity of turbulence, and droplet size are known, then the flame-speed model may be used to obtain the ignition conditions for rate-controlled combustion to occur. The main criterion then becomes the ratio of flame speed to spray velocity; i.e., if the speed of the propagating flame is fast enough to overcome the spray velocity, then the flame will remain rooted at the base of the plume. Conversely, if the spray characteristics are such that the spray velocity is greater than the flame speed, then upon injection the spray will "punch" a hole through the pre-existing pilot flame zone resulting in flame liftoff from the injector orifice and poor combustion of the fuel.

Results of the flame-speed model used to predict ZID combustion of the fuel are shown in Fig. 9. For ratios of flame speed to spray velocity greater than 1, the flame will remain stationary and liftoff will not occur. The relatively sharp increase in the flame speed for small values of X/D is due to the large gradient in turbulence intensity near the exit of the orifice during the initial development of the spray. The results of the model indicate that for droplet sizes greater than ap-

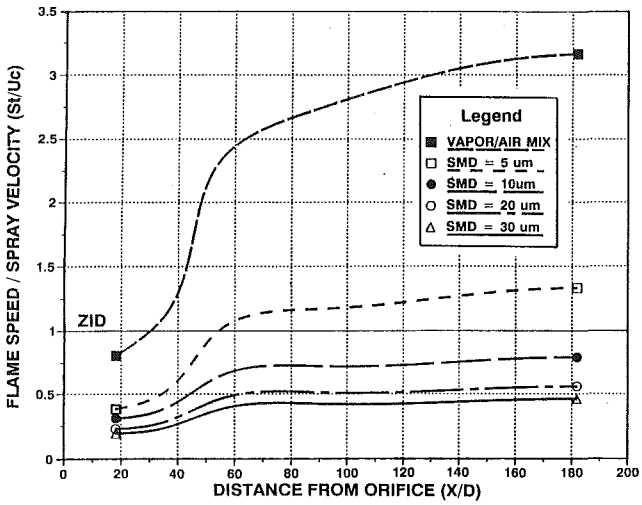

Fig. 9 Prediction of ZID combustion from model

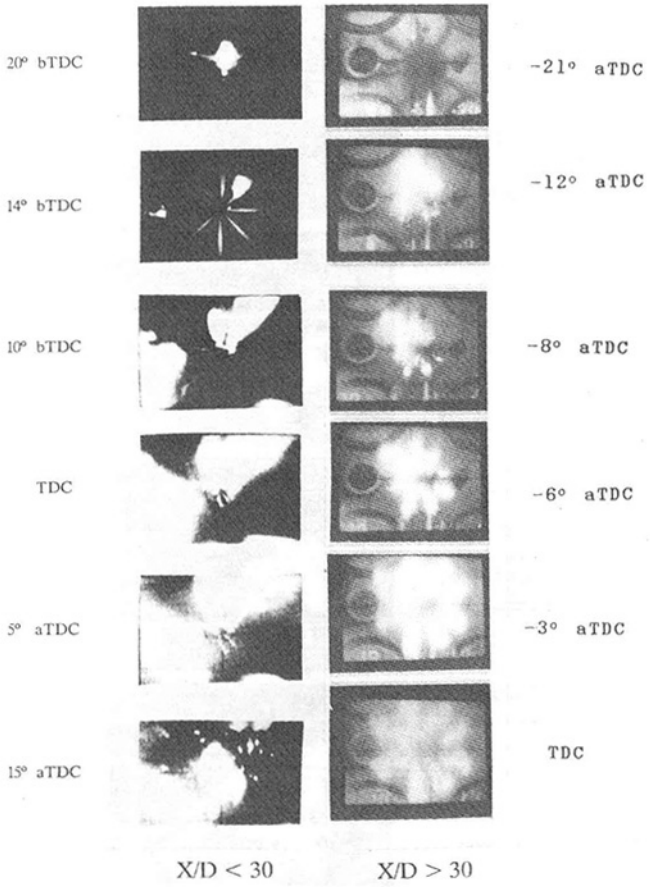

Fig. 10 The two limiting cases of combustion

proximately 8 μm, flame liftoff will occur and heat release will not be controlled by rate of injection. For a droplet size of 5 μm, the model predicts a stationary flame front at X/D equal to 55. When the droplet size is decreased to zero (pure vapor), the model predicts a limiting distance of X/D equal to 30. Therefore, for rate-controlled combustion to occur (assuming nearly complete vapor/air mixture at the edge of the spray), the combustion zone due to the pilot fuel charge must at least be allowed to develop to a distance of 30 orifice diameters from the nozzle tip before the main injection event can take place.

The sequence of photographs for the two limiting cases of combustion ($S_t/U_c<1$ and $S_t/U_c>1$) for the combustion of the low-cetane fuel is shown in Fig. 10. For the first case, X/D for the pilot charge combustion equals approximately 18. Immediately prior to the injection of the fuel, the residual fuel in the sac volume of the nozzle was ignited by a spark resulting in a small flame kernel around the injector nozzle. Upon injection a majority of the pre-existing flame is extinguished with the exception of a small flamelet that is carried up by one of the spray plumes. Five degrees after the injection event several plumes are ignited by the flamelet that was carried up with the fuel spray. As the combustion continuous, the fuel in the vicinity of the nozzle continues to burn while the combustion of the spray plumes dies out. The overall combustion of the fuel is poor, and heat release is not controlled by rate injection.

For the second case shown in Fig. 10, X/D for the pilot charge combustion equals approximately 80. The combustion zone due to the pilot charge of the fuel is clearly visible in the photographs. During the secondary injection event, the main fuel charge immediately ignites upon injection with no ignition delay visible in the photographs. As more fuel is injected into the cylinder, the combustion takes place at the edge of the fuel spray with heat release being controlled by rate of injection. No knock is visible in the photographs with the majority of the fuel burning to completion. Clearly, optimizing this type of rate-controlled combustion will extend the use of low-cetane fuels in the Diesel engine.

Conclusions

From the results of the investigation, several conclusions can be made:

1 The speed of the initial combustion flame through the premixed portion of the Diesel fuel spray may be represented by Wohl's equation for turbulent flames

$$\frac{S_T}{S_L}=1+\left[2\left(\frac{u'}{S_L}-1+\exp\right)\frac{-u'}{S_L}\right)\right]^{\frac{1}{2}}$$

The equation takes into account the effect of droplet size, equivalence ratio, and turbulence intensity on flame speed.

2 From the results of the flame-speed model, the flame speed of the mixture was found to be inversely related to droplet size with an increase in flame speed as the droplet size was decreased. The effect of droplet size on flame speed was less apparent at larger droplet sizes due to the limiting factor of vaporization of the fuel.

3 From the results of the flame-speed model, the flame speed of the mixture was found to be directly related to the intensity of turbulence with an increase in flame speed as the intensity of turbulence was increased. The effect of turbulence was found to be less apparent at larger values of turbulence.

4 When compared to the flame-speed model, the results of the experiment for the low-cetane fuel as well as Diesel fuel indicate that the premix zone at the edge of the spray may be represented by a mixture of fuel vapor and air containing very small droplets of size less than 5 μm. In fact, using a vapor/air mixture to model the edge of the spray results in little error when compared to the flame speeds obtained from the photographs.

5 When used to predict the occurrence of rate-controlled combustion (ZID), the results of the flame model indicate that for droplet sizes greater than approximately 5 μm, flame liftoff will occur and heat release will not be controlled by rate of injection. For a droplet size of 5 μm, the model predicts a stationary flame front at X/D equal to 55. When the droplet size is decreased to zero, the model predicts a limiting distance of X/D equal to 30. Therefore, for rate-controlled combustion to occur, the combustion zone due to the pilot fuel charge

must at least be allowed to develop to a distance of 30 orifice diameters from the nozzle tip before the main injection event can take place.

6 The results of the model as related to rate-controlled combustion were verified by experimental results for the combustion for the low-cetane fuel using the two limiting cases of X/D less than 30 and X/D greater than 30. However, for the case of X/D greater than 30, the fuel ignited upon injection into the cylinder and heat release was controlled by rate of injection.

In summary, the successful combustion of low-cetane fuels is seen to be dependent on several factors including droplet size, intensity of turbulence, and the location (as related to the spray) of the first occurrence of flame. Although not investigated in this paper, other techniques such as fuel preheating and high-pressure injection may also enhance the combustion of low-cetane fuels. In any event, a useful combination of the above factors should enhance the combustion of low-cetane fuels and extend their usage in the Diesel engine.

References

1 Abata, D. L. Fritz, S. G., and Stroia, B. J., SAE Paper No. 860066, 1986.

2 Fritz, S. G., and Abata, D. L., SAE Paper No. 871674, 1987.

3 Fritz, S. G., "An Optical Investigation of the Cold Starting Characteristics of Alternate Fuel Sprays in a Spark-Assisted Direct Injection Diesel Engine Using High-Speed Photography," M. S. Thesis, Michigan Technological University, 1986.

4 Stroia, B. J., "The Use of Auxiliary Ignition Devices to Improve the Combustion of a Low Cetane–High Volatility Fuel in a Direct Injection Diesel Engine," M. S. Thesis, Michigan Technological University, 1987.

5 Stroia, B. J., and Abata, D. L., SAE Paper, No. 880428, 1988.

6 Abata, D. L., et al., SAE Paper No. 880298, 1988.

7 El Wakil, M. M., Myers, P. S., and Uyehara, O. A., *SAE Transactions*, Vol. 63, 1955.

8 Ha, J., et al., SAE Paper No. 830451, 1983.

9 Chiang, C. W., Myers, P. S., and Uyehara, O. A., *SAE Transactions*, Vol. 68, 1960.

10 Henein, N. A., Fragoulis, A. N., and Luo, L., SAE Paper No. 850266, 1985.

11 Henein, N. A., and Akasaka, Y., SAE Paper No. 871617, 1987.

12 Spalding, D. B., *Some Fundamentals of Combustion*, Butterworths, London, 1955.

13 Ballal, D. R., and Lefebvre, A. H., *Eighteenth Symposium (International) on Combustion*, The Combustion Institute, 1981.

14 Myers, G. D., and Lefebvre, A. H., *Combustion and Flame*, Vol. 66, 1986, pp. 193–210.

15 Cekalin, E. K., *Eighth Symposium (Int.) on Combustion*, The Combustion Institute, 1960.

16 Mizutani, Y., and Nishimoto, T., *Combustion Science and Technology*, Vol. 6, 1972, pp. 1–10.

17 Chan, K. K., and Wu, S. R., SAE Paper No. 870099, 1987.

18 Westbrook, C. K., and Dryer, F. L., *Combustion Science and Technology*, Vol. 27, 1981, pp. 31–43.

19 Kadota, T., and Hiroyasu, H., *Trans. JSME*, Vol. 19, No. 138, 1976.

20 Jin, J. D., and Borman, G. L., SAE Paper No. 850264, 1985.

21 Redlich, O., and Kwong, J. N. S., *Chemistry Reviews*, Vol. 44, 1948.

22 Chueh, P. L., and Prausnitz, J. M., *Ind. Eng. Chem.*, Vol. 60, No. 3, 1968.

23 Chueh, P. L., and Prausnitz, J. M., *I&EC Fund.*, Vol. 6, No. 4, 1969.

24 Lee, B. I., and Kesler, M. G., *AIChE Journal*, Vol. 21, 1975, p. 510.

25 Ried, R. C., Prausnitz, J. M., and Poling, B. E., *The Properties of Gases and Liquids*, 4th ed., McGraw-Hill, New York, 1986.

26 Blizard, N. C., and Keck, J. C., SAE Paper, No. 740191, 1974.

27 Tabaczynski, R. J., *Prog. Energy Combust. Sci.*, Vol. 2, 1976, pp. 143–165.

28 McCuiston, F. D., Lavoie, G. A., and Kauffman, C. W., SAE Paper No. 770045, 1977.

29 Groff, E. G., and Matekunas, F. A., SAE Paper No. 800133, 1980.

30 Fraser, R. A., et al., SAE Paper No. 860021, 1986.

31 Lancaster, D. R., et al., SAE Paper No. 760160, 1976.

32 Hinze, J. O., *Turbulence*, 2nd ed., McGraw-Hill, New York, 1975.

33 Damkohler, G., NACA TM 1112, 1947.

34 Shchelkin, K. I., *J. Tech. Phys.* (USSR), Vol. 13, 1943, pp. 520–530; English translation: NACA TM 1110, 1947.

35 Karlovitz, B., Denniston, D. V., and Wells, F. E., *J. Chem. Phys.*, Vol. 19, 1951, p. 541.

36 Wohl, K., et al., *Fourth Symposium (Int.) on Combustion*, 1953, pp. 620–635.

37 Faeth, G. M., AIAA Paper No. 86-0136, 1986.

38 Shuen, J. S., et al., *AIAA Journal*, Vol. 23, 1985, pp. 396–404.

39 Obtained under research contract #DAAE07-83-G-R007 with United States Army TACOM, Oct. 1987.

40 Stroia, B. J., "An Investigation of Injection Rate Controlled Heat Release of Selected Alternate Fuels in a Direct Injection Diesel Engine," Ph.D. Thesis, Michigan Technological University, 1989.

Diesel Engine Cold Starting: P-C Based Comprehensive Heat Release Model: Part I—Single Cycle Analysis

A. R. Zahdeh[1]

N. A. Henein
Professor, Director.

Center for Automotive Research,
Wayne State University,
Warren, MI 48090

W. Bryzik

US Army Automotive Command,
Warren, MI 48090

A portable PC-based heat release model for diesel engines with an emphasis on cold starting was developed to be used on an IBM PC or compatible. The model features normalized variables, the inclusion of blowby and heat transfer models, smoothing using a combination of error detection methods and low pass FFT. The derivative of the pressure data was calculated using cubical splines, from which the analytical first and second derivatives were derived. This method had the advantage of no data shifting, the ability to calculate the derivatives at any point (intermediate or original data point) and the error of both the first and second derivatives of the same order. The inclusion of the blowby model during starting was essential as losses due to blowby were found to be just as significant as other major loss factors. Smoothing angular velocity and the pressure signal using polynomial and cubical splines did not prove to be as efficient or as accurate as using the combination of error detection methods and FFT. Combustion during cold starting is mostly of the premixed type.

Background

The development of a heat release analysis provides a valuable tool for assessing the performance (i.e., power, efficiency, starting behavior, smoke formation and noise) of a diesel engine. Some initial efforts in this line were made by Austen and Lyn [1], Lyn [2], and Shipinski et al. [3]. The most significant work is that of Krieger and Borman [4], which couples the heat release analysis concept to detailed chemical equilibrium properties.

In this work, a heat release model was developed. The immediate aims are:

- Cold startability and white smoke analysis for a single cylinder, air-cooled, four-stroke, DI Deutz F1L 210 diesel engine.
- Autoignition of different fuels at low ambient temperatures and low speeds in a single cylinder Labeco DI diesel engine. This program can be used on any other engine.

The heat release model is based on the normalized approach of Ferguson [5]. This approach was taken in order to reduce the dependency of the model on uncertain or difficult-to-measure quantities like the trapped mass in the cylinder during each cycle. This model also takes into account the losses due to heat transfer to the cylinder walls and the blowby losses through the piston rings. The experimental ($\omega - \theta$) data are used as an input for this model instead of the average engine speed, which has been used in all previous models. The experimental ($P - \theta$) and ($\omega - \theta$) data are smoothed using a smoothing technique specially developed for this analysis. The numerical computations for the model are performed on an IBM PC.

Heat Release Analysis

The foundation of the heat release model is the first law of thermodynamics with attention being focused on the combustion process. Certain assumptions and approximations are

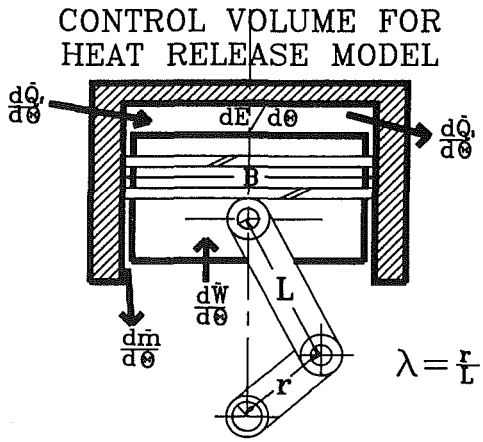

Fig. 1 Heat release model control volume

[1]Current address: General Motors Corporation, Warren, MI.

Contributed by the Internal Combustion Engine Division and presented at the Energy-Sources Technology Conference and Exhibition, Houston, Texas, January 20-24, 1991. Manuscript received by the Internal Combustion Engine Division September 1990. Paper No. 91-ICE-15.

made in the model because of the complex interaction of the physical and chemical natures of the combustion in a diesel engine. The following assumptions are made in the model:

- Uniform properties throughout the combustion chamber.
- Specific heat is taken as a function of temperature.
- Temperature and pressure gradient, fuel vaporization, and mixing are ignored.
- No dissociation of the chemical species.

Figure 1 represents an engine control volume at a specific instant of time. Based upon the above assumptions an energy balance according to the first law of thermodynamics is written as

$$\frac{dE}{d\theta}=\frac{dQ_T}{d\theta}-\frac{dW}{d\theta}-\frac{\dot{m}_i h}{\omega} \tag{1}$$

or in terms of the specific heat the first law can be written as

$$C_v T\frac{dm}{d\theta}+C_v m\frac{dT}{d\theta}=Q_\epsilon\frac{dx}{d\theta}-\frac{dQ_t}{d\theta}-P\frac{dV}{d\theta}-\frac{\dot{m}_i C_p T}{\omega} \tag{2}$$

where $\dot{m}_i$ is the instantaneous blowby rate assumed to be out of the cylinder and taking away hot gases, which are characterized by the enthalpy of the cylinder content, namely C_pT. The fraction of fuel burned is given by $dx/d\theta$.

In order to solve equation (2), additional relationships are required. The equation of state is used as the second equation:

$$PV=mRT \tag{3}$$

Taking the logarithm of the above equation and differentiating with respect to the crank angle we obtain

$$\frac{1}{P}\frac{dP}{d\theta}+\frac{1}{V}\frac{dV}{d\theta}=\frac{1}{m}\frac{dm}{d\theta}+\frac{1}{T}\frac{dT}{d\theta} \tag{4}$$

Eliminating $dT/d\theta$ between equations (2) and (4) we obtain

$$\frac{1}{P}\frac{dP}{d\theta}+\frac{1}{V}\frac{dV}{d\theta}=\frac{Q_\epsilon}{C_v mT}\frac{dx}{d\theta}-\frac{1}{mC_v T}\frac{dQ_t}{d\theta}-\frac{P}{mC_v T}\frac{dV}{d\theta}-\frac{\dot{m}_i}{m}\frac{\gamma}{\omega} \tag{5}$$

Equation (5) reduces to

$$\frac{dP}{d\theta}=-\gamma\frac{P}{V}\frac{dV}{d\theta}+\frac{\gamma+1}{V}Q_\epsilon\frac{dx}{d\theta}-\frac{dQ_t}{d\theta}-\frac{\dot{m}_i}{m}\frac{\gamma P}{\omega} \tag{6}$$

The continuity equation gives

$$\frac{dm}{d\theta}=-\frac{\dot{m}_i}{\omega} \tag{7}$$

From the definition of work

$$\frac{dW}{d\theta}=P\frac{dV}{d\theta} \tag{8}$$

and from heat transfer

$$\frac{dQ_T}{d\theta}=Q_\epsilon\frac{dx}{d\theta}-\frac{dQ_t}{d\theta} \tag{9}$$

The term dQ takes into account the heat added from combustion of fuel and the heat loss by the gases in the cylinder due to convection. dQ_t is given by

$$\frac{dQ_t}{dt}=hA(T-T_w) \tag{10}$$

Using the dimensionless variables

$$\begin{aligned}
&\overline{Q}_\epsilon=\frac{Q_\epsilon}{P_l V_l} && \overline{Q}_t=\frac{Q_t}{P_l V_l} && \overline{W}=\frac{W}{P_l V_l}\\
&\overline{T}=\frac{T}{T_l} && \overline{T}_w=\frac{T_w}{T_l} && \overline{P}=\frac{P}{P_l}\\
&\overline{V}=\frac{V}{V_l} && \overline{m}=\frac{m}{m_l} && \overline{A}=\frac{A}{A_l}\\
&\overline{h}=\frac{hT_l\left(A_0-\frac{4V_0}{b}\right)}{P_l V_l\omega} && \beta=\frac{4V_l}{b\left(A_0-\frac{4V_0}{b}\right)}
\end{aligned} \tag{11}$$

substituting these normalized variables in the equations for heat transfer, work, continuity and $dp/d\theta$, we obtain the governing equations required for the analysis.

$$\frac{d\overline{P}}{d\theta}=-\gamma\frac{\overline{P}}{\overline{V}}\frac{d\overline{V}}{d\theta}+\frac{(\gamma-1)}{\overline{V}}\left(\overline{Q}_\epsilon\frac{dx}{d\theta}-\overline{h}(1+\beta\overline{V})(\overline{T}-\overline{T}_w)\right)-\frac{\dot{m}_i}{m_l}\frac{\gamma\overline{P}}{\overline{m}\omega} \tag{12}$$

$$\frac{d\overline{Q}_t}{d\theta}=\overline{h}(1+\beta\overline{V})(\overline{T}-\overline{T}_w) \tag{13}$$

$$\frac{d\overline{W}}{d\theta}=\overline{P}\frac{d\overline{V}}{d\theta} \tag{14}$$

$$\frac{d\overline{m}}{d\theta}=-\frac{\dot{m}_i}{m_l}\frac{l}{\omega} \tag{15}$$

Equation (12) gives the rate of change of pressure with re-

Nomenclature

$\overline{A}$ = normalized area
A = total area of the heat transfer surface
A_0 = area of combustion chamber at BDC
A_1 = area of combustion chamber at TDC
b = bore of the engine
$\overline{C}_p$ = normalized specific heat at constant pressure = C_p/R
C_d = discharge coefficient for the orifice
C_p = specific heat at constant pressure
CR = compression ratio
C_v = specific heat at constant volume
d = diameter of the nozzle orifice
D = cylinder diameter
E = internal energy
h = cylinder gas-to-wall heat transfer coefficient
$\overline{h}$ = normalized heat transfer coefficient
L_n = needle lift
$\dot{m}_i$ = instantaneous blowby rate
m = mass
N = rpm
$\overline{P}$ = normalized pressure
P = pressure
P_1 = ambient pressure
Q_ϵ = LHV of the fuel multiplied by total fuel mass
$\overline{Q}_t$ = normalized heat transfer
Q = heat transfer
Q_f = amount of fuel injected
Q_l = losses due to heat transfer
Q_T = total heat transfer
r = crank throw radius
R = gas constant
s = stroke
$\overline{T}$ = normalized temperature
T = temperature
T_1 = inlet temperature
T_w = cylinder wall temperature
$\overline{V}$ = normalized volume
V = volume
V_1 = volume at end of intake stroke
V_m = mean piston speed
$\overline{W}$ = normalized work
W = work
x = fraction of burned fuel
β = normalized constant
γ = ratio of specific heats
θ = crank angle
ρ = fuel density
ω = angular velocity

spect to crank angle. For heat release analysis it can be written as

$$\overline{Q}_\epsilon \frac{dx}{d\theta} = \left(\frac{\overline{V}}{\gamma - 1}\right) \frac{d\overline{P}}{d\theta} + \left(\frac{\gamma}{\gamma - 1}\right) \overline{P} \frac{d\overline{V}}{d\theta} + \overline{h}(1 + \beta \overline{V}) \left(\frac{\overline{P}\,\overline{V}}{\overline{m}} - \overline{T}_w\right) + \left(\frac{\gamma}{\gamma - 1}\right) \overline{P}\,\overline{V} \frac{\dot{m}_i}{m_l} \frac{l}{\omega} \quad (16)$$

Equations (13) to (16) represent a set of four ordinary differential equations that are solved simultaneously using the measured cylinder pressure and the rate of pressure change calculated from the experimental data along with the cylinder volume and rate of change of cylinder volume as calculated from the slider crank equations. A detailed derivation of the governing equations is given in [6]. The equations for the specific heats are given below:

$$\gamma = \left(\frac{\overline{C}_p}{\overline{C}_p - 1}\right) \quad (17)$$

where C_p is given for $T < 1000$ K:

$$\overline{C}_p = \left(3.6359 - 1.33736 \frac{T}{1000} + 3.29421 \frac{T^2}{10^6} - 1.91142 \frac{T^3}{10^9} + 0.275462 \frac{T^4}{10^{12}}\right) \quad (18)$$

and for $T > 1000$ K:

$$\overline{C}_p = \left(3.04473 + 1.33805 \frac{T}{1000} - 0.488256 \frac{T^2}{10^6} + 0.0855475 \frac{T^3}{10^9} - 0.00570132 \frac{T^4}{10^{12}}\right) \quad (19)$$

Model for Heat Transfer

Hohenberg's [7] correlation is used to model the heat transfer coefficient between the cylinder gases and the wall. In this simple method, allowance is made for the rise in gas velocity with increasing engine speed as well as the variations in velocity with crank angle. Hohenberg's heat transfer coefficient can be expressed as

$$h = C_1 V^{-0.06} P^{0.8} T^{-0.4} (V_m + C_2)^{0.8} \quad (20)$$

where C_1 and C_2 are empirical constants, C_2 accounts for the combustion turbulence. Their values are

$$C_1 = 160.0$$
$$C_2 = 1.4$$
$$V_m = \frac{2r\omega}{60} \quad (21)$$

The gas-to-wall heat transfer area is calculated by

$$A = A_{\text{cylinder}} + A_{\text{pictor}} + (A_{\text{liner}} + \pi DS) \quad (22)$$

Model for Blowby

The blowby model used in this study represents the gas flow path by a series of volumes connected by square-edged orifices (ring gaps). The mass flow between these volumes is expressed in terms of the pressure ratio and the stagnation conditions by the formulas used for one-dimensional unsteady, compressible adiabatic flow through square orifices, with a constant discharge coefficient [8]. The mass flow rate m_{ij} between adjacent volumes i and j can be expressed as:

For subsonic flow when:

$$\frac{P_j}{P_i} > \left(\frac{2}{\gamma + 1}\right)^{\frac{\gamma}{\gamma - 1}} \quad (23)$$

$$m_{ij} = C_d \frac{A_i P_i}{(RT_i)^{0.5}} \left(\frac{P_j}{P_i}\right)^{\frac{1}{\gamma}} \left(\frac{2\gamma}{\gamma - 1} \left(1 - \left(\frac{P_j}{P_i}\right)^{\frac{\gamma - 1}{\gamma}}\right)\right)^{0.5} \quad (24)$$

and for choked flow when:

$$\frac{P_j}{P_i} = \left(\frac{2}{\gamma + 1}\right)^{\frac{\gamma}{\gamma - 1}} \quad (25)$$

$$\dot{m}_{ij} = C_d \frac{A_i P_i}{(RT)^{0.5}} \gamma^{0.5} \left(\frac{2}{\gamma + 1}\right)^{\frac{(\gamma + 1)}{2(\gamma - 1)}} \quad (26)$$

From the continuity equation, a mass balance for volumes 1 and 2 can be written as

$$dM_1 = m_{11} - m_{12}$$
$$dM_2 = m_{12} - m_{20} \quad (27)$$

Assuming perfect gas and constant wall temperature, the pressures in volumes 1 and 2 change according to:

$$dP_1 = \frac{R_1 T_1}{V_{1b}} dM_1$$
$$dP_2 = \frac{R_2 T_2}{V_{2b}} dM_2 \quad (28)$$

Thus, for the blowby model there is a system of three equations for each volume to solve, with the boundary condition

$$P_1 = P_{\text{cyl}}$$
$$P_0 = P_{\text{atm}} \quad (29)$$

Numerical Technique and Smoothing

In this section, two important techniques that are being used in data processing will be discussed, as smoothing the pressure and the angular velocity data is crucial when they are used to calculate the heat release. A detailed survey of smoothing techniques is available in [6].

Error Detection Smoothing. In this type of smoothing the function $f(x)$ is assumed to be accurate except for some points that are in error (about 10 percent). It is desirable to detect these points and then compute new values, which will result in a smooth curve. This method is useful for preparation of the data for other smoothing techniques. The disadvantage of this method is that the number of points with errors have to be pre-estimated.

Low-Pass Filters and Fast Fourier Transformations. First the idea of using this method is to remove all the linear trends from the data by low-passing them using Fast Fourier Transform (FFT), re-inserting the linear trends, and finally returning the smoothed data to their previous form (real domain as FFT puts the data in the frequency domain). A smoothing factor has to be entered by the user, which defines the number of data points over which the data should be smoothed. This number can be real or an integer. Zero gives no smoothing at all, while any value larger than half of the number of the data points could result in the introduction of such a large error that it could make the data unsuitable.

This method has been found to be most effective if it is used with the abovementioned error detection method, where errors of large magnitude are first eliminated. Then, the FFT–low-pass filter method can be used to give very satisfactory results.

Another important point that has to be mentioned here is that FFT is extremely fast, which is very important in our case as all these analyses are conducted on an IBM-PC.

Preparation of the Experimental Data for the Model ($dP/d\theta$, ω). From equation (16) we can see that the first derivative of the pressure with respect to crank angle is needed in order to solve the differential equations. Taking a simple derivative

$(\Delta P/\Delta\theta)$ is not recommended, especially for unsmoothed raw data. This will be clear from the following analysis.

Error in the Derivative of the Pressure. Assume that the error of the pressure transducer is $\pm\epsilon$, then the first derivative error will depend on the sign of the error in P_i, P_{i+1}. Two cases are encountered:

Both Errors Have the Same Sign. Then

$$\frac{dP}{d\theta}=\frac{(P_{i+1}+P_{i+1}\epsilon)-(P_i+P_i\epsilon)}{d\theta_{i+1}-d\theta_i} \tag{30}$$

where P_i = pressure data at point i; ϵ = error of the pressure transducer. Assume that the theta reading has no error and that the sampling was taken at every crank angle degree. Then the above equation becomes

$$dV=(P_{i+1}-P_i)(1\pm\epsilon) \tag{31}$$

Then the error of the derivative calculations is

$$=\frac{(P_{i+1}-P_i)(1\pm\epsilon)}{(P_{i+1}-P_i)}$$

$$=1\pm\epsilon \tag{32}$$

As we see, the error in the derivative has the same order of magnitude as the error in the pressure data.

Errors Having Different Signs. Using the same assumption about crank angle as the previous case, the derivative of the pressure is

$$\frac{dP}{d\theta}=\frac{(P_{i+1}+P_{i+1}\epsilon)-(P_i-P_i\epsilon)}{d\theta_{i+1}-d\theta_i}$$

$$=(P_{i+1}-P_i)\pm\epsilon(P_{i+1}+p_i) \tag{33}$$

Then the error will be

$$=\frac{(P_{i+1}-P_i)\pm\epsilon(P_{i+1}-P_i)}{(P_{i+1}-P_i)}$$

$$=1\pm\epsilon\left(\frac{P_{i+1}+P_i}{P_{i+1}-P_i}\right) \tag{34}$$

Unfortunately in this case the error could be out of bounds if $P_{i+1}=P_i$. This is the case when the piston is near BDC and also during the intake stroke. The error could be minimal if the $P_{i+1}+P_i=0$, or $P_{i+1}=-P_i$; however, this case is rarely encountered in engine applications, since the part of heat release that is of great importance for us is near TDC where the pressure never changes its sign.

For a pressure transducer with an accuracy of ± 1 percent, $P_2=100$, $P_1=95$, an error of ± 39 percent will be inflected on the derivative of the pressure.

Finding of Data Derivatives. It was shown previously that simple derivatives are not recommended for use due to error magnification. Another important fact is that a shift of data reading forward or backward could be inflected into the data (if forward or backward differences are used). The nine-point polynomial was recommended in the literature, but in the above sections it was noticed that a simple polynomial should be avoided due to its asymptotic behavior and the unlocalized perturbation effects.

This problem can be solved if the calculation of the derivative is performed by defining a spline with a spline factor C. C is a matrix of dimension $i\times 3$, where i is the number of data points and 3 is the cubical polynomial coefficient. Analytical derivatives can be taken for the polynomial at the location corresponding to the original data points, or at any intermediate points located between the data points. The error in this case for both the first and second derivatives is of the same order.

The advantages of using this method are:

1 No data shifting.

2 The ability to calculate the derivatives at any point (intermediate or at original data points).

3 The errors for both derivatives are of the same order.

The second derivative is important for:

1 From the second derivative one can establish whether the smoothing was performed in the proper manner or not. This implies that if ripples are still found in the second derivative, then the data are undersmoothed, while if some of the expected details were not found in the second derivative, then the data are oversmoothed.

2 Taking a reliable second derivative could reveal valuable information about the data. For instance, the second derivative of the pressure data clearly indicates the start of fuel injection, the end of ignition delay, and the total duration of the combustion event (second derivatives correlate well with the rate of heat release).

3 Second derivative of angular velocity (jerk) can be used to characterize the level of roughness of engine operation.

Model Structure and Techniques. The input data required for model calculation were read from a file. This file can be modified very easily to accommodate any other engine. A sample of this file for the Deutz engine is shown in Table 1.

Pressure and angular velocity were smoothed using a combination of error detection method and low-pass-filter with FFT. Cubical spline factor was calculated for both the angular velocity and pressure data. The first and second derivatives were also calculated. The smoothing factors of both angular velocity and pressure are then chosen. A smoothing factor between 5 and 20 was sufficient to produce very acceptable results (if the smoothing factor is large than half of the number of the data points, then the accuracy is seriously compromised).

The predictor and corrector methods was used to solve the ordinary differential equations. Individual subroutines were written for the gas properties and the engine geometry.

Input Data for the Model

The input data required for the heat release model are:

1 Experimental P–θ diagram
2 Experimental ω–θ diagram
3 Engine dimensions
4 Fuel type, LHV, specific gravity
5 Mass of air flow or volumetric efficiency
6 Discharge coefficient C_d
7 Ambient temperature

Cylinder Pressure Measurement

An AVL piezo-electric heat shielded cylinder pressure transducer was used for the measurement of the P–θ trace. It was

Table 1

ENGINE BORE D [M]	= 0.095
ENGINE STROKE S [M]	= 0.095
CONNECTING ROD LENGTH L [M]	= 0.16
COMPRESSION RATIO CR [ ]	= 17.0
ATMOSPHERIC PRESSURE P1 [N/M2]	= 101325.0
ATMOSPHERIC TEMPERATURE T1 [°K]	= 293.0
CYLINDER WALL TEMPERATURE TW [°K]	= 400.0
AREA OF THE COMBUSTION CHAMBER A0 [M2]	= 0.03282943
NUMBER OF C.A TO SHIFT THE TDC TT [°]	= 0.0
BLOW-BY COEFFICIENT BB [ ]	= 0.8
VOLUMETRIC EFFICIENCY Y(5) [ ]	= 0.97
CONVERSION OF THE PRESSURE TO BARS UONV [ ]	= 14.69

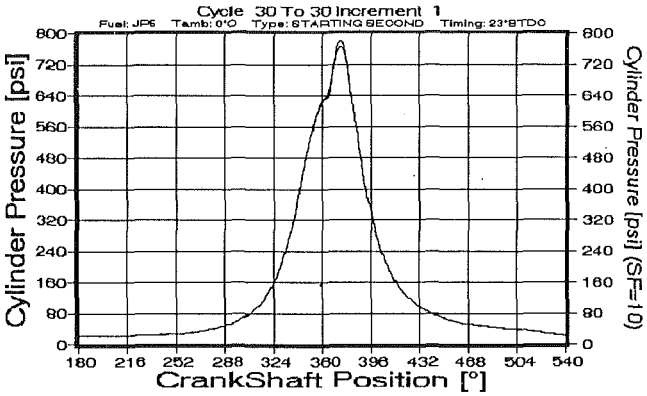

Fig. 2 Unsmoothed cylinder pressure data

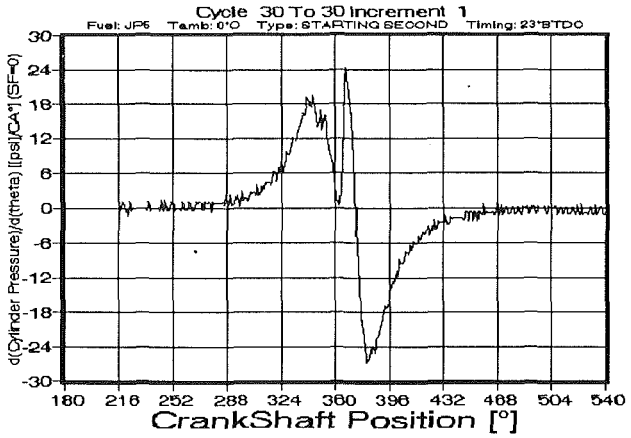

Fig. 3 First derivative of pressure data (smoothing factor 0)

found that the model is extremely sensitive to the smoothness of the input P–θ diagram: A slight perturbation in the input P–θ trace causes oscillations in the pressure derivative, which in turn caused oscillations in the heat release.

Results and Discussion

Data Smoothing. Figure 2 shows a plot of unsmoothed pressure data superimposed on the same data with a smoothing factor of 10. From the figure, smoothing factor 10 followed the data trend satisfactorily. A larger smoothing factor (20) could result in some discrepancy, especially near the TDC.

Smooth and error-free signals will be in great demand when further analyses are performed on the data, especially when first and second derivatives are needed. A typical analysis is one where heat release and instantaneous friction derivatives are required. To calculate the heat release, the first derivative of the pressure data has to be taken, but as the derivative of a discontinuity or a jump blows up toward infinity, the reconstruction of a smooth error-free signal is essential.

Figures 3 and 4 show the effect of smoothing of a signal when its derivatives are needed. Smoothing factors of 0 (no smoothing) and 10 were used to calculate the first derivatives of the cylinder pressure signal presented in the previous graphs.

Even though the effect of smoothing on the original signal was hardly noticeable, the ramifications of the errors on the derivative were obvious from the ripples seen in the $dp/d\theta$ graph with no smoothing. Figures 5 and 6 show the second derivative of the cylinder pressure data with no smoothing and smoothing of 10. One can determine that the unsmoothed second derivative has no physical meaning.

Figure 7 shows the effect of smoothing on angular acceleration. From the previous discussions one can conclude that first and second derivatives have to be matched between sampled data to continue the analysis. The method presented successfully achieved this goal.

From the above discussion it was shown that smoothing the data is essential to reconstruct the continuity of the original signal for further numerical manipulations and analysis. The use of cubical splines to take the first and second derivatives with the same order of error was achieved.

Figures 8 and 9 show graphs of the cumulative rate of heat release for the same cycle with a smoothing factor of 10 and 0 (unsmoothed). The effect of the error in the data (noise or transducer) is manifested by the ripples in the curve with no smoothing.

Figures 10 and 11 show the rate of heat release under the same smoothing conditions for cycle 30. One can see that the noise is more obvious in the rate of heat release as it is derived from the pressure derivative. Derivatives are known to amplify the noise, while integration processes (as in the case of cumulative heat release) are known to suppress it. One can ob-

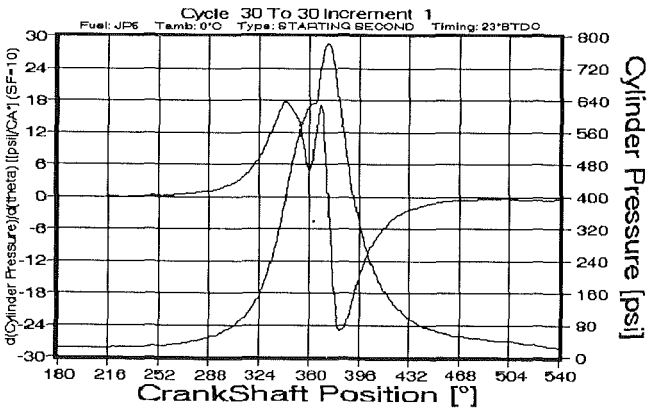

Fig. 4 First derivative of pressure data (smoothing factor 10)

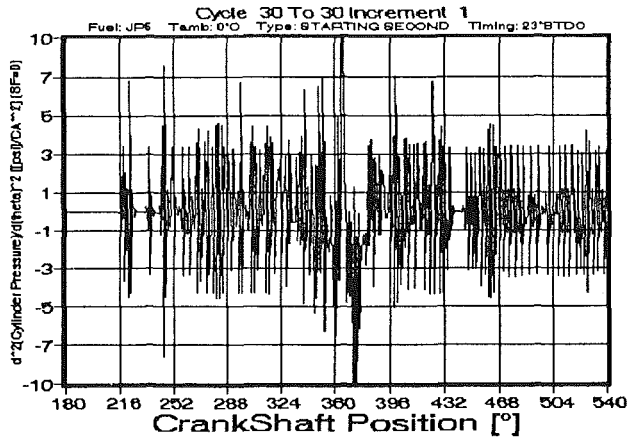

Fig. 5 Pressure second derivative (smoothing factor = 0)

serve that the noise in the rate of heat release signal is more noticeable when the pressure is at its lowest level.

Figures 12 and 13 show the cylinder temperature calculated from the model with and without smoothing.

Finding a reliable first and second derivative can provide valuable information such as establishing the start of the fuel injection. The ignition delay can be found from the second derivative of the pressure data. First and second derivatives of the cylinder pressure can be used as an indicator of the roughness of the combustion process.

From the above statements one can see the need for satisfying the continuity between the sample points (interface). This could be achieved by having a signal with an equal first and second derivative between the sample points.

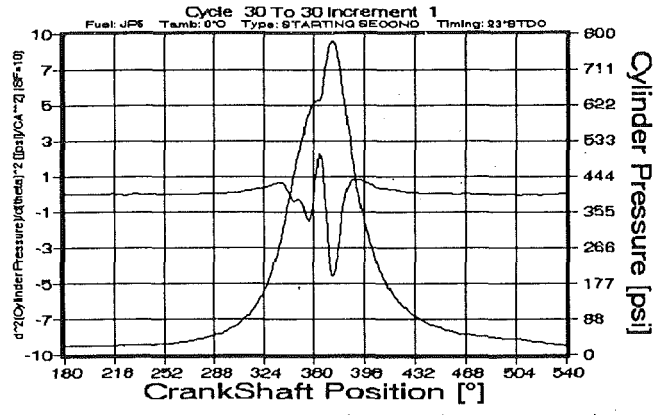

Fig. 6 Pressure second derivative (smoothing factor = 10)

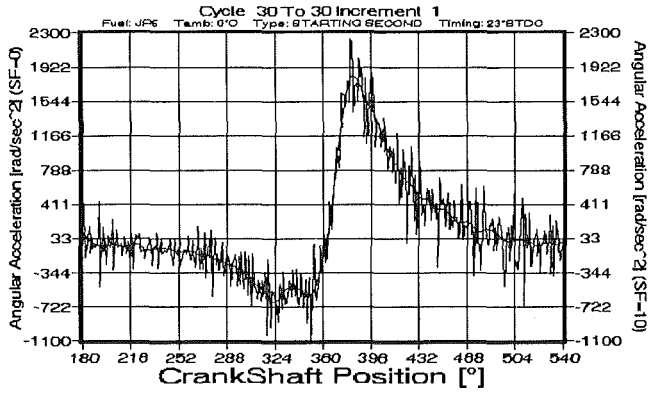

Fig. 7 Effect of smoothing on angular acceleration

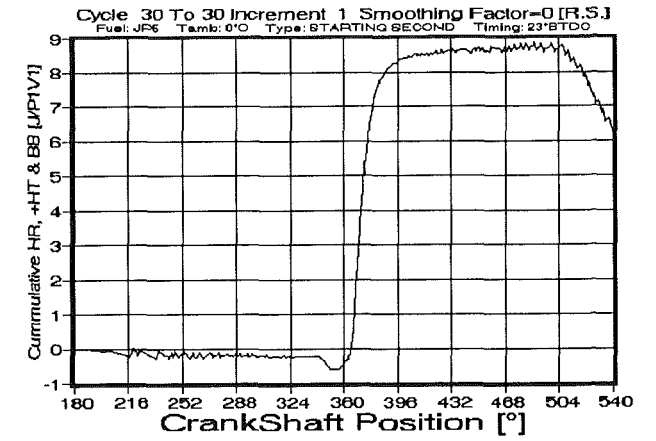

Fig. 8 Cumulative heat release (smoothing factor = 0)

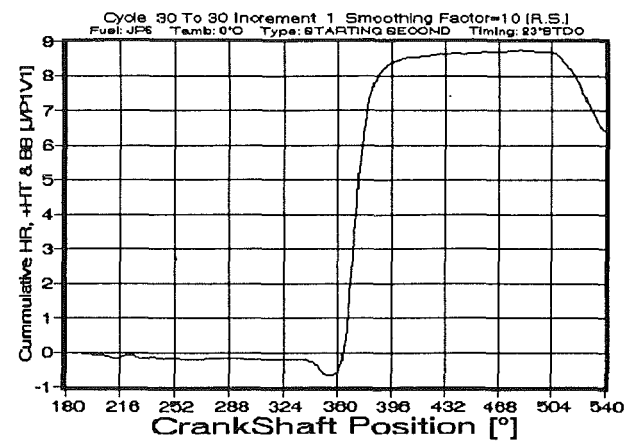

Fig. 9 Cumulative heat release (smoothing factor = 10)

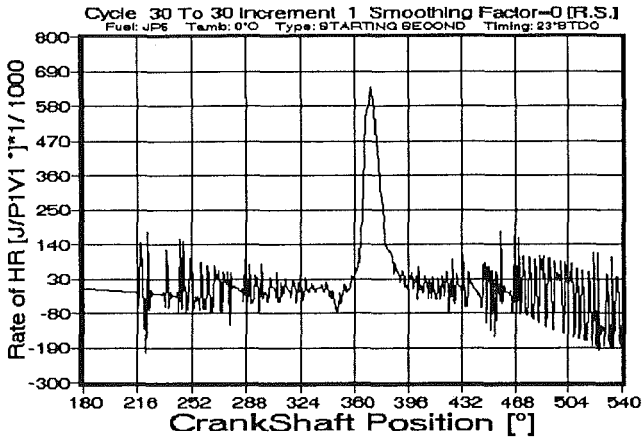

Fig. 10 Rate of heat release (smoothing factor = 0)

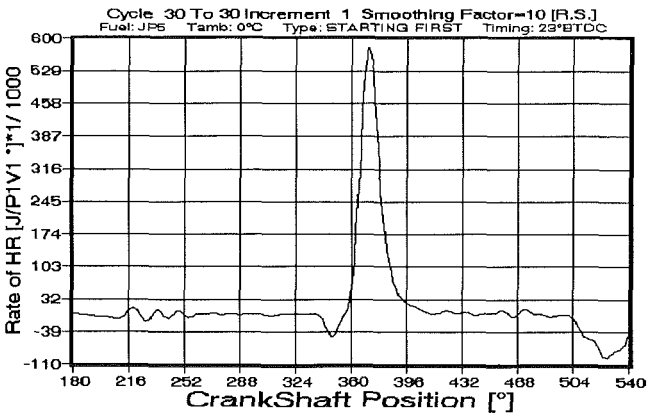

Fig. 11 Rate of heat release (smoothing factor = 10)

Heat Release Model. Careful consideration was given to memory and efficiency of calculation of heat release. 29 seconds were needed to complete the heat release calculation of one cycle (360 CA°). All of the calculations were conducted on an 80286 IBM-compatible PC with 10 MHz clock speed. In the following section the output results from the heat release program will be presented with a brief description.

Rate of Heat Release dQ/dθ (RHR). The rate of heat release was calculated by solving equation (16). It incorporates the effect of the heat transfer and blowby losses. Figure 13 shows the typical rate of heat release for an engine during its starting period. The needle lift signal was superimposed to show the start of the fuel injection.

The following information can be obtained from the Fig. 13:

1 The rate at which the injected fuel is being burned.

2 The start of the fuel injection from the needle lift sensor coincides with the point when the RHR dips into the negative direction. This dip indicates the heat loss of the combustion chamber gases due to the evaporation of the fuel. The start of the fuel injection and the point when the RHR changes to a negative direction coincides only if there is no fuel accumulation.

3 The combustion during starting is considered to be in the premixed mode. The maximum rate of heat release signifies the roughness of the combustion.

Cumulative Heat Release (CHR). The CHR was calculated by integrating equation (16) over a specified period. Equation (16) was divided into three components: First was the theo-

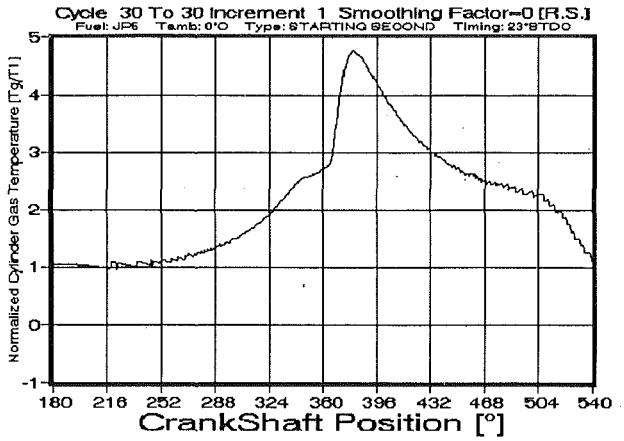

Fig. 12 Cylinder gas temperature (smoothing factor = 0)

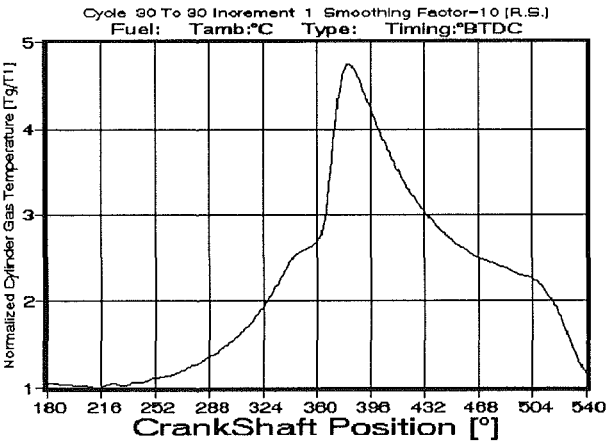

Fig. 13(*a*) Cylinder gas temperature (smoothing factor = 10)

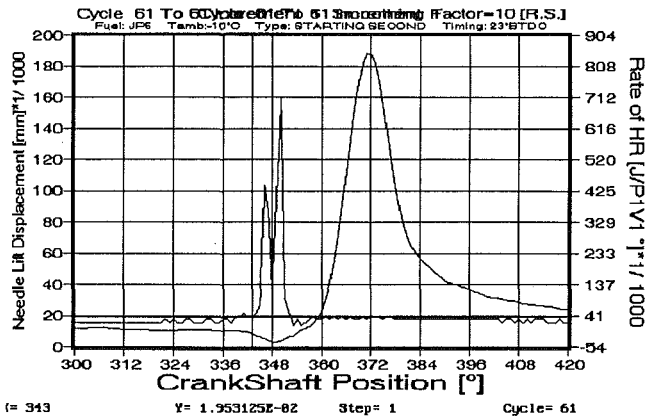

Fig. 13(*b*) Rate of heat release and needle lift

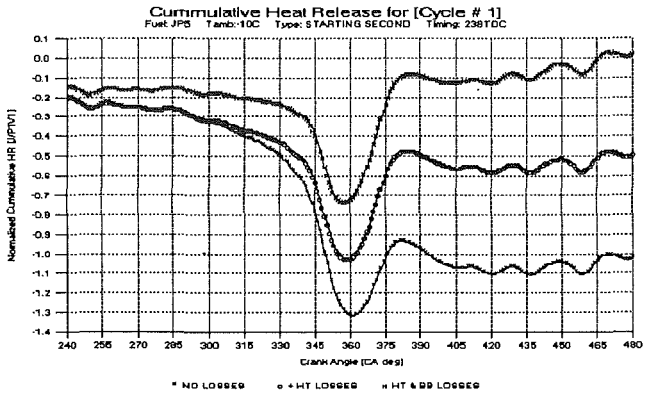

Fig. 14(*a*) Cumulative heat release during starting (−10°C, cycle 1)

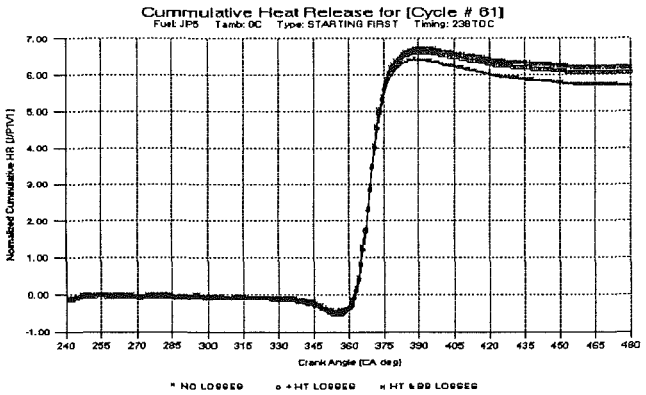

Fig. 14(*b*) Cumulative heat release during starting (−10°C, cycle 61)

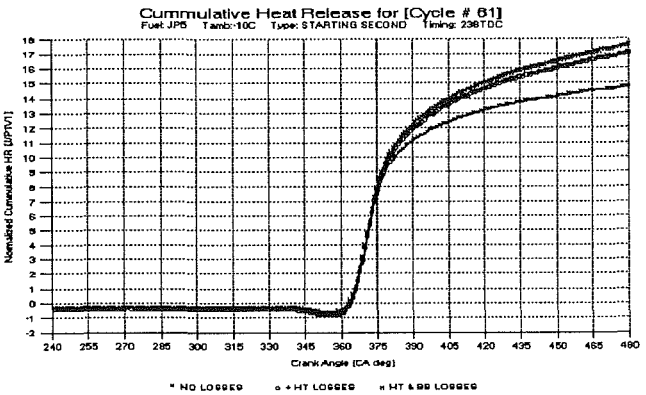

Fig. 14(*c*) Cumulative heat release during starting (0°C, cycle 61)

retical heat release where no losses were considered, second was the CHR with the addition of the effect of blowby losses, and third was the effect of the heat released with all the loss components. Figure 14 shows the three curves of CHR, where the first curve from the top represents the total fuel burned, the second curve from the top represents the mass of fuel that would have burned if the blowby losses were nonexistent, while the third from the top is the theoretical fuel needed if all the losses were to be eliminated. The distance between the first and second curves represents the effect of the blowby, while the distance between the second and the third represents the effect of heat transfer losses.

From the CHR graphs the following information can be found:

1 Total mass of the fuel burned during the cycle.

2 The energy required for the fuel evaporation and the endothermic decomposition reactions.

3 The steepness of the CHR curves, indicating the roughness and the spontaneity of the combustion.

4 The contribution of the blowby and heat transfer losses.

Several observations can be drawn from Fig. 14: A summary of the contribution of the heat transfer and the blowby during engine starting under two different conditions are given in Table 2.

A comparison of the blowby cycle by cycle in the two runs concludes that: At low temperature and during starting, the blowby is as significant as heat transfer. Blowby decreases as time progresses due to the shrinking of the ring gaps and the appearance of an oil film on the cylinder.

Table 2

Cycle #	BLOWBY LOSSES $\frac{J}{P_1V_1°}$	HEAT TRANSFER LOSSES $\frac{J}{P_1V_1°}$
Temperature -10°C		
1	.5	.5
15	.5	.5
61	.7	2.
Temperature 0°C		
1	.8	.18
15	.42	.65
61	.2	.8

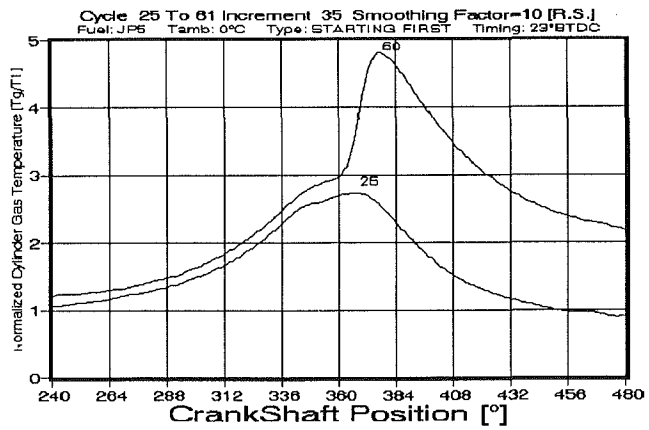

Fig. 15(*a*) Cylinder gas temperature during starting (0°C cycles 25, 61)

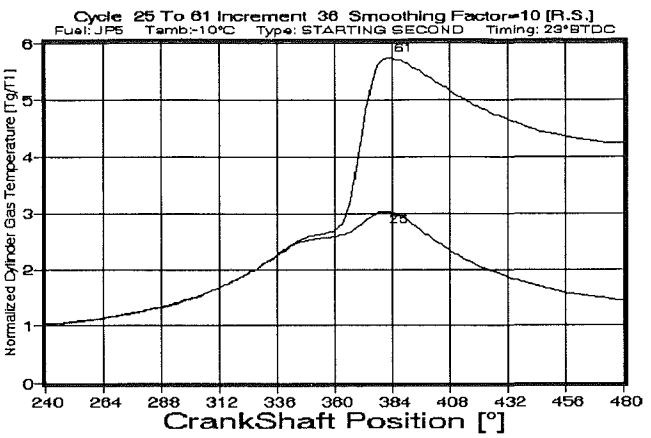

Fig. 15(*b*) Cylinder gas temperature during starting (−10°C cycles 15, 61)

Cylinder Gas Temperature. The mass average cylinder gas temperature was calculated from the state equation where the mass depreciation due to blowby was taken from the blowby model. The state equation is

$$T_\theta = \frac{P_\theta V_\theta}{m_\theta R} \tag{35}$$

By using P_1, V_1, T_1, and m_1 to normalize the variables, the equation becomes:

$$\overline{T}T_1 = \frac{\overline{P}P_1\overline{V}V_1}{\overline{m}m_1R} \tag{36}$$

Finally the state equation in normalized form is

$$\overline{T} = \frac{\overline{P}\,\overline{V}}{\overline{m}} \tag{37}$$

The gas constant R cancels out in the previous equation as

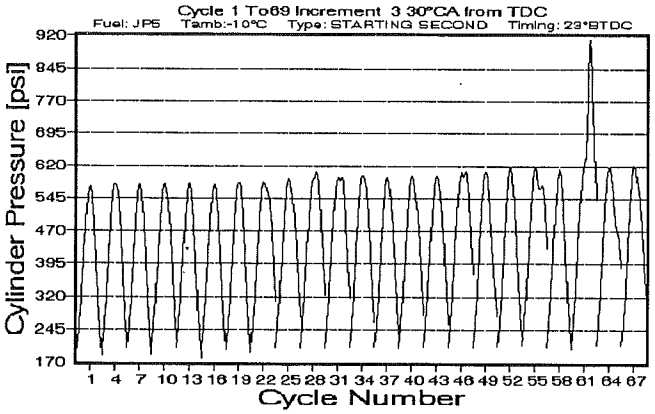

Fig. 16(*a*) Cylinder pressure during starting (−10°C)

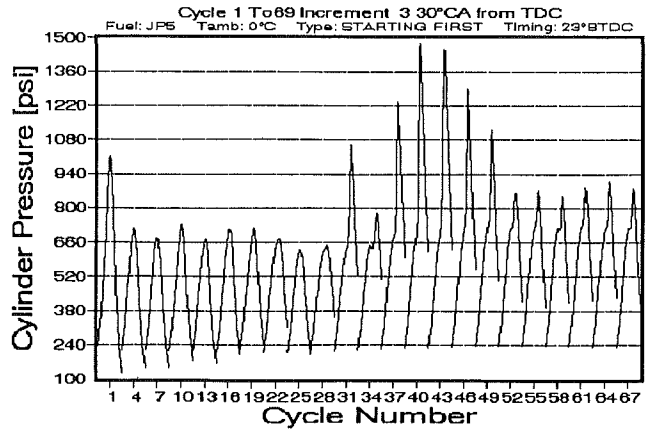

Fig. 16(*b*) Cylinder pressure during starting (0°C)

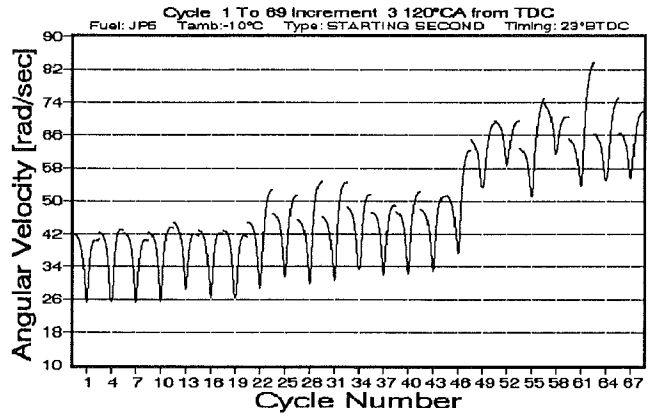

Fig. 17(*a*) Angular velocity during starting (−10°C)

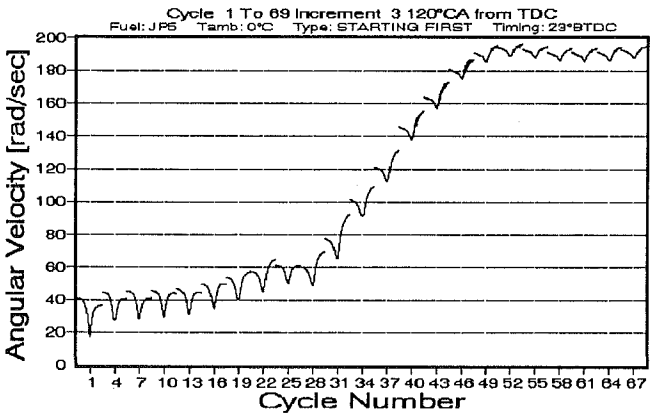

Fig. 17(*b*) Angular velocity during starting (0°C)

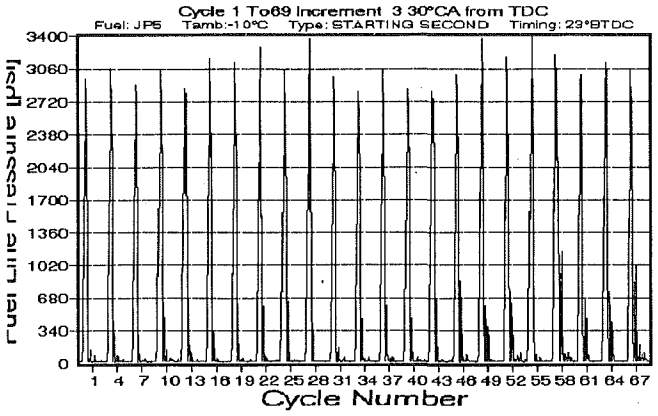

Fig. 18(*a*) Fuel line pressure during starting (−10°C)

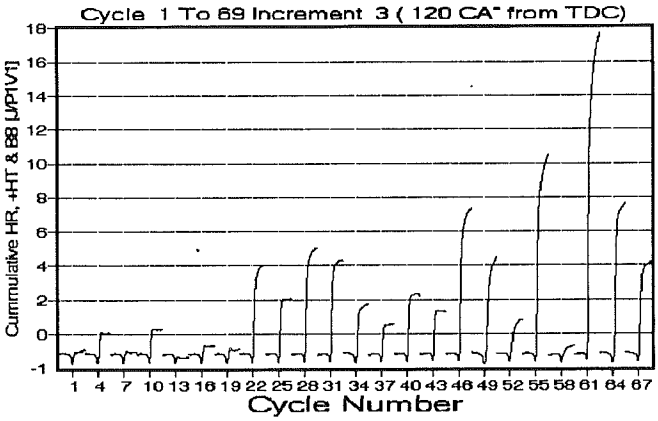

Fig. 19(*a*) Cumulative heat release during starting (−10°C)

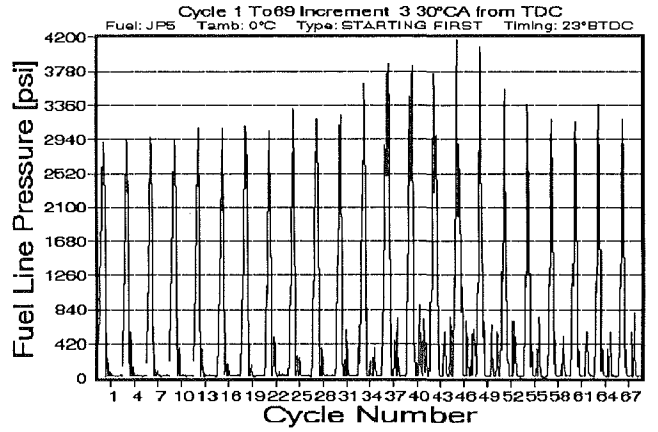

Fig. 18(*b*) Fuel line pressure during starting (0°C)

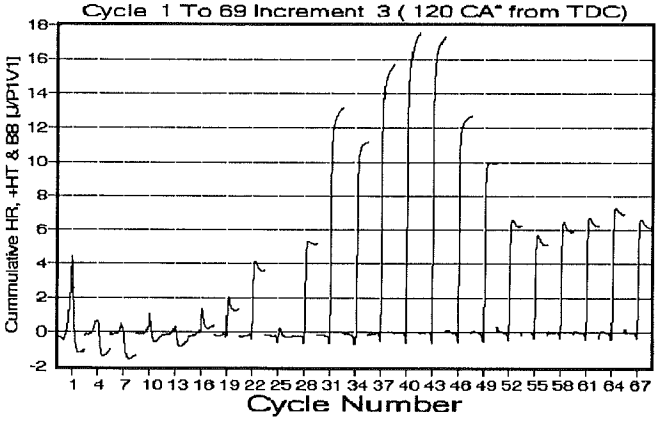

Fig. 19(*b*) Cumulative heat release during starting (0°C)

$$R = \frac{P_1 V_1}{m_1 T_1} \tag{47}$$

In the above equation the cylinder pressure is measured, the cylinder volume is calculated by using the equations in Appendix A, and the mass friction was calculated as a function of CA's. This shows greater accuracy in the calculation of the cylinder gas temperature shown in Fig. 15. Another feature of the normalized dimensions is that the units of the measured parameters are immaterial for the model calculation.

In Fig. 15, two starting attempts were presented, one at 0°C and 10°C. Figure 15(*a*) showed cycles 25 and 60 for a starting attempt at 0°C where an increase in the compression temperature between these two cycles could be attributed to the decrease in the heat transfer losses to the cylinder wall from heating. Figure 15(*b*) shows a starting attempt at a temperature of −10°C. The lower the ambient temperature the more significant the losses and consequently, the lower the compression temperature and pressure.

In the next discussion a comparison will be drawn between the aforementioned two starting attempts for the entire starting procedure. The cycles will be presented from cycle 1 to 67 with an increment of three cycles. Figure 16(*a*) shows the cylinder pressure at −10°C and Fig. 16(*b*) shows the cylinder pressure at 0°C. From the graphs one can determine that the rise in the pressure at low temperatures is much slower, not to mention that the maximum compression pressure was lower due to large ring gaps and intensive heat transfer. The firing cycles could be characterized as late-firing. In Fig. 16(*b*) one can see that the maximum compression pressure was much higher than the previous run and firing occurred more frequently.

Figure 17(*a*) demonstrates the angular velocity for the run at −10°C. The angular velocity traces show a slow increase in the engine speed up to cycle 22 where the first firing occurred. The maximum angular velocity reached by this run was 82 rad/s. In the run with 0°C a smooth and gradual increase in the angular velocity began at cycle 16, reaching a maximum of 200 rad/s at cycle 67. The trend can be attributed to a couple of factors: (1) There is a higher frequency of combustion at higher temperatures; (2) the oil viscosity is lower and the battery can deliver more charge at higher temperatures.

Figure 18(*a*) shows the fuel line pressure with the attempt at −10°C. The average maximum pressure in this run is about 3000 psi, while in Fig. 18(*b*) for the run at 0°C the pressure averaged 3200 psi and in some cycles reached 4200 psi (cycle 46). The higher pressure at higher temperatures can be attributed to the increase in the angular velocity.

Figures 19(*a*) and 19(*b*) showed the cumulative heat release for the same previously mentioned runs. Three significant observations can be made about these starting attempts: (1) At low temperatures the amount of fuel burned per cycle is very small, especially in the earlier cycles, as compared with similar runs at higher temperatures. (2) At lower temperatures the firing cycles are more sporadic than at higher temperatures. (3) During the compression and expansion strokes there is a significant amount of heat loss at lower temperatures, which can be seen in Fig. 19(*a*). Figure 19(*b*) showed that during the compression and expansion strokes the heat release curve was right on the zero line, which signifies less vigorous heat transfer to the cylinder walls.

Figures 20(*a*) and 20(*b*) show the rate of heat release for the above attempts. At lower temperatures the rates were very slow while at higher temperatures the rates of heat release were much faster. The combustion during starting can be described as premixed combustion.

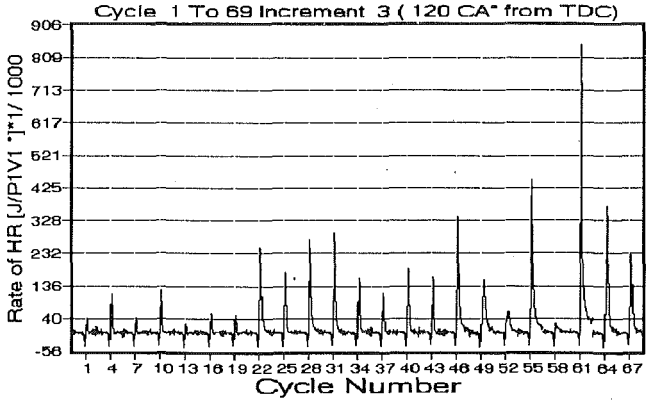

Fig. 20(*a*) Rate of heat release during starting (−10°C)

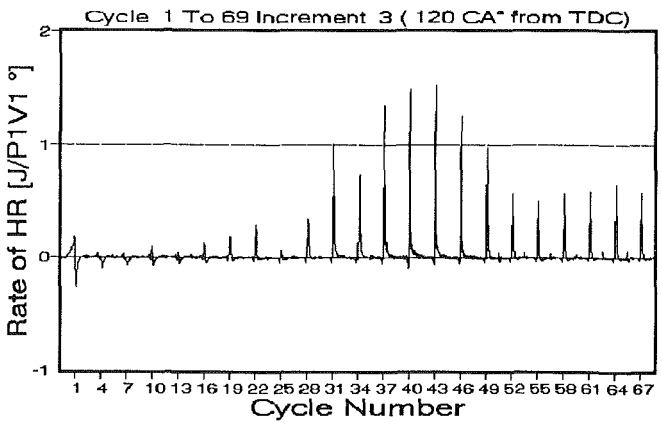

Fig. 20(*b*) Rate of heat release during starting (0°C)

Conclusions

1 A portable heat release program was written to be used on a PC. The program is user-friendly and fast in execution.

2 The blowby losses during starting are as important as the heat transfer losses and their inclusion in any heat release model for starting analysis is essential.

3 Recovering the continuity of measured pressure data for heat release is essential. This was achieved by smoothing the data using the combination of FFT and error detection method.

4 During starting most of the combustion was of the premixed type, which means a fine atomization of fuel could improve the starting of the engine by increasing the evaporation of the fuel.

References

1 Austin, A. E. W., and Lyn, W. T., "Relation Between Fuel Injection and Heat Release in a Direct Injection Engine and the Nature of the Combustion Processes," *Proceedings, Institution of Mechanical Engineers (A.D.)*, 1960–61, pp. 47–62.

2 Austen, A. E. W., and Lyn, W. T., "Some Investigation on Cold-Starting Phenomena in Diesel Engines," *Gas and Oil Power*, Annual Technical Review Number, 1959.

3 Shipinski, J., Uyehara, O. A., Myers, P. S., "Experimental Correlation Between Rate of Injection and Rate of Heat Release in a Diesel Engine," ASME Paper No. 68-DGP-11, 1968.

4 Krieger, R. B., and Borman, G. L., "The Computation of Apparent Heat Release for Internal Combustion Engines," ASME Paper No. 66-WA/DGP-4, 1966.

5 Ferguson, C. R., *Internal Combustion Engines, Applied Thermosciences*, Wiley, New York, 1986.

6 Zahdeh, A. R., "Diesel Engine Startability and White Smoke Formation Under Cold Temperature Conditions," Ph.D. dissertation, Wayne State University, Wayne, MI, 1990.

7 Hohenberg, G. F., "Advanced Approach for Heat Transfer Calculations," SAE Paper No. 790825, 1979.

8 Heywood, J. B., *Internal Combustion Engine Fundamentals*, McGraw-Hill, New York, 1988.